Transcriptomic Profiling of Non-Cardiomyocytes During Both Early and Late Stages of Adverse Remodelling in Hypertrophic Cardiomyopathy (HCM)

Siwei Deng

Wolfson College

University of Oxford

A thesis submitted for the degree of

Doctor of Philosophy

Trinity 2025

Acknowledgements

Personal

First and foremost, I would like to express my deepest gratitude to my college advisor, Dr. Antoniya Georgieva, my former Director of Graduate Studies, Prof. Afsie Sabokbar, and the Senior Tutor of Wolfson College, Ms Emily Eastham. Their unwavering support, particularly during the challenging period following my first year and the completion of my Transfer of Status, was instrumental in ensuring a smooth transition to my current research group. Their guidance and encouragement have left a lasting impact on my academic journey.

Upon joining my current group, I was fortunate to receive exceptional support from my outstanding supervisory team: Prof. Hugh Watkins, Prof. Charles Redwood, Dr. Calliope Dendrou, and Dr. Ying-Jie Wang. Their expertise, patience, and insightful advice have been invaluable throughout my research. I am immensely grateful for the opportunities they provided, the trust they placed in me, and their unwavering commitment to my development as a researcher.

Within the group, I have had the privilege of collaborating with talented colleagues, including Jacky Fung, Dr. Kamayani Singh, and Dr. Sunitha Balaraju. Their contributions, particularly in wet lab experiments and the generation of valuable omics data for my project, have been crucial to the success of my research. I am especially grateful to Dr. Ying-Jie Wang, who not only served as one of my co-supervisors but also provided significant support in both experimental and analytical aspects of my work. In turn, I was glad to contribute to their projects through bioinformatics analyses, fostering a truly collaborative and enriching environment.

Beyond the lab, I am deeply thankful for the friendships I have formed during my time in Oxford. Jacky Fung is not only a trusted colleague but also one of my closest friends. From sharing meals after work to planning future reunions in Shenzhen, his companionship has been a source of joy and support. I am equally grateful to my friends outside the lab, including Dr. Yongcheng Jin, Tianyao Zhou, and Prof. Lei Sha. Their camaraderie and shared aspirations have made my time in Oxford truly memorable, and I am confident that our projects will flourish in the years to come.

I owe an immeasurable debt of gratitude to my parents, Ziming Deng and Zhijun Tian, whose unwavering love and support have been the foundation of all my achievements. Their belief in me has been a constant source of strength, and I am forever grateful for their sacrifices and encouragement throughout my academic journey.

Institutional

I would like to extend my heartfelt thanks to the China Scholarship Council (CSC) and the University of Oxford for their generous financial support, which made it possible for me to pursue my studies at Oxford. I am also profoundly grateful to Prof. Hugh Watkins for providing additional funding to support my living expenses during the final months of my doctoral studies, enabling me to complete my research after the conclusion of the CSC-Oxford funding period. Without the generous support of these institutions and individuals, the completion of my project within such a short timeframe would not have been possible. Their contributions have been pivotal to my academic and personal growth, and I will always remain deeply appreciative of their support.

Abstract

Background Familial hypertrophic cardiomyopathy (HCM) is an autosomal dominant disease characterised by unexplained ventricular hypertrophy, myocyte disarray, and fibrosis. Although the biophysical mechanisms by which gene variants in sarcomeric proteins disrupt cardiomyocyte function are largely understood, the cellular and molecular pathways leading to the complex, variable, and adverse remodelling of the non-myocyte compartment are not fully characterised. Understanding the molecular mechanisms driving and escalating these pathological processes, particularly during early and late disease stages, is crucial for developing disease modifying therapeutic strategies.

Objectives My aims were i) to characterise the temporal transcriptomic changes in non-cardiomyocytes during HCM progression; ii) to identify potential candidates responsible for additional risks at advanced stage of the disease — specifically, the inflammatory and fibrotic processes that contribute to adverse clinical outcomes; and iii) to explore the early molecular events in non-cardiomyocytes that contribute to disease pathology.

Methods I employed an integrative approach combining bulk temporal RNA sequencing (RNA-seq) and single-cell RNA-seq analyses of a well-established cardiac actin Actc1^{E99K} mouse model, which carries an orthologue of a well known pathogenic variant in HCM patients, thereby recapitulating key features of HCM. For context, I compared findings from the Actc1^{E99K} model with three other established HCM mouse models (i.e., α-MHC^{R403Q}, α-MHC^{R719W}, and Tnt^{R92W}) — which generally show milder phenotypes — and with human HCM samples. Leiden clustering was used to identify co-regulated gene modules with distinct temporal expression patterns. Pathway enrichment analysis, including Pathway RespOnsive GENes for activity inference from gene expression (PROGENy), was performed to identify activated and suppressed pathways.

Results Bulk RNA-seq analysis revealed dynamic gene expression changes throughout HCM progression, with Leiden clustering identifying distinct temporal patterns associated with fibrosis, inflammation, metabolic dysregulation, and

cell cycle control. The fast progressive Actc1^{E99K} model, which shows extensive fibrosis and immune cell infiltration, provided clear insights into the behaviour of non-cardiomyocytes. Single-cell analysis further resolved these processes by delineating cell-type-specific contributions that underlie the remodelling response. Comparison with human HCM samples confirmed a conserved upregulation of immune activation, inflammatory responses, and epithelial–mesenchymal transition (EMT) processes — hallmarks that all play a critical role in cardiac remodelling.

Discussion The data indicate that variation in interferon responses — potentially driven by mitochondrial damage-associated molecular patterns released from cardiomyocytes undergoing a significant stress response, which involves the up-regulation of cell cycle inhibitors — may orchestrate non-cardiomyocyte immune activation. Although many aspects of the non-cardiomyocyte transcriptomic changes were conserved between the Actc1^{E99K} model and human HCM, differences in metabolic regulation and growth factor signalling were also apparent. These interspecies differences highlight the challenges of direct translation from animal models to the clinic while also emphasising the potential of the Actc1^{E99K} model to capture advanced remodelling processes driven by non-cardiomyocytes.

Conclusions My project provides a comprehensive view of the non-myocyte transcriptomic landscape during HCM progression. Transcriptomic analysis of mouse and human HCM hearts reveals chronic inflammation and progressive fibrosis in the classic and advanced stages of the disease. Hallmark analysis, at a single-cell level, shows upregulated inflammatory responses in many non-myocytes, suggesting their contributions to establishing a pro-inflammatory milieu. While the initiating stress signals from mutant cardiomyocytes remain unclear, their downstream effects on non-myocytes indicate chronic inflammation as a key pathogenic process in HCM. This supports future studies on stress signals, fibrosis, and chronic inflammation in HCM, which will help identify valuable biomarkers for early diagnosis and develop novel therapeutics to manage key pathogenic risks. However, translational challenges — such as interspecies differences and sampling variability — warrant caution when interpreting preclinical findings.

Contents

List of Figures **xiii**

List of Tables **xxvii**

1 Introduction **1**

1.1 Overview of hypertrophic cardiomyopathy 1
1.1.1 A historical overview 1
1.1.2 Clinical phenotypes 2
1.2 Molecular and genetic basis 3
1.3 Pathogenesis 7
1.3.1 Genetic basis of HCM 8
1.3.2 Impact on cardiomyocyte physiology 10
1.3.3 Pathophysiological cascade 11
1.4 Clinical management 12
1.4.1 Targeted pharmacotherapy: Cardiac myosin inhibitors . . . 12
1.4.2 Emerging genetic therapies 13
1.4.3 Non-cardiomyocyte pathophysiology: Addressing fibrosis and inflammation 14
1.5 Non-cardiomyocytes: A future direction 14
1.5.1 Inflammation in cardiac remodelling in HCM 15
1.5.2 Fibrosis in cardiac remodelling in HCM 20
1.5.3 Remaining cellular clusters 23
1.6 Animal models of human HCM 24
1.6.1 The α-MHC^{R403Q} model 25
1.6.2 MYBPC3 truncation and knockout models 26
1.6.3 Troponin I (Tnni3) and Troponin T (Tnnt2) models 27
1.6.4 Tropomyosin Tpm1^{E180G} and Tpm1^{D175N} models 27
1.6.5 Cardiac actin Actc1^{E99K} model 28
1.6.6 Integrative discussion and translational perspectives 35
1.7 Objectives 38

2 Methodology **41**
2.1 Bulk RNA-seq 41
2.1.1 Library preparation 41
2.1.2 Data analysis 42
2.2 Single-cell multiplexed gene expression profiling 44
2.2.1 Cell isolation 44
2.2.2 Cell labelling and sorting 44
2.2.3 Library preparation 45
2.2.4 Data analysis 45
2.3 Code availability 48

3 Bulk Temporal Transcriptomic Profiling Reveals Disease Progression in Actc1$^{\mathbf{E99K}}$ HCM Mouse Models **49**
3.1 Mapping the dynamic gene expression landscape in Actc1$^{\mathrm{E99K}}$ HCM mouse model 49
3.1.1 Comparing longitudinal datasets uncovers the evolution of cardiac transcriptional changes 49
3.2 Deciphering temporal clustering reveals distinct waves of gene regulation 60
3.2.1 Gene clusters outline core temporal patterns steering disease evolution 60
3.2.2 Cluster 0: Persistent upregulation indicates chronic remodelling drivers 63
3.2.3 Cluster 1 & 4: Biphasic activation unveils early response and late amplification of inflammatory and apoptotic pathways . 64
3.2.4 Cluster 7: Transient early activation of ECM, innate immune, and signalling pathways precedes decline 65
3.2.5 Cluster 9 & 10: Progressive activation of biosynthetic and metabolic adaptation programmes 67
3.2.6 Cluster 11 & 12: Cyclical regulation mirrors stress response and recovery phases 69
3.2.7 Cluster 2, 3 & 8: Sustained downregulation highlights progressive energy metabolism impairment 71
3.2.8 Cluster 5 & 6: Late-stage declines exacerbate cardiac dysfunction 72
3.3 Discussion: Synthesis of molecular insights bridges transcriptomic dynamics to cardiac remodelling 76

4 Single-cell resolution of adverse remodelling in Actc1^{E99K} hearts 85
4.1 Mapping non-cardiomyocyte populations through multiplexed scRNA-seq reveals cellular diversity . . . 85
4.1.1 Design and overview of the multiplexed scRNA-seq experiment unveil cellular heterogeneity . . . 85
4.1.2 Immune cells shape the inflammatory landscape in remodelled hearts . . . 88
4.1.3 Endothelial cells maintain vascular integrity and influence remodelling dynamics . . . 94
4.1.4 Stromal cells define the cardiac microstructure and mediate fibrotic signaling . . . 95
4.2 Single-cell transcriptomics reveal dynamic regulatory networks in cardiac remodelling . . . 98
4.2.1 Cellular census clarifies sample diversity and annotation precision . . . 98
4.2.2 Pathway profiling highlights stage-specific signalling shifts and metabolic reprogramming . . . 103
4.2.3 Profibrotic cytokine maps reveal key drivers of fibrosis . . . 112
4.2.4 Dynamic RNA analysis traces cellular trajectories and future states in heart remodelling . . . 114
4.3 Discussion: Insights on therapeutic implications for cardiac remodelling 134

5 Targeting fibrosis and inflammation in late-stage mouse and human HCM 141
5.1 Mapping cell populations and expression changes that reveal unique disease dynamics in late-stage HCM . . . 141
5.2 Comparing gene expression landscapes in human and mouse HCM to uncover shared mechanisms and species-specific differences . . . 149
5.2.1 Enrichment analysis uncovers metabolic suppression and heightened immune activation in HCM . . . 149
5.2.2 Comparative pathway activity reveals distinct signalling responses across species . . . 153
5.2.3 Intercellular communication insights reveal crucial crosstalk that drives adverse remodelling . . . 156
5.3 Integrative analysis connects bulk trends with single-cell insights to reveal cell type contributions . . . 159
5.3.1 Cellular drivers of late-stage up-regulated and U-shaped gene clusters . . . 159
5.3.2 Cellular origins of down-regulated gene clusters in late-stage HCM . . . 160

5.4 Discussion: Synthesis of insights and therapeutic perspectives for advancing treatment in late-stage HCM 161

6 Early events leading to adverse remodelling in mouse and human HCM 163

6.1 Mapping cellular diversity to uncover early expression patterns in human HCM 163

6.2 Comparing transcriptional landscapes reveals early disease signatures 171

6.2.1 Divergent pathway enrichment highlights species-specific signalling 171

6.2.2 Functional signalling patterns expose key activity changes . 175

6.2.3 Intercellular dialogue uncovers critical remodelling cues . . . 179

6.3 Integrating bulk trends with single-cell insights reveals early HCM changes 181

6.3.1 Cellular origins of early-active and biphasic gene clusters . . 181

6.4 Discussion: Early HCM mechanisms and emerging intervention targets 182

7 Conclusion and discussion 185

7.1 Connecting the threads: Unravelling temporal and cellular dynamics in HCM 185

7.2 Human and the Actc1^{E99K} mouse model of HCM: Immune parallels and metabolic contrasts 187

7.3 Harnessing therapeutic windows in HCM 187

7.4 Evolving phases in HCM: Recognising the shift from silence to inflammation 188

7.5 Innovative therapeutic strategies and future perspectives in HCM . 188

7.6 Concluding reflections on HCM research 190

Appendices

A Bulk RNA-seq sample details 193

A.1 Temporal bulk E99K samples 193

A.2 Bulk RNA-seq samples from other mouse models 194

A.3 Bulk RNA-seq samples from HCM human patients 195

B Expression of marker genes in mouse scRNA-seq samples 199

C Intercellular communication insights reveal crucial crosstalk that drives adverse remodelling 205

C.1 T cell communication illuminates adaptive immune dynamics in the diseased heart . . . 205

C.2 Macrophage signalling reveals inflammatory and repair cues shaping remodelling . . . 206

C.3 Endothelial and lymphatic cell interactions underpin vascular remodelling and immune recruitment . . . 209

C.4 Fibroblast signalling orchestrates extracellular matrix remodelling and fibrosis . . . 212

C.5 Pericyte and VSMC interactions maintain vascular stability and influence fibrotic changes . . . 217

C.6 Neuronal signalling patterns impact cardiac innervation and structural remodelling . . . 221

D Integrative analysis connects bulk trends with single-cell insights to reveal cell type contributions 225

D.1 Cluster 1 & 4: Early activation followed by a late surge signals diverse functional changes in HCM . . . 225

D.2 Cluster 9 & 10: Gradual expression increase points to ongoing cellular adaptations in the failing heart . . . 271

D.3 Cluster 11 & 12: Biphasic expression patterns reveal dynamic shifts in stress response and repair mechanisms . . . 317

D.4 Cluster 5 & 6: Progressive down-regulation in key clusters signals metabolic and functional decline during HCM . . . 348

E Intercellular dialogue uncovers critical remodelling cues 397

F Integrating bulk trends with single-cell insights reveals early HCM changes 403

F.1 Cluster 7: Early activation then decline reveals specific modulations of cellular processes . . . 403

F.2 Cluster 11 & 12: Biphasic expression patterns reflect shifting cellular homeostasis . . . 415

References 433

List of Figures

1.1 Sarcomere mutations in HCM. 4
1.2 Schematic representation of the revised pathogenesis of HCM . . . 8
1.3 Progressive cardiac phenotypes in the Actc1^{E99K} HCM mouse model 30
1.4 Chronic immune cell infiltration in HCM patients 31
1.5 Temporal dynamics of immune cell infiltration in Actc1^{E99K} mouse hearts 32

3.1 Principal component analysis (PCA) of bulk RNA-seq data from Actc1^{E99K} HCM mice across all time points 51
3.2 Principal component analysis of bulk RNA-seq data from public mouse and human datasets 54
3.3 Breakdown of differentially expressed genes by biotype 56
3.4 Gene set enrichment analysis for bulk RNA-seq 58
3.5 PROGENy pathway activity analysis for bulk RNA-seq 59
3.6 Differentially expressed gene clusters in temporal Actc1^{E99K} mouse data 62
3.7 Temporal cluster 0: Consistent up-regulation 64
3.8 Temporal cluster 1 & 4: Early up-regulation followed by a late surge 66
3.9 Temporal cluster 7: Early up-regulation followed by a late decline . 68
3.10 Temporal cluster 9 & 10: Increasing expression over time 70
3.11 Temporal cluster 11 & 12: U-shaped trends 71
3.12 Temporal cluster 2, 3 & 8: Consistent down-regulation 73
3.13 Temporal cluster 5 & 6: Down-regulation and late declines 75
3.14 Summary of temporal expression waves and top pathways 76

4.1 Early and late stage multiplexed single-cell RNA-seq experimental design 87
4.2 Dotplot of T cell markers in CD45$^+$ samples 90
4.3 Dotplot of myeloid cell markers in CD45$^+$ samples 92
4.4 Dotplot of other immune cell markers in CD45$^+$ samples 93
4.5 Integrated UMAP of annotated cell clusters in the CD45$^+$ population 94
4.6 Dotplot of endothelial cell markers in CD31$^+$ samples 95
4.7 Integrated UMAP of annotated cell clusters in the CD31$^+$ population 96
4.8 Dotplot of stromal cell markers in CD45$^-$CD31$^-$ samples 97

4.9 Integrated UMAP of annotated cell clusters in the CD45^{-}CD31^{-} population 98
4.10 Stacked bar plots for cell types in early-stage mouse samples 102
4.11 Stacked bar plots for cell types in late-stage mouse samples 104
4.12 GSEA analysis of hallmark pathways in early-stage Actc1^{E99K} mouse samples 106
4.13 GSEA analysis of hallmark pathways in late-stage Actc1^{E99K} mouse samples 107
4.14 PROGENy pathway activity analysis in early-stage Actc1^{E99K} mouse samples 109
4.15 PROGENy pathway activity analysis in late-stage Actc1^{E99K} mouse samples 111
4.16 Expression of profibrotic cytokines in bulk RNA-seq data 113
4.17 Expression of profibrotic cytokines in scRNA-seq data 115
4.18 Integrated trajectory analysis of CD45^{+} immune cells from combined early and late stages 117
4.19 Integrated trajectory analysis of CD31^{+} endothelial cells from combined early and late stages 119
4.20 Integrated trajectory analysis of CD45^{-}CD31^{-} stromal cells from combined early and late stages 121
4.21 Trajectory and velocity length in early-stage CD45^{+} Actc1^{E99K}/WT samples 122
4.22 Trajectory and velocity length in late-stage CD45^{+} Actc1^{E99K}/WT samples 123
4.23 Trajectory and velocity length in early-stage CD31^{+} Actc1^{E99K}/WT samples 125
4.24 Trajectory and velocity length in late-stage CD31^{+} Actc1^{E99K}/WT samples 126
4.25 Trajectory and velocity length in early-stage CD45^{-}CD31^{-} Actc1^{E99K}/WT samples 127
4.26 Trajectory and velocity length in late-stage CD45^{-}CD31^{-} Actc1^{E99K}/WT samples 128
4.27 Velocity pseudotime in early-stage CD45^{+} Actc1^{E99K}/WT samples . 129
4.28 Velocity pseudotime in late-stage CD45^{+} Actc1^{E99K}/WT samples . 130
4.29 Velocity pseudotime in early-stage CD31^{+} Actc1^{E99K}/WT samples . 131
4.30 Velocity pseudotime in late-stage CD31^{+} Actc1^{E99K}/WT samples . 132
4.31 Velocity pseudotime in early-stage CD45^{-}CD31^{-} Actc1^{E99K}/WT samples 133
4.32 Velocity pseudotime in late-stage CD45^{-}CD31^{-} Actc1^{E99K}/WT samples 134

4.33 Targeting profibrotic cytokines in early- and late-stage HCM 137

5.1 UMAP for late-stage human HCM snRNA-seq cell type annotation 143
5.2 Marker expression in stromal cell types from late-stage human HCM snRNA-seq data 144
5.3 Marker expression in immune cell types from late-stage human HCM snRNA-seq data 145
5.4 Stacked bar plots for cell types in late-stage human samples 147
5.5 GSEA analysis of hallmark pathways in late-stage human snRNA-seq samples 152
5.6 PROGENy pathway activity analysis in late-stage human samples . 153
5.7 Overview of cell-cell communication in late-stage HCM 157

6.1 UMAP for mid-stage human HCM snRNA-seq cell type annotation 165
6.2 Marker expression in main cell types from mid-stage human HCM snRNA-seq data 166
6.3 Marker expression in fibroblasts, pericytes, and VSMCs from mid-stage human HCM snRNA-seq data 167
6.4 Marker expression in immune cell types from mid-stage human HCM snRNA-seq data 168
6.5 Stacked bar plots for cell types in mid-stage human samples 170
6.6 GSEA analysis of hallmark pathways in mid-stage human snRNA-seq samples 175
6.7 PROGENy pathway activity analysis in mid-stage human samples . 176
6.8 Overview of cell-cell communication in early-to-mid-stage HCM . . 180

A.1 Principal component analysis (PCA) of bulk RNA-seq data from Actc1^{E99K} HCM mice 197

B.1 **UMAP projections showing the expression of individual T cell marker genes within the CD45$^+$ cell population.** These visualisations complement the summary dotplot in Figure 4.2 by showing the spatial distribution of expression for each marker gene on the UMAP. The data are integrated from both WT and Actc1^{E99K} mice (N=3 per genotype) at (A) the early stage (5 weeks) and (B) the late stage (60 weeks). In each plot, cells are coloured according to their log-normalised expression level for the specified gene, with the scale shown by the colour bar. 200

B.2 **UMAP projections showing the expression of individual myeloid cell marker genes within the CD45$^+$ cell population.**These visualisations complement the summary dotplot in Figure 4.3 by showing the spatial distribution of expression for each marker gene on the UMAP. The data are integrated from both WT and Actc1^{E99K} mice (N=3 per genotype) at (A) the early stage (5 weeks) and (B) the late stage (60 weeks). In each plot, cells are coloured according to their log-normalised expression level for the specified gene, with the scale shown by the colour bar. 201

B.3 **UMAP projections showing the expression of other immune cell marker genes within the CD45$^+$ cell population.**These visualisations complement the summary dotplot in Figure 4.4 by showing the spatial distribution of expression for each marker gene on the UMAP. The data are integrated from both WT and Actc1^{E99K} mice (N=3 per genotype) at (A) the early stage (5 weeks) and (B) the late stage (60 weeks). In each plot, cells are coloured according to their log-normalised expression level for the specified gene, with the scale shown by the colour bar. 202

B.4 **UMAP projections showing the expression of individual endothelial cell marker genes within the CD31$^+$ cell population.**These visualisations complement the summary dotplot in Figure 4.6 by showing the spatial distribution of expression for each marker gene on the UMAP. The data are integrated from both WT and Actc1^{E99K} mice (N=3 per genotype) at (A) the early stage (5 weeks) and (B) the late stage (60 weeks). In each plot, cells are coloured according to their log-normalised expression level for the specified gene, with the scale shown by the colour bar. 203

B.5 **UMAP projections showing the expression of individual stromal cell marker genes within the CD45$^-$CD31$^-$ cell population.**These visualisations complement the summary dotplot in Figure 4.8 by showing the spatial distribution of expression for each marker gene on the UMAP. The data are integrated from both WT and Actc1^{E99K} mice (N=3 per genotype) at (A) the early stage (5 weeks) and (B) the late stage (60 weeks). In each plot, cells are coloured according to their log-normalised expression level for the specified gene, with the scale shown by the colour bar. 204

C.1 Cell-cell communication involving T cells in late-stage HCM 207

C.2 Cell-cell communication involving macrophages in late-stage HCM . 210

C.3 Cell-cell communication involving endothelial cells in late-stage HCM213

C.4 Cell-cell communication involving fibroblasts in late-stage HCM . . 217
C.5 Cell-cell communication involving pericytes and VSMCs in late-stage HCM 222
C.6 Cell-cell communication involving neuronal cells in late-stage HCM 224

D.1 Gene set scoring and statistics of cluster 1 (early up-regulation followed by a late surge) in late-stage human cell types 227
D.2 Gene set scoring for MCL sub-cluster 1 of Cluster 1 (early up-regulation followed by a late surge) in late-stage human cell types 228
D.3 Gene set scoring for MCL sub-cluster 2 of Cluster 1 (early up-regulation followed by a late surge) in late-stage human cell types 229
D.4 Gene set scoring for MCL sub-cluster 3 of Cluster 1 (early up-regulation followed by a late surge) in late-stage human cell types 230
D.5 Gene set scoring for MCL sub-cluster 4 of Cluster 1 (early up-regulation followed by a late surge) in late-stage human cell types 231
D.6 Gene set scoring for MCL sub-cluster 5 of Cluster 1 (early up-regulation followed by a late surge) in late-stage human cell types 232
D.7 Gene set scoring for MCL sub-cluster 6 of Cluster 1 (early up-regulation followed by a late surge) in late-stage human cell types 233
D.8 Gene set scoring for MCL sub-cluster 7 of Cluster 1 (early up-regulation followed by a late surge) in late-stage human cell types 234
D.9 Gene set scoring for MCL sub-cluster 8 of Cluster 1 (early up-regulation followed by a late surge) in late-stage human cell types 235
D.10 Gene set scoring for MCL sub-cluster 9 of Cluster 1 (early up-regulation followed by a late surge) in late-stage human cell types 236
D.11 Gene set scoring for MCL sub-cluster 10 of Cluster 1 (early up-regulation followed by a late surge) in late-stage human cell types 237
D.12 Gene set scoring and statistics of cluster 1 (early up-regulation followed by a late surge) in late-stage mouse cell types 238
D.13 Gene set scoring for MCL sub-cluster 1 of Cluster 1 (early up-regulation followed by a late surge) in late-stage mouse cell types 239
D.14 Gene set scoring for MCL sub-cluster 2 of Cluster 1 (early up-regulation followed by a late surge) in late-stage mouse cell types 240
D.15 Gene set scoring for MCL sub-cluster 3 of Cluster 1 (early up-regulation followed by a late surge) in late-stage mouse cell types 241
D.16 Gene set scoring for MCL sub-cluster 4 of Cluster 1 (early up-regulation followed by a late surge) in late-stage mouse cell types 242
D.17 Gene set scoring for MCL sub-cluster 5 of Cluster 1 (early up-regulation followed by a late surge) in late-stage mouse cell types 243

D.18 Gene set scoring for MCL sub-cluster 6 of Cluster 1 (early up-regulation followed by a late surge) in late-stage mouse cell types 244
D.19 Gene set scoring for MCL sub-cluster 7 of Cluster 1 (early up-regulation followed by a late surge) in late-stage mouse cell types 245
D.20 Gene set scoring for MCL sub-cluster 8 of Cluster 1 (early up-regulation followed by a late surge) in late-stage mouse cell types 246
D.21 Gene set scoring for MCL sub-cluster 9 of Cluster 1 (early up-regulation followed by a late surge) in late-stage mouse cell types 247
D.22 Gene set scoring for MCL sub-cluster 10 of Cluster 1 (early up-regulation followed by a late surge) in late-stage mouse cell types 248
D.23 Gene set scoring and statistics of Cluster 4 (early up-regulation followed by a late surge) in late-stage human cell types 250
D.24 Gene set scoring for MCL sub-cluster 1 of Cluster 4 (early up-regulation followed by a late surge) in late-stage human cell types 251
D.25 Gene set scoring for MCL sub-cluster 2 of Cluster 4 (early up-regulation followed by a late surge) in late-stage human cell types 252
D.26 Gene set scoring for MCL sub-cluster 3 of Cluster 4 (early up-regulation followed by a late surge) in late-stage human cell types 253
D.27 Gene set scoring for MCL sub-cluster 4 of Cluster 4 (early up-regulation followed by a late surge) in late-stage human cell types 254
D.28 Gene set scoring for MCL sub-cluster 5 of Cluster 4 (early up-regulation followed by a late surge) in late-stage human cell types 255
D.29 Gene set scoring for MCL sub-cluster 6 of Cluster 4 (early up-regulation followed by a late surge) in late-stage human cell types 256
D.30 Gene set scoring for MCL sub-cluster 7 of Cluster 4 (early up-regulation followed by a late surge) in late-stage human cell types 257
D.31 Gene set scoring for MCL sub-cluster 8 of Cluster 4 (early up-regulation followed by a late surge) in late-stage human cell types 258
D.32 Gene set scoring for MCL sub-cluster 9 of Cluster 4 (early up-regulation followed by a late surge) in late-stage human cell types 259
D.33 Gene set scoring for MCL sub-cluster 10 of Cluster 4 (early up-regulation followed by a late surge) in late-stage human cell types 260
D.34 Gene set scoring and statistics of cluster 4 (early up-regulation followed by a late surge) in late-stage mouse cell types 261
D.35 Gene set scoring for MCL sub-cluster 1 of Cluster 4 (early up-regulation followed by a late surge) in late-stage mouse cell types 262
D.36 Gene set scoring for MCL sub-cluster 2 of Cluster 4 (early up-regulation followed by a late surge) in late-stage mouse cell types 263
D.37 Gene set scoring for MCL sub-cluster 3 of Cluster 4 (early up-regulation followed by a late surge) in late-stage mouse cell types 264

D.38 Gene set scoring for MCL sub-cluster 4 of Cluster 4 (early up-regulation followed by a late surge) in late-stage mouse cell types 265
D.39 Gene set scoring for MCL sub-cluster 5 of Cluster 4 (early up-regulation followed by a late surge) in late-stage mouse cell types 266
D.40 Gene set scoring for MCL sub-cluster 6 of Cluster 4 (early up-regulation followed by a late surge) in late-stage mouse cell types 267
D.41 Gene set scoring for MCL sub-cluster 7 of Cluster 4 (early up-regulation followed by a late surge) in late-stage mouse cell types 268
D.42 Gene set scoring for MCL sub-cluster 8 of Cluster 4 (early up-regulation followed by a late surge) in late-stage mouse cell types 269
D.43 Gene set scoring for MCL sub-cluster 9 of Cluster 4 (early up-regulation followed by a late surge) in late-stage mouse cell types 270
D.44 Gene set scoring for MCL sub-cluster 10 of Cluster 4 (early up-regulation followed by a late surge) in late-stage mouse cell types 271
D.45 Gene set scoring and statistics of Cluster 9 (increasing expression over time) in late-stage human cell types 273
D.46 Gene set scoring for MCL sub-cluster 1 of Cluster 9 (increasing expression over time) in late-stage human cell types 274
D.47 Gene set scoring for MCL sub-cluster 2 of Cluster 9 (increasing expression over time) in late-stage human cell types 275
D.48 Gene set scoring for MCL sub-cluster 3 of Cluster 9 (increasing expression over time) in late-stage human cell types 276
D.49 Gene set scoring for MCL sub-cluster 4 of Cluster 9 (increasing expression over time) in late-stage human cell types 277
D.50 Gene set scoring for MCL sub-cluster 5 of Cluster 9 (increasing expression over time) in late-stage human cell types 278
D.51 Gene set scoring for MCL sub-cluster 6 of Cluster 9 (increasing expression over time) in late-stage human cell types 279
D.52 Gene set scoring for MCL sub-cluster 7 of Cluster 9 (increasing expression over time) in late-stage human cell types 280
D.53 Gene set scoring for MCL sub-cluster 8 of Cluster 9 (increasing expression over time) in late-stage human cell types 281
D.54 Gene set scoring for MCL sub-cluster 9 of Cluster 9 (increasing expression over time) in late-stage human cell types 282
D.55 Gene set scoring for MCL sub-cluster 10 of Cluster 9 (increasing expression over time) in late-stage human cell types 283
D.56 Gene set scoring and statistics of Cluster 9 (increasing expression over time) in late-stage mouse cell types 284
D.57 Gene set scoring for MCL sub-cluster 1 of Cluster 9 (increasing expression over time) in late-stage mouse cell types 285

D.58 Gene set scoring for MCL sub-cluster 2 of Cluster 9 (increasing expression over time) in late-stage mouse cell types 286
D.59 Gene set scoring for MCL sub-cluster 3 of Cluster 9 (increasing expression over time) in late-stage mouse cell types 287
D.60 Gene set scoring for MCL sub-cluster 4 of Cluster 9 (increasing expression over time) in late-stage mouse cell types 288
D.61 Gene set scoring for MCL sub-cluster 5 of Cluster 9 (increasing expression over time) in late-stage mouse cell types 289
D.62 Gene set scoring for MCL sub-cluster 6 of Cluster 9 (increasing expression over time) in late-stage mouse cell types 290
D.63 Gene set scoring for MCL sub-cluster 7 of Cluster 9 (increasing expression over time) in late-stage mouse cell types 291
D.64 Gene set scoring for MCL sub-cluster 8 of Cluster 9 (increasing expression over time) in late-stage mouse cell types 292
D.65 Gene set scoring for MCL sub-cluster 9 of Cluster 9 (increasing expression over time) in late-stage mouse cell types 293
D.66 Gene set scoring for MCL sub-cluster 10 of Cluster 9 (increasing expression over time) in late-stage mouse cell types 294
D.67 Gene set scoring and statistics of Cluster 10 (increasing expression over time) in late-stage human cell types 296
D.68 Gene set scoring for MCL sub-cluster 1 of Cluster 10 (increasing expression over time) in late-stage human cell types 297
D.69 Gene set scoring for MCL sub-cluster 2 of Cluster 10 (increasing expression over time) in late-stage human cell types 298
D.70 Gene set scoring for MCL sub-cluster 3 of Cluster 10 (increasing expression over time) in late-stage human cell types 299
D.71 Gene set scoring for MCL sub-cluster 4 of Cluster 10 (increasing expression over time) in late-stage human cell types 300
D.72 Gene set scoring for MCL sub-cluster 5 of Cluster 10 (increasing expression over time) in late-stage human cell types 301
D.73 Gene set scoring for MCL sub-cluster 6 of Cluster 10 (increasing expression over time) in late-stage human cell types 302
D.74 Gene set scoring for MCL sub-cluster 7 of Cluster 10 (increasing expression over time) in late-stage human cell types 303
D.75 Gene set scoring for MCL sub-cluster 8 of Cluster 10 (increasing expression over time) in late-stage human cell types 304
D.76 Gene set scoring for MCL sub-cluster 9 of Cluster 10 (increasing expression over time) in late-stage human cell types 305
D.77 Gene set scoring for MCL sub-cluster 10 of Cluster 10 (increasing expression over time) in late-stage human cell types 306

D.78 Gene set scoring and statistics of Cluster 10 (increasing expression over time) in late-stage mouse cell types 307
D.79 Gene set scoring for MCL sub-cluster 1 of Cluster 10 (increasing expression over time) in late-stage mouse cell types 308
D.80 Gene set scoring for MCL sub-cluster 2 of Cluster 10 (increasing expression over time) in late-stage mouse cell types 309
D.81 Gene set scoring for MCL sub-cluster 3 of Cluster 10 (increasing expression over time) in late-stage mouse cell types 310
D.82 Gene set scoring for MCL sub-cluster 4 of Cluster 10 (increasing expression over time) in late-stage mouse cell types 311
D.83 Gene set scoring for MCL sub-cluster 5 of Cluster 10 (increasing expression over time) in late-stage mouse cell types 312
D.84 Gene set scoring for MCL sub-cluster 6 of Cluster 10 (increasing expression over time) in late-stage mouse cell types 313
D.85 Gene set scoring for MCL sub-cluster 7 of Cluster 10 (increasing expression over time) in late-stage mouse cell types 314
D.86 Gene set scoring for MCL sub-cluster 8 of Cluster 10 (increasing expression over time) in late-stage mouse cell types 315
D.87 Gene set scoring for MCL sub-cluster 9 of Cluster 10 (increasing expression over time) in late-stage mouse cell types 316
D.88 Gene set scoring for MCL sub-cluster 10 of Cluster 10 (increasing expression over time) in late-stage mouse cell types 317
D.89 Gene set scoring and statistics of Cluster 11 (U-shaped trends) in late-stage human cell types 319
D.90 Gene set scoring for MCL sub-cluster 1 of Cluster 11 (U-shaped trends) in late-stage human cell types 320
D.91 Gene set scoring for MCL sub-cluster 2 of Cluster 11 (U-shaped trends) in late-stage human cell types 321
D.92 Gene set scoring for MCL sub-cluster 3 of Cluster 11 (U-shaped trends) in late-stage human cell types 322
D.93 Gene set scoring for MCL sub-cluster 4 of Cluster 11 (U-shaped trends) in late-stage human cell types 323
D.94 Gene set scoring for MCL sub-cluster 5 of Cluster 11 (U-shaped trends) in late-stage human cell types 324
D.95 Gene set scoring for MCL sub-cluster 6 of Cluster 11 (U-shaped trends) in late-stage human cell types 325
D.96 Gene set scoring for MCL sub-cluster 7 of Cluster 11 (U-shaped trends) in late-stage human cell types 326
D.97 Gene set scoring for MCL sub-cluster 8 of Cluster 11 (U-shaped trends) in late-stage human cell types 327

D.98 Gene set scoring for MCL sub-cluster 9 of Cluster 11 (U-shaped trends) in late-stage human cell types 328
D.99 Gene set scoring for MCL sub-cluster 10 of Cluster 11 (U-shaped trends) in late-stage human cell types 329
D.100 Gene set scoring and statistics of Cluster 11 (U-shaped trends) in late-stage mouse cell types 330
D.101 Gene set scoring for MCL sub-cluster 1 of Cluster 11 (U-shaped trends) in late-stage mouse cell types 331
D.102 Gene set scoring for MCL sub-cluster 2 of Cluster 11 (U-shaped trends) in late-stage mouse cell types 332
D.103 Gene set scoring for MCL sub-cluster 3 of Cluster 11 (U-shaped trends) in late-stage mouse cell types 333
D.104 Gene set scoring for MCL sub-cluster 4 of Cluster 11 (U-shaped trends) in late-stage mouse cell types 334
D.105 Gene set scoring for MCL sub-cluster 5 of Cluster 11 (U-shaped trends) in late-stage mouse cell types 335
D.106 Gene set scoring for MCL sub-cluster 6 of Cluster 11 (U-shaped trends) in late-stage mouse cell types 336
D.107 Gene set scoring for MCL sub-cluster 7 of Cluster 11 (U-shaped trends) in late-stage mouse cell types 337
D.108 Gene set scoring for MCL sub-cluster 8 of Cluster 11 (U-shaped trends) in late-stage mouse cell types 338
D.109 Gene set scoring for MCL sub-cluster 9 of Cluster 11 (U-shaped trends) in late-stage mouse cell types 339
D.110 Gene set scoring for MCL sub-cluster 10 of Cluster 11 (U-shaped trends) in late-stage mouse cell types 340
D.111 Gene set scoring and statistics of Cluster 12 (U-shaped trends) in late-stage human cell types 342
D.112 Gene set scoring for MCL sub-cluster 1 of Cluster 12 (U-shaped trends) in late-stage human cell types 343
D.113 Gene set scoring for MCL sub-cluster 2 of Cluster 12 (U-shaped trends) in late-stage human cell types 344
D.114 Gene set scoring for MCL sub-cluster 3 of Cluster 12 (U-shaped trends) in late-stage human cell types 345
D.115 Gene set scoring and statistics of Cluster 12 (U-shaped trends) in late-stage mouse cell types 346
D.116 Gene set scoring for MCL sub-cluster 1 of Cluster 12 (U-shaped trends) in late-stage mouse cell types 347
D.117 Gene set scoring for MCL sub-cluster 2 of Cluster 12 (U-shaped trends) in late-stage mouse cell types 348

D.118 Gene set scoring for MCL sub-cluster 3 of Cluster 12 (U-shaped trends) in late-stage mouse cell types 349
D.119 Gene set scoring and statistics of Cluster 5 (down-regulation and late declines) in late-stage human cell types 351
D.120 Gene set scoring for MCL sub-cluster 1 of Cluster 5 (down-regulation and late declines) in late-stage human cell types 352
D.121 Gene set scoring for MCL sub-cluster 2 of Cluster 5 (down-regulation and late declines) in late-stage human cell types 353
D.122 Gene set scoring for MCL sub-cluster 3 of Cluster 5 (down-regulation and late declines) in late-stage human cell types 354
D.123 Gene set scoring for MCL sub-cluster 4 of Cluster 5 (down-regulation and late declines) in late-stage human cell types 355
D.124 Gene set scoring for MCL sub-cluster 5 of Cluster 5 (down-regulation and late declines) in late-stage human cell types 356
D.125 Gene set scoring for MCL sub-cluster 6 of Cluster 5 (down-regulation and late declines) in late-stage human cell types 357
D.126 Gene set scoring for MCL sub-cluster 7 of Cluster 5 (down-regulation and late declines) in late-stage human cell types 358
D.127 Gene set scoring for MCL sub-cluster 8 of Cluster 5 (down-regulation and late declines) in late-stage human cell types 359
D.128 Gene set scoring for MCL sub-cluster 9 of Cluster 5 (down-regulation and late declines) in late-stage human cell types 360
D.129 Gene set scoring for MCL sub-cluster 10 of Cluster 5 (down-regulation and late declines) in late-stage human cell types 361
D.130 Gene set scoring and statistics of Cluster 5 (down-regulation and late declines) in late-stage mouse cell types 362
D.131 Gene set scoring for MCL sub-cluster 1 of Cluster 5 (down-regulation and late declines) in late-stage mouse cell types 363
D.132 Gene set scoring for MCL sub-cluster 2 of Cluster 5 (down-regulation and late declines) in late-stage mouse cell types 364
D.133 Gene set scoring for MCL sub-cluster 3 of Cluster 5 (down-regulation and late declines) in late-stage mouse cell types 365
D.134 Gene set scoring for MCL sub-cluster 4 of Cluster 5 (down-regulation and late declines) in late-stage mouse cell types 366
D.135 Gene set scoring for MCL sub-cluster 5 of Cluster 5 (down-regulation and late declines) in late-stage mouse cell types 367
D.136 Gene set scoring for MCL sub-cluster 6 of Cluster 5 (down-regulation and late declines) in late-stage mouse cell types 368
D.137 Gene set scoring for MCL sub-cluster 7 of Cluster 5 (down-regulation and late declines) in late-stage mouse cell types 369

D.138 Gene set scoring for MCL sub-cluster 8 of Cluster 5 (down-regulation and late declines) in late-stage mouse cell types 370
D.139 Gene set scoring for MCL sub-cluster 9 of Cluster 5 (down-regulation and late declines) in late-stage mouse cell types 371
D.140 Gene set scoring for MCL sub-cluster 10 of Cluster 5 (down-regulation and late declines) in late-stage mouse cell types 372
D.141 Gene set scoring and statistics of Cluster 6 (down-regulation and late declines) in late-stage human cell types 374
D.142 Gene set scoring for MCL sub-cluster 1 of Cluster 6 (down-regulation and late declines) in late-stage human cell types 375
D.143 Gene set scoring for MCL sub-cluster 2 of Cluster 6 (down-regulation and late declines) in late-stage human cell types 376
D.144 Gene set scoring for MCL sub-cluster 3 of Cluster 6 (down-regulation and late declines) in late-stage human cell types 377
D.145 Gene set scoring for MCL sub-cluster 4 of Cluster 6 (down-regulation and late declines) in late-stage human cell types 378
D.146 Gene set scoring for MCL sub-cluster 5 of Cluster 6 (down-regulation and late declines) in late-stage human cell types 379
D.147 Gene set scoring for MCL sub-cluster 6 of Cluster 6 (down-regulation and late declines) in late-stage human cell types 380
D.148 Gene set scoring for MCL sub-cluster 7 of Cluster 6 (down-regulation and late declines) in late-stage human cell types 381
D.149 Gene set scoring for MCL sub-cluster 8 of Cluster 6 (down-regulation and late declines) in late-stage human cell types 382
D.150 Gene set scoring for MCL sub-cluster 9 of Cluster 6 (down-regulation and late declines) in late-stage human cell types 383
D.151 Gene set scoring for MCL sub-cluster 10 of Cluster 6 (down-regulation and late declines) in late-stage human cell types 384
D.152 Gene set scoring and statistics of Cluster 6 (down-regulation and late declines) in late-stage mouse cell types 385
D.153 Gene set scoring for MCL sub-cluster 1 of Cluster 6 (down-regulation and late declines) in late-stage mouse cell types 386
D.154 Gene set scoring for MCL sub-cluster 2 of Cluster 6 (down-regulation and late declines) in late-stage mouse cell types 387
D.155 Gene set scoring for MCL sub-cluster 3 of Cluster 6 (down-regulation and late declines) in late-stage mouse cell types 388
D.156 Gene set scoring for MCL sub-cluster 4 of Cluster 6 (down-regulation and late declines) in late-stage mouse cell types 389
D.157 Gene set scoring for MCL sub-cluster 5 of Cluster 6 (down-regulation and late declines) in late-stage mouse cell types 390

D.158 Gene set scoring for MCL sub-cluster 6 of Cluster 6 (down-regulation and late declines) in late-stage mouse cell types 391
D.159 Gene set scoring for MCL sub-cluster 7 of Cluster 6 (down-regulation and late declines) in late-stage mouse cell types 392
D.160 Gene set scoring for MCL sub-cluster 8 of Cluster 6 (down-regulation and late declines) in late-stage mouse cell types 393
D.161 Gene set scoring for MCL sub-cluster 9 of Cluster 6 (down-regulation and late declines) in late-stage mouse cell types 394
D.162 Gene set scoring for MCL sub-cluster 10 of Cluster 6 (down-regulation and late declines) in late-stage mouse cell types 395

E.1 Cell-cell communication involving endothelial cells in early-to-mid-stage HCM 398
E.2 Cell-cell communication involving fibroblasts in early-to-mid-stage HCM 401

F.1 Gene set scoring and statistics of Cluster 7 (early upregulation followed by late decline) in late-stage mouse cell types 405
F.2 Gene set scoring for MCL sub-cluster 1 of Cluster 7 (early upregulation followed by late decline) in late-stage mouse cell types 406
F.3 Gene set scoring for MCL sub-cluster 2 of Cluster 7 (early upregulation followed by late decline) in late-stage mouse cell types 407
F.4 Gene set scoring for MCL sub-cluster 3 of Cluster 7 (early upregulation followed by late decline) in late-stage mouse cell types 408
F.5 Gene set scoring for MCL sub-cluster 4 of Cluster 7 (early upregulation followed by late decline) in late-stage mouse cell types 409
F.6 Gene set scoring for MCL sub-cluster 5 of Cluster 7 (early upregulation followed by late decline) in late-stage mouse cell types 410
F.7 Gene set scoring for MCL sub-cluster 6 of Cluster 7 (early upregulation followed by late decline) in late-stage mouse cell types 411
F.8 Gene set scoring for MCL sub-cluster 7 of Cluster 7 (early upregulation followed by late decline) in late-stage mouse cell types 412
F.9 Gene set scoring for MCL sub-cluster 8 of Cluster 7 (early upregulation followed by late decline) in late-stage mouse cell types 413
F.10 Gene set scoring for MCL sub-cluster 9 of Cluster 7 (early upregulation followed by late decline) in late-stage mouse cell types 414
F.11 Gene set scoring for MCL sub-cluster 10 of Cluster 7 (early upregulation followed by late decline) in late-stage mouse cell types 415
F.12 Gene set scoring and statistics of Cluster 11 (U-shaped trends) in late-stage mouse cell types 417

F.13 Gene set scoring for MCL sub-cluster 1 of Cluster 11 (U-shaped trends) in late-stage mouse cell types 418
F.14 Gene set scoring for MCL sub-cluster 2 of Cluster 11 (U-shaped trends) in late-stage mouse cell types 419
F.15 Gene set scoring for MCL sub-cluster 3 of Cluster 11 (U-shaped trends) in late-stage mouse cell types 420
F.16 Gene set scoring for MCL sub-cluster 4 of Cluster 11 (U-shaped trends) in late-stage mouse cell types 421
F.17 Gene set scoring for MCL sub-cluster 5 of Cluster 11 (U-shaped trends) in late-stage mouse cell types 422
F.18 Gene set scoring for MCL sub-cluster 6 of Cluster 11 (U-shaped trends) in late-stage mouse cell types 423
F.19 Gene set scoring for MCL sub-cluster 7 of Cluster 11 (U-shaped trends) in late-stage mouse cell types 424
F.20 Gene set scoring for MCL sub-cluster 8 of Cluster 11 (U-shaped trends) in late-stage mouse cell types 425
F.21 Gene set scoring for MCL sub-cluster 9 of Cluster 11 (U-shaped trends) in late-stage mouse cell types 426
F.22 Gene set scoring for MCL sub-cluster 10 of Cluster 11 (U-shaped trends) in late-stage mouse cell types 427
F.23 Gene set scoring and statistics of Cluster 12 (U-shaped trends) in late-stage mouse cell types 429
F.24 Gene set scoring for MCL sub-cluster 1 of Cluster 12 (U-shaped trends) in late-stage mouse cell types 430
F.25 Gene set scoring for MCL sub-cluster 2 of Cluster 12 (U-shaped trends) in late-stage mouse cell types 431
F.26 Gene set scoring for MCL sub-cluster 3 of Cluster 12 (U-shaped trends) in late-stage mouse cell types 432

List of Tables

3.1 Summary of temporal bulk Actc1^{E99K} samples 51
3.2 Summary of public HCM mouse model samples 52
3.3 Summary of human bulk RNA-seq samples 53
3.4 Summary of statistical power analysis for bulk RNA-seq datasets . 53
3.5 Summary of differential expression analysis of human and mouse bulk RNA-seq data 57
3.6 Number of genes within differentially expressed gene clusters in temporal Actc1^{E99K} mouse data 63

4.1 The number of cells sorted for the early- and late-stage multiplexed single-cell RNA-seq sample 87
4.2 Summary of cells and cell numbers in early-stage multiplexed scRNA-seq Actc1^{E99K} mouse samples 99
4.3 Summary of cells and cell numbers in late-stage multiplexed scRNA-seq Actc1^{E99K} mouse samples 100

5.1 Summary of cells and cell numbers in late-stage human HCM snRNA-seq data 146
5.2 Number of DEGs for each cell type in human late-stage HCM snRNA-seq data 148
5.3 Number of DEGs for each cell type in mouse late-stage Actc1^{E99K} scRNA-seq data 148

6.1 Summary of cells and cell numbers in mid-stage human HCM snRNA-seq data 169
6.2 Number of DEGs for each cell type in human mid-stage HCM snRNA-seq data 170
6.3 Number of DEGs for each cell type in mouse early-stage Actc1^{E99K} scRNA-seq data 171

A.1 Temporal bulk Actc1^{E99K} samples 193
A.2 α-MHC^{R403Q} and α-MHC^{R719W} mouse samples 194
A.3 Tnt^{R92W} sample information 195
A.4 HCM human bulk RNA-seq sample information 195

Abbreviations

ADT antibody-derived tag

AF atrial fibrillation

AMPK AMP-activated protein kinase

ATAC-seq Assay for Transposase-Accessible Chromatin with high-throughput sequencing

CAR chimeric antigen receptor

CCL C-C motif chemokine ligand

cGAMP cyclic GMP-AMP

CITE-seq Cellular Indexing of Transcriptomes and Epitopes by sequencing

DAMP damage-associated molecular pattern

DC dendritic cell

DCM dilated cardiomyopathy

DEG differentially expressed gene

DN double-negative

DP double-positive

DRX disordered relaxed state

ECM extracellular matrix

EF ejection fraction

EGFR epidermal growth factor receptor

EHT engineered heart tissue

EMT epithelial-mesenchymal transition

ENCODE Encyclopedia of DNA Elements

ER endoplasmic reticulum

FACS fluorescence-activated cell sorting

FAP fibroblast activation protein

FB feature barcode

FDR False Discovery Rate

GSEA Gene Set Enrichment Analysis

GWAS genome-wide association studies

HCM hypertrophic cardiomyopathy

HDR homology-directed repair

HF heart failure

HIF hypoxia-inducible factor

IFN-γ interferon-gamma

IHSS idiopathic hypertrophic subaortic stenosis

IL interleukin

iPSC-CM induced pluripotent stem cell-derived cardiomyocyte

IVS interventricular septum

JAK-STAT Janus kinase-signal transducer and activator of transcription

LGE late gadolinium enhancement

LV left ventricular

LVEF left ventricular ejection fraction

LVH left ventricular hypertrophy

LVOT left ventricular outflow tract

LVOTO left ventricular outflow tract obstruction

MAPK mitogen-activated protein kinase

MCL Markov Cluster

MHC-I major histocompatibility complex class I

MHC-II major histocompatibility complex class II

MRI magnetic resonance imaging

mRNA messenger RNA

MSigDB Molecular Signatures Database

mTOR mammalian target of rapamycin

mTORC1 mammalian target of rapamycin complex 1

NES normalised enrichment score

NF non-failing

NF-κB nuclear factor kappa B

NFAT nuclear factor of activated T-cells

NK natural killer

NMD nonsense-mediated decay

NYHA New York Heart Association

PCA Principal Component Analysis

PCR Polymerase Chain Reaction

PI3K phosphatidylinositol 3-kinase

PPI protein-protein interaction

PROGENy Pathway RespOnsive GENes for activity inference from gene expression

pVO_2 peak oxygen consumption

RNA-seq RNA sequencing

ROS reactive oxygen species

SASP senescence-associated secretory phenotype

SCD sudden cardiac death

scRNA-seq single-cell RNA sequencing

snRNA-seq single-nucleus RNA sequencing

TAC transverse aortic constriction

TCA tricarboxylic acid

TGF-β transforming growth factor β

TMM Trimmed Mean of M-value

TNF tumour necrosis factor

Treg regulatory T cell

UMAP Uniform Manifold Approximation and Projection

UMI unique molecular identifier

UPS ubiquitin-proteasome system

VEGF vascular endothelial growth factor

VSMC vascular smooth muscle cell

VT ventricular tachycardia

WT wild-type

1 Introduction

1.1 Overview of hypertrophic cardiomyopathy

1.1.1 A historical overview

The journey to understanding hypertrophic cardiomyopathy (HCM) began in 1868 when Vulpian first described it as "idiopathic hypertrophic subaortic stenosis" due to its anatomical features [1]. This initial identification was soon followed by similar observations by Liouville and Hallopeau in 1869 [2, 3]. Fast forward to 1957, Brock in England reported on cases of left ventricular outflow tract (LVOT) hypertrophy [4], attributing it to systemic hypertension. A year later, in 1958, Teare brought more clarity with his publication of eight autopsy cases that revealed "asymmetrical hypertrophy" causing sudden deaths [5]. The same year saw Bercu *et al.* describing "pseudoaortic stenosis" [6], a condition they initially misunderstood as aortic stenosis but later identified as marked myocardial hypertrophy with normal aortic valve cusps.

The pivotal moment came in 1961 when the condition was distinctly recognised as idiopathic hypertrophic subaortic stenosis (IHSS) [7], setting it apart from aortic stenosis. Brockenbrough made significant strides by developing a diagnostic method that leveraged the dynamic nature of the obstruction in HCM [7],

specifically through the body's physiological response to premature ventricular contractions.

By 1963, Braunwald *et al.* had brought to light the nonobstructive form of HCM [8]. They noted patients who exhibited hypertrophy without the left ventricular outflow tract obstruction, paving the way for a broader understanding of the condition. Eventually, in 1972, M-Mode echocardiography emerged as a valuable diagnostic tool for identifying non-obstructive HCM [9], enhancing our ability to diagnose and understand this complex disease.

1.1.2 Clinical phenotypes

Familial HCM is now recognised as one of the most common inherited heart diseases [9, 10], with its prevalence estimated at 0.16%–0.29% in the general adult population [11–14]. HCM can manifest at any age, although it is most commonly diagnosed in clinical practice between the ages of 20 and 50 [15, 16], particularly among individuals with a strong genetic predisposition. A more specific figure comes from a meta-analysis of genetically predisposed individuals (relatives of HCM probands carrying pathogenic or likely pathogenic variants), which identified a mean age of onset of 38 years (95% CI [36, 40]) [17]. HCM presents a wide range of clinical manifestations, which can include exertional dyspnea, syncope, and in severe cases, sudden cardiac death (SCD) [18, 19]. These symptoms stem from ventricular diastolic dysfunction, cardiac arrhythmias, and left ventricular outflow tract obstruction (LVOTO) [18, 19]. Interestingly, the severity of symptoms does not always match the extent of LVOTO or the degree of left ventricular hypertrophy (LVH) [20]. Many young patients remain asymptomatic or experience only mild symptoms throughout their lives [20]. Nevertheless, SCD, the most devastating complication of HCM, can occur suddenly, especially in young competitive athletes [21, 22].

Heart failure (HF) in HCM patients is characterised by severe exertional dyspnea, triggered by factors such as intravascular volume depletion, impaired diastolic

filling, and arrhythmias [23]. Impaired myocardial function, potentially exacerbated by myocardial ischaemia arising from microvascular dysfunction, also contributes significantly to HF [24–26]. This ischaemia is not typically caused by epicardial coronary disease but arises from coronary microvascular dysfunction, underpinned by adverse structural remodelling of the small intramural arteries [25, 26]. Pathological evidence points to medial hypertrophy and intimal hyperplasia of these vessels, leading to luminal narrowing [26, 27]. This remodelling impairs the capacity for coronary vasodilation, resulting in blunted myocardial blood flow during stress, which can lead to myocyte injury, replacement fibrosis, and progressive ventricular dysfunction [24, 28]. Furthermore, LVOTO playing a significant role in acute and intermittent symptoms [23].

Arrhythmias, particularly atrial fibrillation (AF) and ventricular tachycardia (VT), are prevalent in HCM patients, often preceding or complicating the development of HF. Studies show that one in three to one in five HCM patients develop AF, a major risk factor for thromboembolic stroke [18, 29, 30]. The prevalence of AF increases with the severity of the New York Heart Association (NYHA) functional class, from under 10% in NYHA I to around 50% in NYHA IV [31]. Potential mechanisms sustaining AF in HCM include left atrial dilation, remodelling, and mutated protein expression [30].

HCM is characterised by various patterns of LVH, which can affect any part of the left ventricle asymmetrically. Typically, this involves the thickening of the basal anterior septal wall, leading to LVOTO. Histopathologically, HCM features myocyte hypertrophy and disarray, along with myocardial fibrosis [18, 32]. While myocyte disarray is a hallmark of HCM, it is also seen in other cardiac diseases. The link between genetic aetiology and morphological changes in HCM remains not fully understood and requires further investigation [33].

1.2 Molecular and genetic basis

In up to 60% of adult cases, HCM is caused by mutations in genes encoding cardiac sarcomere proteins, following a predominantly autosomal dominant inher-

itance pattern [34–38]. While autosomal recessive and X-linked modes of inheritance have been described, they are rare [39, 40]. The most common pathogenic variants are found in the genes for myosin heavy chain 7 (*MYH7*) and myosin-binding protein C (*MYBPC3*), which together account for approximately 45% of familial HCM cases (Figure 1.1) [41–44]. Mutations in other sarcomeric genes, including troponin I and T (*TNNI3* and *TNNT2*) and tropomyosin alpha-1 chain (*TPM1*), are responsible for fewer than 10% of cases [36–38, 43–46].
Other recognised but less common genetic mutations include cardiac α-actin (*ACTC1*), myosin light chain 2 (*MYL2*), myosin light chain 3 (*MYL3*), and cysteine and glycine rich protein 3 (*CSRP3*) [47–49]. These pathogenic mutations often lead to severe cardiac outcomes such as increased hypertrophy, myocardial fibrosis, hypercontractility, impaired relaxation, higher energy demands on the heart, and a greater risk of SCD [50–56].

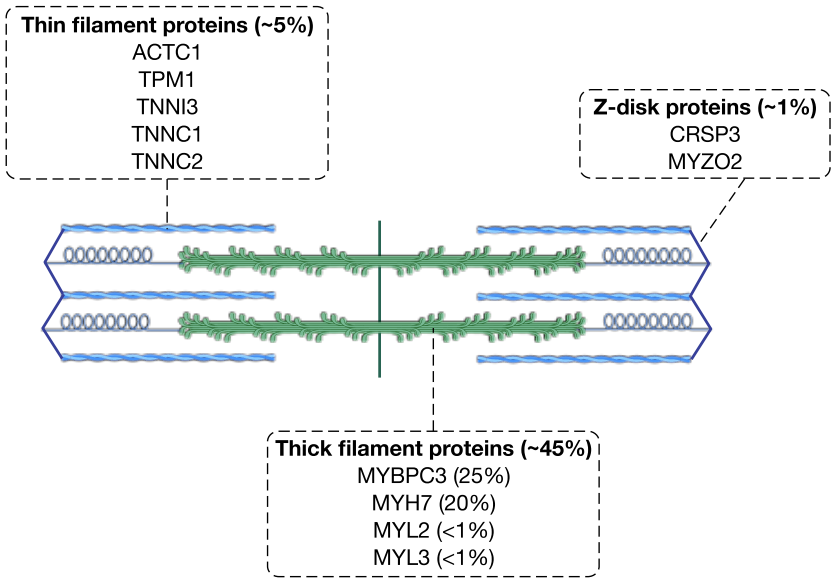

Figure 1.1. Sarcomere mutations in HCM.
The schematic structure of a sarcomere shows thick and thin filaments and Z-discs. Listed are established causal genes for HCM and their population frequencies (Adapted from Marian *et al.*, 2017) [18].

Additionally, mutations in genes such as titin (*TTN*), titin-cap (*TCAP*), myozenin 2 (*MYOZ2*), tripartite motif containing 63 (*TRIM63*), and four and a half LIM domains 1 (*FHL1*) have been linked to HCM, primarily seen in sporadic cases and smaller family groups [57–64]. Other genes, including troponin C1

(*TNNC1*), myosin heavy chain 6 (*MYH6*), phospholamban (*PLN*), caveolin 3 (*CAV3*), α kinase 3 (*ALPK3*), and junctophilin 2 (*JPH2*), have also been associated with HCM cases [65–70]. However, the evidence supporting these mutations as direct causes of HCM remains inconclusive, since only a subset of pathogenic variants—those that exhibit pronounced phenotypic consequences, high penetrance, and clear co-segregation with the disease phenotype in large HCM families—can be confidently considered causal mutations.

Genetic variants with mild phenotypic effects—i.e., variants that confer only modest alterations in protein function, result in minimal changes in cellular performance detectable in functional assays, or demonstrate limited co-segregation with the clinical phenotype—often display incomplete penetrance. These low- to moderate-effect variants are susceptible to modification by additional genetic and environmental influences [71–75]. Their occurrence in patients with sporadic HCM or in smaller familial clusters complicates the ability to firmly establish a direct causal role. Furthermore, the extensive genetic diversity in human populations, characterised by population-specific variant frequencies and the presence of thousands of coding variants per exome that may be potentially pathogenic, further obscures the distinction between variants that are truly causal and those that are incidental findings.

HCM is primarily caused by rare mutations in genes coding for sarcomere and sarcomere proteins. Because of this, most pathogenic mutations are rare within the HCM population. Notable exceptions include the Arg502Trp (or R502W) mutation in MYBPC3, found in approximately 1.5% to 3% of HCM patients [53, 76, 77], and the Val762Asp (or V762D) mutation in MYBPC3, present in 3.9% of the Japanese population [78]. Almost all other mutations occur at a frequency of less than 1% in the HCM population, with about half identified in a single proband or family [53].

The relatively high frequencies of these mutations might suggest “hot spots” or a founder effect [77]. However, these elevated frequencies are not observed in genetically independent HCM populations and may be specific to the study

populations reported. Thus, except for the aforementioned mutations, no clear "hot spots" for mutations have been identified in any known genes [79–81].
Most mutations causing HCM are missense mutations, except for *MYBPC3*, which often has insertion/deletion mutations and premature truncation mutations due to frameshift [41, 43]. Missense mutations can alter protein structure and function by changing the amino acid composition of the encoded protein. For instance, *MYH7* gene mutations frequently occur in the globular head and hinge region of the myosin heavy chain protein, with some noted in the rod domain as well [82–85]. In most cases, a clear relationship between the precise location of mutations within protein domains and the overall HCM phenotype is elusive; however, exceptions exist, such as mutations in the converter domain and on a flat surface of the *MYH7* globular head, which have been associated with an earlier disease onset [85]. Insertion/deletion mutations that cause frameshift in the protein are frequently targeted for degradation by nonsense-mediated decay (NMD). Similarly, prematurely truncated proteins are degraded by the ubiquitin-proteasome system (UPS), leading to haploinsufficiency. Rare deletion mutations in genes such as *MYH7* and *TNNT2* have also been reported [82, 83].
Although the majority of HCM has historically been attributed to mutations in genes encoding sarcomeric proteins, accumulating evidence over recent years has revealed that alterations in non-sarcomeric genes may also contribute to the development of the disease [86]. For example, variants affecting the AMP-activated protein kinase (AMPK) pathway have been implicated [87], highlighting the role of myocardial metabolic regulation in disease pathogenesis. AMPK is central to the maintenance of cellular energy homeostasis, and its dysregulation can perturb myocardial substrate utilisation and stress response mechanisms, ultimately promoting the hypertrophic and fibrotic changes observed in HCM [87].
Moreover, contemporary genetic studies have demonstrated that up to 40% of HCM cases do not carry identifiable mutations in established sarcomeric genes [88, 89]. In these genotype-negative individuals, the cumulative effect of common

genetic variants—as captured by polygenic risk scores—appears to substantially influence disease susceptibility [90].

Building on these insights, the current project focuses on the common pathological processes of adverse myocardial remodeling and fibrosis, which are critical contributors to the progression of HCM.

1.3 Pathogenesis

HCM is a paradigmatic example of a genetically mediated disease that arises from a spectrum of mutations. The underlying genetic defects initiate a series of interrelated molecular events that culminate in the histopathological and clinical manifestations of the disease. In the sections that follow, I first delineate the mutational landscape—from the predominant sarcomere mutations, both missense and truncating, to the contribution of non-sarcomere variants as indicated by polygenic analyses. Thereafter, I discuss the prevailing model wherein these distinct genetic insults are thought to converge upon a common pathway that perturbs cardiomyocyte physiology. This cascade, illustrated for the canonical sarcomeric mutations in Figure 1.2, encompasses enhanced calcium sensitivity, compensatory hypertrophy, metabolic derangements and fibrotic remodelling. However, it is important to acknowledge that this concept of a single, unified pathway is being increasingly scrutinised. Recent single-cell transcriptomic studies in other inherited cardiomyopathies, such as dilated cardiomyopathy, have revealed that different pathogenic variants can initiate distinct downstream signalling events and cellular responses [91]. Although similar detailed studies in HCM are still emerging, it is plausible that mutation-specific mechanisms may also be at play in HCM, representing an important area for future investigation. This challenges the traditional view and suggests that the road from genotype to phenotype may be more varied than previously appreciated.

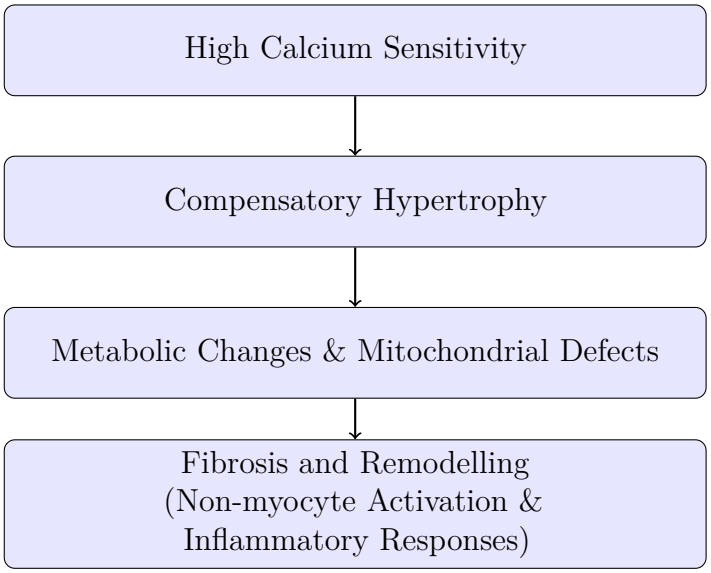

Figure 1.2. Schematic representation of the revised pathogenesis of HCM. This flowchart depicts the canonical cascade of events thought to be initiated by the majority of HCM-causing sarcomeric protein mutations. It begins with increased myofilament calcium sensitivity, which leads to a compensatory hypertrophic response. This, in turn, progresses to metabolic reprogramming (including mitochondrial defects), and culminates in fibrosis and remodelling driven by non-cardiomyocyte activation and inflammatory responses. It is important to note that non-sarcomeric mutations may operate through different initial triggers [91].

1.3.1 Genetic basis of HCM

Sarcromere mutations: Missense variants

HCM is predominantly linked to heterozygous missense mutations within sarcomere-encoding genes. These mutations induce the single amino acid substitutions that impair the structure and function of contractile proteins. In affected individuals, both wild-type and mutant alleles are transcribed and translated, although the mutant allele often demonstrates reduced expression efficiency—plausibly a consequence of suboptimal codon usage [92–94]. The resultant imbalance not only affects sarcomere assembly but also alters key aspects of the acto-myosin cross-bridge cycling. In particular, modifications in calcium sensitivity and ATPase activity are frequently observed, with reported mutant-to-wild-type protein incorporation ratios ranging between 30% and 80% [94–96]. These molecular perturbations underlie the diminished contractile performance characteristic of early HCM phenotypes.

Sarcromere mutations: Truncated variants

In contrast to missense mutations, a subset of HCM cases is associated with truncated variants—most notably in the *MYBPC3* gene. These truncated mutations arise from premature stop codons or frame shifts, and the resulting transcripts are typically targeted for clearance by quality control mechanisms such as NMD and No-Go decay [97–100]. The ensuing reduction in functional protein levels leads to haploinsufficiency, a mechanism that differs fundamentally from the dominant-negative effects seen with missense mutations. Although truncating mutations are less common, their impact on sarcomere integrity remains a crucial determinant of the HCM phenotype [44, 101, 102]. Notably, transcripts harbouring premature stop codons that partly escape NMD are further degraded by the ubiquitin proteasome system, as corroborated by mouse model studies [103, 104].

Non-sarcromere genetic influences: Polygenic contributions

Beyond primary sarcomere defects, recent genetic studies have highlighted the involvement of non-sarcomeric variants in HCM. The polygenic component of HCM is largely driven by a broad spectrum of common variants that each confer modest risk. In contrast, the classical sarcomere gene variants that lead to sarcomere-positive HCM are typically rare and of large effect [105]. These rare variants represent the established drivers of monogenic HCM, whereas the polygenic risk score is constructed from many common variants distributed across the genome that are not concentrated within the classical sarcomere genes [105]. Most patients with a clear familial form of HCM carry rare, pathogenic variants in key sarcomere genes (e.g., *MYBPC3* and *MYH7*), which have a strong effect on disease risk and are traditionally considered “disease-causing” mutations in clinical genetic testing. In contrast, genome-wide association studies (GWAS) and subsequent analyses demonstrate that common variants—each with a relatively small effect size—collectively contribute to the overall HCM risk [105]. These common variants are largely independent of the rare, high-impact sarcomeric mutations and are often found outside of the canonical sarcomere genes. The

constructed polygenic risk score, which aggregates the effects of 27 independent variants under a 5% FDR threshold, can be predictive of HCM risk across both sarcomere-positive and sarcomere-negative individuals [105].
Importantly, there is no clear evidence to suggest that there exists an additional burden of small-effect variants within the sarcomere genes themselves that further contributes to the polygenic risk [105]. Instead, the genetic architecture appears to be dichotomous: rare, high-impact variants in sarcomere genes drive the disease in sarcomere-positive individuals, while many common variants—largely residing in non-sarcomere genes—collectively account for the polygenic susceptibility observed, especially among sarcomere-negative HCM patients. Therefore, while the polygenic contributions to HCM emanate from numerous common, small-effect variants, these do not appear to include a significant burden of additional small-effect alterations within the classical sarcomere genes, thereby underscoring that high-impact sarcomere mutations and the polygenic background represent largely independent axes of genetic susceptibility in HCM.

1.3.2 Impact on cardiomyocyte physiology

Despite the heterogeneity in the underlying genetic defects, the resultant cardiomyocyte dysfunction exhibits several common features. In cases of sarcomere missense mutations, the dominant-negative interference causes variable incorporation of dysfunctional proteins into the contractile apparatus, thereby altering both calcium sensitivity and ATPase kinetics [106–110]. Conversely, truncating mutations exert their deleterious effects predominantly through haploinsufficiency, leading to a reduction in overall sarcomere protein content. Non-sarcomere variants appear to modulate these effects further, contributing to the observed mosaic of gene expression and functional deficits within the myocardium. In MYH7-expressing cardiomyocytes, for example, mutations have been shown to reduce the efficiency of actin-myosin dissociation in the presence of ATP, thereby impairing force generation [96, 111]. Such variability in mutation-induced dysfunction partially explains the clinical heterogeneity of HCM.

1.3.3 Pathophysiological cascade

The initial mutational defects trigger a cascade of secondary and tertiary events that extend from the molecular to the histological level. The characterisation of this cascade has been largely established using genetically engineered mouse models carrying human pathogenic mutations, with key findings consistently corroborated in human cardiac tissue obtained from patients during surgical procedures [18]. A salient early event is the increase in calcium sensitivity within cardiomyocytes. This has been demonstrated to be a primary consequence of many sarcomeric mutations in both mouse models and human myocardial preparations [112], and is considered a critical initiating step. Enhanced binding of calcium to contractile proteins elevates ATPase activity and engenders a persistent hypercalcaemic state that activates calcium-sensitive signalling cascades, including the calcineurin–nuclear factor of activated T-cells (NFAT) pathway [113, 114]. This upregulation of pro-hypertrophic genes represents an early compensatory mechanism aimed at preserving contractile function.

As the disease progresses, the compensatory hypertrophic response becomes maladaptive. The initial increase in cardiomyocyte volume is accompanied by extensive reprogramming of gene expression, driven in part by the activation of stress-responsive pathways such as mitogen-activated protein kinase (MAPK) and transforming growth factor β (TGF-β) signalling [63, 115]. The activation of these pathways is not confined to animal models; for instance, elevated TGF-β signalling is a prominent feature in myocardial tissue from human HCM patients, where it correlates with the degree of fibrosis [116]. Concurrently, the sustained hypertrophic stimulus precipitates significant alterations in myocardial metabolism. Specifically, the chronic energy demand shifts the balance from fatty acid oxidation towards glycolysis, while mitochondrial dysfunction—including impaired ATP production and increased reactive oxygen species (ROS) generation—further compromises contractile performance. This energetic deficit has been thoroughly characterised and confirmed in human HCM hearts, which exhibit

profound reductions in ATP and the molecular machinery for fatty acid oxidation, thus validating observations from experimental models [117].
The ensuing energetic deficit and sustained cellular stress eventually extend the remodelling process beyond cardiomyocytes. Paracrine factors released by stressed cells, along with aberrant mitochondrial metabolites, activate non-myocyte populations such as cardiac fibroblasts and inflammatory cells. Under the influence of profibrotic cytokines, notably TGF-β, fibroblasts differentiate into myofibroblasts that secrete excessive extracellular matrix proteins, resulting in extensive interstitial fibrosis [118, 119]. This fibrotic process, a key hallmark of the human condition, is faithfully recapitulated in chronic animal models and is understood to be a major contributor to diastolic dysfunction and arrhythmogenesis. The fibrotic process, could potentially be further amplified by a local chronic inflammatory milieu, disrupts normal myocardial architecture and impairs electrical conductance, thereby contributing to arrhythmogenesis and potentially promoting the eventual manifestation of HF.
In summary, the pathogenesis of HCM reflects a complex interplay between distinct genetic mutations and a cascading series of cellular responses. From the initial defects in sarcomere protein structure and function to the progressive remodelling of myocardial tissue, each step in this cascade represents a potential target for therapeutic intervention. A more detailed elucidation of these spatio-temporal processes—particularly through high-resolution transcriptomic analyses of both experimental models and human specimens—remains essential for the development of tailored therapeutic strategies.

1.4 Clinical management

1.4.1 Targeted pharmacotherapy: Cardiac myosin inhibitors

Cardiac myosin inhibitors have emerged as a paradigm shift in the management of HCM, as they directly address the underlying molecular mechanism of the disease. Excessive myosin-actin cross-bridge formation in the cardiomyocyte sarcomeres is a key driver of the hypercontractile state and subsequent LVOT

obstruction. In this context, the myosin inhibitors mavacamten and aficamten represent the first class of drugs that not only alleviate symptoms but also modify the core pathophysiology of HCM.

Mavacamten, the first-in-class agent, has been extensively evaluated in several phase 3 clinical trials—namely, EXPLORER-HCM [120], VALOR-HCM [121], and EXPLORER-CN [122]—demonstrating significant reductions in LVOT gradients, improvements in peak oxygen consumption (pVO_2), and enhanced quality of life compared with placebo. By reversibly binding to myosin, mavacamten decreases the density of myosin-actin cross-bridges, thereby mitigating the hypercontractile state that leads to the characteristic myocardial hypertrophy and obstruction. However, careful dose titration is essential to avoid an excessive inhibition of myosin activity, which may result in a detrimental drop in left ventricular ejection fraction (LVEF).

Aficamten, a second-generation myosin inhibitor, has been developed with an improved pharmacokinetic profile. This agent allows for more rapid dose titration while minimising the risk of excessive myosin inhibition. Its design aims to maintain the efficacy in reducing LVOT obstruction while mitigating adverse inotropic effects observed with earlier agents. Early phase 3 data suggest that aficamten achieves similar degrees of haemodynamic improvement with a lower incidence of LVEF reduction [123], thereby offering a safer option for long-term management of symptomatic obstructive HCM. Collectively, these findings underscore that myosin inhibition is currently the only pharmacological intervention that directly addresses the core mechanism of HCM at a molecular level.

1.4.2 Emerging genetic therapies

Concurrently, considerable efforts are being directed towards gene-based approaches to correct the underlying genetic mutations that account for nearly half of HCM cases. The rationale behind gene therapy lies in its potential to modify the primary cause of the disease rather than merely alleviating its phenotypic manifestations. Current strategies under investigation include gene replacement therapy

[124–126], gene silencing [127], genome editing [128], exon skipping [124, 129], and RNA trans-splicing [130, 131]. Each modality aims to restore or compensate for the impaired function of mutated proteins within the cardiac sarcomere. For instance, gene replacement therapy has shown promise in preclinical models by reintroducing the wild-type copy of a defective gene, particularly in cases involving *MYBPC3* mutations [124]. However, these innovative approaches remain in the early stages of clinical research and require further validation to assess their long-term safety and efficacy.

1.4.3 Non-cardiomyocyte pathophysiology: Addressing fibrosis and inflammation

While cardiac myosin inhibitors offer a targeted approach to ameliorate the hypercontractility observed in HCM, treatment options directed at other pathological components remain conspicuously scarce. In particular, the mechanisms driving myocardial fibrosis and inflammatory processes are poorly understood, and no current therapeutic agents directly target these non-cardiomyocyte components. The absence of effective antifibrotic or anti-inflammatory drugs highlights a critical gap in the comprehensive management of HCM. Given that fibrosis and inflammation can contribute to adverse remodelling and deteriorating cardiac function, there is a pressing need for basic and translational research to elucidate these pathways. Addressing these mechanisms is a major objective of the present study, with the long-term aim of identifying novel targets for therapeutic intervention [132–134].

1.5 Non-cardiomyocytes: A future direction

HCM has long been conceptualised as a primary disease of the cardiomyocytes, with pathogenic mutations in sarcomeric proteins provoking abnormal contractile function and hypertrophy. However, growing evidence indicates that non-cardiomyocytes—comprising immune cells, cardiac fibroblasts, vascular smooth muscle cells (VSMCs), pericytes, and other stromal cell types—may play critical roles not only in the

initiation but also in the progression of the disease phenotype. These cells may actively participate in the remodelling process by modulating both inflammatory and fibrotic cascades that ultimately contribute to adverse clinical outcomes. Recent advances in single-nucleus RNA sequencing (snRNA-seq) have afforded an unprecedented resolution in characterising cellular heterogeneity and dynamic transcriptional profiles in the HCM heart [135, 136]. These transcriptomic approaches now reveal that non-cardiomyocyte populations are remarkably plastic, and their phenotypic transitions—often occurring before overt hypertrophy—may serve as early diagnostic markers or even as targets for disease-modifying therapies.

In this context, two fundamental processes underlie pathological cardiac remodelling in HCM: inflammation and fibrosis. Although the inflammatory response is essential for tissue repair, its aberrant activation can become deleterious. Likewise, the activation of cardiac fibroblasts leads to the deposition of extracellular matrix (ECM) proteins that disrupt myocardial architecture and impair electrical conduction. Notably, effective antifibrotic interventions are typically feasible only during the early stages of disease progression, as once advanced fibrosis is established, targeting the process becomes exceedingly challenging. A precise understanding of the temporal and spatial dynamics of these processes is therefore critical: early detection of subclinical inflammation or fibrotic signalling could enable timely interventions that delay or reverse disease progression, whereas strategies aimed at mitigating chronic fibrosis in advanced disease stages may have limited therapeutic benefit.

1.5.1 Inflammation in cardiac remodelling in HCM

Inflammation is an evolutionarily conserved response, originally evolved to protect tissues against injury and infection through a well-orchestrated cascade of cellular and molecular events. In the myocardium, a controlled and transient inflammatory reaction is essential for repair and regeneration following injury. However, in HCM, the sustained presence of a chronic low-grade inflammatory

response is observed, and its precise contributions to disease pathogenesis are an area of ongoing research; it is being explored whether this inflammatory state might influence cardiomyocyte dysfunction and contribute to maladaptive remodelling processes, such as fibrosis and electrical instability [132, 137–139].

The current understanding of inflammatory involvement in HCM is informed by clinical observations, histopathological studies, and advanced transcriptomic investigations. Histological analyses of myocardial biopsies from certain cohorts of HCM patients (e.g., those with specific mutations such as $TPM1^{D175N}$ [132]) and findings from preclinical models [140] have indicated the presence of inflammatory cell infiltration—even in the absence of overt myocarditis—and the activation of key inflammatory pathways, including those mediated by nuclear factor kappa B (NF-κB). However, a comprehensive characterisation of inflammatory cell infiltration and activation across the broader spectrum of HCM has remained an area requiring more detailed investigation, to which recent studies and the work within this thesis aim to contribute. These findings are complemented by serological studies that reveal elevations in circulating cytokines—including tumour necrosis factor (TNF), interleukin (IL)-1β, IL-6, and IL-10—in patients bearing HCM-causing mutations [141–143]. In parallel, recent snRNA-seq studies have unveiled extensive heterogeneity within the cardiac immune compartment, identifying distinct subpopulations of macrophages, T cells, and dendritic cells (DCs) that are differentially activated across varied stages of HCM [135, 136]. Notably, the resolution afforded by single-nucleus transcriptomics has provided unprecedented insights into the dynamic interplay between immune cells and other resident cell types in the myocardium. For instance, sub-clustering of cardiac macrophages has identified distinct circulating and resident populations. While these populations can exhibit a spectrum of functional states, including those associated with pro-inflammatory or reparative activities, their precise roles and the balance of these activities in HCM are complex, with evidence suggesting a mixture of phenotypes rather than a strict functional dichotomy based on origin [144, 145]. Importantly, alterations in the relative abundance or activation

states of these macrophage subsets appear to occur in HCM, with potential implications for the secretion of cytokines and chemokines involved in inflammatory cell recruitment and fibroblast proliferation [145]. In some cases, these alterations have been detected even prior to the onset of overt hypertrophy, suggesting that inflammation might represent an early biomarker or even a targetable initiator of subsequent pathological remodelling.

Cellular mediators of inflammation in HCM

At the cellular level, multiple non-cardiomyocyte populations contribute to the inflammatory milieu in the HCM heart. Among these, macrophages have received the most attention. Cardiac macrophages fulfil a spectrum of functions, from maintaining homeostasis and facilitating electrical conduction to mediating inflammation and tissue repair [146–149]. In pathological states such as HCM, the balance of these macrophage activities can be disrupted. Indeed, studies have identified diverse macrophage subsets within the diseased myocardium, some of which exhibit heightened pro-inflammatory and pro-fibrotic profiles [150–155]. These populations, characterised by distinct transcriptional signatures including upregulation of inflammatory cytokines and MAPK signalling components, are implicated in exacerbating myocardial injury and promoting adverse remodelling through paracrine interactions with cardiomyocytes and fibroblasts.
T lymphocytes also contribute significantly to the inflammatory landscape in HCM. Evidence suggests that cytotoxic $CD8^+$ T cells, in conjunction with pro-inflammatory $CD4^+$ T helper cells, can infiltrate the myocardium and secrete cytokines such as interferon-gamma (IFN-γ) and interleukins that modulate the function of both cardiomyocytes and fibroblasts [156, 157]. In contrast, regulatory T cells (Tregs) are endowed with immunosuppressive properties that normally help attenuate excessive inflammation. Disruption of Treg activity has been linked to heightened inflammatory responses and is associated with worse outcomes in cardiac diseases [158–162].

Additional immune cell types, such as neutrophils and DCs, have been implicated through both animal models and human tissue studies. Neutrophils, typically among the first responders to tissue injury, may contribute to myocardial damage by releasing proteolytic enzymes and ROS, thereby amplifying tissue injury and promoting subsequent fibrosis [163, 164]. DCs, though less abundant, have also been observed to participate in antigen presentation and T-cell activation, potentially linking innate and adaptive immune responses in the diseased myocardium.

Molecular pathways and cytokine signalling in inflammatory remodelling

Central to the orchestration of the inflammatory response in HCM is the activation of several key molecular pathways. Foremost among these is the NF-κB pathway, a critical regulator of immune responses and inflammation. Histopathological analyses of endomyocardial biopsies from HCM patients have provided evidence of NF-κB pathway activation, although its extent and cellular localisation appear variable. For instance, one study detected nuclear positivity for NF-κB in a subset of patient samples; this was observed in cardiomyocytes in some cases, with varying proportions of positive nuclei, and in inflammatory or endothelial cells in other instances, while control myocardial specimens showed no such nuclear positivity [132]. These findings, while indicative of NF-κB involvement, also highlight the heterogeneity of this response in HCM hearts. Activation of NF-κB is known to enhance the transcription of a broad array of pro-inflammatory cytokine genes, including TNF, IL-1β, and IL-6, which are critical in stimulating inflammatory cascades [165, 166]. While elevated circulating levels of such cytokines have been reported in HCM patients [141–143], the direct contribution of NF-κB-mediated cytokine transcription within the HCM myocardium to the local inflammatory state requires further elucidation. Nevertheless, the potential for chronic activation of this pathway to contribute to persistent low-grade inflammation and adverse remodelling in HCM remains an important area of investigation [132].

In addition to NF-κB, the Janus kinase-signal transducer and activator of transcription (JAK-STAT) pathway is recognised as a pivotal mediator of inflammatory signalling in various cardiac conditions, and its role in the HCM heart is an area of active investigation [167–170]. Cytokines such as IL-6, which can be elevated in cardiac stress, exert their effects by binding to the gp130 receptor complex and activating STAT3. Activated STAT3 then translocates to the nucleus to modulate the expression of genes involved in cell survival, hypertrophy, and inflammation [171–174]. Aberrant STAT activation has been associated with both protective and deleterious effects in cardiac pathology generally, underscoring the complexity of cytokine signalling and its potential implications for HCM [170, 175–177].

Moreover, chemokine signalling, particularly involving the C-C motif chemokine ligand (CCL) family, orchestrates the recruitment and migration of inflammatory cells. Elevated levels of chemokines such as CCL2 (monocyte chemoattractant protein-1) have been reported in HCM patients and correlate with increased macrophage infiltration in myocardial tissue [178–180]. This chemotactic gradient not only serves to perpetuate the inflammatory response but may also induce phenotypic shifts in resident stromal cells, thereby linking inflammation with subsequent fibrosis.

Implications for early diagnosis and therapeutic intervention

Understanding the inflammatory processes in HCM at single-cell level opens up several potential avenues for early diagnosis and targeted intervention. Given that the inflammatory cascade appears to be activated at a very early stage—prior to the full establishment of hypertrophy—there is an opportunity to identify high-risk individuals through minimally invasive tests based on circulating inflammatory markers or even through tissue sampling using next-generation sequencing technologies.

Therapeutically, modulating the inflammatory response holds promise for altering the disease course. Early intervention aimed at restoring the balance between

pro-inflammatory and anti-inflammatory mediators may mitigate the progression of myocardial remodelling. For example, therapies designed to enhance the reparative functions of cardiac macrophages or to boost the activity of regulatory T cells may help to temper the damaging effects of chronic inflammation. Similarly, pharmacological agents that specifically inhibit detrimental cytokine signalling (such as inhibitors of NF-κB or the JAK-STAT pathway) are currently under investigation and may offer novel strategies to limit inflammation-driven damage in HCM [181–185].

1.5.2 Fibrosis in cardiac remodelling in HCM

Fibrosis represents one of the key pathological hallmarks of HCM. In HCM, fibrosis manifests primarily as the excessive deposition of ECM proteins, such as collagen types I and III, in discrete regions of the myocardium. Unlike acute reparative fibrosis following myocardial infarction, the fibrotic process in HCM is predominantly reactive or interstitial in nature, developing in the absence of widespread cardiomyocyte death. The resultant accumulation of ECM not only disrupts the normal contractile mechanics of the heart but also alters electrical conduction, predisposing affected patients to arrhythmias and functional deterioration over time [133]. Recent advances in snRNA-seq have, for the first time, afforded the resolution necessary to delineate the heterogeneity among non-cardiomyocyte populations implicated in fibrotic remodelling [135, 136].

The cellular basis of myocardial fibrosis

At the core of myocardial fibrosis lie cardiac fibroblasts [186–188]. Under steady-state conditions, these cells play an essential role in maintaining the structural integrity of the myocardium by regulating the synthesis and degradation of ECM proteins and associated enzymes [133]. However, in HCM, fibroblasts become persistently activated, adopting a myofibroblast phenotype characterised by the *de novo* expression of contractile proteins and an exuberant production of ECM proteins [133, 189, 190]. Importantly, this fibroblast activation and subsequent

fibrotic remodelling in HCM often occur in the absence of widespread cardiomyocyte necrosis, as significant cell death is not a predominant feature of most stages of HCM [140, 191]. This indicates that fibroblast activation plays a primary pathological role in the adverse remodelling characteristic of HCM, rather than being a mere secondary repair response to extensive cell death. It is thus considered an early and active pathological process in the disease course.

The transition of quiescent cardiac fibroblasts to activated myofibroblasts is primarily regulated by a network of paracrine and autocrine signals. Among these, the TGF-β signalling pathway has emerged as the most seminal driver of myocardial fibrosis in HCM [140, 192]. TGF-β is typically secreted in a latent form and becomes activated through proteolytic cleavage by a range of enzymes, including thrombospondin 1, matrix metalloproteinases, and specific sheddases such as furin and ADAMTS family members [133, 193–195]. Once activated, bioactive TGF-β binds to its heterodimeric receptors (TβR-I/TβR-II) on the surface of cardiac fibroblasts, initiating both canonical and non-canonical signalling cascades. The canonical pathway involves the phosphorylation of Smad2 and Smad3, their association with Smad4, and subsequent nuclear translocation, where the complex regulates the transcription of a myriad of profibrotic genes, including those encoding collagens, periostin, and tissue inhibitors of metalloproteinases [116, 136]. In contrast, the non-canonical pathways involve signalling mechanisms such as the MAPK pathway, phosphatidylinositol 3-kinase (PI3K), and Rho GTPase pathways, all of which synergise to modulate ECM turnover and fibroblast activation [133, 196–198].

Single-nucleus transcriptomic analyses have been pivotal in reformulating our understanding of fibroblast heterogeneity in the HCM myocardium [135]. Still, the interplay between fibrosis and other facets of non-cardiomyocyte activity in HCM further underscores the necessity of an integrated perspective on cardiac remodelling [132]. Immune cells and vascular components, as discussed in the previous section on inflammation, directly influence the fibrotic milieu [132]. Pro-inflammatory cytokines released by macrophages and T cells can enhance fibrob-

last activation [148, 152, 153, 199–201], while altered vascular perfusion may induce hypoxic conditions that further potentiate profibrotic signalling [157, 202, 203]. Moreover, emerging evidence suggests that certain fibroblast populations themselves may adopt immunomodulatory roles, secreting cytokines that influence both their own activation state and the behaviour of neighbouring immune cells [204, 205]. This bidirectional communication between immunological and fibrotic processes creates a self-reinforcing cycle that drives the progression of myocardial remodelling and underscores the potential impact of targeted anti-fibrotic therapies in HCM.

Implications for therapeutic intervention

From a therapeutic standpoint, the implications of these insights are profound. In the early stages of HCM, when the fibrotic process remains reversible, there exists a real prospect of developing treatments that not only alleviate symptoms but also modify the disease trajectory by curtailing profibrotic signalling. For example, partial inhibition of TGF-β—while avoiding the complete suppression that could lead to adverse outcomes such as ventricular dilation and dysfunction—has been achieved in preclinical studies using agents such as Pirfenidone [182, 184, 206]. Moreover, the highly specific profiles of fibroblast subpopulations revealed by single-nucleus transcriptomics may allow for the design of novel targeted therapies. For instance, therapeutic strategies targeting specific fibroblast markers, such as fibroblast activation protein (FAP), are being explored; one such approach involves chimeric antigen receptor (CAR) T cell therapy. Recent studies have shown that *in vivo* generated FAP-CAR T cells, produced by delivering modified messenger RNA (mRNA) via T cell-targeted lipid nanoparticles, can effectively reduce cardiac fibrosis and improve cardiac function in preclinical models of HF [207]. Nanoparticle-mediated delivery systems, for instance, could also be employed to directly target fibroblasts that exhibit a maladaptive transcriptomic signature, thereby limiting systemic toxicity and maximising local therapeutic efficacy [208].

In addition to therapeutic interventions, the precise characterisation of fibrotic cells by single-cell RNA sequencing (scRNA-seq) and snRNA-seq holds promise for the development of new biomarkers for early diagnosis and prognostication in HCM. Subclinical fibrosis, detectable through minimally invasive sampling or advanced imaging techniques augmented by transcriptomic profiles, could serve as a harbinger of future adverse remodelling.

1.5.3 Remaining cellular clusters

Beyond the extensive roles of immune cells and fibroblasts already discussed, emerging evidence indicates that other non-cardiomyocyte populations also contribute to the complex pathogenesis of HCM. In addition to the inflammatory and fibrotic cascades, vascular cells—including endothelial cells, VSMCs, and pericytes—also help to modulate myocardial homeostasis and remodelling. Endothelial cells are not only responsible for governing vascular tone and permeability, but they also function as key regulators of local inflammation. In transverse aortic constriction (TAC) or AngII-induced cardiac hypertrophy, several recent studies have reported subtle yet significant changes in endothelial cell phenotypes, including the upregulation of adhesion molecules and chemokines, which may facilitate the local recruitment of immune cells and create a microenvironment conducive to both inflammation and fibrosis [209–212]. Such observations suggest that endothelial dysfunction could contribute to HCM pathogenesis, and further research may explore the potential for endothelial-targeted therapies aimed at restoring microvascular integrity.

Similarly, VSMCs have been implicated in the remodelling process by influencing both local ECM turnover and paracrine signalling networks [213, 214]. VSMCs in HCM have been observed to undergo phenotypic modulation, characterised by a reduction in contractile markers and an increased expression of pro-inflammatory and profibrotic mediators. Such phenotypic shifts may arise from chronic mechanical stress and altered biochemical cues in the hypertrophied myocardium. This modulation suggests that these cells may not remain inert bystanders but,

in fact, actively contribute to the progression of fibrosis and to the dysregulation of vascular tone—a combination of events that may heighten the arrhythmic risk and impair myocardial perfusion in HCM.

Pericytes, which function in close association with endothelial cells, represent yet another intriguing cluster within the non-cardiomyocyte compartment. These cells, crucial for capillary stability and microvascular remodelling, have been shown to display changes in gene expression that suggest an involvement in the early fibrotic signalling cascade [215–220]. Although the precise mechanistic roles of pericytes in HCM remain to be fully delineated, their interactions with both fibroblasts and vascular endothelial cells indicate that they might help coordinate the balance between ECM deposition and degradation.

Taken together, these additional non-cardiomyocyte populations significantly expand our view of the cellular ecosystem within the HCM heart. Single-cell and single-nucleus transcriptomic technologies offer a powerful lens through which researchers can identify and track the dynamic transitions in these cell populations—from a relatively quiescent state to one of activation and pathogenic remodelling. This comprehensive cellular profiling is critical for establishing early diagnostic biomarkers that may, when integrated with advanced imaging modalities such as cardiac magnetic resonance imaging (MRI) with late gadolinium enhancement (LGE) and T1 mapping (a quantitative MRI technique that measures the longitudinal relaxation time of myocardial tissue to sensitively detect diffuse fibrosis and other subtle tissue alterations), enable precise risk stratification of patients at the subclinical stage of disease. Moreover, by identifying specific cell-surface markers and unique transcriptomic signatures of pathogenic subpopulations, these approaches pave the way for the development of targeted, cell-specific therapeutic interventions.

1.6 Animal models of human HCM

Animal models harbouring human HCM–causing mutations have been instrumental in elucidating the mechanistic underpinnings of this disease. Among these, ro-

dent models, particularly mice, have become the mainstay for the genetic dissection of HCM. Their short gestation, ready amenability to transgenic and knockout techniques, and relatively low maintenance costs facilitate rapid generation and phenotyping of disease alleles [221, 222]. Despite physiological differences when compared to humans—such as heart rate, myosin isoform predominance and calcium handling dynamics—murine models have yielded unparalleled molecular and cellular detail regarding sarcomeric dysfunction and its consequences, providing crucial insights into HCM pathogenesis. These models allow researchers to recapitulate defined sarcomeric defects in a controlled environment, enabling the dissection of the cascade from molecular perturbation to organ-level remodelling and the testing of therapeutic interventions.

1.6.1 The α-MHC$^{\mathbf{R403Q}}$ model

The α-MHC$^{\mathrm{R403Q}}$ mutation in the myosin heavy chain is one of the most extensively studied genetic alterations associated with HCM. Published for the first time in a mouse model by Geisterfer-Lowrance *et al.* in *Science* (1996) [223], the α-MHC$^{\mathrm{R403Q}}$ mouse model marked a significant milestone in HCM research. Initial transgenic mice overexpressed the human α–myosin heavy chain (α-MHC) harbouring the α-MHC$^{\mathrm{R403Q}}$ substitution under the control of the cardiac-specific α-MHC promoter [223]. Although human hearts predominantly express β-MHC, the murine myocardium is α-MHC–dominant; this mismatch complicates direct extrapolation but nonetheless yields valuable mechanistic data.

In the α-MHC$^{\mathrm{R403Q}}$ transgenic mice, expression levels reached approximately 10–20% of total myosin, ensuring a heterozygous-like stoichiometry [224]. Phenotypically, these mice developed early onset myocyte disarray, concentric hypertrophy and interstitial fibrosis by 12–16 weeks of age. Echocardiography revealed preserved ejection fraction with diastolic dysfunction, mirroring human non-obstructive HCM. At the cellular level, isolated cardiomyocytes exhibited increased calcium sensitivity of force development and slowed relaxation, attributable

to a shift in the equilibrium of myosin heads towards the disordered relaxed state (DRX) [225].

Biophysically, skinned fibre assays demonstrated a 30–50% increase in ATPase activity and actin-activated sliding velocity in α-MHC^{R403Q}-containing myosins compared with wild type. Paradoxically, intact papillary muscle preparations exhibited decreased work output, reflecting an energetic inefficiency that triggers compensatory hypertrophy [225]. Transcriptomic profiling of left ventricular tissue at early disease stages uncovered up-regulation of pro-hypertrophic genes (e.g., *Nppa*, *Myh7*) and extracellular matrix components (e.g., *Col1a1*, *Tgfb2*) prior to overt wall thickening [226]. These molecular signatures implicate an early fibrotic priming that precedes histological fibrosis.

It is important to recognise, however, that although the α-MHC^{R403Q} mouse model faithfully reproduces several hallmarks of human HCM, there remain significant differences between murine and human cardiac physiology. Mice, for instance, have a much higher basal heart rate and altered calcium dynamics relative to humans, which can modulate the effects of sarcomeric mutations on contractility and remodelling [222, 227]. These disparities underscore the need for caution when extrapolating findings from the α-MHC^{R403Q} model to the human condition. Nevertheless, the model has proved invaluable in delineating the mutation-specific alterations in contractility and remodelling, and it continues to serve as a platform for evaluating potential therapeutic interventions that target the molecular defects underlying HCM.

1.6.2 MYBPC3 truncation and knockout models

Truncating variants in *MYBPC3* are the most prevalent cause of familial HCM. To model haploinsufficiency, both global and cardiac-specific knockout mice have been generated [101, 228]. Homozygous *Mybpc3* knockouts die in utero due to severe contractile dysfunction, whereas heterozygotes survive but develop late-onset hypertrophy and fibrosis by 9–12 months of age [228]. This delayed phenotype

contrasts with the rapid onset seen in some missense models, reflecting the distinct mechanism of protein insufficiency rather than dominant-negative interference.

1.6.3 Troponin I (Tnni3) and Troponin T (Tnnt2) models

Missense mutations in *Tnni3* and *Tnnt2* perturb the regulatory troponin complex, altering calcium sensitivity and cross-bridge kinetics. The Tnni3$^{\mathrm{R145G}}$ substitution was introduced into mice via transgenic expression under the α-MHC promoter [229]. These mice develop severe diastolic dysfunction by eight weeks, elevated myofibrillar calcium sensitivity and early mortality. Histologically, they display myocyte disarray and patchy fibrosis, with up-regulated natriuretic peptides and fetal gene programme activation [229]. Notably, β-adrenergic blockade improves diastolic parameters but does not prevent fibrosis, indicating a direct pro-fibrotic effect of sustained calcium sensitisation.

In parallel, Tnnt2$^{\mathrm{R92Q}}$ knock-in mice were created by targeted mutagenesis [230]. Heterozygotes manifest mild hypertrophy by six months, whereas homozygotes exhibit perinatal lethality. Detailed mechanical studies on skinned fibres reveal increased calcium affinity and slower rate of tension redevelopment, consistent with an impaired k_{tr} response. Single-cell transcriptomics in Tnnt2$^{\mathrm{R92Q}}$ heterozygotes show up-regulation of *Tgfβ1* and matrix remodelling genes in fibroblasts long before overt hypertrophy, underscoring an early crosstalk between myocytes and non-myocytes [230].

1.6.4 Tropomyosin Tpm1$^{\mathbf{E180G}}$ and Tpm1$^{\mathbf{D175N}}$ models

Mutations in α-tropomyosin (Tpm1), such as Tpm1$^{\mathrm{E180G}}$ and Tpm1$^{\mathrm{D175N}}$, have been recreated in mice to probe their specific molecular consequences. The Tpm1$^{\mathrm{E180G}}$ transgenic model, expressing the human *TPM1* mutant at approximately 20% of total tropomyosin, exhibits early hypertrophy and interstitial fibrosis by ten weeks,

accompanied by increased myofilament calcium sensitivity and impaired relaxation kinetics [231]. Interestingly, these mice display atrial enlargement and predisposition to atrial fibrillation, paralleling the high burden of supraventricular arrhythmias in HCM patients [231].

Conversely, the Tpm1^{D175N} mutation introduced as a knock-in yields subtler phenotypes: heterozygotes show mild left ventricular thickening by six months with preserved systolic function, whereas homozygotes are non-viable. Mechanical assays reveal a smaller increase in calcium affinity compared to Tpm1^{E180G}, suggesting mutation-specific gradations in biophysical impact [232]. These observations support a spectrum of disease severity modulated by the precise location and nature of each residue substitution.

1.6.5 Cardiac actin Actc1^{E99K} model

Another genetically engineered mouse model that has provided important insights into HCM is the Actc1^{E99K} model. Although not as historically seminal as the α-MHC^{R403Q} model, the Actc1^{E99K} model offers distinct advantages in the study of inflammation and fibrosis within the context of cardiac remodelling. Therefore, the Actc1^{E99K} HCM mouse model represents a pivotal tool in our lab's study of HCM. This model was first developed by Song *et al.* [233] and has subsequently been extensively characterised by our group.

The construction of the Actc1^{E99K} HCM mouse model was described in Song *et al.* (2011) [233]. Briefly, The Actc1^{E99K} mutation was inserted into the human cardiac actin sequence. Transgene expression was restricted to the heart using an α-myosin heavy chain promoter construct originally produced in the laboratory of Dr Jeffrey Robbins [234]. This construct includes the promoter region of the α-myosin heavy chain, starting with the 3' untranslated region of the β-myosin heavy chain and the first three non-coding exons of the α-myosin heavy chain. To prepare the transgene expression vector, it was first cut with Hind III and then partially filled in with two nucleotides (AG) using the Klenow fragment. After purification, the vector was digested with Sal I. The mutant cardiac actin

cDNA was removed from the pBSII KS vector by first digesting with Spe I, then filling the 3' end with two nucleotides (C,T) using the Klenow fragment. After purification, the vector was digested with Sal I. This allowed directional cloning of the mutant actin construct into the transgene expression vector using a Sal I site at the 5' end and a Spe I/Hind III hybrid at the 3' end.

Transgenic mice were generated by pronuclear microinjection of gel-purified transgenic constructs (after removal of the plasmid backbone with Not I) into the pronuclei of fertilised mouse eggs on a C57BL10xCBA/Ca hybrid background, following previously described methods. Treated embryos were then returned to a pseudopregnant CD-1 foster mother, generated by mating with a vasectomised male mouse. The resultant pups were identified and genotyped by Polymerase Chain Reaction (PCR) from ear-notch samples.

Immune cell dynamics and cardiac remodelling in the Actc1$^{\mathbf{E99K}}$ HCM mouse model

The model has been rigorously characterised: previous work has demonstrated that, even in the absence of new wet-lab experiments in this thesis, the Actc1$^{\mathrm{E99K}}$ mice reliably recapitulate the key hallmarks of HCM—including early apical hypertrophy, progressive interstitial fibrosis, and eventual decline in ejection fraction.

The cardiac actin Actc1$^{\mathrm{E99K}}$ mouse model recapitulates the clinical features of human HCM caused by the analogous mutation, including apical hypertrophy and fibrosis (Figure 1.3). This model's accelerated disease progression and clear phenotypic presentation of adverse cardiac remodelling make it ideal for studying HCM. At four weeks, mice exhibit apical hypertrophy and fibrosis without left ventricular (LV) thickening or dysfunction, mirroring the stable, early stage of HCM in patients with hypertrophy and fibrosis but preserved ejection fraction (EF) (Figure 1.3, left panel). This early stage offers a critical window for understanding the initiation of adverse remodelling before functional decline.

As the disease progresses, hypertrophy and fibrosis extend to the LV, leading to a reduction in EF, which is characteristic of advanced HCM (Figure 1.3, middle panel). This transition from a stable to a more advanced stage is marked by significant remodelling, including increased fibrosis and a decline in cardiac function. The final stage, observed in a smaller subset of mice, is characterised by substantial LV hypertrophy and fibrosis with severely reduced EF, reflecting the progression to HF seen in some HCM patients (Figure 1.3, right panel). This phenotypic progression underscores the utility of the Actc1^{E99K} model in studying both early and late stages of cardiac remodelling, providing a comprehensive view of disease dynamics.

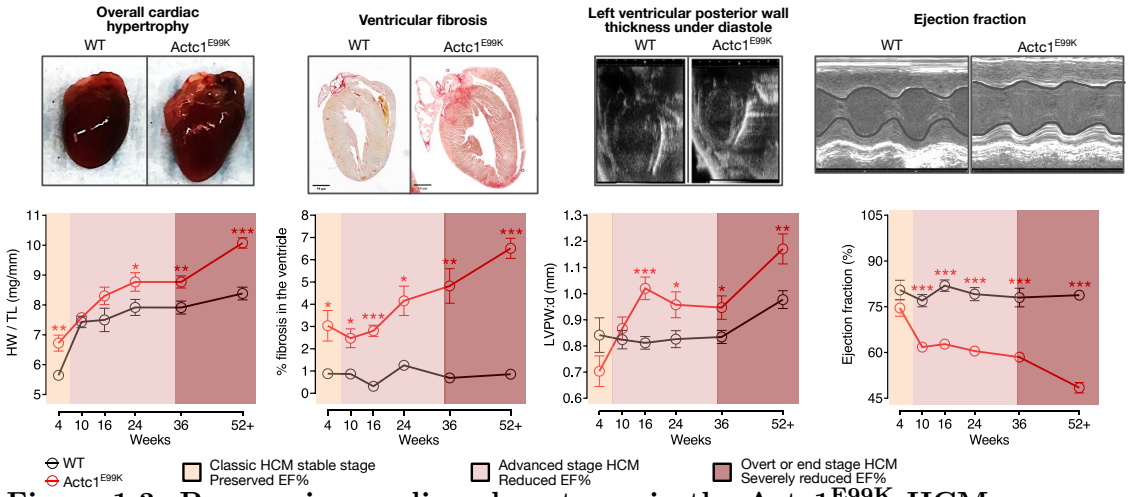

Figure 1.3. Progressive cardiac phenotypes in the Actc1^{E99K} HCM mouse model.
This figure summarises the progressive cardiac phenotypes observed in the Actc1^{E99K} HCM mouse model. Heart weight/tibia length (HW/TL) ratios were calculated to quantify cardiac hypertrophy. Following euthanasia under UK Home Office project licenses, hearts were excised, weighed, and processed for further analyses. Echocardiography was performed on live mice to determine left ventricular posterior wall thickness in diastole (LVPW:d) and ejection fraction (EF%), enabling longitudinal assessment of cardiac structure and function. Ventricular fibrosis was assessed by quantifying the percentage of collagen deposition in picrosirius red-stained heart sections. The collagen fibres, stained red, were quantified microscopically. Group sizes for the analyses were: hypertrophy ($n \geq 8$); echocardiography (LVPW:d and EF%) ($n \geq 5$); and fibrosis ($n \geq 4$). Statistical analysis was performed using a two-way ANOVA with mixed-effects analysis and p-values adjusted using the Benjamini, Krieger, and Yekutieli two-stage step-up method (adjusted p-values: *: < 0.05, **: < 0.01, ***: < 0.001, and ****: <0.0001). Data source: Dr Ying-Jie Wang.

In addition to structural remodelling, immune cell infiltration characterises ad-

verse remodelling in HCM. While less pronounced than in myocarditis, HCM patients exhibit low-grade, focal, chronic infiltration of T cells, myeloid cells, and macrophages (Figure 1.4), contributing to a chronic inflammatory environment that exacerbates remodelling. To investigate the initiation and progression of immune responses in HCM, we employed the Actc1^{E99K} mouse model, which allows for a detailed temporal analysis of immune cell dynamics.

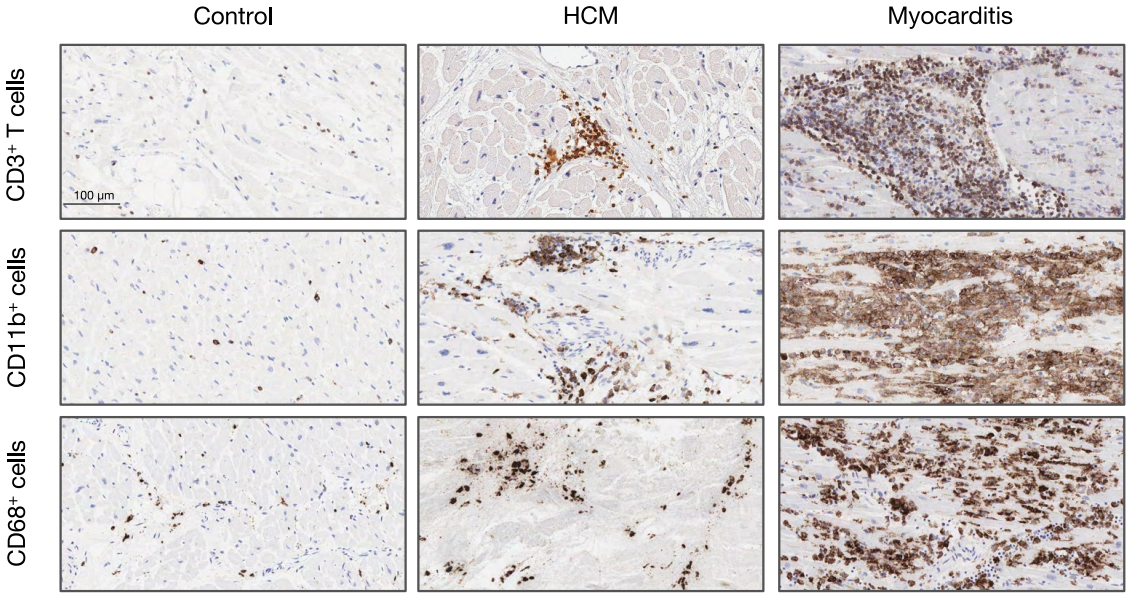

Figure 1.4. Chronic immune cell infiltration in HCM patients. Formalin-fixed, paraffin-embedded (FFPE) human heart samples (healthy controls, HCM, and myocarditis) were obtained postmortem or from explants with patient consent from tissue banks at Cambridge University Hospitals, Royal Papworth Hospital, and Oxford University Hospitals. 3 mm sections were mounted onto slides and stained using immunohistochemistry on a Leica Bond Rx research stainer. Images were captured using a Leica Biosystems anatomic pathology scanner. Data source: Dr Jose Coelho Lima Junior, Prof Elizabeth Soilleux, and Dr Ying-Jie Wang.

In the Actc1^{E99K} mouse hearts, immune cell infiltration follows a distinct temporal pattern (Figure 1.5). With the onset of the advanced stage, macrophages predominate, remaining elevated until a drastic increase in the late stage. Dendritic cells and T lymphocytes show a synchronised, modest increase at 10 weeks, followed by a continuous accumulation. This coordinated infiltration suggests a progressive immune response that parallels the structural remodelling observed in the heart. Monocytes and neutrophils, however, surge dramatically in the

late stage, after 36 weeks. This late-stage monocyte surge is particularly relevant, given reports linking higher monocyte counts to increased survival risk in HCM patients [235, 236]. These findings highlight the importance of immune cell dynamics in the progression of adverse remodelling and suggest that targeting specific immune populations may offer therapeutic avenues.

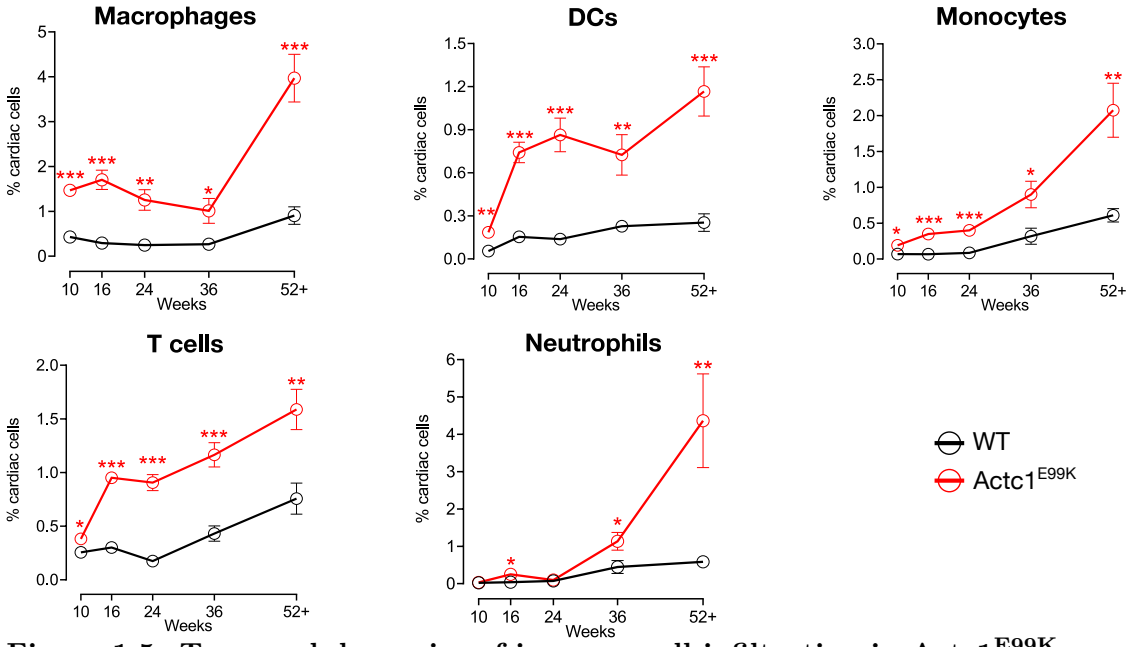

Figure 1.5. Temporal dynamics of immune cell infiltration in Actc1^{E99K} mouse hearts.
Cardiac immune cell infiltration was assessed in Actc1^{E99K} mice and their wild-type littermates at various time points between 10 and 52 weeks of age. Following cardiac cell isolation and cardiomyocyte depletion, live non-cardiomyocyte cells were analysed by multi-colour flow cytometry. Using fluorescently-labelled antibodies against cell-surface and intracellular markers, immune cells were identified and quantified. The pan-leukocyte marker CD45 defined the overall immune cell population. Within this CD45$^+$ population, macrophages (F4/80$^+$), dendritic cells (CD11c$^+$), monocytes (Ly6C$^+$), T cells (CD3e$^+$), and neutrophils (Ly6G$^+$) were identified using a specific gating strategy. Data are presented as the percentage of each cell type within the total live non-cardiomyocyte population (mean ± SEM; n ≥ 3 mice per group). A two-way mixed-effects ANOVA, followed by Benjamini, Krieger, and Yekutieli post-hoc correction for multiple comparisons, was used to determine statistical significance between Actc1^{E99K} and WT mice across time points (adjusted p-values: *: < 0.05, **: < 0.01, ***: < 0.001, and ****: <0.0001). Data source: Dr Ying-Jie Wang.

Choosing the Actc1^{E99K} model as a tool in this study

This project harnesses the power of transcriptomic profiling to uncover the molecular underpinnings of adverse cardiac remodelling in HCM. The Actc1^{E99K} model

was selected because it reproduces key pathological features of human HCM—notably early apical hypertrophy, progressive interstitial fibrosis and chronic inflammation—in a manner that closely mimics the spatial and temporal dynamics of the human disease.

A defining characteristic of the Actc1^{E99K} model is its epicardial, patchy pattern of fibrosis. To place this in context, cardiac fibrosis can be broadly categorised by its histological pattern. 'Replacement fibrosis' is characterised by a dense, focal scar that replaces areas of dead cardiomyocytes, a typical outcome of acute necrotic injury such as myocardial infarction [237, 238]. In contrast, 'interstitial fibrosis' involves a more widespread accumulation of extracellular matrix proteins within the spaces between viable cardiomyocytes, without significant cell loss [237, 239]. This latter type is often described as 'diffuse' to reflect its pervasive, rather than localised, nature [239, 240]. Whereas models based on acute necrotic injury develop dense replacement fibrosis confined to zones of infarction, and pressure-overload paradigms produce predominantly subendocardial fibrosis (fibrosis of the layer just beneath the inner endocardial surface) [241], the Actc1^{E99K} hearts display a sparsely distributed, diffuse collagen network that remodels the extracellular matrix gradually. This low-grade, pervasive interstitial fibrosis parallels the chronic remodelling seen in patients with HCM, in whom interstitial collagen accumulates over decades rather than weeks. Such a pattern creates a tissue milieu in which mechanical stiffness increases modestly and heterogeneously, offering a unique substrate in which to investigate how local variations in matrix composition influence cardiomyocyte signalling and chamber compliance.

Equally important is the inflammatory milieu of the Actc1^{E99K} model. Instead of an acute, high-amplitude immune reaction, these mice manifest a sustained, low-level infiltration of T lymphocytes, macrophages and dendritic cells. Immune cells are dispersed throughout the myocardium rather than clustered around a focal injury, suggesting that persistent, subclinical inflammation drives the activation of profibrotic programmes. This chronic inflammatory tone may engage

signalling pathways—such as TGF-β and NF-κB—in a temporally extended fashion, thereby linking immune cell recruitment to progressive fibroblast activation and collagen deposition.

Together, the distinctive fibrotic architecture and smouldering inflammatory profile of the Actc1^{E99K} model make it particularly well suited to disentangle the crosstalk between inflammation, fibrosis and hypertrophy. The diffuse nature of fibrosis implies the existence of compensatory mechanisms that regulate collagen turnover to preserve myocardial compliance; transcriptomic analyses in this context can pinpoint matrix metalloproteinases, their inhibitors and matricellular proteins that mediate this balance. Likewise, the pattern of immune cell infiltration points to immune–fibroblast interactions that may be absent in models driven by acute or regionalised injury, offering opportunities to identify cytokines and chemokines that sustain low-grade inflammation.

Limitations of genetic engineered mouse models

Despite the substantial advances afforded by the genetic mouse models of HCM, important limitations need to be recognised, especially when comparing these models with the human disease. The fundamental differences in cardiovascular physiology between mice and humans—such as differences in heart rate, ion channel composition, myosin isoform expression, and calcium handling—can significantly influence the phenotype produced by the same genetic mutation. For instance, the α-MHC^{R403Q} mutation in the murine heart may lead to a different degree of contractile dysfunction compared with human hearts due to discrepancies in post-translational modifications and compensatory regulatory mechanisms [242, 243]. Furthermore, the overexpression or variable expression levels of the mutant protein in transgenic systems may not precisely reflect the heterozygous state observed in human patients, thereby complicating direct comparisons between experimental models and clinical manifestations.

In addition to the intrinsic species-specific differences, the stage of disease progression in animal models often differs from that in human HCM. In mice, the

disease may progress much more rapidly and may reach an overt state of dysfunction within weeks to months, whereas human HCM typically develops insidiously over decades. This temporal discrepancy can impact studies aimed at deciphering early molecular events in HCM pathogenesis, as the window for intervention in murine models may be substantially compressed relative to the human condition. Such limitations emphasise the necessity for cautious interpretation of data and underscore the importance of validating findings from mouse models in larger animals or, ultimately, in human studies.

1.6.6 Integrative discussion and translational perspectives

The wealth of mechanistic insights garnered from genetically engineered HCM mouse models underscores both the power and the complexity of recapitulating human disease in the laboratory. Models such as α-MHC$^{\mathrm{R403Q}}$ and Actc1$^{\mathrm{E99K}}$ have unequivocally demonstrated that sarcomeric mutations drive a primary hypercontractile state—manifest as increased myosin ATPase activity, a shift towards the DRX, and sensitisation of the myofilaments to calcium—that precedes overt hypertrophy and fibrosis [225, 231]. Delving deeper, it becomes apparent that this hypercontractile milieu imposes an energetic strain on cardiomyocytes, provoking a cascade of secondary signalling events. For instance, For instance, in mouse models of cardiac pressure overload and genetic cardiomyopathy, the energetic strain is thought to activate hypoxia-inducible factor (HIF)-mediated transcriptional programmes and engages AMPK and mammalian target of rapamycin complex 1 (mTORC1) pathways. These pathways in turn augment profibrotic cytokine production (notably TGF-β isoforms) and extracellular matrix deposition (e.g., *Col1a1*, *Tgfb2*) even before histological fibrosis is evident [226, 244]. This integrative perspective reveals that sarcomeric defects and downstream metabolic stress coalesce to drive a self-sustaining loop of remodelling.

A second key lesson is that the inflammatory response in HCM is neither purely acute nor confined to discrete regions, but rather manifests as chronic, low-grade infiltration by macrophages, dendritic cells and T lymphocytes, as shown in the

Actc1^{E99K} model (Figures 1.4 and 1.5). Mechanistically, it is hypothesised, based on findings from other animal models of cardiac stress, that the initial myocyte stress releases damage-associated molecular patterns (DAMPs). These molecules can engage pattern recognition receptors on resident macrophages, skewing them towards a profibrotic, M2-like phenotype. These macrophages secrete additional TGF-β and IL10, which reinforce fibroblast activation and collagen cross-linking, while also modulating cardiomyocyte viability and calcium handling via paracrine NF-κB and JAK-STAT signals. This layered interpretation—whereby mechanical, metabolic and immune stimuli converge—explains why antifibrotic strategies targeting only one axis often yield incomplete benefit.

Translating these insights into therapeutic avenues has already borne fruit. The small-molecule myosin inhibitor mavacamten, developed to temper aberrant ATPase activity and bias myosin heads back towards the energy-sparing super-relaxed state, emerged directly from observations in the α-MHC^{R403Q} model [225]. Early clinical trials have demonstrated improvements in LVEF, reductions in LVH and amelioration of EF reserve [120–122]. Complementing such sarcomere-centric approaches, interventions aimed at the fibrotic and inflammatory milieu hold promise. Preclinical studies suggest that selective antagonism of TGF-β signalling—whether via neutralising antibodies or receptor kinase inhibitors—can attenuate collagen deposition and preserve diastolic function in mouse models of pressure-overload-induced fibrosis [245, 246]. Similarly, blockade of CCR2 to inhibit monocyte recruitment, or modulation of matrix metalloproteinases and their tissue inhibitors, has shown efficacy in reducing diffuse fibrosis in rodent models of chronic cardiac remodelling [247–249].

Looking ahead, several strategies will be critical to bridge the translational gap. First, the development of larger mammalian HCM models—such as gene-edited pigs bearing precise human mutations—promises to recapitulate human myosin isoform ratios, heart rates and electrophysiological properties more faithfully than mice [250]. Second, advances in genome editing now enable the creation of knock-in alleles that preserve endogenous regulatory elements, thereby avoiding

artefacts of transgene overexpression. Third, integrating longitudinal multi-omics—including single-cell transcriptomics, proteomics and spatial metabolomics—with high-resolution imaging (e.g., strain-encoded MRI, four-dimensional echocardiography) will afford a systems-level map of how mutations translate into organ-level dysfunction over time. Computational models that simulate myofilament mechanics and myocardial energy flux can then test *in silico* the impact of candidate drugs or genetic modifiers, refining hypotheses before *in vivo* validation.

Furthermore, precision medicine approaches in HCM will benefit from patient-derived induced pluripotent stem cell-derived cardiomyocyte (iPSC-CM) platforms, which allow direct comparison of human cardiomyocyte phenotypes with those observed in animal models. By correlating transcriptomic and functional readouts across species, we can identify conserved disease nodes—such as persistent TGF-β activation, which is observed in both human HCM tissue and experimental models, or dysregulated NF-κB signalling—that represent high-value targets for broad-spectrum therapy [116]. Biomarker discovery efforts should focus on circulating signatures of collagen turnover (e.g., PICP, CITP), inflammatory mediators (e.g., TNF, IFN-γ) and specific microRNAs implicated in sarcomeric regulation, enabling real-time monitoring of disease activity and therapeutic response.

In sum, the integrative narrative emerging from HCM animal models reveals a multifaceted pathogenesis in which primary sarcomeric hypercontractility begets metabolic stress, immunological activation and fibrotic remodelling. Translational efforts that combine sarcomere modulators, targeted anti-inflammatory agents and antifibrotic therapies—validated in physiologically relevant large-animal models and human cell systems—hold the greatest promise for altering the natural history of HCM. By continuing to leverage and refine these experimental platforms, we move ever closer to truly mechanism-based, personalised treatments for patients afflicted by this complex and heterogeneous disease.

1.7 Objectives

In light of the comprehensive overview of HCM pathogenesis, genetic and molecular bases, and the distinct patterns of adverse remodelling—particularly the roles of chronic inflammation and fibrosis—this thesis aims to address critical knowledge gaps in the understanding of HCM. The overarching goal is to elucidate the temporal and cellular dynamics of adverse cardiac remodelling, with particular emphasis on non-cardiomyocyte populations. By integrating bulk and single-cell transcriptomic profiling in the Actc1^{E99K} HCM mouse model, and correlating these results with data from human HCM samples, this study strives to identify novel biomarkers and potential therapeutic targets across different disease stages. A central objective of this research is to characterise the temporal progression of gene expression signatures related to fibrosis, chronic inflammation, and metabolic reprogramming in the Actc1^{E99K} mouse model. This analysis will be complemented by a detailed dissection of the cellular heterogeneity among non-cardiomyocytes using single-cell and single-nucleus RNA sequencing techniques. Such high-resolution approaches will delineate cell-type-specific contributions to adverse remodelling and provide insights into the dynamic interplay between different cellular populations. Additionally, by comparing the molecular profiles of late-stage HCM in both mouse and human samples, the study aims to identify conserved pathways—particularly those governing immune activation and profibrotic remodelling—that hold promise as translatable therapeutic targets. Parallelly, early-stage transcriptomic alterations, notably the down-regulation of ECM-receptor interaction genes in fibroblasts, will be investigated as potential diagnostic markers that could enable timely therapeutic intervention prior to the onset of irreversible fibrosis. Based on current literature and preliminary data, the study is built on several key hypotheses. It is hypothesised that adverse remodelling in HCM is accompanied by a temporal shift, where the early disease stage is marked by subtle changes in inflammation and fibrotic signalling that intensify as the disease progresses. Moreover, chronic inflammation within the non-cardiomyocyte compartment is proposed to be a primary contributor to fibrosis, creating a direct mecha-

nistic link between the stress signals emanating from mutant cardiomyocytes and the ensuing matrix remodelling. Furthermore, it is anticipated that a subset of transcriptomic changes—particularly the up-regulation of both profibrotic and immune response genes—will be conserved between the Actc1^{E99K} mouse model and human HCM. Such conservation would validate these molecular alterations as potential targets for therapeutic intervention. In addition, the observed early down-regulation of specific ECM-receptor interaction mediators in fibroblasts may serve as a diagnostic indicator, offering a critical window for pre-emptive intervention before the progression to irreversible remodelling occurs.

By addressing these aims and testing the outlined hypotheses, this thesis intends to advance our understanding of the complex molecular cascades underpinning HCM progression. The insights gained from this integrative transcriptomic approach are expected to provide a framework for stage-specific therapeutic strategies that may ultimately attenuate or even reverse the adverse remodelling processes, thereby improving clinical outcomes for patients with this debilitating cardiac disease.

2 Methodology

Disclaimer: The wet-lab experimental procedures described in the subsequent sections—including sample collection, tissue processing, library preparation, and cell sorting—were developed and executed by wet-lab collaborators, notably Dr Ying-Jie Wang (who provided the detailed method description), Mr Moustafa Attar, Dr Kamayani Singh, Dr Sunitha Balaraju, and Mr Jacky Fung. These wet-lab method descriptions are included solely for the sake of completeness and reference purposes. All bioinformatics analyses, including data preprocessing, statistical interrogation, and visualisation, were conducted exclusively by the author.

2.1 Bulk RNA-seq

2.1.1 Library preparation

Total RNA was extracted from snap-frozen murine hearts using RNeasy Mini Kit (QIAGEN, 75144). Initially, the tissue was pulverised using a mortar and pestle, followed by the addition of an appropriate amount of RLT buffer. The tissue was then homogenised using a 20-gauge needle fitted to an RNase-free syringe. Contaminating proteins and DNA were removed using proteinase K and RNase-free

DNase, respectively. The RNA was eluted in a fresh collection tube with RNase-free water. Total RNA was quantified using the Quant-IT RiboGreen RNA Assay Kit (ThermoFisher Scientific, Invitrogen™, R11490), and the integrity of RNA was assessed using a high sensitivity RNA ScreenTape (Agilent Technologies, 5067-5579). RNA integrity number estimates for all samples were above 8.
The purification of mRNA, generation of double-stranded cDNA, and library construction were performed using the NEBNext® Ultra™ II Directional RNA Library Prep Kit for Illumina® (New England Biolabs, E7760) with minor modifications to the manufacturer's specifications. Oligo d(T) beads were used to enrich mRNA with poly (A) tails. RNA was fragmented, followed by first and second strand cDNA synthesis. Fragments were end-repaired and A-tailed, followed by adaptor ligation. Finally, there was a USER-enzyme digestion and PCR enrichment step. Amplified libraries were analysed for size distribution using the Agilent Tapestation 2200 D1000. Libraries were quantified using Picogreen, and relative volumes were pooled accordingly. Sequencing was performed using the 150PE strategy on an Illumina NovaSeq6000 platform.

2.1.2 Data analysis

Data preprocessing

Reads were quality checked and trimmed using `fastp` v0.23.3 [251, 252]. Specifically, polyG tails and adapters were trimmed, and reads with more than 5 "N" bases or where over 40% of bases had a Phred quality score below 15 were discarded. After trimming, reads shorter than 15 bases were also discarded. Trimmed reads were then aligned to the mouse reference genome (GRCm39) from GENCODE release M35 [253] using `STAR` v2.7.3a [254] following the Encyclopedia of DNA Elements (ENCODE) standard [255]. Reads mapping to the genome were summarised at the gene level using `featureCounts` v1.6.4 [256]. The raw gene count matrix was subsequently imported into the R environment v4.1.0 for further processing and analysis with the `edgeR` package v3.40.2 [257].

Differential expression analysis

Genes with very low expression were excluded based on the following heuristic: to be retained, a gene needed to be expressed at the equivalent of 10 reads or more (after normalising for library size) in at least as many samples as the smallest experimental group considered. The raw counts were then normalised using the Trimmed Mean of M-value (TMM) method [258] in the `edgeR` package v3.40.2 [257] before transforming to z-scores to generate the corresponding heatmaps. Multiple testing correction was performed using `edgeR`'s default Benjamini-Hochberg method for controlling the False Discovery Rate (FDR). Genes with FDR < 0.05 and an absolute $\log_2$-fold change greater than 1 between conditions were considered significantly changed in expression.

Enrichment analysis

Gene Set Enrichment Analysis (GSEA) was performed using `fgsea` v1.24.0 [259] using log2FC ordered gene vector with 1,000 permutations against the gene sets obtained from the Molecular Signatures Database (MSigDB) v2023.1 [260, 261]. Terms with adjusted p-values < 0.05 were considered significant.

Temporal trend analysis

To understand the temporal trend in gene expression changes, I adopted a single-cell method for processing bulk temporal data. The traditional single-cell Leiden clustering method can cluster cells with similar expression profiles before annotation. Here, I clustered genes with similar trends over time by considering the cells in the single-cell data as genes and the genes in single-cell data as time points, using the Leiden clustering approach to effectively cluster genes with similar temporal trend profiles.

After clustering, I manually combined the clusters with similar trends and then extracted the genes with these similar temporal trends. To understand their biological functions, I performed enrichment analysis using the `PANTHER` classification system [262] and `g:Profiler` [263] version e111_eg58_p18_30541362.

2.2 Single-cell multiplexed gene expression profiling

2.2.1 Cell isolation

Single cell suspension of non-cardiomyocytes were prepared from age- and gender-matched wild-type (WT) and Actc1^{E99K} hearts (N = 3 each). Hearts were perfused with cold 1 x HBSS (Life Technologies, 14065072), dissected, and then enzymatically digested in 5 mL of 1 x HBSS containing 300 U/mL collagenase II (Life Technologies, 17101015) and 10 U/mL DNase I (VWR, A3778.0500). Digestion was performed in a C-tube (Miltenyi Biotec, 130-093-237) using a gentleMACS Dissociator (Miltenyi Biotec, 130-093-235) with a tailored programme for 45 minutes at 37°C on a rolling station. A second programmed digestion step, followed by filtration through a 70 μm filter to remove large debris and erythrocyte depletion (BioLegend, 420302), yielded a clear single-cell suspension in PBS containing 2 mM EDTA. Non-cardiomyocytes were then blocked for one hour at 4°C in Stain Buffer (BD Biosciences, 554656) containing 2% mouse FcR blocker (Miltenyi Biotec, 130-092-575) and a cocktail of 10% rat (Life Technologies, 10710C), rabbit (Life Technologies, 16120099), and goat serum (Merck, G6767-100ML).

2.2.2 Cell labelling and sorting

Cells were then labelled for one hour at 4°C with the following antibodies: FITC anti-mouse CD45 (BioLegend, 103108, 1:100 dilution), AF647 anti-mouse FAP (Biotechne, FAB9727R, 1:100 dilution), BV421 anti-mouse CD31 (Biosciences, 563356, 1:50 dilution), BUV395 anti-mouse CD90.2 (Biosciences, 565257, 1:100 dilution), and the live/dead marker FVS620 (Biosciences, 564996, 1:2000 dilution). A hashtag staining approach was employed for multiplexing. Individual samples were stained with one of the following TotalSeq™ anti-mouse hashtag antibodies according to the manufacturer's instructions: Hashtag 1 (barcode

ACCCACCAGTAAGAC, BioLegend, 155861), Hashtag 2 (barcode GGTCGAGAGCATTCA, BioLegend, 155863), or Hashtag 3 (barcode CTTGCCGCATGTCAT, BioLegend, 155865). Cells of the same genotype were pooled and sorted using a five-laser (355 nm, 405 nm, 488 nm, 561 nm, 640 nm) BD FACSAria™ Fusion Cell Sorter. Live cells were sorted into the following populations: immune cells ($CD45^+CD31^-$), endothelial cells ($CD45^-CD31^+$), stromal cells ($Thy1^+Fap^-$, $Thy1^-Fap^+$, and $Thy1^+Fap^+$), and an unknown ($Thy1^-Fap^-$) population.

2.2.3 Library preparation

The densities of cell suspensions were determined using acridine orange/propidium iodide fluorescence on a LUNA-FX7 cell counter (Logos Biosystems). A quantity of 14,000–30,000 cells per sample were loaded onto the 10x Genomics Chromium Controller (Chip K). Gene expression and feature barcoding libraries ($CD45^+$ fractions) were prepared using the 10x Genomics Single Cell 5' Reagent Kits v2 (Dual Index) following the manufacturer's user guide (CG000330 Rev B). The final libraries were diluted to 10 nM for storage. The 10nM library was denatured and further diluted prior to loading on the NovaSeq6000 sequencing platform (Illumina, v1.5 chemistry, 150bp paired end).

2.2.4 Data analysis

Gene expression data preprocessing

Raw data were pre-processed using the 10x Genomics `cellRanger count` v7.1.0 pipeline [264] with the mouse reference genome mm10 provided by 10x Genomics (version 2020-A). The pipeline first extracts and corrects the cell barcodes and unique molecular identifier (UMI) from the feature library, then matches the feature barcode (FB) reads against the list of features declared in the FB reference, outputting the counts for each feature in the feature-barcode matrix. Since droplet-based scRNA-seq experiments capture ambient mRNAs along with cell-specific mRNAs, this ambient RNA contamination was removed using `SoupX` v1.6.0 [265], and doublets (or multiplets) were removed using `DoubletFinder`

v2.0 [266]. The processed data were then imported into `scanpy` v1.10.1 [267], and potential batch effects between samples were corrected using `harmony` v0.1 [268].

Cell annotation

Cells were filtered for mitochondrial genes (`percent_mit` $< 20\%$), number of features/genes ($500 <$ `nFeature_RNA` $< 5{,}000$), and ribosomal genes (`percent_ribo` $< 20\%$). Samples were then integrated using `harmony` v0.1 [268]. Cells were clustered using the Leiden algorithm [269] in `scanpy` v1.10.3 [267] and annotated based on their marker genes using the `scanpy.tl.rank_genes_groups` method.

Differential expression analysis

Differential expression analysis was performed using a "pseudobulk" approach. Specifically, the pseudobulk profiles were generated using `decoupler-py` v1.6.0 [270], a faster and memory-efficient Python implementation of the `decoupler` R package. Low-quality samples were filtered using the recommended threshold, which is to have at least 10 cells with 1000 accumulated counts. Then, downstream differential expression analysis was performed using the `limma-voom` pipeline v3.60.2 [271], where genes with FDR < 0.05 and an absolute $\log_2$-fold change greater than 1 between conditions were considered significantly changed in expression. Cell types with fewer than 50 cells in at least two independent biological replicates were excluded from pseudobulk aggregation and thus omitted from all downstream analyses, including differential expression, enrichment analysis, pathway activity inference, and cell–cell communication.

Enrichment analysis

Similar to bulk RNA-seq analysis, GSEA was performed using `fgsea` v1.24.0 [259] using log2FC ordered gene vector with 1,000 permutations against the gene sets obtained from the MSigDB v2023.1 [260, 261]. Terms with adjusted p-values < 0.05 were considered significant. All GSEA analyses were performed only on pseudobulk profiles derived from cell types meeting the minimum representation criteria (≥ 50 cells in ≥ 2 replicates).

Pathway activity analysis

Pathway RespOnsive GENes for activity inference from gene expression (PROGENy) is a method used to infer the activity of biological pathways from gene expression data by utilising a vast collection of perturbation experiments to identify common pathway-responsive genes [272]. It overcomes the limitations of traditional mapping methods and provides insights into driver mutations, drug indications, and pathway distinctions [272]. Although the original study was developed for human data, a recent benchmark study shows that PROGENy is also applicable to mouse data [273]. Additionally, it has been shown that PROGENy can be applied to scRNA-seq data [274]. Therefore, I inferred the pathway activities in the mouse scRNA-seq data using the `progeny` R package v1.26.0. Pathway activity inference by PROGENy was restricted to cell types that satisfied the inclusion threshold (≥ 50 cells in ≥ 2 replicates).

Cell-cell communication analysis

Cell-cell communication analysis enables the exploration of how cells interact and signal to each other, which is crucial for understanding complex biological processes and disease mechanisms. In this dissertation, I used `LIANA+` v1.2.0, which is an all-in-one cell-cell communication framework in Python [275]. `LIANA+` offers several advantages, including the decoupling of methods from their respective resources, allowing any resource to be combined with any method. It also features a robust and extendable architecture, aggregates ranked results from multiple methods, and provides access to a customisable plethora of resources.

RNA velocity analysis

RNA velocity analysis was performed using `velocyto` (v0.17) [276] to calculate spliced and unspliced RNA profiles. These profiles were then integrated into a `scanpy` `AnnData` object for each sample using `scvelo`'s (v0.3.2) `read_loom` method [277]. RNA velocities were subsequently derived by modelling the transcriptional dynamics of splicing kinetics. This involved fitting a steady-state ratio

of unspliced (pre-mature) and spliced (mature) mRNA counts for each gene, representing a constant transcriptional state. Velocities were calculated as the residuals from this steady-state ratio. A positive velocity, indicating up-regulation, corresponds to a higher abundance of unspliced mRNA than expected at steady state. Conversely, negative velocity signifies down-regulation.
By combining velocities across genes, the future state of individual cells was estimated. To project these velocities onto a lower-dimensional embedding, transition probabilities between cells were estimated based on the cosine correlation between potential cell-to-cell transitions and the velocity vector. This resulted in a velocity graph, a matrix storing these probabilities. Finally, the velocities were projected onto a Uniform Manifold Approximation and Projection (UMAP) embedding for visualisation.

Human single-nucleus RNA-seq data analysis

Human late-stage snRNA-seq data, comprising 15 LV samples with HCM and 16 non-failing (NF) LV samples, were obtained from a publicly available dataset [135]. Mid-stage snRNA-seq data, also publicly available [136], comprised LV interventricular septum (IVS) tissue from 10 male HCM patients undergoing usrgical myectomy and two male healthy heart transplant donors. To ensure comparability between human and mice results, the same downstream analysis methods were applied to both species unless otherwise stated.

2.3 Code availability

All the code used for processing the data has been deposited in the GitHub repository (https://github.com/siwei-deng/DPhil-thesis-project.git).

3

Bulk Temporal Transcriptomic Profiling Reveals Disease Progression in Actc1^{E99K} HCM Mouse Models

3.1 Mapping the dynamic gene expression landscape in Actc1^{E99K} HCM mouse model

3.1.1 Comparing longitudinal datasets uncovers the evolution of cardiac transcriptional changes

To characterise the transcriptomic landscape of the Actc1^{E99K} HCM mouse model, bulk RNA sequencing was performed at four time points, representing different stages of disease progression (Figure A.1). A summary of the samples analysed at each time point is provided in Table 3.1, with full details available in Appendix A.1, Table A.1. At 5 weeks, the early stage is characterised by cardiac hypertrophy and fibrosis with preserved systolic function. By 10 weeks, significantly reduced systolic function and increased immune cell infiltration were observed in Actc1^{E99K} mice, suggesting a transition to a more advanced stage of HCM. The 24-week time point represents a mid-advanced stage, characterised by increasing cardiac hypertrophy and fibrosis with slowly progressive systolic dysfunction. Finally, the 60-week time point represents a later stage with se-

vere fibrosis and rapid deterioration of systolic function, mirroring overt human HCM. This temporal dataset enabled the tracking of progressive transcriptional changes, providing insights into the molecular mechanisms underlying adverse remodelling.

Principal Component Analysis (PCA) of the combined dataset from all time points reveals a clear separation between Actc1^{E99K} and WT mice, as well as a distinct temporal trajectory of disease progression (Figure 3.1 and A.1). The WT samples from all time points cluster together, indicating a stable transcriptomic profile over time. In contrast, the Actc1^{E99K} samples show a progressive shift away from the WT cluster as the animals age. The distance between the Actc1^{E99K} and WT groups is smallest at 5 weeks and greatest at 60 weeks, illustrating the cumulative impact of the mutation on the cardiac transcriptome. This pattern highlights that the most significant transcriptional alterations occur at later stages of the disease.

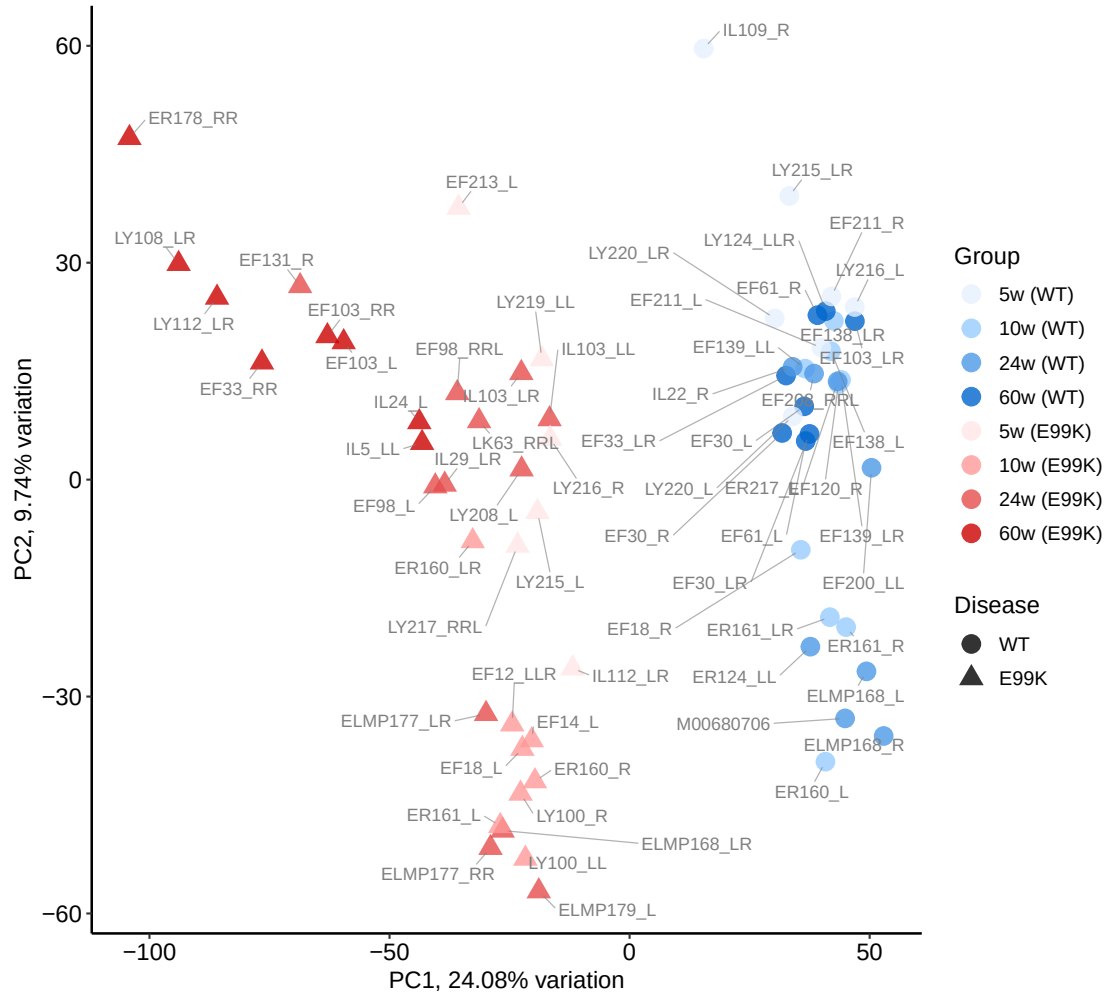

Figure 3.1. Principal component analysis (PCA) of bulk RNA-seq data from Actc1^{E99K} HCM mice across all time points.
PCA plot of all samples from the 5, 10, 24, and 60-week time points, following correction for inter-individual batch effects. Wild-type (WT) samples are shown as blue circles and Actc1^{E99K} samples as red triangles. The colour saturation for each point corresponds to the time point, becoming darker with increasing age.

Table 3.1. Summary of temporal bulk Actc1^{E99K} samples. The table provides a breakdown of the number of wild-type (WT) and Actc1^{E99K} mice analysed at each of the four time points (5, 10, 24, and 60 weeks), categorised by sex. Full sample details are provided in Appendix A.1, Table A.1.

Group	Genotype	N (Total)	N (Female)	N (Male)
5 weeks	WT	7	3	4
	Actc1^{E99K}	6	3	3
10 weeks	WT	9	4	5
	Actc1^{E99K}	8	4	4
24 weeks	WT	8	4	4
	Actc1^{E99K}	12	8	4

Continued on next page

Group	Genotype	N (Total)	N (Female)	N (Male)
60 weeks	WT	8	4	4
	Actc1^{E99K}	8	4	4

These findings were contextualised by comparing them with publicly available bulk RNA-seq datasets from other HCM mouse models at the classic stage, including the α-MHC^{R403Q} and α-MHC^{R719W} models [140] and the Tnt^{R92W} model [278]. A summary of these public mouse model samples is presented in Table 3.2, with complete details in Appendix A.2 (Tables A.2 and A.3). These models displayed clear transcriptomic separation between mutant and WT mice (Figure 3.2A and B).

Table 3.2. Summary of public HCM mouse model samples. This table outlines the key characteristics of the external mouse model datasets incorporated into this study, including the specific model, genotype, age at sampling, total number of samples (N), and average mapping rate. Full details are available in Appendix A.2, Tables A.2 and A.3.

Model	Genotype	Age (weeks)	N (Total)	Avg Mapping Rate (%)
Teekakirikul [140]	WT	38–76	9	80.66
	α-MHC^{R403Q}	46–48	8	84.76
	α-MHC^{R719W}	35–36	5	85.97
Vakrou [278]	WT	24	3	97.87
	Tnt^{R92W}	24	3	97.05

To further extend the analysis, I incorporated publicly available bulk RNA sequencing (RNA-seq) data from human HCM patient samples [279]. This dataset included 28 HCM samples collected during septal myectomy surgery, comprising nine female and 19 male patients. This dataset included samples from 28 HCM patients and nine non-failing donor hearts, as summarised in Table 3.3 (see Appendix A.3, Table A.4 for full details). Importantly, these samples represented classic-stage HCM, providing a relevant comparison to the classic-stage Actc1^{E99K} mouse model. The data quality was high, and PCA clearly separated the HCM and control groups (Figure 3.2C). This cross-species comparison allowed for the identification of conserved and species-specific transcriptional signatures.

Table 3.3. Summary of human bulk RNA-seq samples from hypertrophic cardiomyopathy patients and non-failing donor hearts. The table details the human cohort from Liu et al. (2019) [279], summarising the number of control and HCM samples, their distribution by sex, and the average mapping rate. These samples, obtained during septal myectomy, represent an established stage of human HCM. Full details are in Appendix A.3, Table A.4.

Group	N (Total)	N (Female)	N (Male)	Avg Mapping Rate (%)
Control	9	1	8	97.41
HCM	28	9	19	97.26

To ensure the statistical robustness of the differential expression analysis, a post-hoc power calculation was performed using the `RNASeqPower` R package (version 1.30.0) [280]. The analysis was based on the number of mapped reads for each dataset, assuming a moderate biological coefficient of variation of 0.3, a significance level of 0.05, and a fold change of 2. As detailed in Table 3.4, the statistical power was high across all datasets, ranging from 0.80 for the Tnt^{R92W} model to over 0.99 for the human and Actc1^{E99K} datasets. This confirms that the sequencing depth and number of biological replicates were sufficient to confidently detect true differential expression with the chosen effect size threshold.

Table 3.4. Post-hoc statistical power analysis confirms the robustness of all bulk RNA-seq datasets. The power to detect a true differential expression effect (fold change of 2) was calculated for each dataset using the `RNASeqPower` R package (v1.30.0) [280]. The analysis assumed a biological coefficient of variation of 0.3 and a significance level (α) of 0.05. The consistently high power across all datasets (ranging from 0.80 to >0.99) confirms that the sample sizes and sequencing depths were sufficient for robust differential expression analysis.

Dataset	Avg Mapped Reads per Sample	Avg Read Pairs	Avg Depth Coverage	Power
Actc1^{E99K} @ 5 weeks	83,934,135	41,967,067	1,582.59	0.991
Actc1^{E99K} @ 10 weeks	152,734,131	76,367,065	2,879.82	0.998
Actc1^{E99K} @ 24 weeks	113,746,688	56,873,344	2,144.71	0.999
Actc1^{E99K} @ 60 weeks	112,748,118	56,374,059	2,125.88	0.996
α-MHC^{R403Q}	61,682,111	30,841,055	1,448.62	0.998
α-MHC^{R719W}	43,302,300	21,651,150	1,016.96	0.990
Tnt^{R92W}	25,014,064	12,507,032	651.71	0.801
Human	113,228,187	56,614,093	1,502.26	>0.999

Comprehensive transcriptomic analysis of the Actc1^{E99K} model revealed significant insights into HCM's molecular underpinnings (Table 3.5). Differential gene expression analysis across four time points in the Actc1^{E99K} model—5, 10, 24,

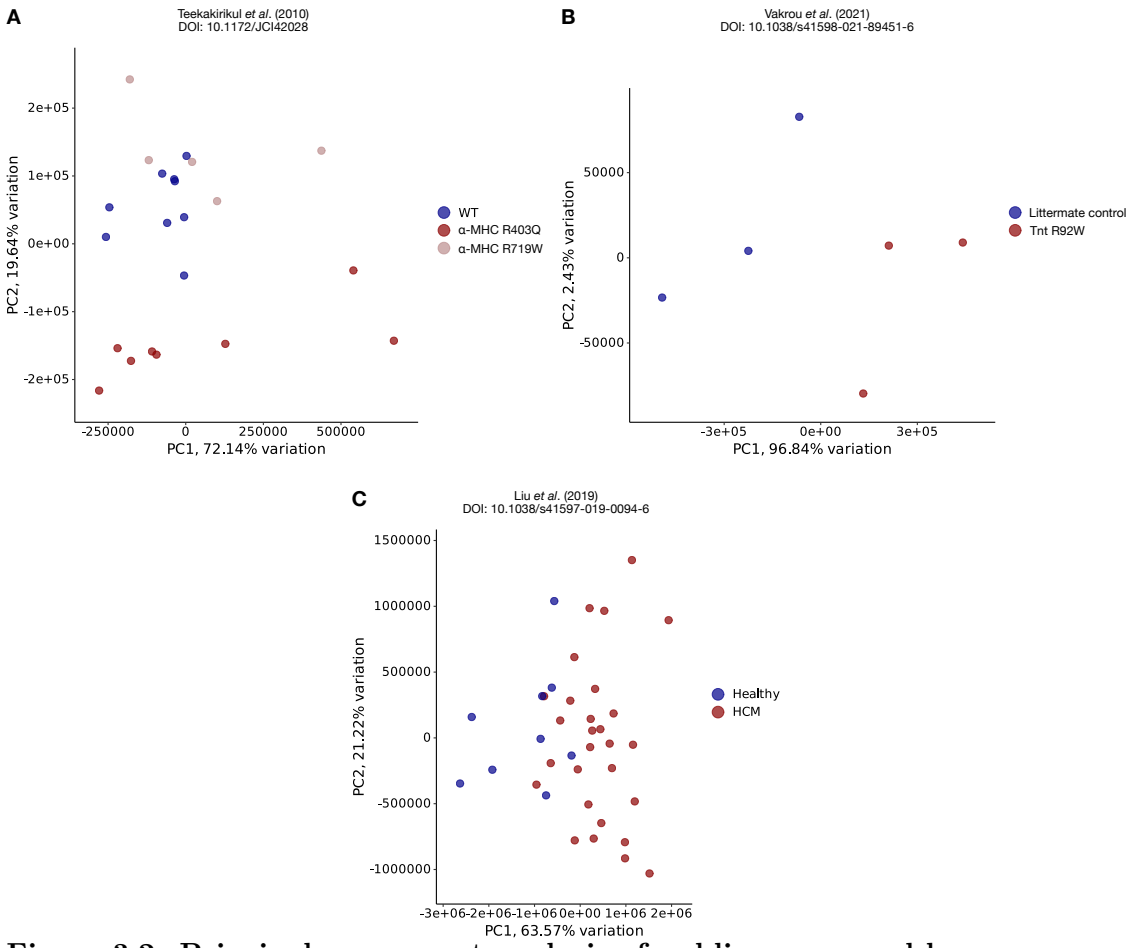

Figure 3.2. Principal component analysis of public mouse and human datasets demonstrates clear transcriptomic separation between HCM and control samples.
PCA plots show the transcriptomic profiles of publicly available datasets used for comparison. In all three independent cohorts, a clear separation is observed between control (blue) and HCM (red/pink) samples along the first principal component. (A) Data from α-MHC$^{\mathrm{R403Q}}$ and α-MHC$^{\mathrm{R719W}}$ mouse models [140]. (B) Data from the Tnt$^{\mathrm{R92W}}$ mouse model [278]. (C) Data from human septal myectomy tissue from HCM patients and non-failing donor hearts [279]. This consistent separation validates these datasets for comparative analysis of HCM-related gene expression signatures.

and 60 weeks—demonstrated progressively increasing transcriptional changes. The number of differentially expressed genes (DEGs) rose from 5,565 at 5 weeks to 9,495 at 60 weeks (adjusted p-value < 0.05). DEGs with an absolute $\log_2$ fold change greater than 1 also increased substantially, from 1,017 at 5 weeks to 2,887 at 60 weeks, indicating a substantial escalation in the magnitude of transcriptional alterations as the disease progresses. This trend underscores the dynamic nature of gene expression changes associated with disease progression in

the Actc1^{E99K} model, reflecting the increasing complexity of adverse remodelling over time.

To further characterise these transcriptional changes, the differentially expressed genes were categorised by their annotated gene biotype (Figure 3.3). This analysis revealed that protein-coding genes consistently constituted the vast majority of DEGs across all time points and statistical thresholds, typically accounting for around 90% of the total. Long non-coding RNAs represented the second most frequent biotype, though they comprised less than 10% of the identified genes. Other biotypes, such as pseudogenes and small non-coding RNAs, were present in much smaller proportions. This distribution remained stable throughout the disease progression in the Actc1^{E99K} model, indicating that the observed transcriptomic dysregulation is predominantly driven by changes in protein-coding gene expression.

In comparison, other HCM mouse models exhibited fewer transcriptional differences. α-MHC^{R403Q} at 48 weeks and α-MHC^{R719W} at 36 weeks yielded 2,665 and 592 DEGs, respectively (adjusted p-value < 0.05), and even fewer with substantial fold changes (Table 3.5). This disparity highlights the Actc1^{E99K} model's heightened sensitivity in capturing the transcriptional landscape of HCM, aligning more closely with human mid-stage HCM samples, which exhibited 6,524 DEGs (Table 3.5). This similarity in DEG numbers between the Actc1^{E99K} model's early to mid-stages and human mid-stage samples suggests a potential translational relevance of the Actc1^{E99K} model for understanding human HCM.

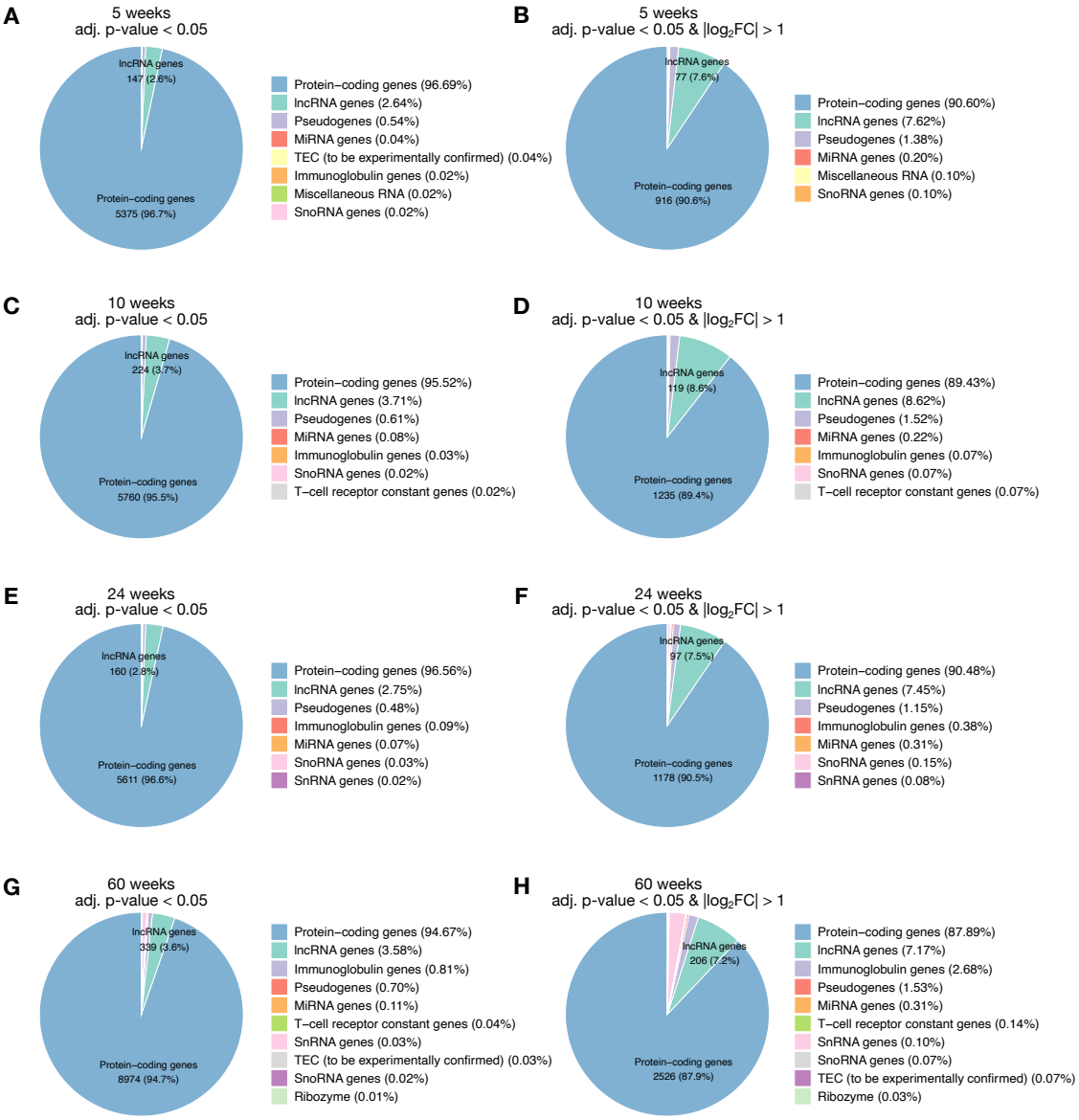

Figure 3.3. Protein-coding genes consistently constitute the majority of differentially expressed genes throughout disease progression in the Actc1^{E99K} model.

The pie charts illustrate the proportion of different gene biotypes among the differentially expressed genes (DEGs) at each time point. Gene annotations were based on the mouse reference genome (GRCm39) from GENCODE release M35 [253]. The analysis is shown for all DEGs (adjusted p-value < 0.05; panels A, C, E, G) and for those with a more stringent fold-change threshold ($|\log_2 FC| > 1$; panels B, D, F, H). Across all time points and thresholds, protein-coding genes represent the vast majority (90%) of transcriptional changes, indicating that the core pathology is driven by alterations in the protein-coding transcriptome.

Table 3.5. Summary of differential expression analysis across all human and mouse bulk RNA-seq datasets. The table quantifies the number of differentially expressed genes (DEGs) identified in each dataset, comparing the Actc1^{E99K} model at different ages with other mouse models and human HCM samples. The number of DEGs is shown at two statistical thresholds: a standard significance level (adjusted p-value < 0.05) and a more stringent threshold that also requires a substantial change in expression ($|\log_2 FC| > 1$).

Dataset	Age (weeks)	adj.p < 0.05	adj.p < 0.05 & |log2FC| > 1
Actc1^{E99K}	5	5,565	1,017
Actc1^{E99K}	10	6,040	1,389
Actc1^{E99K}	24	5,821	1,311
Actc1^{E99K}	60	9,495	2,887
α-MHC^{R403Q}	48	2,665	450
α-MHC^{R719W}	36	592	99
Tnt^{R92W}	24	108	33
Human	Mid-stage	6,524	1,335

GSEA further elucidated the pathway-level changes across the samples (Figure 3.4). Down-regulation of oxidative phosphorylation and fatty acid metabolism was consistent across mouse and human samples, indicating shared metabolic dysregulation. Conversely, pathways such as epithelial-mesenchymal transition and inflammatory response were up-regulated in the Actc1^{E99K} model, with significant normalised enrichment scores (NESs) at various time points, particularly at 60 weeks (NES = 2.264 for inflammatory response, adjusted p-value $= 2.572 \times 10^{-12}$). These pathways were not similarly up-regulated in human samples, suggesting potential species-specific differences in pathway activation or varying stages of disease progression.

The PROGENy pathway activity analysis corroborated these findings (Figure 3.5). Pathway activity scores were calculated using the PROGENy method within the `decoupleR` framework v1.26.0 [270], which estimates the activity of 14 signalling pathways from gene expression data. The activity for each pathway was determined using a univariate linear model, yielding a score (t-value) and a corresponding p-value, which was subsequently adjusted for multiple testing. This analysis revealed that TGF-β, JAK-STAT, and MAPK pathways showed increased activity in the Actc1^{E99K} model, with TGF-β showing a particularly pronounced increase across all time points (e.g., score = 11.897 at 10 weeks, p

Figure 3.4. Gene set enrichment analysis reveals conserved metabolic dysregulation and divergent inflammatory signalling across HCM models. Gene Set Enrichment Analysis (GSEA) was performed on Hallmark gene sets (MSigDB v2023.1 [260, 261]). Analyses for mouse and human datasets were conducted separately using species-specific gene sets and then combined for visualisation. Sample sizes (N) for each group are as follows: Actc1^{E99K} 5w (WT=7, Actc1^{E99K}=6), 10w (WT=9, Actc1^{E99K}=8), 24w (WT=8, Actc1^{E99K}=12), 60w (WT=8, Actc1^{E99K}=8); α-MHC^{R403Q} (WT=9, α-MHC^{R403Q}=8); α-MHC^{R719W} (WT=9, α-MHC^{R719W}=5); Tnt^{R92W} (WT=3, Tnt^{R92W}=3); Human (Control=9, HCM=28). Results shown are significant following 1,000 permutations.

$< 1.63 \times 10^{-32}$). In contrast, these pathways were less activated or even down-regulated in human samples, indicating a divergence in pathway activation between species. Androgen signalling was consistently down-regulated in both Actc1^{E99K} model and human samples, suggesting a conserved pathway alteration in HCM pathogenesis.

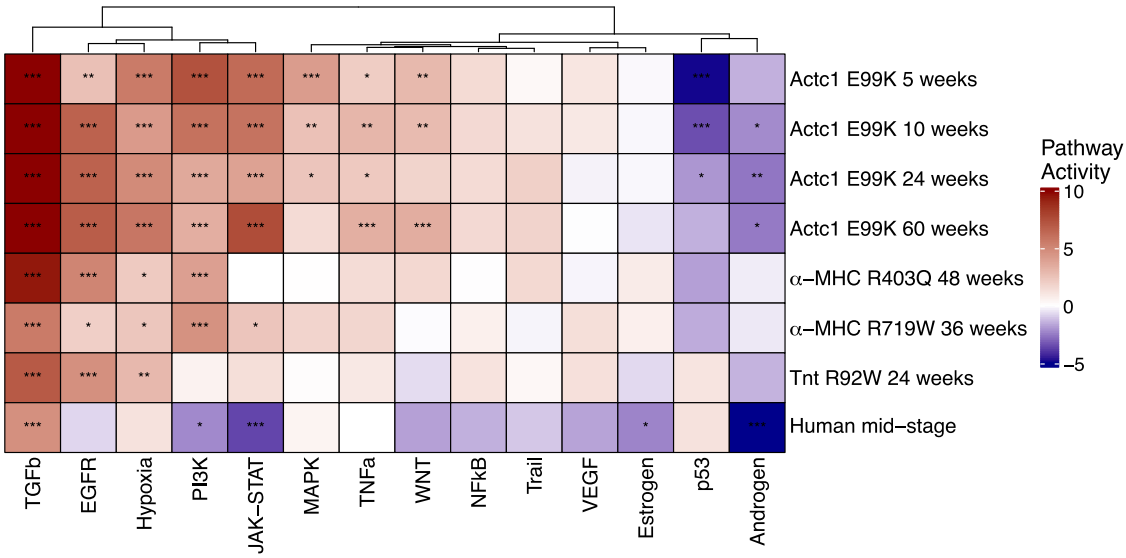

Figure 3.5. PROGENy analysis highlights divergent activity of key signalling pathways between mouse models and human HCM.
This plot shows the inferred activity of 14 key signalling pathways, estimated from gene expression data using the PROGENy method within the `decoupleR` framework (v1.26.0) [270]. The activity score (t-value from a univariate linear model) indicates the degree of pathway activation (positive score) or inhibition (negative score) in HCM versus control samples. Notably, pathways like TGF-β and JAK-STAT show strong activation in the Actc1^{E99K} model, particularly at later stages, but are less active or even down-regulated in human samples, highlighting important species-specific differences. Significance levels are derived from adjusted p-values: * $p < 0.05$, ** $p < 0.01$, *** $p < 0.001$.

These results highlight the Actc1^{E99K} model's utility in capturing the complex transcriptional and pathway-level changes associated with HCM, offering valuable insights into potential therapeutic targets and biomarkers. The observed differences between mouse models and human samples underscore the importance of careful translation of findings across species, particularly in the context of pathway activation and disease progression.

3.2 Deciphering temporal clustering reveals distinct waves of gene regulation

To analyse the temporal dynamics of gene expression in the Actc1^{E99K} mouse model, a bespoke analytical strategy was required. Several established methods for time-series RNA-seq analysis were considered, including regression-based approaches such as `maSigPro` [281, 282] and those based on impulse-response models like `ImpulseDE2` [283, 284]. These methods are powerful for identifying genes with statistically significant temporal changes by fitting expression data to predefined mathematical models, for instance polynomial or impulse functions. However, the primary objective of this study was not merely to identify differentially expressed genes, but to perform an unsupervised, data-driven discovery of co-regulated gene modules based on the overall similarity of their expression trajectories. Model-based approaches were deemed less suitable as they impose assumptions on the shape of expression profiles, which could potentially obscure novel or complex patterns not conforming to these models. The chosen strategy, therefore, was to adapt a method from a different domain to better suit this exploratory aim.

3.2.1 Gene clusters outline core temporal patterns steering disease evolution

In my investigation of the Actc1^{E99K} HCM mouse model, I employed an innovative method to elucidate temporal trends in gene expression. This approach, adapted from single-cell methodologies, involves the application of the Leiden clustering technique to bulk temporal data. Traditionally, the Leiden method is utilised to cluster cells with analogous expression profiles in single-cell analyses. However, in this study, I repurposed this paradigm by treating genes as the primary units of analysis, analogous to cells, and time points as analogous to genes. This application allowed for the clustering of genes exhibiting similar temporal expression trends, thereby offering a refined and unbiased understanding of

the transcriptional dynamics underpinning disease progression in the Actc1^{E99K} model.

Upon clustering, I identified 13 distinct clusters, which were subsequently consolidated into seven functional groups, with one cluster remaining unclassified due to its ambiguous trend (Figure 3.6 and Table 3.6). Clustering was performed at a resolution of 0.8, determined optimal for capturing the complex temporal expression changes. The analysis revealed diverse temporal expression patterns, including consistent up-regulation, early up-regulation followed by a late surge, consistent down-regulation, late declines, and U-shaped trends (Figure 3.6B–H).

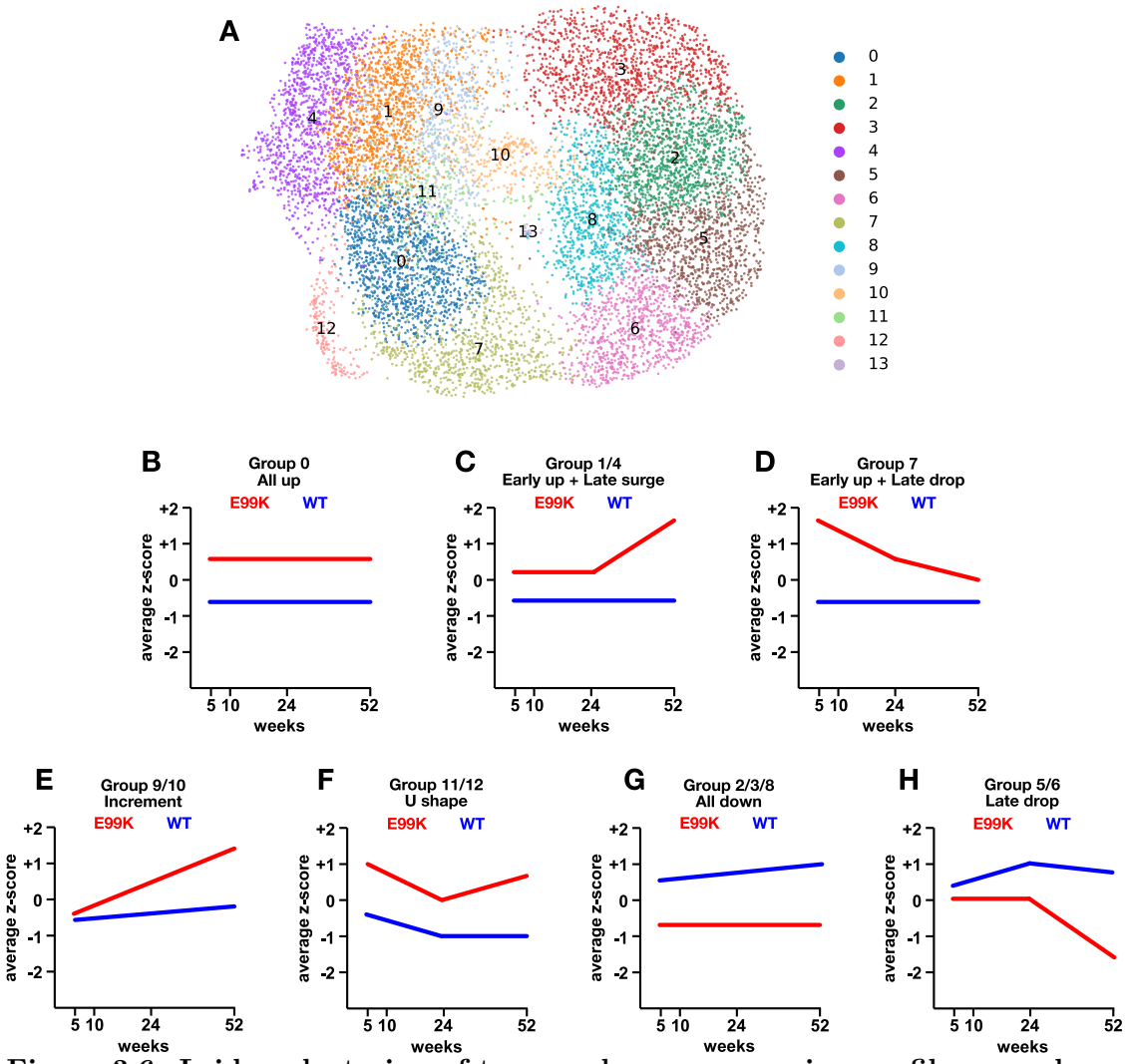

Figure 3.6. Leiden clustering of temporal gene expression profiles reveals distinct regulatory waves.

(A) UMAP visualisation of the 13 gene clusters identified by applying the Leiden algorithm to the temporal expression profiles of differentially expressed genes. Each point represents a single gene, coloured by cluster membership. (B–H) Schematic representations of the seven major functional trend groups derived by consolidating the 13 initial clusters. These groups capture the core temporal patterns of gene regulation during disease progression, from consistent up-regulation (B) to complex biphasic (C, D) or U-shaped (F) trends. Cluster 13 was excluded from functional grouping due to its small size and ambiguous trend.

Table 3.6. Distribution of differentially expressed genes across temporal clusters. The table lists the 13 primary clusters identified by the Leiden algorithm, the functional group to which each cluster was assigned, and the number of genes within each cluster.

Cluster	Group	Number of Genes
0	All up	1,353
1	Early up + Late surge	1,280
2	All down	1,209
3	All down	1,200
4	Early up + Late surge	1,133
5	Late drop	1,084
6	Late drop	890
7	Early up + Late drop	861
8	All down	812
9	Increment	681
10	Increment	369
11	U shape	332
12	U shape	195
13	Unclear	15

3.2.2 Cluster 0: Persistent upregulation indicates chronic remodelling drivers

Cluster 0, comprising 1,353 consistently up-regulated genes (Figure 3.7), was further analysed using protein-protein interaction (PPI) analysis using the STRING database and the Markov Cluster (MCL) algorithm with an inflation parameter of 3. This approach effectively identifies functionally coherent gene clusters within tightly connected sub-networks.

The top ten functional clusters within Cluster 0 revealed a range of biological processes. The most prominent cluster, comprising 43 genes, was associated with collagen formation (e.g., *Postn*, *Tgfb2*, *Col1a1*), highlighting the role of ECM remodelling in HCM pathogenesis. Another significant cluster, involving 22 genes, was linked to the Ras signalling pathway, highlighting its involvement in cellular growth and differentiation processes. Additionally, a cluster of 17 genes was associated with cellular responses to interferon-beta and antiviral mechanisms, suggesting an interplay between immune response and cardiac remodelling. Further clusters included those involved in chondroitin sulphate metabolism, ECM-receptor interaction, endoplasmic reticulum to Golgi vesicle-mediated transport,

necroptotic processes, and ribosome biogenesis, providing insights into cellular stress responses and altered protein synthesis during disease progression.

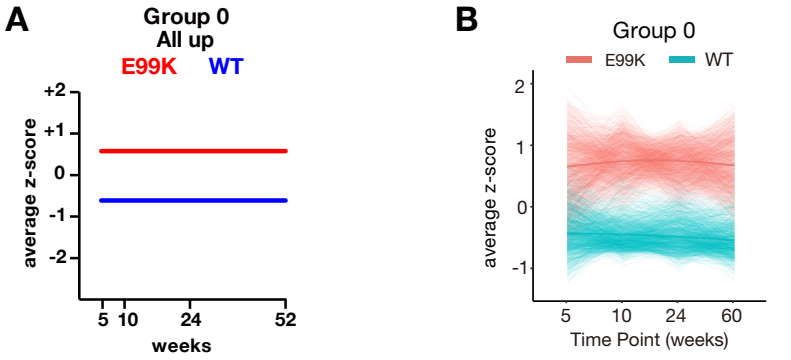

Group 0 main functional clusters

- Collagen formation
  `Postn, Tgfb2, Col18a1, Serpinh1, Lum, Plod2, Fmod, Col1a2, Col1a1, Col6a2, Islr, P4ha1, Ccdc80, Col20a1, Mfap5, Lox, Col22a1, Col4a6, Col9a2, Col24a1, Fbln2, Colgalt1, Fstl1, P3h2, Col8a1, Aspn, Col12a1, Col11a1, Col5a2, Col14a1, Itgbl1, Dpt, Sulf1, Mfap4, Cdh11, Tnmd, Omd, Cilp, Loxl4, Moxd1, Cdkl2, Fkbp9, Svep1`
- Ras signalling pathway
  `Ngfr, Egfr, Shc4, Ereg, Pdgfc, Shc2, Areg, Shc3, Fgf21, Hgf, Fgf6, Fgf5, Hbegf, Gab2, Met, Flt4, E2f3, Tgm2, Ptprj, Rhbdf1, Cdcp1, Tns3`
- Mixed, incl. cellular response to interferon- , and antiviral mechanism by IFN-stimulated genes
  `Eif2ak2, Ifit2, Xaf1, Irgm1, Irf9, Stat2, Rsad2, Nlrc5, Phf11d, Lgals3bp, Trim30a, Gbp3, Parp9, Herc6, Rtp4, Oasl2, Trim30d`
- Chondroitin sulfate/dermatan sulfate metabolism
  `Cspg4, Adamts1, Bgn, Tgfb3, Dcn, Ccn4, Lrrc59, Tmprss6, Sdc2, Chst10, Chst3, Chsy1, Chsy3, Ust, Chst15, Dsel, Dse`
- ECM-receptor interaction
  `Cd44, Cd34, Thbs3, Itga4, Itga2, Itga5, Ddr1, Sele, Tiam2, Serpinb1c, Serpinb8, Serpinb6b`
- Endoplasmic reticulum to Golgi vesicle-mediated transport
  `Sec31a, Arfgap3, Stx5a, Gosr2, Kdelr3, Copg1, Vti1a, Sec23b, Lman1l, Stx11, Stx2, Golim4`
- Uncharacterised
  `Ifrd1, Cul7, Rpl3, Kcnd1, Eif5a2, Eif1a, Zcchc4, Fam111a, Pbp2, Ccdc8`
- Nicotinate and nicotinamide metabolism
  `Adcy7, Adcy2, Enpp1, Acp2, Nmrk2, Nmnat2, Upp1, Pde1a, Pde8a, Slc20a1`
- Necroptotic process
  `Casp8, Tnfrsf10b, Casp12, Mlkl, Bcl10, Ripk1, Gsdma, Tnfrsf23, Capn2, Pigk`
- Maturation of SSU-rRNA
  `Riok1, Heatr1, Wdr43, Gcc1, Rrp12, Tsr1, Ddx21, Pum3, Iffo2`

Figure 3.7. Functional analysis of Cluster 0 identifies persistently up-regulated pathways driving chronic remodelling.
(A) Schematic representation of the consistent up-regulation trend. (B) The averaged, z-scored expression profile of the 1,353 genes in this group across the five time points. The shaded area represents the 95% confidence interval. (C) The primary functional modules identified within this group using protein-protein interaction network analysis with the MCL (Markov Cluster) algorithm. Each module is presented with its top functional annotation and the corresponding genes.

3.2.3 Cluster 1 & 4: Biphasic activation unveils early response and late amplification of inflammatory and apoptotic pathways

Clusters 1 (1,280 genes) and 4 (1,133 genes) exhibited an early up-regulation followed by a late surge in expression (Figure 3.8). In Cluster 1, the primary cluster (32 genes) was associated with ribosome biogenesis, indicating an up-regulation of protein synthesis machinery. Key genes such as *Nol12*, *Rrp15*, and

Gnl1 are implicated in preribosome assembly, underscoring the heightened cellular activity during this phase. Another prominent pathway (22 genes) involved the release of cytochrome c from mitochondria and p53 signalling (e.g., *Trp53* and *Bax*), suggesting an early apoptotic response that intensifies later. The RHO GTPases pathway (20 genes; e.g., *Actb*, *Vim*) highlighted cytoskeletal dynamics and cellular motility. A histone deacetylase complex cluster (e.g., *Hdac1*, *Sin3b*) pointed to epigenetic regulation, while the COPI-dependent Golgi-to-ER retrograde traffic pathway (e.g., *Arf6*, *Scamp2*) emphasised intracellular transport processes.

Cluster 4 was dominated by cytokine-cytokine receptor interactions (129 genes; e.g., *Icam1*, *Il6*), indicating a robust inflammatory response. This was complemented by an adaptive immune response cluster (89 genes; e.g., *Cd3e*, *Cd8a*). The complement and coagulation cascades (18 genes; e.g., *C3*, *C5ar1*) suggested an interplay between immune activation and coagulation. Pathways related to FcϵRI-mediated calcium mobilisation and B cell receptor complex (17 genes; e.g., *Inpp5d*, *Vav1*) highlighted calcium signalling in immune cell activation. The Wnt signalling pathway (e.g., *Wnt10a*, *Fzd7*) implicated this pathway in cellular proliferation and differentiation during remodelling.

3.2.4 Cluster 7: Transient early activation of ECM, innate immune, and signalling pathways precedes decline

Cluster 7, characterised by an early up-regulation followed by a late decline (861 genes; Figure 3.9), provided further insights into the dynamic molecular processes associated with adverse remodelling. The primary cluster (42 genes) focused on ECM-receptor interaction, featuring key basement membrane components (e.g., *Itgb1*, *Col6a1*, *Tnxb*). This suggested an initial increase in ECM remodelling activity that diminishes in later stages, potentially indicating early structural adaptations preceding pathological remodelling.

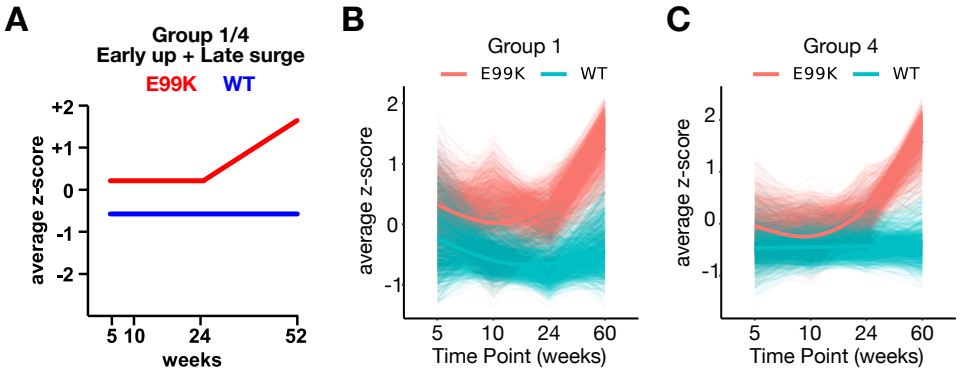

Group 1 main functional clusters

- Ribosome biogenesis
  Nol12, Rrp15, Gnl1, Spout1, Trmt61a, Mettl1, Zfp593, Ddx54, 3110082I17Rik, Nop16, Nolc1, Nop2, Ddx27, Pwp2, Zfp622, Rrp8, Ddx31, Grwd1, Bop1, Noc2l, Rrp1, Surf6, Ebna1bp2, Ppan, Trmt1, Wdr4, Car11, Nle1, Hgh1, Rexo4, Pmepa1, Jsrp1
- Release of cytochrome c from mitochondria
  Pkmyt1, Cdc25b, Trp53, Cdk4, Snai1, Hspb1, Bbc3, Ddit3, Bad, Bok, Bax, Bid, Il2rg, Ccn1, Brd3, Sfn, Sertad1, Gadd45b, Irf2, Gadd45g, Sp140, Banp
- Mixed, incl. RHO GTPases activate WASPs and WAVEs, and formin, FH2 domain
  Actb, Lmnb2, Nes, Vim, Dpf1, Evl, Pfn1, Mrtfa, Lmna, Itgb5, Myo7a, Myh9, Vasp, Arpc1b, Actn1, Myl6b, Whamm, Tmsb10, Itga10, Parvg
- Histone deacetylase complex
  Hdac1, Sin3b, Macroh2a1, Gatad2a, Wdr73, Sap30, Hdac10, H2aj, Rnf220, Taf1c, Ubtf, Fhl3, Foxp4, Tgif2, Zbtb7b
- COPI-dependent Golgi-to-ER retrograde traffic
  Arf6, Scamp2, Arf5, Arf3, Psd, Arfip2, Arap1, Klc3, Kif26b, Cyth2, Kifc5b, Arfip1, Tbc1d10a
- Positive regulation of interferon-β production
  Irf1, Uba7, Oas1a, Oas1g, Oas2, Dhx58, Isg15, Ifi35, Oas1c, Bst2, Ghdc, Fbxl19
- Ionotropic glutamate receptor complex
  Begain, Dlg3, Dlg4, Grik5, Cpt1c, Olfm2, Grin2c, Nlgn2, Cnp, Lrfn3, Igsf9, Kirrel3
- Regulator of G protein signalling domain
  Grk4, Gna15, Rgs16, Rgs10, Gnai2, Rgs11, Ptger4, Tbxa2r, Gng8, Rgs3, Nucb2
- RET signalling
  Ephb3, Src, Shc1, Pelp1, Robo3, Csk, Sirpa, Unc5a, Adam15, Dok1, Nrtn
- Tumour necrosis factor receptor binding
  Traf5, Tnfrsf1a, Cd40, Ripk3, Tradd, Fadd, Tnfsf12, Ltbr, Tnfsf13, Il17rc, Madd

Group 4 main functional clusters

- Cytokine-cytokine receptor interaction
  Icam1, Tlr9, Il6, Csf1r, Flt3, Fgfr2, Ccl2, Ikbke, Vegfd, Irak4, Procr, Il10ra, Nfkbiz, Ctsb, Cyba, Lcp1, Itgal, Il17ra, Cd47, Csf3r, Cd209a, Ncf1, Irf5, Tnfsf13b, Osm, Casp4, Mefv, Tnfrsf1b, Lif, Angpt2, Serpinb9b, Il11, Ctss, Olr1, Fcgr1, Cxcl3, Il1r1, Cxcl14, Ptx3, Fcgr2b, Tnfaip6, Nlrp3, Cybb, Mmp12, Tlr1, Itgb2, Casp1, Selp, Il33, Il12b, Il4ra, Ly6c2, Cd14, Cxcl16, Il6ra, Itgax, Ccl19, Il7, Cxcl13, Socs3, Fcgr3, Itgam, Adgre1, Il1rn, Mmp9, Cd68, Ccl22, Ccl3, Mmp3, Xcr1, Cxcr6, Ccl9, Vcam1, Cxcl5, Ifng, Ccl8, Cxcl10, Ccr7, Ccl12, Ccl4, Ccl5, Ccl6, Cxcr3, Ccr1, Ccr5, Ccr2, Ccl7, Il18rap, Tlr13, Csf2rb, Batf3, Gm2a, Il12rb1, Ebi3, Card9, Il27, Zc3h12d, Il21r, Stat4, Il23r, Ltb, Csf2rb2, Nlrc4, Fpr1, Tnfsf8, Tnfsf15, Il9r, Chil1, Tnfsf14, Cd207, Ctsc, Aim2, Ptpn1, Unc93b1, Klhl35, Irak3, Bcl3, Ticam2, Litaf, Naip5, Tlr11, Tlr12, Cd163l1, 5830411N06Rik, Il18bp, Nlrp1b, Naip2, Klrg2, Neurl3
- Adaptive immune response
  Ncam1, Il7r, Irf8, Tnfrsf9, Cd3e, Cd8a, Tbx21, Klrk1, Itgae, Cd74, Cd6, Havcr2, Pdcd1, Gzmb, Foxp3, Ptprc, Cd4, Cd244a, Cd5, Zap70, Cd2, Spn, Lck, Cd52, Cd27, Cd48, Slamf7, Nkg7, H2-Eb1, H2-Ab1, Cd3d, H2-Aa, Itk, Tnfrsf8, Ikzf1, Cd37, Cd22, Siglecg, Maf, Eomes, Batf, Il2rb, Gzmk, Tigit, Klrd1, Cst7, Cd3g, Cd8b1, Ikzf3, Slamf6, Icosl, Btla, Tnfrsf4, Tcf7, Runx3, Gimap3, H2-Eb2, H2-M11, H2-T22, Ctsw, H2-M2, H2-M3, Ptpn22, H2-K1, Ciita, Pax5, Sh2d2a, Spib, Vsir, Ly9, Lax1, Tnfrsf13c, H2-D1, Fam3c, Tnfrsf13b, March1, H2-DMa, H2-Ob, H2-Oa, H2-DMb2, H2-DMb1, Emb, Izumo1r, Basp1, Sit1, Pdcd7, Bmx, H60b, Gnaz
- Mixed, incl. antifungal innate immune response, and immunoglobulin
  Tyrobp, Fcgr4, Fcer1g, Clec4e, Lyz2, Trem1, Trem2, Aif1, Cd300a, Ly86, Mpeg1, Lair1, Ncf2, Ncf4, Laptm5, Cd53, Clec10a, Clec5a, Clec4a2, Clec12a, Hcst, Clec4d, Siglece, Igsf6, Lst1, Ms4a7, Ifi211, Clec4n, Clec4a3, Cd300c2, Ms4a6d, P2ry6, Sirpb1a, Clec4b1, Gm5150, Cd300ld, Cd200r4, A530064D06Rik, Cd300e, Sirpb1c, Cd300lb, Klra2, Fcrlb
- Complement and coagulation cascades
  C5ar1, Cfb, C3, C3ar1, Vsig4, C4b, Cfp, C6, A2m, C5ar2, Cfi, C2, C1ra, C1s1, Serpina3n, Serpina3i, C7, Cfhr2
- FcεRI-mediated Ca^{2+} mobilisation, and B cell receptor complex
  Inpp5d, Fyb, Lcp2, Fermt3, Vav1, Lat, Skap1, Arhgap30, Dennd1c, Rasal3, Card11, Ccdc88b, Sla, Rasgrp1, Carmil2, Lat2, Skap2
- Mixed, incl. cellular response to interferon-beta, and antiviral mechanism by IFN-stimulated genes
  Ifit3, Irf7, Ifit1, Oasl1, Usp18, Slfn2, Epsti1, Zbp1, Sp100, Oas3, Ifi205, Batf2, Sp110, Ifi209, Ifit3b
- Plasma lipoprotein particle
  Abcg1, Msr1, Saa3, Apoe, Lsr, Apol11a, Apobr, Apol9a, Pltp, Itih3
- WNT signalling pathway
  Myoc, Wnt10a, Wnt7a, Wnt4, Dkk2, Fzd7, Rspo1, Rspo3, Foxl2, Rspo2
- Phosphatidylcholine metabolism
  Lpcat1, Cyp4f18, Pla2g2d, Pafah1b3, Lpcat4, Lpcat2, Pla2g15, Pemt, Plppr3
- Mostly uncharacterised, incl. GTPase GIMA/IAN/Toc, and GTPase-activator protein for Rho-like GTPases
  Arhgap9, Lpxn, Myo1f, Rac2, Myo1g, Arhgap45, Nckap1, Wdfy4, Ralbp1

Figure 3.8. Functional analysis of Clusters 1 & 4 reveals biphasic activation of apoptotic and inflammatory pathways.

(A) Schematic representation of the biphasic trend. (B, C) The averaged, z-scored expression profiles for genes in Cluster 1 (B) and Cluster 4 (C) across the five time points. The shaded area represents the 95% confidence interval. (D) The primary functional modules identified within these groups using protein-protein interaction network analysis with the MCL (Markov Cluster) algorithm. Each module is presented with its top functional annotation and the corresponding genes.

A second cluster (23 genes) associated with digestive system development (e.g., *Pdgfra*, *Pten*, *Ctnnb1*) highlighted pathways regulating cellular growth and differentiation, potentially co-opted during cardiac remodelling. A 14-gene cluster (e.g., *Ifnar1*, *Cmpk2*) involved in interferon-β response and antiviral mechanisms suggested a transient early immune activation. Regulation of RAS by GAPs (14 genes; e.g., *Kras*, *Nf1*) pointed to modulation of signalling pathways like the MAPK cascade, crucial for cell proliferation and survival, with early activity tapering off.

Smooth muscle cell differentiation (11 genes; e.g., *Ednrb*, *Mrtfb*) indicated early changes in vascular smooth muscle. Genes involved in striated muscle contraction (e.g., *Dmd*, *Utrn*) further underscored early alterations in muscle function. Additional clusters highlighted rRNA processing (e.g., *Utp20*, *Ppic*), Golgi-associated vesicle biogenesis (e.g., *Eps15*, *Cltc*), and apoptosis (e.g., *Casp3*, *Nos2*), reflecting early cellular and metabolic activities, and an initial apoptotic response that subsequently diminishes.

3.2.5 Cluster 9 & 10: Progressive activation of biosynthetic and metabolic adaptation programmes

Clusters 9 (681 genes) and 10 (369 genes) comprise genes whose expression increases steadily from 5 to 60 weeks, reflecting a progressive intensification of both biosynthetic and metabolic adaptation processes as hypertrophic cardiomyopathy advances (Figure 3.10).

In Cluster 9, the primary cluster (121 genes) centred on cytoplasmic translation and ribosome function (e.g., *Rpl23a*, *Psmd7*, *Eif3g*), indicating up-regulation of translational machinery and increased protein synthesis demands as the disease progresses. Preribosome and ribosome biogenesis (e.g., *Kri1*, *Mybbp1a*) further underscored heightened ribosomal activity. Genes involved in the precatalytic spliceosome (e.g., *Prpf31*, *Cwc27*) indicated active RNA processing. Chemokine receptor binding (e.g., *Cxcl2*, *Timp1*) suggested an ongoing inflammatory response.

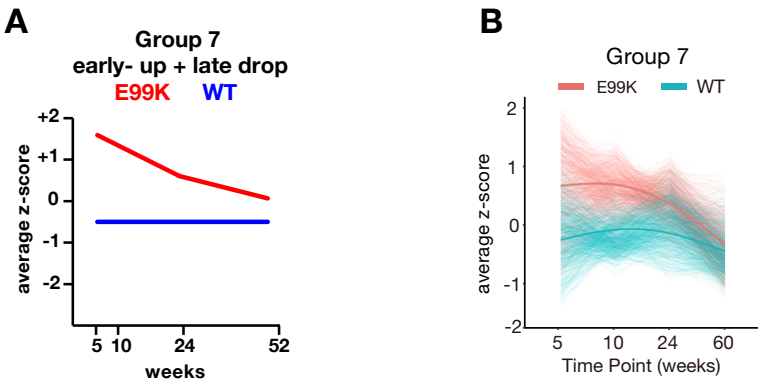

Group 7 main functional clusters

- ECM-receptor interaction
  `Itgb1, Col6a1, Tnxb, Pdgfrb, Nid2, Col28a1, Col4a4, Hspg2, Col4a5, Lama4, Adamts2, Col5a3, Sparc, Ptk2, Lamc1, Nid1, Itga9, Itga6, Itgb8, Lama2, Lamb1, Col15a1, Col5a1, Col4a2, Itgav, Col4a1, Col3a1, Col6a3, Angptl4, Vtn, Bmp1, Col4a3, Ddr2, Loxl2, Parva, Prrx1, Fap, Spon2, Fras1, Lgals8, Pla2r1, Gm19410`
- Digestive system development
  `Pdgfra, Pten, Ctnnb1, Hif1a, Igf1, Prkci, Apcdd1, Psmc6, Lin54, Wls, Pkd1, Gli3, Wnt5b, Tjp2, Dchs1, Cdh13, Zeb1, Nr5a2, Magi1, Amer1, Ctnnbip1, Frk, Klf8`
- Mixed, incl. cellular response to interferon- , and antiviral mechanism by IFN-stimulated genes
  `Ifnar1, Cmpk2, Dtx3l, Gbp6, Rnf213, Parp14, Znfx1, Ddx60, Ifi44, Ifih1, Ifnlr1, Ifi203, Morc3, Ro60`
- Regulation of RAS by GAPs
  `Kras, Nf1, Vav3, Spred1, Rasa1, Erbin, Ptpn12, Ppp1r15b, Shoc2, Rgl1, Dab2ip, Stag2, Il17rd, Rps6ka3`
- Smooth muscle cell differentiation
  `Ednrb, Mrtfb, S1pr3, Gna13, Arhgef12, Gpsm2, Grm7, F2rl3, Aplnr, Lpar4, Ackr3`
- Striated muscle contraction
  `Tmod3, Dmd, Utrn, Casq1, Klhl41, Myot, Myl1, Dysf, Tmod2, Sntb2`
- Small-subunit processome, and positive regulation of rRNA processing
  `Utp20, Ppic, Dhx33, Dhx32, Pus7, Dimt1, Mdn1, Utp6, Wdr75`
- COPI-independent Golgi-to-ER retrograde traffic
  `Rab6a, Galnt1, Bicd1, Tmf1, Vps33b, Dennd5a, Lca5, B4galnt3`
- Clathrin coat assembly
  `Eps15, Tbc1d8b, Cpd, Picalm, Snap91, Cltc, Ap1s2, Ror1`
- Apoptosis - multiple species
  `Casp3, Nos2, Apaf1, Papss2, Casp2, Map2, Cast, Gas2`

Figure 3.9. Functional analysis of Cluster 7 highlights transient activation of ECM and innate immune pathways.
(A) Schematic representation of the transient up-regulation trend. (B) The averaged, z-scored expression profile of the 861 genes in this group across the five time points. The shaded area represents the 95% confidence interval. (C) The primary functional modules identified within this group using protein-protein interaction network analysis with the MCL (Markov Cluster) algorithm. Each module is presented with its top functional annotation and the corresponding genes.

Glutathione metabolism (e.g., *Nqo1*, *Gss*) highlighted oxidative stress management. The aryl hydrocarbon receptor signalling pathway (e.g., *Hsp90ab1*, *Fkbp1a*) pointed to the regulation of xenobiotic metabolism and cellular stress responses. Mitophagy (e.g., *Becn1*, *Bcl2l1*) indicated the removal of damaged mitochondria. Amino acids regulating mTORC1 (e.g., *Atp6v1f*, *Castor1*) suggested a role in nutrient sensing and energy metabolism.

In Cluster 10, the primary function was tight junction assembly (e.g., *Cdh1*, *Tjp3*), maintaining cellular barriers and tissue integrity. Phase I functionalisation of compounds (e.g., *Aldh1a1*, *Cyp2f2*) highlighted detoxification processes. CoA-ligase activity (e.g., *Acsl5*, *Acat2*) was involved in fatty acid metabolism. Ax-

onemal dynein complex and inner dynein arm assembly (e.g., *Ccdc103*, *Rsph9*) indicated roles in cellular motility and structural organisation.

3.2.6 Cluster 11 & 12: Cyclical regulation mirrors stress response and recovery phases

Clusters 11 (332 genes) and 12 (195 genes) exhibited U-shaped expression patterns (Figure 3.11). In Cluster 11, the primary cluster (12 genes) was associated with the regulation of transcription from the RNA polymerase II promoter in response to stress (e.g., *Cd83*, *Fos*, *Egr1*). Genes such as *Btg2* and *Atf3* suggested roles in early growth response and transcription factor activity. Homologous recombination repair (11 genes; e.g., *Ubfd1*, *Rad51b*) highlighted DNA repair mechanisms. Ceramide metabolism (e.g., *Elovl1*, *Cers5*) suggested a role in lipid signalling and apoptosis regulation. The RHO GTPases pathway (e.g., *Cdc42*, *Rap1b*) pointed to the regulation of cytoskeletal dynamics and cell motility. The polysomal ribosome cluster (e.g., *Eef1a1*, *Rpl39*) underscored the continued importance of protein synthesis.

In cluster 12, comprising 195 genes, the mitotic spindle checkpoint and mitotic sister chromatid segregation dominate, with 169 genes including *Uhrf1* and *Troap*. These genes are crucial for cell cycle regulation and genomic integrity, indicating active cell division and proliferation processes during remodelling. The presence of genes like *Cenpi* and *Kif18b* further underscores the complexity of mitotic regulation.

A smaller cluster, comprising three genes, includes *Stat1* and *Cx3cr1*, which are involved in immune signalling and chemokine receptor activity, suggesting a nuanced role in immune modulation. The tenascin complex, with genes such as *Tnc* and *Tnr*, highlights the involvement of extracellular matrix components in structural remodelling and tissue integrity.

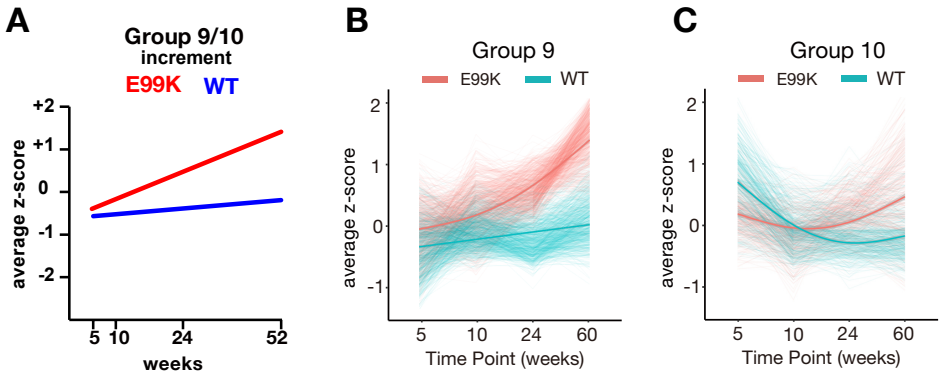

Group 9 main functional clusters

- Cytoplasmic translation
  `Tsen2, Stambp, Psmc4, Rpl23a, Psmd7, Psmc1, Psmc5, Rps12, Nhp2, Efl1, Rpp38, Mrto4, Pa2g4, Psma3, Psmd11, Rack1, Rpl19, Eif3g, Eif3b, Psma7, Psmd1, Eif4a1, Drg1, Psma5, Psmd4, Psmd2, Lsg1, Gtpbp4, Nob1, Fcf1, Ftsj3, Ltv1, Ngdn, Ddx18, Bud23, Prmt1, Eif4b, Eif3h, Exosc1, Rpl10a, Rpl13a, Rpl22, Rpl17, Rpl37, Rpl18a, Rpl21, Rpl27a, Rpl23, Rpl34, Rpl14, Fbl, Rpl32, Rpl4, Lyar, Mak16, Nsa2, Pes1, Rps11, Exosc9, Zc3h15, Fam207a, Sbds, Mettl27, Ptma, Sec61b, Eif3j2, Ubb, Habp4, Btf3, Ppia, Eif3a, Rrp7a, Utp11, Rpl36a, Rplp1, Rplp2, Rpl29, Mrpl33, Rpl10, Rps9, Rps27, Rps25, Rps23, Rps14, Rps24, Rps19, Rpl5, Rps6, Rps26, Rps4x, Rps28, Rpl12, Rps27a, Rps18, Rps8, Fau, Rps16, Rps29, Rpl28, Rps5, Pop4, Psmd8, Tsr2, Hif3a, Axin1, Ccdc92, Psmd10, Psmb1, Vwa7, Serf2, Llph, Larp1, Rnf181, Ube2e2, Mindy1, Uchl1, Esd, Ccdc86, Pop7, Cnksr1, Ccdc149`
- Mixed, incl. preribosome, and ribosome biogenesis
  `Kri1, Mybbp1a, Aatf, Wdr46, Dcaf13, Utp14a, Gpatch4, Nop14, Pinx1, Abt1, Mphosph10, Utp3, Znhit6, Gar1, Ddx50, Rbm34, Nop58, Resf1, Rnf17`
- Precatalytic spliceosome, and U4/U6 x U5 tri-snRNP complex
  `Prpf31, Cwc27, Ddx23, Cwc22, Rbmx2, Sf3a3, Htatsf1, Snrnp35, Thumpd1, Rbm17, Slc25a14, Upf3a`
- Chemokine receptors bind chemokines
  `Tmsb4x, Cxcl2, Spp1, Serpinb6a, Timp1, Serpine1, Edn1, Timp3, Ccl17, Mif, Prg4, Pf4`
- Glutathione metabolism
  Nqo1, Cyb5r3, Osgin1, Gss, Ephx1, Gm3776, Gsta1, Gsr, Srxn1, Gclm, Txndc12
- Aryl hydrocarbon receptor signalling
  `Hsp90ab1, Fkbp1a, Ppp3ca, Dnajb6, Tmem59l, H1f2, Fkbpl, Aip`
- Mitophagy - animal
  `Becn1, Bcl2l1, Atg3, Bnip3, Uvrag, Dnajc14, Bcl2l2, Gabarapl1`
- Amino acids regulate mTORC1
  `Atp6v1f, Castor1, Rragc, Atp6v0e2, Atp6v0d2, Atp6v0e, Atp6v0d1`
- Vesicle fusion with vacuole
  `Chmp1a, Zfyve19, Hgs, Chmp4b, Chmp5, Chmp3`
- S-100/ICaBP type calcium binding domain
  `S100a6, Csrp1, Fxyd5, Ahnak, Crip1, S100a13`

Group 10 main functional clusters

- Tight junction assembly
  `Cdh1, Krt17, Crb3, Wwc1, Foxa1, Foxa2, Tjp3, Cldn2, Ephb2, Krt7, Cldn4, Cd24a, Krt19, Cldn3, Krt8, Krt18, Cldn1`
- Phase I - Functionalization of compounds
  `Aldh1a1, Cyp2f2, Fmo3, Cbr2, Cyp4f15, Cyp2a5, Aox3, Mgst2, Cyp2s1, Cyp2e1, Fmo1, Aldh3b2, Chac1`
- CoA-ligase activity
  `Acsl5, Slc25a1, Acat2, Aacs, Pcx, Acss2, Acox2, Acaa1b, Acss3, Thrsp`
- Axonemal dynein complex, and inner dynein arm assembly
  `Ccdc103, Ppil6, Ccdc39, Rsph9, Rsph1, Drc1, Drc3, Dnajb13, Ropn1l`
- Tektin, and establishment of left/right asymmetry
  Efhc1, Cfap52, Fhad1, Ccdc180, Dlec1, Ribc1, Lrrc23, Tekt4, Cfap45
- Inner dynein arm
  `Pih1d2, Dnah2, Dnah6, Cfap43, Dnah10, Dnah12, Cfap58`
- Myosin II complex, and mesenchyme migration
  `Cnn1, Mylk, Tagln, Lmod1, Myh11, Spire2, Tnnt3`
- Adrenaline,noradrenaline inhibits insulin secretion
  `Vpreb3, Gng3, Gnai1, Adra2a, Hcar1, Htr1b`
- Wnt, and frizzled/secreted frizzled-related protein
  Wnt2, Sfrp4, Wnt10b, Wnt16, Gpc3, Tbx4
- Mixed, incl. surface film, and alveolar lamellar body
  `Scgb1a1, Sftpb, Scgb3a2, Ager, Sec14l3, Gprc5a`

Figure 3.10. Functional analysis of Clusters 9 & 10 shows progressive activation of biosynthetic and metabolic adaptation programmes.
(A) Schematic representation of the incremental up-regulation trend. (B, C) The averaged, z-scored expression profiles for genes in Cluster 9 (B) and Cluster 10 (C) across the five time points. The shaded area represents the 95% confidence interval. (D) The primary functional modules identified within these groups using protein-protein interaction network analysis with the MCL (Markov Cluster) algorithm. Each module is presented with its top functional annotation and the corresponding genes.

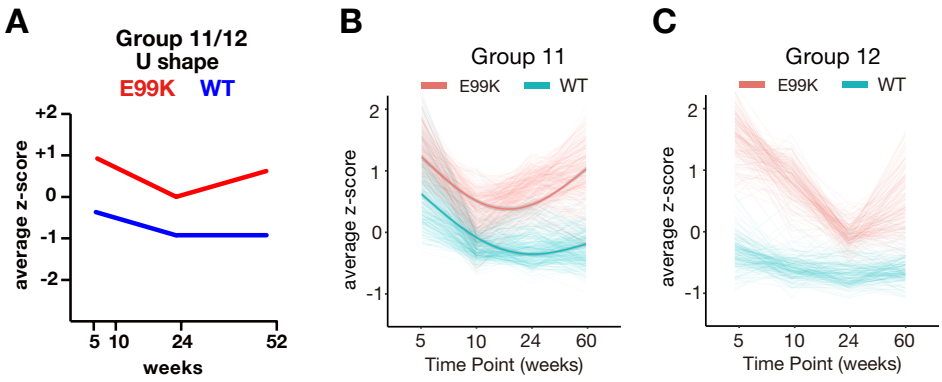

Group 11 main functional clusters

- Regulation of transcription from RNA polymerase II promoter in response to stress
  `Cd83, Fos, Egr1, Btg2, Sik1, Atf3, Klf2, Nr4a2, Nr4a3, Cebpb, Fosl2, Errfi1`
- HDR through Homologous Recombination (HRR)
  `Gm11808, Ubfd1, Orc6, Rfc3, Bub3, Rad51b, Rps18-ps5, Ostc, Kcna5, Otud1, Ube2z`
- Ceramide metabolism
  `Elovl1, Cers5, Cers2, Kdsr, Plpp1, Sgpl1, Ugcg, Gorasp2`
- RHO GTPases activate WASPs and WAVEs
  `Cdc42, Rap1b, Actr3, Rhob, Tagap, Arpc5, Arpc2, Arhgap1`
- Polysomal ribosome
  Eef1a1, Rpl10-ps3, Rpl39, Rpl41, Rps20, Nme1
- Mixed, incl. homeobox
  `Ndufb4, Tmem254b, 2310022B05Rik, mt-Co3, Duxbl1`
- Procollagen-proline dioxygenase activity
  `P4hb, B2m, Creb3l1, Lgals9, P3h1`
- Response to interleukin-18
  `Anxa5, Capns1, Il18, Gpx1, Ripk2`
- Nuclear-transcribed mRNA catabolism, nonsense-mediated decay
  `Parn, Ncbp1, Usp39, Ddx39, Pcid2`
- Tubulin/FtsZ family, C-terminal domain
  `Tubb5, Tbcd, Tuba1a, Cnn3`

Group 12 main functional clusters

- Mitotic spindle checkpoint, and mitotic sister chromatid segregation
  `Uhrf1, Troap, Ska3, Chtf18, Parpbp, Depdc1b, Cenpi, Mcm10, Tyms, Ccnf, Tpx2, Brip1, Ercc6l, Fbxo5, Sgo1, Ndc80, Spc25, Rad54l, Pole2, Smc2, Lmnb1, Kif18b, Pimreg, Cenpe, Racgap1, Ska1, Mybl2, Kif15, Kif20b, Orc1, Kifc1, Mad2l1, Incenp, Nek2, Aspm, Pole, Eme1, Chek1, Kif4, Ncapg, Dlgap5, Fanci, Cdca2, Kif23, Trip13, Tk1, Dscc1, Ttk, Rrm1, Prim1, Clspn, Cenph, Ccnb1, Fignl1, Ckap2, Cdt1, Nuf2, E2f1, Rad51ap1, Cdca7, Espl1, Aurka, Ncaph, Shcbp1, Tacc3, Kntc1, Atad2, Plk1, Ccnb2, Chaf1b, Melk, Cdca3, Kif22, Nusap1, Zwilch, Ect2, Cep55, Spag5, Mcm4, Bub1b, Prc1, Ncapg2, Tcf19, Exo1, Foxm1, E2f8, Mcm2, Rad51, Mcm3, Kif11, Fancd2, Mcm6, Pclaf, Ube2c, Kif20a, Bub1, Kif2c, Aurkb, Cdc20, Cdca5, Mki67, Cdk1, Mcm5, Pbk, Hells, Top2a, Cdca8, Dtl, Cdc6, Birc5, Rrm2, Brca1, Ccna2, Lig1, Dnmt1, Tubb6, Tonsl, Mtfr2, Neil3, Mastl, Stmn1, Ticrr, Cip2a, Haspin, Mis18bp1, Stil, Kif14, Mxd3, Arhgef39, E2f7, Oip5, Esco2, Fam83d, Depdc1a, Iqgap3, Pif1, Ckap2l, Arhgap11a, Dbf4, Gtse1, Nsl1, Hmmr, Anln, Plk4, Knstrn, Knl1, Bard1, Cenpm, Cdkn3, Cdc25c, Spdl1, Cks2, Dck, Rbl1, Dna2, Prim2, Wdhd1, Mms22l, Diaph3, Cit, Prr11, Arl6ip1, Traip, Ankle1, Pask, Sapcd2, Ddias, Trim59, Arhgap33`
- Uncharacterised
  `Stat1, Serpinb1a, Cx3cr1`
- Tenascin complex
  `Tnc, Tnr`

Figure 3.11. Functional analysis of Clusters 11 & 12 reveals cyclical regulation of stress response and cell cycle pathways.
(A) Schematic representation of the U-shaped trend. (B, C) The averaged, z-scored expression profiles for genes in Cluster 11 (B) and Cluster 12 (C) across the five time points. The shaded area represents the 95% confidence interval. (D) The primary functional modules identified within these groups using protein-protein interaction network analysis with the MCL (Markov Cluster) algorithm. Each module is presented with its top functional annotation and the corresponding genes.

3.2.7 Cluster 2, 3 & 8: Sustained downregulation highlights progressive energy metabolism impairment

Clusters 2 (1,209 genes), 3 (1,200 genes), and 8 (812 genes) exhibited consistent down-regulation (Figure 3.12). In Cluster 2, the primary cluster (48 genes) centred on the tricarboxylic acid (TCA) cycle (e.g., *Sdhd*, *Immt*, *Pdhx*), suggesting a

decrease in mitochondrial activity and energy metabolism. Fatty acid β-oxidation (38 genes; e.g., *Etfdh*, *Hadhb*) further underscored reduced lipid metabolism. Mitochondrial translation (17 genes; e.g., *Mrpl10*, *Mtrf1*) and protein targeting to mitochondria (e.g., *Timm44*, *Grpel1*) indicated compromised mitochondrial function and import mechanisms.

In Cluster 3, mitochondrial translation (113 genes; e.g., *Chchd1*, *Eef1d*) and oxidative phosphorylation (83 genes; e.g., *Cox5a*, *Atp5mpl*) were prominent, indicating reduced ATP production. Ubiquitin-mediated proteolysis (32 genes; e.g., *Rbx1*, *Ube2n*) suggested down-regulation of protein degradation pathways. RNA polymerase activity (17 genes; e.g., *Polr2f*, *Med16*) indicated decreased transcriptional activity.

Cluster 8 featured the Wnt signalling pathway (12 genes; e.g., *Dvl1*, *Frat2*). Regulation of TOR signalling (11 genes; e.g., *Itfg2*, *Mlst8*) highlighted a reduction in nutrient sensing and growth regulation. Salivary secretion (10 genes; e.g., *Prkaca*, *Rps6ka5*) suggested decreased secretory processes. Long-chain fatty acid-CoA ligase activity (7 genes; e.g., *Ppard*, *Acsl3*) pointed to reduced lipid metabolism and energy storage.

3.2.8 Cluster 5 & 6: Late-stage declines exacerbate cardiac dysfunction

Clusters 5 (1,084 genes) and 6 (890 genes) exhibited a pattern of down-regulation with late declines (Figure 3.13). In Cluster 5, the primary cluster (17 genes) centred on ribonucleoside monophosphate metabolism (e.g., *L2hgdh*, *Rdh13*, *Thnsl1*), suggesting a decreased capacity for nucleotide synthesis, potentially impacting cellular proliferation and repair. Cardiac muscle cell contraction (11 genes; e.g., *Hey2*, *Cacnb2*) indicated a decline in contractile function, potentially contributing to reduced ejection fraction. The nucleoid and regulation of mitochondrial translation (11 genes; e.g., *Grsf1*, *Mterf4*) suggested disruptions in mitochondrial gene expression and energy production. Vesicle tethering involved in exocytosis

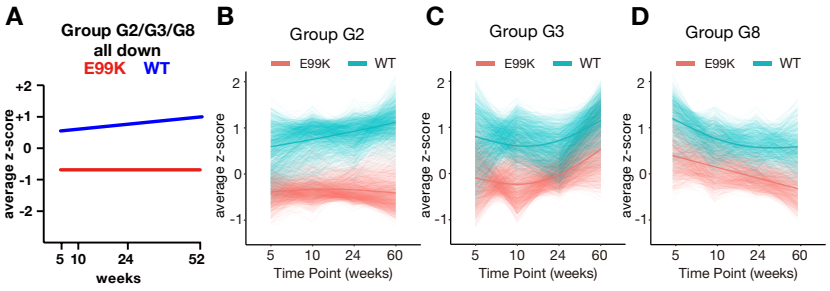

Group 2 main functional clusters

- Tricarboxylic acid cycle
  Sdhd, Immt, Pdhx, Ogdhl, Ndufa10, Slc25a11, Idh1, Idh3g, Dlat, Prdx3, Cs, Pdhb, Mdh1, Idh3b, Ndufv1, Idh2, Ndufs7, Ogdh, Aco2, Uqcrc1, Dlst, Idh3a, Mdh2, Ndufs4, Ndufs1, Ndufs2, Suclg2, Ndufa9, Sucla2, Fh1, Suclg1, Sdhb, Sdha, Sdhc, Foxred1, Glud1, Aldh5a1, Aldh4a1, Bckdha, Mpc1, Ldhb, Me3, Acad9, Apoo, Pdp2, Dmac2, Tmem126b, Ldhd
- Fatty acid -oxidation
  Etfdh, Etfa, Hadhb, Echs1, Ech1, Eci2, Acadl, Acad8, Acadm, Hsd17b4, Scp2, Hadha, Eci1, Hadh, Gcdh, Echdc2, Acadvl, Cpt2, Ivd, Acat1, Acad11, Mccc2, Pccb, Acaa2, Acads, Mlycd, Auh, Pcca, Acsm5, Slc25a20, Crat, Mccc1, Decr1, Acsl6, Hsd17b10, Hibadh, Acad12, Prxl2a
- Mitochondrial translation
  Mrpl10, Mtrf1, Rpl3l, Mrpl50, Mrpl37, Mrps27, Mrpl39, Mrpl45, Mrpl9, Mrpl44, Mrpl46, Mrpl3, Mrpl49, Mrpl4, Metap1, Zfp30, Hhatl
- Protein targeting to mitochondrion, and ATP-dependent peptidase activity
  Timm44, Timm23, Grpel1, Trap1, Phb, Afg3l1, Clpb, Hspd1, Hspa9, Afg3l2, Dnajb12, Hspa12b, 6430571L13Rik, Tmx1
- Formation of ATP by chemiosmotic coupling
  Slc25a3, Atp5b, Atp5g1, Atp5g3, Atp5c1, Atp5a1, Atp5pb, Cyc1, Ndufb9, Atpaf2, mt-Atp8, Atpaf1, Dmac2l
- tRNA aminoacylation
  Aars2, Vars2, Cars2, Gatb, Fars2, Sars2, Lrrc47, Qars, Hars2, Wars, Pars2, Nars2
- Ether lipid metabolism
  Enpp2, Ptdss2, Pisd, Pla2g5, Pla2g2c, Pla2g2f, Plb1, Cyp4f14, Cyp4a32, Pafah2, Plbd1, Ttpa
- Mixed, incl. muscle protein, and myofibril assembly
  Ckm, Ckmt2, Itgb1bp2, Unc45b, Tcap, Ano5, Fhl2, Hrc, Sgca, Tmod4, Myl3, Popdc2
- Purine metabolism
  Gmpr, Pde11a, Pde2a, Adsl, Nt5c3b, Entpd6, Entpd5, Slc25a19, Ak4, Ak1, Pde4a
- Peroxisome
  Pex7, Acot3, Pex11a, Abcd1, Pex19, Gnpat, Fndc5, Pex10, Amacr, Fam185a, Acot2

Group 3 main functional clusters

- Mitochondrial translation
  Chchd1, Eef1d, Mrpl42, Rpl7a, Mrps7, Mrps11, Rps13, Mrps12, Mrps15, Imp3, Ssbp1, Mrps5, Mrpl28, Gadd45gip1, Mrpl21, Mrps36, Mrpl40, Mrpl41, Mrps33, Mrpl43, Mrps21, Mrpl55, Mrpl58, Mrpl30, Mrpl2, Aurkaip1, Mrps34, Pdcd2l, Rps2, Mrps28,Mrpl14, Mrpl13, Mrps22, Mrpl22, Ears2, Noa1, Hsppb1, Mrpl11, Malsu1, Tars2, Mrps9, Rpl8, Psmg1, Mrpl32, Mrps14, Mrpl24,Ccdc124, Mrps18a, Mrpl27, Tsfm, Mrpl16, Mrps16, Mrpl36, Mrpl20, Mrpl12, Btf3l4, Nme5, Farsa, Farsb, Kcng2, Cisd3, Mrm2,Ak2, Pdcd5, Nop53, Abcf3, Sec61g, 1700021F05Rik, Srp19, Mrm3, Pebp1, Abcf2, Srp68, Mtg1, Rps17, Edf1, Mrps17, Hmgn2,Hmgn1, Mrps23, Mrps26, Mrpl23, Mrps24, Mrpl38, Mrps18c, Mrpl51, Eif5a, Rpl7l1, Rpl36, Mrps25, Mrpl48, Mrpl18, Mrps35,Mrpl34, Dap3, Mrpl15, Mrpl19, Eif1, Eif3k, Tpt1, Eif1b, Eif3j1, Dgcr2, Dgcr6, Rbfa, Mrm1, Smim11, Slc7a4, 2510002D24Rik, Rsph3b, Cfap410, Pepd, Patz1
- Oxidative phosphorylation
  Cox5a, Atp5mpl, Timm8b, Wbp2, Cox16, Cox14, Coa3, R3hdm4, Cox17, Cox11, Atp5e, Higd2a, Atp5g2, Atp5md, Ndufb1-ps, Ndufv3, Ndufa3, Atp5j2, Ndufc1, Yjefn3, Ndufa11, Higd1a, Ndufa7, Ndufb11, Atp5j, Ndufs5, Atp5l, Ndufb3, Cox8b, Ndufa13, Atp5k, Coa6, Ndufa2, Pmpcb, Cox6b2, Ndufa5, Ndufab1, Ndufb7, Cox7a2l, Ndufb4, Cox7a1, Atp5o, Atp5d, Ndufs6, Ndufa6, Cox7a2, Ndufa8, Ndufb10, Ndufb5, Ndufb8, Ndufs8, Atp5h, Ndufv2, Ndufa12, Ndufa4, Ndufs3, Uqcrh, Ndufb6, Cox7b, Cox6a2, Cox4i1, Cox7c, Uqcrfs1, Uqcr10, Cox6c, Uqcr11, Cox6b1, Uqcrq, Uqcrb, Cox5b, Spa17, Ndufaf7, Smdt1, Ndufaf6, Romo1, Timmdc1, Phpt1, Dmac1, Ndufaf2, Ndufaf3, Ndufaf1, Ndufaf8, Uqcc2
- Ubiquitin mediated proteolysis
  Rbx1, Ube2n, Rad23a, Ube2m, Cops7a, Cops6, Anapc11, Btbd6, Commd1, Commd3, Commd9, Dcun1d5, Rnf7, Ube2l3, Ube2s, Ube2k, Ube2j2, Neurl2, Ube2e3, Ube2a, Ankrd9, Ube2r2, Ube2f, Cdc34, Anapc16, Anapc13, Phc1, Pttg1, Tbc1d22a, Trpc4ap, Zfp706, Tmem243
- RNA polymerase
  Polr2f, Polr2c, Nelfcd, Nelfb, Med16, Med25, Med4, Polr2l, Polr2i, Polr2k, Polr2j, Elof1, Rtf1, Polr3gl, Maf1, Snapc5, Pcp4l1
- Regulation of ornithine decarboxylase (ODC)
  Psmb6, Psmb4, Psmc3, Psmb5, Psmb7, Oaz2, Akirin2, Oaz1, Mpnd, Psmg2, Psme1, Psmd12, Psmb2, Psmb3
- U12-type spliceosomal complex
  Ubl5, Zcrb1, Sf3b2, Cwc15, Snrnp25, Scnm1, Lsm6, Snrnp48, Snrpb, Rnf113a2, Snrpd3, Snrpd2, Snrpf, Tmem258
- Drug metabolism - cytochrome P450
  Ddt, Gstt2, Gstp1, Gstm5, Adh1, Gstp2, Gstm6, Gstm1, Mgst3, Mgst1, Gstm2, Prdx6, Gsto1
- Iron-sulfur cluster assembly
  Hscb, Lyrm4, Iscu, Bola1, Isca2, Glrx5, Nfu1, Ciapin1, Glrx2, Lias, Bola3, Kcmf1
- Anchoring of the basal body to the plasma membrane
  Rab11a, Rab11b, Rab3ip, Rabl6, Cep63, Ehd1, Cep131, Nde1, Rab4a, Ggnbp1, Rab2a, Poc1a
- Mixed, incl. HDACs deacetylate histones, and Sin3 complex
  Ctbp1, Hdac2, Cbx4, Ss18l2, Csnk2b, Sap30l, Hmg20b, Sap18, Rcor2, Deaf1

Group 8 main functional clusters

- Wnt signalling pathway
  Dvl1, Frat2, Ptch1, Wnt5a, Wif1, Fzd6, Fzd3, Fzd8, Notum, Celsr3, Prickle1, Dixdc1
- Regulation of TOR signalling
  Itfg2, Mlst8, Flcn, Slc38a9, Tbc1d7, Castor2, Rragb, Nprl3, Wdr24, Szt2, Tbc1d22b
- Salivary secretion
  Prkaca, Rps6ka5, Phka2, Olfr78, Adrb1, Atp1b2, Pde4c, Adcy6, Akap5, Adra1b
- Mixed, incl. long-chain fatty acid-CoA ligase activity, and carnitine O-palmitoyltransferase N-terminus
  Ppard, Acsl3, Slc27a1, Ucp3, Pdk4, Srebf1, Cpt1b
- RET signalling
  Vav2, Ret, Gdnf, Gab1, Plcg1, Ntf3, Impa2
- Histone lysine demethylation
  Setd1b, Kdm4b, Kdm4a, Kdm6b, Setd1a, Kdm8, Has3
- Cell communication involved in cardiac conduction
  Jup, Actc1, Gja1, Dsc2, Gja5, Ptgfr
- Kinesin complex
  Kifc2, Ywhae, Kif28, Kif26a, Mlf1, Nav2
- RNA polymerase II preinitiation complex assembly
  Med24, Taf4, Ercc2, Med26, Ddb2, Cops8
- Peroxisomal protein import
  Acot1, Nudt19, Zfand6, Pex26, Pex5, Mb21d2

Figure 3.12. Functional analysis of Clusters 2, 3 & 8 highlights a sustained and progressive failure of energy metabolism.
(A) Schematic representation of the consistent down-regulation trend. (B–D) The averaged, z-scored expression profiles for genes in Cluster 2 (B), Cluster 3 (C), and Cluster 8 (D) across the five time points. The shaded area represents the 95% confidence interval. (E) The primary functional modules identified within these groups using protein-protein interaction network analysis with the MCL (Markov Cluster) algorithm. Each module is presented with its top functional annotation and the corresponding genes.

(e.g., *Tbc1d4*, *Rab10*) highlighted potential impairments in vesicular transport and insulin processing.

In Cluster 6, autophagy (14 genes; e.g., *Mtor*, *Rb1cc1*) was prominent, suggesting reduced cellular clearance and recycling. Histone H3 acetylation (11 genes; e.g., *Spen*, *Ep300*) indicated decreased chromatin remodelling and gene expression regulation. Nucleocytoplasmic carrier activity (10 genes; e.g., *Cse1l*, *Xpo7*) suggested impaired nucleocytoplasmic transport. The thyroid hormone signalling pathway (e.g., *Med1*, *Med13l*) pointed to disruptions in hormonal regulation. The dystrophin-associated glycoprotein complex (e.g., *Itga7*, *Lama5*) highlighted down-regulation of structural components, potentially affecting muscle integrity. Cardiac muscle cell development (e.g., *Actn2*, *Ttn*) suggested a decline in muscle development and maintenance, contributing to cardiac dysfunction.

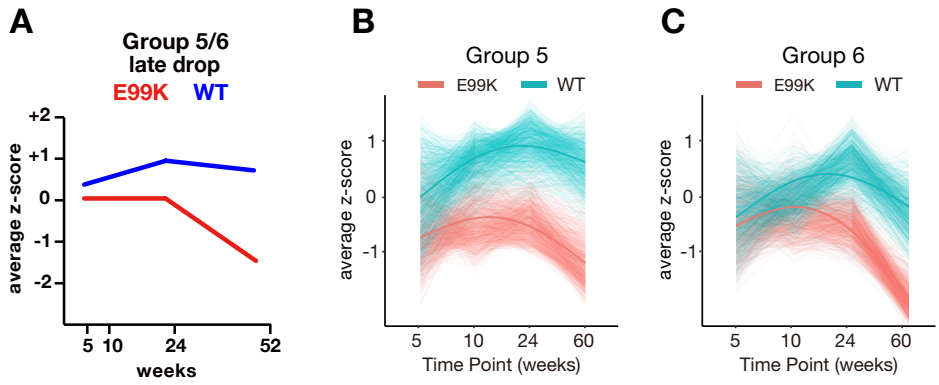

Group 5 main functional clusters

- Ribonucleoside monophosphate metabolism
  `L2hgdh, Rdh13, Thnsl1, Nudt15, Paics, Gart, Mthfd1, Pank4, Dpyd, Pcmtd1, Cyb5rl, Slc28a2, Amd2, Amd1, Srr, Prps2, Prps1`
- Cardiac muscle cell contraction
  `Hey2, Cacnb2, Camk2g, Scn5a, Gpd1l, Abcc9, Dsg2, Kcnj12, Kcnj2, Fgf13, Kcnn2`
- Mixed, incl. nucleoid, and regulation of mitochondrial translation
  `Grsf1, Mterf4, Fastkd1, Ptcd1, Gtpbp10, Fastkd2, Mtpap, Mterf3, Mterf2, Ttc33, Fastkd5`
- BTB and C-terminal Kelch
  `Cul2, Wwp1, Senp8, Cul3, Dcun1d2, Btbd1, Dcun1d4, Klhl15, Ociad1, Klhl23, Kbtbd4`
- Vesicle tethering involved in exocytosis
  `Tbc1d4, Rab10, Myo5b, Rab21, Snap29, Rab14, Exoc8, Exoc7, Exoc3, Exoc6, Rilpl1`
- Cysteine-type deubiquitinase activity
  `Usp13, Usp14, Josd1, Ecpas, Usp10, Ublcp1, Usp15, Ubl4a, Katnal1, Ppp6r2`
- mRNA surveillance pathway
  `Ppp2r2a, Ppp2ca, Ppp2r3c, Ppp2r5c, Ccng1, Fgfr1op2, Fgfr1op, Ppp2r3a, Ppp2r5e`
- Mitochondrial translation
  `Mrpl1, Eif1ax, Mtrf1l, Ptcd3, Mtif2, Mrpl35, Mtif3, Mrrf, Tarsl2`
- Complex I biogenesis
  `Ndufaf4, mt-Nd4, mt-Nd3, mt-Nd2, mt-Nd6, mt-Nd5, mt-Nd4l, Tmem186`
- Propanoate metabolism
  `Hibch, Abat, Acox1, Acadsb, Echdc1, Aldh6a1, Acsl1, Acacb`

Group 6 main functional clusters

- Autophagy - animal
  `Mtor, Rb1cc1, Nbr1, Ulk2, Fyco1, Stx17, Atg9a, Rptor, Pik3r4, Prkaa2, Fnip1, Bmt2, Tecpr2, Pfkfb2`
- Histone H3 acetylation
  `Spen, Ep300, Ncoa2, Kat6b, Rora, Ncoa6, Kat6a, Jade1, Prdm2, Prox1, Jmy`
- Nucleocytoplasmic carrier activity
  `Cse1l, Xpo7, Xpo5, Kpna6, Tnpo1, Xpo4, Kpna3, Kpna4, Ipo11, Tmem64`
- Thyroid hormone signalling pathway
  `Med1, Med13l, Med13, Rarb, Med23, Med14, Thrb, Ncoa1, Med12l, Fam120b`
- U2-type spliceosomal complex, and spliceosomal complex
  `Sf3a1, Prpf18, Rnpc3, Srrm2, Prpf8, Ddx46, Snrnp200, Dhx36, Prpf4b`
- Dystrophin-associated glycoprotein complex
  `Itga7, Lama5, Dag1, Dtna, Sspn, Sgcg, Sgcd, Fktn, Large1`
- Mixed, incl. ECM-receptor interaction, and cell-extracellular matrix interactions
  `Vcl, Flnb, Fermt2, Tln2, Itga1, Lims1, Ctnna3, Cd28`
- Clathrin-dependent endocytosis
  `Itsn2, Epn2, Trim23, Arl5a, Fcho2, Chrm2, Fnbp1l`
- Cardiac muscle cell development
  `Actn2, Ttn, Myo18b, Nebl, Obscn, Rbm20, Myom1`
- Cul3-RING ubiquitin ligase complex
  `Spopl, Kbtbd8, Klhl9, Kbtbd7, Klhl20, Klhl13, Klhl11`

Figure 3.13. Functional analysis of Clusters 5 & 6 points to a late-stage decline in contractile and cellular maintenance pathways.
(A) Schematic representation of the late-drop trend. (B, C) The averaged, z-scored expression profiles for genes in Cluster 5 (B) and Cluster 6 (C) across the five time points. The shaded area represents the 95% confidence interval. (D) The primary functional modules identified within these groups using protein-protein interaction network analysis with the MCL (Markov Cluster) algorithm. Each module is presented with its top functional annotation and the corresponding genes.

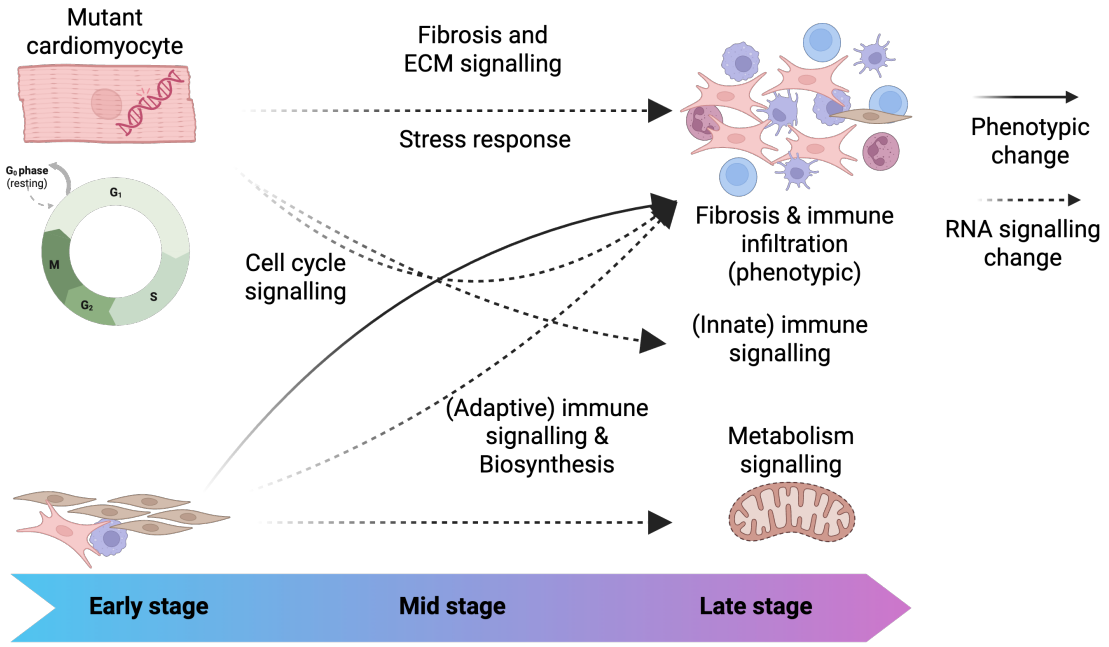

Figure 3.14. Integrative model of the transcriptomic waves driving HCM progression.
The schematic illustrates the progression from an early-stage to a late-stage phenotype, driven by the mutant cardiomyocyte (solid arrow). Key transcriptomic waves are mapped onto this timeline (dashed arrows), showing persistent up-regulation of fibrosis and stress responses; U-shaped activation of cell cycle pathways; an early, transient peak in innate immune signalling; late-stage activation of adaptive immunity and biosynthesis; and sustained down-regulation of metabolism.

To synthesise these complex temporal dynamics, a summary schematic was created to illustrate the interplay between the key transcriptomic waves and the overarching pathophysiological progression of the disease (Figure 3.14). This model integrates the persistent, transient, and progressive changes in signalling pathways with the key phenotypic hallmarks of disease, such as immune infiltration and fibrosis, providing a holistic view of HCM evolution in the Actc1^{E99K} model.

3.3 Discussion: Synthesis of molecular insights bridges transcriptomic dynamics to cardiac remodelling

Transcriptomic profiling of the Actc1^{E99K} HCM mouse model reveals dynamic gene expression changes throughout disease progression. This transcriptional

dysregulation mirrors the phenotypic progression of HCM in this model, highlighting the importance of temporal analyses for dissecting disease mechanisms. Applying Leiden clustering to bulk RNA-seq data provides a powerful framework for organising and interpreting these changes, revealing distinct temporal gene expression patterns and offering insights into the evolving molecular processes underlying HCM. The number of DEGs increases over time, nearly doubling by 60 weeks compared to 5 weeks, reflecting intensifying molecular derangements as the disease advances, from initial apical hypertrophy to severe left ventricular dysfunction and widespread fibrosis. Comparisons with other HCM mouse models and human HCM samples reveal shared features, such as down-regulation of metabolic pathways, alongside species-specific differences in pathway activation, underscoring the complexities of translating preclinical findings to human disease.

Leiden clustering identified seven functional gene groups with unique temporal expression profiles, offering a more nuanced understanding than traditional pathway analysis by capturing co-regulated gene modules that may not fall within predefined pathway boundaries. This clustering framework helps dissect the complex interplay of molecular processes driving HCM progression.

Cluster 0, consistently up-regulated throughout the disease course, highlights processes central to adverse remodelling in HCM. Enrichment of collagen formation genes (e.g., *Postn*, *Tgfb2*, *Col1a1*) implicates sustained fibrotic pathway activation, consistent with increased fibrosis observed in the Actc1^{E99K} model. Concurrent up-regulation of the Ras signalling pathway suggests a potential link between hypertrophic signalling and fibrosis. Ras activation promotes cell growth and proliferation, [285–290] potentially contributing to both hypertrophic and fibrotic phenotypes in HCM. Up-regulation of genes involved in interferon-β response and antiviral mechanisms raises questions about the role of innate immune activation in HCM's chronic inflammatory environment [178, 291, 292]. This interferon response could be triggered by cellular stress or damage associated with remodelling. Other processes within Cluster 0, including chondroitin

sulphate metabolism, ECM-receptor interaction, vesicle transport, necroptosis, and ribosome biogenesis, further underscore the multifaceted molecular changes in HCM. Ribosome biogenesis up-regulation may reflect increased protein synthesis demands associated with hypertrophic growth and fibrotic remodelling.

Clusters 1 and 4, both exhibiting early up-regulation followed by a late surge, represent processes initially activated and then amplified as the disease progresses. In Cluster 1, enrichment of ribosome biogenesis genes (e.g., *Nol12*, *Rrp15*, *Gnl1*) suggests increased protein synthesis demands in early-stage HCM, potentially related to the initial hypertrophic response. Activation of cytochrome c release and p53 signalling (e.g., *Trp53*, *Bax*) indicates early engagement of apoptotic pathways, possibly due to cellular stress [293–298]. The involvement of RHO GTPases (e.g., *Actb*, *Vim*) suggests altered cytoskeletal dynamics and cell motility, potentially contributing to cardiac remodelling [299–303]. Genes related to the histone deacetylase complex and Golgi-to-ER retrograde traffic implicate epigenetic modifications and protein trafficking in early HCM. Cluster 4, on the other hand, exhibits a strong inflammatory signature, with marked enrichment of genes involved in cytokine-cytokine receptor interactions, adaptive immune response, and complement and coagulation cascades. This late surge in inflammatory activity (e.g., *Icam1*, *Il6*, *Cd3e*, *Cd8a*, *C3*, *C5ar1*) suggests progressive intensification of the inflammatory response, consistent with increased immune cell infiltration observed in the Actc1^{E99K} model at later time points. Activation of Wnt signalling (e.g., *Wnt10a*, *Fzd7*) further implicates this pathway in late-stage HCM progression. Wnt signalling is known to play a role in cardiac development and remodelling [304–310], potentially contributing to ongoing structural and functional changes in the heart.

Cluster 7, showing early up-regulation followed by late decline, represents processes initially activated then suppressed as the disease progresses. Enrichment of ECM-receptor interaction genes (e.g., *Itgb1*, *Col6a1*, *Tnxb*) suggests an initial extracellular matrix remodelling response. The subsequent decline may indicate a shift in the remodelling process or compensatory down-regulation in

response to excessive ECM deposition. The involvement of genes related to digestive system development (e.g., *Pdgfra*, *Pten*, *Ctnnb1*) warrants further investigation. Although seemingly unrelated to cardiac function, these genes could reflect broader developmental or metabolic changes in HCM. Similar to Cluster 0, the presence of interferon-β response and antiviral mechanism genes raises questions about innate immune activation in HCM. However, the transient nature of this response in Cluster 7 suggests an initial attempt to control inflammation that is eventually overwhelmed. Regulation of RAS by GAPs (e.g., *Kras*, *Nf1*) suggests dynamic interplay between Ras signalling and its negative regulators, potentially reflecting attempts to fine-tune Ras activity during HCM progression. The involvement of smooth muscle cell differentiation genes (e.g., *Ednrb*, *Mrtfb*) suggests contributions from vascular smooth muscle cells to the remodelling process. Genes related to striated muscle contraction, rRNA processing, Golgi vesicle biogenesis, and apoptosis highlight the complex interplay of cellular processes in early-stage HCM.

Clusters 9 and 10, both exhibiting increasing expression over time, represent progressively activated processes. In Cluster 9, strong enrichment of cytoplasmic translation and ribosome function genes (e.g., *Rpl23a*, *Psmd7*, *Eif3g*) suggests sustained increases in protein synthesis, potentially reflecting ongoing hypertrophic growth, fibrotic remodelling, or both. Genes involved in preribosome and ribosome biogenesis, the pre-catalytic spliceosome, and chemokine receptor binding further support increased protein synthesis and inflammatory activity in later-stage HCM. Pathways related to glutathione metabolism [298, 311, 312], aryl hydrocarbon receptor signalling, mitophagy [313], and amino acid regulation of mTORC1 [314–317] suggest potential roles for oxidative stress, xenobiotic metabolism, mitochondrial quality control, and metabolic regulation in HCM progression. Cluster 10, although smaller, shows increasing expression of genes related to tight junction assembly (e.g., *Cdh1*, *Tjp3*), suggesting alterations in cell-cell adhesion and barrier function, potentially contributing to structural and functional changes in the heart. Genes related to phase I functionali-

sation of compounds and CoA-ligase activity point to potential changes in drug metabolism and fatty acid metabolism, respectively. The presence of axonemal dynein complex and inner dynein arm assembly genes warrants further investigation. Typically associated with cilia and flagella function, their up-regulation in the heart could reflect novel roles in cardiac cell biology or contributions from non-cardiomyocyte cell types.

Clusters 11 and 12, both displaying U-shaped trends, represent processes that are activated, suppressed, and then reactivated, suggesting complex regulatory mechanisms. In Cluster 11, enrichment of transcriptional regulation genes (e.g., *Cd83*, *Fos*, *Egr1*) suggests an initial transcriptional response, followed by relative quiescence, and then resurgence, potentially reflecting waves of gene expression changes. The involvement of homologous recombination repair genes (e.g., *Ubfd1*, *Rad51b* [318]) suggests potential DNA damage and repair responses, with the U-shaped trend possibly indicating an initial insult, a repair period, and then recurrence of DNA damage. Genes related to ceramide metabolism, the RHO GTPases pathway, and the polysomal ribosome implicate lipid signalling, cytoskeletal dynamics, and protein synthesis in HCM's complex temporal regulation. Cluster 12 is dominated by mitotic spindle checkpoint and sister chromatid segregation genes (e.g., *Uhrf1*, *Troap*). The U-shaped trend here suggests initial activation of cell cycle processes, followed by suppression, and then reactivation. This could reflect attempts at compensatory cardiomyocyte proliferation, followed by cell cycle arrest, and then a potential resurgence of proliferative activity, possibly driven by fibrotic or inflammatory signals. Genes related to immune signalling and chemokine receptor activity (e.g., *Stat1*, *Cx3cr1*) further support interplay between cell cycle regulation and inflammation in HCM.

Clusters 2, 3, and 8, all exhibiting consistent down-regulation, represent processes progressively suppressed throughout disease progression. This sustained down-regulation suggests fundamental shifts in cellular function and metabolism in HCM. Cluster 2 displays a strong metabolic signature, with marked down-regulation of TCA cycle and fatty acid β-oxidation genes (e.g., *Sdhd*, *Immt*, *Pdhx*,

Etfdh, *Hadhb*). This aligns with observed energetic deficits in HCM and suggests progressive mitochondrial dysfunction [319–322]. Concurrent down-regulation of mitochondrial translation and protein targeting genes further supports this. Cluster 3 reinforces this metabolic theme, with prominent down-regulation of mitochondrial translation and oxidative phosphorylation genes (e.g., *Chchd1*, *Eef1d*, *Cox5a*, *Atp5mpl*), further emphasising declining mitochondrial function and suggesting its potential as a therapeutic target. Down-regulation of ubiquitin-mediated proteolysis genes (e.g., *Rbx1*, *Ube2n*) suggests impaired protein quality control, potentially contributing to misfolded protein accumulation and cellular stress. Down-regulation of RNA polymerase activity genes (e.g., *Polr2f*, *Med16*) suggests global transcriptional suppression, potentially reflecting broader cellular dysfunction. Cluster 8 shows consistent down-regulation of Wnt signalling genes (e.g., *Dvl1*, *Frat2*). This contrasts with Cluster 4's up-regulation, suggesting complex and dynamic regulation of this pathway in HCM. Down-regulation of TOR signalling genes (e.g., *Itfg2*, *Mlst8*) further implicates altered metabolic signalling. The involvement of genes related to salivary secretion and long-chain fatty acid-CoA ligase activity requires further investigation.

Clusters 5 and 6, both characterised by down-regulation followed by a late decline, represent processes initially suppressed and then further down-regulated, suggesting a gradual loss of function. In Cluster 5, down-regulation of ribonucleoside monophosphate metabolism genes (e.g., *L2hgdh*, *Rdh13*, *Thnsl1*) suggests potential alterations in nucleotide biosynthesis and metabolism. Down-regulation of cardiac muscle cell contraction genes (e.g., *Hey2*, *Cacnb2*) directly implicates impaired contractile function, aligning with the observed decline in ejection fraction in the Actc1^{E99K} model. Down-regulation of nucleoid and mitochondrial translation regulation genes (e.g., *Grsf1*, *Mterf4*) further supports mitochondrial dysfunction. The involvement of genes related to vesicle tethering and exocytosis suggests potential alterations in protein trafficking and secretion. Cluster 6 exhibits down-regulation of autophagy genes (e.g., *Mtor*, *Rb1cc1*). This could impair cellular quality control, contributing to damaged protein and organelle

accumulation [323–325]. Down-regulation of histone H3 acetylation genes (e.g., *Spen*, *Ep300*) suggests altered epigenetic regulation. Genes related to nucleocytoplasmic carrier activity, thyroid hormone signalling, the dystrophin-associated glycoprotein complex, and cardiac muscle cell development highlight the complex interplay of affected cellular processes. Their progressive down-regulation suggests a gradual decline in cellular function and adaptation, contributing to the worsening cardiac phenotype.

This comprehensive temporal analysis of gene expression in the Actc1^{E99K} HCM mouse model provides valuable insights into the dynamic molecular processes underlying disease progression. Leiden clustering reveals distinct temporal patterns, highlighting the interplay of fibrosis, inflammation, metabolic dysregulation, and cell cycle control. These clusters provide a framework for later studies dissecting these processes' specific roles in single-cell or single-nucleus resolution and identifying potential therapeutic targets. In summary, this study provides a uniquely detailed and dynamic map of the transcriptomic changes that drive the progression of HCM in the Actc1^{E99K} model. The key finding is that the molecular pathology of HCM is not a monolithic state, but rather a sequence of distinct, temporally-ordered waves of gene expression. I have delineated a persistent wave of fibrotic and stress-related gene activation, a progressive and sustained collapse of cardiac metabolism, and a biphasic immune response characterised by early innate and later adaptive immune pathway activation.

This longitudinal approach represents a significant advance over previous transcriptomic studies in HCM, which have largely provided static snapshots of established disease [140, 279]. By tracking the heart from a compensated to a failing state, my work provides a much-needed temporal context, revealing a molecular timeline of pathogenesis. For instance, the identification of a transient, early activation of ECM remodelling and innate immunity (Cluster 7) followed by a late, dramatic surge in inflammatory signalling (Cluster 4) offers novel insights into the evolving nature of cardiac inflammation. This dynamic view moves beyond

simply identifying which pathways are dysregulated, and instead begins to uncover when and in what sequence they contribute to the disease. This improved understanding of the molecular choreography of HCM progression is critical, as it highlights potential stage-specific windows for therapeutic intervention that a single-timepoint analysis would miss, thereby providing a more sophisticated foundation for future translational research.

4

Single-cell resolution of adverse remodelling in Actc1^{E99K} hearts

4.1 Mapping non-cardiomyocyte populations through multiplexed scRNA-seq reveals cellular diversity

4.1.1 Design and overview of the multiplexed scRNA-seq experiment unveil cellular heterogeneity

Having established the global transcriptional landscape of the Actc1^{E99K} HCM mouse model, I next sought to dissect the cellular heterogeneity underlying these observed changes. This deeper resolution is crucial for understanding the complex interplay of cell types contributing to adverse remodelling in HCM. To achieve this, we employed multiplexed Cellular Indexing of Transcriptomes and Epitopes by sequencing (CITE-seq), a technique that combines scRNA-seq with antibody-derived tags (ADTs) to simultaneously profile gene expression and cell surface markers at single-cell resolution (Figure 4.1). Both early (5 weeks) and late (60 weeks) stage Actc1^{E99K} and WT mice were used (N = 3 for both genotypes at each time point). Cardiac tissue was harvested and processed for scRNA-seq. Due to their large size and rod shape, which can obstruct microfluidic channels

within the 10x Genomics platform, cardiomyocytes were excluded from the single-cell library preparation. The remaining non-cardiomyocytes were then sorted into distinct populations using fluorescence-activated cell sorting (FACS). $CD45^+$ immune cells and $CD31^+$ endothelial cells were isolated, while the $CD45^-CD31^-$ population was further subdivided based on Thy1 and Fap expression into $Thy1^-Fap^-$ and $Thy1^+$ and/or Fap^+ cells (encompassing $Thy1^+Fap^+$, $Thy1^+Fap^-$, and $Thy1^-Fap^+$ cells).

To facilitate multiplexing of samples, TotalSeq-C antibodies conjugated to unique oligonucleotide barcodes (hashtags) were used. Each of the three biological replicates within a given condition (WT or $Actc1^{E99K}$, at either early or late stage) was labelled with a distinct hashtag: TotalSeq™-C0301 (`ACCCACCAGTAAGAC`), TotalSeq™-C0302 (`GGTCGAGAGCATTCA`), and TotalSeq™-C0303 (`CTTGCCGCATGTCAT`). This resulted in eight distinct samples for each time point: $CD45^+$, $CD31^+$, $Thy1^-Fap^-$, and $Thy1^+$ and/or Fap^+ cells from both WT and $Actc1^{E99K}$ hearts. These labelled samples were then pooled into four separate libraries for gene expression analysis and four corresponding hashtag libraries for demultiplexing. These libraries were subsequently sequenced, and the resulting data were processed to identify distinct cell populations and characterise their transcriptional profiles. The number of cells sorted for the early- and late-stage samples are outlined in Table 4.1.

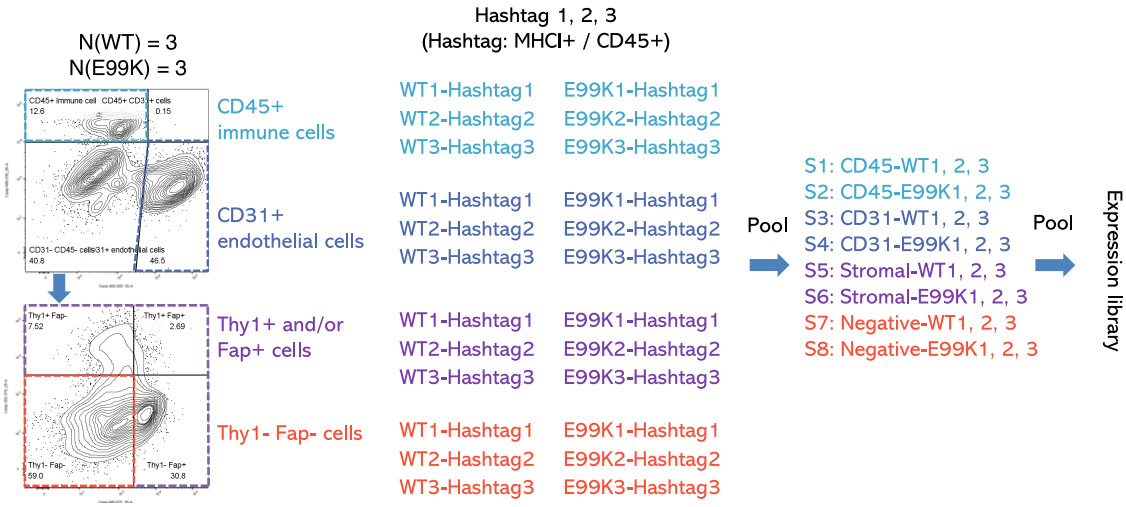

Figure 4.1. Multiplexed single-cell RNA-sequencing experimental design for early and late-stage non-cardiomyocytes.
Illustration of multiplexed single-cell RNA-seq experimental design of sorting non-cardiomyocytes from Actc1^{E99K} mouse hearts. Compensatory beads were used to set up compensation for the panel of five antibodies. Single antibody staining was tested to confirm the existence of the individual cell population, including AF488-CD45 (30-F11) for immune cells, APC-FAPa (FAB9727R) for activated fibroblasts, BV421-CD31 for endothelial cells, PE-Dazzle-FVS620 for live/dead cells, and BUV395-CD90.2 for pericytes or immunofibroblasts. Fluorescence minus one (FMO) strategy was then employed to verify the similar level of detection as in single antibody staining with established compensation matrix. Single non-cardiomyocytes, following heart tissue digestion, were stained with hashtag antibodies to label individual mice from Actc1^{E99K} or WT groups. Samples with the same genotype pooled together and then stained with a cocktail of five antibodies (described above) before cell sorting. Gating strategy was shown to firstly separate CD45^{+} immune cells and CD31^{+} endothelial cells and secondly FAPa^{+} and/or CD90.2^{+} stromal cell types from the CD45^{-}CD31^{-} cell population. 10x platform was then used to prepare libraries for sequencing.

Table 4.1. Cell counts for sorted non-cardiomyocyte populations from early- and late-stage hearts. This table details the number of cells recovered for each of the eight sorted samples (four populations from each genotype) prior to loading onto the 10x Genomics platform. Each sample represents a pool of three biological replicates, individually labelled with a distinct hashtag antibody (TotalSeq™-C0301, C0302, or C0303).

Sample	Sample description	Early-stage	Late-stage
S1	CD45-WT (Hashtag C0301, C0302, C0303)	14,144	31,923
S2	CD45-E99K (Hashtag C0301, C0302, C0303)	12,207	83,808
S3	CD31-WT (Hashtag C0301, C0302, C0303)	68,557	142,652
S4	CD31-E99K (Hashtag C0301, C0302, C0303)	56,857	177,003
S5	Stromal-WT (Hashtag C0301, C0302, C0303)	9,325	62,681
S6	Stromal-E99K (Hashtag C0301, C0302, C0303)	6,287	96,835
S7	Negative-WT (Hashtag C0301, C0302, C0303)	25,778	66,416
S8	Negative-E99K (Hashtag C0301, C0302, C0303)	31,114	90,509

After establishing the multiplexed scRNA-seq experimental design, I characterised

the non-cardiomyocyte cell types. The FACS sorting, which relied on surface protein expression, was successfully performed. For the principal downstream transcriptional analyses, the sorted cells were grouped into three primary populations: $CD45^+$ cells, $CD31^+$ cells, and $CD45^-CD31^-$ cells. The latter group comprised the cells from the $CD45^-CD31^-$ fraction that were initially further sorted based on Thy1 and Fap surface markers (into $Thy1^-Fap^-$ and $Thy1^+$ and/or Fap^+ subpopulations) but were subsequently combined for these analyses. Using multiplexed scRNA-seq data from these three primary populations, I then identified the distinct cell types within each in both early and late-stage $Actc1^{E99K}$ and WT hearts. In the following sections, cell populations are defined by marker gene expression, which is summarised in dotplots. For detailed spatial visualisation, UMAPs showing the log-normalised expression of each individual marker gene are available in Appendix B.

4.1.2 Immune cells shape the inflammatory landscape in remodelled hearts

T cells exhibit diverse activation states and functional profiles

T cells (Figures 4.2 and 4.5), key components of the adaptive immune system, were identified using a combination of cellular markers. This identification began with their expression of *Ptprc* (CD45), a universal marker for all nucleated haematopoietic cells [326, 327]. T cells were then further confirmed by the expression of T cell receptor complex components: *Cd3d*, *Cd3e*, and *Cd3g*. These genes encode the CD3 chains essential for T cell receptor signalling and activation [328, 329]. Several T cell subsets were subsequently identified. $CD8^+$ cytotoxic T cells (Tc) expressed *Cd8a* and *Cd8b1*, which encode the CD8 co-receptor that interacts with major histocompatibility complex class I (MHC-I) molecules [330]. $CD4^+$ conventional T cells (Tconv) expressed *Cd4*, encoding the CD4 co-receptor that interacts with major histocompatibility complex class II (MHC-II) molecules [331]. Regulatory T cells (Tregs), a $CD4^+$ T cell subset crucial for

immune homeostasis, expressed both *Foxp3* and *Il2ra* (CD25). Foxp3, a lineage-defining transcription factor, is essential for Treg development and suppressive function [332, 333]. Il2ra, the high-affinity IL-2 receptor α chain, contributes to Treg survival and function [334, 335]. In late-stage samples, additional T cell subsets emerged, including Gzmk$^+$ CD8$^+$ Tc cells (expressing granzyme K, a cytotoxic molecule [336]), Lag3$^+$ CD4$^+$ Tconv cells (expressing the immune checkpoint receptor LAG3 [337]), and proliferating T cells (expressing the cell cycle progression markers *Mki67*, *Stmn1*, and *Birc5* [338–340]). $\gamma\delta$T cells, expressing *Trdv4* and either *Trgv2* or *Trdc* (encoding the γ and δ chains of the $\gamma\delta$T cell receptor), were also observed. Two late-stage $\gamma\delta$T cell subsets were identified: Lgals3$^+$ $\gamma\delta$T cells (expressing galectin-3, implicated in inflammation and fibrosis [341–344]) and Sox13^{hi} $\gamma\delta$T cells (expressing high levels of the transcription factor SOX13 [345]). Finally, double-negative (DN) and double-positive (DP) T cells, lacking both CD4 and CD8 or expressing both, respectively, were also present in late-stage samples.

Myeloid and dendritic populations drive inflammatory and phagocytic responses

Myeloid cells (Figures 4.3 and 4.5), encompassing monocytes, macrophages, and DCs, expressed *Cd68*, *Itgam* (CD11b), *Lyz2* (lysozyme), *Fcgr3* (CD16/32), *Csf1r* (CSF-1 receptor), and *Adgre1* (F4/80). These markers reflect the phagocytic and antigen-presenting functions of myeloid cells [346–351]. Macrophages were further distinguished by *Mrc1* (CD206), *C1qa*, *C1qb*, and *C1qc* expression. These genes are involved in phagocytosis, complement activation, and tissue homeostasis [352, 353]. Three macrophage subsets were identified based on differential expression of *Timd4*, *Lyve1*, *Folr2*, *H2-Ab1* (MHC-II), and *Ccr2* [354]: TLF$^+$ macrophages (Timd4$^+$ and/or Lyve1$^+$ and/or Folr2$^+$), Ccr2$^+$ macrophages (Timd4$^-$Lyve1$^-$Folr2$^-$Ccr2$^+$), and MHC-II^{hi} macrophages (Timd4$^-$Lyve1$^-$Folr2$^-$Ccr2$^-$MHC-II^{hi}). Monocytes were identified by *Cd14* expression, delineating CD14^{hi} and CD14^{lo} subsets. DCs expressed *Cd209a* (DC-SIGN).

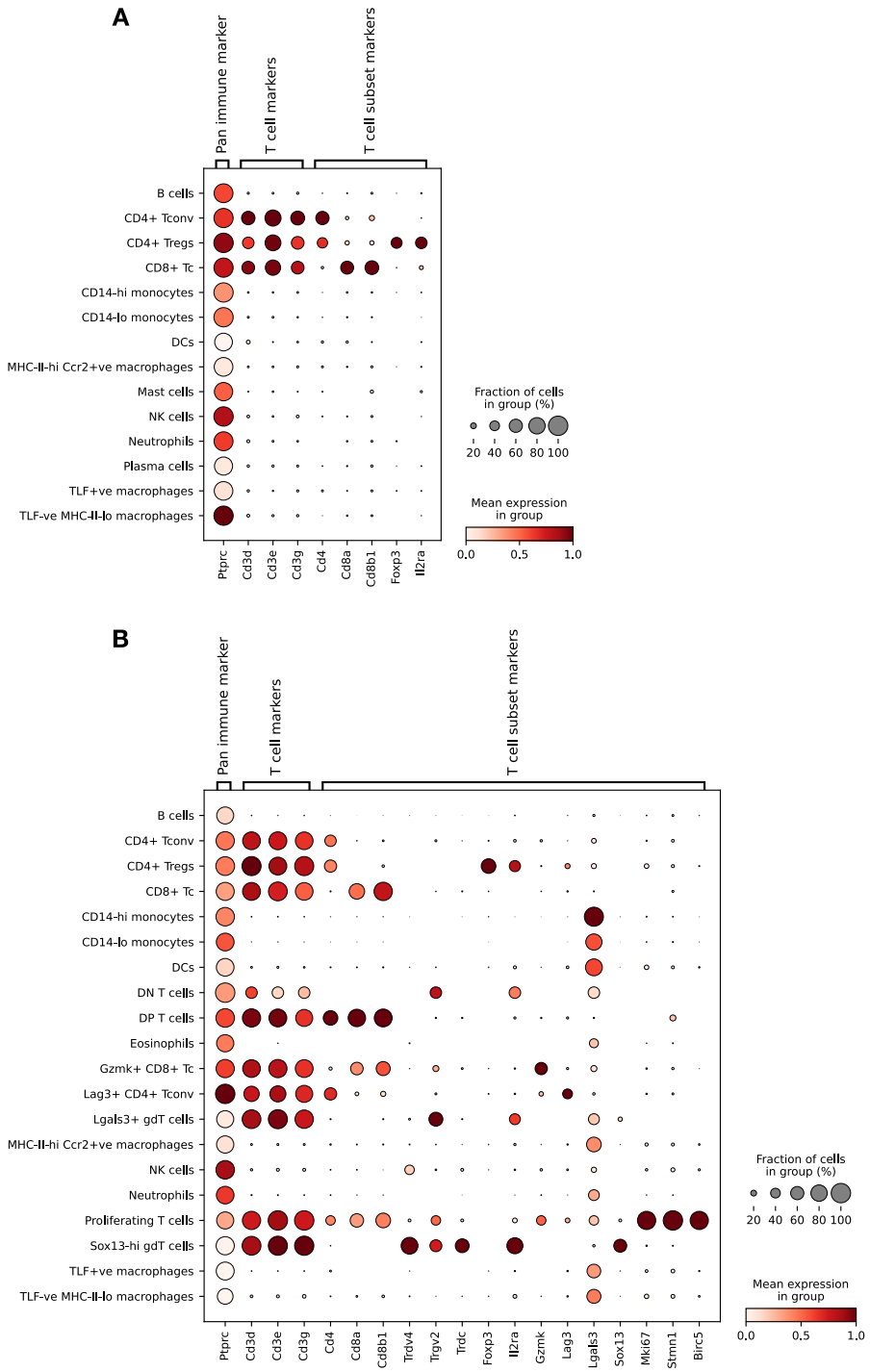

Figure 4.2. Canonical marker gene expression defining T cell populations within the CD45$^+$ fraction.
Data are shown for (A) early-stage (5 weeks) and (B) late-stage (60 weeks) samples. Each dot represents a specific cell cluster, as annotated on the y-axis. The size of the dot indicates the percentage of cells within that cluster expressing the gene, while the colour intensity reflects the mean expression level in expressing cells. Mean expression values are scaled from 0 to 1 for each gene (x-axis) to allow for comparison across different markers. Data were generated from N=3 mice per genotype. The spatial relationship between these clusters is shown in the UMAP visualisation in Figure 4.5.

Additional immune effectors enhance adaptive and innate responses

B cells (Figures 4.4 and 4.5), responsible for humoral immune response, were identified by the expression of *Cd79a*, *Cd79b*, *Cd19*, and *Ms4a1* (CD20), which encode B cell receptor components and are essential for B cell development and function [355–357]. Plasma cells, the antibody-secreting effector B cells, were identified by *Mzb1* expression, essential for their differentiation and integrin function [358]. Eosinophils, belonging to granulocytes involved in allergic reactions and parasitic infections, expressed *Siglecf*. Natural killer (NK) cells, cytotoxic innate lymphoid cells, were identified through the expression of NK cell receptors (*Klrd1*, *Klrb1a*, *Klrb1b*, *Klrb1c*, *Klrb1f*) and cytotoxic molecules (*Gzma*, *Gzmb*, *Prf1*). Neutrophils, the most abundant granulocytes and key first responders to infection, expressed *Ly6g*, *Cxcr2*, *S100a8*, *S100a9*, *Lcn2*, *Retnlg*, and *Csf3r*. Finally, mast cells, implicated in allergic reactions and tissue homeostasis, were identified by the expression of *Kit* and *Fcer1a*.

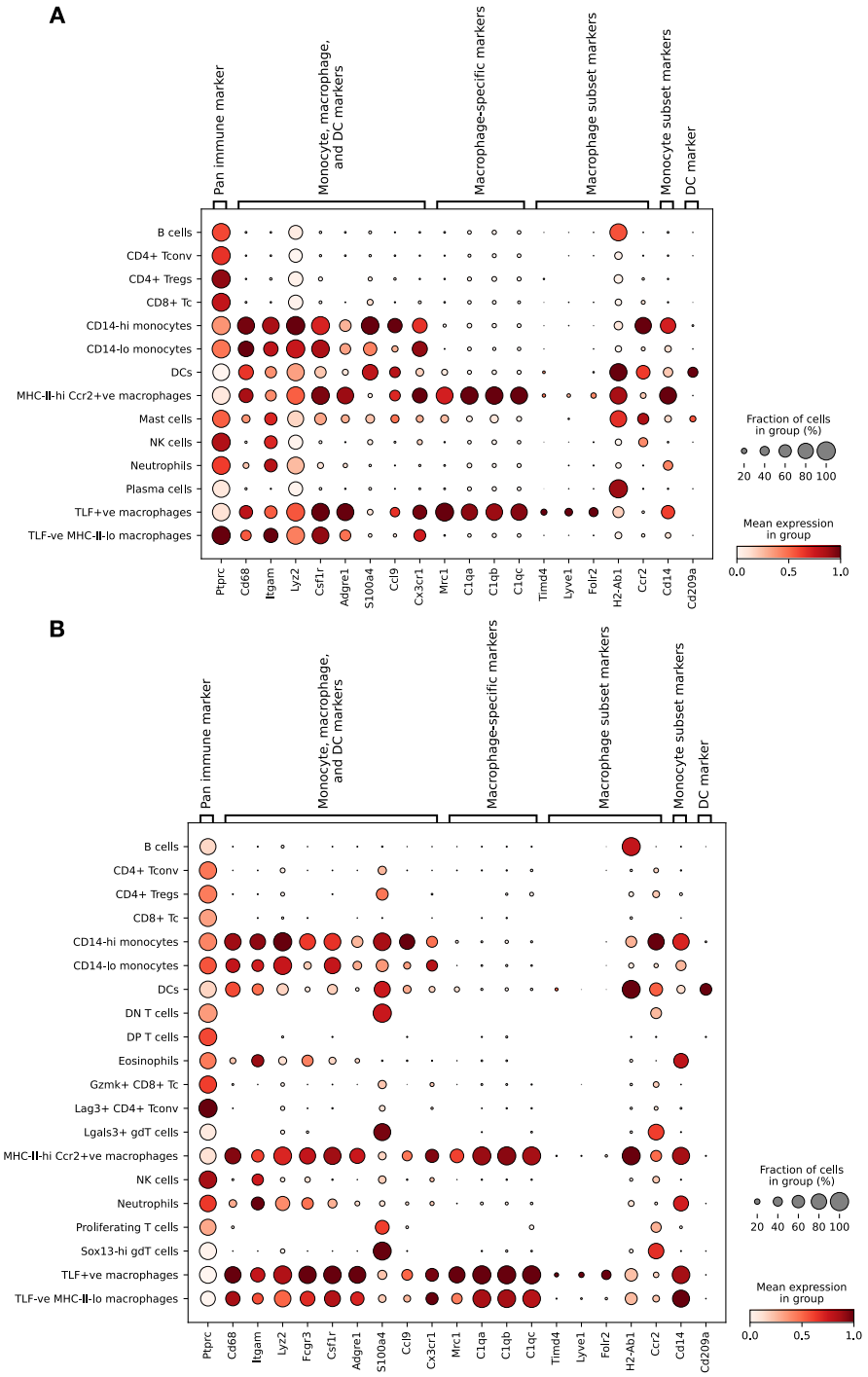

Figure 4.3. Canonical marker gene expression defining myeloid and dendritic cell populations within the CD45$^+$ fraction.
Data are shown for (A) early-stage (5 weeks) and (B) late-stage (60 weeks) samples. Each dot represents a specific cell cluster, as annotated on the y-axis. The size of the dot indicates the percentage of cells within that cluster expressing the gene, while the colour intensity reflects the mean expression level in expressing cells. Mean expression values are scaled from 0 to 1 for each gene (x-axis) to allow for comparison across different markers. Data were generated from N=3 mice per genotype. The spatial relationship between these clusters is shown in the UMAP visualisation in Figure 4.5.

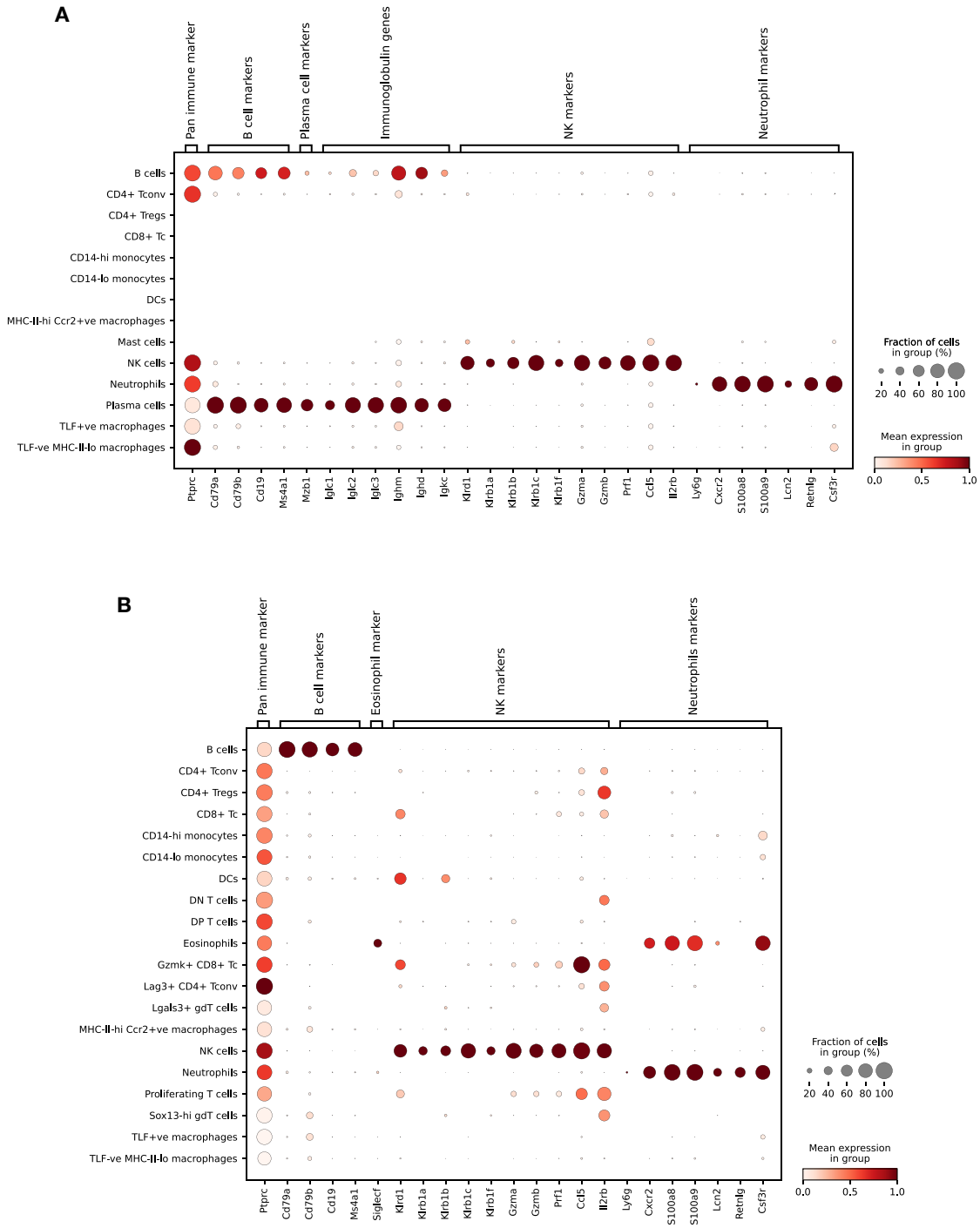

Figure 4.4. Canonical marker gene expression defining additional immune cell populations within the CD45$^+$ fraction.
Data are shown for (A) early-stage (5 weeks) and (B) late-stage (60 weeks) samples. Each dot represents a specific cell cluster, as annotated on the y-axis. The size of the dot indicates the percentage of cells within that cluster expressing the gene, while the colour intensity reflects the mean expression level in expressing cells. Mean expression values are scaled from 0 to 1 for each gene (x-axis) to allow for comparison across different markers. Data were generated from N=3 mice per genotype. The spatial relationship between these clusters is shown in the UMAP visualisation in Figure 4.5.

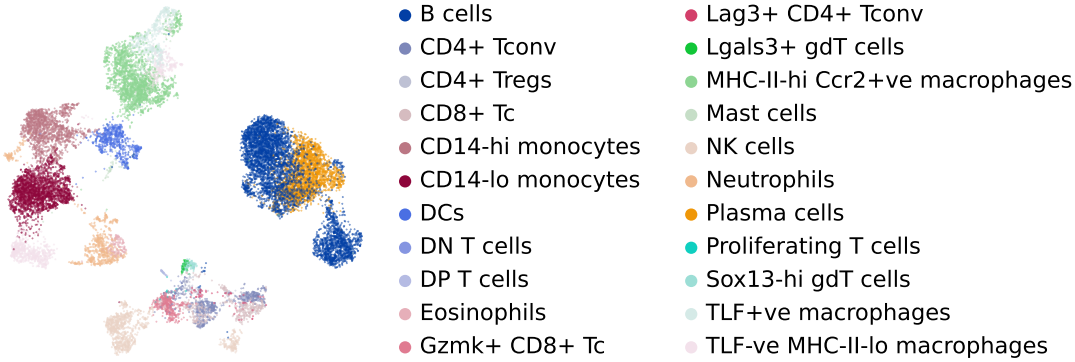

Figure 4.5. Integrated UMAP visualisation of annotated cell clusters within the CD45$^+$ immune cell population from both early and late-stage samples. The plot shows data from early-stage (5 weeks) and late-stage (60 weeks) WT and Actc1^{E99K} mice (N=3 per genotype per time point) integrated using the Harmony algorithm. Each point represents a single cell, positioned based on its integrated transcriptional profile. Colours correspond to the cell type annotations described in the text and detailed in the marker dotplots in Figures 4.2, 4.3, and 4.4.

4.1.3 Endothelial cells maintain vascular integrity and influence remodelling dynamics

Endothelial cells (Figures 4.6 and 4.7), constituents of blood vessel linings, were identified by *Pecam1* (CD31), *Cdh5* (VE-cadherin), *Emcn* (endomucin), and *Flt1* (VEGFR1) expression. These markers are characteristic of endothelial cells and contribute to vascular development, angiogenesis, and permeability [359–362]. Lymphatic endothelial cells, which line lymphatic vessels, expressed *Lyve1* and *Prox1*. LYVE1, a lymphatic vessel endothelial hyaluronan receptor, facilitates hyaluronan transport and lymphatic drainage [363]. PROX1, a transcription factor, is essential for lymphatic endothelial cell fate specification and maintenance [364–366]. *Vwf* (von Willebrand factor) was highly expressed in lymphatic endothelial cells and expressed at lower levels in endothelial cells. While typically associated with platelet adhesion and haemostasis in endothelial cells [367], its role in lymphatic endothelial cells may involve lymphatic vessel development and function [368, 369]. Conversely, *Cldn5* (claudin-5) showed high expression in endothelial cells and lower expression in lymphatic endothelial cells. Claudin-5, a

tight junction protein, maintains blood-brain barrier integrity and regulates vascular permeability in endothelial cells [370]. Its reduced expression in lymphatic endothelial cells may reflect the differing permeability of lymphatic vessels [371, 372].

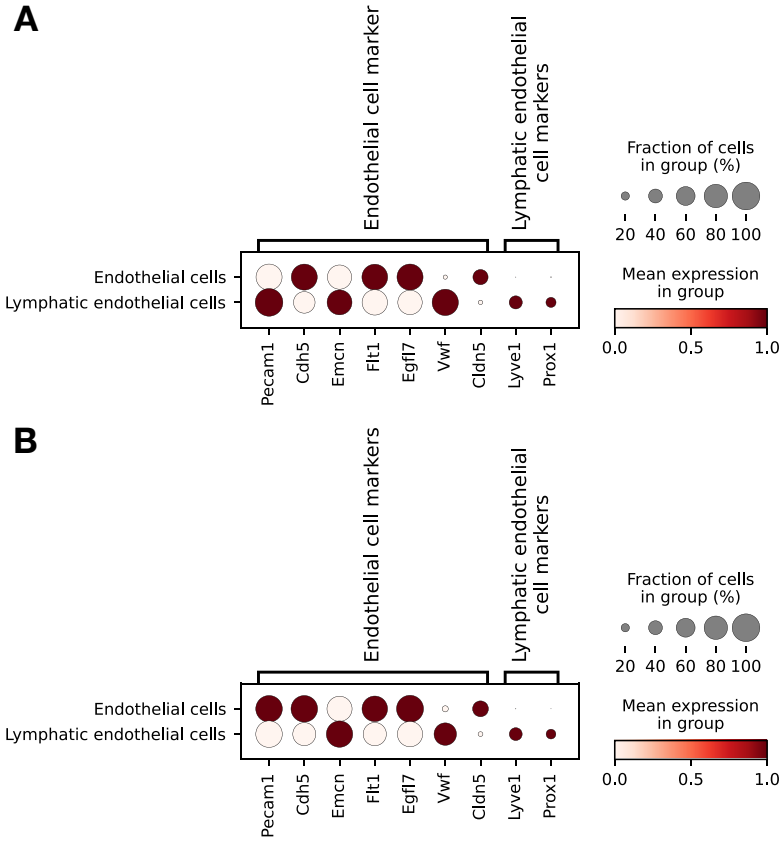

Figure 4.6. Dotplot of canonical marker genes used to identify endothelial cell populations in CD31^{+} cells.
Data are shown for (A) early-stage (5 weeks) and (B) late-stage (60 weeks) samples. Each dot represents a specific cell cluster, as annotated on the y-axis. The size of the dot indicates the percentage of cells within that cluster expressing the gene, while the colour intensity reflects the mean expression level in expressing cells. Mean expression values are scaled from 0 to 1 for each gene (x-axis) to allow for comparison across different markers. Data were generated from N=3 mice per genotype. The spatial relationship between these clusters is shown in the UMAP visualisation in Figure 4.7.

4.1.4 Stromal cells define the cardiac microstructure and mediate fibrotic signaling

Fibroblasts (Figures 4.8 and 4.9), the predominant cell type in the cardiac interstitium, expressed collagen genes (*Col1a1*, *Col1a2*, *Col3a1*, *Col5a1*) and *Loxl1* (ly-

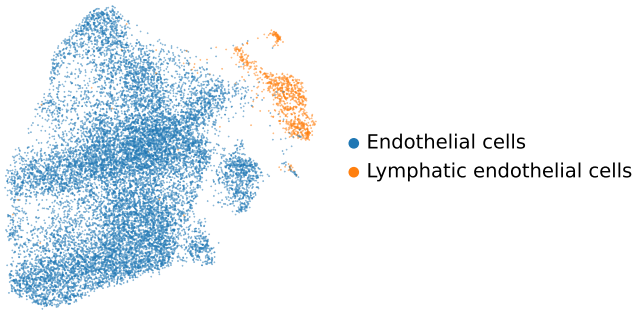

Figure 4.7. Integrated UMAP visualisation of annotated cell clusters within the CD31$^+$ endothelial cell population from both early and late-stage samples.
The plot shows data from early-stage (5 weeks) and late-stage (60 weeks) WT and Actc1^{E99K} mice (N=3 per genotype per time point) integrated using the Harmony algorithm. Each point represents a single cell, positioned based on its integrated transcriptional profile. Colours correspond to the cell type annotations described in the text and detailed in the marker dotplot in Figure 4.6.

syl oxidase-like 1). These genes encode extracellular matrix components and contribute to collagen synthesis and crosslinking, vital for maintaining cardiac structural integrity [373, 374]. Fibroblast subsets, distinguished by *Thy1* (CD90) and *Fap* (fibroblast activation protein) expression, included Thy1$^+$Fap$^+$, Thy1$^+$Fap^{lo} (observed only in late-stage samples), Thy1^{lo}Fap$^+$, and Thy1^{lo}Fap^{lo} fibroblasts. These subsets may represent different stages of fibroblast activation or differentiation, potentially playing distinct roles in tissue homeostasis and repair [375]. Pericytes, mural cells surrounding capillaries and microvessels, and VSMCs, comprising the medial layer of larger vessels, expressed *Pdgfrb* (PDGFRβ), *Rgs5* (regulator of G protein signalling 5), *Ano1* (anoctamin 1), and *Notch3* (Figures 4.8 and 4.9). These shared markers reflect their roles in vascular development, tone regulation, and blood flow control [376–379]. VSMCs were further characterised by *Tagln* (transgelin), *Acta2* (smooth muscle α-actin), *Myh11* (smooth muscle myosin heavy chain 11), *Cav1* (caveolin 1), *Lmod1* (leiomodin 1), and *Mylk* (myosin light chain kinase) expression. These genes participate in smooth muscle contraction and regulation [380–384]. Pericytes were further distinguished by *Cspg4* (NG2) and *Abcc9* (ATP-binding cassette sub-family C member 9) expression, reflecting their roles in vascular stability and blood-brain barrier maintenance

[385–387]. Neuronal cells expressed markers such as *Kcna1*, *Kcna2*, *Kcna6*, *Mbp* (myelin basic protein), *Sox10*, *Ncam1* (neural cell adhesion molecule 1), *L1cam*, *S100b*, *Gfra3* (GDNF family receptor α3), and *Erbb3*, indicating diverse functions including sensory innervation and autonomic regulation [388–396].

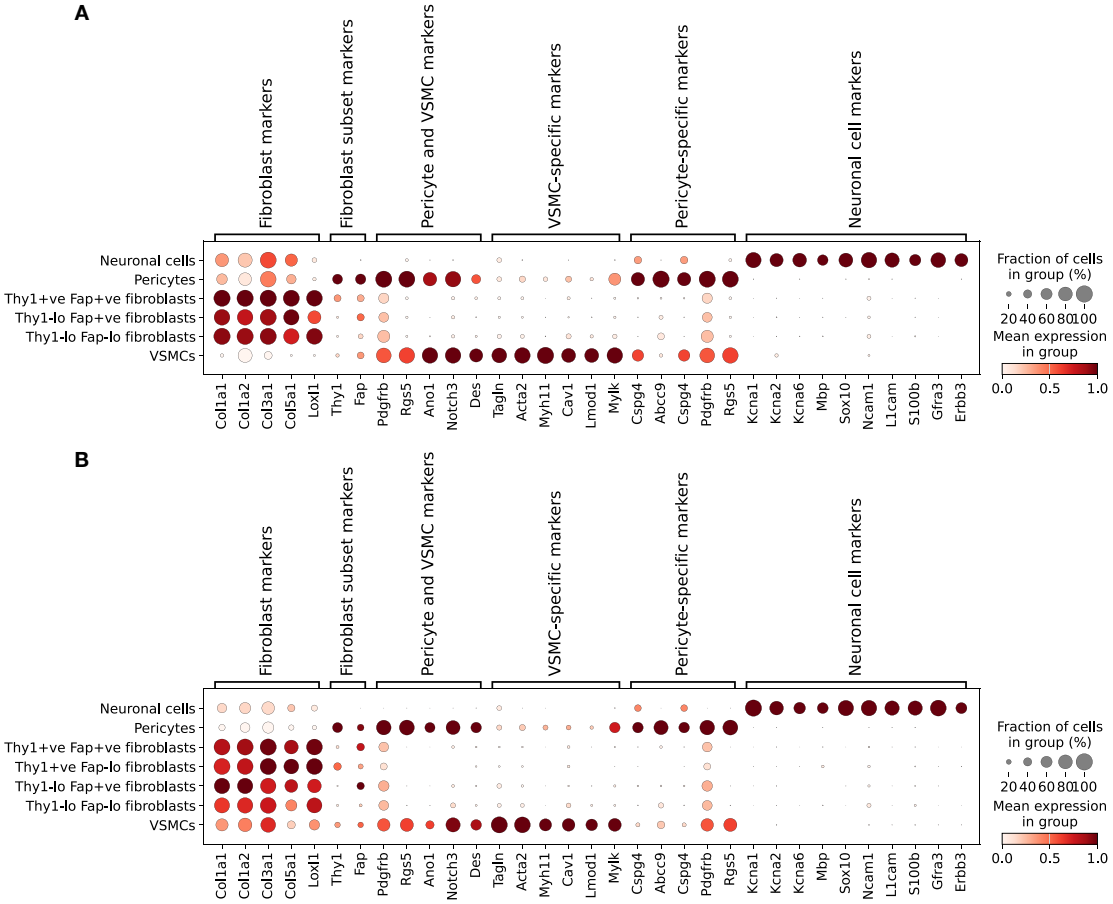

Figure 4.8. Dotplot of canonical marker genes used to identify stromal cell populations in CD45$^-$CD31$^-$ cells.
Data are shown for (A) early-stage (5 weeks) and (B) late-stage (60 weeks) samples. Each dot represents a specific cell cluster, as annotated on the y-axis. The size of the dot indicates the percentage of cells within that cluster expressing the gene, while the colour intensity reflects the mean expression level in expressing cells. Mean expression values are scaled from 0 to 1 for each gene (x-axis) to allow for comparison across different markers. Data were generated from N=3 mice per genotype. The spatial relationship between these clusters is shown in the UMAP visualisation in Figure 4.9.

This analysis revealed a complex cellular landscape within the non-cardiomyocyte compartment of the Actc1^{E99K} HCM mouse model. Characterising these distinct cell populations provides a basis for further investigation into their roles in HCM pathogenesis and the development of targeted therapies.

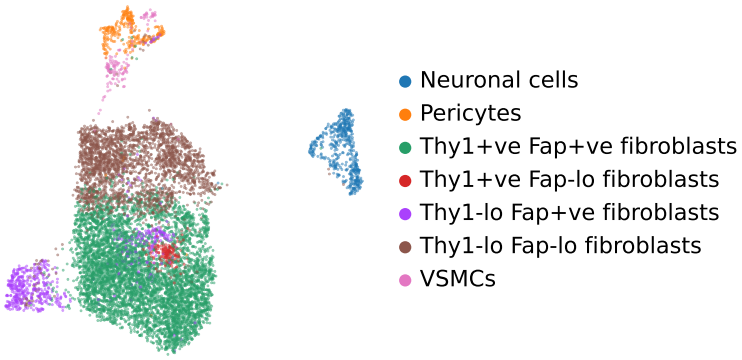

Figure 4.9. Integrated UMAP visualisation of annotated cell clusters within the CD45$^-$CD31$^-$ stromal cell population from both early and late-stage samples.
The plot shows data from early-stage (5 weeks) and late-stage (60 weeks) WT and Actc1^{E99K} mice (N=3 per genotype per time point) integrated using the Harmony algorithm. Each point represents a single cell, positioned based on its integrated transcriptional profile. Colours correspond to the cell type annotations described in the text and detailed in the marker dotplot in Figure 4.8.

4.2 Single-cell transcriptomics reveal dynamic regulatory networks in cardiac remodelling

4.2.1 Cellular census clarifies sample diversity and annotation precision

After characterising the non-cardiomyocyte cell types, I examined their transcriptional dynamics in the Actc1^{E99K} HCM model at both early (5 weeks) and late (60 weeks) stages. To determine differential gene expression between WT and Actc1^{E99K} samples, we used a pseudobulk approach with limma-voom [271], aggregating reads for each cell type and condition to create representative samples. This approach mitigated the impact of technical noise and dropout events inherent to scRNA-seq, improving statistical power. It also facilitated differential expression analysis by enabling the use of established statistical methods designed for bulk RNA-seq data.

However, this method requires adequate representation of each cell type across all conditions. Some cell types were absent or sparsely represented, preventing their inclusion in the pseudobulk differential expression analysis (Tables 4.2 and 4.3). In particular, DP T cells, DN T cells, proliferating T cells and $\gamma\delta$T cells

as well as eosinophils were observed only in the late-stage samples and not at 5 weeks—consistent with the chronic inflammatory milieu of advanced HCM—whereas they were undetectable in early-stage hearts. For example, eosinophils numbered 113 cells in late-stage E99K versus 4 cells in WT, and $\gamma\delta$T cells appeared exclusively at 60 weeks. Conversely, DN T cells (n = 2), DP T cells (n = 38), proliferating T cells (n = 13) and neuronal cells (n = 1) were present at very low abundance (fewer than 50 cells total or detected in only a single biological replicate), rendering any statistical comparison under-powered. Because we require at least 50 cells in at least two independent samples to obtain reliable pseudobulk estimates, these scarcely populated clusters were excluded from all downstream analyses. Consequently, the differential expression and pathway profiling focus only on cell types with sufficient representation ($\geq$ 50 cells in $\geq$ 2 replicates).

To assess how these filtering steps and the Actc1^{E99K} mutation alter the global cellular landscape, I next quantified both the absolute and relative abundances of each annotated cell type in early– and late–stage hearts (Figure 4.10 and Figure 4.11).

Table 4.2. Cell type composition and counts in early-stage hearts. This table summarises the number of biological replicates (Sample Count) and total cells (Cell Count) identified for each annotated cell type in the early-stage (5 weeks) Actc1^{E99K} and WT groups. These counts were used to determine which cell types had sufficient representation for robust downstream differential expression analysis.

Cell Type	Group	Sample Count	Cell Count
B cells	E99K	3	370
B cells	WT	3	731
CD4$^+$ Tconv	E99K	3	78
CD4$^+$ Tconv	WT	3	215
CD4$^+$ Tregs	E99K	1	3
CD4$^+$ Tregs	WT	2	27
CD8$^+$ Tc	E99K	3	65
CD8$^+$ Tc	WT	3	291
CD14^{hi} monocytes	E99K	3	70
CD14^{hi} monocytes	WT	3	152
CD14^{lo} monocytes	E99K	3	174
CD14^{lo} monocytes	WT	3	214
DCs	E99K	3	15
DCs	WT	2	38
Endothelial cells	E99K	3	1462
Endothelial cells	WT	3	1968

Continued on next page

Cell Type	Group	Sample Count	Cell Count
Lymphatic endothelial cells	E99K	2	10
Lymphatic endothelial cells	WT	3	36
MHC-II^{hi}Ccr2^{+} macrophages	E99K	3	64
MHC-II^{hi}Ccr2^{+} macrophages	WT	3	229
Mast cells	E99K	3	21
Mast cells	WT	2	35
NK cells	E99K	3	115
NK cells	WT	3	320
Neuronal cells	E99K	1	1
Neuronal cells	WT	3	87
Neutrophils	E99K	3	35
Neutrophils	WT	3	100
Pericytes	E99K	0	0
Pericytes	WT	3	72
Plasma cells	E99K	3	440
Plasma cells	WT	3	1879
TLF^{+} macrophages	E99K	3	104
TLF^{+} macrophages	WT	3	251
TLF^{-}MHC-II^{lo} macrophages	E99K	3	161
TLF^{-}MHC-II^{lo} macrophages	WT	3	424
Thy1^{+}Fap^{+} fibroblasts	E99K	3	78
Thy1^{+}Fap^{+} fibroblasts	WT	3	167
Thy1^{lo}Fap^{+} fibroblasts	E99K	3	149
Thy1^{lo}Fap^{+} fibroblasts	WT	3	153
Thy1^{lo}Fap^{lo} fibroblasts	E99K	3	247
Thy1^{lo}Fap^{lo} fibroblasts	WT	3	106
VSMCs	E99K	2	2
VSMCs	WT	3	14

Table 4.3. Cell type composition and counts in late-stage hearts. This table summarises the number of biological replicates (Sample Count) and total cells (Cell Count) identified for each annotated cell type in the late-stage (60 weeks) Actc1^{E99K} and WT groups. These counts were used to determine which cell types had sufficient representation for robust downstream differential expression analysis.

Cell Type	Group	Sample Count	Cell Count
B cells	E99K	3	1319
B cells	WT	3	1796
CD14^{hi} monocytes	E99K	3	847
CD14^{hi} monocytes	WT	3	261
CD14^{lo} monocytes	E99K	3	1143
CD14^{lo} monocytes	WT	3	405
CD4^{+} Tconv	E99K	3	105
CD4^{+} Tconv	WT	3	99
CD4^{+} Tregs	E99K	3	44
CD4^{+} Tregs	WT	3	4
CD8^{+} Tc	E99K	3	50
CD8^{+} Tc	WT	3	51
DCs	E99K	3	397
DCs	WT	3	125
DN T cells	E99K	0	0
DN T cells	WT	2	2
DP T cells	E99K	3	35
DP T cells	WT	2	3

Continued on next page

Cell Type	**Group**	**Sample Count**	**Cell Count**
Endothelial cells	E99K	3	5341
Endothelial cells	WT	3	5791
Eosinophils	E99K	3	113
Eosinophils	WT	2	4
Gzmk^{+}CD8^{+} Tc	E99K	3	223
Gzmk^{+}CD8^{+} Tc	WT	3	89
Lag3^{+}CD4^{+} Tconv	E99K	3	49
Lag3^{+}CD4^{+} Tconv	WT	3	15
Lgals3^{+} $\gamma\delta$T cells	E99K	3	18
Lgals3^{+} $\gamma\delta$T cells	WT	3	27
Lymphatic endothelial cells	E99K	3	114
Lymphatic endothelial cells	WT	3	723
MHC-II^{hi}Ccr2^{+} macrophages	E99K	3	1246
MHC-II^{hi}Ccr2^{+} macrophages	WT	3	399
NK cells	E99K	3	263
NK cells	WT	3	159
Neuronal cells	E99K	3	58
Neuronal cells	WT	3	332
Neutrophils	E99K	3	304
Neutrophils	WT	3	209
Pericytes	E99K	3	50
Pericytes	WT	3	155
Proliferating T cells	E99K	3	7
Proliferating T cells	WT	1	6
Sox13^{hi} $\gamma\delta$T cells	E99K	3	28
Sox13^{hi} $\gamma\delta$T cells	WT	3	71
TLF^{+} macrophages	E99K	3	129
TLF^{+} macrophages	WT	3	35
TLF^{-}MHC-II^{lo} macrophages	E99K	3	228
TLF^{-}MHC-II^{lo} macrophages	WT	3	25
Thy1^{+}Fap^{+} fibroblasts	E99K	3	2021
Thy1^{+}Fap^{+} fibroblasts	WT	3	2752
Thy1^{+}Fap^{lo} fibroblasts	E99K	3	51
Thy1^{+}Fap^{lo} fibroblasts	WT	3	102
Thy1^{lo}Fap^{+} fibroblasts	E99K	3	208
Thy1^{lo}Fap^{+} fibroblasts	WT	3	77
Thy1^{lo}Fap^{lo} fibroblasts	E99K	3	818
Thy1^{lo}Fap^{lo} fibroblasts	WT	3	1238
VSMCs	E99K	3	36
VSMCs	WT	3	78

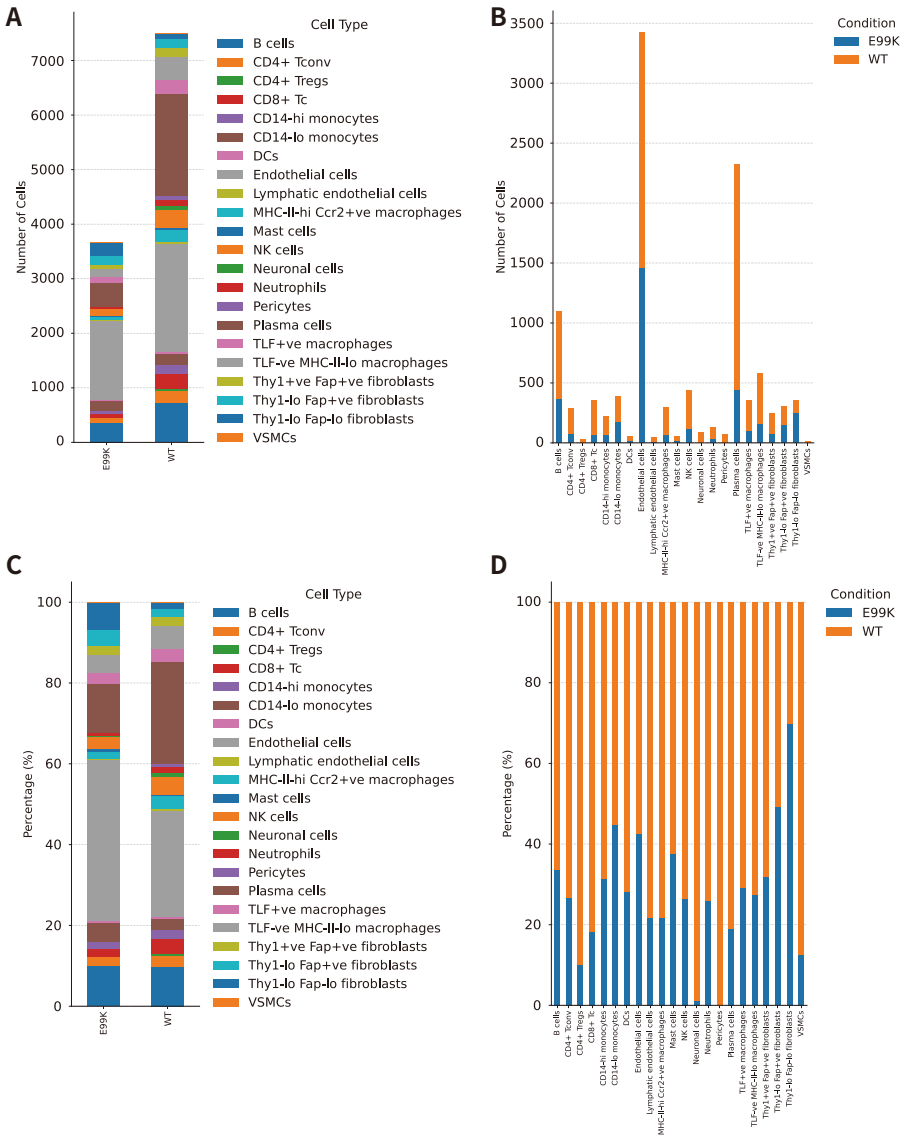

Figure 4.10. Cellular composition of non-cardiomyocyte populations in early-stage (5 weeks) hearts.
(A) Stacked bar plot showing the total number of cells recovered from Actc1^{E99K} (blue) and WT (orange) hearts, with contributions from each cell type indicated by coloured segments. (B) Bar plot showing the absolute cell counts for each annotated cell type, comparing Actc1^{E99K} and WT. (C) Stacked bar plot showing the relative abundance (percentage) of each cell type within the total non-cardiomyocyte pool for Actc1^{E99K} and WT hearts. (D) Bar plot showing the relative abundance of each cell type. These plots provide a descriptive summary of the cellular composition; no statistical tests for differential abundance are depicted.

4.2.2 Pathway profiling highlights stage-specific signalling shifts and metabolic reprogramming

To investigate altered functional pathways within each cell population, I performed GSEA [259] using the MSigDB hallmark gene sets v2023.1 [260, 261]. This revealed distinct pathway regulation between the early and late stages of the Actc1^{E99K} model (Figures 4.12 and 4.13). Early-stage samples showed fewer significantly enriched pathways than late-stage samples, with predominant pathway downregulation across most cell types. Thy1^{lo}Fap^{lo} fibroblasts were a notable exception, exhibiting consistent upregulation of pathways related to adipogenesis, cholesterol homeostasis, DNA repair, E2F targets, fatty acid metabolism, hypoxia, MTORC1 signalling, MYC targets V1 and V2, oxidative phosphorylation, peroxisome, TNF signalling via NF-κB, and UV response up. Endothelial cells displayed a mixed pattern, with upregulation of E2F targets, G2M checkpoint, inflammatory response, MYC targets V1 and V2, and oxidative phosphorylation, alongside downregulation of epithelial-mesenchymal transition, myogenesis, and UV response down.

Late-stage samples, conversely, were marked by widespread pathway upregulation (Figure 4.13). Adipogenesis was downregulated in several cell types, including pericytes, VSMCs, lymphatic endothelial cells, neuronal cells, Thy1^{+}Fap^{lo} fibroblasts, and Thy1^{+}Fap^{+} fibroblasts, yet upregulated in eosinophils, Lag3^{+}CD4^{+} conventional T cells, CD14^{hi} monocytes, and all macrophage populations. Allograft rejection pathways were consistently upregulated across diverse cell types in the late stage, suggesting an elevated immune response.

In early-stage Actc1^{E99K} hearts (Figure 4.12), the allograft rejection pathway was broadly downregulated across various immune cell populations, including all macrophage subtypes, CD14^{lo} monocytes, B cells, plasma cells, and neutrophils, suggesting a dampened or delayed early immune response. The KRAS signalling down pathway was upregulated in plasma cells, CD8^{+} T cells, CD4^{+} conventional T cells, and TLF^{-}MHC-II^{lo} macrophages, but not significantly altered

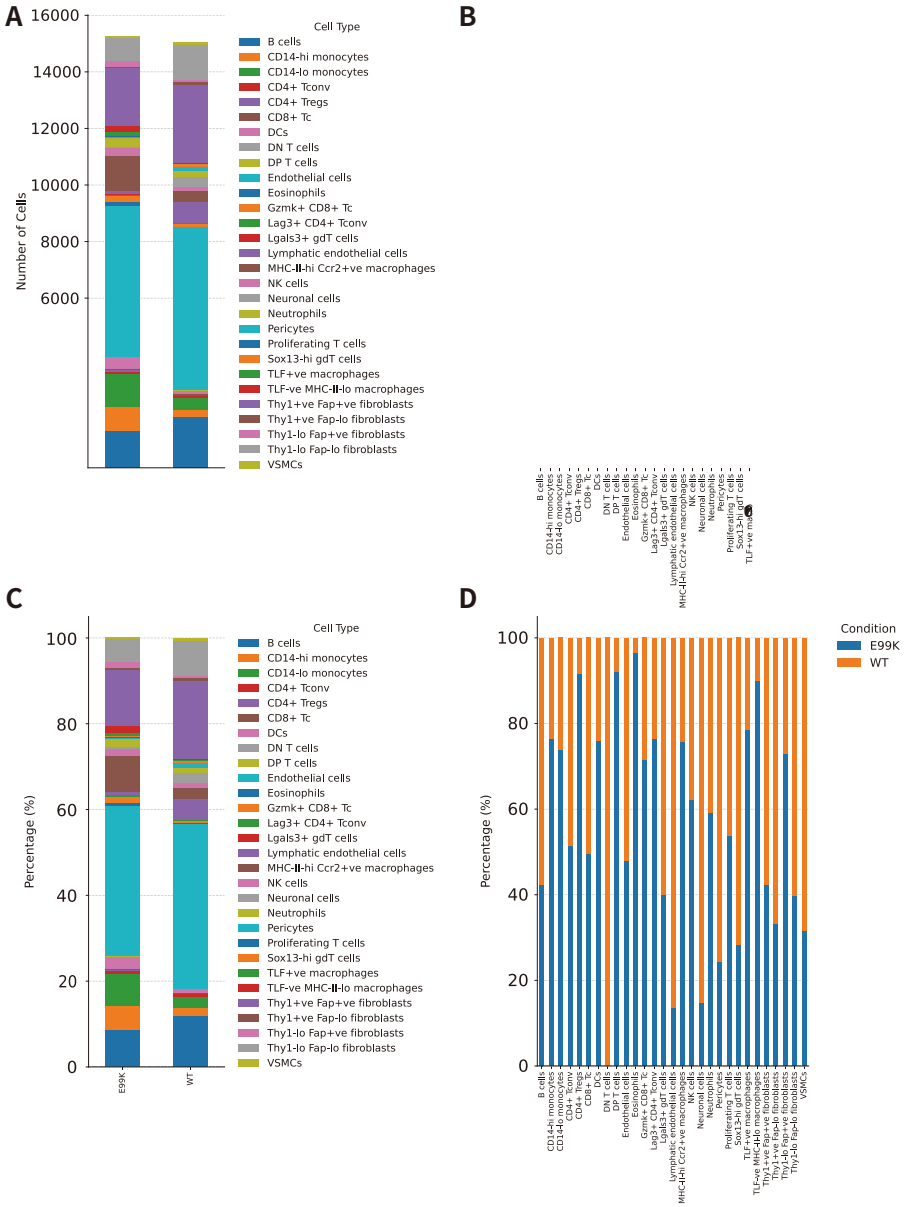

Figure 4.11. Cellular composition of non-cardiomyocyte populations in late-stage (60 weeks) hearts.
(A) Stacked bar plot showing the total number of cells recovered from Actc1^{E99K} (blue) and WT (orange) hearts, with contributions from each cell type indicated by coloured segments. (B) Bar plot showing the absolute cell counts for each annotated cell type, comparing Actc1^{E99K} and WT. (C) Stacked bar plot showing the relative abundance (percentage) of each cell type within the total non-cardiomyocyte pool for Actc1^{E99K} and WT hearts. (D) Bar plot showing the relative abundance of each cell type. These plots provide a descriptive summary of the cellular composition; no statistical tests for differential abundance are depicted.

in other cell types. Oxidative phosphorylation was predominantly downregulated in most cell types, including MHC-II^{hi}Ccr2^{+} macrophages, TLF^{-}MHC-II^{lo} macrophages, all monocyte and lymphocyte subtypes, mast cells, dendritic cells, Thy1^{+}Fap^{+} fibroblasts, and VSMCs, yet upregulated in endothelial cells, Thy1^{lo}Fap^{lo}fibroblasts, and TLF^{+} macrophages. Both interferon-α and interferon-γ response pathways were consistently downregulated in mast cells, neutrophils, NK cells, plasma cells, all monocyte subtypes, and TLF^{-}MHC-II^{lo} macrophages, with interferon-γ response also downregulated in MHC-II^{hi}Ccr2^{+} macrophages. The epithelial-mesenchymal transition pathway was downregulated in VSMCs, endothelial cells, Thy1^{+}Fap^{+} fibroblasts, and Thy1^{lo}Fap^{+} fibroblasts, but upregulated in NK cells. Finally, MYC targets V1 and V2 showed complex regulation, with downregulation in many cell types, but upregulation in endothelial cells and Thy1^{lo}Fap^{lo} fibroblasts (both V1 and V2), and uniquely in VSMCs for V2.
Late-stage Actc1^{E99K} hearts (Figure 4.13), in contrast, exhibited a marked shift towards pathway upregulation. The allograft rejection pathway, downregulated in the early stage, was significantly upregulated in almost all cell types, indicating a robust immune response in later-stage HCM. This aligns with the increased immune cell infiltration observed phenotypically in late-stage Actc1^{E99K} hearts (Figure 1.5). Widespread upregulation of immune activation and inflammation pathways, including complement, inflammatory response, interferon-α and interferon-γ responses, and TNF signalling, further underscores the prominent role of inflammation in late-stage HCM pathogenesis. Metabolic pathways, including cholesterol homeostasis, glycolysis, and oxidative phosphorylation, also showed distinct regulatory patterns. While cholesterol homeostasis was upregulated in several cell types, oxidative phosphorylation was predominantly downregulated, particularly in endothelial cells and various fibroblast populations. Growth and development pathways, such as E2F targets, MYC targets V1, and G2M checkpoint, were also largely upregulated, suggesting continued cellular remodelling and proliferation. These findings highlight the complex interplay of cellular processes and pathways in HCM progression, transitioning from a

relatively quiescent early stage to a highly activated and inflamed late stage. This detailed characterisation of adverse remodelling in HCM provides a valuable framework for identifying potential therapeutic targets and developing novel strategies for early intervention and disease management.

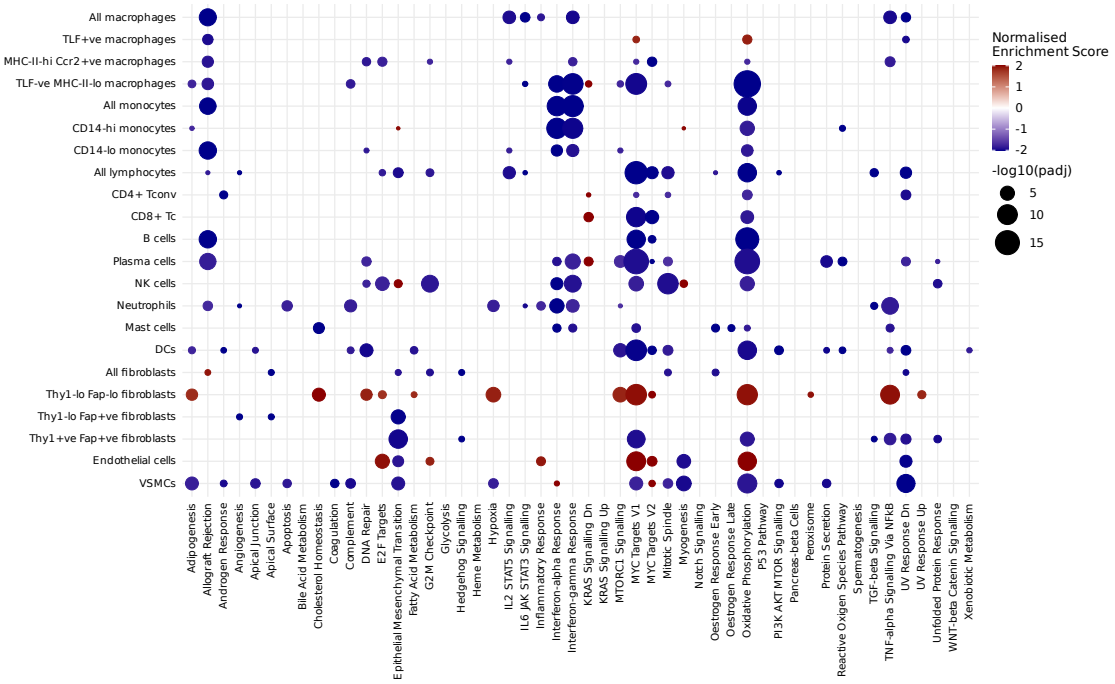

Figure 4.12. GSEA analysis of hallmark pathways in early-stage Actc1^{E99K} mouse samples.
Dotplot summarising Gene Set Enrichment Analysis (GSEA) results for hallmark pathways in each cell type at 5 weeks. The colour of each dot indicates the normalised enrichment score (NES), with red signifying upregulation and blue signifying downregulation of the pathway in Actc1^{E99K} versus WT samples. The size of the dot is proportional to the statistical significance (adjusted p-value). Only pathways with an adjusted p-value < 0.05 are displayed.

To investigate signalling dynamics within non-cardiomyocytes, I used PROGENy, a pathway activity inference method. PROGENy, leveraging a compendium of publicly available perturbation experiments (primarily in cancer models), defines a core set of pathway-responsive genes for both human and mouse [272–274]. While acknowledging the limitations of applying cancer-derived data to cardiac contexts, PROGENy offers a valuable resource for inferring pathway activities from transcriptomic data, enabling us to explore the broader functional consequences of gene expression changes in HCM. Critically, PROGENy assesses

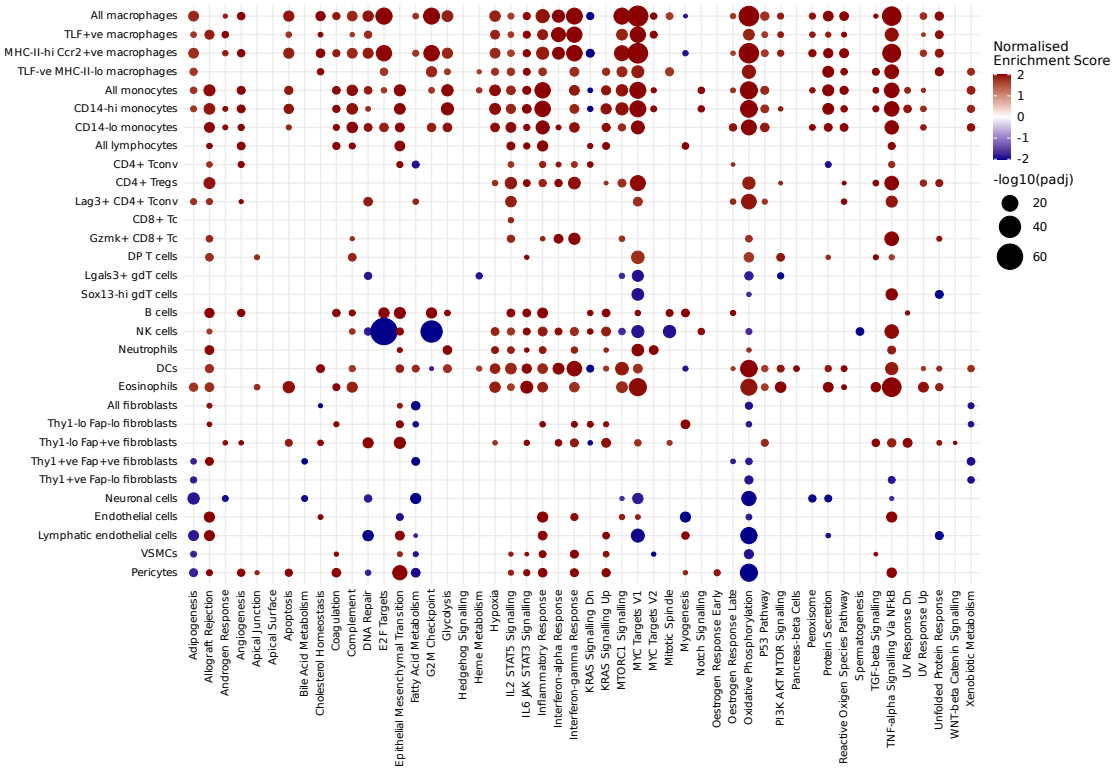

Figure 4.13. GSEA analysis of hallmark pathways in late-stage Actc1^{E99K} mouse samples.
Dotplot summarising Gene Set Enrichment Analysis (GSEA) results for hallmark pathways in each cell type at 60 weeks. The colour of each dot indicates the normalised enrichment score (NES), with red signifying upregulation and blue signifying downregulation of the pathway in Actc1^{E99K} versus WT samples. The size of the dot is proportional to the statistical significance (adjusted p-value). Only pathways with an adjusted p-value < 0.05 are displayed.

pathway *activity* (a measure of a pathway's overall effect) rather than pathway *enrichment* (over-representation of pathway-related genes). Therefore, we discuss changes in pathway activity rather than individual gene up- or down-regulation. I analysed fourteen key signalling pathways: growth factor signalling (epidermal growth factor receptor (EGFR), vascular endothelial growth factor (VEGF), TGF-β); hormone signalling (androgen, oestrogen); stress and inflammatory signalling (hypoxia, NF-κB, TNF, Trail); key intracellular signalling pathways (JAK-STAT, MAPK, PI3K, WNT); and the p53 tumour suppressor pathway (Figures 4.14 and 4.15).

In early-stage Actc1^{E99K} hearts, pathway activity changes were relatively small, with a mix of increases and decreases, suggesting that initial adverse remodelling

phases are characterised by relatively mild signalling perturbations (Figure 4.14). Increased Trail pathway activity was observed, potentially indicating an early role for apoptosis. Conversely, reduced JAK-STAT pathway activity was observed across most cell types except VSMCs. In lymphocytes, EGFR, hypoxia, NF-κB, and p53 pathway activities were increased, suggesting early activation within the immune compartment. More specifically, B cells showed increased Androgen and Hypoxia pathway activity, while CD14^{lo} monocytes and neutrophils displayed reduced Androgen and JAK-STAT activity. Elevated EGFR pathway activity was observed in CD4^{+} conventional T cells, CD8^{+} cytotoxic T cells, endothelial cells, and NK cells. Within fibroblast populations, Thy1^{lo}Fap^{lo} fibroblasts exhibited increased Oestrogen and p53 pathway activity, while Thy1^{lo}Fap^{+} fibroblasts showed increased NF-κB and PI3K activity.

In contrast, late-stage Actc1^{E99K} hearts displayed more pronounced pathway activity shifts, reflecting amplified signalling perturbations in advanced adverse remodelling (Figure 4.15). A general trend towards increased pathway activity was observed across multiple cell types and pathways. NF-κB activity, a key regulator of inflammation, was elevated in endothelial cells, lymphatic endothelial cells, VSMCs, and pericytes, but not in fibroblasts, suggesting that while NF-κB signalling may contribute to the late-stage inflammatory milieu in HCM, its role in fibroblast activation may be less direct. Within fibroblasts, TGF-β signalling showed the most substantial activity increase, consistent with its established role in fibrosis. Additionally, other growth and remodelling pathways, including PI3K, VEGF, MAPK, and WNT, also showed increased activity in certain fibroblast subtypes. Increased NF-κB activity was also observed in B cells, $\gamma\delta$T cells, NK cells, neutrophils, and myeloid cells. These findings highlight the complex interplay of signalling pathways within the diverse cellular landscape of the remodelling heart. For example, Androgen pathway activity was increased in B cells and CD4^{+} regulatory T cells but reduced in neuronal cells. Similarly, Oestrogen pathway activity was increased in pericytes but reduced in eosinophils.

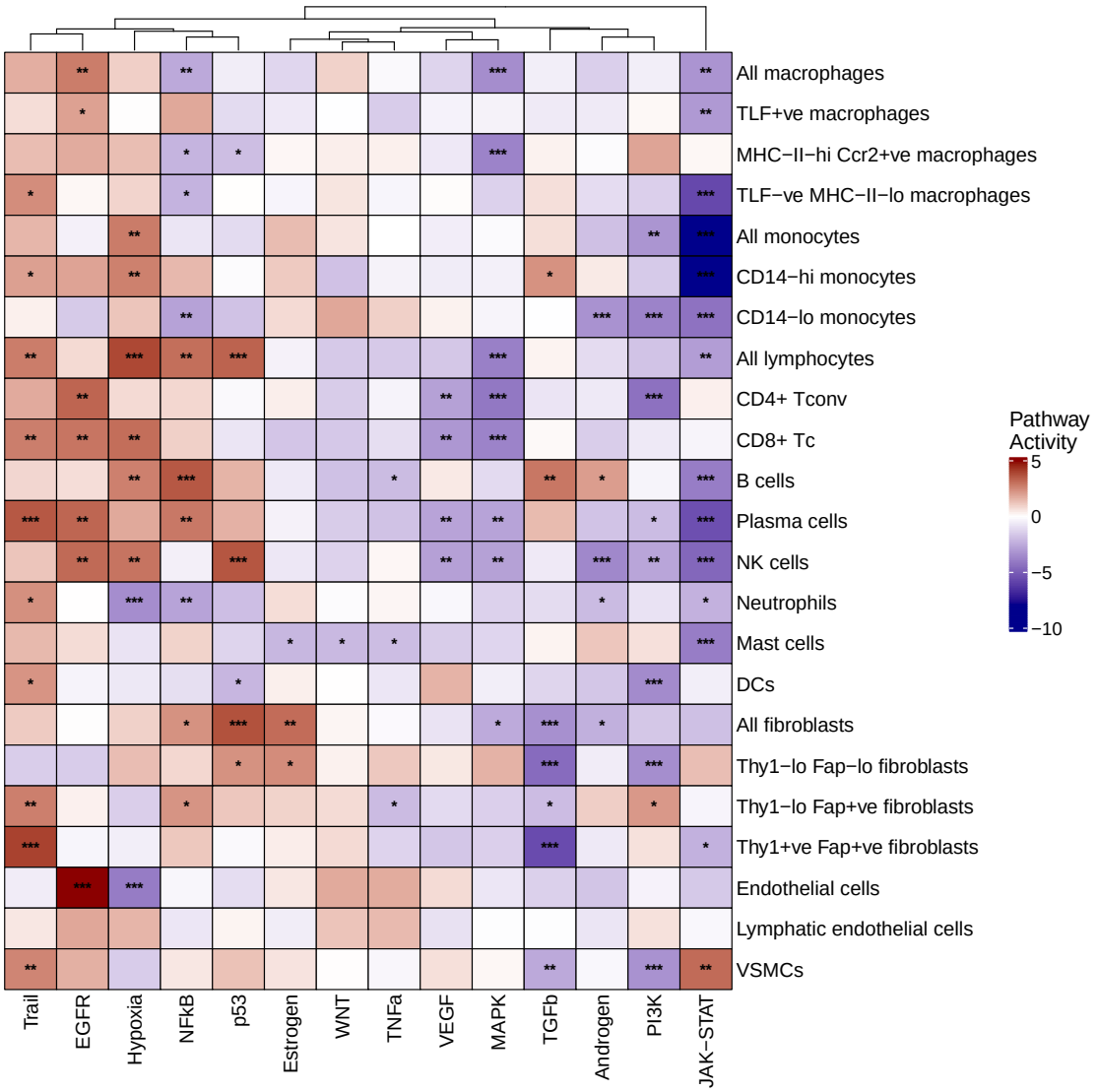

Figure 4.14. PROGENy analysis of signalling pathway activity in early-stage hearts.
This heatmap displays the inferred activity scores for fourteen key signalling pathways across different cell types at 5 weeks, comparing Actc1^{E99K} to WT samples. PROGENy infers pathway activity based on the collective expression of downstream target genes. The colour scale represents the activity score, with red indicating increased activity and blue indicating decreased activity in Actc1^{E99K} hearts. Significance levels derived from statistical comparison are indicated as follows: * $p < 0.05$, ** $p < 0.01$, *** $p < 0.001$.

This intricate network of signalling changes underscores the need for cell-type-specific analyses to fully understand HCM pathogenesis.

Hypoxia pathway activity was broadly increased in late-stage Actc1^{E99K} hearts, affecting diverse cell types including monocytes, DCs, endothelial cells, eosinophils, lymphatic endothelial cells, NK cells, neuronal cells, pericytes, macrophages, and Thy1^{lo}Fap^{+} fibroblasts. This widespread activation likely reflects compromised tissue oxygenation common in advanced cardiac remodelling [397–400]. JAK-STAT pathway activity, generally suppressed in the early stage, showed increased activity in the late stage across several cell types, including CD4^{+} T cells, CD4^{+} regulatory T cells, DCs, endothelial cells, CD8^{+} cytotoxic T cells, macrophages, NK cells, neuronal cells, and fibroblasts, but remained suppressed in DP T cells and Lag3^{+}CD4^{+} T cells. MAPK pathway activity was elevated in monocytes, endothelial cells, macrophages, neutrophils, and fibroblasts, suggesting its involvement in both inflammatory and fibrotic processes. Increased PI3K activity was observed in B cells, monocytes, CD4^{+} T cells, endothelial cells, lymphatic endothelial cells, neuronal cells, pericytes, and fibroblasts. TGF-β signalling, as noted previously, was broadly activated across various cell types, including monocytes, CD4^{+} regulatory T cells, CD8^{+} cytotoxic T cells, lymphatic endothelial cells, neuronal cells, pericytes, macrophages, and fibroblasts, reinforcing its central role in driving the fibrotic response in HCM.

Furthermore, TNF pathway activity was increased in CD4^{+} regulatory T cells, neuronal cells, and Thy1^{lo}Fap^{lo} fibroblasts, while Trail pathway activity was elevated in monocytes, lymphatic endothelial cells, NK cells, and neuronal cells. VEGF signalling, crucial for angiogenesis, showed increased activity in monocytes, DCs, endothelial cells, CD8^{+} cytotoxic T cells, macrophages, and fibroblasts. WNT pathway activity was also increased in several cell types, including monocytes, CD4^{+} T cells, lymphatic endothelial cells, macrophages, and fibroblasts. Finally, p53 pathway activity was elevated in monocytes, DCs, eosinophils, Lag3^{+}CD4^{+} T cells, and NK cells.

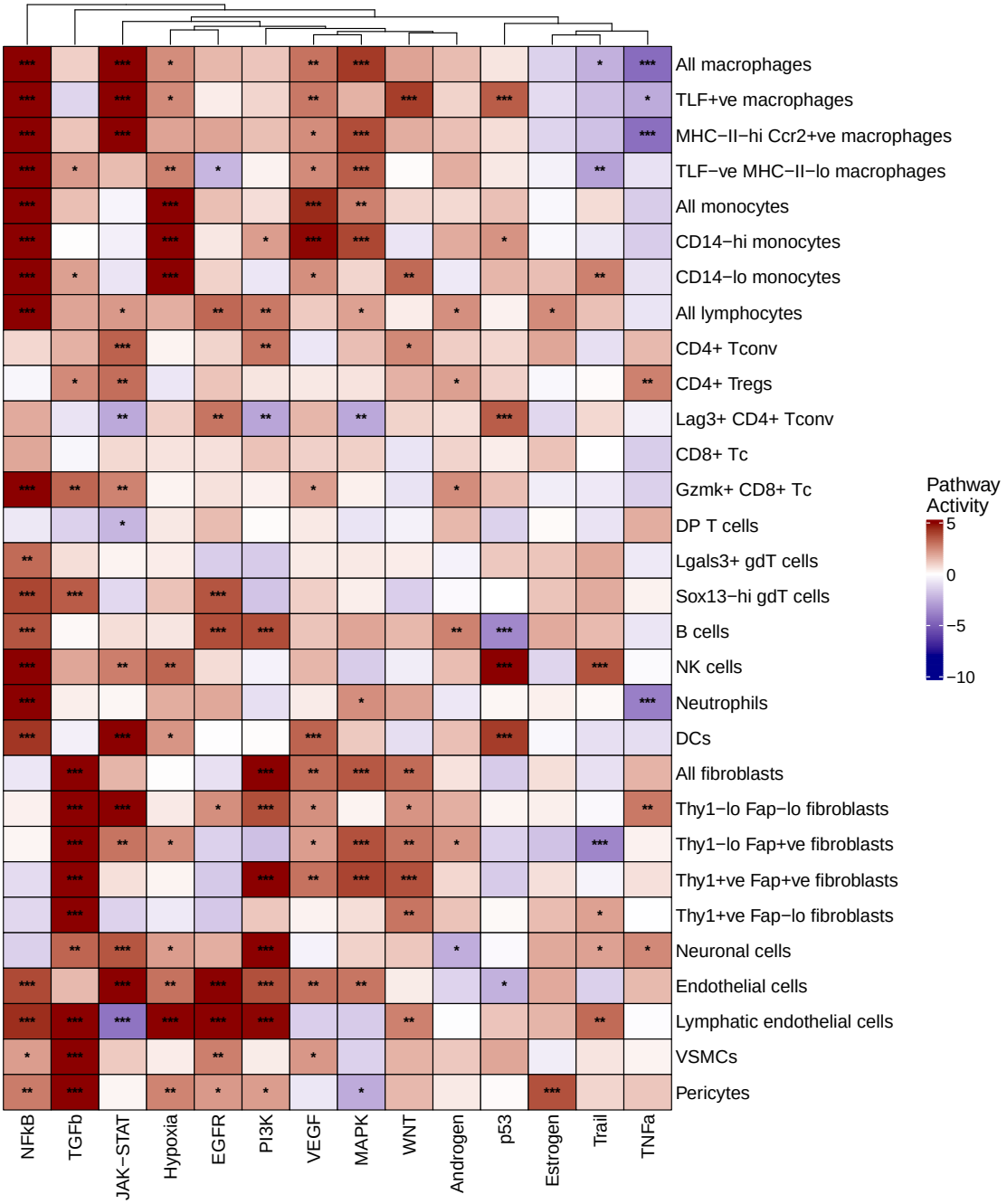

Figure 4.15. PROGENy analysis of signalling pathway activity in late-stage hearts.
This heatmap displays the inferred activity scores for fourteen key signalling pathways across different cell types at 60 weeks, comparing Actc1^{E99K} to WT samples. The colour scale represents the activity score, with red indicating increased activity and blue indicating decreased activity in Actc1^{E99K} hearts. Significance levels derived from statistical comparison are indicated as follows: * $p < 0.05$, ** $p < 0.01$, *** $p < 0.001$.

These detailed pathway activity analyses reveal a complex, dynamic interplay of signalling cascades within the non-cardiomyocyte compartment during HCM progression. The observed shifts highlight the diverse roles of different cell types in adverse remodelling. For instance, widespread Hypoxia and TGF-β signalling activation underscores their importance in HCM pathogenesis. Furthermore, cell-type-specific changes, such as increased NF-κB activity in immune cells but not fibroblasts, provide valuable insights into the complex cellular crosstalk driving the remodelling process.

4.2.3 Profibrotic cytokine maps reveal key drivers of fibrosis

Profibrotic cytokines are key drivers of adverse cardiac remodelling, particularly fibrosis, a hallmark of HCM progression and a major contributor to declining cardiac function [140, 178]. To understand their roles in the non-cardiomyocyte compartment of Actc1^{E99K} hearts, I investigated the cellular sources and temporal dynamics of these signalling molecules. Bulk RNA-sequencing data from various Actc1^{E99K} HCM mouse models consistently revealed upregulation of *Tgfb2* and *Tgfb3* (Figure 4.16). Furthermore, increased expression of *Tgfb1* and *Il11* was primarily observed in the Actc1^{E99K} and α-MHC^{R403Q} models, while *Il6* upregulation was more prominent in the Actc1^{E99K} model (Figure 4.16). This complex interplay of profibrotic cytokines warrants single-cell resolution analysis to pinpoint their cellular origins and provide crucial insights into the fibrotic mechanisms driving HCM, ultimately informing targeted therapeutic development.
Analysis of single-cell data from 5-week-old Actc1^{E99K} hearts revealed the cellular origins of these profibrotic signals during early adverse remodelling (Figure 4.17, left panel). Within the stromal compartment, *Tgfb2* and *Tgfb3* were significantly upregulated in Actc1^{E99K} VSMCs compared to WT controls. This upregulation was largely specific to VSMCs, with negligible differences in fibroblasts or other non-cardiomyocyte populations. Conversely, *Il6* and *Il11* expression showed no discernible differences between Actc1^{E99K} and WT cells within the

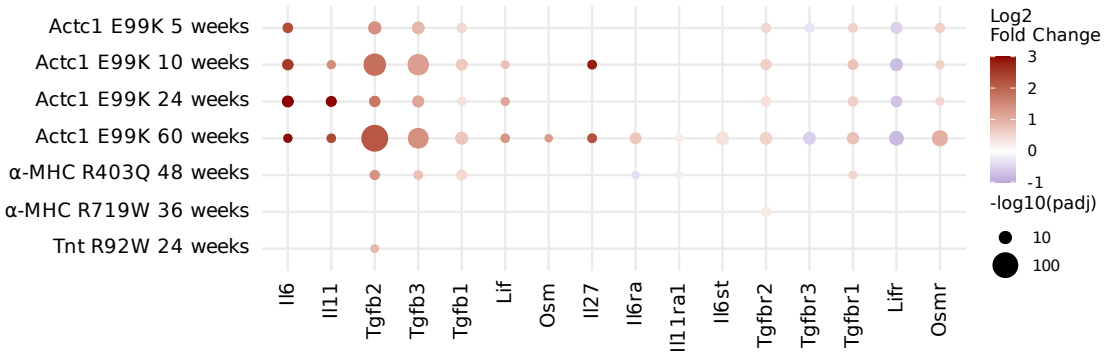

Figure 4.16. Expression of key profibrotic cytokines across multiple HCM mouse models from bulk RNA-sequencing data.
The heatmap displays the log2 fold change in expression for profibrotic cytokine genes in whole heart tissue from different mouse models of HCM compared to their respective wild-type controls. This analysis provides a global overview of cytokine dysregulation in HCM, setting the context for the single-cell investigation.

non-cardiomyocyte compartment at this stage. While the absence of *Il11* upregulation is consistent with the bulk RNA-seq data, the lack of detectable *Il6* differences at the single-cell level, despite its bulk tissue upregulation in Actc1^{E99K} hearts, suggests a potential source outside the examined non-cardiomyocyte populations. Mutant cardiomyocytes may contribute to this early *Il6* upregulation, a hypothesis warranting further investigation.

In 60-week-old Actc1^{E99K} hearts, the profibrotic cytokine expression landscape shifts (Figure 4.17, right panel). While VSMCs maintain elevated *Tgfb3*, *Tgfb2* upregulation is less pronounced than at the earlier stage. However, *Il6* and *Tgfb1* expression increases significantly in VSMCs at this later time point. Moreover, this upregulation extends to other stromal cells, including endothelial cells and certain fibroblast subpopulations, suggesting a more complex profibrotic signalling network in late-stage HCM. *Tgfb1* appears more ubiquitously expressed across stromal and immune cells, while *Tgfb2*, *Tgfb3*, *Il6*, and *Il11* expression is predominantly localised within the stromal compartment. Despite the less pronounced *Tgfb2* upregulation in late-stage VSMCs at the single-cell level, its persistent elevation in bulk RNA-seq data from whole Actc1^{E99K} hearts suggests

cardiomyocytes may be a significant source, particularly in late-stage disease, a hypothesis requiring further investigation. This dynamic interplay of profibrotic cytokines underscores the need for cell-type-specific therapeutic targeting in HCM.

4.2.4 Dynamic RNA analysis traces cellular trajectories and future states in heart remodelling

RNA velocity analysis leverages the ratio of unspliced to spliced mRNA to provide insights into the dynamics of cellular populations [276, 277]. This ratio serves as a proxy for transcriptional activity: a higher ratio indicates active transcription, while a lower ratio suggests reduced activity or increased mRNA degradation. This concept underpins "RNA velocity," which projects a cell's future transcriptional state based on this balance. By modelling splicing kinetics, RNA velocity predicts the direction and magnitude of transcriptional changes, effectively forecasting a cell's trajectory through transcriptional space.
Trajectory inference connects individual cell velocities, forming a continuous path representing the likely developmental or differentiation course. Transition probabilities between cells are calculated based on the alignment of their velocity vectors. Cells with similar velocities and aligned trajectories are more likely to be connected, creating a directed graph representing the overall flow of cellular states. Pseudotime, a measure of a cell's progression along a trajectory, is inferred by ordering cells based on their position. Cells at the trajectory's beginning are assigned lower pseudotime values, increasing as cells progress, providing a quantitative measure of cellular differentiation or developmental stage, independent of experimental time.

Integrated trajectory analysis across time points offers a holistic view of cellular progression

To capture the full developmental trajectories of non-cardiomyocyte populations over the entire disease course, the early- and late-stage datasets were integrated

Figure 4.17. Cell-type-specific expression of profibrotic cytokines in early- and late-stage Actc1^{E99K} hearts.

These dot plots show the distribution of normalised expression for key profibrotic cytokine genes across all major non-cardiomyocyte populations, comparing Actc1^{E99K} and WT samples. The left panel shows data from the early stage (5 weeks), and the right panel shows data from the late stage (60 weeks). This analysis pinpoints the specific cellular sources of these important signalling molecules and reveals how their expression patterns change over the course of disease progression. Vascular smooth muscle cells (VSMCs) are highlighted with a red box to draw attention to their significant contribution.

for a combined RNA velocity analysis. This approach aims to construct a single, continuous map of cellular progression. However, it is important to note a key technical limitation: the early- and late-stage samples derive from different sequencing batches, creating a confounding variable between the biological time point and the technical batch. While batch correction was applied to mitigate inter-sample variation, residual technical effects may still influence the integrated trajectories. Therefore, this analysis should be interpreted as a complementary perspective to the stage-specific analyses presented previously.

Integrated immune cell trajectories reveal conserved and divergent dynamics The integrated analysis of $CD45^+$ immune cells highlights both conserved and genotype-specific dynamics over time (Figure 4.18). In both $Actc1^{E99K}$ and WT hearts, neutrophils consistently exhibited high velocity lengths, indicating a persistently dynamic transcriptional state throughout the disease process. The most striking difference was observed in B cell trajectories, which flowed in opposite directions between the $Actc1^{E99K}$ and WT models, suggesting a fundamental alteration in B cell activation or differentiation pathways in the diseased state. Pseudotime analysis further clarified these dynamics. In $Actc1^{E99K}$ hearts, the trajectory appeared to progress from neutrophils through monocytes, macrophages, and T cells, terminating at B cells. In contrast, the WT trajectory also began with neutrophils and progressed through myeloid cells, but then proceeded to B cells before ending with T cells. This suggests a different sequence of immune cell activation and resolution in the context of the $Actc1^{E99K}$ mutation. A minor separation of the B cell population is apparent in the integrated UMAP, which may reflect a residual technical artefact or genuine biological heterogeneity between B cells at the two time points.

Integrated endothelial cell analysis shows opposing progression patterns In the integrated $CD31^+$ endothelial cell dataset, the overall trajectory streamlines and velocity lengths appeared broadly similar between $Actc1^{E99K}$

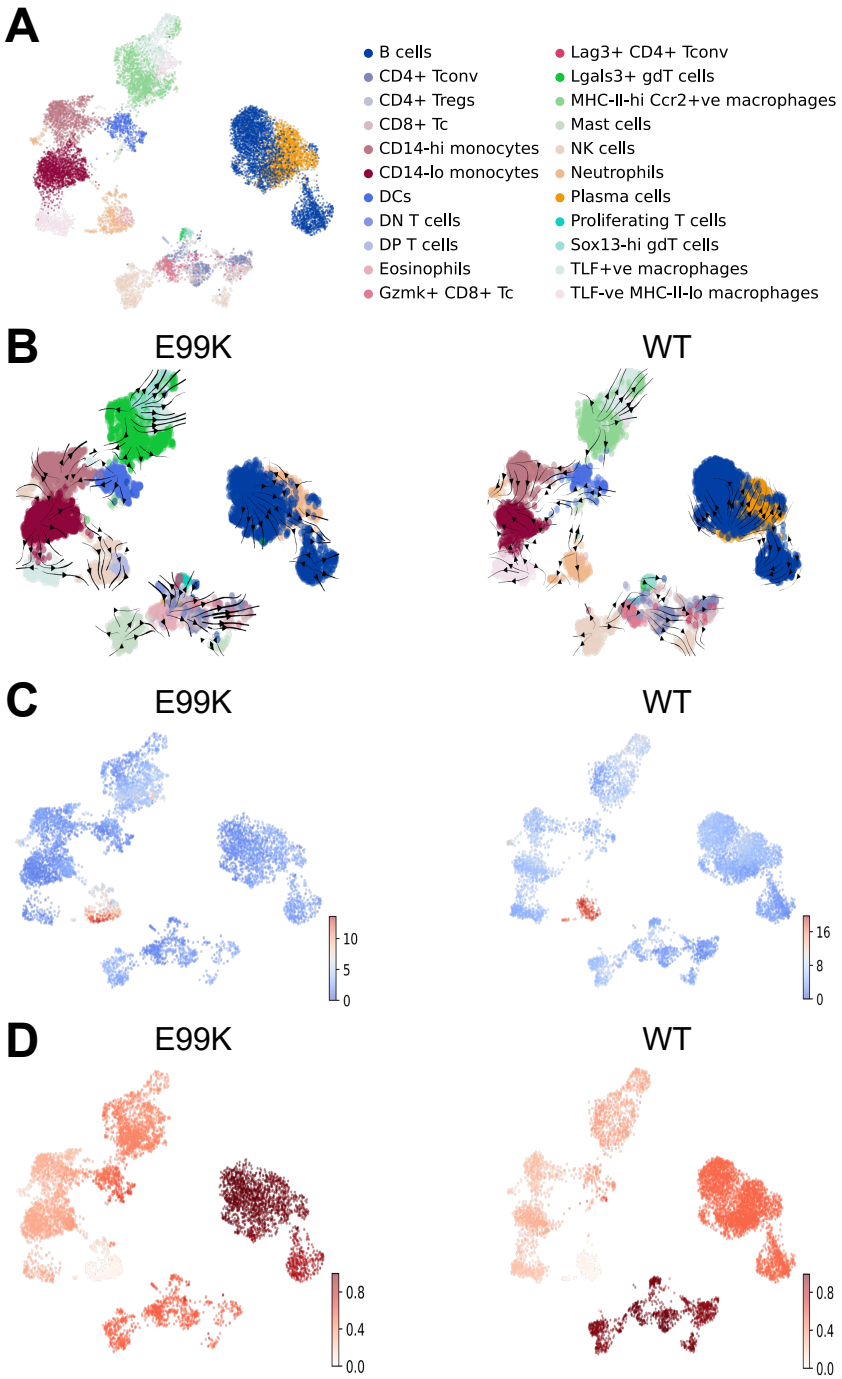

Figure 4.18. Integrated trajectory analysis of CD45$^+$ immune cells from combined early and late stages.
(A) UMAP of integrated CD45$^+$ cells from Actc1^{E99K} and WT mice, annotated by cell type. (B) Streamline plots illustrating RNA velocity trajectories for Actc1^{E99K} (left) and WT (right) samples. Arrows indicate the direction of transcriptional flow. (C) Velocity length, representing the magnitude of transcriptional change, for Actc1^{E99K} (left) and WT (right) samples. Warmer colours indicate higher velocity. (D) Velocity pseudotime, ordering cells along the inferred trajectory, for Actc1^{E99K} (left) and WT (right) samples. Red intensity corresponds to later pseudotime.

and WT samples (Figure 4.19). In both genotypes, a small subset of endothelial cells displayed high velocity, suggesting a subpopulation undergoing active transcriptional changes. Despite the similar velocity patterns, the pseudotime analysis revealed a stark contrast. The inferred cellular progression in Actc1^{E99K} hearts was almost the complete reverse of that seen in WT hearts. This opposing directionality suggests that while the moment-to-moment transcriptional activity might appear similar, the long-term developmental or response trajectory of the endothelial compartment is fundamentally altered over the course of disease progression in the Actc1^{E99K} model.

Integrated stromal cell trajectories point to a common origin with subtle disease-specific shifts The integrated analysis of CD45$^-$CD31$^-$ stromal cells showed that trajectories in both genotypes appeared to originate from the neuronal cell population, which consistently displayed the highest velocity length (Figure 4.20). This suggests that neuronal cells may represent a progenitor-like or highly active population within the stromal compartment. While the overall flow was similar, a subtle difference emerged in the pseudotime analysis. In WT hearts, the trajectory progressed directly from neuronal cells to the other stromal populations. In Actc1^{E99K} hearts, the trajectory appeared to originate from both neuronal cells and Thy1^{lo}Fap$^+$ fibroblasts before progressing towards other cell types. This may indicate that in the diseased heart, activated Thy1^{lo}Fap$^+$ fibroblasts also contribute significantly to the early phase of the stromal cell differentiation or activation continuum.

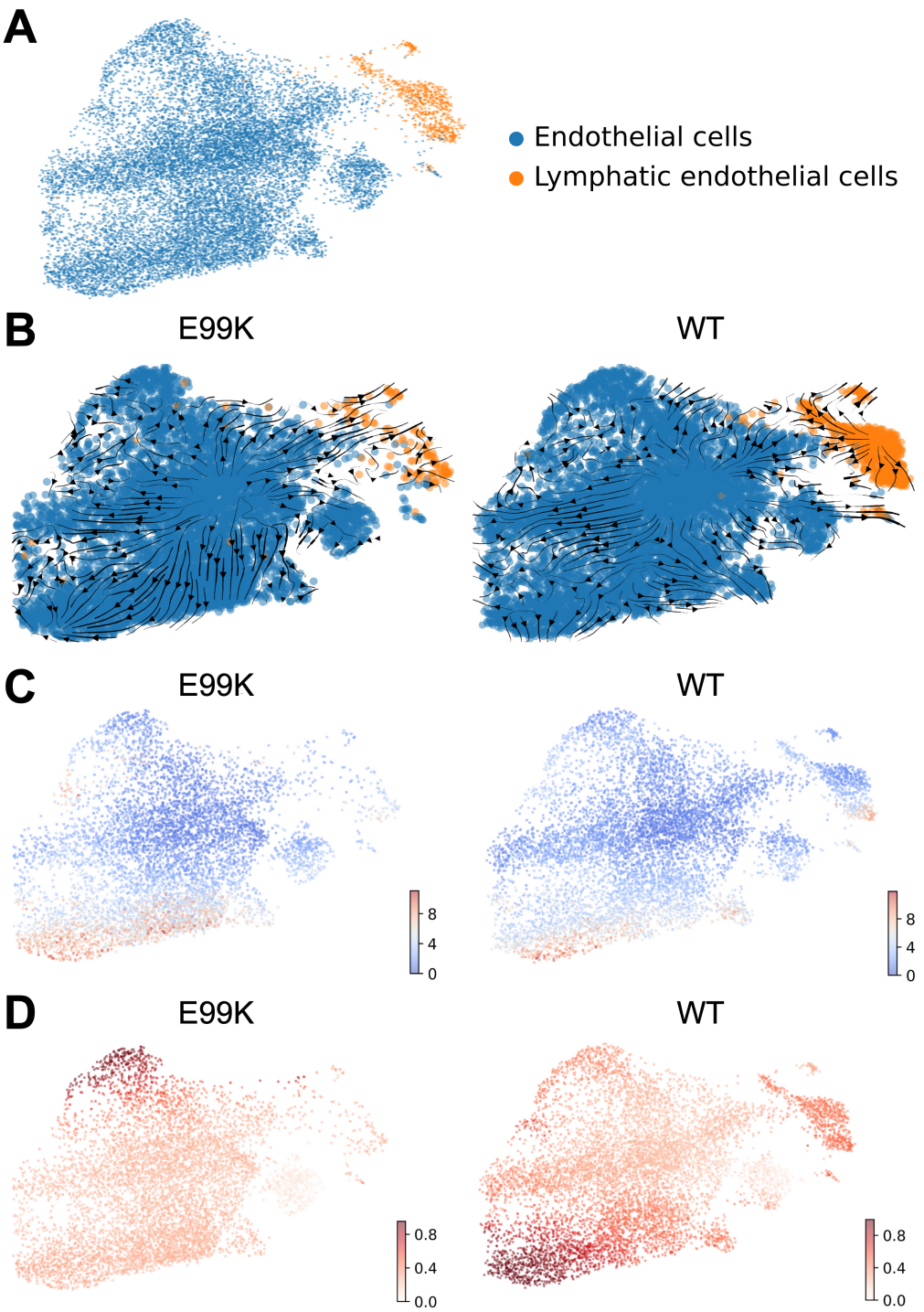

Figure 4.19. Integrated trajectory analysis of CD31$^+$ endothelial cells from combined early and late stages.
(A) UMAP of integrated CD31$^+$ cells. (B) Streamline plots of RNA velocity trajectories for Actc1^{E99K} (left) and WT (right). (C) Velocity length for Actc1^{E99K} (left) and WT (right). (D) Velocity pseudotime for Actc1^{E99K} (left) and WT (right), showing opposing progression patterns. Red intensity corresponds to later pseudotime.

Trajectories and velocity measurements differentiate cellular responses in normal and diseased hearts

Immune cell trajectories highlight distinct transcriptional dynamics across stages Early-stage $CD45^+$ immune cell trajectories were broadly similar between WT and $Actc1^{E99K}$ mice, with notable differences in neutrophil trajectories, which exhibited opposite directions (Figure 4.21). Velocity length, reflecting the magnitude of transcriptional change, also varied. In WT samples, plasma cells displayed higher velocities than B cells, suggesting a trajectory from plasma to B cells (Figure 4.21). Within the myeloid compartment, neutrophils and some macrophages exhibited the highest velocities, while lymphocytes generally exhibited lower velocities (Figure 4.21). $Actc1^{E99K}$ samples, conversely, showed uniformly high velocities across all immune cell types, with no significant difference between B cells and plasma cells, suggesting a more dynamic early-stage transcriptional landscape.

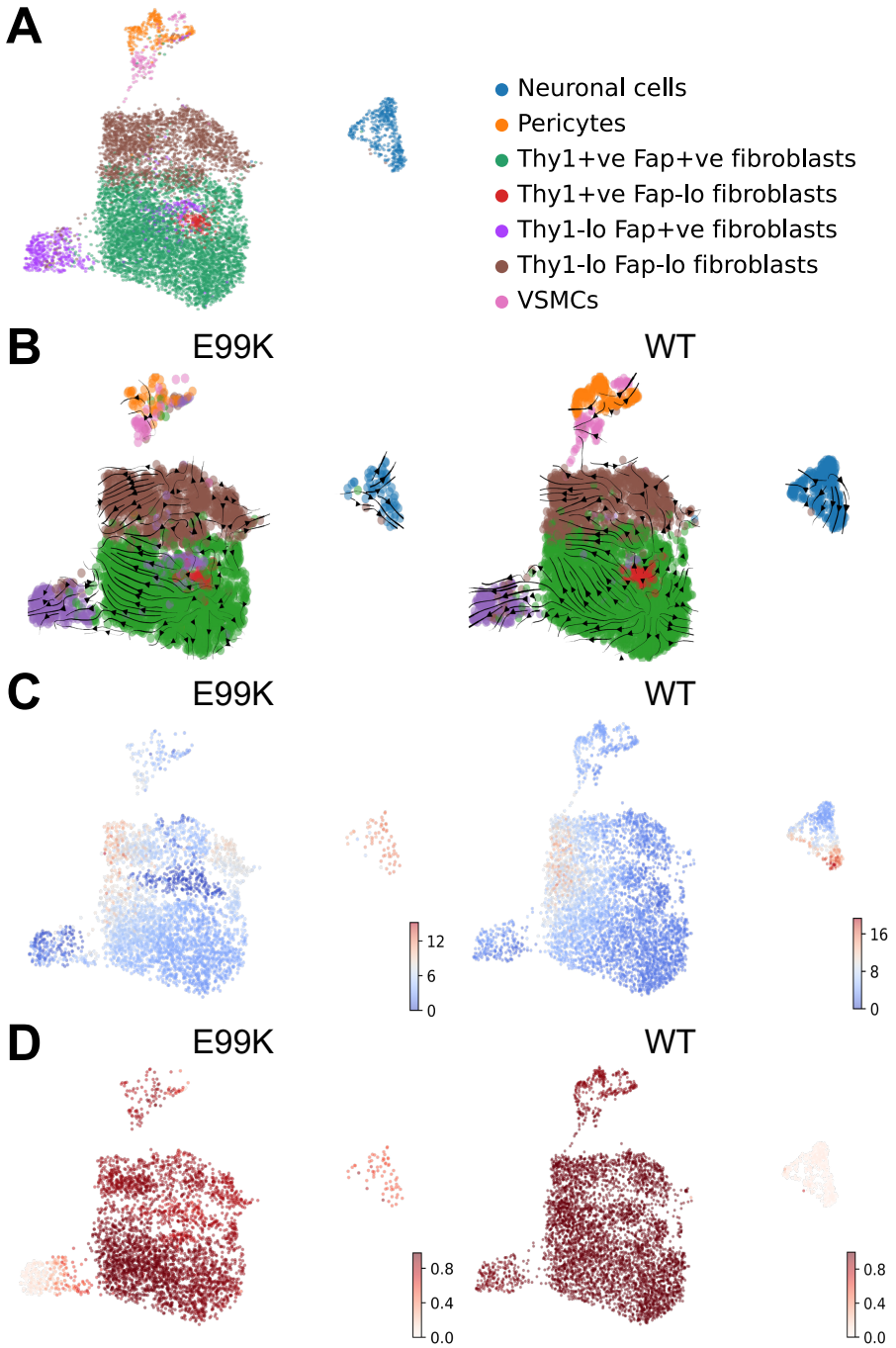

Figure 4.20. Integrated trajectory analysis of CD45$^-$CD31$^-$ stromal cells from combined early and late stages.
(A) UMAP of integrated CD45$^-$CD31$^-$ cells, annotated by cell type. (B) Streamline plots of RNA velocity trajectories for Actc1^{E99K} (left) and WT (right). (C) Velocity length for Actc1^{E99K} (left) and WT (right), with neuronal cells showing high velocity. (D) Velocity pseudotime for Actc1^{E99K} (left) and WT (right). Red intensity corresponds to later pseudotime.

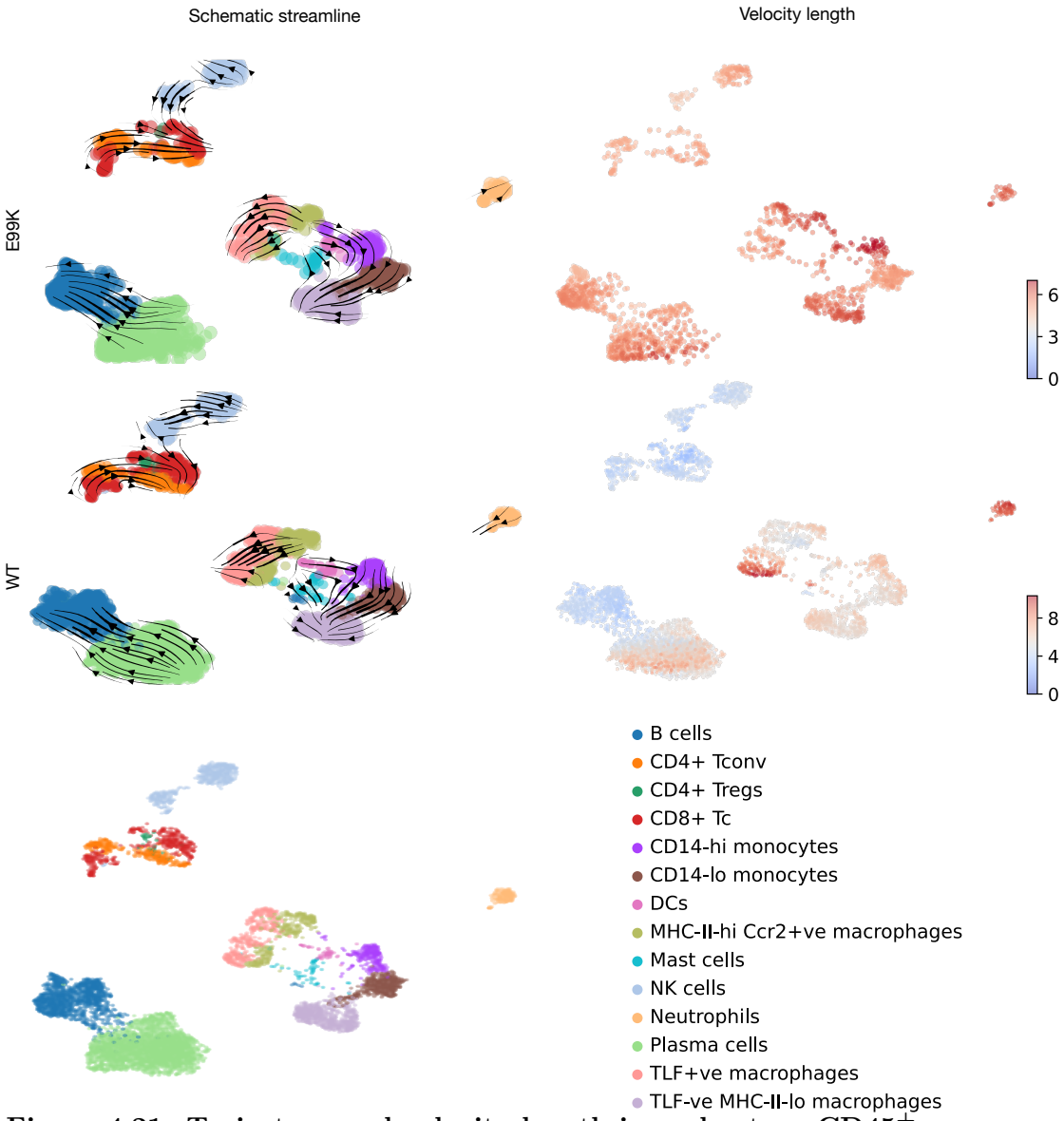

Figure 4.21. Trajectory and velocity length in early-stage CD45^{+} Actc1^{E99K}/WT samples.
Upper panel shows the schematic streamline plots to illustrate the trajectory (left). The velocity lengths are shown on the right. The lower panel shows the cell types identified in the sample.

In late-stage CD45^{+} cells, trajectory and velocity length were more similar between genotypes (Figure 4.22). Neutrophils, eosinophils, and CD14^{lo} monocytes exhibited high velocities in both. However, B cells showed a contrasting pattern: high velocity in WT and low velocity in Actc1^{E99K} mice. A subtle difference in trajectory direction between CD14^{hi} and CD14^{lo} monocytes potentially reflects altered monocyte differentiation dynamics in the Actc1^{E99K} model.

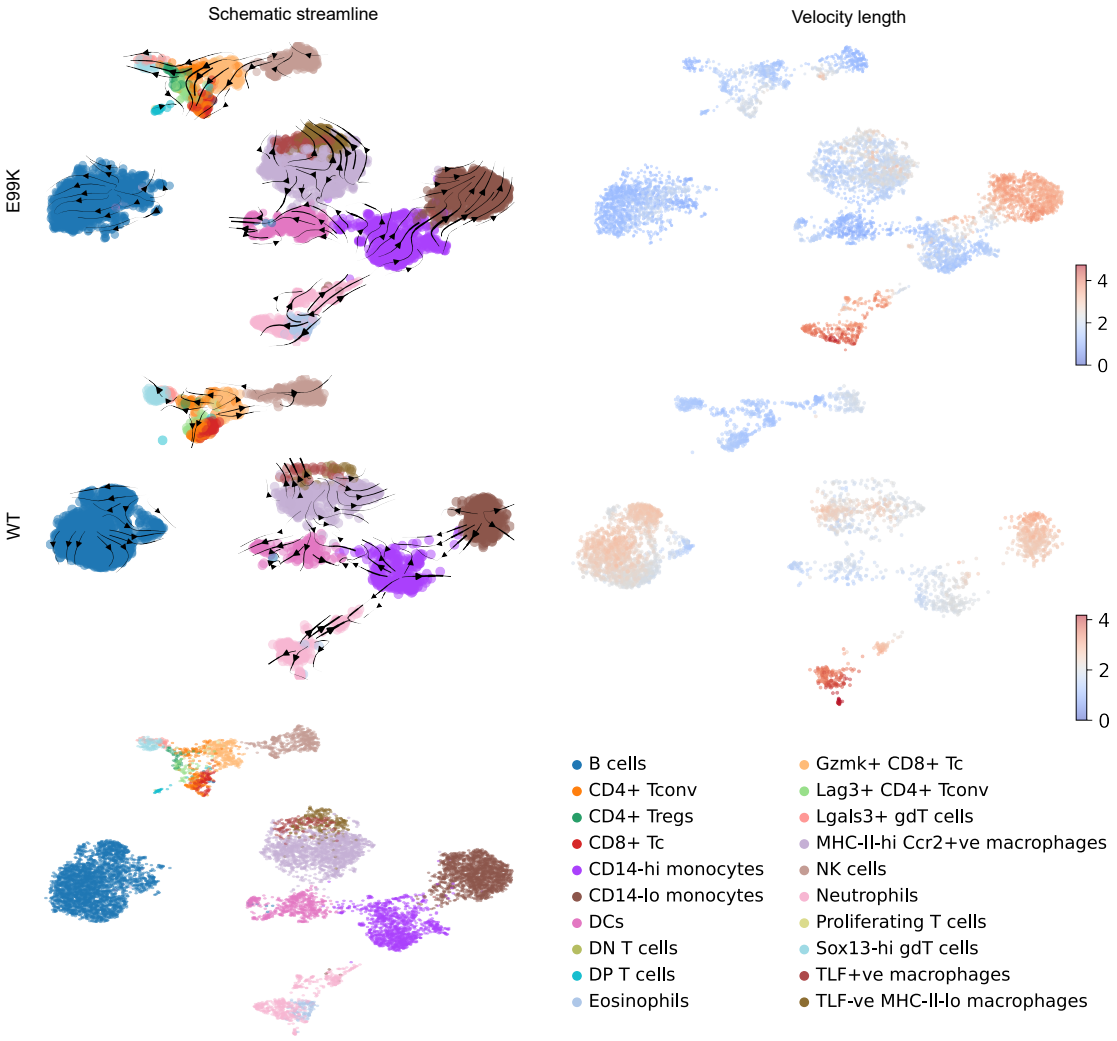

Figure 4.22. Trajectory and velocity length in late-stage CD45$^+$ Actc1^{E99K}/WT samples.
Upper panel shows the schematic streamline plots to illustrate the trajectory (left). The velocity lengths are shown on the right. The lower panel shows the cell types identified in the sample.

Endothelial cell dynamics show early uniformity with later divergence

Early-stage CD31$^+$ endothelial cells showed highly similar trajectories and velocity lengths between genotypes (Figure 4.23). A subpopulation of endothelial cells, potentially representing a more actively differentiating or responsive subset, exhibited higher velocities in both genotypes, with a seemingly greater proportion in Actc1^{E99K} samples. Late-stage CD31$^+$ cell trajectory patterns diverged, particularly within the lower portion of the endothelial cell cluster (Figure 4.24). Overall velocity length was low in both genotypes at this stage, suggesting re-

duced transcriptional dynamism.

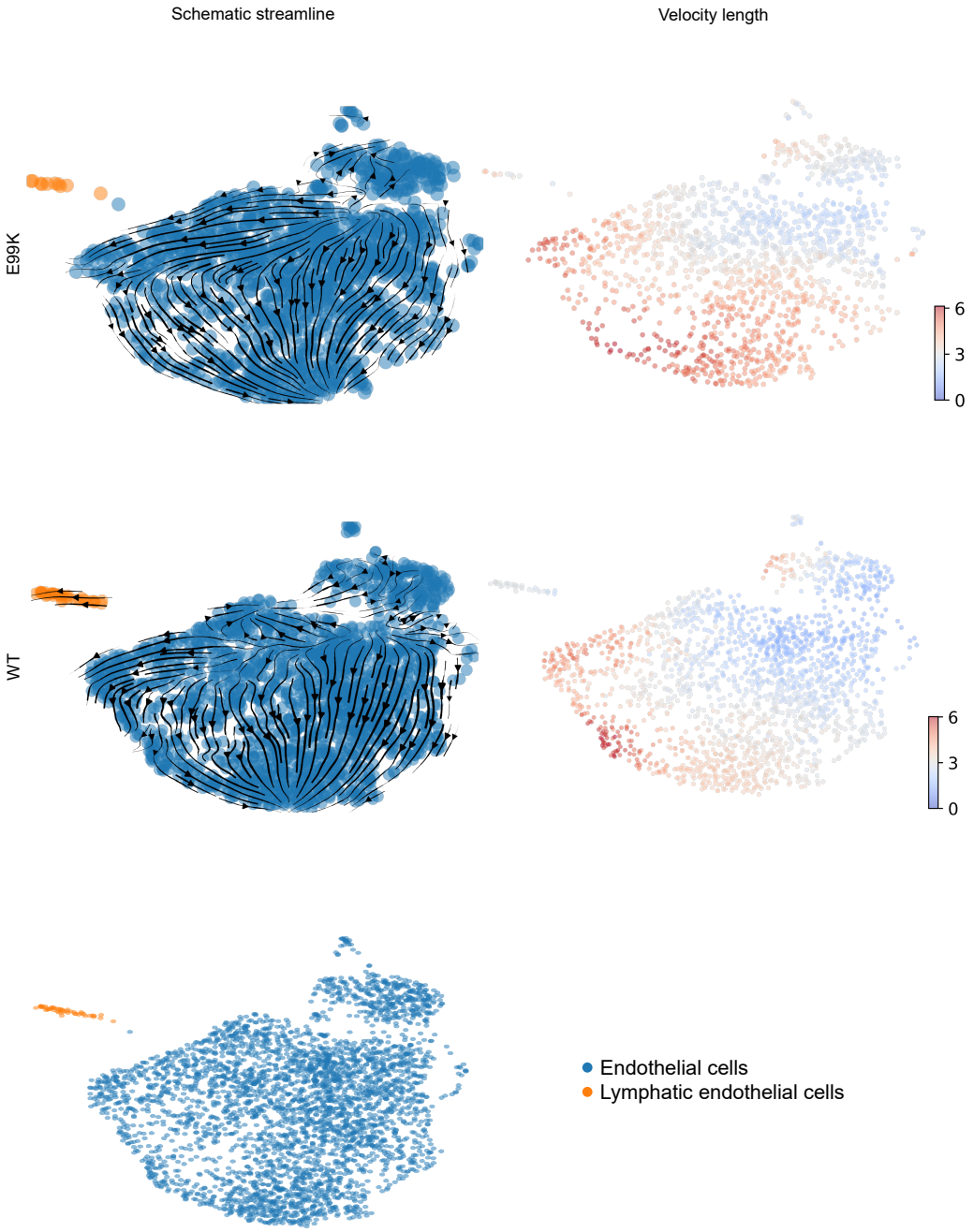

Figure 4.23. Trajectory and velocity length in early-stage CD31^{+} Actc1^{E99K}/WT samples.
Upper panel shows the schematic streamline plots to illustrate the trajectory (left). The velocity lengths are shown on the right. The lower panel shows the cell types identified in the sample.

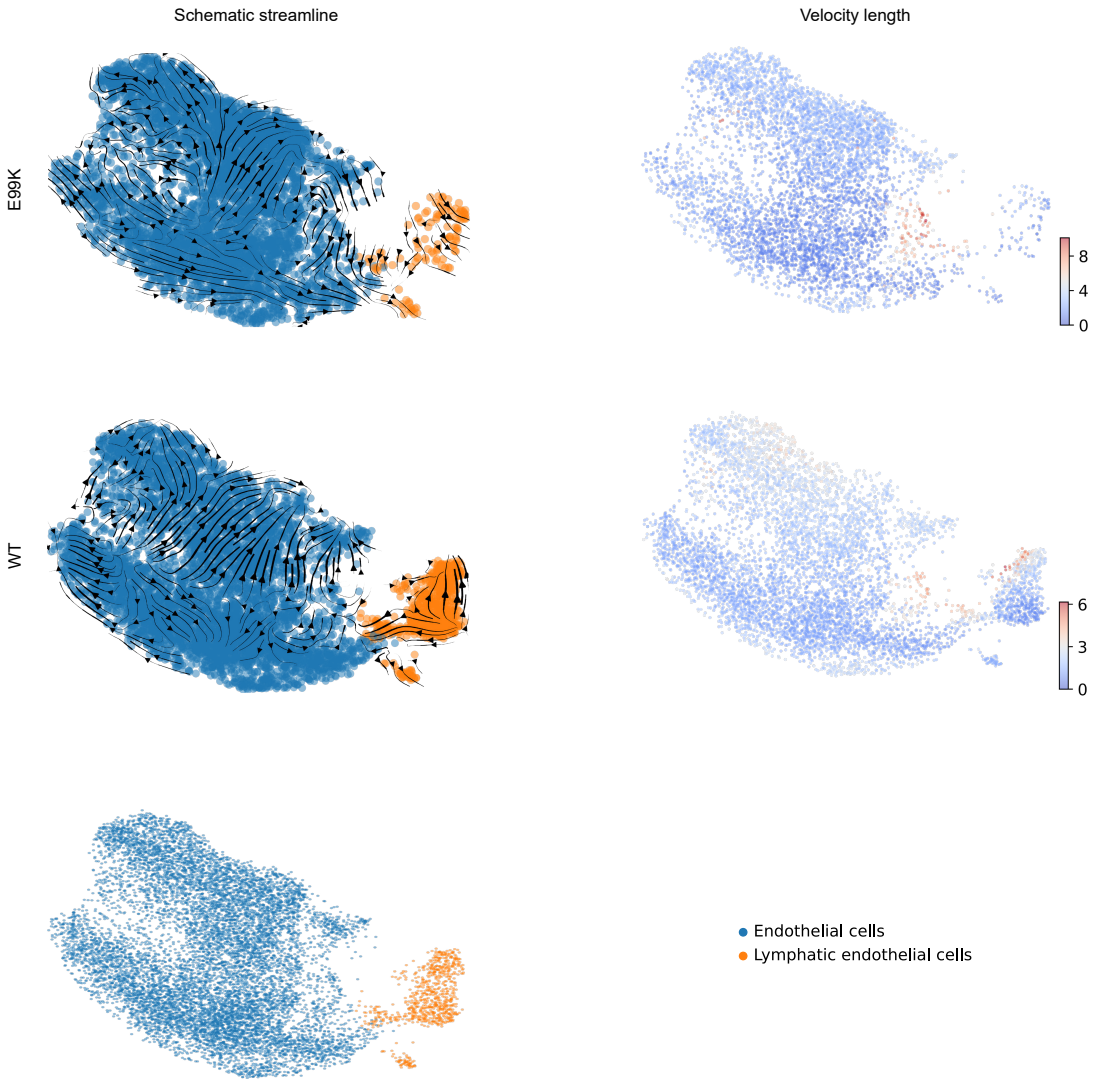

Figure 4.24. Trajectory and velocity length in late-stage CD31$^+$ Actc1^{E99K}/WT samples.
Upper panel shows the schematic streamline plots to illustrate the trajectory (left). The velocity lengths are shown on the right. The lower panel shows the cell types identified in the sample.

Stromal cell trajectories reflect heterogeneous activation and differentiation patterns Early-stage CD45$^-$CD31$^-$ stromal cell trajectories were similar between genotypes, except for neuronal cells, pericytes, and VSMCs, less abundant in Actc1^{E99K} samples (Figure 4.25). In WT samples, these cell types, along with Thy1^{lo}Fap$^+$ fibroblasts, displayed high velocities, with neuronal cells showing the highest. Velocity length could not be reliably inferred in Actc1^{E99K}

samples due to low cell numbers in these populations. In late-stage CD45$^-$CD31$^-$ cells, trajectories and velocity lengths were again similar (Figure 4.26). Some neuronal cells showed high velocities in WT but low velocities in Actc1^{E99K} mice. Thy1^{lo}Fap$^+$ fibroblasts exhibited higher velocities than other stromal cell types in both genotypes.

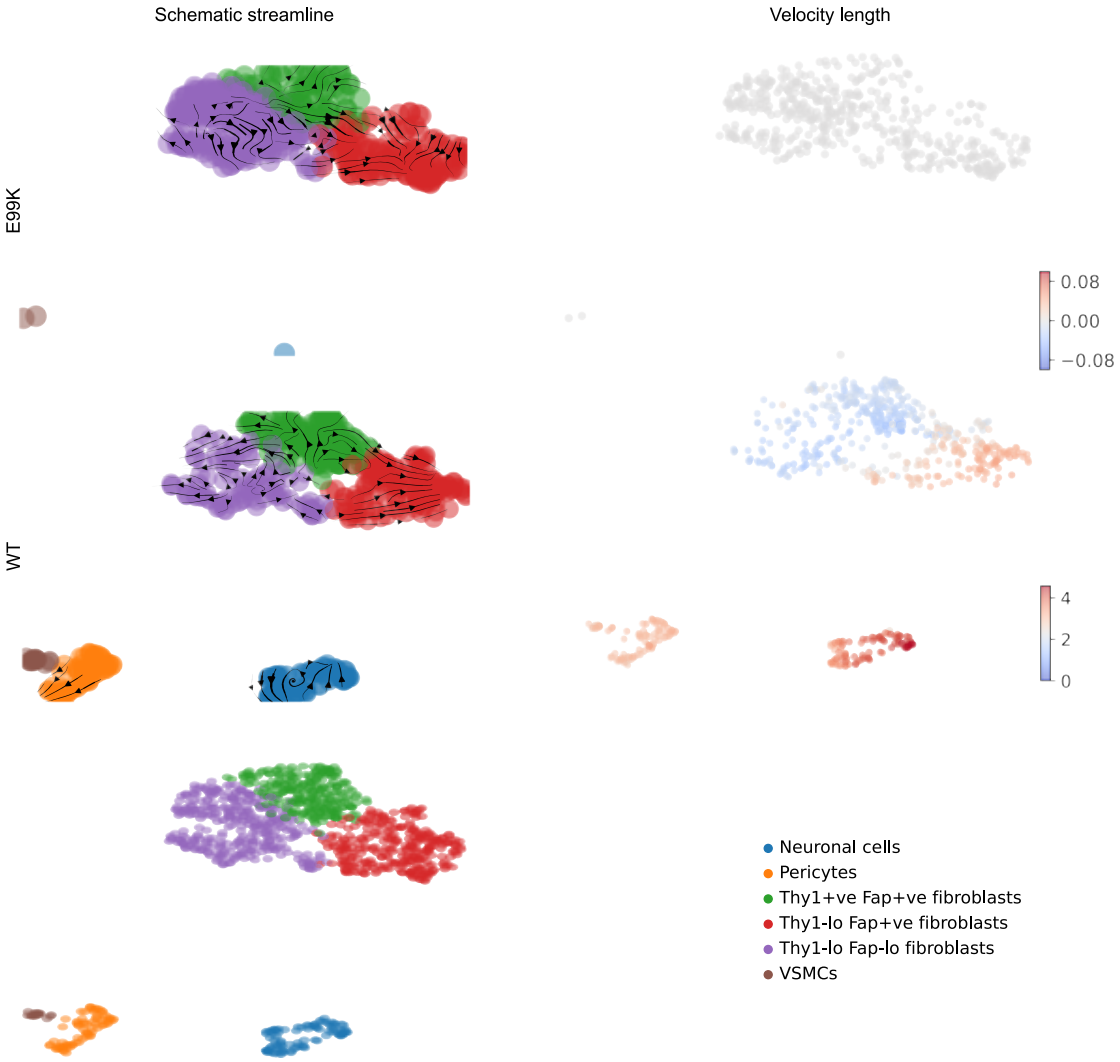

Figure 4.25. Trajectory and velocity length in early-stage CD45$^-$CD31$^-$ Actc1^{E99K}/WT samples.
Upper panel shows the schematic streamline plots to illustrate the trajectory (left). The velocity lengths are shown on the right. The lower panel shows the cell types identified in the sample.

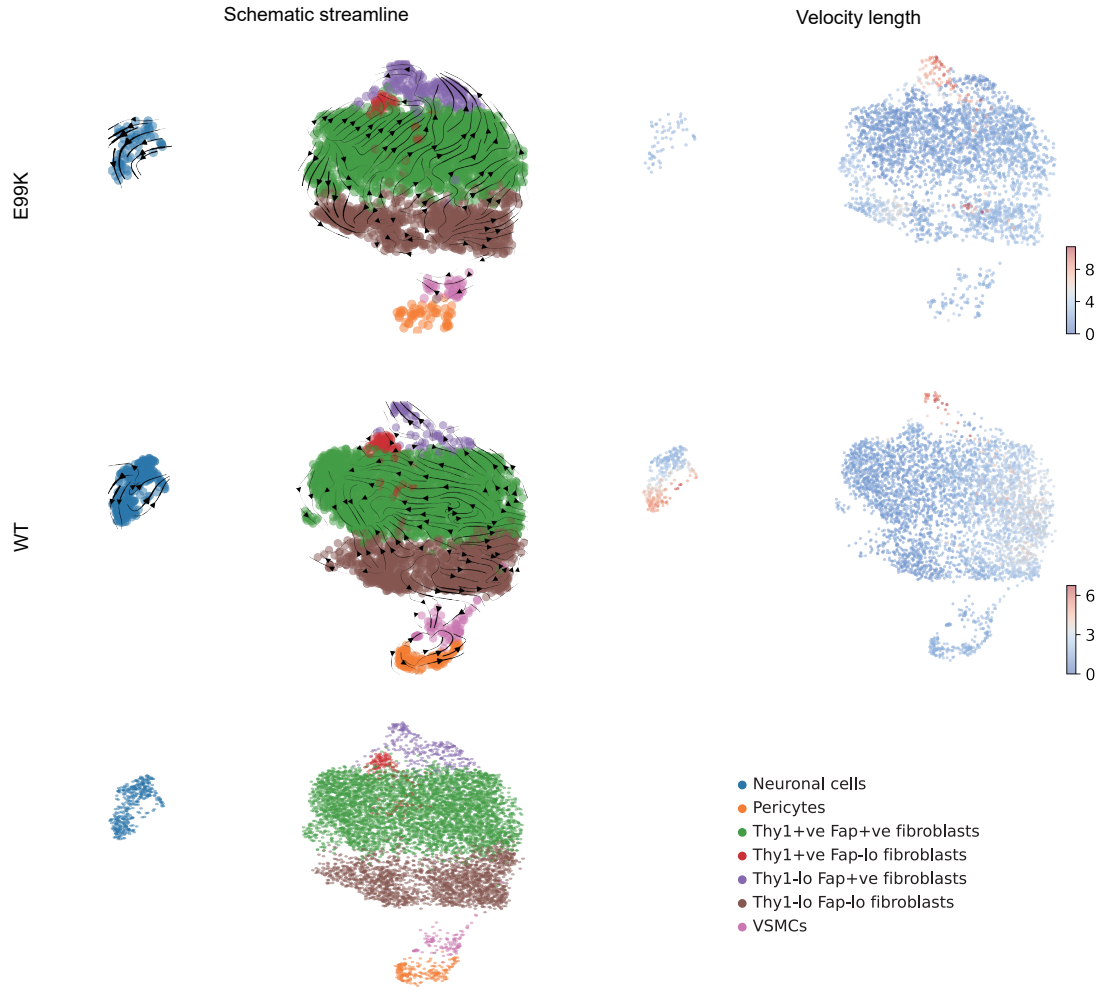

Figure 4.26. Trajectory and velocity length in late-stage CD45$^-$CD31$^-$ Actc1^{E99K}/WT samples.
Upper panel shows the schematic streamline plots to illustrate the trajectory (left). The velocity lengths are shown on the right. The lower panel shows the cell types identified in the sample.

Pseudotime analysis uncovers divergent cellular progression in immune, endothelial, and stromal compartments

Pseudotime analysis provides a quantitative measure of cellular progression along a defined trajectory, offering insights into the temporal dynamics of cellular differentiation and state transitions. This analysis was applied to further dissect temporal changes within non-cardiomyocyte populations in both WT and Actc1^{E99K} mice.

Immune cell pseudotime reveals distinct activation sequences in health and disease Early-stage CD45^{+} immune cells exhibited distinct pseudotime orderings between genotypes (Figure 4.27). In Actc1^{E99K} samples, pseudotime progressed from neutrophils, macrophages, monocytes, DCs, and mast cells to T and NK cells, and finally to B and plasma cells, suggesting a potential developmental or activation sequence with myeloid cells preceding lymphoid cells. The WT pseudotime trajectory followed a different order: neutrophils preceded macrophages, monocytes, DCs, mast cells, B and plasma cells, which in turn preceded T and NK cells. This difference highlights the distinct early-stage immune cell dynamics in the Actc1^{E99K} model.

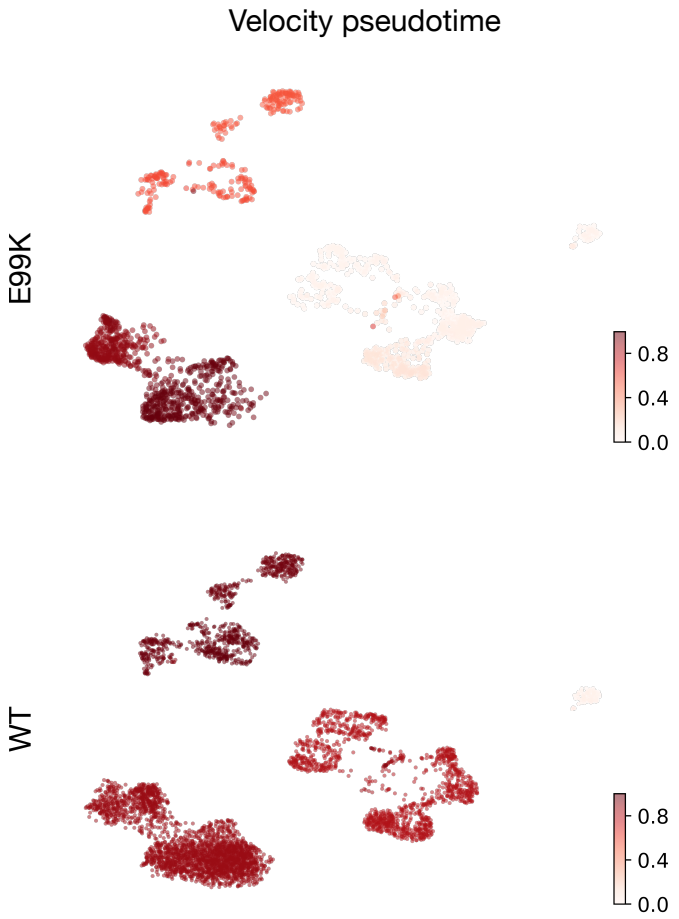

Figure 4.27. Velocity pseudotime in early-stage CD45^{+} Actc1^{E99K}/WT samples.
Pseudotime heatmaps are shown for Actc1^{E99K} (upper panel) and WT (lower panel) samples. Red intensity corresponds to later pseudotime.

In late-stage CD45^{+} cells, pseudotime trajectories also differed (Figure 4.28). In

Actc1^{E99K} samples, progression was from neutrophils and eosinophils to myeloid cells, T and NK cells, followed by B cells. In WT samples, the order was neutrophils and eosinophils, followed by monocytes, then macrophages and DCs, then B cells, and finally T and NK cells. These distinct orderings suggest altered differentiation and activation pathways within the late-stage Actc1^{E99K} immune compartment.

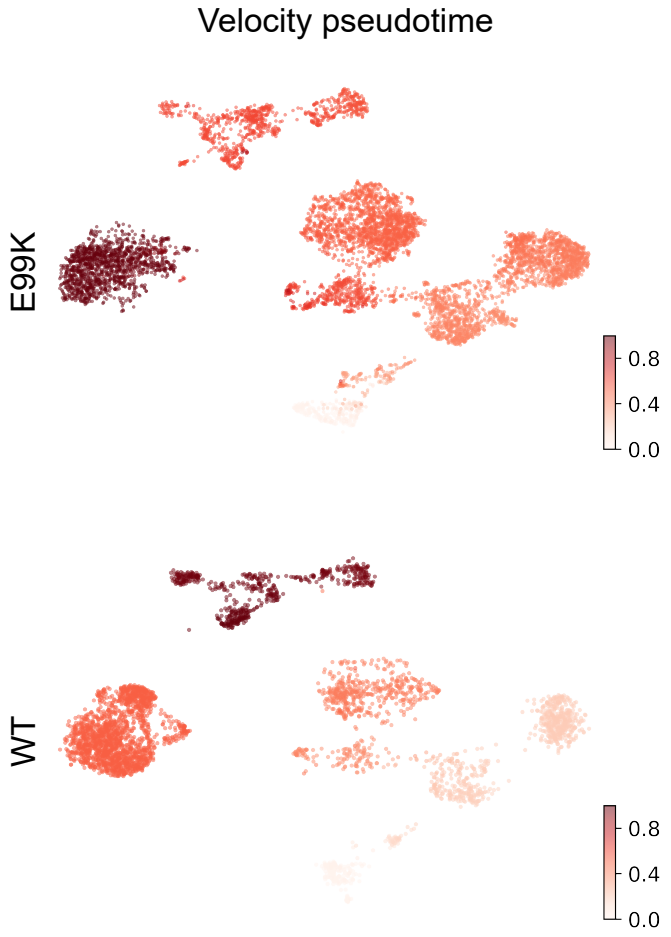

Figure 4.28. Velocity pseudotime in late-stage CD45$^+$ Actc1^{E99K}/WT samples.
Pseudotime heatmaps are shown for Actc1^{E99K} (upper panel) and WT (lower panel) samples. Red intensity corresponds to later pseudotime.

Endothelial pseudotime patterns distinguish normal and diseased states

Early-stage CD31$^+$ endothelial cell pseudotime trajectories were similar between genotypes (Figure 4.29). While specific subpopulations were not explicitly defined, pseudotime appeared to progress from the upper to the lower portion of

the endothelial cell cluster in both, suggesting a common early-stage developmental or activation pathway.

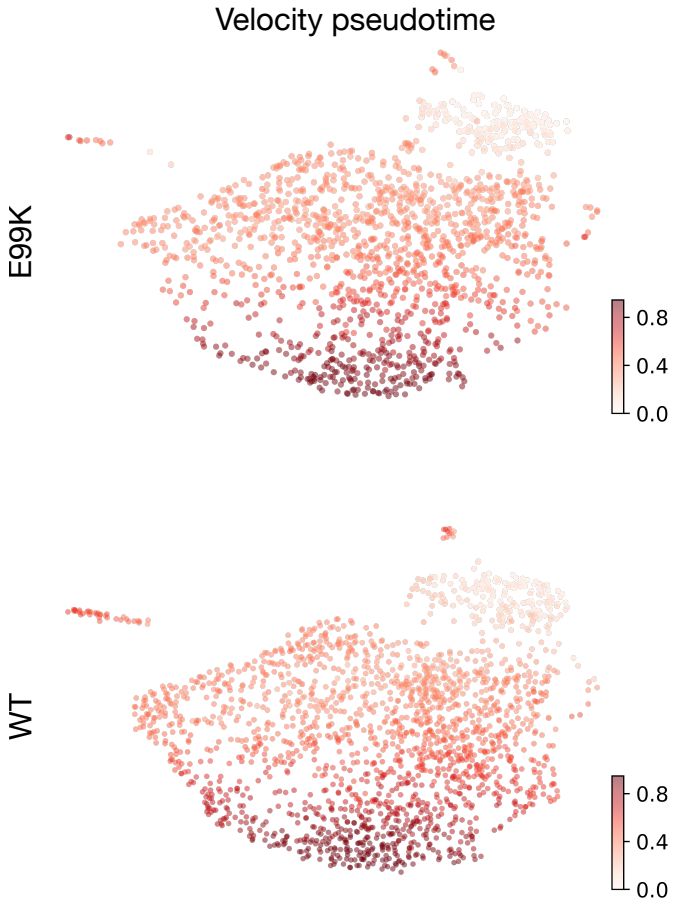

Figure 4.29. Velocity pseudotime in early-stage CD31$^+$ Actc1^{E99K}/WT samples.
Pseudotime heatmaps are shown for Actc1^{E99K} (upper panel) and WT (lower panel) samples. Red intensity corresponds to later pseudotime.

Late-stage CD31$^+$ cell pseudotime trajectories, however, were reversed between genotypes (Figure 4.30). The Actc1^{E99K} trajectory progressed from the upper to the lower portion of the cluster, while the WT trajectory followed the opposite direction. This reversal suggests a fundamental difference in late-stage endothelial cell dynamics in the Actc1^{E99K} model.

Stromal cell pseudotime indicates converging trajectories in late-stage remodelling Early-stage CD45$^-$CD31$^-$ stromal cell pseudotime trajectories differed markedly between genotypes (Figure 4.31). In Actc1^{E99K} samples, pseu-

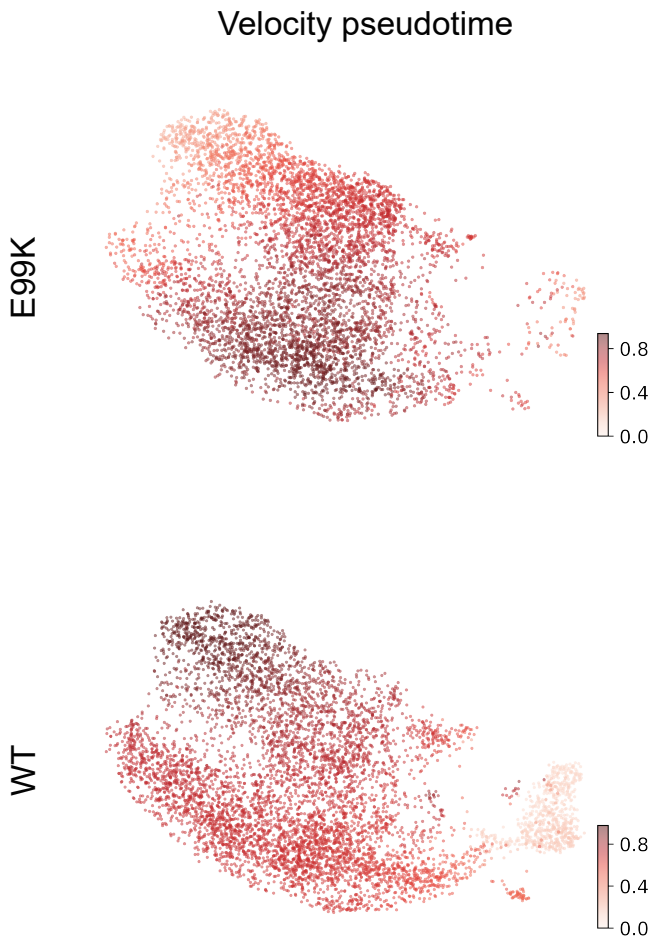

Figure 4.30. Velocity pseudotime in late-stage CD31$^+$ Actc1^{E99K}/WT samples.
Pseudotime heatmaps are shown for Actc1^{E99K} (upper panel) and WT (lower panel) samples. Red intensity corresponds to later pseudotime.

dotime ordering was less clear, potentially due to the lower abundance of cell types like pericytes, VSMCs, and neuronal cells. A tentative trajectory from Thy1^{lo}Fap$^+$ to Thy1^{lo}Fap^{lo} and Thy1$^+$Fap$^+$ fibroblasts was observed, though this requires further investigation. In WT samples, a clear trajectory progressed from neuronal cells to pericytes and VSMCs, and finally to all fibroblast populations, suggesting a defined developmental or differentiation hierarchy within the early-stage WT stromal compartment.

Late-stage CD45$^-$CD31$^-$ cell pseudotime trajectories were similar (Figure 4.32), progressing from neuronal cells to all other cell types (fibroblasts, pericytes, and VSMCs). This shared trajectory suggests a convergence in stromal cell dynam-

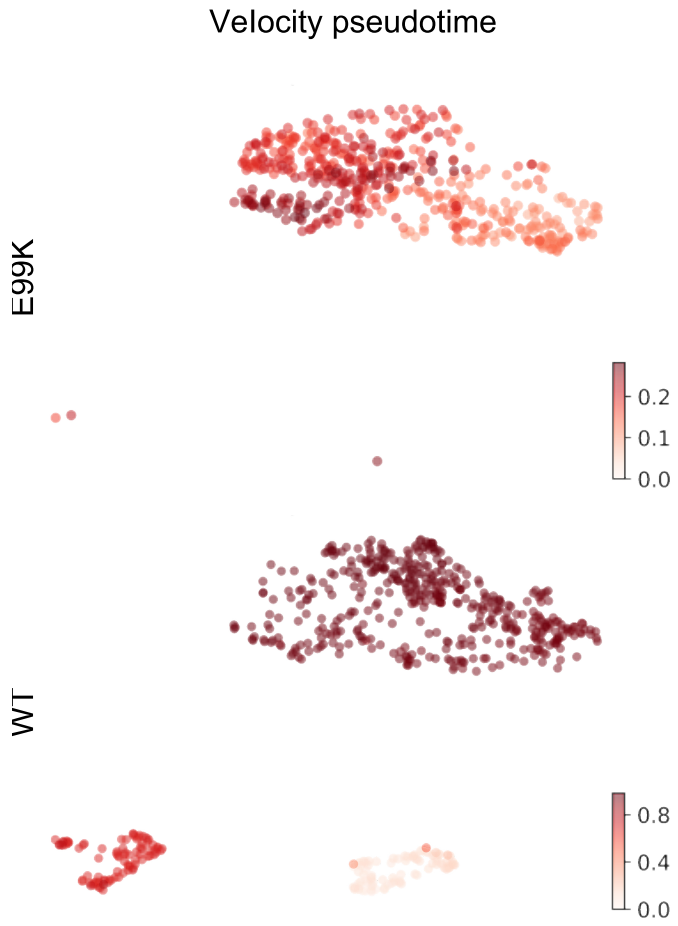

Figure 4.31. Velocity pseudotime in early-stage CD45$^-$CD31$^-$ Actc1^{E99K}/WT samples.
Pseudotime heatmaps are shown for Actc1^{E99K} (upper panel) and WT (lower panel) samples. Red intensity corresponds to later pseudotime.

ics in the late-stage Actc1^{E99K} model and WT mice. The observed early-stage pseudotime trajectory differences, particularly in the Actc1^{E99K} model, may be attributed to altered cellular composition and reduced abundance of certain stromal cell populations. Further investigation is needed to fully elucidate the functional implications of these temporal changes in the context of adverse remodelling in HCM.

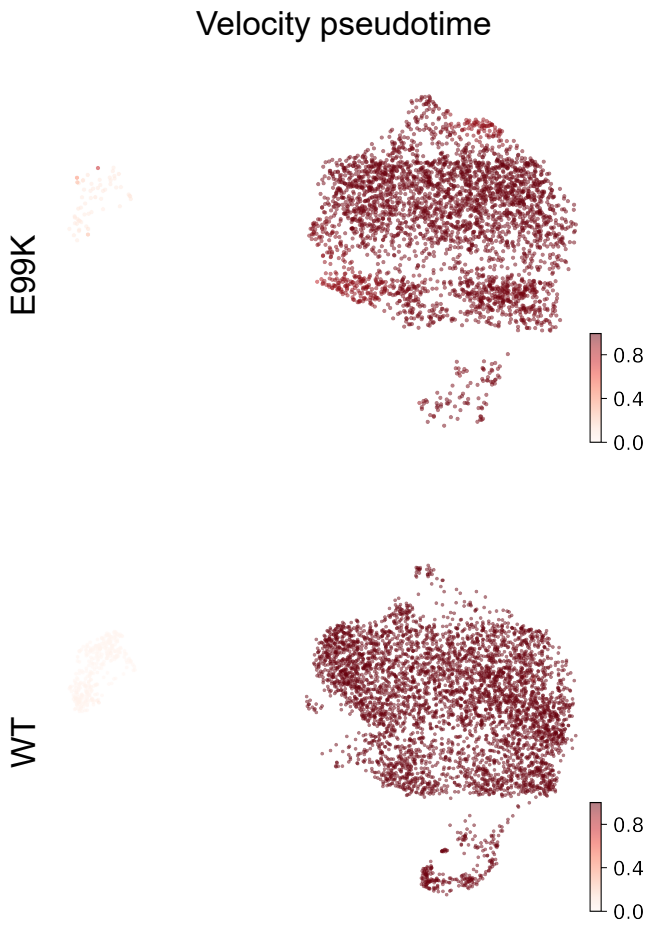

Figure 4.32. Velocity pseudotime in late-stage CD45$^-$CD31$^-$ Actc1^{E99K}/WT samples.
Pseudotime heatmaps are shown for Actc1^{E99K} (upper panel) and WT (lower panel) samples. Red intensity corresponds to later pseudotime.

4.3 Discussion: Insights on therapeutic implications for cardiac remodelling

Single-cell transcriptomic analysis of non-cardiomyocytes in the Actc1^{E99K} HCM mouse model reveals a complex interplay of cellular and molecular changes driving adverse remodelling across both early (5 weeks) and late (60 weeks) disease stages. The progression of HCM is underscored by the shift from relatively subtle alterations in pathway activity at the early stage to widespread upregulation in the late stage. Understanding these temporal dynamics is crucial for developing effective therapeutic strategies.

Early-stage HCM is characterised by a dampened immune response, evidenced by

downregulation of the allograft rejection pathway in various immune cell populations. This suggests either delayed immune activation or active early inflammation suppression. This relative quiescence in the early remodelling phase is further corroborated by the generally low pathway activity changes observed. However, certain cell types, such as lymphocytes, exhibit increased activity in EGFR, hypoxia, NF-κB, and p53 pathways. This early lymphocyte activation could represent an initial response to the cellular stress induced by the *Actc1* mutation in cardiomyocytes, potentially triggering paracrine signalling that contributes to subsequent remodelling [178]. Increased Trail pathway activity, potentially indicative of apoptosis, raises the question of whether early cell death contributes to the initiation of adverse remodelling. Apoptotic signals released by dying cells could trigger inflammatory responses and fibroblast activation, initiating fibrosis [178, 401]. Upregulation of cell growth and metabolism pathways, such as E2F targets, MYC targets, and oxidative phosphorylation, specifically in Thy1^{lo}Fap^{lo} fibroblasts during the early stage, suggests early metabolic reprogramming in these cells, potentially driven by altered energy demands or nutrient availability surrounding the hypertrophic cardiomyocytes [321, 402, 403]. Conversely, downregulation of oxidative phosphorylation in other cell types, including immune cells and VSMCs, indicates a cell-type-specific metabolic response to early-stage HCM. This raises questions about how these metabolic shifts contribute to the overall remodelling process and whether targeting these pathways could offer early therapeutic opportunities.

In stark contrast, late-stage HCM is dominated by widespread pathway upregulation, reflecting a highly activated and inflamed state. Marked upregulation of the allograft rejection pathway across almost all cell types signifies a robust immune response, consistent with the increased immune cell infiltration observed phenotypically. This suggests a transition from early immune suppression or quiescence to overt immune activation, potentially driven by the accumulation of DAMPs released by stressed or dying cardiomyocytes [178, 404–406]. Widespread upregulation of inflammatory pathways, including complement, interferon responses,

and TNF signalling, further underscores inflammation's prominent role in late-stage HCM pathogenesis. Whether this inflammatory response drives adverse remodelling or results from it remains a key question. A chronic inflammatory environment may perpetuate fibrosis by stimulating fibroblast activation and ECM deposition [178]. Increased Hypoxia pathway activity across diverse cell types likely reflects compromised tissue oxygenation, a common feature of advanced cardiac remodelling. This hypoxic environment could exacerbate inflammation and fibrosis by activating HIF signalling [407–411].

Elevated TGF-β signalling activity in fibroblasts, coupled with increased activity in other growth and remodelling pathways such as PI3K, VEGF, MAPK, and WNT, strongly implicates these pathways in the fibrotic response. This study significantly advances our understanding beyond previous work, which often relied on bulk tissue analysis. While bulk transcriptomics could identify a general increase in fibrotic markers in HCM, it could not resolve the cellular origins of these signals. My single-cell approach pinpoints specific cell populations responsible for producing key profibrotic cytokines. For instance, the identification of VSMCs as a primary source of *Tgfb2* and *Tgfb3* in early disease, and later *Il6* and *Tgfb1*, is a novel finding that would be obscured in whole-tissue measurements. This distinction is critical, as it suggests that VSMCs, not just fibroblasts, are key initiators and modulators of the fibrotic process in this model. This is further supported by increased expression of profibrotic cytokines like *Tgfb1*, *Tgfb2*, *Tgfb3*, *Il6*, and *Il11*, primarily within the stromal compartment. The dynamic expression patterns of these cytokines, with VSMCs transitioning from producing *Tgfb2* and *Tgfb3* early on to *Il6* and *Tgfb1* in the late stage, suggests complex cellular crosstalk driving fibrosis. The potential contribution of cardiomyocytes to *Il6* and *Tgfb2* expression, particularly in the late stage, warrants further investigation. Targeting these cytokines and their downstream signalling pathways represents a potential therapeutic avenue (Figure 4.33). For example, targeting IL6/IL11 with bispecific antibodies or targeting gp130 in late-stage Actc1$^{\mathrm{E99K}}$ mice may be a promising therapeutic strategy. Similarly,

targeting Tgfb2/3 with a bispecific antibody in the early stage may prevent or delay fibrosis.

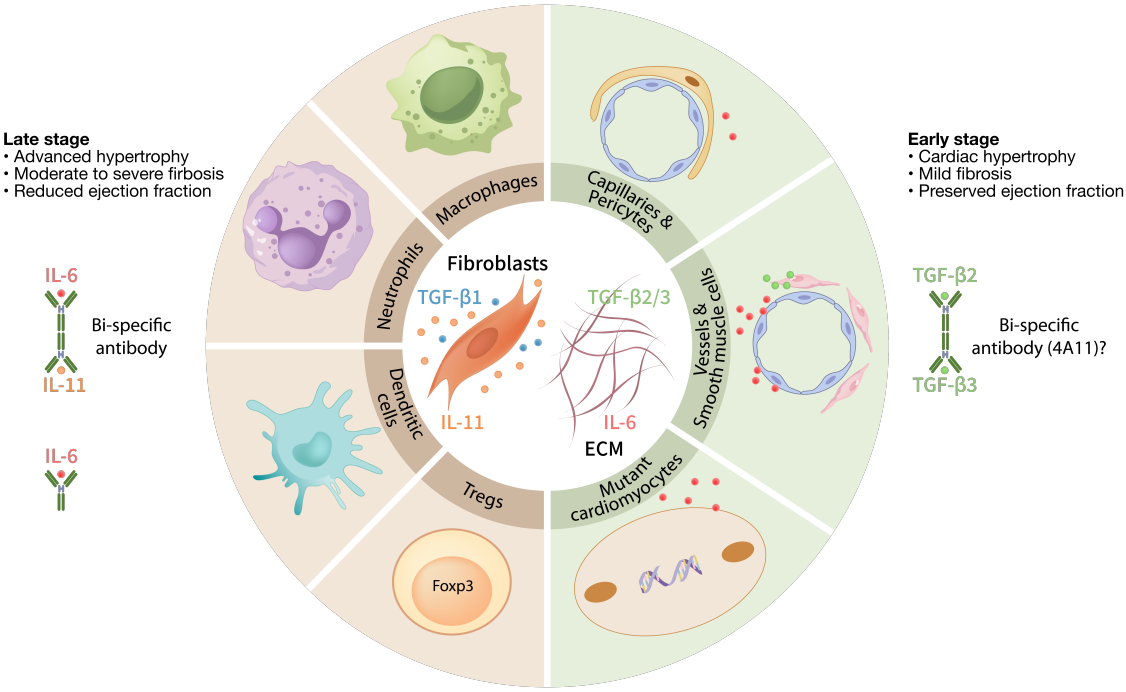

Figure 4.33. Schematic of dynamic profibrotic signalling and potential therapeutic strategies in HCM.
This diagram summarises the key findings regarding the cellular sources and temporal expression of profibrotic cytokines in the Actc1^{E99K} model. In the early stage, VSMCs are identified as a primary source of TGFB2 and TGFB3. In the late stage, a broader range of stromal cells, including VSMCs and endothelial cells, upregulate *IL6* and *TGFB1*. Based on these dynamics, the diagram proposes stage-specific therapeutic interventions, such as targeting TGFB2/3 in early disease and the IL6/gp130 axis in late-stage disease.

The integrated trajectory analysis, combining early and late time points, offers a complementary perspective, albeit one that must be interpreted with caution due to the confounding of time and sequencing batch. This holistic view reinforces certain stage-specific findings while revealing overarching dynamics. For instance, the consistently high velocity of neutrophils in both genotypes across time suggests they are a persistently active population, rather than one confined to a specific disease stage. The starkly divergent trajectories of B cells and the opposing pseudotime progression of endothelial cells in the integrated model strongly suggest a sustained, long-term reprogramming of these cell lineages in the Actc1^{E99K} heart. While this integrated view helps to conceptualise the

entire disease course as a single process, the stage-specific analyses remain crucial for dissecting the distinct mechanisms and cellular states that characterise the initiation versus the established phases of adverse remodelling, thereby avoiding the potential misinterpretation of technical artefacts as biological progression.
RNA velocity and pseudotime analyses provide further insights into the dynamic cellular transitions during HCM progression. Contrasting neutrophil trajectories in early-stage $CD45^+$ immune cells between WT and $Actc1^{E99K}$ mice suggest an altered neutrophil differentiation or activation programme in the $Actc1^{E99K}$ model, potentially driven by the altered cytokine milieu or other early-stage microenvironmental cues [178, 412, 413]. Higher velocities across all early-stage $Actc1^{E99K}$ immune cell types compared to WT indicate a more dynamic transcriptional landscape, potentially reflecting heightened cellular activation or responsiveness.
In late-stage $CD45^+$ cells, similar trajectory and velocity patterns between genotypes suggest converging immune cell dynamics, potentially reflecting a common inflammatory response endpoint. Contrasting B cell velocities—high in WT and low in $Actc1^{E99K}$ mice—raise the question of whether this reflects impaired B cell response in late-stage HCM, potentially due to B cell exhaustion or suppressive microenvironmental signals [178, 414–416]. The subtle trajectory divergence between $CD14^{hi}$ and $CD14^{lo}$ monocytes in $Actc1^{E99K}$ mice could indicate altered monocyte differentiation dynamics, potentially contributing to the inflammatory response.
Similar early-stage trajectories and velocity lengths in $CD31^+$ endothelial cells between genotypes suggest that early endothelial cell activation follows a similar path regardless of the *Actc1* mutation. Higher velocities in a subpopulation of potentially more actively differentiating or responsive endothelial cells raise questions about the drivers of this heterogeneity and these cells' specific role in early remodelling. Diverging late-stage $CD31^+$ cell trajectory patterns, coupled with the overall low velocity length, suggest a more complex and potentially less

dynamic endothelial response in late-stage HCM. This could reflect a shift from active early angiogenesis or remodelling to a more quiescent late stage.

RNA velocity analysis of CD45$^-$CD31$^-$ stromal cells reveals distinct temporal dynamics. High velocities in early-stage WT neuronal cells, pericytes, and VSMCs suggest active transcriptional changes during early development. The inability to reliably infer velocity length in early-stage Actc1^{E99K} samples due to low cell numbers represents a study limitation and underscores the need for larger sample sizes. Higher velocities of Thy1^{lo}Fap$^+$ fibroblasts compared to other late-stage stromal cell types in both genotypes suggest these fibroblasts play a particularly active role in late remodelling, potentially related to their involvement in ECM production and deposition.

Pseudotime analysis further supports the notion of distinct temporal dynamics. Different early-stage CD45$^+$ immune cell pseudotime orderings between genotypes suggest altered differentiation and activation pathways in the Actc1^{E99K} model. Myeloid-to-lymphoid cell progression in the Actc1^{E99K} pseudotime trajectory raises the question of whether myeloid cells initiate or amplify the adaptive immune response in HCM. Similar early-stage CD31$^+$ endothelial cell pseudotime trajectories suggest a common early developmental or activation pathway, while reversed late-stage trajectories indicate a fundamental difference in endothelial cell dynamics in late-stage HCM. The less clear early-stage CD45$^-$CD31$^-$ stromal cell pseudotime ordering in Actc1^{E99K} samples, potentially due to lower cell type abundance, again highlights the need for larger sample sizes. Similar late-stage stromal cell pseudotime trajectories suggest converging stromal cell dynamics in late-stage HCM.

Study limitations include low cell numbers in certain populations and the use of cancer-derived data (PROGENy) for pathway activity inference. Nevertheless, this work provides a uniquely high-resolution map of the non-cardiomyocyte landscape during HCM progression, moving beyond the limitations of bulk analysis to define cell-type-specific contributions and dynamic temporal shifts. By

identifying specific fibroblast subsets, pinpointing VSMCs as key cytokine producers, and modelling the trajectories of cellular change, this study provides a more nuanced understanding of adverse remodelling in HCM than has previously been possible. This comprehensive single-cell analysis provides valuable insights into the cellular and molecular changes driving adverse remodelling in HCM. Further research, including larger-scale single-cell studies, functional validation of identified pathways, and investigation of cardiomyocyte-non-cardiomyocyte interplay, is needed to fully elucidate HCM progression mechanisms and develop targeted therapeutic strategies. This study provides a strong foundation for future investigations and offers promising therapeutic avenues.

5

Targeting fibrosis and inflammation in late-stage mouse and human HCM

5.1 Mapping cell populations and expression changes that reveal unique disease dynamics in late-stage HCM

Having established the temporal transcriptional landscape of adverse remodelling in the Actc1^{E99K} HCM mouse model at both bulk and single-cell resolution, this investigation now assesses the translational relevance of these findings for human HCM. A critical step is comparing the late-stage Actc1^{E99K} mouse model with late-stage human HCM. This comparison uses a publicly available snRNA-seq dataset from explanted hearts of patients undergoing heart transplants due to advanced cardiomyopathy [135]. This analysis aims to reveal shared and divergent molecular mechanisms driving adverse remodelling in both species.

The human dataset includes samples from 16 HCM patients, 12 dilated cardiomyopathy (DCM) patients, and non-failing donor hearts with no history of heart failure. All LV free wall samples were collected from a non-infarcted region, predominantly the anterior wall, midway between the apex and base. This consistent sampling strategy minimises regional gene expression variability.

The first step in analysing the human snRNA-seq data was to identify non-cardiomyocyte cell populations. Following the same cell type annotation strategy used in the mouse scRNA-seq analysis (section 4.1), cell types were assigned based on established canonical markers. The rationale for these markers, their functions, and suitability for human and mouse cell type identification have been previously discussed and are applied here accordingly. The original authors' annotation identified cardiomyocytes, adipocytes, pericytes, VSMCs, fibroblasts, activated fibroblasts, mast cells, endothelial cells, lymphatic endothelial cells, proliferating macrophages, macrophages, lymphocytes, neuronal cells, epicardial cells, and endocardial cells (Figure 5.1, upper panel; Figures 5.2 and 5.3). To further resolve the immune landscape, the lymphocyte population was sub-clustered based on marker expression, revealing $CD4^+$ conventional T cells (Tconv), $CD4^+$ regulatory T cells (Tregs), $CD4^+$ naïve T cells, $CD4^+/CD8^+$ DP T cells, $CD8^+$ cytotoxic T cells, and NK cells (Figure 5.1, lower panel; Figure 5.3). This granular characterisation allows a more nuanced understanding of the immune response in late-stage human HCM. Table 5.1 and Figure 5.4 summarise the cell numbers for each cell type in each condition, providing a quantitative assessment of the cellular composition.

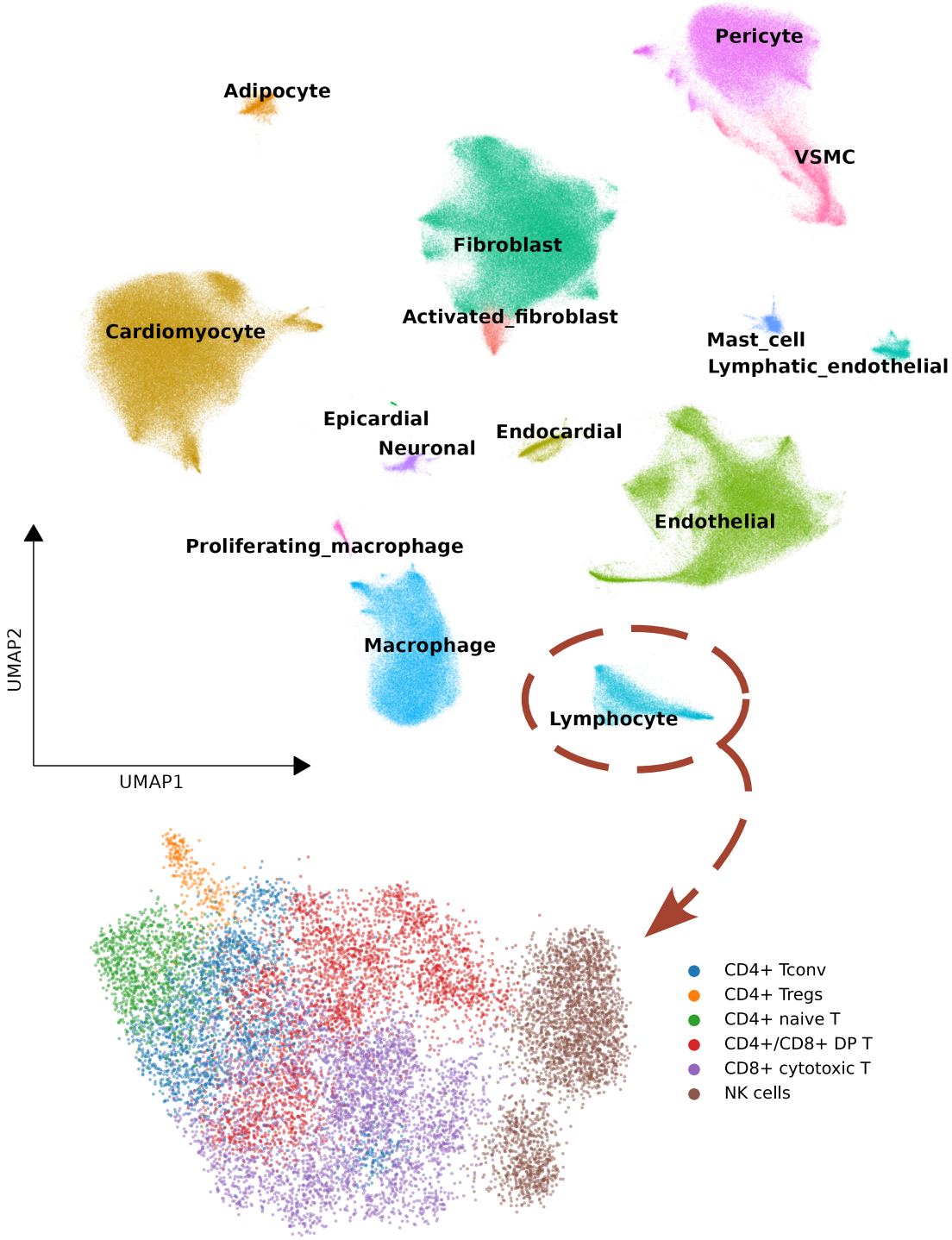

Figure 5.1. UMAP projection of single-nucleus transcriptomes from late-stage human HCM and non-failing (NF) hearts.
The upper panel displays cell clusters annotated according to the original study's classification. The lower panel shows a refined annotation of the lymphocyte population, sub-clustering them into distinct T cell and NK cell subsets based on canonical marker gene expression.

Figure 5.2. Dot plot illustrating the expression of canonical marker genes used to identify stromal cell populations in the late-stage human HCM dataset.

The size of each dot corresponds to the percentage of cells within a population expressing the gene, while the colour intensity reflects the average expression level.

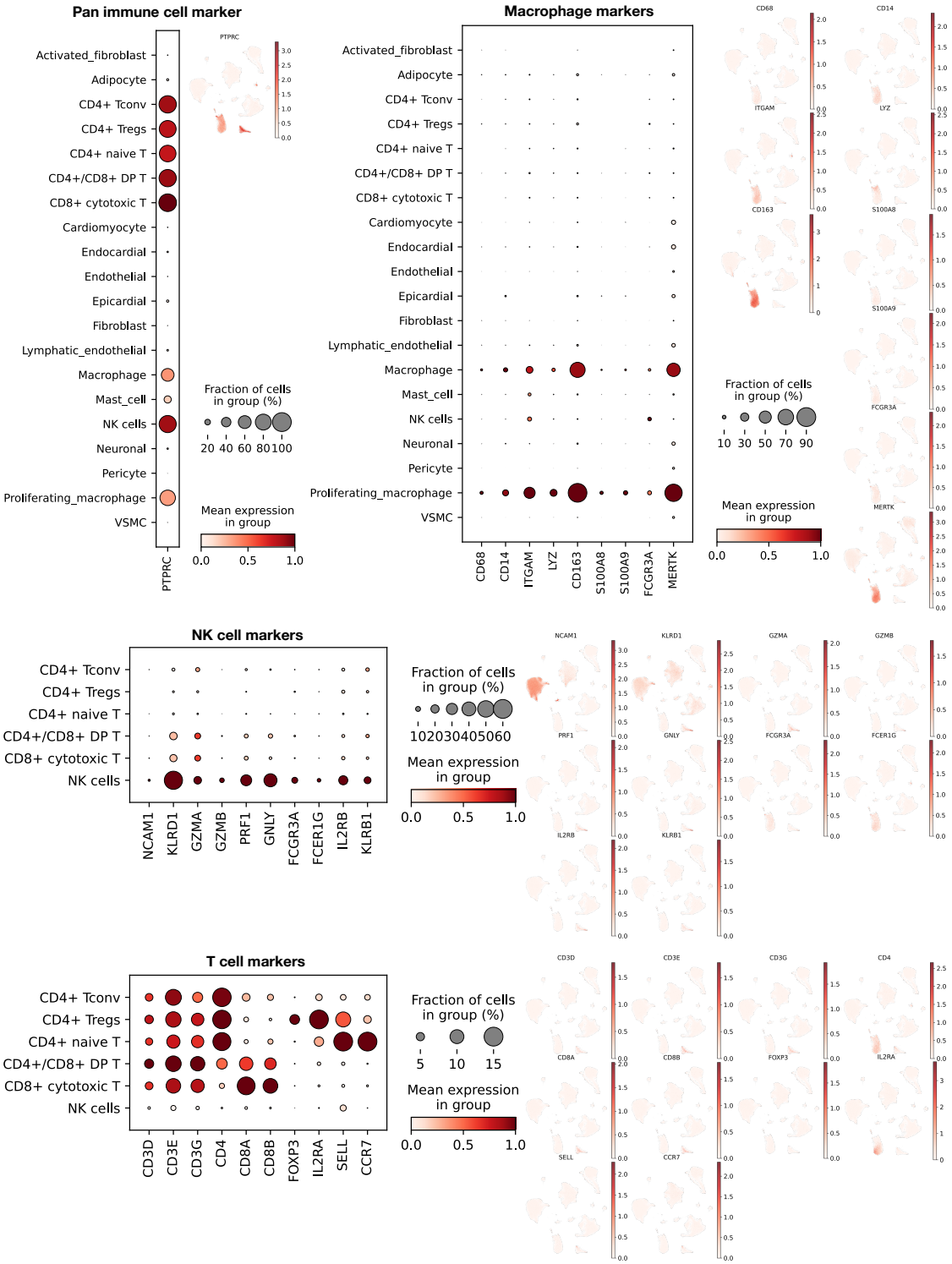

Figure 5.3. Dot plot showing the expression of canonical marker genes for the annotation of immune cell populations, including refined lymphocyte subsets, in the late-stage human HCM dataset.
Dot size indicates the percentage of cells expressing the gene, and colour intensity represents the average expression level.

Table 5.1. Summary of absolute cell counts for each annotated cell type from the late-stage human HCM and non-failing (NF) single-nucleus RNA-seq dataset. The table details the number of samples in which each cell type was detected and the total cell count per condition.

Cell Type	Disease	Sample Count	Cell Count
Activated fibroblasts	HCM	30	2196
Activated fibroblasts	NF	14	25
Adipocytes	HCM	30	2445
Adipocytes	NF	30	1437
$CD4^+$ Tconv	HCM	28	782
$CD4^+$ Tconv	NF	29	629
$CD4^+$ Tregs	HCM	26	111
$CD4^+$ Tregs	NF	20	86
$CD4^+$ naïve T cells	HCM	29	410
$CD4^+$ naïve T cells	NF	29	276
$CD4^+/CD8^+$ DP T cells	HCM	29	1092
$CD4^+/CD8^+$ DP T cells	NF	29	728
$CD8^+$ cytotoxic T cells	HCM	28	1418
$CD8^+$ cytotoxic T cells	NF	30	1324
Cardiomyocytes	HCM	30	58680
Cardiomyocytes	NF	30	63682
Endocardial cells	HCM	30	2207
Endocardial cells	NF	30	2239
Endothelial cells	HCM	30	46840
Endothelial cells	NF	30	26412
Epicardial cells	HCM	12	202
Epicardial cells	NF	0	0
Fibroblast cells	HCM	30	55448
Fibroblast cells	NF	30	38194
Lymphatic endothelial cells	HCM	30	2671
Lymphatic endothelial cells	NF	30	1107
Macrophages	HCM	30	21399
Macrophages	NF	30	14377
Mast cells	HCM	30	1120
Mast cells	NF	30	1855
NK cells	HCM	29	1000
NK cells	NF	29	400
Neuronal cells	HCM	30	1538
Neuronal cells	NF	30	1407
Pericytes	HCM	30	25696
Pericytes	NF	30	26433
Proliferating macrophages	HCM	30	148
Proliferating macrophages	NF	30	1008
VSMCs	HCM	30	8589
VSMCs	NF	30	3449

A comparative differential expression analysis was then performed between late-stage human HCM samples and the late-stage $Actc1^{E99K}$ mouse model to identify genes with significantly different expression levels within corresponding cell types. The results reveal substantial numbers of DEGs in both human and mouse (Tables 5.2 and 5.3, respectively), although the magnitude varies across cell types. This underscores the importance of single-cell resolution for cross-species compar-

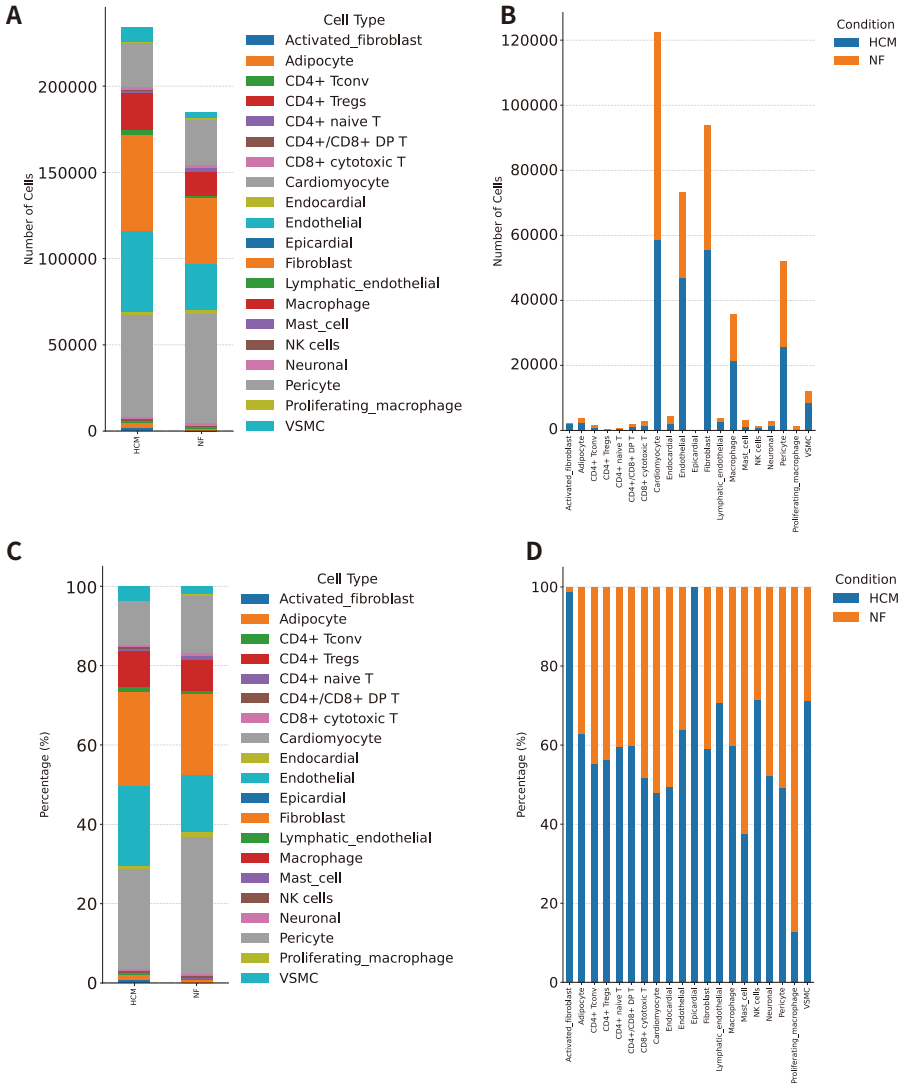

Figure 5.4. Cellular composition of single nucleus populations in late-stage and non-failing (NF) human hearts.
(A) Total cell counts recovered from HCM (blue) and NF (orange) hearts, with cell types stacked.
(B) Per-cell-type bar plot of absolute counts: each bar is one cell type, with blue (HCM) and orange (NF) segments.
(C) As in (A), but normalised to percentage of total cells.
(D) As in (B), but normalised to percentage.
These plots provide a descriptive summary of the cellular composition; no statistical tests for differential abundance are depicted.

isons and highlights the potential for divergent molecular mechanisms underlying seemingly similar disease phenotypes.

Table 5.2. Summary of differentially expressed genes (DEGs) between HCM and non-failing (NF) conditions for each cell type in the late-stage human dataset. DEGs were identified based on an adjusted p-value < 0.05. The table lists the total number of genes detected, and the number of significantly up-regulated and down-regulated genes in HCM versus NF.

Cell Type	Genes Detected	Upregulation	Downregulation
Adipocytes	27846	996	896
All T cells	26304	184	0
Cardiomyocytes	21622	6135	4759
$CD4^+/CD8^+$ DP T cells	21519	63	116
$CD4^+$ naïve T cells	17614	8	25
$CD4^+$ Tconv	20915	27	90
$CD8^+$ cytotoxic T cells	22985	35	114
Endocardial cells	27720	415	519
Endothelial cells	27475	2322	3128
Fibroblasts	26392	5387	5540
Lymphatic endothelial cells	26752	1047	10835
Lymphocytes	27257	487	677
Macrophages	28804	1879	2339
Mast cells	23704	7705	791
Neuronal cells	25256	465	517
NK cells	20292	94	83
Pericytes	28413	5517	2976
Proliferating macrophages	23844	10669	1161
VSMCs	27792	2090	12580

Table 5.3. Summary of differentially expressed genes (DEGs) between late-stage $Actc1^{E99K}$ and wild-type (WT) mice for each cell type. DEGs were identified using an adjusted p-value < 0.05. The table shows the total genes detected, and the number of significantly up-regulated and down-regulated genes in the $Actc1^{E99K}$ model.

Cell Type	Genes Detected	Upregulation	Downregulation
All fibroblasts	22025	2327	2251
All lymphocytes	18677	41	44
All macrophages	18172	660	692
All monocytes	17184	584	418
All T cells	15761	105	125
B cells	16977	42	57
$CD14^{hi}$ monocytes	16005	486	388
$CD14^{lo}$ monocytes	15318	452	272
$CD4^+$ Tconv	12350	24	38
$CD4^+$ Tregs	10422	6	2
$CD8^+$ Tc	10963	9	20
DCs	15709	253	259
DP T cells	9142	3	0
Endothelial cells	20745	886	744
Eosinophils	10586	486	1957
$Gzmk^+CD8^+$ Tc	13052	31	15
$Lag3^+CD4^+$ Tconv	10763	5	0

Continued on next page

Cell Type	Genes Detected	Upregulation	Downregulation
Lgals3^{+} $\gamma\delta$T cells	10284	9	19
Lymphatic endothelial cells	17412	458	151
MHC-II^{hi}Ccr2^{+} macrophages	17675	587	610
Neuronal cells	14596	51	27
Neutrophils	13482	282	216
NK cells	13550	0	0
Pericytes	14356	642	354
Sox13^{hi} $\gamma\delta$T cells	11727	43	15
Thy1^{lo}Fap^{lo} fibroblasts	19471	1203	864
Thy1^{lo}Fap^{+} fibroblasts	15974	295	345
Thy1^{+}Fap^{lo} fibroblasts	14336	104	125
Thy1^{+}Fap^{+} fibroblasts	20854	1862	1998
TLF^{-}MHC-II^{lo} macrophages	13779	77	157
TLF^{+} macrophages	13302	100	91
VSMCs	13695	191	176

5.2 Comparing gene expression landscapes in human and mouse HCM to uncover shared mechanisms and species-specific differences

5.2.1 Enrichment analysis uncovers metabolic suppression and heightened immune activation in HCM

GSEA was conducted on differentially expressed genes identified between late-stage human and mouse HCM samples to explore coordinated pathway alterations. This approach aimed to elucidate broader functional changes beyond individual gene expression differences, providing insights into shared and divergent molecular mechanisms driving late-stage disease progression in both species. The analysis encompassed a comprehensive set of hallmark gene sets representing a wide spectrum of biological processes relevant to HCM pathogenesis, including fibrosis, inflammation, and metabolic remodelling.

GSEA revealed both concordant and discordant pathway alterations between the species. An expected finding was the widespread down-regulation of metabolic pathways in the human HCM samples. Across diverse cell types, including adipocytes, endocardial cells, endothelial cells, fibroblasts, lymphocytes, macrophages, neuronal cells, pericytes, and VSMCs, adipogenesis, androgen response, cholesterol homeostasis, fatty acid metabolism, and glycolysis were significantly down-regulated (Figure 5.5). This suggests a potential metabolic shift in the late-stage human

HCM heart, warranting further investigation [56, 321, 417]. In contrast, these metabolic pathways did not exhibit consistent down-regulation in the mouse samples (Figure 4.13). While this observation could point towards a potential species-specific difference in metabolic remodelling during HCM progression [278], it is also important to consider that variations in experimental methodologies between the human and mouse studies may contribute to these divergent findings. Factors such as differences in sample preparation (e.g., predominantly frozen human samples versus fresh mouse samples), the RNA sequencing techniques employed (snRNA-seq for human versus multiplexed scRNA-seq for mouse), and the specific cardiac regions sampled (human LV free wall versus whole mouse heart) can critically influence metabolic signals and their downstream interpretation.
Conversely, several pathways related to immune activation and stress response were up-regulated in both human and mouse samples (Figures 5.5 and 4.13). Allograft rejection, complement, apoptosis, and interferon responses were up-regulated in various cell types, including cardiomyocytes, endothelial cells, lymphocytes, and NK cells. This shared up-regulation suggests a conserved role for immune activation and inflammation in late-stage HCM across species. However, the specific cell types exhibiting these changes differed. For example, allograft rejection was up-regulated in several T cell subsets in human samples, whereas in mouse samples, up-regulation was observed across a broader range of immune cell types. This difference may reflect interspecies variation in the adaptive immune response.
Further GSEA revealed intriguing differences in pathways related to cell growth and signalling. Epithelial-mesenchymal transition (EMT), implicated in fibrosis, was up-regulated in both human and mouse samples, predominantly in cardiomyocytes, endocardial cells, endothelial cells, fibroblasts, and pericytes (Figures 5.5 and 4.13). This reinforces the importance of EMT in HCM-related fibrosis and suggests that targeting this pathway could be a viable therapeutic strategy [418–420]. However, the down-regulation of EMT in human macrophages and VSMCs

(Figure 5.5), contrasting with its up-regulation in the mouse (Figure 4.13), warrants further investigation to understand the cell-type-specific regulation of EMT in HCM.

Several growth factor signalling pathways also exhibited differential regulation. While KRAS signalling was up-regulated in both species, primarily in cardiomyocytes, endocardial cells, endothelial cells, fibroblasts, and pericytes, other pathways, such as mTORC1 signalling and MYC targets, showed contrasting patterns (Figures 5.5 and 4.13). mTORC1 signalling, a key regulator of cell growth and metabolism, was down-regulated in multiple human cell types, including adipocytes, endocardial cells, fibroblasts, macrophages, neuronal cells, pericytes, and VSMCs (Figure 5.5). This down-regulation could represent a compensatory mechanism counteracting the hypertrophic growth observed in HCM [315, 421–423]. Conversely, mTORC1 signalling was up-regulated in several mouse immune cell types (Figure 4.13), suggesting a potential role in the inflammatory response.

GSEA also highlighted alterations in cellular stress response pathways. The unfolded protein response, activated by endoplasmic reticulum (ER) stress, was up-regulated in human cardiomyocytes, endothelial cells, lymphocytes, and NK cells (Figure 5.5). This suggests that ER stress contributes to the pathogenesis of late-stage HCM and could be a potential therapeutic target [424–429]. However, its down-regulation in several mouse cell types, including adipocytes, endocardial cells, fibroblasts, neuronal cells, pericytes, and VSMCs (Figure 4.13), indicates potential species-specific differences in the cellular response to ER stress.

In summary, GSEA revealed a complex interplay of conserved and divergent pathway alterations between late-stage human and mouse HCM. Both species exhibited up-regulation of pathways related to immune activation, inflammation, and EMT process. However, substantial differences were observed in metabolic pathways, growth factor signalling, and cellular stress responses. The widespread down-regulation of metabolic pathways in the human samples, for instance, coupled with the contrasting regulation of mTORC1 signalling and the unfolded

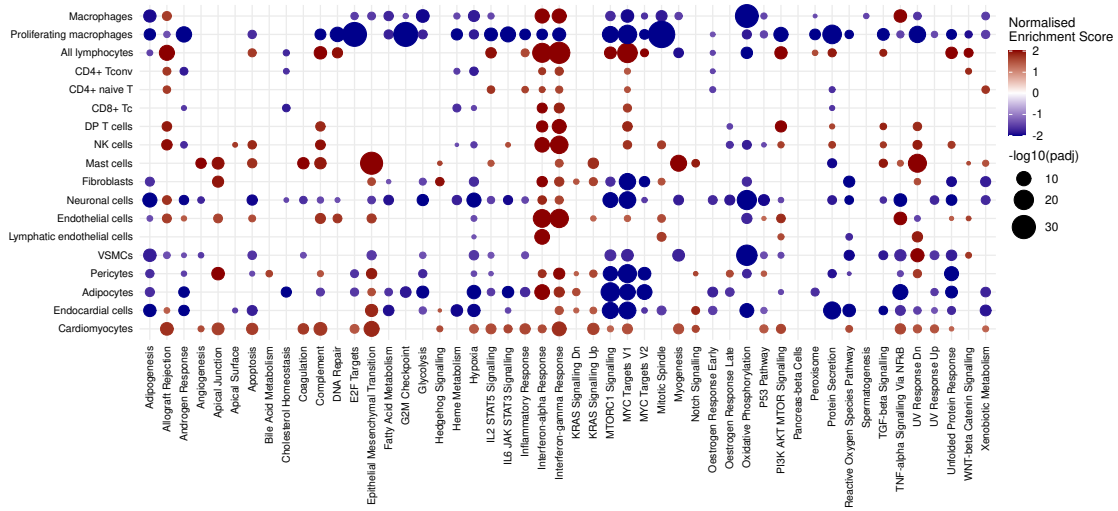

Figure 5.5. GSEA analysis of hallmark pathways in late-stage human snRNA-seq samples.
The dot plot summarises pathway activity across different cell types. The normalised enrichment score (NES), indicated by colour, shows whether a pathway is up-regulated (red) or down-regulated (blue) in HCM. The size of the dot is proportional to the statistical significance (adjusted p-value). Only pathways with an adjusted p-value <0.05 are shown.

protein response, may not solely reflect species-specific differences in the underlying molecular mechanisms of late-stage HCM. It is crucial to acknowledge that methodological variations, including differences in sample procurement and processing (such as the use of frozen human tissue versus predominantly fresh mouse tissue), RNA sequencing technologies (snRNA-seq versus multiplexed scRNA-seq), and the anatomical regions analysed (e.g., human LV versus whole mouse heart), could also significantly contribute to these observed divergences, particularly for sensitive metabolic signals. These findings underscore the importance of considering such confounding factors alongside potential biological differences when developing therapeutic strategies for HCM and emphasise the need for further research to elucidate the functional implications of these observed differences. Furthermore, the discrepancies reinforce the inherent limitations of cross-species comparisons and highlight the necessity for cautious interpretation when translating findings from preclinical models to human disease.

5.2.2 Comparative pathway activity reveals distinct signalling responses across species

GSEA of the global transcriptional landscape informed subsequent characterisation of key signalling pathway activities within non-cardiomyocytes in late-stage human and mouse HCM. Using PROGENy, I inferred activity for fourteen signalling pathways across diverse cell types in both species (Figures 5.6 and 4.15). This cross-species comparison revealed notable differences in pathway activity, suggesting distinct species-specific responses to HCM.

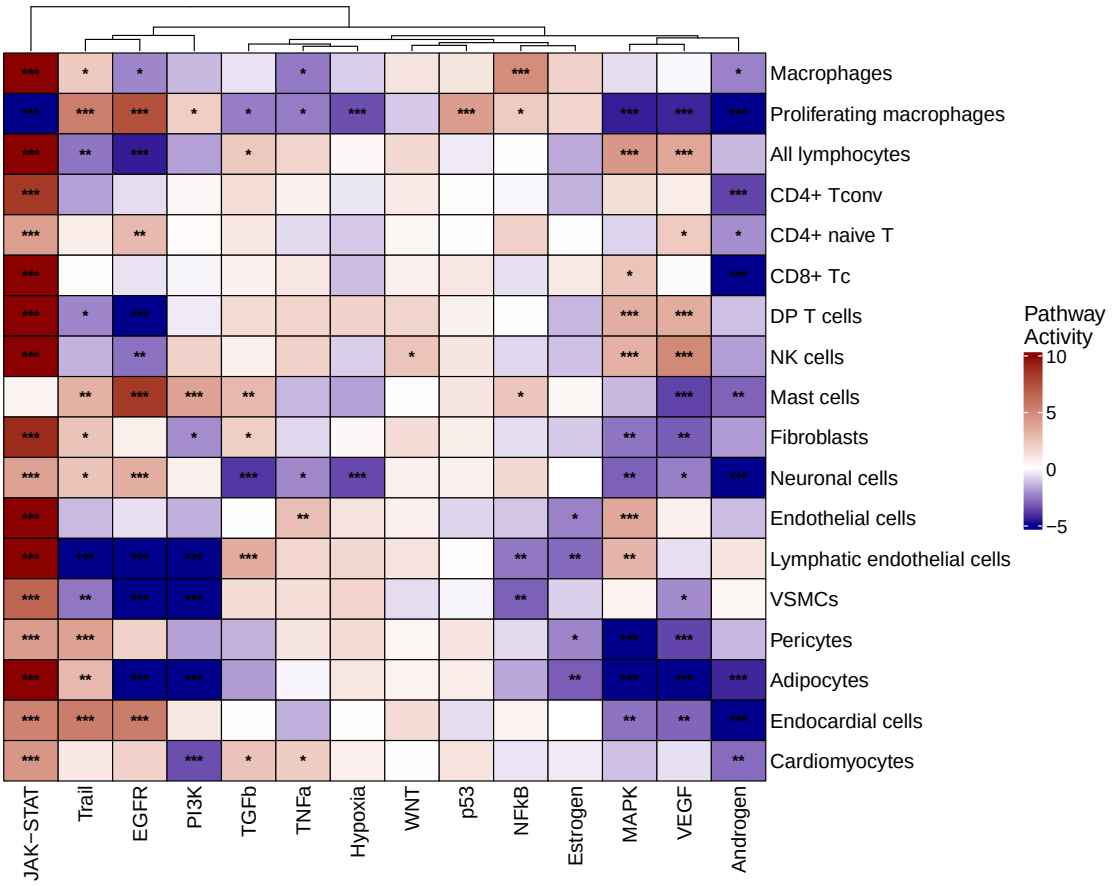

Figure 5.6. Heatmap summary of PROGENy pathway activity analysis in late-stage human samples.
The score represents the differential activity of 14 key pathways across various cell types. Red indicates activation and blue indicates inhibition of the pathway in HCM compared to non-failing controls. Significance levels are indicated as follows: * $p < 0.05$, ** $p < 0.01$, *** $p < 0.001$.

Androgen signalling, for example, was broadly inhibited across various human cell types, including adipocytes, several T cell subsets ($CD4^+$ conventional, $CD4^+$

naïve, $CD8^+$ cytotoxic), cardiomyocytes, endocardial cells, macrophages, mast cells, neuronal cells, and proliferating macrophages. Conversely, in the $Actc1^{E99K}$ mouse model, this pathway showed activation in B cells, $CD4^+$ regulatory T cells, $Gzmk^+$ $CD8^+$ cytotoxic T cells, and $Thy1^{lo}Fap^+$ fibroblasts, with inhibition restricted to neuronal cells. This marked divergence suggests a potentially human-specific role for androgen signalling modulation in late-stage HCM. EGFR signalling exhibited a more complex pattern in human samples. While activated in $CD4^+$ naïve T cells, endocardial cells, mast cells, neuronal cells, and proliferating macrophages, EGFR signalling was inhibited in adipocytes, $CD4^+CD8^+$ double-positive T cells, lymphatic endothelial cells, lymphocytes, macrophages, NK cells, and VSMCs. This contrasts with the mouse model, where EGFR signalling was predominantly activated across several cell types, including B cells, endothelial cells, and fibroblasts. Oestrogen signalling was largely inhibited in human adipocytes, endothelial cells, lymphatic endothelial cells, and pericytes, while in mouse, it was activated in pericytes and inhibited in eosinophils. Finally, hypoxia signalling was inhibited in human neuronal cells and proliferating macrophages, contrasting with its widespread activation across various myeloid and endothelial cell populations in the mouse model.

The JAK-STAT pathway showed prominent activation in human HCM across a broad range of cell types, including adipocytes, various T cell subsets, cardiomyocytes, endothelial cells, fibroblasts, lymphatic endothelial cells, lymphocytes, macrophages, NK cells, neuronal cells, pericytes, and VSMCs. Inhibition was restricted to proliferating macrophages. This widespread activation contrasted with the more limited activation observed in the mouse model, primarily in T cells, DCs, endothelial cells, and macrophages. MAPK signalling also exhibited distinct interspecies patterns. In human HCM, activation occurred in $CD4^+CD8^+$ double-positive T cells, $CD8^+$ cytotoxic T cells, endothelial cells, lymphatic endothelial cells, lymphocytes, and NK cells, while inhibition was noted in adipocytes, endocardial cells, fibroblasts, neuronal cells, pericytes, and proliferating macrophages.

The mouse model, conversely, showed MAPK activation predominantly in myeloid cells and fibroblasts.

NF-κB signalling was activated in human macrophages, mast cells, and proliferating macrophages, but inhibited in lymphatic endothelial cells and VSMCs. This contrasted with the mouse model, which exhibited widespread NF-κB activation across various immune and stromal cell populations. Similarly, PI3K signalling, activated in human mast cells and proliferating macrophages, was inhibited in human adipocytes, cardiomyocytes, fibroblasts, lymphatic endothelial cells, and VSMCs. This differed from the mouse, where PI3K activation was more prevalent, particularly in myeloid cells, endothelial cells, and fibroblasts. TGF-β signalling was activated in human cardiomyocytes, fibroblasts, lymphatic endothelial cells, lymphocytes, and mast cells, with inhibition observed in neuronal cells and proliferating macrophages. This contrasted with the widespread TGF-β activation across various myeloid, lymphoid, and stromal cell populations in the mouse. TNF signalling was activated in human cardiomyocytes and endothelial cells, but inhibited in macrophages, neuronal cells, and proliferating macrophages. In the mouse model, TNF activation occurred in regulatory T cells, neuronal cells, and fibroblasts.

Trail signalling was broadly activated in human adipocytes, endocardial cells, fibroblasts, macrophages, mast cells, neuronal cells, pericytes, and proliferating macrophages, while inhibited in $CD4^+CD8^+$ double-positive T cells, lymphatic endothelial cells, lymphocytes, and VSMCs. The mouse model displayed a more restricted Trail activation pattern. Finally, VEGF signalling, activated in human $CD4^+CD8^+$ double-positive T cells, $CD4^+$ naïve T cells, lymphocytes, and NK cells, was inhibited in human adipocytes, endocardial cells, fibroblasts, mast cells, neuronal cells, pericytes, proliferating macrophages, and VSMCs. This contrasted with the widespread VEGF activation observed in the mouse. WNT activation was observed only in human NK cells, and p53 activation was restricted to proliferating macrophages. These findings underscore the complex landscape

of pathway activation in late-stage HCM and highlight potentially important interspecies differences.

5.2.3 Intercellular communication insights reveal crucial crosstalk that drives adverse remodelling

Global transcriptional and pathway-level dysregulation in late-stage HCM, as revealed by GSEA and PROGENy analyses, prompted investigation of intercellular communication networks within the myocardial microenvironment. This analysis aimed to identify key cell-cell interactions contributing to adverse remodelling in both human and mouse late-stage HCM.

Initial cross-species analysis revealed fibroblasts, cardiomyocytes, and endothelial cells as the predominant "source" cells (initiating signals) in late-stage human HCM (Figure 5.7). Macrophages, fibroblasts, and pericytes were the main "target" cells (receiving signals). A similar pattern emerged in the mouse model, with fibroblast subtypes ($Thy1^{+}Fap^{+}$, $Thy1^{lo}Fap^{lo}$, and $Thy1^{lo}Fap^{+}$), endothelial cells, and pericytes as primary "source" cells, and fibroblast subtypes, eosinophils, and macrophages as primary "target" cells (Figure 5.7). This highlighted the central role of fibroblasts, endothelial cells, and immune cells, particularly macrophages, in late-stage HCM intercellular communication across both species. However, notable differences were observed, particularly regarding specific immune cell populations, potentially reflecting species-specific inflammatory responses during HCM progression.

Key communication hubs show conserved roles and species-specific signalling

To streamline the analysis, I focused on the most active and functionally relevant cell populations. Detailed investigation of T cells, macrophages, endothelial cells, fibroblasts, and pericytes/VSMCs revealed both conserved themes and critical species-specific differences in the signalling networks driving late-stage disease. Analysis of T cell communication highlighted divergent adaptive immune responses (Figure C.1). In human HCM, T cells engaged in complex, widespread

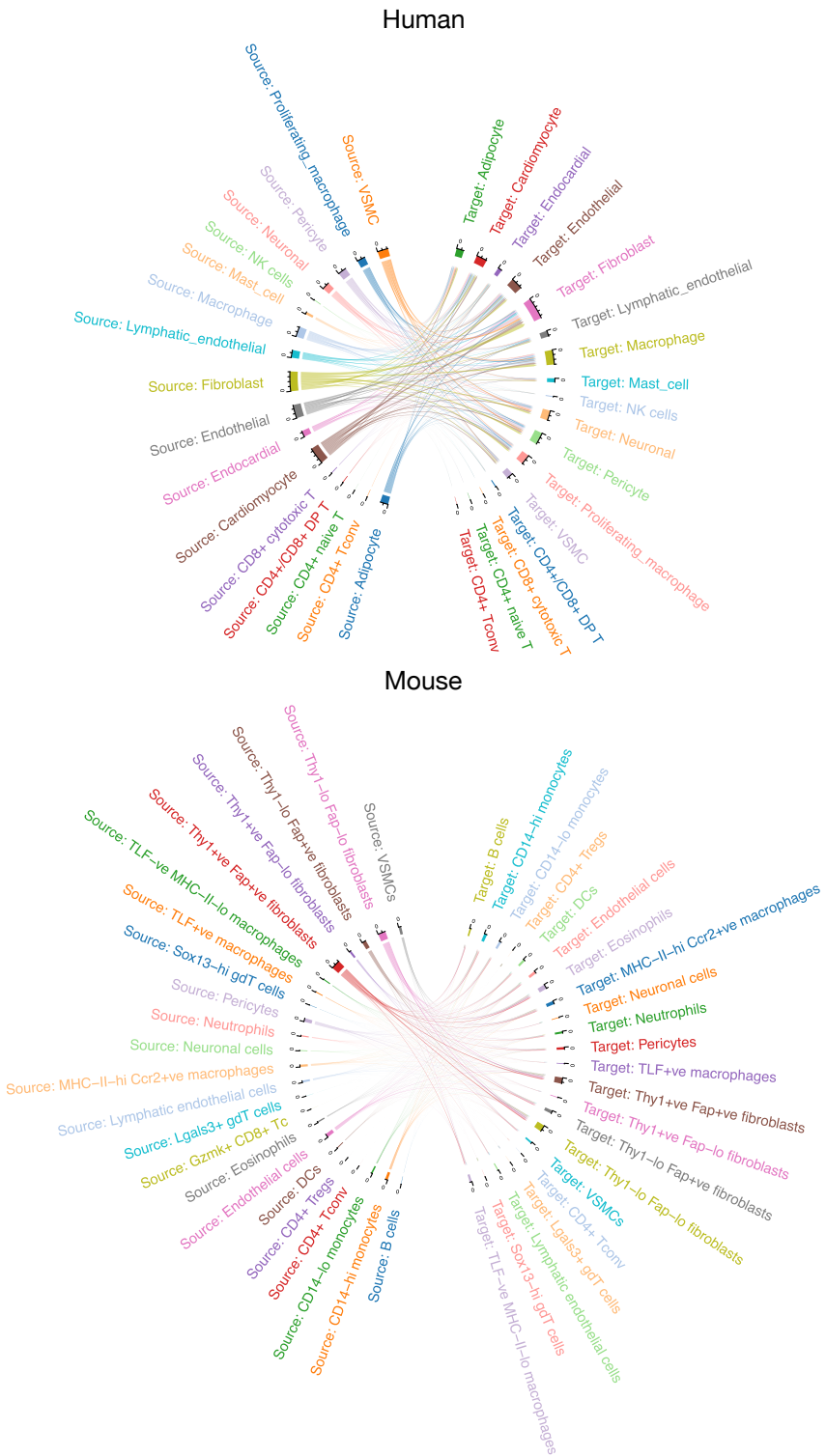

Figure 5.7. Overview of cell-cell communication in late-stage human and mouse HCM.
This circos plot depicts cell-cell communication, with ligand-secreting source cells (left) and receptor-expressing target cells (right). Ribbon width indicates interaction strength; wider ribbons represent more interactions. Human interactions are shown in the upper half, and mouse interactions in the lower half.

signalling with both stromal and myeloid cells, suggesting a broad immunomodulatory role. In contrast, the mouse model showed a more focused response, dominated by pro-inflammatory chemokine signalling from $CD8^+$ T cells to myeloid cells, indicating a potential difference in T cell effector function.

Macrophages, key drivers of inflammation and repair, also showed distinct communication profiles (Figure C.2). Human macrophages displayed altered GAS6-MERTK signalling, suggesting changes in efferocytosis and cardiomyocyte interaction. The mouse model, however, was characterised by strong chemokine signalling (e.g., Ccl2/4) between macrophage subtypes and other myeloid cells, pointing to a greater emphasis on immune cell recruitment.

Endothelial and lymphatic endothelial cells, critical for vascular function, exhibited complex and largely species-specific signalling changes (Figure C.3). Human endothelial cells showed altered CALM1 and EFNB2 signalling, implicated in vascular tone and remodelling, while mouse endothelial cells displayed significant changes in collagen and ApoE signalling, suggesting different mechanisms of vascular and metabolic adaptation.

Fibroblasts, central to ECM remodelling, were major signalling hubs in both species but utilised different pathways (Figure C.4). Human fibroblasts showed increased signalling through non-fibrillar collagens like COL14A1 and COL12A1. In contrast, the different fibroblast subtypes in the mouse model were characterised by complex changes in Adm, ApoE, and Adam metalloproteinase signalling, in addition to fibrillar collagen signalling.

Finally, pericytes and VSMCs displayed significant alterations related to vascular stability and fibrosis (Figure C.5). Human pericytes showed prominent upregulation of FGF1 signalling, whereas their mouse counterparts were dominated by Bgn and ApoE signalling. These differences underscore the divergent pathways activated in the mural cells of the two species during late-stage disease.

A comprehensive list of all significantly altered interactions for these and other cell types, including neuronal cells, is provided in Appendix C, Figures C.1–C.6.

5.3 Integrative analysis connects bulk trends with single-cell insights to reveal cell type contributions

Having established a comparative framework between human and mouse late-stage HCM at single-cell/nucleus resolution, we now turn to investigate the specific cell types contributing to the late-stage adverse remodelling signals observed in the bulk RNA-seq data. This integrative analysis aims to deconstruct the bulk temporal gene expression clusters from Chapter 3 by identifying their cellular origins, focusing on the most salient findings for brevity. A gene set score was calculated for each cluster in each cell type to assess its activity. A detailed breakdown of the scores for all sub-clusters across all cell types is available in Appendix D, Figures D.1–D.152.

5.3.1 Cellular drivers of late-stage up-regulated and U-shaped gene clusters

Clusters 1 and 4, which show an early up-regulation followed by a late surge, were primarily driven by non-myeloid cells in human HCM. Cluster 1, associated with ribosome biogenesis and stress responses, was significantly upregulated in activated fibroblasts, endothelial cells, and cardiomyocytes. Cluster 4, enriched for immune and inflammatory responses, was similarly driven by activated fibroblasts, NK cells, and cardiomyocytes. These findings pinpoint a broad activation of protein synthesis and inflammatory signalling in structural and lymphoid cells as a key feature of late-stage human disease. In contrast, the mouse model showed sparse and divergent changes, suggesting these specific temporal dynamics are not well conserved at the cellular level (Figures D.1, D.12, D.23, and D.34).

Clusters 9 and 10, characterised by a gradual increase in expression over time, also showed significant activity in human non-myeloid cells. Cluster 9, linked to translation and metabolism, was upregulated in activated fibroblasts, NK cells, and lymphatic endothelial cells, while being suppressed in macrophages. Cluster

10, associated with cell junctions and signalling, was similarly active in activated fibroblasts, cardiomyocytes, and VSMCs. This suggests that progressive adverse remodelling involves a sustained increase in translational and structural gene programs in fibroblasts and other stromal cells. Again, the mouse model showed different patterns, with monocytes and fibroblasts being the main drivers (Figures D.45, D.56, D.67, and D.78).

The U-shaped clusters, 11 and 12, which are active in early and late disease, were also predominantly active in human non-myeloid cells in the late stage. Cluster 11 (stress response, DNA repair) and Cluster 12 (cell cycle) were both significantly upregulated in activated fibroblasts, endothelial cells, VSMCs, and cardiomyocytes, while being suppressed in macrophages. This may indicate an abortive attempt by terminally differentiated cells to re-enter the cell cycle as a stress response, a phenomenon that warrants further investigation. The mouse model showed a contrasting pattern, with myeloid cells and VSMCs upregulating the cell cycle cluster, highlighting another key species difference (Figures D.89, D.100, and D.111, D.115).

5.3.2 Cellular origins of down-regulated gene clusters in late-stage HCM

Clusters 5 and 6, which are progressively down-regulated in the bulk tissue analysis, revealed a paradoxical pattern at the single-cell level. While these clusters, associated with metabolism (Cluster 5) and autophagy (Cluster 6), were indeed down-regulated in human macrophages, they were surprisingly up-regulated in activated fibroblasts, lymphatic endothelial cells, and VSMCs. This suggests that the overall down-regulation seen in bulk tissue is likely driven by a dominant signal from macrophages and potentially cardiomyocytes, masking a contrasting up-regulation in specific stromal cell types that may be adapting their metabolic and catabolic machinery to the diseased environment. The mouse model showed a more consistent down-regulation across various cell types, suggesting a less complex cellular response (Figures D.119, D.130, D.141, and D.152).

5.4 Discussion: Synthesis of insights and therapeutic perspectives for advancing treatment in late-stage HCM

This chapter's cross-species analysis of late-stage HCM provides a granular, cell-type-specific view of the molecular changes underpinning adverse remodelling. By comparing the Actc1^{E99K} mouse with human transplant-stage disease, we have identified both conserved pathogenic pathways and critical species-specific differences that have significant implications for therapeutic development. The key findings of this chapter are threefold: first, the confirmation of conserved inflammatory and fibrotic signalling networks across species; second, the discovery of a profound and likely human-specific metabolic shutdown in the failing heart; and third, the deconstruction of bulk gene expression signals into their constituent cellular sources, resolving previous ambiguities.

My work reinforces the central role of inflammation and fibrosis in HCM progression. The shared up-regulation of pathways related to immune activation (e.g., interferon and complement signalling) and EMT in both human and mouse non-cardiomyocytes provides a strong rationale for developing therapies that target these processes. This aligns with previous studies that have implicated these pathways in cardiac remodelling [430, 431]. However, where previous work, often based on bulk tissue analysis, provided a blended view of these signals, my single-cell resolution pinpoints the specific cell types driving these changes, such as fibroblasts and endothelial cells in the case of EMT, offering more precise targets for intervention.

Perhaps the most significant contribution of this analysis is the identification of divergent pathways, which highlight the limitations of preclinical models. I observed a widespread down-regulation of metabolic pathways—including fatty acid metabolism and glycolysis—across multiple human non-cardiomyocyte populations. This was not recapitulated in the mouse model, suggesting a human-specific metabolic collapse in the end-stage failing heart. This finding challenges the direct translatability of metabolic therapies developed in mice and suggests

that restoring metabolic function could be a uniquely important therapeutic goal in human HCM. Similarly, the contrasting regulation of key growth pathways like mTORC1 signalling, which was suppressed in human stromal cells but activated in mouse immune cells, underscores the need for caution when extrapolating signalling pathway data across species [432].

Finally, by integrating these single-cell data with the temporal bulk RNA-seq profiles from Chapter 3, we have been able to assign cellular origins to previously opaque gene expression trends. For instance, the progressive down-regulation of metabolic genes (Cluster 5) in bulk tissue was revealed to be a more complex phenomenon: a strong suppressive signal from macrophages masks a paradoxical up-regulation in activated fibroblasts and VSMCs. This level of insight, which resolves conflicting cellular responses within a single tissue, is unattainable with bulk sequencing and demonstrates the power of a single-cell approach to refine our understanding of disease mechanisms [135].

These findings chart a clear path for future research. First, the profound metabolic suppression observed in human HCM must be functionally validated. This will require the use of targeted metabolomics and metabolic flux analysis on human cardiac tissue and iPSC-CM-based multicellular systems to determine if this metabolic failure is a driver of, or a response to, cardiac decline. Second, the conserved ligand-receptor interactions identified in our cell-cell communication analysis, particularly those involving inflammatory signalling, represent high-priority therapeutic targets. The efficacy of blocking these interactions should be tested using neutralising antibodies or small molecules in human engineered heart tissue (EHT) models that incorporate both immune and stromal cells. Third, to overcome the limitations of cross-species comparisons, spatial transcriptomics should be applied to human HCM tissue. This would validate our predicted cell-cell interactions in their native context and provide a spatial map of the metabolic and inflammatory changes we have identified. Such work will be critical for translating the discoveries from this thesis into tangible therapeutic strategies for patients with advanced HCM.

6

Early events leading to adverse remodelling in mouse and human HCM

6.1 Mapping cellular diversity to uncover early expression patterns in human HCM

Having explored late-stage adverse remodelling characteristics in human and mouse HCM and identified potential therapeutic targets, we now focus on earlier disease stages. This shift aims to identify targets for early intervention or detection, ideally before significant fibrosis and immune infiltration. While early-stage human samples are scarce, we leveraged a publicly available dataset of mid-stage human HCM samples for comparison with our early-stage Actc1^{E99K} mouse model data. Acknowledging the inherent limitations of comparing different disease stages across species [433, 434], this approach allows us to explore potential parallels in early molecular events that may contribute to later adverse remodelling.

The human dataset comprises cardiac IVS tissues from ten male HCM patients undergoing surgical myectomy and two male healthy heart transplant donors, representing a mid-stage disease point [136]. The original study characterised several key cell populations within these samples, including fibroblasts, neuronal cells, VSMCs, pericytes, cardiomyocytes, endothelial cells, lymphoid cells, myeloid

cells, and lymphatic endothelial cells [136] (Figure 6.1, upper panel). To refine my analysis and facilitate comparison with my mouse data, I further annotated lymphoid, myeloid, and fibroblast populations (Figure 6.1, lower panel). Following the cell annotation strategy detailed previously for the mouse single-cell data (section 4.1), and using similar functionally validated markers for both human and mouse, I identified the following subpopulations: $CD4^+$ conventional T cells, $CD4^+$ naïve T cells, $CD8^+$ T cells, $\gamma\delta$T cells, and B cells (lymphoid lineage); MHC-$II^{hi}CCR2^+$ macrophages and TLF^+ macrophages (myeloid lineage); and $Thy1^+Fap^+$ and $Thy1^{lo}Fap^{lo}$ fibroblasts (Figure 6.1, lower panel). The rationale and functional significance of these markers in both human and mouse contexts have been previously discussed (section 4.1). UMAP and dot plot visualisations (Figures 6.1, 6.2, 6.3, and 6.4) further support the accuracy of these refined cell type annotations. Cell counts for each identified cell type in both HCM and control conditions are summarised in Table 6.1 and Figure 6.5.

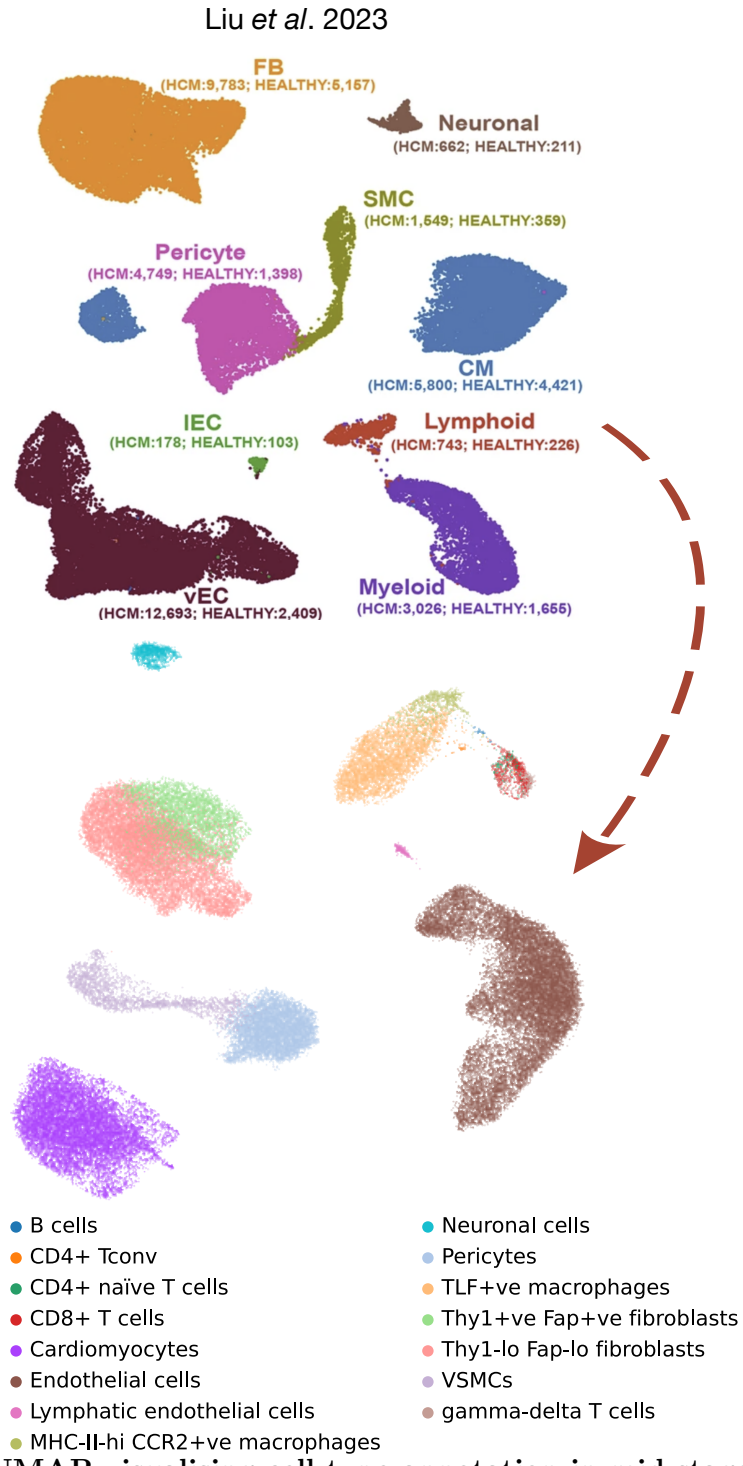

Figure 6.1. UMAP visualising cell type annotation in mid-stage human HCM snRNA-seq data.
UMAP plots of single-nucleus RNA-sequencing data from interventricular septum tissue of mid-stage HCM patients (n=10) and healthy donors (n=2). The upper panel displays the cell type annotations as provided in the original study [136]. The lower panel shows the refined annotation performed for this thesis, resolving distinct immune and fibroblast subpopulations.

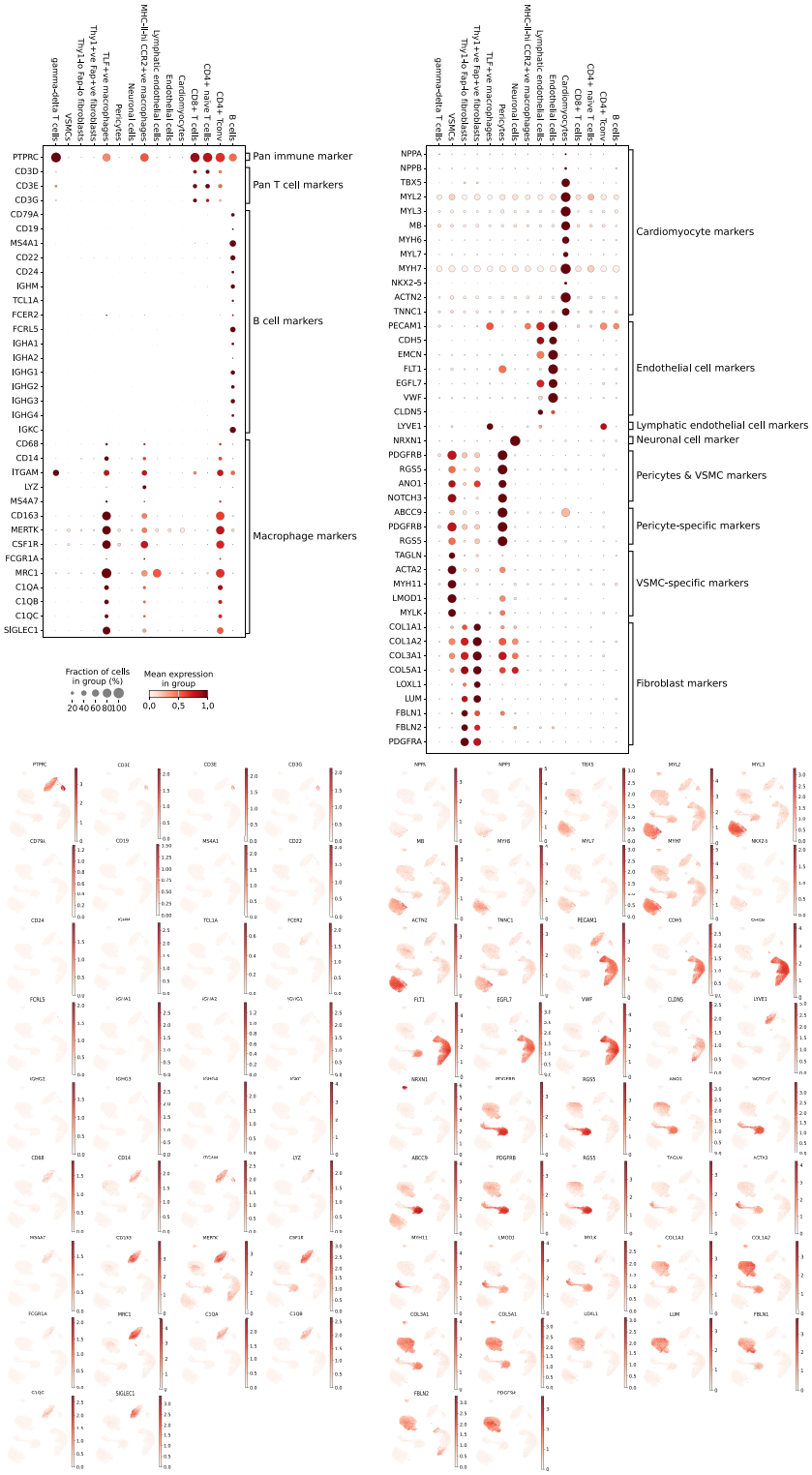

Figure 6.2. Expression of canonical marker genes validates the annotation of major cell lineages in mid-stage human hearts.
Dot size corresponds to the percentage of cells within a given population expressing a specific gene, while the colour intensity indicates the average expression level. This plot confirms the identity of the broad cell types annotated in Figure 6.1.

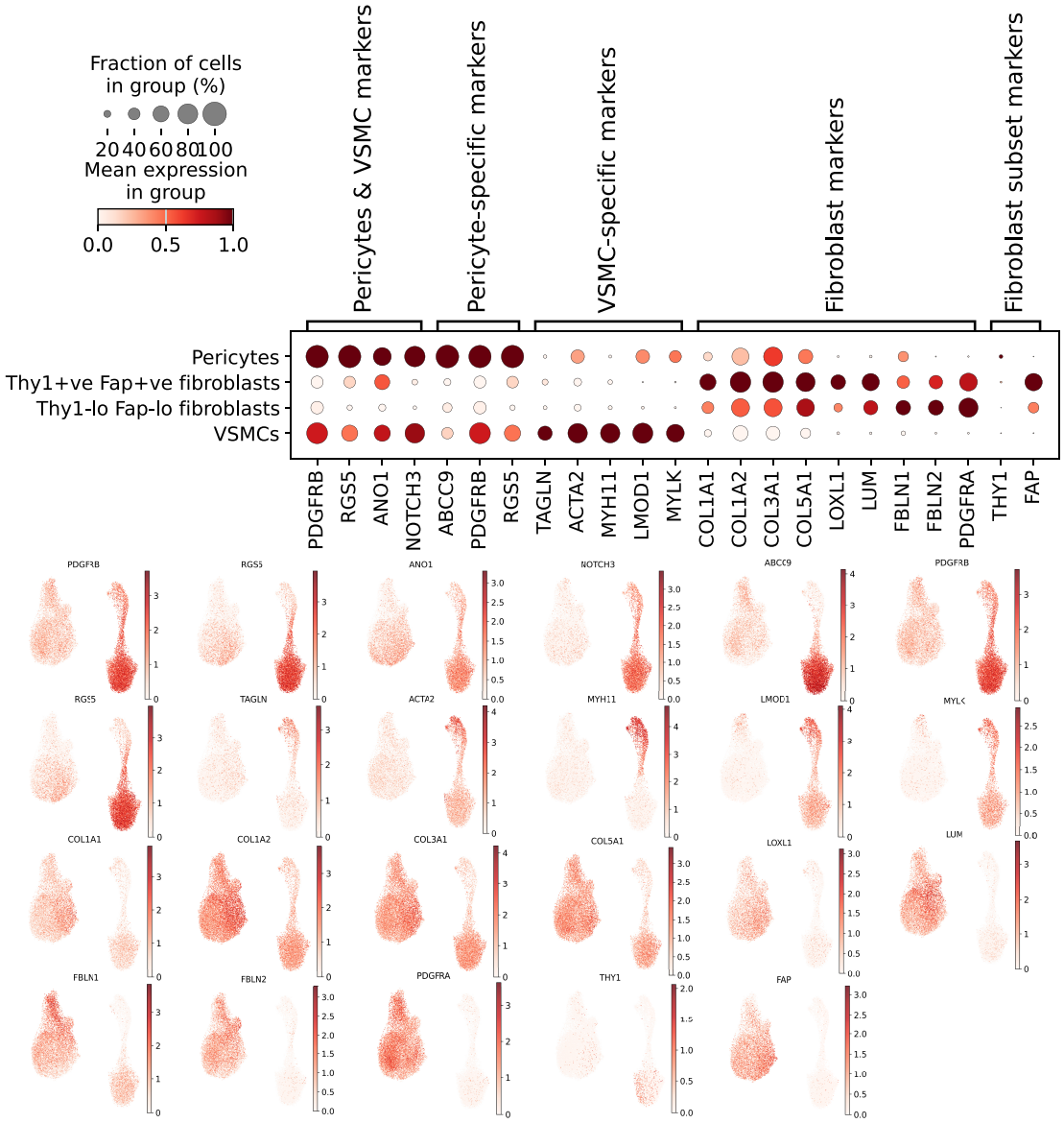

Figure 6.3. Expression of marker genes used to distinguish fibroblast, pericyte, and vascular smooth muscle cell (VSMC) populations.
Dot size corresponds to the percentage of cells within a population expressing a gene; colour intensity indicates the average expression level. These markers support the specific annotations of stromal and vascular cell types shown in Figure 6.1.

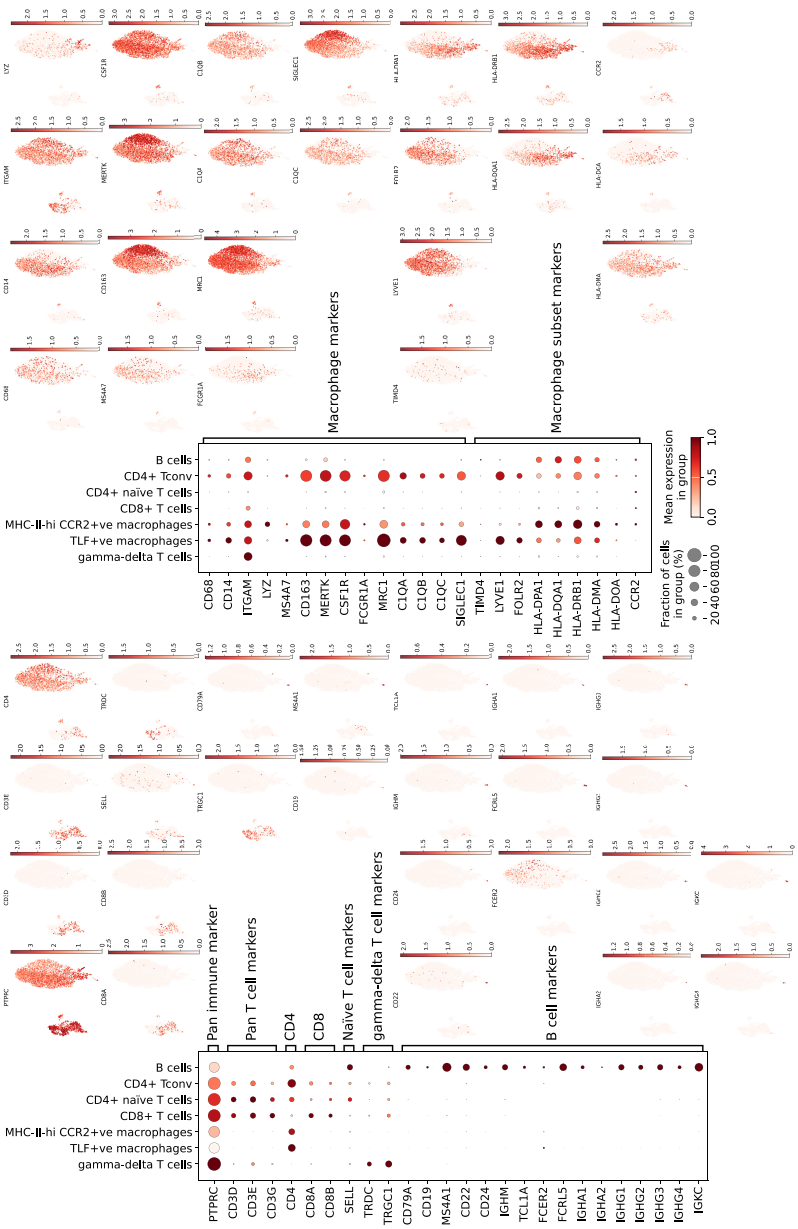

Figure 6.4. Validation of immune subpopulation annotations using established marker genes.
Dot size represents the percentage of cells in each subpopulation expressing the marker, and colour intensity reflects the average expression level. This analysis confirms the identity of the refined lymphoid and myeloid subpopulations annotated in Figure 6.1.

Table 6.1. Summary of cells and cell numbers in mid-stage human HCM snRNA-seq data.

Cell Type	Disease	Sample Count	Cell Count
B cells	HCM	8	22
B cells	Control	2	4
$CD4^+$ Tconv	HCM	9	42
$CD4^+$ Tconv	Control	2	21
$CD4^+$ naïve T cells	HCM	9	103
$CD4^+$ naïve T cells	Control	2	34
$CD8^+$ T cells	HCM	10	382
$CD8^+$ T cells	Control	2	147
Cardiomyocytes	HCM	10	5802
Cardiomyocytes	Control	2	4447
Endothelial cells	HCM	10	12720
Endothelial cells	Control	2	2400
Lymphatic endothelial cells	HCM	10	144
Lymphatic endothelial cells	Control	2	91
MHC-$II^{hi}CCR2^+$ macrophages	HCM	10	413
MHC-$II^{hi}CCR2^+$ macrophages	Control	2	243
Neuronal cells	HCM	10	662
Neuronal cells	Control	2	212
Pericytes	HCM	10	4473
Pericytes	Control	2	1379
TLF^+ macrophages	HCM	10	2600
TLF^+ macrophages	Control	2	1408
$Thy1^+Fap^+$ fibroblasts	HCM	10	3210
$Thy1^+Fap^+$ fibroblasts	Control	2	854
$Thy1^{lo}Fap^{lo}$ fibroblasts	HCM	10	6576
$Thy1^{lo}Fap^{lo}$ fibroblasts	Control	2	4297
VSMCs	HCM	10	1825
VSMCs	Control	2	374
$\gamma\delta$T cells	HCM	9	209
$\gamma\delta$T cells	Control	2	28

Differential expression analysis comparing mid-stage human and early-stage mouse samples revealed a striking difference in DEGs. Human samples exhibited substantially more DEGs across various cell types than the early-stage mouse model (Tables 6.2 and 6.3, respectively). This disparity suggests that while bulk RNA-seq analysis may reveal comparable transcriptional changes between human and mouse HCM, underlying cellular heterogeneity and cell-type-specific responses, particularly in early disease stages, may differ significantly. This underscores the importance of single-cell resolution for dissecting the complex interplay of cellular contributions to disease pathogenesis.

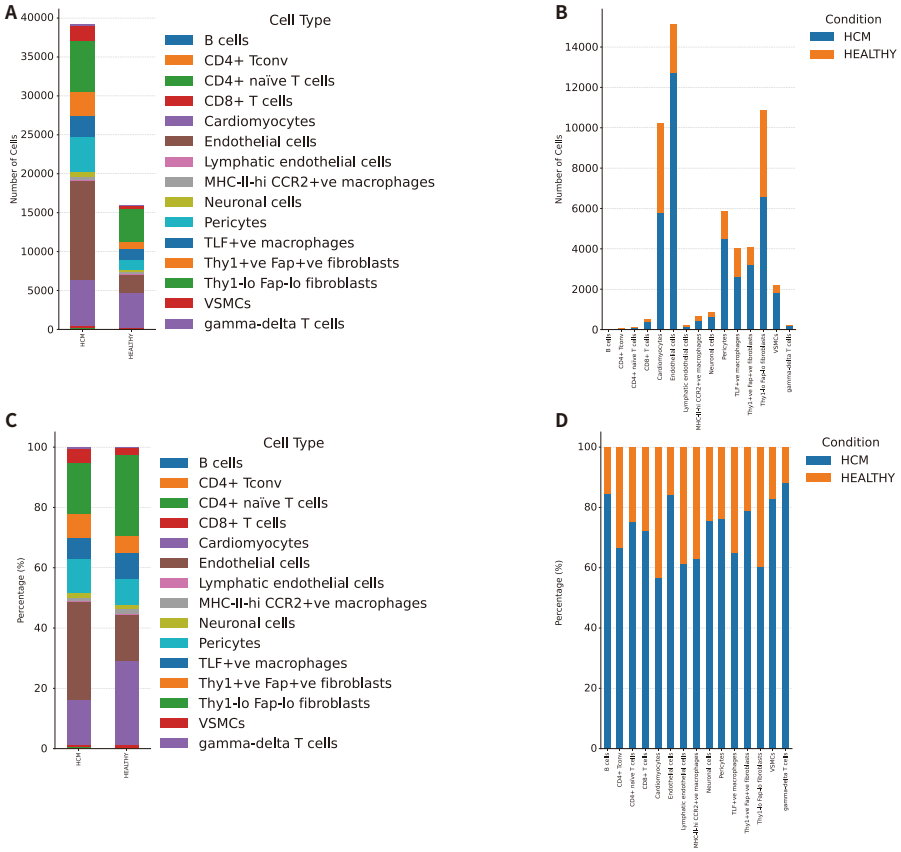

Figure 6.5. Cellular composition of single nucleus populations in mid-stage and healthy human hearts.
(A) Total cell counts recovered from HCM (blue) and healthy (orange) hearts, with cell types stacked.
(B) Per-cell-type bar plot of absolute counts: each bar is one cell type, with blue (HCM) and orange (healthy) segments.
(C) As in (A), but normalised to percentage of total cells.
(D) As in (B), but normalised to percentage.
These plots provide a descriptive summary of the cellular composition; no statistical tests for differential abundance are depicted.

Table 6.2. Summary of differentially expressed genes (DEGs) between mid-stage HCM and control human samples for each cell type. DEGs were identified using a pseudo-bulk analysis with an adjusted p-value < 0.05.

Cell Type	Genes Detected	Upregulation	Downregulation
All fibroblasts	30502	2053	2384
All lymphocytes	23978	136	414
All macrophages	27977	1532	1964
All T cells	23752	152	467
B cells	12890	4	0
Cardiomyocytes	29924	3378	2675
$CD4^+$ naïve T cells	17255	62	63
$CD4^+$ Tconv	16834	8	27
$CD8^+$ T cells	21274	67	403
Endothelial cells	29991	189	795

Continued on next page

Cell Type	Genes Detected	Upregulation	Downregulation
$\gamma\delta$T cells	19048	389	822
Lymphatic endothelial cells	20256	35	56
MHC-II^{hi}CCR2^{+} macrophages	23126	141	366
Neuronal cells	23643	369	415
Pericytes	28029	1138	1303
Thy1^{lo}Fap^{lo} fibroblasts	30028	1925	2511
Thy1^{+}Fap^{+} fibroblasts	28713	595	851
TLF^{+} macrophages	27471	1290	1936
VSMCs	26468	344	389

Table 6.3. Summary of differentially expressed genes (DEGs) between early-stage Actc1^{E99K} and wild-type mouse hearts for each cell type. DEGs were identified using a pseudo-bulk analysis with an adjusted p-value < 0.05.

Cell Type	Genes Detected	Upregulation	Downregulation
All fibroblasts	19142	285	436
All lymphocytes	18509	4	0
All macrophages	17619	0	0
All monocytes	15196	5	1
All T cells	16208	0	0
B cells	16029	41	39
CD14^{hi} monocytes	13816	3	3
CD14^{lo} monocytes	13684	22	5
CD4^{+} Tconv	13966	0	0
CD8^{+} Tc	15015	0	0
DCs	12158	2	14
Endothelial cells	19448	62	51
Lymphatic endothelial cells	12144	4	5
Mast cells	11849	0	0
MHC-II^{hi}CCR2^{+} macrophages	15085	1	0
Neutrophils	10339	0	0
NK cells	14575	9	3
Plasma cells	17481	10	1
Thy1^{lo}Fap^{lo} fibroblasts	16810	85	138
Thy1^{lo}Fap^{+} fibroblasts	16220	96	75
Thy1^{+}Fap^{+} fibroblasts	16099	35	30
TLF^{-}MHC-II^{lo} macrophages	14638	8	7
TLF^{+} macrophages	15383	0	2
VSMCs	9106	0	9

6.2 Comparing transcriptional landscapes reveals early disease signatures

6.2.1 Divergent pathway enrichment highlights species-specific signalling

To explore coordinated biological pathway changes in HCM, GSEA was performed following differential gene expression analysis between human mid-stage and

mouse early-stage HCM. This comparative approach aimed to elucidate shared and divergent molecular mechanisms underlying early disease pathogenesis. GSEA revealed distinct pathway modulation patterns across cell types in both species. For example, the adipogenesis pathway showed contrasting regulation. While down-regulated in human $CD4^+$ Tconv, $CD8^+$ T cells, MHC-$II^{hi}CCR2^+$ macrophages, pericytes, TLF^+ macrophages, and $Thy1^{lo}Fap^{lo}$ fibroblasts (Figure 6.6), it was up-regulated in mouse $Thy1^{lo}Fap^{lo}$ fibroblasts and down-regulated in several other mouse myeloid populations (Figure 4.12). This difference suggests potential species-specific adipogenic regulation during early HCM development. The Allograft Rejection pathway also exhibited divergent regulation. Up-regulated in human B cells, $CD4^+$ naïve T cells, $CD8^+$ T cells, MHC-$II^{hi}CCR2^+$ macrophages, and $\gamma\delta$T cells, it was down-regulated in human endothelial cells, pericytes, $Thy1^+Fap^+$ fibroblasts, and VSMCs (Figure 6.6). Conversely, this pathway was down-regulated across various immune cells in the mouse model (Figure 4.12), highlighting the complex interplay of immune responses in early HCM and the need for further investigation into species-specific immune cell roles.

The EMT pathway was up-regulated in human neuronal cells, $Thy1^+Fap^+$ fibroblasts, $Thy1^{lo}Fap^{lo}$ fibroblasts, and VSMCs, but down-regulated in human $CD4^+$ Tconv, $CD4^+$ naïve T cells, $CD8^+$ T cells, MHC-$II^{hi}CCR2^+$ macrophages, TLF^+ macrophages, and $\gamma\delta$T cells (Figure 6.6). In the mouse model, this pathway was up-regulated in $CD14^{hi}$ monocytes and NK cells but down-regulated in endothelial cells, $Thy1^+Fap^+$ fibroblasts, $Thy1^{lo}Fap^+$ fibroblasts, and VSMCs (Figure 4.12). This suggests complex cell-type interactions in regulating the EMT during early HCM progression, potentially influencing fibrosis development [418–420]. Finally, interferon response pathways also diverged between species. While interferon-α response and interferon-γ response were predominantly up-regulated in various human cell types (Figure 6.6), these pathways were down-regulated in several mouse immune cell populations (Figure 4.12), suggesting potential differences in the early interferon response between human and mouse HCM.

Further analysis identified pathways consistently down-regulated in both human and mouse early-stage HCM. The Apical Junction pathway was down-regulated across diverse cell types in both species, including $CD4^+$ Tconv, $CD8^+$ T cells, cardiomyocytes, lymphatic endothelial cells, MHC-$II^{hi}CCR2^+$ macrophages, pericytes, TLF^+ macrophages, and both $Thy1^+Fap^+$ and $Thy1^{lo}Fap^{lo}$ fibroblasts (Figures 6.6 and 4.12). This suggests potential disruption of cell-cell adhesion and communication within the cardiac microenvironment during early disease progression [435–437]. Similarly, cell cycle regulation pathways, such as E2F Targets and G2M Checkpoint, were down-regulated in several immune cell populations in both species (Figures 6.6 and 4.12), indicating potential alterations in cell proliferation and differentiation [438].

Metabolic pathways also showed significant alterations. Cholesterol Homeostasis was down-regulated in human $CD4^+$ naïve T cells, pericytes, TLF^+ macrophages, and both $Thy1^+Fap^+$ and $Thy1^{lo}Fap^{lo}$ fibroblasts (Figure 6.6). In mice, it was down-regulated in mast cells but up-regulated in $Thy1^{lo}Fap^{lo}$ fibroblasts (Figure 4.12). Glycolysis was down-regulated across a broad range of cell types in both species, including B cells, $CD4^+$ Tconv, $CD8^+$ T cells, MHC-$II^{hi}CCR2^+$ macrophages, pericytes, TLF^+ macrophages, and both $Thy1^+Fap^+$ and $Thy1^{lo}Fap^{lo}$ fibroblasts (Figures 6.6 and 4.12). These findings point to potential metabolic reprogramming in early HCM, possibly contributing to disease pathogenesis [56, 321, 417]. In contrast, Oxidative Phosphorylation showed divergent regulation. It was up-regulated in several human cell types, including $CD4^+$ naïve T cells, $CD8^+$ T cells, endothelial cells, neuronal cells, VSMCs, and $\gamma\delta$T cells (Figure 6.6), but down-regulated in mouse TLF^+ macrophages and other cell types (Figure 4.12).

Several other pathways exhibited notable cell-type-specific alterations. Heme Metabolism was down-regulated in human cardiomyocytes, pericytes, TLF^+ macrophages, $Thy1^{lo}Fap^{lo}$ fibroblasts, VSMCs, and $\gamma\delta$T cells (Figure 6.6), potentially indicating altered iron handling and oxygen transport within the heart during early HCM [439–443]. The Inflammatory Response pathway was generally down-regulated in both species (Figures 6.6 and 4.12), particularly in human endothelial cells,

lymphatic endothelial cells, neuronal cells, pericytes, Thy1^{+}Fap^{+} fibroblasts, Thy1^{lo}Fap^{lo} fibroblasts, VSMCs, and $\gamma\delta$T cells, and in mouse neutrophils. This observation, while potentially unexpected given the established role of inflammation in HCM progression, may reflect the early disease stage examined [178, 444]. Further investigation is needed to fully characterise inflammatory pathway dynamics throughout HCM development.

Growth factor signalling pathways also showed distinct modulation patterns. mTORC1 signalling was down-regulated in human CD4^{+} Tconv, MHC-II^{hi}CCR2^{+} macrophages, pericytes, TLF^{+} macrophages, and Thy1^{lo}Fap^{lo} fibroblasts (Figure 6.6), but up-regulated in mouse Thy1^{lo}Fap^{lo} fibroblasts (Figure 4.12), while being down-regulated in several other mouse cell types. PI3K/AKT/mammalian target of rapamycin (mTOR) Signalling was down-regulated across various cell types in both species (Figures 6.6 and 4.12), suggesting potential alterations in growth and survival signalling [315, 445, 446]. The TGF-β Signalling pathway, crucial for fibrosis development, was down-regulated in human CD4^{+} Tconv, MHC-II^{hi}CCR2^{+} macrophages, and TLF^{+} macrophages (Figure 6.6), and in mouse neutrophils and Thy1^{+}Fap^{+} fibroblasts (Figure 4.12). This seemingly paradoxical finding, considering the eventual fibrosis in later-stage HCM, may reflect the complex and dynamic regulation of TGF-β signalling during disease progression [447].

In summary, GSEA revealed a complex landscape of pathway alterations in early-stage HCM, highlighting shared and divergent molecular mechanisms between human and mouse models. These findings provide valuable insights into early HCM pathophysiology and may inform the identification of therapeutic targets for early intervention. Further research is needed to validate these findings and explore the functional consequences of these pathway alterations.

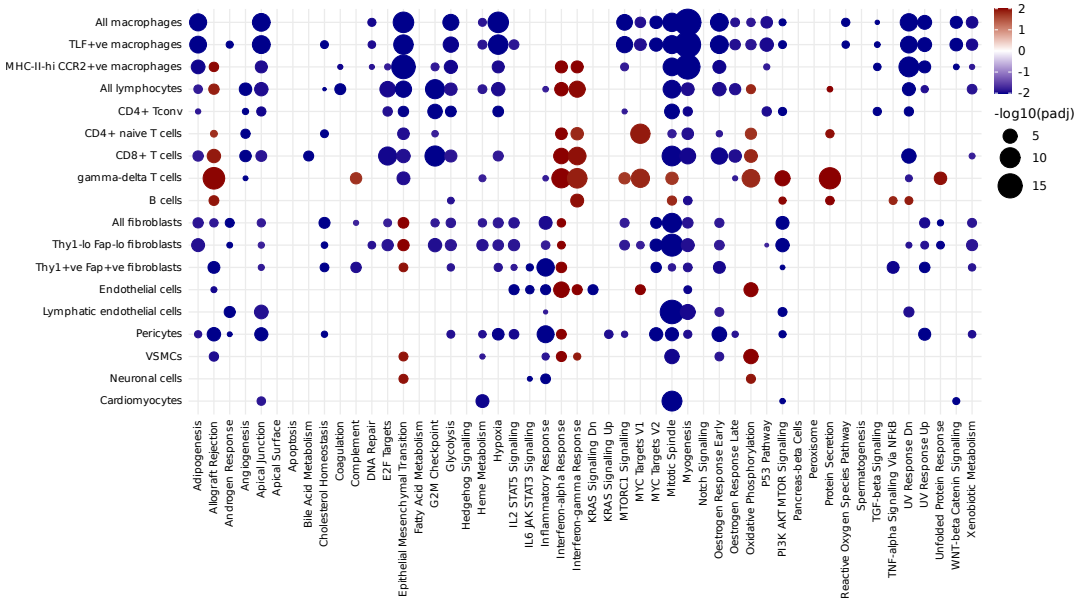

Figure 6.6. Hallmark pathway enrichment analysis reveals distinct transcriptional programmes in mid-stage human HCM.
Dot size represents significance. Only significant terms (adjusted p-value < 0.05) are displayed. Colour indicates the direction of regulation (positive or negative normalised enrichment score), where up-regulation signifies increased expression in HCM samples compared to control, and vice versa.

6.2.2 Functional signalling patterns expose key activity changes

To investigate functional changes in gene expression, I used PROGENy pathway analysis to characterise signalling pathway activity within non-cardiomyocyte populations in mid-stage human and early-stage mouse HCM hearts (Figures 6.7 and 4.14). While acknowledging the inherent limitations of cross-species and cross-disease stage comparisons, this approach allowed us to move beyond differential gene expression and examine the activity of specific signalling cascades. In mid-stage human HCM, PROGENy analysis revealed distinct patterns of pathway modulation across various cell types. Androgen signalling was broadly suppressed in $CD8^+$ T cells, cardiomyocytes, endothelial cells, lymphatic endothelial cells, MHC-$II^{hi}CCR2^+$ macrophages, neuronal cells, pericytes, TLF^+ macrophages, $Thy1^+Fap^+$ fibroblasts, $Thy1^{lo}Fap^{lo}$ fibroblasts, and VSMCs. Conversely, EGFR signalling showed a more nuanced pattern, with activation in cardiomyocytes and $Thy1^{lo}Fap^{lo}$ fibroblasts, but inhibition in B cells, $CD4^+$ naïve

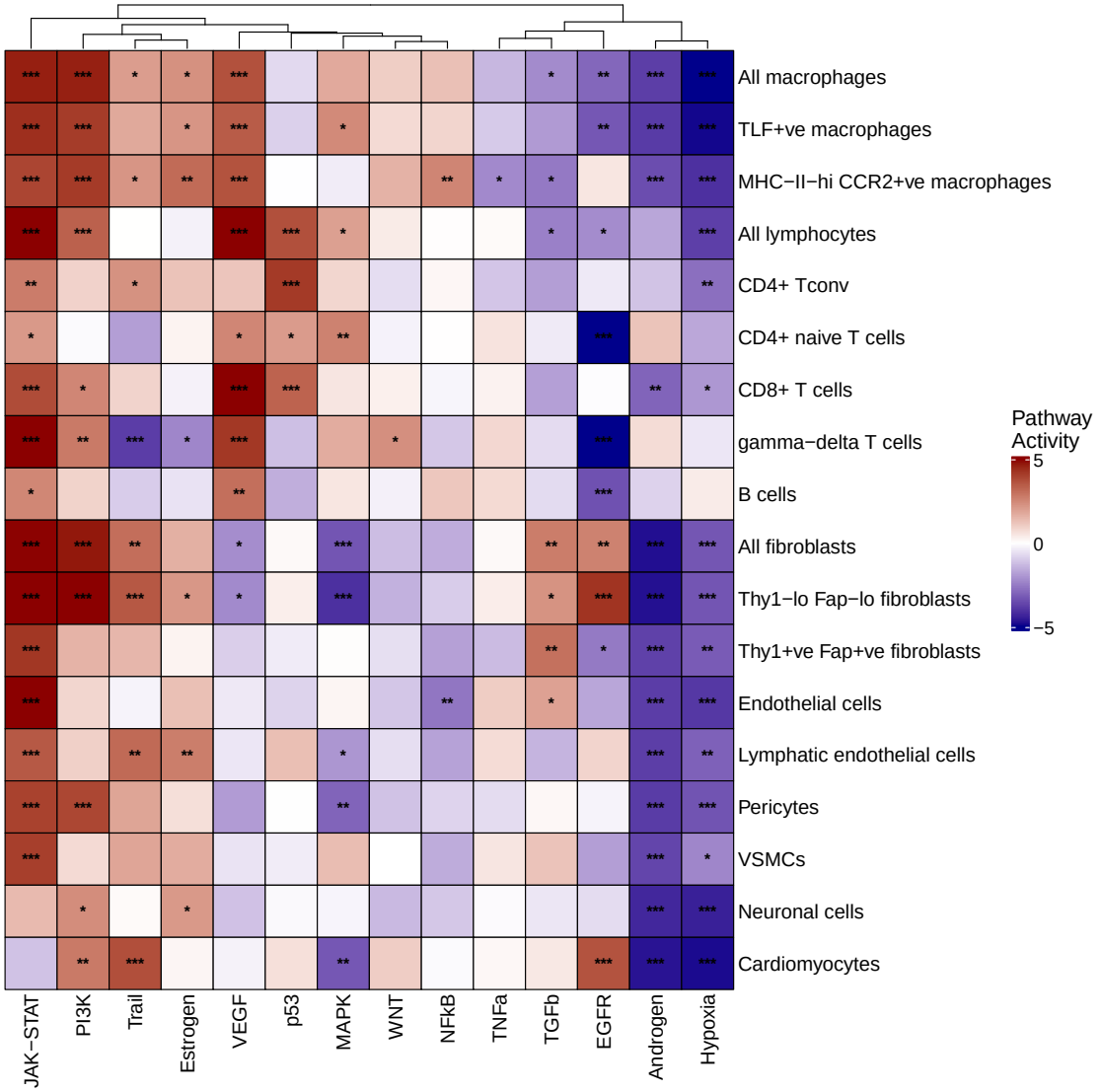

Figure 6.7. Heatmap summary of PROGENy pathway activity analysis in mid-stage human samples.
The heatmap displays the PROGENy activity scores for 14 key signalling pathways across annotated cell types, comparing HCM with control samples. Red indicates significantly increased pathway activity in HCM, while blue indicates significantly decreased activity. Significance levels are denoted by asterisks (* $p < 0.05$, ** $p < 0.01$, *** $p < 0.001$).

T cells, TLF$^+$ macrophages, Thy1$^+$Fap$^+$ fibroblasts, and $\gamma\delta$T cells. Oestrogen signalling was predominantly activated in lymphatic endothelial cells, MHC-II^{hi}CCR2$^+$ macrophages, neuronal cells, TLF$^+$ macrophages, and Thy1^{lo}Fap^{lo} fibroblasts, with inhibition restricted to $\gamma\delta$T cells. Hypoxia signalling, similar to androgen signalling, was broadly suppressed across multiple cell types. In contrast, JAK-STAT signalling was broadly activated across most non-cardiomyocyte populations. MAPK signalling displayed a mixed profile, with activation in CD4$^+$ naïve T cells and TLF$^+$ macrophages, and inhibition in cardiomyocytes, lymphatic endothelial cells, pericytes, and Thy1^{lo}Fap^{lo} fibroblasts. NF-κB signalling was activated in MHC-II^{hi}CCR2$^+$ macrophages and inhibited in endothelial cells. PI3K signalling was activated in CD8$^+$ T cells, cardiomyocytes, MHC-II^{hi}CCR2$^+$ macrophages, neuronal cells, pericytes, TLF$^+$ macrophages, Thy1^{lo}Fap^{lo} fibroblasts, and $\gamma\delta$T cells. TGFβ signalling was activated in endothelial cells, Thy1$^+$Fap$^+$ fibroblasts, and Thy1^{lo}Fap^{lo} fibroblasts, but inhibited in MHC-II^{hi}CCR2$^+$ macrophages. TNF signalling was inhibited in MHC-II^{hi}CCR2$^+$ macrophages. Trail signalling was activated in CD4$^+$ Tconv cells, cardiomyocytes, lymphatic endothelial cells, MHC-II^{hi}CCR2$^+$ macrophages, and Thy1^{lo}Fap^{lo} fibroblasts, and inhibited in $\gamma\delta$T cells. Finally, VEGF signalling was activated in B cells, CD4$^+$ naïve T cells, CD8$^+$ T cells, MHC-II^{hi}CCR2$^+$ macrophages, TLF$^+$ macrophages, and $\gamma\delta$T cells, but inhibited in Thy1^{lo}Fap^{lo} fibroblasts. WNT signalling activation was observed in $\gamma\delta$T cells, and p53 activation was seen in CD4$^+$ Tconv cells, CD4$^+$ naïve T cells, and CD8$^+$ T cells.

PROGENy analysis of the early-stage mouse HCM model revealed both similarities and differences in pathway activity compared to the mid-stage human samples (Figure 4.14). While androgen signalling was suppressed in several mouse myeloid populations (CD14^{lo} monocytes, NK cells, and neutrophils), mirroring the broader suppression observed in human samples, it was also activated in mouse B cells, contrasting with the human data. EGFR signalling activation was observed in several mouse cell types, including CD4$^+$ Tconv cells, CD8$^+$ T cells, endothelial cells, NK cells, plasma cells, and TLF$^+$ macrophages, overlapping

with, but not identical to, the human cell types exhibiting activation. Oestrogen signalling was activated in Thy1^{lo}Fap^{lo} fibroblasts in both mouse and human samples, suggesting a potentially conserved role for this pathway in this specific fibroblast population. Hypoxia signalling, broadly suppressed in human HCM, showed a more complex pattern in the mouse model, with activation in B cells, CD14^{hi} monocytes, CD8^{+} T cells, and NK cells, and inhibition in endothelial cells and neutrophils. JAK-STAT signalling, broadly activated in human HCM, was predominantly inhibited in the mouse model across various myeloid and lymphoid populations, as well as fibroblasts, highlighting a potential key difference in the inflammatory landscape between species and disease stages. MAPK signalling inhibition was observed in several mouse immune cell populations, including CD4^{+} Tconv cells, CD8^{+} T cells, MHC-II^{hi}CCR2^{+} macrophages, NK cells, and plasma cells, partially overlapping with the human findings. NF-κB signalling activation was observed in mouse B cells, plasma cells, and Thy1^{lo}Fap^{+} fibroblasts, contrasting with the more restricted activation observed in human MHC-II^{hi}CCR2^{+} macrophages. PI3K signalling, activated in several human cell types, was predominantly inhibited in the mouse model, particularly in myeloid cells and fibroblasts. TGF-β signalling activation was observed in mouse B cells and CD14^{hi} monocytes, differing from the human profile. TNF signalling inhibition was observed in mouse B cells, mast cells, and Thy1^{lo}Fap^{+} fibroblasts, partially overlapping with the human findings. TRAIL signalling, activated in several human cell types, was also activated in a broader range of mouse cell types, including myeloid, lymphoid, and fibroblast populations. VEGF signalling, activated in several human immune cell populations, was inhibited in similar mouse populations, suggesting a potential divergence in the role of VEGF signalling. Finally, WNT signalling was inhibited in mouse mast cells, contrasting with the activation observed in human $\gamma\delta$T cells, and p53 activation was observed in mouse NK cells and Thy1^{lo}Fap^{lo} fibroblasts, partially overlapping with the human findings.

6.2.3 Intercellular dialogue uncovers critical remodelling cues

Following global transcriptional and pathway analyses using GSEA and PROGENy, cell-cell communication within the myocardial microenvironment was investigated in mid-stage human and early-stage mouse HCM. This aimed to identify key intercellular interactions contributing to adverse remodelling, particularly during early disease development.

A striking difference was observed between the two conditions (Figure 6.8). The mid-stage human samples revealed a complex and active communication network, with $Thy1^{lo}Fap^{lo}$ fibroblasts, cardiomyocytes, and TLF^{+} macrophages acting as major signalling hubs. In contrast, the early-stage mouse model displayed a much simpler network, driven almost exclusively by fibroblasts targeting endothelial cells. This suggests that while fibroblasts are early players in both species, the broader, multi-cellular crosstalk that characterises advanced disease has not yet been established in the early-stage mouse heart.

Fibroblast and endothelial cell interactions in early disease

Given their central role, I examined the key outgoing signals from fibroblasts and endothelial cells. In mid-stage human HCM, these cells exhibited complex signalling changes, with dozens of up- and down-regulated interactions targeting nearly every other cell type in the heart (Figures E.1 and E.2). For instance, both cell types showed broad downregulation of FGF12 signalling, potentially disrupting vascular homeostasis. In contrast, the early-stage mouse model showed very few significant changes. The most notable were a downregulation of Thbs1 signalling between fibroblast subtypes and an upregulation of Col4a1-Cd93 signalling between endothelial cells. This relative quiescence in the mouse model underscores the early nature of the disease stage being studied and its divergence from the more established pathology in the human samples. A comprehensive list of all significantly altered interactions is provided in Appendix E, Figures E.1–E.2.

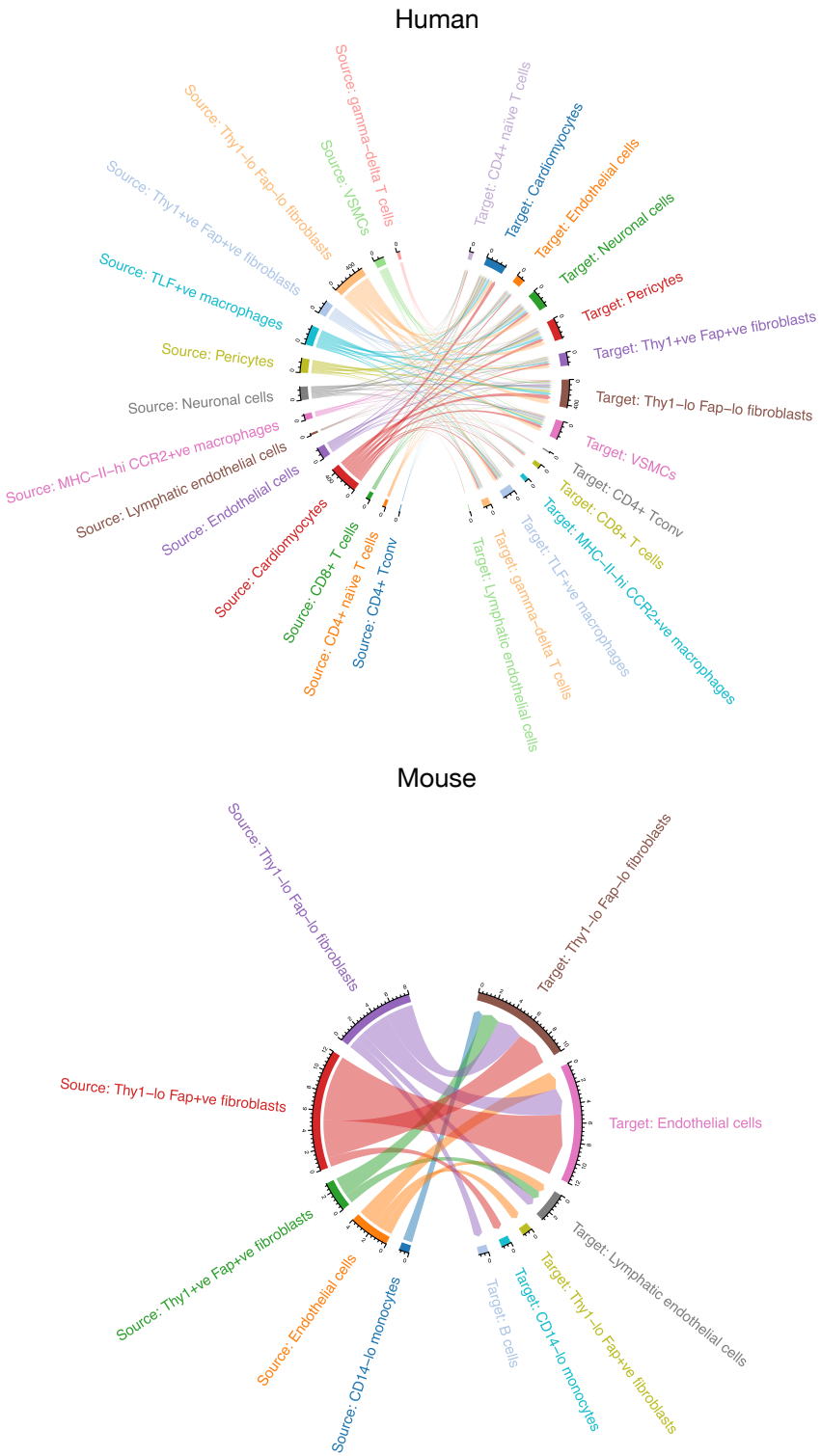

Figure 6.8. Overview of cell-cell communication in mid-stage human and early-stage mouse HCM.
This circos plot depicts cell-cell communication, with ligand-secreting source cells (left) and receptor-expressing target cells (right). Ribbon width indicates interaction strength; wider ribbons represent more interactions. Human interactions are shown in the upper half, and mouse interactions in the lower half.

6.3 Integrating bulk trends with single-cell insights reveals early HCM changes

Having explored the cross-species comparison between mid-stage human and early-stage Actc1^{E99K} mouse hearts, we now turn to an integrative analysis leveraging the temporal dynamics observed in the bulk RNA-seq data (Chapter 3). This section aims to identify the cellular origins of gene expression programs active in the early, pre-fibrotic stage of the Actc1^{E99K} mouse model. The analysis is restricted to the mouse data due to the limited number of healthy controls in the human dataset. The goal is to pinpoint cell types and pathways that could serve as targets for early intervention. A detailed breakdown of the scores for all sub-clusters is available in Appendix F, Figures F.1–F.23.

6.3.1 Cellular origins of early-active and biphasic gene clusters

Cluster 7, defined by early up-regulation followed by a decline, is enriched for ECM-receptor interaction genes. Intriguingly, this signature was significantly down-regulated in *Thy1*^{lo}*Fap*$^{+}$ and *Thy1*$^{+}$*Fap*$^{+}$ fibroblasts in the early-stage mouse heart (Figure F.1). This finding is a key insight of this chapter, suggesting that a paradoxical suppression of ECM interaction pathways in specific fibroblast populations precedes the development of overt fibrosis. This may represent an early, perhaps maladaptive, cellular response to the underlying mutation.
The U-shaped clusters, 11 and 12, which are active in both early and late disease, showed more subtle changes at this early timepoint. The overall signature of Cluster 11 (stress response) was downregulated in endothelial cells and *Thy1*$^{+}$*Fap*$^{+}$ fibroblasts, perhaps indicating an initial failure to mount an effective stress response (Figure F.12). In contrast, Cluster 12 (cell cycle) showed no significant changes in any non-cardiomyocyte population, suggesting that cell cycle re-entry is not a feature of these cell types at this early stage of disease in the Actc1^{E99K} model (Figure F.23).

In summary, this integrative analysis pinpoints a key, counter-intuitive event in early HCM pathogenesis: the down-regulation of ECM-receptor signalling in fibroblasts. This occurs before significant fibrosis is established and may be a critical initiating event in the journey towards adverse remodelling.

6.4 Discussion: Early HCM mechanisms and emerging intervention targets

This chapter sought to identify the earliest molecular events in non-cardiomyocytes that precede adverse remodelling in HCM. By integrating temporal bulk transcriptomics with single-cell data from the pre-fibrotic Actc1^{E99K} mouse, this analysis provides a unique window into the initiation of disease. The central finding is a paradoxical and transient suppression of ECM-receptor interaction pathways in specific fibroblast populations, an event that occurs before the establishment of significant fibrosis. This counter-intuitive discovery challenges the conventional model of fibroblast activation and suggests a more complex, potentially biphasic, role for fibroblasts in HCM pathogenesis.

Previous studies on early HCM have largely focused on cardiomyocyte-intrinsic defects in calcium handling and energetics, with fibrosis considered a secondary reaction [18]. My work provides a novel, non-myocyte-centric view. The finding that *Thy1*^{lo}*Fap*$^{+}$ and *Thy1*$^{+}$*Fap*$^{+}$ fibroblasts down-regulate genes associated with ECM interaction (Cluster 7) at an early stage is a key insight. It suggests that the initial response of these cells to myocyte stress is not immediate activation, but rather a suppression of their connection to the matrix. This may represent a maladaptive response that destabilises the myocardial environment, creating a permissive state for the subsequent development of fibrosis. This finding reframes our understanding of the fibroblast's role from a simple reactor to an early, dynamic participant in disease initiation.

The analysis also highlights the limitations of comparing different disease stages across species. The mid-stage human samples displayed a far more active and complex transcriptional and communication network than the early-stage mouse

model. This divergence, particularly in immune signalling pathways like JAK-STAT, suggests that while the fundamental disease trigger is genetic, the ensuing inflammatory and remodelling responses may follow different trajectories and timelines in mice and humans. This underscores the importance of using caution when extrapolating findings from early-stage animal models to established human disease.

The insights from this chapter point towards specific and tangible avenues for future research aimed at early diagnosis and intervention. First, the functional consequences of the paradoxical fibroblast signature must be validated. This requires isolating fibroblast subpopulations from early-stage Actc1^{E99K} mouse hearts and assessing their adhesive, migratory, and matrix-depositing properties *in vitro*. Confirming a functional deficit would solidify this as a key initiating event. Second, the upstream mechanisms driving this suppression need to be identified. Performing Assay for Transposase-Accessible Chromatin with high-throughput sequencing (ATAC-seq) on sorted fibroblast populations from early-stage hearts could reveal changes in chromatin accessibility and identify the transcription factors responsible for shutting down the ECM-receptor program. These factors would represent prime targets for therapies aimed at preventing fibrosis before it starts. Finally, the down-regulated genes in the Cluster 7 signature, especially those encoding secreted or cell-surface proteins, are strong candidates for novel, early-stage biomarkers. Developing sensitive assays to detect these proteins or their transcripts in patient plasma could facilitate the diagnosis of HCM at a pre-clinical stage, before the development of irreversible structural changes, opening a critical window for preventative treatment.

7

Conclusion and discussion

7.1 Connecting the threads: Unravelling temporal and cellular dynamics in HCM

This integrated project, encompassing bulk and single-cell transcriptomics across different stages of HCM in both human and mouse models, reveals a complex interplay of conserved and divergent molecular mechanisms. One of the most striking observations is the dynamic regulation of interferon responses throughout HCM progression. In both mid- and late-stage human HCM, interferon responses are elevated in most non-cardiomyocytes, suggesting a sustained innate immune activation. This is mirrored in the Actc1^{E99K} mouse model, where interferon responses are initially elevated only in VSMCs at the early stage but become widespread across most cell types in the late stage. This temporal pattern, coupled with the observation of increased JAK-STAT pathway activity, which is downstream of interferon signalling, further supports the notion of progressive immune activation in HCM. The fact that cardiomyocytes do not exhibit early interferon response activation suggests that non-cardiomyocytes, particularly VSMCs, may be the initial responders to cellular stress signals emanating from mutant cardiomyocytes. This raises the intriguing possibility that VSMCs play a crucial role in initiating and propagating the inflammatory response in HCM.

One hypothesis posits that mutant cardiomyocytes may undergo a significant stress response, which includes the up-regulation of canonical cell cycle inhibitors such as *p21*, *p16*, and *p53*. The subsequent release of damage-associated molecular patterns (for example mitochondrial DNA) from these stressed cells could then offer a mechanistic link to non-cardiomyocyte interferon activation. In this scenario, cytosolic mitochondrial DNA would engage the cGAS–STING axis in neighbouring stromal and immune cells, generating cyclic GMP-AMP (cGAMP) and driving downstream interferon responses. While this state shares features with classical senescence, cardiomyocytes are terminally differentiated; whether they truly undergo a full senescence-associated secretory phenotype (SASP) or instead enact a distinct "senescence-like" stress programme remains to be determined. Nevertheless, targeting either mitochondrial DNA release or cGAS–STING signalling could represent a viable therapeutic axis [448, 449].

Given the sustained activation of the JAK-STAT pathway in my late-stage analyses, repurposing clinically approved JAK inhibitors emerges as an attractive therapeutic avenue. Small-molecule agents such as tofacitinib (JAK1/3) [450], ruxolitinib (JAK1/2) [451, 452] and baricitinib (JAK1/2) [453, 454] are already licensed for inflammatory diseases—including ulcerative colitis, rheumatoid arthritis and myelofibrosis—and have well-characterised safety profiles. By attenuating cytokine-driven JAK-STAT signalling, these inhibitors reduce immune cell infiltration and fibrogenic gene expression in preclinical cardiac injury models [455, 456]. Indeed, in murine pressure-overload settings, JAK inhibition mitigated adverse remodelling, decreased interstitial fibrosis and preserved left ventricular function [457–459]. Deploying JAK inhibitors in HCM could therefore blunt the late-stage inflammatory cascade—particularly the interferon- and cytokine-mediated feed-forward loops—and slow progression to irreversible fibrosis. Given their clinical availability, safety record, and mechanistic alignment with our pathway findings, these agents merit rapid translational evaluation in HCM.

7.2 Human and the Actc1^{E99K} mouse model of HCM: Immune parallels and metabolic contrasts

The Actc1^{E99K} mouse model recapitulates several key features of human HCM, including the progressive up-regulation of immune activation and inflammation pathways. This shared feature strengthens the model's validity for studying these aspects of HCM pathogenesis and testing potential therapeutic interventions targeting inflammation. However, the model also exhibits some notable differences from human HCM, particularly in the regulation of metabolic pathways. The widespread down-regulation of metabolic pathways observed in late-stage human HCM is not consistently recapitulated in the mouse model. This discrepancy highlights the limitations of cross-species comparisons and underscores the need for caution when extrapolating findings from the mouse model to human disease. Further research is needed to determine the underlying reasons for these metabolic differences and to identify more human-specific models for studying metabolic dysregulation in HCM.

7.3 Harnessing therapeutic windows in HCM

For late-stage HCM, targeting the conserved up-regulation of immune activation, inflammation, and EMT represents a promising therapeutic strategy. Inhibiting inflammatory signalling pathways, such as the complement cascade or interferon response, could attenuate the inflammatory response and improve cardiac function. Similarly, targeting EMT, perhaps by inhibiting TGF-β signalling, could reduce fibrosis and improve myocardial compliance. For early-stage HCM, the down-regulation of ECM-receptor interaction genes in fibroblasts emerges as a potential diagnostic marker and therapeutic target. Monitoring the expression of these genes could enable early detection of HCM before the onset of significant fibrosis, allowing for timely intervention. Targeting this pathway, perhaps through receptor agonists or antagonists, could also represent a novel therapeutic

strategy to prevent or delay fibrosis development. The up-regulation of digestive system development genes in neutrophils, while requiring further investigation, also warrants exploration as a potential early diagnostic or therapeutic target.

7.4 Evolving phases in HCM: Recognising the shift from silence to inflammation

The early stage of HCM is characterised by a relatively quiescent immune response, with limited interferon response activation and subtle changes in pathway activity. This contrasts sharply with the late stage, which is dominated by widespread immune activation, inflammation, and fibrosis. This transition from quiescence to overt activation highlights the dynamic nature of HCM progression and underscores the importance of stage-specific therapeutic strategies. Early interventions may focus on preventing or delaying the activation of inflammatory and fibrotic pathways, while late-stage interventions may need to address the established inflammatory and fibrotic environment.

7.5 Innovative therapeutic strategies and future perspectives in HCM

The findings from this study have significant implications for the development of novel therapeutic strategies for HCM. The identification of conserved pathways and molecules involved in both human and mouse HCM provides promising targets for therapeutic intervention. Specifically, targeting the cGAS-STING pathway, mitigating mitochondrial DNA release from senescent cardiomyocytes, inhibiting inflammatory signalling pathways like the complement cascade or interferon response, and modulating EMT represent potential therapeutic avenues for late-stage HCM. For early-stage disease, targeting ECM-receptor interactions in fibroblasts and exploring the role of neutrophils in digestive system development could offer novel preventative or disease-modifying strategies.

However, the observed interspecies differences highlight the need for careful consideration of species-specific effects when translating preclinical findings to human trials. The divergent regulation of metabolic pathways, growth factor signalling, and cellular stress responses underscores the importance of validating preclinical findings in human samples and developing therapeutic agents that selectively target the relevant cell types in human disease. Furthermore, the dynamic nature of HCM progression necessitates stage-specific therapeutic approaches. Early interventions may focus on preventing or delaying the activation of inflammatory and fibrotic pathways, while late-stage interventions may need to address the established inflammatory and fibrotic environment.

Several key areas warrant further investigation to advance our understanding and treatment of HCM. Validating the functional consequences of the identified pathway and molecular alterations in human HCM is crucial. This includes conducting mechanistic studies to confirm the role of these pathways in disease pathogenesis and exploring the therapeutic potential of modulating their activity. Developing and testing targeted therapies that specifically modulate these pathways and molecules is another critical step. This requires the development of novel therapeutic agents, such as small molecules, antibodies, or gene therapies, that selectively target the identified pathways in the relevant cell types. Identifying biomarkers that can predict response to therapy and monitor disease progression is also essential for personalising treatment strategies and optimising patient outcomes. This involves identifying molecular signatures that correlate with disease severity, progression, and response to therapy.

Exploring the interplay between different cell types and their contributions to adverse remodelling could reveal novel therapeutic targets and strategies for modulating the myocardial microenvironment. This includes investigating the role of cell-cell communication, paracrine signalling, and ECM interactions in HCM pathogenesis. Integrating multi-omics data, such as proteomics and metabolomics, with transcriptomic data could provide a more comprehensive understanding of the molecular mechanisms driving HCM and identify novel therapeutic targets.

By pursuing these lines of investigation, we can gain deeper insights into the complex pathobiology of HCM and develop more effective therapeutic strategies to improve outcomes for patients with this disease.

7.6 Concluding reflections on HCM research

This integrative analysis has provided valuable insights into the complex molecular mechanisms driving HCM. By comparing human and mouse models, this study has identified several conserved pathways and molecules that represent promising therapeutic targets. Specifically, targeting the cGAS-STING pathway, modulating interferon responses, and inhibiting EMT are potential therapeutic strategies for late-stage HCM. For early-stage disease, targeting ECM-receptor interactions and exploring the role of neutrophils in digestive system development warrant further investigation. However, the observed interspecies differences underscore the need for careful consideration of species-specific effects when translating preclinical findings to human trials. Further research is crucial to validate these findings in human HCM and develop targeted therapeutic strategies to improve outcomes for patients with this devastating disease.

Appendices

A

Bulk RNA-seq sample details

A.1 Temporal bulk Actc1^{E99K} samples

Table A.1. Temporal bulk Actc1^{E99K} samples.

Sample ID	Sex	Actc1 mutation	Age (week)	Group	Mapping rate (%)	Reads mapped
IL109_R	F	WT	5	5 weeks	81.03%	93547757
LY216_L	F	WT	5	5 weeks	82.81%	102634924
LY220_L	F	WT	5	5 weeks	82.75%	107184595
LY219_LL	M	E99K	5	5 weeks	82.30%	103915331
EF213_L	M	E99K	5	5 weeks	79.90%	87713326
LY220_LR	F	WT	5	5 weeks	81.65%	60001536
LY215_LR	M	WT	5	5 weeks	81.41%	58030288
LY215_L	M	E99K	5	5 weeks	81.59%	78190573
LY216_R	F	E99K	5	5 weeks	78.65%	66109901
LY217_RRL	F	E99K	5	5 weeks	79.42%	81201189
EF211_R	M	WT	6	5 weeks	80.06%	75260899
EF211_L	M	WT	6	5 weeks	86.06%	98318106
IL112_LR	M	E99K	6	5 weeks	78.07%	79035328
ER160_LR	F	E99K	8	10 weeks	96.48%	208280006
ER161_L	M	E99K	8	10 weeks	97.22%	169917331
ER160_L	F	WT	8	10 weeks	97.68%	160431240
ER161_R	M	WT	8	10 weeks	97.80%	168136528
LY100_R	F	E99K	8	10 weeks	96.96%	161753089
ER160_R	F	E99K	8	10 weeks	96.96%	188912792
ER161_LR	M	WT	8	10 weeks	97.71%	167390281
LY100_LL	F	E99K	8	10 weeks	97.05%	173733587
EF18_R	F	WT	10	10 weeks	97.63%	169241486
EF18_L	F	E99K	10	10 weeks	96.89%	210274396
EF139_LL	F	WT	11	10 weeks	97.48%	106781380
EF12_LLR	M	E99K	12	10 weeks	96.88%	158969866
EF14_L	M	E99K	12	10 weeks	96.89%	164670389
EF120_R	M	WT	12	10 weeks	97.60%	109408690
EF138_L	M	WT	13	10 weeks	97.95%	88830342
EF139_LR	F	WT	13	10 weeks	97.66%	94248992

Continued on next page

Sample ID	Sex	Actc1 mutation	Age (week)	Group	Mapping rate (%)	Reads mapped
EF138_LR	M	WT	13	10 weeks	97.70%	95499831
LY208_L	M	E99K	21	24 weeks	85.12%	98349509
IL103_LL	M	E99K	22	24 weeks	83.23%	83992149
LK63_RRL	M	E99K	22	24 weeks	82.11%	71537141
IL103_LR	M	E99K	23	24 weeks	83.86%	71795839
EF131_R	M	E99K	23	24 weeks	97.05%	88886665
ELMP179_L	F	E99K	24	24 weeks	97.03%	139474027
M00680706	M	WT	24	24 weeks	97.36%	190079553
ER124_LL	M	WT	25	24 weeks	97.40%	163975882
ELMP177_RR	F	E99K	25	24 weeks	96.55%	136960125
ELMP177_LR	F	E99K	25	24 weeks	96.89%	160431048
IL22_R	M	WT	25	24 weeks	97.87%	97210201
EF208_RRL	F	WT	26	24 weeks	82.43%	98024328
IL29_LR	F	E99K	26	24 weeks	96.45%	74193120
EF98_L	F	E99K	27	24 weeks	97.04%	80036330
EF98_RRL	F	E99K	27	24 weeks	96.97%	83981525
ELMP168_LR	F	E99K	28	24 weeks	96.56%	136286441
ELMP168_L	F	WT	28	24 weeks	97.30%	149624879
ELMP168_R	F	WT	28	24 weeks	97.67%	186874722
ER217_L	F	WT	28	24 weeks	85.34%	74275641
EF200_LL	F	WT	29	24 weeks	85.24%	88944635
EF103_L	M	E99K	48	60 weeks	96.74%	94120549
EF103_RR	M	E99K	49	60 weeks	96.60%	91400301
EF103_LR	M	WT	49	60 weeks	97.77%	78864760
IL24_L	M	E99K	51	60 weeks	96.52%	83674453
LY124_LLR	M	WT	52	60 weeks	97.76%	113637796
ER178_RR	F	E99K	53	60 weeks	95.85%	139857968
LY112_LR	F	E99K	54	60 weeks	96.34%	118409191
LY108_LR	F	E99K	56	60 weeks	96.35%	137142573
IL5_LL	M	E99K	56	60 weeks	97.02%	96665148
EF61_R	F	WT	56	60 weeks	97.43%	80181632
EF61_L	F	WT	56	60 weeks	96.98%	92300304
EF33_LR	M	WT	58	60 weeks	96.68%	104244582
EF33_RR	M	E99K	58	60 weeks	96.34%	149903530
EF30_R	F	WT	61	60 weeks	97.15%	135223003
EF30_L	F	WT	61	60 weeks	96.96%	159711020
EF30_LR	F	WT	61	60 weeks	97.14%	128633081

A.2 Bulk RNA-seq samples from other mouse models

Table A.2. α-MHC^{R403Q} and α-MHC^{R719W} mouse samples [140].

Sample ID	Age (weeks)	Group	Mapping Rate (%)	Reads mapped
4422_A	62	WT	81.67	54289870
4422_B	missing	WT	81.86	53486024
4423_A	76	WT	80.84	40162455
4423_B	missing	WT	80.30	54033590
4426_A	62	WT	79.16	42833390
4427_A	62	WT	81.70	48214955
4445_A	57	WT	79.71	49545811
4445_B	missing	WT	79.08	46134635
4932_RN	38	WT	82.64	49741477

Continued on next page

Sample ID	Age (weeks)	Group	Mapping Rate (%)	Reads mapped
4937_NA	48	α-MHC^{R403Q}	83.17	72616637
4937_NB	missing	α-MHC^{R403Q}	84.66	64732105
4939_NA	48	α-MHC^{R403Q}	84.03	85992399
4939_NB	missing	α-MHC^{R403Q}	83.80	66616288
4942_NA	46	α-MHC^{R403Q}	89.67	89402354
4942_NB	missing	α-MHC^{R403Q}	83.29	83842554
4944_NA	46	α-MHC^{R403Q}	85.12	71103055
4944_NB	missing	α-MHC^{R403Q}	83.31	75848285
6908	35	α-MHC^{R719W}	85.78	35084469
6910	35	α-MHC^{R719W}	85.90	30659873
6913	35	α-MHC^{R719W}	85.84	33130490
72	36	α-MHC^{R719W}	86.20	29917268
73	36	α-MHC^{R719W}	86.13	38997886

Table A.3. Tnt^{R92W} sample information [278].

SRA Run ID	Age (weeks)	BioProject	Group	Sex	Mapping Rate (%)	Reads mapp
SRR9937849	24	PRJNA559482	Littermate control	Male	97.65	27047387
SRR9937850	24	PRJNA559482	Littermate control	Male	97.95	26636586
SRR9937853	24	PRJNA559482	Tnt^{R92W} mutant	Male	97.20	22852822
SRR9937854	24	PRJNA559482	Tnt^{R92W} mutant	Male	96.67	21065439
SRR9937855	24	PRJNA559482	Littermate control	Male	98.01	27647843
SRR9937856	24	PRJNA559482	Tnt^{R92W} mutant	Male	97.29	24834308

A.3 Bulk RNA-seq samples from HCM human patients

Table A.4. HCM human bulk RNA-seq sample information [279].

SRA Run ID	Age (years)	BioProject	Group	Sex	Mapping Rate (%)	Reads mapped
SRR8586402	29	PRJNA522931	Control	Female	97.73	112591273
SRR8586403	39	PRJNA522931	Control	Male	97.83	117032579
SRR8586404	36	PRJNA522931	Control	Male	97.53	129867717
SRR8586405	46	PRJNA522931	Control	Male	97.71	122200710
SRR8586406	35	PRJNA522931	Control	Male	97.75	148350402
SRR8586407	47	PRJNA522931	Control	Male	97.68	113290811
SRR8586408	37	PRJNA522931	Control	Male	97.86	108653709
SRR8586409	21	PRJNA522931	HCM	Male	97.65	123415153
SRR8586410	25	PRJNA522931	HCM	Male	97.76	123778640
SRR8586411	39	PRJNA522931	HCM	Male	97.01	114583012
SRR8586412	36	PRJNA522931	HCM	Female	97.31	99261318
SRR8586413	43	PRJNA522931	HCM	Male	97.19	80980482
SRR8586414	47	PRJNA522931	HCM	Female	97.14	112649790
SRR8586415	30	PRJNA522931	HCM	Male	97.15	111148489
SRR8586416	36	PRJNA522931	HCM	Female	97.10	104215348
SRR8586417	47	PRJNA522931	HCM	Male	97.14	110546578
SRR8586418	31	PRJNA522931	HCM	Female	97.12	119593985
SRR8586419	32	PRJNA522931	HCM	Male	97.27	114052967
SRR8586420	31	PRJNA522931	HCM	Female	97.20	93954091
SRR8586421	38	PRJNA522931	HCM	Male	97.83	115796383

Continued on next page

SRA Run ID	Age (years)	BioProject	Group	Sex	Mapping Rate (%)	Reads mapped
SRR8586422	40	PRJNA522931	HCM	Male	97.02	131554402
SRR8586423	30	PRJNA522931	HCM	Male	97.52	97894100
SRR8586424	25	PRJNA522931	HCM	Male	97.35	101802411
SRR8586425	20	PRJNA522931	HCM	Male	96.80	98217053
SRR8586426	48	PRJNA522931	HCM	Male	97.62	132163206
SRR8586427	42	PRJNA522931	HCM	Male	97.30	114031272
SRR8586428	32	PRJNA522931	HCM	Male	96.98	101089321
SRR8586429	30	PRJNA522931	Control	Male	95.62	106273888
SRR8586430	40	PRJNA522931	Control	Male	97.59	143138192
SRR8586431	19	PRJNA522931	HCM	Male	97.29	101633410
SRR8586432	36	PRJNA522931	HCM	Female	97.64	116363770
SRR8586433	41	PRJNA522931	HCM	Female	97.11	106023021
SRR8586434	30	PRJNA522931	HCM	Female	97.12	119664784
SRR8586435	28	PRJNA522931	HCM	Male	97.29	120823225
SRR8586436	37	PRJNA522931	HCM	Male	97.61	129211444
SRR8586437	24	PRJNA522931	HCM	Male	97.71	93281337
SRR8586438	28	PRJNA522931	HCM	Female	97.03	100314630

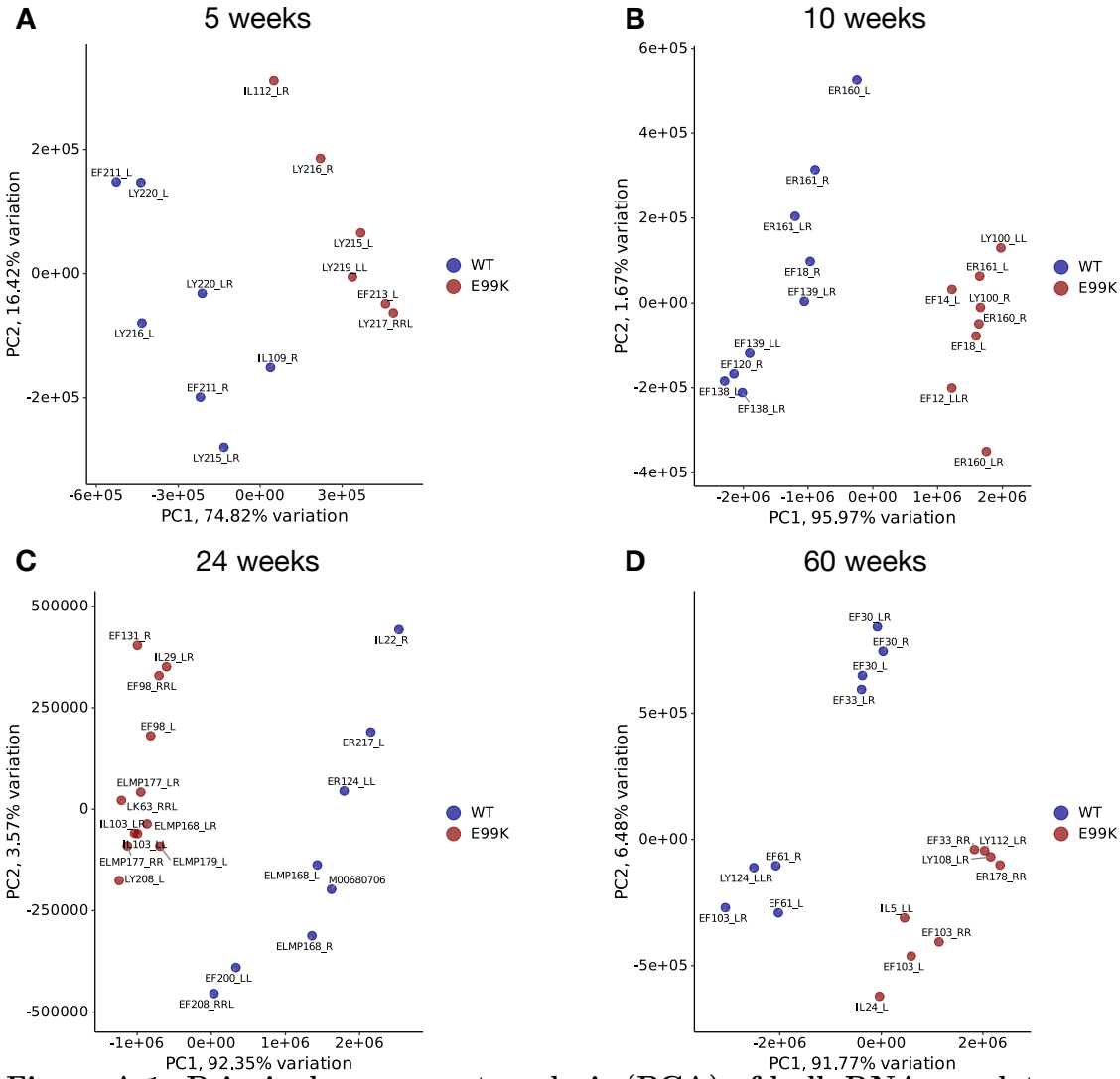

Figure A.1. Principal component analysis (PCA) of bulk RNA-seq data from Actc1^{E99K} HCM mice.
PCA plots are shown for 5 weeks (A), 10 weeks (B), 24 weeks (C), and 60 weeks (D). Blue and red dots represent wild-type and Actc1^{E99K} HCM mice, respectively.

B

Expression of marker genes in mouse scRNA-seq samples

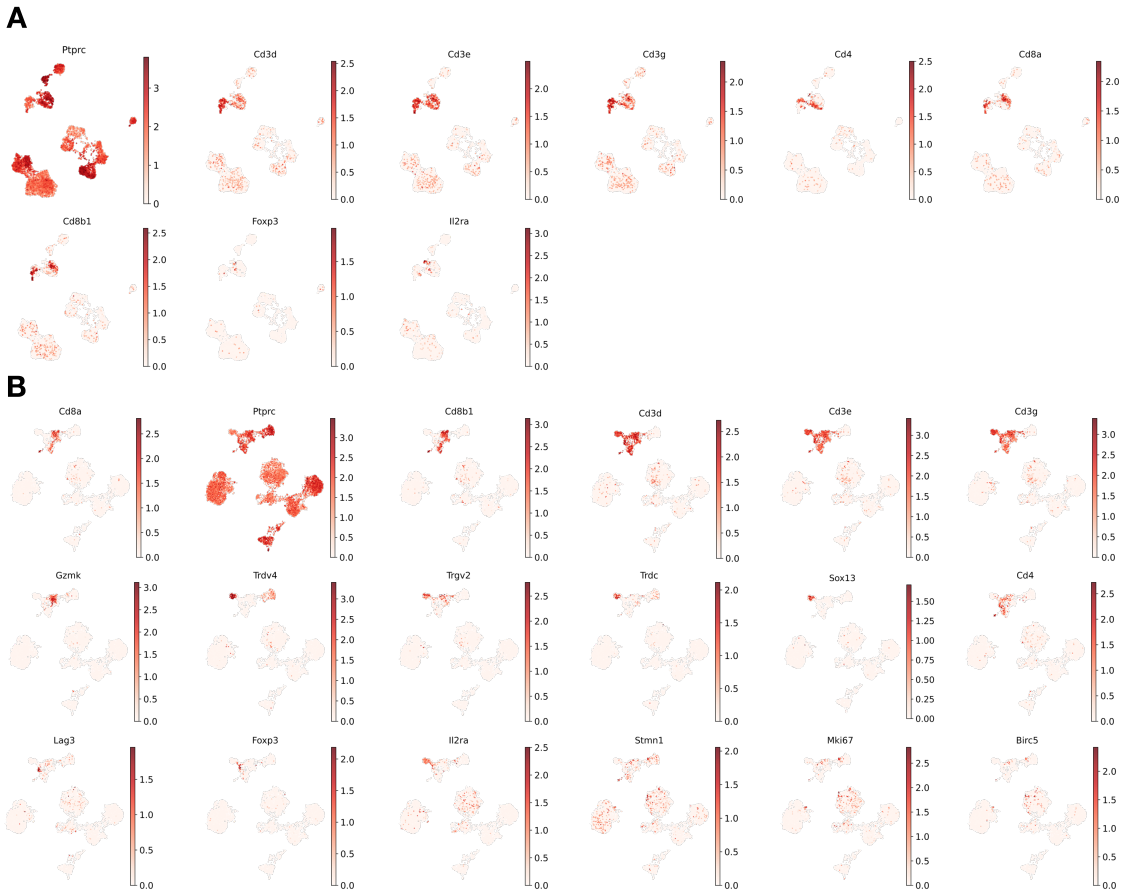

Figure B.1. UMAP projections showing the expression of individual T cell marker genes within the CD45$^+$ cell population. These visualisations complement the summary dotplot in Figure 4.2 by showing the spatial distribution of expression for each marker gene on the UMAP. The data are integrated from both WT and Actc1^{E99K} mice (N=3 per genotype) at (A) the early stage (5 weeks) and (B) the late stage (60 weeks). In each plot, cells are coloured according to their log-normalised expression level for the specified gene, with the scale shown by the colour bar.

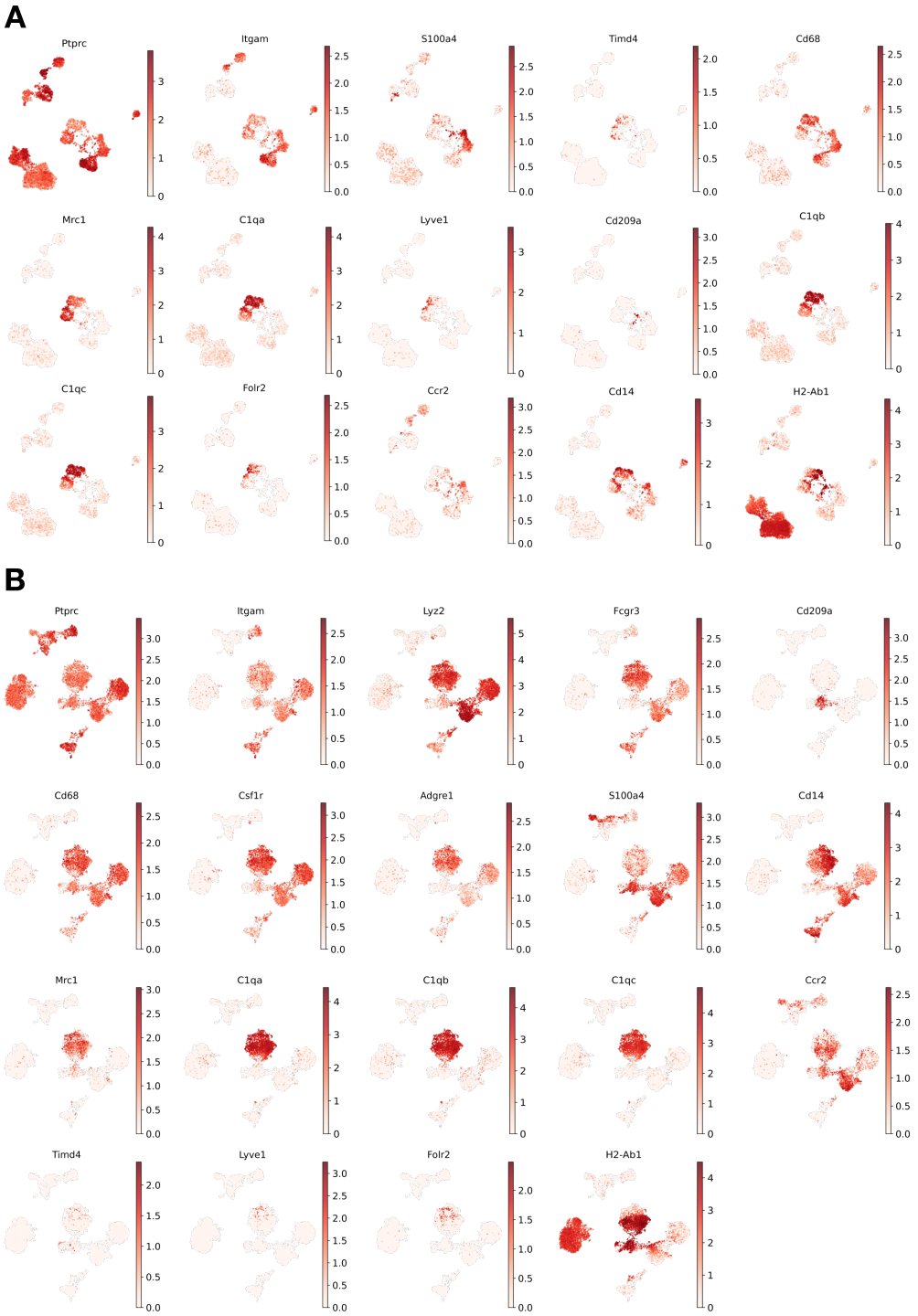

Figure B.2. UMAP projections showing the expression of individual myeloid cell marker genes within the CD45$^+$ cell population. These visualisations complement the summary dotplot in Figure 4.3 by showing the spatial distribution of expression for each marker gene on the UMAP. The data are integrated from both WT and Actc1^{E99K} mice (N=3 per genotype) at (A) the early stage (5 weeks) and (B) the late stage (60 weeks). In each plot, cells are coloured according to their log-normalised expression level for the specified gene, with the scale shown by the colour bar.

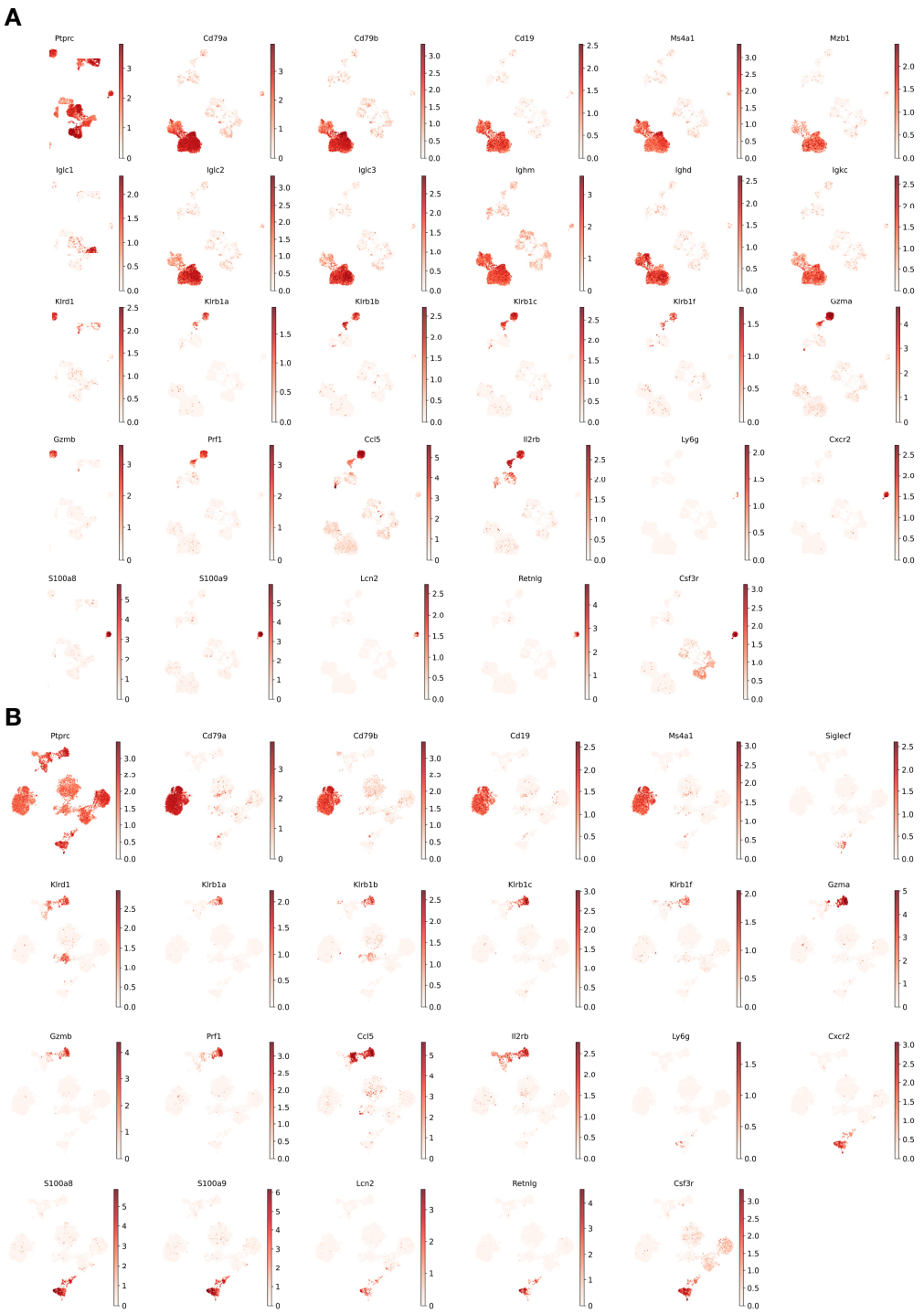

Figure B.3. UMAP projections showing the expression of other immune cell marker genes within the CD45$^+$ cell population. These visualisations complement the summary dotplot in Figure 4.4 by showing the spatial distribution of expression for each marker gene on the UMAP. The data are integrated from both WT and Actc1^{E99K} mice (N=3 per genotype) at (A) the early stage (5 weeks) and (B) the late stage (60 weeks). In each plot, cells are coloured according to their log-normalised expression level for the specified gene, with the scale shown by the colour bar.

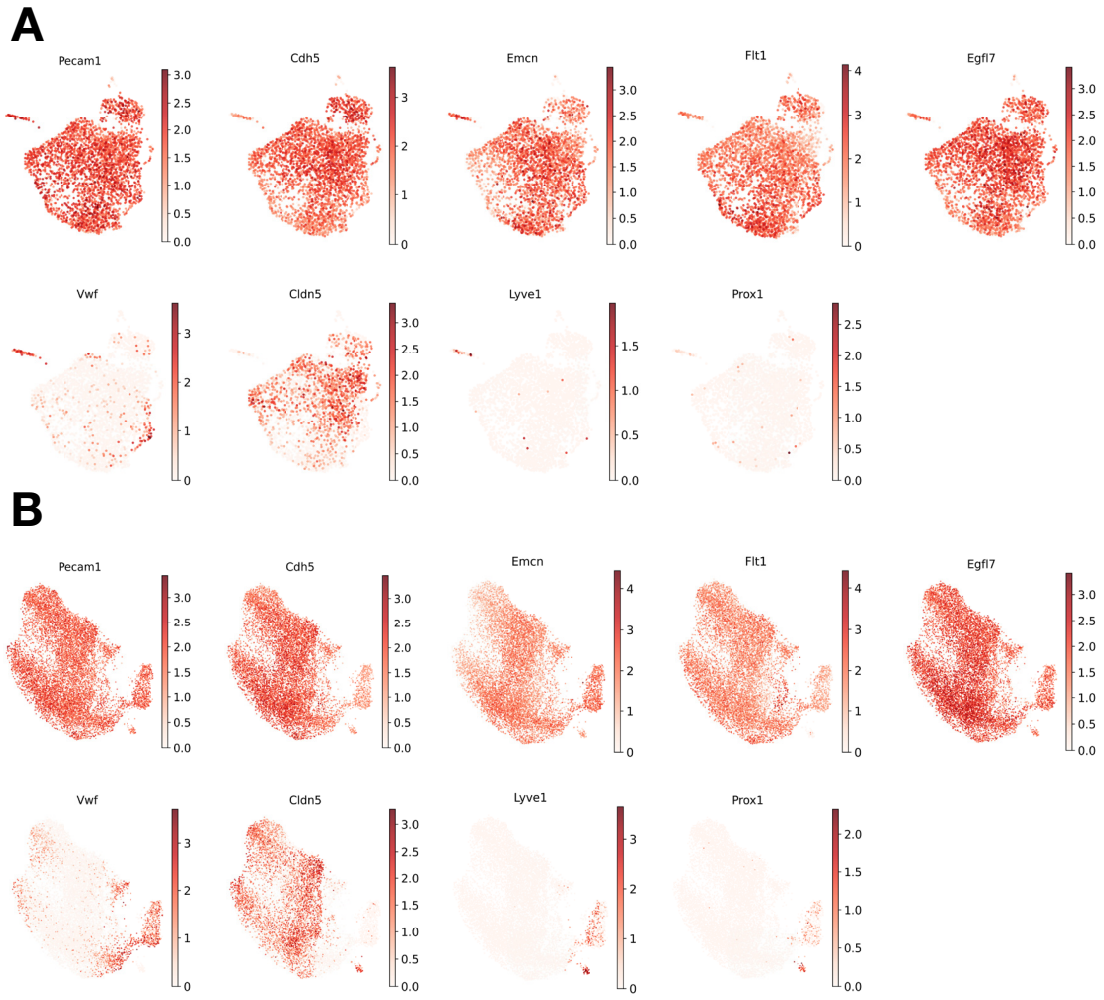

Figure B.4. UMAP projections showing the expression of individual endothelial cell marker genes within the CD31$^+$ cell population. These visualisations complement the summary dotplot in Figure 4.6 by showing the spatial distribution of expression for each marker gene on the UMAP. The data are integrated from both WT and Actc1^{E99K} mice (N=3 per genotype) at (A) the early stage (5 weeks) and (B) the late stage (60 weeks). In each plot, cells are coloured according to their log-normalised expression level for the specified gene, with the scale shown by the colour bar.

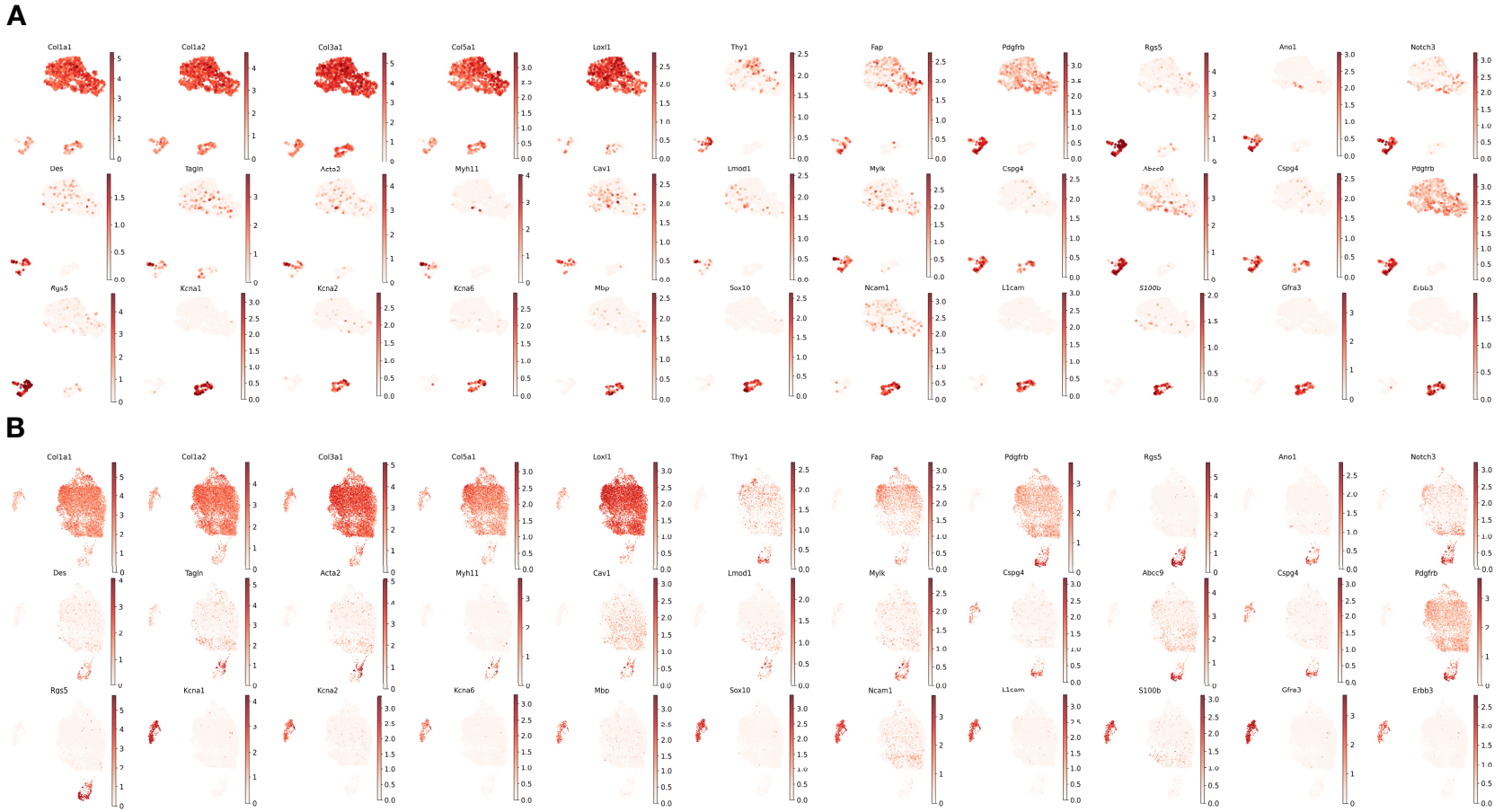

Figure B.5. UMAP projections showing the expression of individual stromal cell marker genes within the CD45$^-$CD31$^-$ cell population. These visualisations complement the summary dotplot in Figure 4.8 by showing the spatial distribution of expression for each marker gene on the UMAP. The data are integrated from both WT and Actc1^{E99K} mice (N=3 per genotype) at (A) the early stage (5 weeks) and (B) the late stage (60 weeks). In each plot, cells are coloured according to their log-normalised expression level for the specified gene, with the scale shown by the colour bar.

C

Intercellular communication insights reveal crucial crosstalk that drives adverse remodelling

C.1 T cell communication illuminates adaptive immune dynamics in the diseased heart

Given the cross-species nature of this study, subsequent analyses focused on T cells (Figure C.1), key mediators of adaptive immunity and present in both datasets. Within the $CD4^+$ Tconv cell population in late-stage human HCM, the analysis revealed complex alterations in signalling pathways. TG-TPO interaction was significantly downregulated between $CD4^+$ Tconv cells and both endothelial and endocardial cells. Similarly, A2M-LRP1 interaction decreased between $CD4^+$ Tconv cells and macrophages, proliferating macrophages, and fibroblasts. Conversely, ST6GAL1-EGFR interaction was upregulated between $CD4^+$ Tconv cells and VSMCs, endocardial cells, and pericytes. PAM-FAP interaction also increased between $CD4^+$ Tconv cells and fibroblasts. In contrast, the $CD4^+$ Tconv cell communication profile in the mouse model was less complex. The most prominent change was the upregulation of the Ifng-Ifngr1/2 axis between $CD4^+$ Tconv cells and endothelial cells and $Thy1^+Fap^+$ fibroblasts. Down-

regulation of the Hspa1a-tlr4 interaction was observed between $CD4^+$ Tconv cells and $CD14^{hi}$ monocytes and endothelial cells.

In late-stage human HCM (Figure C.1), $CD8^+$ cytotoxic T cells exhibited marked downregulation of SPON2-ITGA5 interaction with fibroblasts and decreased TG-TPO signalling to endothelial cells. Several SPON2 interactions were also reduced, including SPON2-ITGAM and SPON2-ITGB1/2 with macrophages, and SPON2-ITGA5 with proliferating macrophages and lymphatic endothelial cells. Additionally, PDGFD-PDGFRA/B signalling between $CD8^+$ cytotoxic T cells and fibroblasts was diminished. Conversely, mirroring the pattern observed in $CD4^+$ Tconv cells, ST6GAL1-EGFR interaction increased between $CD8^+$ cytotoxic T cells and VSMCs, endocardial cells, and pericytes. A modest increase in PAM-FAP signalling between $CD8^+$ cytotoxic T cells and fibroblasts was also detected.

In contrast, the mouse model revealed a distinct $CD8^+$ cytotoxic T cell communication profile (Figure C.1). A striking upregulation of Ccl4-Ccr1/5 signalling, predominantly targeting $CD14^{hi}$ monocytes, DCs, and MHC-$II^{hi}Ccr2^+$ macrophages, was observed. Conversely, Lgals1-Ptprc interaction with neutrophils and Hspa1a-tlr4 signalling to $CD14^{hi}$ monocytes and endothelial cells were downregulated. These findings underscore the divergent roles of $CD8^+$ cytotoxic T cells in intercellular communication within the human and mouse late-stage HCM myocardial microenvironment, potentially reflecting differences in the cytotoxic T cell response and its contribution to adverse remodelling.

C.2 Macrophage signalling reveals inflammatory and repair cues shaping remodelling

Following analysis of T cell interactions, the investigation focused on macrophages, key components of the innate immune system and implicated in adverse cardiac remodelling.

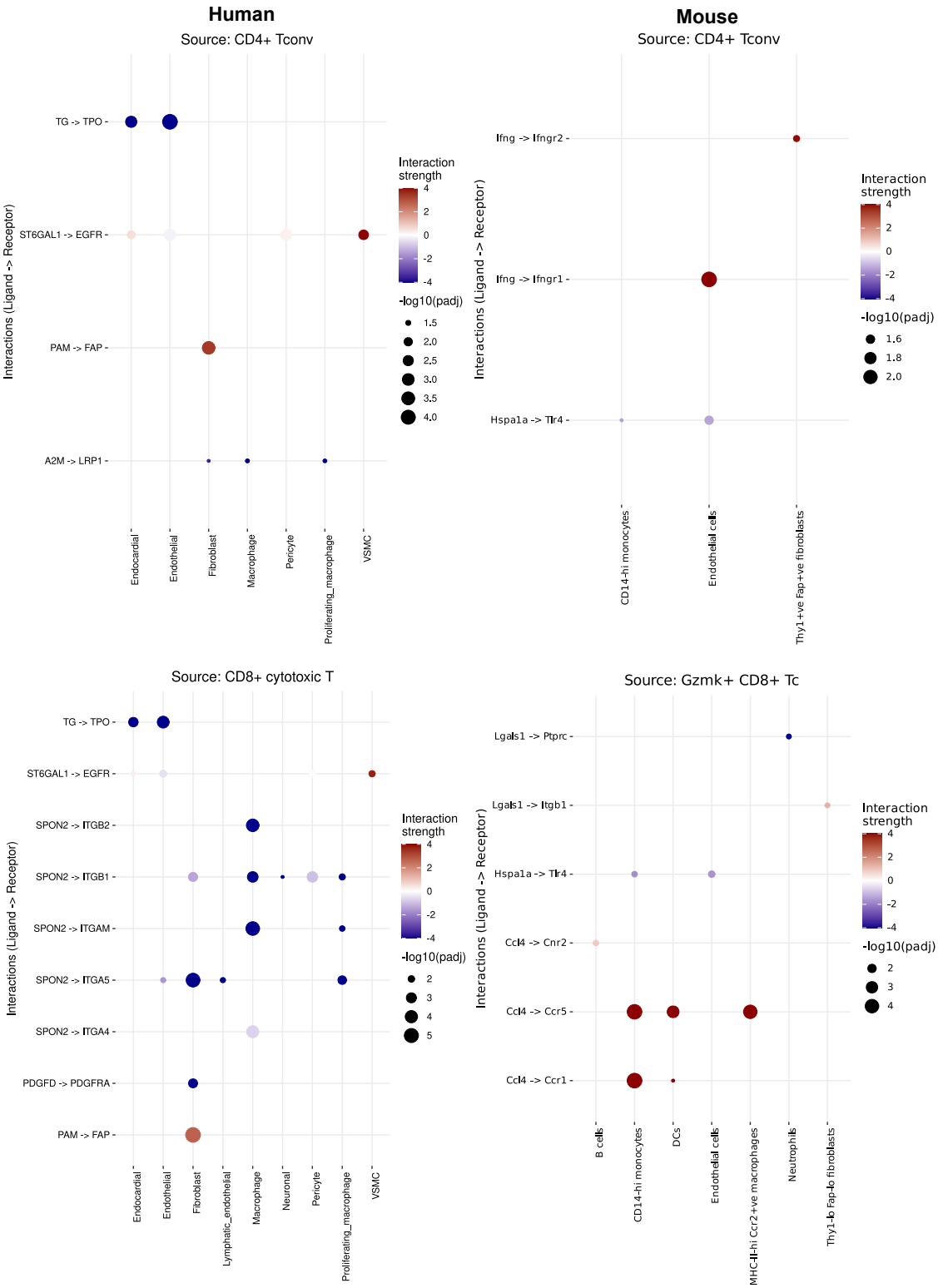

Figure C.1. Cell-cell communication involving T cells in late-stage human and mouse HCM.

Positive interaction strength indicates up-regulation of ligand-receptor genes in HCM or Actc1^{E99K} samples, while negative strength indicates down-regulation. P-values were adjusted using the Benjamini-Hochberg method. Human interactions appear on the left and mouse interactions on the right.

In late-stage human HCM, macrophages exhibited a complex interaction profile (Figure C.2). Downregulation of GAS6-MERTK signalling in macrophage self-interaction suggests diminished efferocytosis or other MERTK-mediated processes [460–463]. Reduced ANXA2-TLR2 interaction in macrophage self-interaction potentially indicates altered inflammatory responses [464]. Conversely, increased GAS6-MERTK signalling between macrophages and proliferating macrophages may reflect a compensatory mechanism for clearing apoptotic cells during proliferation [145]. Increased interaction via GNAS-ADCY1 and GNAS-ADCY9 axes between macrophages and fibroblasts may influence fibroblast activity and ECM remodelling [465, 466]. Furthermore, increased GAS6-MERTK signalling between macrophages and cardiomyocytes possibly indicates a role in cardiomyocyte survival or clearance [467]. Upregulation of several other interactions, including GAS6-AXL with fibroblasts, VSMCs, and pericytes, and CKLF-LRP6 with fibroblasts, endothelial cells, and lymphatic endothelial cells, suggests a broad macrophage influence on the myocardial microenvironment. Downregulation of interactions, such as C1QB-LRP1 with macrophages and proliferating macrophages, and ADAM17-ITGA5 with fibroblasts, indicates a complex interplay of activating and inhibitory signals.

In the mouse model, however, the macrophage communication landscape differed markedly (Figure C.2). MHC-II^{hi}Ccr2^{+} macrophages exhibited prominent upregulation of chemokine signalling, particularly Ccl2-Ccr1/2/5 and Ccl4-Ccr1/5, primarily targeting other myeloid cells, including CD14^{hi} monocytes and DCs. This suggests a strong chemotactic drive, potentially contributing to immune cell recruitment and inflammation in late-stage mouse HCM [468–470]. Downregulation of F13a1-Itga4 interaction with CD14^{hi} monocytes, DCs, neutrophils, and eosinophils potentially indicates altered cell adhesion or migration [471, 472]. TLF^{-}MHC-II^{lo} macrophages displayed a different communication profile, with upregulation of Gdf15-Tgfbr2 signalling to fibroblasts and Lpl-Cd44 interaction with various cell types, including fibroblasts, neutrophils, and neuronal cells. This suggests their potential role in ECM remodelling and tissue repair [473–476].

TLF^+ macrophages exhibited yet another distinct profile, characterised by increased Gdf15-Tgfbr2 signalling to fibroblasts and Ccl4-Ccr1/5 signalling to $CD14^{hi}$ monocytes and DCs, similar to MHC-$II^{hi}Ccr2^+$ macrophages. They also showed downregulation of Lyz2-Itgal interaction with several myeloid cell types, potentially indicating altered phagocytic activity or other Itgal-mediated processes [477, 478].

The observed differences in macrophage communication between the human and mouse models merit further consideration. While both species exhibited altered signalling pathways related to inflammation and ECM remodelling, the specific ligands, receptors, and target cell types often differed. For instance, the prominent Ccl2/4-Ccr1/2/5 chemokine signalling in mouse macrophages was less evident in the human dataset. This discrepancy may reflect species-specific differences in chemokine networks or the involvement of other chemotactic factors in human HCM. Similarly, the downregulation of F13a1-Itga4 interaction in mouse macrophages lacked a human counterpart, suggesting potential divergence in integrin-mediated interactions and cell adhesion between species. Furthermore, the distinct communication profiles of different macrophage subpopulations in the mouse model, such as TLF^+ and TLF^- macrophages, highlight the heterogeneity of macrophage responses in HCM. Whether similar subpopulations exist in human HCM with comparable communication patterns remains to be determined [479, 480].

C.3 Endothelial and lymphatic cell interactions underpin vascular remodelling and immune recruitment

Following the analysis of macrophage interactions, the investigation shifted to endothelial and lymphatic endothelial cells, crucial players in maintaining vascular integrity and regulating immune cell trafficking within the myocardium. These cell types are known to be involved in the adverse remodelling processes observed in HCM [481–485].

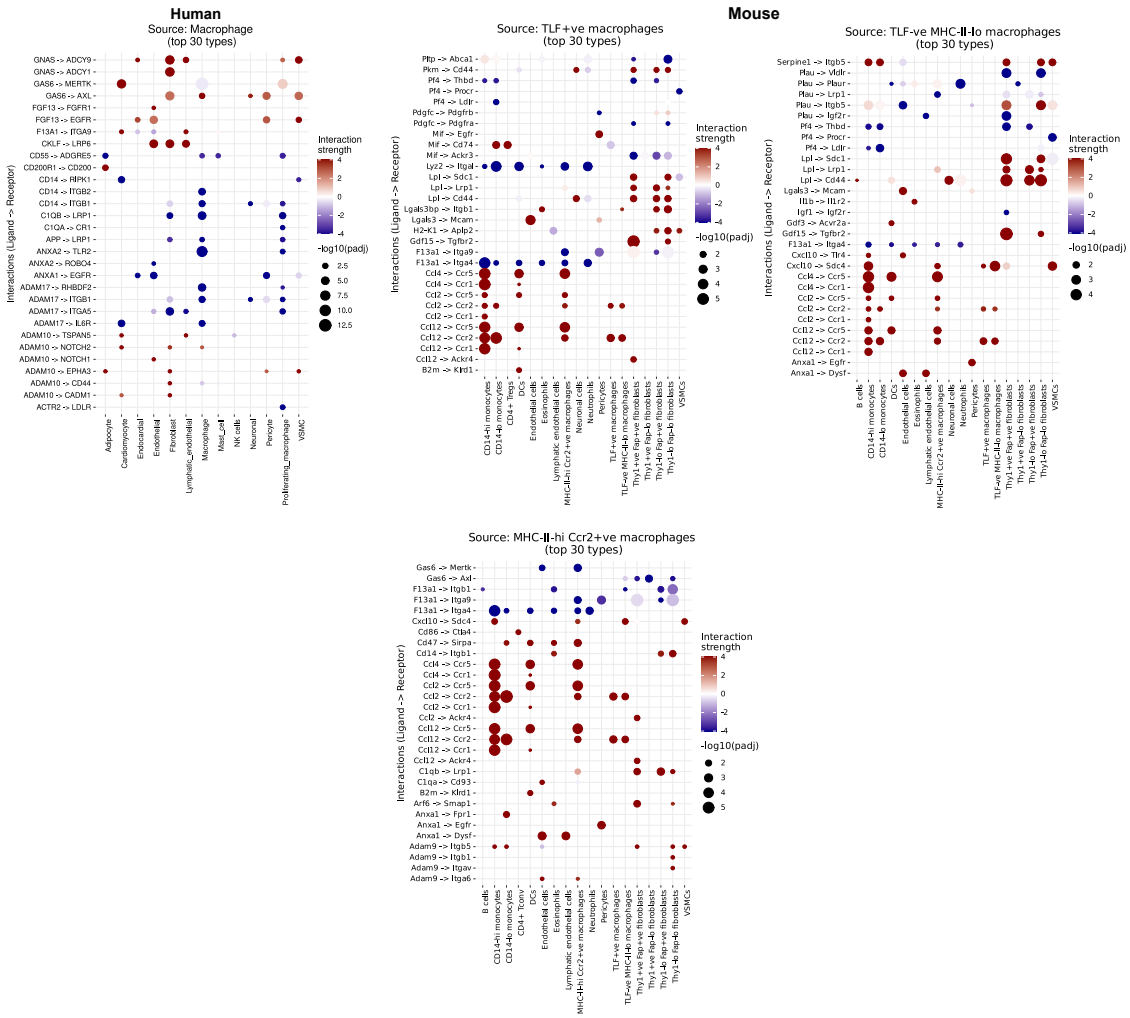

Figure C.2. Cell-cell communication involving macrophages in late-stage human and mouse HCM.
Positive interaction strength indicates up-regulation of ligand-receptor genes in HCM or Actc1^{E99K} samples, while negative strength indicates down-regulation. P-values were adjusted using the Benjamini-Hochberg method. Human interactions appear on the left and mouse interactions on the right.

In late-stage human HCM, endothelial cells displayed a complex pattern of altered interactions (Figure C.3). Increased signalling through CALM1-PDE1A/C axes, targeting cardiomyocytes, pericytes, adipocytes, VSMCs, and fibroblasts, suggests a role for CALM1 in modulating vascular tone and ECM remodelling via its interaction with PDE1 isoforms [486–489]. Elevated EFNB2-EPHA3 signalling between endothelial cells and fibroblasts, adipocytes, and VSMCs further implicates Eph/ephrin signalling in vascular remodelling and angiogenesis [490–492]. Conversely, downregulation of CXCL12-ITGA5 [180], CD59-STAB1,

ANXA2-TLR2 [493–496], F8-LRP1 [497], ADAM10-TSPAN14 [498, 499], and APP-LRP1 interactions [497, 500–502], primarily targeting macrophages and fibroblasts, suggests modulation of inflammatory responses and cell adhesion within the human myocardial microenvironment.

In the mouse model, endothelial cell communication exhibited a distinct profile (Figure C.3). Upregulation of Col15a1-Itga1/Itgb1 and Col18a1-Itga1/Itgb1 interactions, primarily with fibroblasts and eosinophils, suggests a potential role for these collagens in ECM remodelling and immune cell adhesion [503–507]. Increased Adam9-Itgb5 signalling to fibroblasts, VSMCs, and monocytes further supports the involvement of integrin signalling in cell adhesion and migration within the mouse myocardium [508–510]. Downregulation of Apoe signalling through interactions with Abca1, Vldlr, Sorl1, Lrp6, and Lrp1, on various cell types including fibroblasts, neutrophils, pericytes, and macrophages, suggests a role for Apoe in modulating lipid metabolism and inflammation [511, 512].

In late-stage human HCM, lymphatic endothelial cells exhibited a distinct communication profile (Figure C.3) marked by increased signalling through IGF1-IGF2R/INSR and MAML2-NOTCH1/2/3/4 axes. These interactions, targeting endothelial cells, cardiomyocytes, VSMCs, pericytes, and NK cells, suggest a role for lymphatic endothelial cells in regulating vascular growth, cardiomyocyte survival, and immune cell recruitment [513–515]. Increased LAMA4-CD44 and SEMA3D-NRP1/PLXNA4 signalling to fibroblasts further implicates lymphatic endothelial cells in ECM remodelling and cell migration [516–519]. Conversely, downregulation of CD59-STAB1 [520, 521], FBN1-ITGA5 [522, 523], and LAMB1-DAG1 [524] interactions, primarily targeting macrophages and neuronal cells, suggests modulation of inflammatory responses and cell adhesion within the human myocardial microenvironment.

In the mouse model, lymphatic endothelial cell communication displayed a different pattern (Figure C.3). Upregulation of Adam9-Itgb5 [509, 525, 526], Col1a2-Cd44/Cd93 [527–531], Bgn-Tlr2/4 [532, 533], Adam15-Itga9 [534], and Bmp4-Lrp6 [535, 536] interactions, targeting fibroblasts, endothelial cells, monocytes,

and macrophages, suggests a role for lymphatic endothelial cells in ECM remodelling, immune cell recruitment, and inflammation. Downregulation of Apoe signalling via interactions with Abca1, Vldlr, Sorl1, Lrp6, and Lrp1, mirroring the pattern observed in mouse endothelial cells, further supports the involvement of Apoe in modulating lipid metabolism and inflammation [537, 538].
Differences in endothelial and lymphatic endothelial cell communication between human and mouse models highlight the complexity of translating findings from animal models to human disease. While both species exhibited altered signalling related to vascular remodelling, inflammation, and cell adhesion, the specific ligands, receptors, and target cell types often differed. These interspecies variations underscore the limitations of cross-species and cross-disease stage comparisons and emphasise the need for further research using human samples and *in vitro* models to validate these findings and identify therapeutically relevant targets for human HCM.

C.4 Fibroblast signalling orchestrates extracellular matrix remodelling and fibrosis

Following an analysis of endothelial and lymphatic endothelial cell interactions, we then focused on fibroblasts, key mediators of ECM remodelling and fibrosis in HCM [178, 539]. In late-stage human HCM (Figure C.4), fibroblasts exhibited increased collagen signalling, notably COL14A1 and COL12A1. Elevated COL14A1 signalling, via CD44 and ITGB1, targeted fibroblasts, pericytes, mast cells, and adipocytes, suggesting a role in ECM organisation and cell adhesion within the human myocardium [540]. Similarly, increased COL12A1 and COL24A1 signalling through ITGB1, primarily targeting pericytes and fibroblasts, further implicates these collagens in ECM remodelling and cell-matrix interactions [541, 542]. Conversely, human fibroblasts showed decreased signalling of ANGPT1 and ANGPTL1 through ITGA5, TEK, and ITGB1, targeting fibroblasts, endothelial cells, and neuronal cells. This downregulation suggests potential modulation of angiogenesis and vascular remodelling in the human HCM heart [543–545].

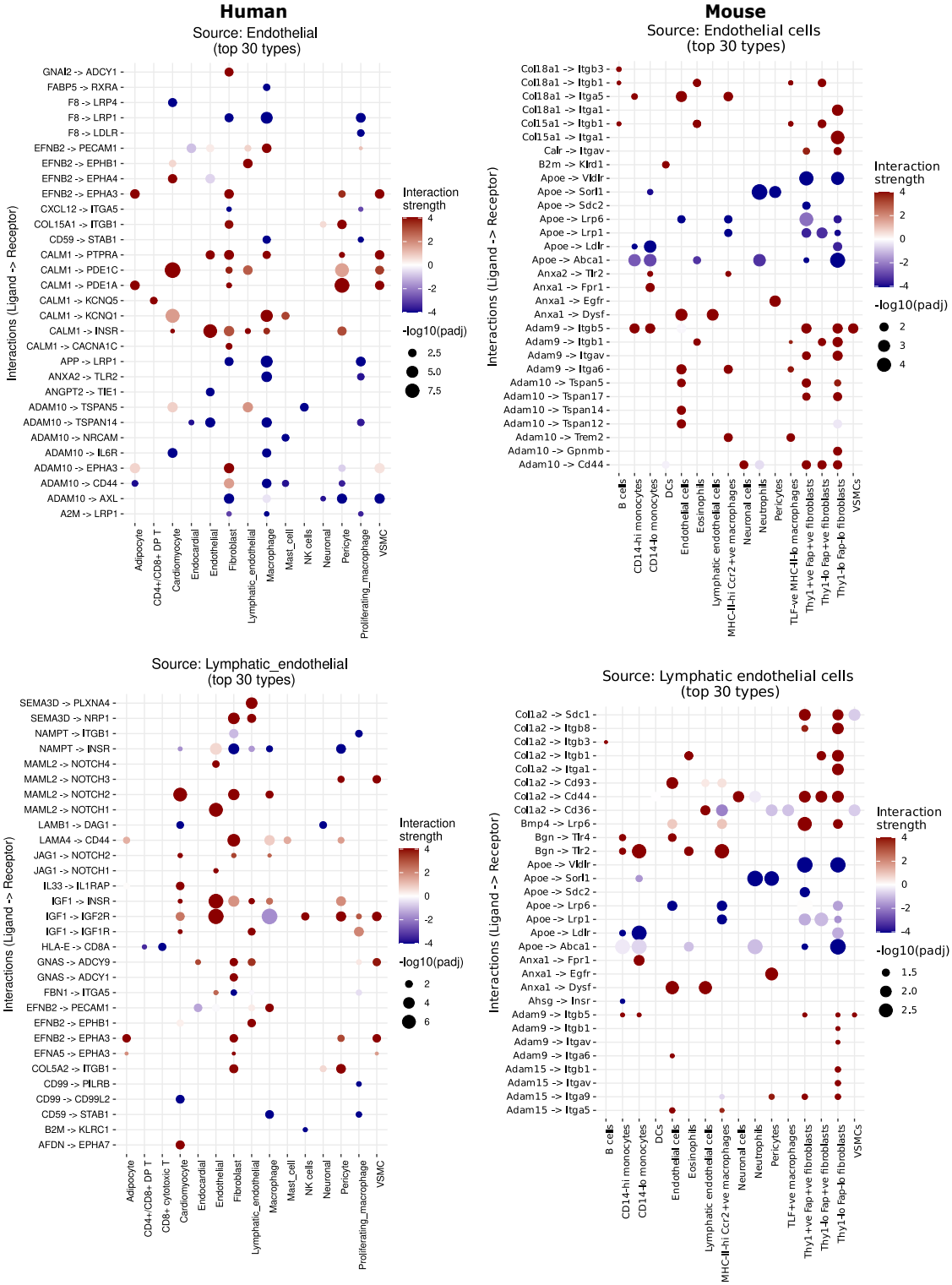

Figure C.3. Cell-cell communication involving endothelial cells in late-stage human and mouse HCM.

Positive interaction strength indicates up-regulation of ligand-receptor genes in HCM or Actc1^{E99K} samples, while negative strength indicates down-regulation. P-values were adjusted using the Benjamini-Hochberg method. Human interactions appear on the left and mouse interactions on the right.

Furthermore, reduced signalling through C3, ANXA2, COL4A1, COL1A1, and ADAM10, interacting with ITGAM, LRP1, TLR2, CD44, ITGA5, DDR2, and TSPAN14, and primarily targeting macrophages, adipocytes, mast cells, and fibroblasts, suggests modulation of inflammatory responses, cell adhesion, and ECM turnover within the myocardial microenvironment [546–550]. Increased ANOS1 signalling, via SDC2 and FGFR1, targeting cardiomyocytes and endothelial cells, suggests a role in regulating cell proliferation and differentiation in human HCM [551, 552]. Finally, increased COL1A1 signalling through FLT4 to lymphatic endothelial cells may influence lymphatic vessel remodelling [553–555]. The downregulation of AFDN-EPHA7 interaction between fibroblasts and cardiomyocytes suggests potential disruption of cell-cell adhesion and signalling in human HCM [556, 557].

In the Actc1^{E99K} mouse model, three distinct fibroblast populations (Thy1^{lo}Fap^{lo}, Thy1^{lo}Fap^{+}, and Thy1^{+}Fap^{lo}) were identified, each exhibiting unique communication profiles (Figure C.4). Thy1^{lo}Fap^{lo} fibroblasts displayed prominent downregulation of Adm and Apoe signalling. Decreased Adm signalling through Ackr3, Ramp2, Gpr182, Adrb2, and Adcyap1r1, targeting various cell types, including other fibroblast populations, lymphatic endothelial cells, monocytes, eosinophils, and DCs, suggests modulation of immune cell recruitment and vascular function [558]. Similarly, downregulation of Apoe signalling through interactions with Abca1, Ldlr, Lrp1, and Lrp5, targeting fibroblasts, macrophages, monocytes, and $\gamma\delta$T cells, suggests a role for Apoe in modulating lipid metabolism and inflammation [559]. Conversely, Thy1^{lo}Fap^{lo} fibroblasts exhibited increased Adam9 and Adam10 signalling through Itgb5, Itgb1, Itga6, Cd44, and Tspan5, primarily targeting fibroblasts, endothelial cells, macrophages, and monocytes, suggesting a role for these metalloproteinases in ECM remodelling and cell adhesion [560–563]. Upregulation of Angptl4 signalling through Cdh11 and Sdc3, targeting fibroblasts and endothelial cells, further supports the involvement of angiopoietin-like proteins in vascular remodelling [564–566]. Increased Anxa1 signalling through Dysf and Fpr1, targeting lymphatic and endothelial cells, and monocytes, suggests a

role in regulating inflammation and cell migration [567]. Downregulation of the Alcam-Nrp1 interaction between $Thy1^{lo}Fap^{lo}$ fibroblasts and monocytes, and other fibroblasts, suggests potential alteration of cell guidance and migration [568, 569].

$Thy1^{lo}Fap^{+}$ fibroblasts in the $Actc1^{E99K}$ mouse model exhibited a distinct communication profile (Figure C.4) characterised by increased collagen signalling. Elevated Col1a1 signalling, via Cd44, Cd93, Ddr1, Itga1, Itga5, and Cd36, targeted other fibroblast populations, endothelial cells, lymphatic endothelial cells, neuronal cells, DCs, neutrophils, macrophages, and monocytes, suggesting a central role for this collagen in ECM deposition and cell-matrix interactions [374]. Increased Col11a1 and Col12a1 signalling, via Ddr1, Itga1, and Itgb1, targeting DCs, fibroblasts, B cells, eosinophils, and macrophages, further implicates these collagens in ECM remodelling and immune cell modulation [570, 571]. Increased Col18a1 signalling through Itgb5 and Ptprs, targeting fibroblasts, endothelial cells, monocytes, and VSMCs, suggests a role in regulating cell adhesion and vascular remodelling [507]. Conversely, $Thy1^{lo}Fap^{+}$ fibroblasts displayed downregulation of C3, Cd34, Apoe, and Angptl1 signalling. Decreased C3 signalling, via Cd81 and Nrp1, targeting DCs, pericytes, VSMCs, monocytes, and other fibroblasts, suggests modulation of complement-mediated immune responses [572]. Downregulation of Cd34 signalling via Sell, targeting B cells, neutrophils, and $CD4^{+}$ Tconv cells, suggests potential alteration in haematopoietic progenitor cell recruitment and differentiation [573]. Decreased Apoe signalling, through interactions with Abca1 and Vldlr, targeting fibroblasts, monocytes, neutrophils, and eosinophils, further supports the involvement of Apoe in modulating lipid metabolism and inflammation [559]. Finally, downregulation of Angptl1 signalling through Tek, targeting endothelial cells, suggests modulation of angiogenesis and vascular remodelling [574]. Increased Angptl2-Pirb signalling between $Thy1^{lo}Fap^{+}$ fibroblasts and monocytes and macrophages suggests a role in regulating inflammatory responses [575, 576]. Increased Col1a1-Itga9 interaction within $Thy1^{lo}Fap^{+}$

fibroblasts suggests a potential autocrine mechanism regulating ECM remodelling [374].

Finally, Thy1^{+}Fap^{lo} and Thy1^{+}Fap^{+} fibroblasts shared similar communication patterns, notably downregulation of Adm signalling through Ackr3, Ramp2, and Gpr182, targeting other fibroblast populations, endothelial cells, lymphatic endothelial cells, and pericytes (Figure C.4). This suggests a conserved role for Adm in regulating inter-fibroblast communication and vascular function [577]. Both populations also exhibited downregulation of Apoe signalling through Abca1, Vldlr, Lrp1, Lrp6, and Sdc2, targeting fibroblasts, monocytes, neutrophils, eosinophils, endothelial cells, and macrophages, further supporting Apoe's involvement in lipid metabolism and inflammation [559]. However, these fibroblast populations also displayed distinct signalling patterns. Thy1^{+}Fap^{lo} fibroblasts exhibited increased Bgn signalling through Tlr2 and Tlr4, targeting monocytes, macrophages, eosinophils, and endothelial cells, suggesting a role for this proteoglycan in regulating inflammatory responses [532, 533, 578–582]. Increased Cfh-Itgam interaction between Thy1^{+}Fap^{lo} fibroblasts and macrophages further supports the involvement of complement factors in inflammation [583–585]. Increased Comp signalling, via Sdc1, Itga5, Cd47, and Cd36, targeting other fibroblasts, endothelial cells, macrophages, DCs, and lymphatic endothelial cells, suggests a role for this complement component in modulating immune cell activity and vascular function [586]. Thy1^{+}Fap^{+} fibroblasts displayed increased Adam9, Adam10, Adam15, and Anxa1 signalling, targeting various cell types, including fibroblasts, endothelial cells, monocytes, macrophages, B cells, pericytes, and lymphatic endothelial cells, suggesting a role for these proteins in ECM remodelling, cell adhesion, and inflammation [560–563, 567]. Downregulation of the Ccl11-Dpp4 interaction in Thy1^{+}Fap^{lo} fibroblasts, targeting other fibroblasts and lymphatic endothelial cells, suggests modulation of chemokine signalling [587–589]. Downregulation of the Adm-Pth1r interaction between Thy1^{+}Fap^{+} fibroblasts and other fibroblasts and VSMCs suggests potential alteration in vascular tone and remodelling [590–592].

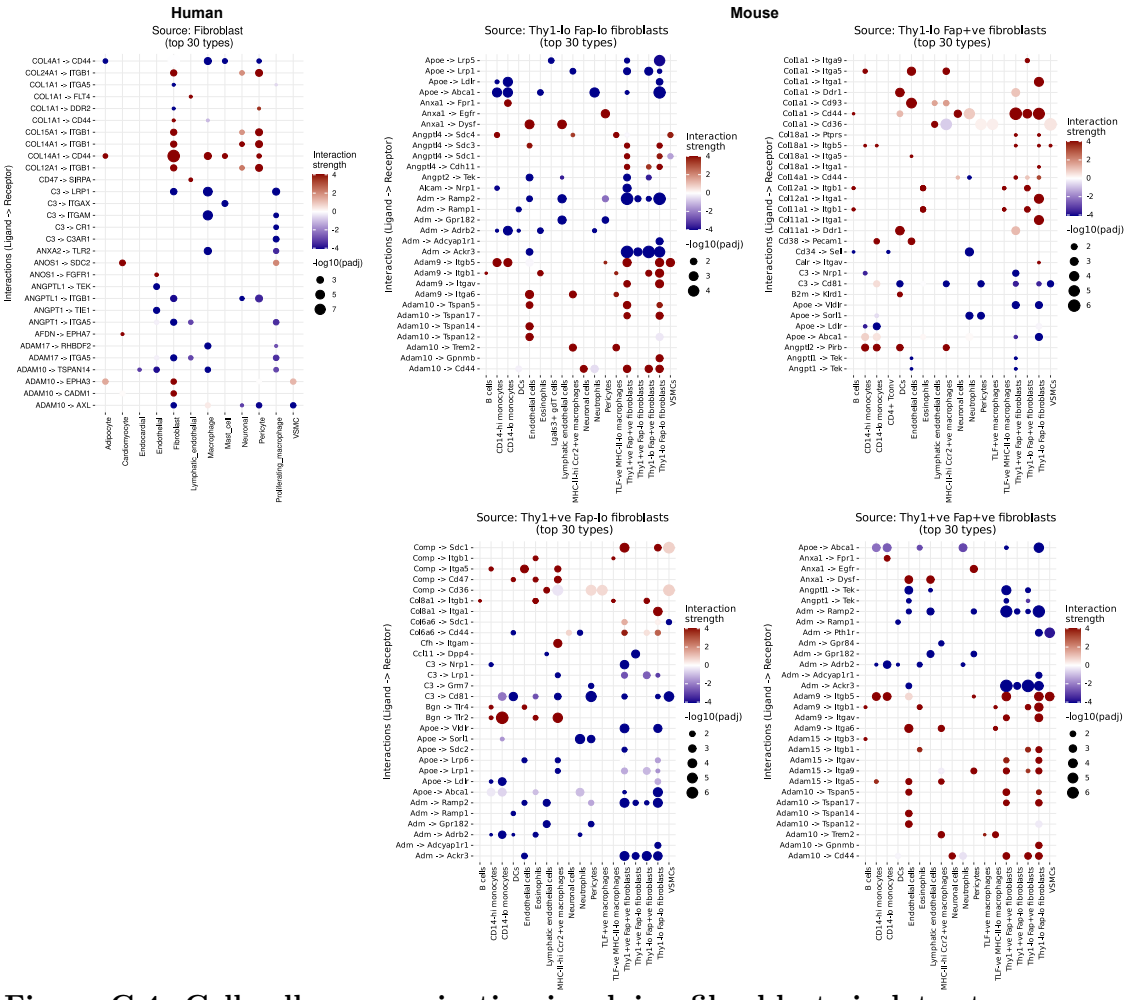

Figure C.4. Cell-cell communication involving fibroblasts in late-stage human and mouse HCM.
Positive interaction strength indicates up-regulation of ligand-receptor genes in HCM or Actc1^{E99K} samples, while negative strength indicates down-regulation. P-values were adjusted using the Benjamini-Hochberg method. Human interactions appear on the left and mouse interactions on the right.

C.5 Pericyte and VSMC interactions maintain vascular stability and influence fibrotic changes

Pericytes and VSMCs are essential for vascular integrity, blood flow regulation, and ECM deposition [217, 593, 594]. Their intercellular communication is crucial in the adverse cardiac remodelling seen in HCM [217, 218, 595].

In late-stage human HCM, pericytes displayed a complex signalling profile (Figure C.5). FGF1 signalling was markedly upregulated, primarily via interactions with CD44, NRP1, TGFBR3, EGFR, FGFR1, and CSPG4, targeting diverse

cell types, including fibroblasts, other pericytes, VSMCs, NK cells, $CD4^+/CD8^+$ DP T cells, macrophages, lymphatic endothelial cells, mast cells, and adipocytes. This increased FGF1 activity may contribute to the vascular remodelling and inflammation characteristic of HCM, given its established roles in angiogenesis, cell proliferation, and differentiation [364, 596]. Conversely, human pericytes showed reduced signalling of several molecules. Downregulation of COL18A1 signalling (via ITGA5 and PTPRS) to fibroblasts and neuronal cells may alter ECM composition and structure [597]. Decreased CD38 signalling via PECAM1 to endothelial, endocardial, and lymphatic endothelial cells could impact intercellular communication and vascular function [598, 599]. Reduced ANGPT2 signalling (through TIE1 and TEK) to endothelial cells, and decreased AGT signalling (through ENPEP) to VSMCs and other pericytes, suggests modulation of angiogenesis, vascular remodelling, and blood pressure regulation [600–604]. Furthermore, decreased COL4A1 and COL4A2 signalling, interacting with CD44 and ITGAV, and targeting macrophages, adipocytes, mast cells, fibroblasts, and neuronal cells, suggests altered ECM turnover and cell adhesion within the myocardium [605–607]. Increased signalling was observed for several other molecules. Upregulated FARP2 (through PLXNA4 and PLXNA2) targeting endocardial cells, lymphatic endothelial cells, fibroblasts, cardiomyocytes, and macrophages, suggests involvement in cell migration and axon guidance [608, 609]. Increased CD99 signalling through PILRA to macrophages may modulate immune cell activity [610–612]. Increased COL3A1 (through DDR2) to other pericytes and VSMCs, COL5A1 and COL5A2 (through ITGB1) to other pericytes, fibroblasts, and neuronal cells, may influence ECM remodelling and organisation, respectively [597, 613, 614]. Finally, decreased COL1A2 signalling (via CD36) to endothelial cells and cardiomyocytes, and decreased COL27A1 (via ITGB1) to neuronal cells and other pericytes, suggest potential alterations in lipid metabolism and inflammation, and cartilage development and ECM organisation, respectively [615–618].

In the Actc1^{E99K} mouse model, pericyte intercellular communication differed substantially from the human HCM profile (Figure C.5). A prominent feature was the upregulation of Bgn signalling, primarily through Tlr2 and Tlr4. This signalling targeted various immune cells, including CD14^{lo} monocytes, MHC-II^{hi}Ccr2^{+} macrophages, eosinophils, and endothelial cells. Given Bgn's role in ECM organisation and inflammation, this increased signalling likely contributes to the inflammatory and fibrotic processes observed in this HCM model [619]. Increased Apoe signalling was also observed, interacting with Lrp1, Lrp5, Lrp6, Abca1, Lsr, Trem2, Ldlr, Scarb1, and Sorl1, and targeting fibroblasts, monocytes, macrophages, $\gamma\delta$T cells, neutrophils, eosinophils, DCs, and endothelial cells. This upregulation of Apoe, involved in lipid metabolism and transport, may reflect altered lipid handling and inflammatory responses within the Actc1^{E99K} mouse heart [559]. Furthermore, mouse pericytes exhibited increased signalling of several collagens, including Col1a1, Col14a1, and Col15a1, primarily through interactions with Cd44, Cd93, Ddr1, Itga1, and Itgb1. These collagens targeted various cell types, including fibroblasts, endothelial cells, lymphatic endothelial cells, neuronal cells, and immune cells (DCs, neutrophils, macrophages, monocytes, and B cells), suggesting active ECM remodelling and deposition [597, 620]. Several other signalling pathways were also upregulated in mouse pericytes. Increased Cfh signalling (via Itgam) to MHC-II^{hi}Ccr2^{+} macrophages points to the involvement of complement factors in the inflammatory response [621–624]. Increased Anxa1 and Anxa2 signalling (through Dysf, Egfr, Fpr1, and Tlr2) targeting lymphatic and endothelial cells, monocytes, macrophages, and eosinophils, suggests roles in inflammation regulation, cell migration, and proliferation [548, 625]. Increased Comp signalling (via Cd36) targeting lymphatic endothelial cells, VSMCs, macrophages, pericytes, and DCs suggests modulation of complement activation and immune cell activity [626–628]. Increased B2m signalling (via Klrd1) to DCs may influence antigen presentation and subsequent immune responses [629, 630]. Increased Col8a1 signalling (via Itga1 and Itgb1) to fibroblasts, B cells, and macrophages, Col3a1 signalling (via Ddr1) to DCs and fibrob-

lasts, and Col18a1 signalling (through Itgb3) to B cells, suggest roles in cell adhesion, migration, ECM remodelling, and immune modulation [597, 607, 631–633]. Finally, increased Bmp4 signalling (through Lrp6) to fibroblasts and endothelial cells suggests a role in cell differentiation and proliferation [634–636]. Conversely, decreased Ccl11 signalling (via Dpp4) to fibroblasts and lymphatic endothelial cells suggests modulation of chemokine signalling and immune cell recruitment [588, 637].

VSMCs in late-stage human HCM exhibited a distinct communication profile (Figure C.5), notably altered collagen signalling. COL4A5 signalling was increased (via CD47) targeting fibroblasts and cardiomyocytes. This upregulation of COL4A5, a basement membrane component, may contribute to vascular remodelling and stiffness in human HCM [638]. Conversely, several other collagen genes (COL18A1, COL4A1, and COL4A2) showed decreased signalling (through ITGA5, PTPRS, CD44, and ITGAV) targeting fibroblasts, macrophages, adipocytes, mast cells, pericytes, and neuronal cells. This downregulation suggests complex alterations in ECM composition and cell-matrix interactions within the diseased myocardium [597, 639]. Furthermore, increased signalling of COL14A1, APP, ANGPT1, COL1A2, COL6A1, COL5A1, COL5A2, and BMP5 (through various receptors including CD44, CD74, ITGB1, ITGA5, FLT4, LRP6, and BMPR2) targeting a range of cell types, including fibroblasts, macrophages, endothelial cells, lymphatic endothelial cells, pericytes, cardiomyocytes, endocardial cells, and neuronal cells, suggests their involvement in ECM remodelling, cell adhesion, and intercellular signalling. Decreased FBN1 signalling (via ITGA5) to fibroblasts, endothelial cells, and proliferating macrophages suggests potential disruption of elastic fibre assembly and microfibril formation [640]. Decreased COL3A1 signalling (via DDR2) to fibroblasts and pericytes, alongside increased CD99 signalling (via PILRA) to macrophages, and increased CNTN4 signalling (via PTPRG) to a broad range of cell types, may influence ECM remodelling, immune cell activity, cell adhesion, and axon guidance, respectively [610, 612, 613, 620, 641–645].

In the Actc1^{E99K} mouse model, VSMCs also displayed altered intercellular communication, mirroring some aspects of the human HCM profile (Figure C.5). Similar to mouse pericytes, Bgn signalling was upregulated (via Tlr2 and Tlr4), targeting immune cells and endothelial cells, suggesting a conserved role for Bgn in the inflammatory response [619]. Increased signalling of several collagens (Col1a1, Col1a2, Col18a1, Col8a1, Col3a1, and Col15a1) through various receptors, targeting a range of cell types, suggests active ECM remodelling and deposition [597]. Increased Cfh signalling (via Itgam) to MHC-II^{hi}Ccr2^{+} macrophages further implicates complement factors in the inflammatory response [621–624]. Increased Comp signalling (via Cd36) and Anxa1 signalling (via Fpr1) suggest roles in complement activation, immune cell activity, inflammation regulation, and cell migration [548, 625–628]. Finally, decreased Ccl11 signalling (via Dpp4) suggests modulation of chemokine signalling and immune cell recruitment [588, 637].

C.6 Neuronal signalling patterns impact cardiac innervation and structural remodelling

Neuronal cells are integral to cardiac innervation and function, and play a crucial role in the pathogenesis of HCM [646]. In human HCM hearts, neuronal cells exhibited complex altered signalling interactions (Figure C.6). Downregulation of interactions between LAMA2, HSPG2, and LAMA3 with receptors such as DAG1, PTPRS, LRP1, and integrins (ITGB1, ITGAV) was prominent. These interactions primarily targeted other neuronal cells, cardiomyocytes, fibroblasts, and macrophages. Laminins (LAMA2, LAMA3) and perlecan (HSPG2) are key ECM components. Their decreased signalling could disrupt cell adhesion, migration, and ECM organisation, potentially contributing to structural and functional abnormalities observed in HCM [647–649]. Conversely, neuronal cells showed increased JAG1 signalling via NOTCH receptors (NOTCH1, NOTCH2, NOTCH3, NOTCH4), targeting endothelial cells, cardiomyocytes, fibroblasts, and VSMCs. This NOTCH signalling upregulation, known to regulate cell fate and differentiation, could influence cellular composition and remodelling processes within the

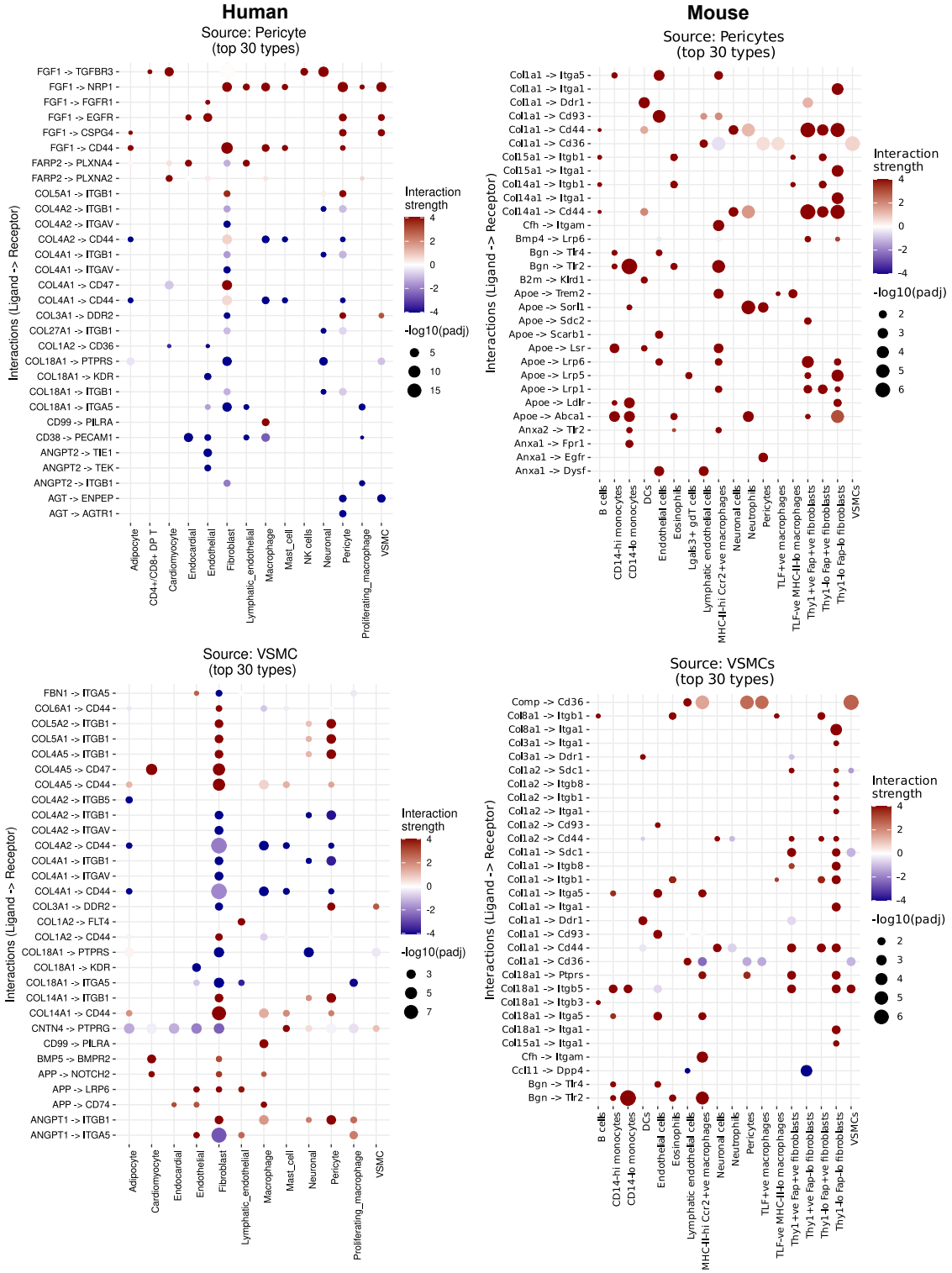

Figure C.5. Cell-cell communication involving pericytes and VSMCs in late-stage human and mouse HCM.

Positive interaction strength indicates up-regulation of ligand-receptor genes in HCM or Actc1^{E99K} samples, while negative strength indicates down-regulation. P-values were adjusted using the Benjamini-Hochberg method. Human interactions appear on the left and mouse interactions on the right.

diseased heart [650–652]. Additionally, altered signalling of collagens (COL4A1, COL18A1) and CD59 was observed. Increased COL4A1 signalling via CD47 to fibroblasts, and increased COL18A1 signalling via PTPRS to adipocytes and VSMCs, suggest roles in ECM remodelling and vascular function [597]. Decreased COL4A1 and COL4A2 signalling through CD44 and integrins, targeting macrophages, adipocytes, and fibroblasts, alongside decreased CD59 signalling via STAB1 to macrophages, may influence ECM turnover, cell adhesion, and complement regulation [597].

In the Actc1^{E99K} mouse model, neuronal cell communication differed from the human HCM profile (Figure C.6). Increased signalling of various collagens (Col6a1, Col18a1, Col8a1, Col28a1) and versican (Vcan) was a striking observation, primarily targeting fibroblasts, endothelial cells, and immune cells (monocytes, macrophages, B cells, and eosinophils). This upregulation of ECM components suggests active ECM remodelling and deposition, potentially contributing to the fibrotic phenotype observed in this model [597, 653, 654]. Apoe signalling, interacting with receptors such as Abca1, Vldlr, Sorl1, and Lrp6, and targeting fibroblasts, monocytes, neutrophils, pericytes, and endothelial cells, was significantly downregulated. This downregulation of Apoe, involved in lipid metabolism and transport, may reflect altered lipid handling and inflammatory responses within the Actc1^{E99K} mouse heart [559]. Furthermore, increased Lgals3bp signalling via Itgb1 to fibroblasts, and decreased Alcam signalling via Nrp1 to fibroblasts, suggest potential roles in cell adhesion, migration, and axon guidance [569, 655, 656]. Finally, altered signalling of Nrxn1, Sostdc1, C4b, and Lgi1 was also observed, indicating potential modulation of neuronal function, Wnt signalling, complement activation, and synaptic transmission [657–660].

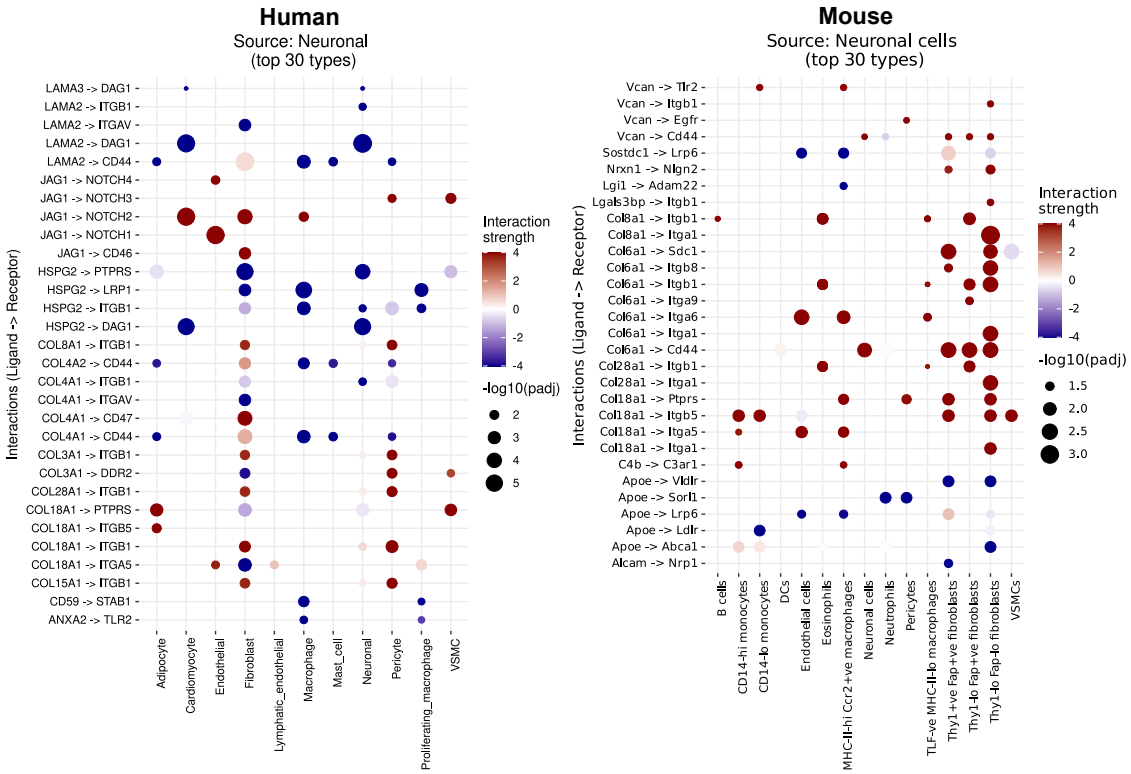

Figure C.6. Cell-cell communication involving neuronal cells in late-stage human and mouse HCM.

Positive interaction strength indicates up-regulation of ligand-receptor genes in HCM or Actc1^{E99K} samples, while negative strength indicates down-regulation. P-values were adjusted using the Benjamini-Hochberg method. Human interactions appear on the left and mouse interactions on the right.

D

Integrative analysis connects bulk trends with single-cell insights to reveal cell type contributions

D.1 Cluster 1 & 4: Early activation followed by a late surge signals diverse functional changes in HCM

Cluster 1, characterised by an initial upregulation followed by a further surge in expression during the late stage of disease, was functionally diverse (Figures D.1 and D.12). Sub-cluster analysis revealed enrichment for various processes, including ribosome biogenesis (MCL sub-cluster 1; Figure D.2), release of cytochrome c from mitochondria (MCL sub-cluster 2; Figure D.3), regulation of RHO GTPases (MCL sub-cluster 3; Figure D.4), histone deacetylase complex activity (MCL sub-cluster 4; Figure D.5), Golgi-to-ER retrograde traffic (MCL sub-cluster 5; Figure D.6), interferon-β production (MCL sub-cluster 6; Figure D.7), ionotropic glutamate receptor complex assembly (MCL sub-cluster 7; Figure D.8), G protein signalling (MCL sub-cluster 8; Figure D.9), RET signalling (MCL sub-cluster 9; Figure D.10), and tumour necrosis factor receptor binding (MCL sub-cluster 10; Figure D.11). In late-stage human HCM samples, the overall cluster 1 signa-

ture was significantly upregulated in activated fibroblasts, NK cell, endothelial cells, lymphatic endothelial cells, VSMCs, and cardiomyocytes, while downregulated in proliferating macrophages and pericytes (Figure D.1). Further examination of individual sub-clusters revealed more nuanced cell-type specific patterns. For instance, the ribosome biogenesis sub-cluster (MCL sub-cluster 1; Figure D.2) showed upregulation in activated fibroblasts and lymphatic endothelial cells, and downregulation in proliferating macrophages and pericytes. The release of cytochrome c from mitochondria sub-cluster (MCL sub-cluster 2; Figure D.3) was upregulated in fibroblasts, VSMCs, and pericytes, and downregulated in mast cells and proliferating macrophages. In contrast, the mouse scRNA-seq data revealed fewer significant changes for cluster 1 (Figure D.12). Only NK cells exhibited significant downregulation of the overall cluster 1 signature, while sub-cluster analysis revealed upregulation of the ribosome biogenesis sub-cluster (MCL sub-cluster 1; Figure D.13) in $CD14^{lo}$ monocytes, downregulation of the release of cytochrome c from mitochondria sub-cluster (MCL sub-cluster 2; Figure D.14) in a subset of fibroblasts ($Thy1^{lo}Fap^{lo}$ fibroblasts), and upregulation of the histone deacetylase complex sub-cluster (MCL sub-cluster 4; Figure D.16) in two fibroblast populations ($Thy1^{lo}Fap^{lo}$ and $Thy1^{lo}Fap^{+}$ fibroblasts).

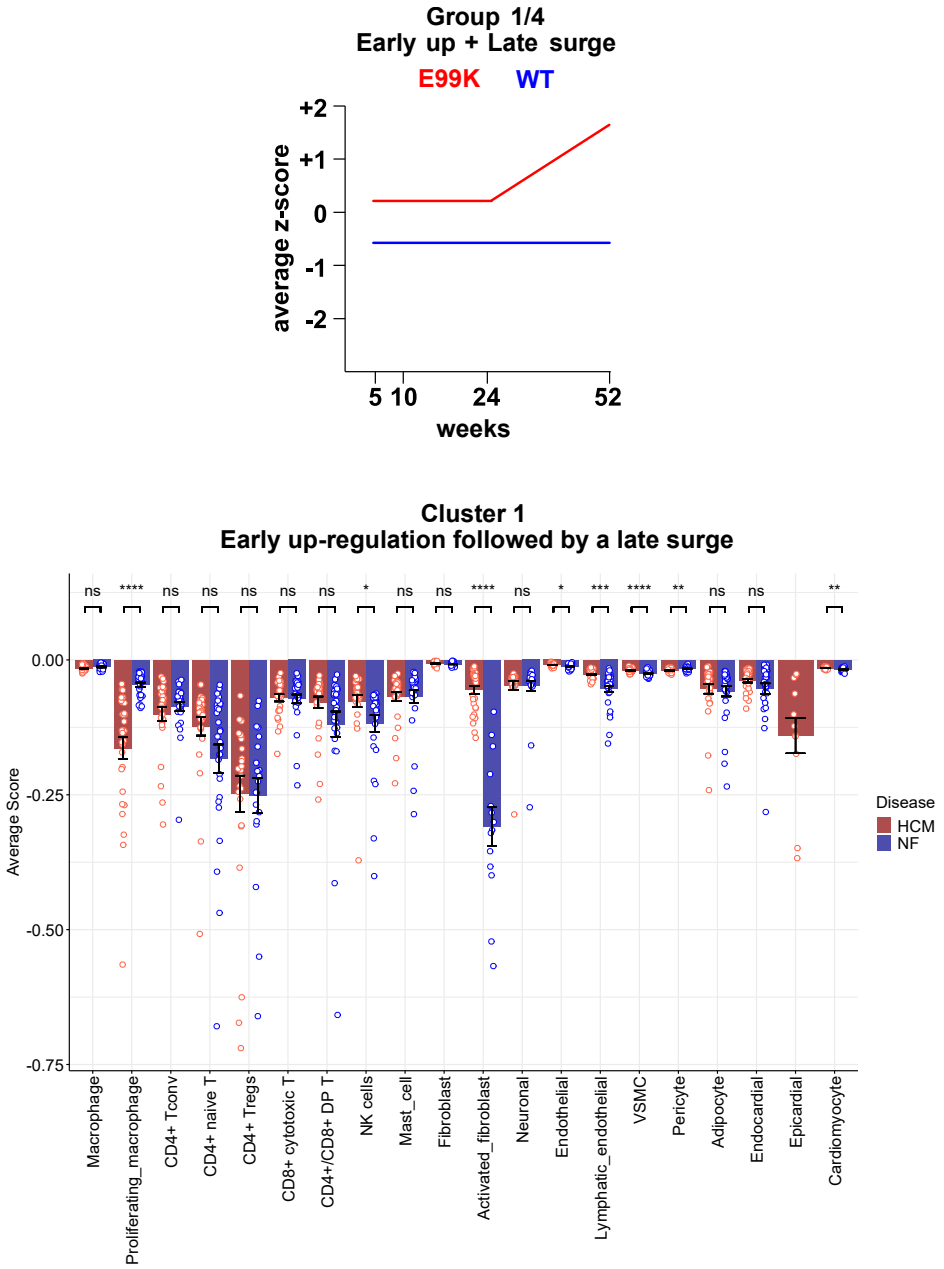

Figure D.1. Gene set scoring and statistics of cluster 1 (early up-regulation followed by a late surge) in late-stage human cell types.
The upper panel schematically illustrates the temporal expression trend for Cluster 1, derived from bulk RNA-seq data of Actc1^{E99K} (red line) and wild-type (blue line) hearts over time. The lower panel displays the gene set score for all genes within Cluster 1 across various cell types identified in late-stage human HCM snRNA-seq data. Scores were calculated for each sample using the `score_genes` function in `scanpy` v1.10.1 [267]. Bars represent the mean score, with error bars indicating the standard error of the mean. Statistical significance between disease and control samples was determined using a t-test, with p-values adjusted for multiple comparisons using the Benjamini-Hochberg method. Asterisks denote significance levels: * $p < 0.05$, ** $p < 0.01$, *** $p < 0.001$, **** $p < 0.0001$.

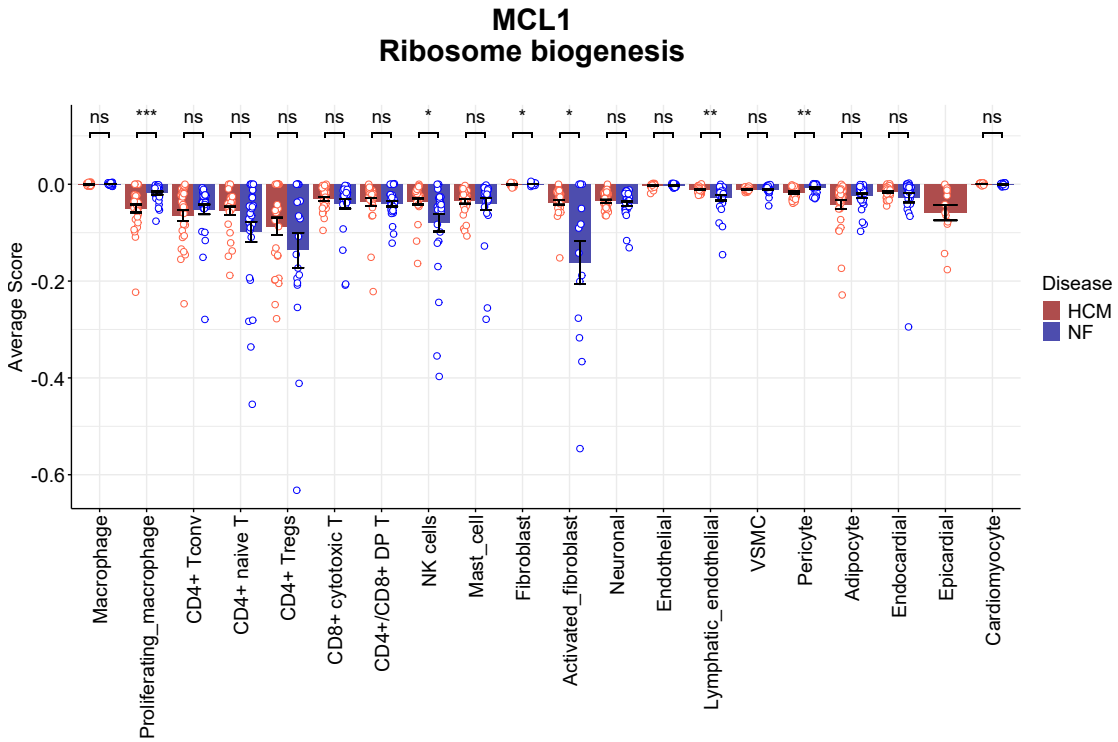

Figure D.2. Gene set scoring for MCL sub-cluster 1 of Cluster 1 (early up-regulation followed by a late surge) in late-stage human cell types.
This sub-cluster is a constituent of Cluster 1. The bar chart displays the gene set score for this specific sub-cluster across various cell types from late-stage human HCM snRNA-seq data. Scores were calculated for each sample using the `score_genes` function in `scanpy` v1.10.1 [267]. Bars represent the mean score, with error bars indicating the standard error of the mean. Statistical significance between disease and control samples was determined using a t-test, with p-values adjusted for multiple comparisons using the Benjamini-Hochberg method. Asterisks denote significance levels: * $p < 0.05$, ** $p < 0.01$, *** $p < 0.001$, **** $p < 0.0001$.

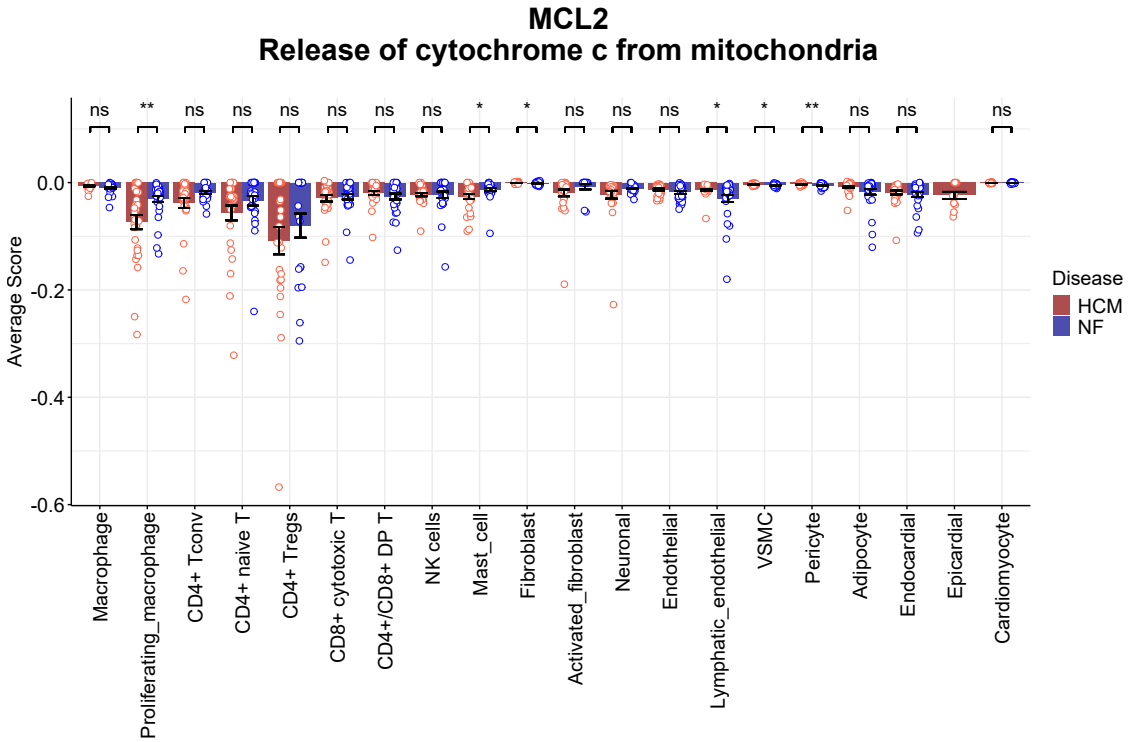

Figure D.3. Gene set scoring for MCL sub-cluster 2 of Cluster 1 (early up-regulation followed by a late surge) in late-stage human cell types.
This sub-cluster is a constituent of Cluster 1. The bar chart displays the gene set score for this specific sub-cluster across various cell types from late-stage human HCM snRNA-seq data. Scores were calculated for each sample using the `score_genes` function in `scanpy` v1.10.1 [267]. Bars represent the mean score, with error bars indicating the standard error of the mean. Statistical significance between disease and control samples was determined using a t-test, with p-values adjusted for multiple comparisons using the Benjamini-Hochberg method. Asterisks denote significance levels: * $p < 0.05$, ** $p < 0.01$, *** $p < 0.001$, **** $p < 0.0001$.

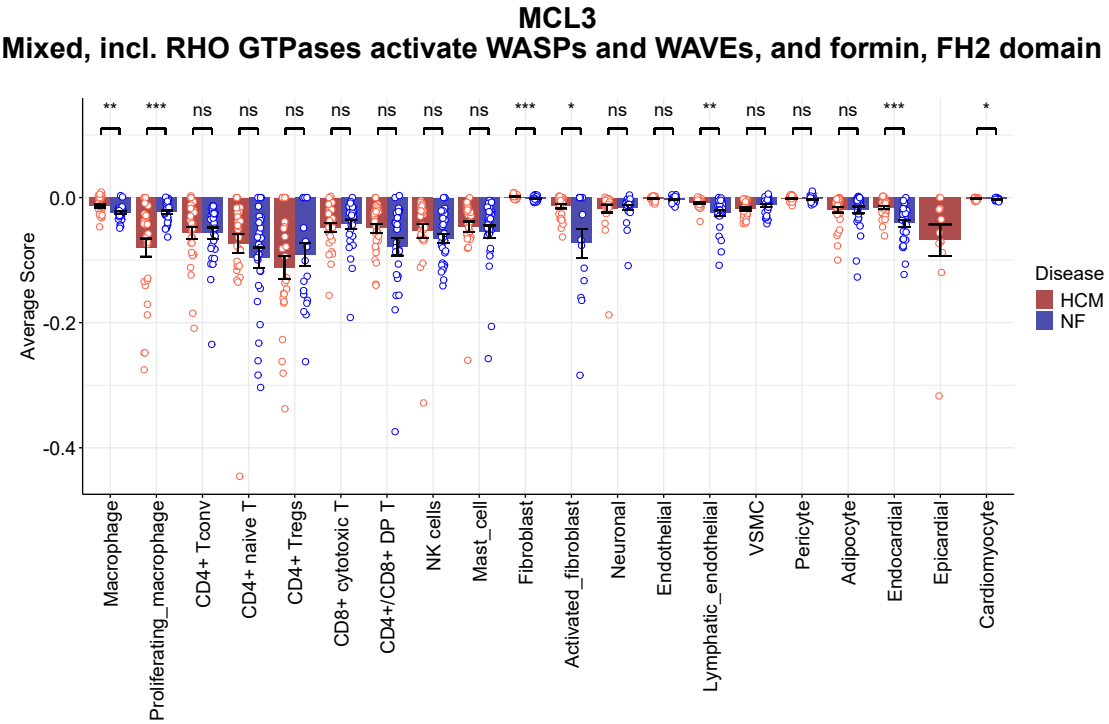

Figure D.4. Gene set scoring for MCL sub-cluster 3 of Cluster 1 (early up-regulation followed by a late surge) in late-stage human cell types.
This sub-cluster is a constituent of Cluster 1. The bar chart displays the gene set score for this specific sub-cluster across various cell types from late-stage human HCM snRNA-seq data. Scores were calculated for each sample using the `score_genes` function in `scanpy` v1.10.1 [267]. Bars represent the mean score, with error bars indicating the standard error of the mean. Statistical significance between disease and control samples was determined using a t-test, with p-values adjusted for multiple comparisons using the Benjamini-Hochberg method. Asterisks denote significance levels: * $p < 0.05$, ** $p < 0.01$, *** $p < 0.001$, **** $p < 0.0001$.

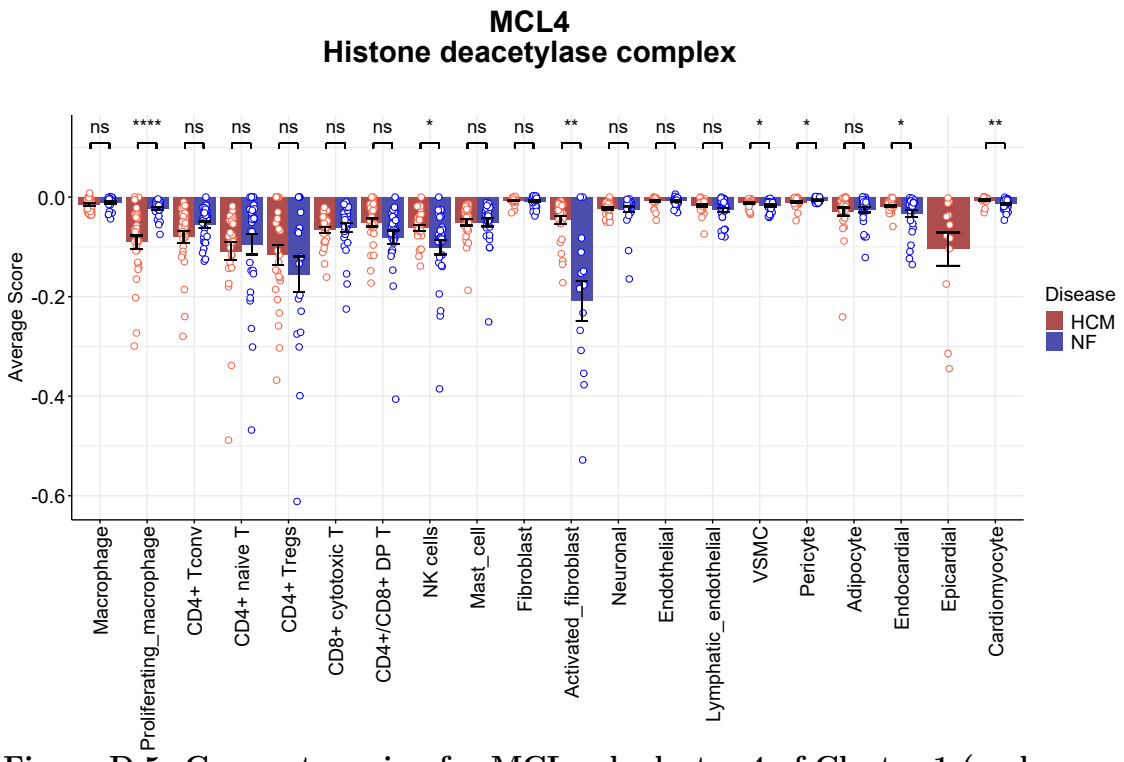

Figure D.5. Gene set scoring for MCL sub-cluster 4 of Cluster 1 (early up-regulation followed by a late surge) in late-stage human cell types.
This sub-cluster is a constituent of Cluster 1. The bar chart displays the gene set score for this specific sub-cluster across various cell types from late-stage human HCM snRNA-seq data. Scores were calculated for each sample using the `score_genes` function in `scanpy` v1.10.1 [267]. Bars represent the mean score, with error bars indicating the standard error of the mean. Statistical significance between disease and control samples was determined using a t-test, with p-values adjusted for multiple comparisons using the Benjamini-Hochberg method. Asterisks denote significance levels: * $p < 0.05$, ** $p < 0.01$, *** $p < 0.001$, **** $p < 0.0001$.

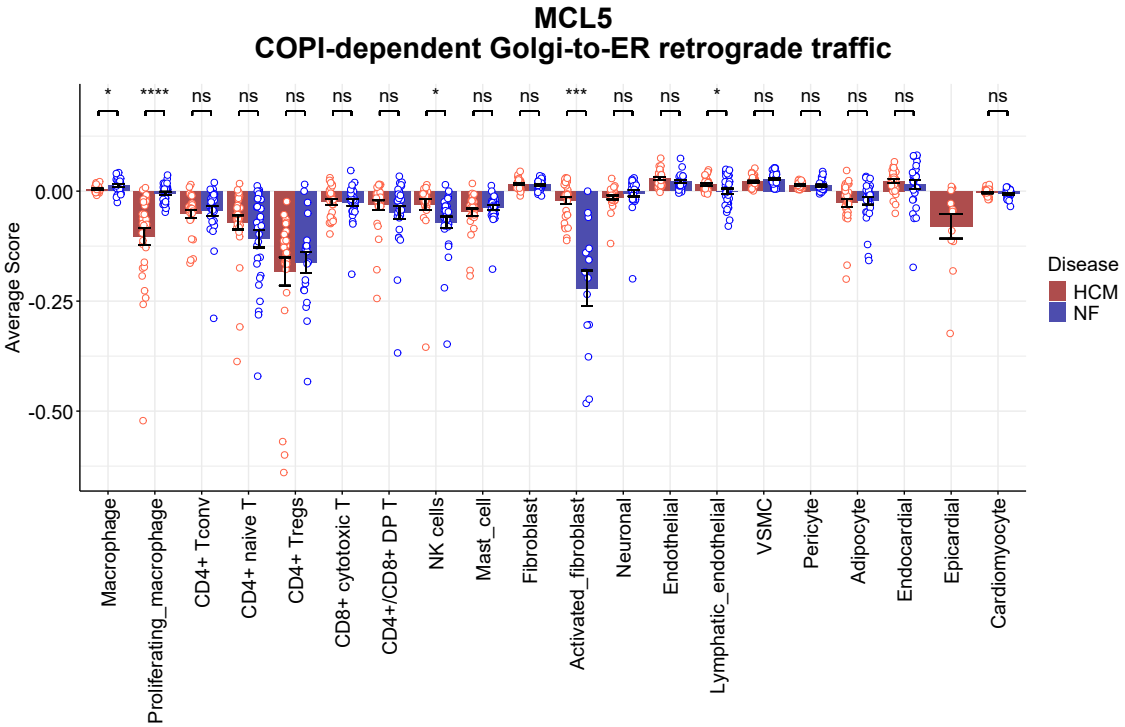

Figure D.6. Gene set scoring for MCL sub-cluster 5 of Cluster 1 (early up-regulation followed by a late surge) in late-stage human cell types.
This sub-cluster is a constituent of Cluster 1. The bar chart displays the gene set score for this specific sub-cluster across various cell types from late-stage human HCM snRNA-seq data. Scores were calculated for each sample using the `score_genes` function in `scanpy` v1.10.1 [267]. Bars represent the mean score, with error bars indicating the standard error of the mean. Statistical significance between disease and control samples was determined using a t-test, with p-values adjusted for multiple comparisons using the Benjamini-Hochberg method. Asterisks denote significance levels: * $p < 0.05$, ** $p < 0.01$, *** $p < 0.001$, **** $p < 0.0001$.

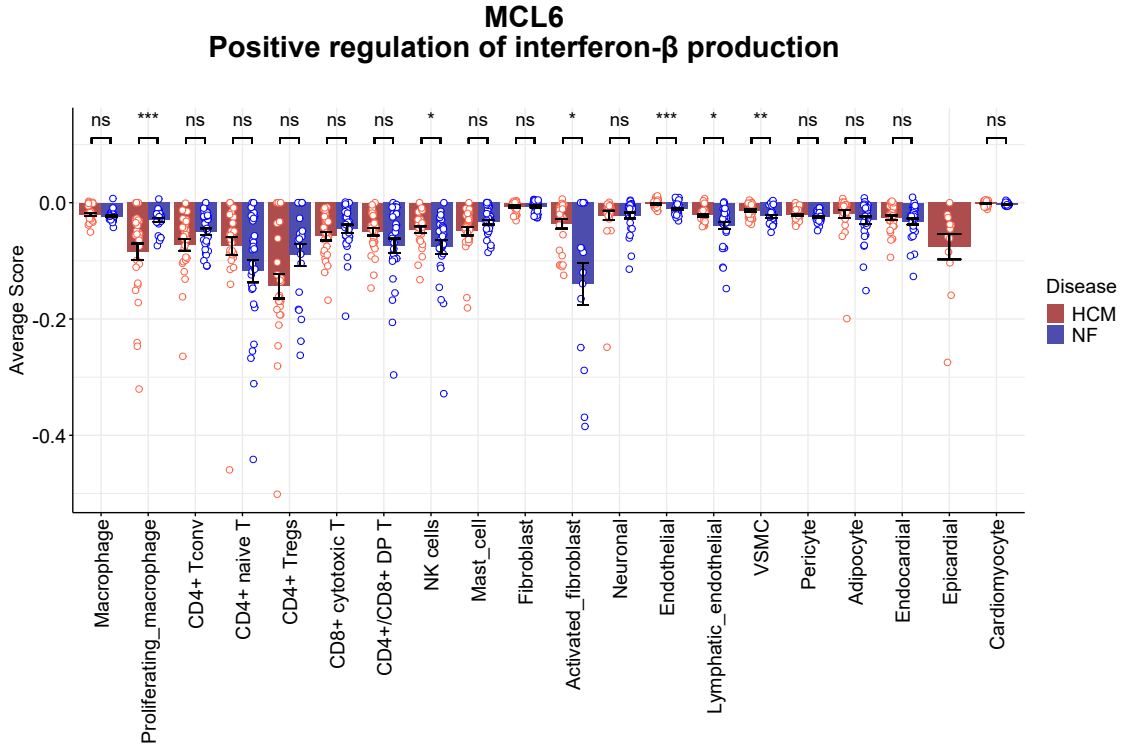

Figure D.7. Gene set scoring for MCL sub-cluster 6 of Cluster 1 (early up-regulation followed by a late surge) in late-stage human cell types.
This sub-cluster is a constituent of Cluster 1. The bar chart displays the gene set score for this specific sub-cluster across various cell types from late-stage human HCM snRNA-seq data. Scores were calculated for each sample using the `score_genes` function in `scanpy` v1.10.1 [267]. Bars represent the mean score, with error bars indicating the standard error of the mean. Statistical significance between disease and control samples was determined using a t-test, with p-values adjusted for multiple comparisons using the Benjamini-Hochberg method. Asterisks denote significance levels: * $p < 0.05$, ** $p < 0.01$, *** $p < 0.001$, **** $p < 0.0001$.

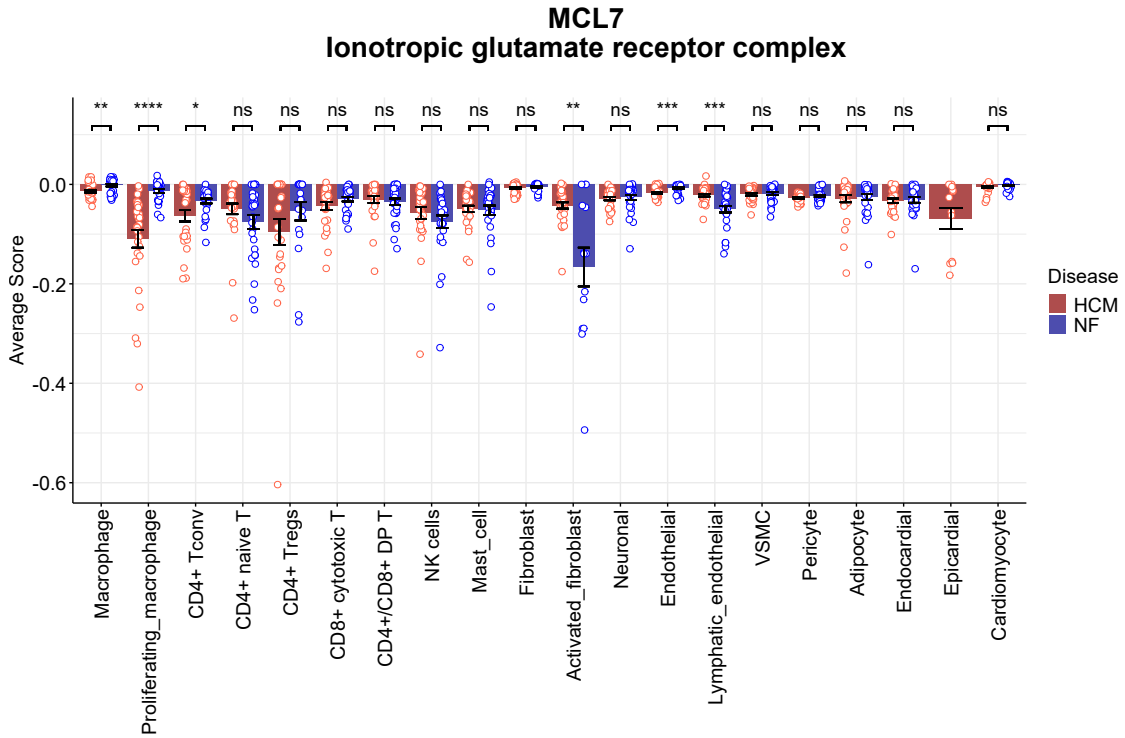

Figure D.8. Gene set scoring for MCL sub-cluster 7 of Cluster 1 (early up-regulation followed by a late surge) in late-stage human cell types.
This sub-cluster is a constituent of Cluster 1. The bar chart displays the gene set score for this specific sub-cluster across various cell types from late-stage human HCM snRNA-seq data. Scores were calculated for each sample using the `score_genes` function in `scanpy` v1.10.1 [267]. Bars represent the mean score, with error bars indicating the standard error of the mean. Statistical significance between disease and control samples was determined using a t-test, with p-values adjusted for multiple comparisons using the Benjamini-Hochberg method. Asterisks denote significance levels: * $p < 0.05$, ** $p < 0.01$, *** $p < 0.001$, **** $p < 0.0001$.

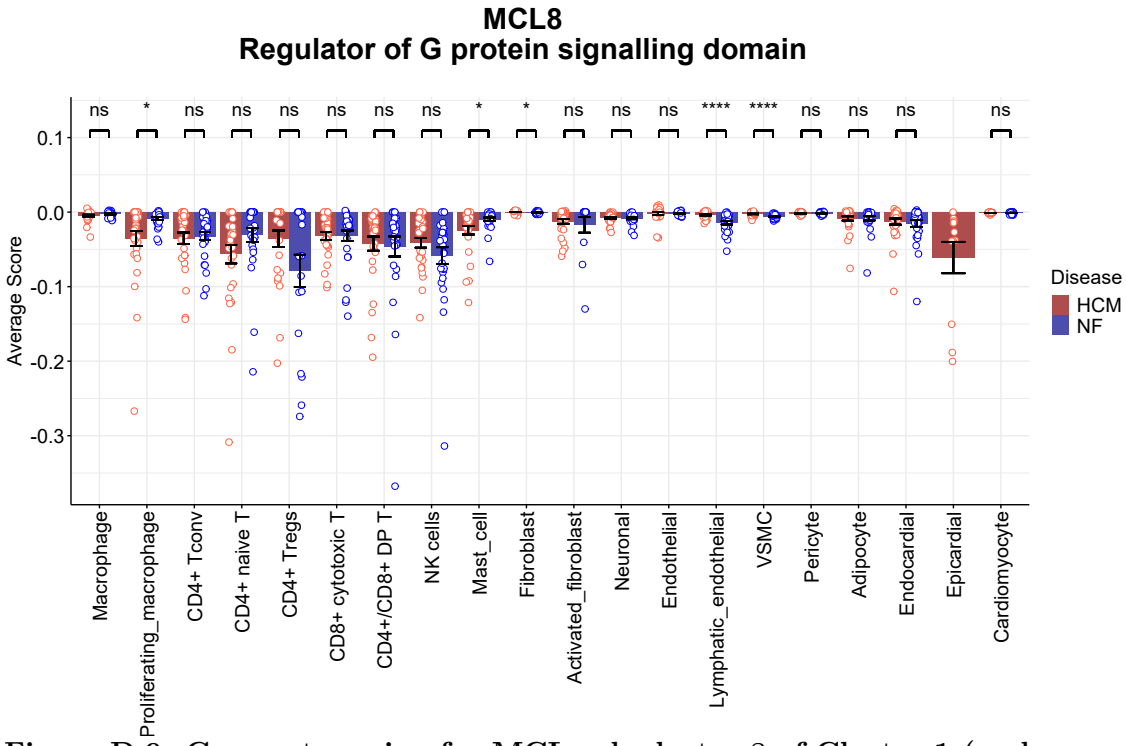

Figure D.9. Gene set scoring for MCL sub-cluster 8 of Cluster 1 (early up-regulation followed by a late surge) in late-stage human cell types.
This sub-cluster is a constituent of Cluster 1. The bar chart displays the gene set score for this specific sub-cluster across various cell types from late-stage human HCM snRNA-seq data. Scores were calculated for each sample using the `score_genes` function in `scanpy` v1.10.1 [267]. Bars represent the mean score, with error bars indicating the standard error of the mean. Statistical significance between disease and control samples was determined using a t-test, with p-values adjusted for multiple comparisons using the Benjamini-Hochberg method. Asterisks denote significance levels: * $p < 0.05$, ** $p < 0.01$, *** $p < 0.001$, **** $p < 0.0001$.

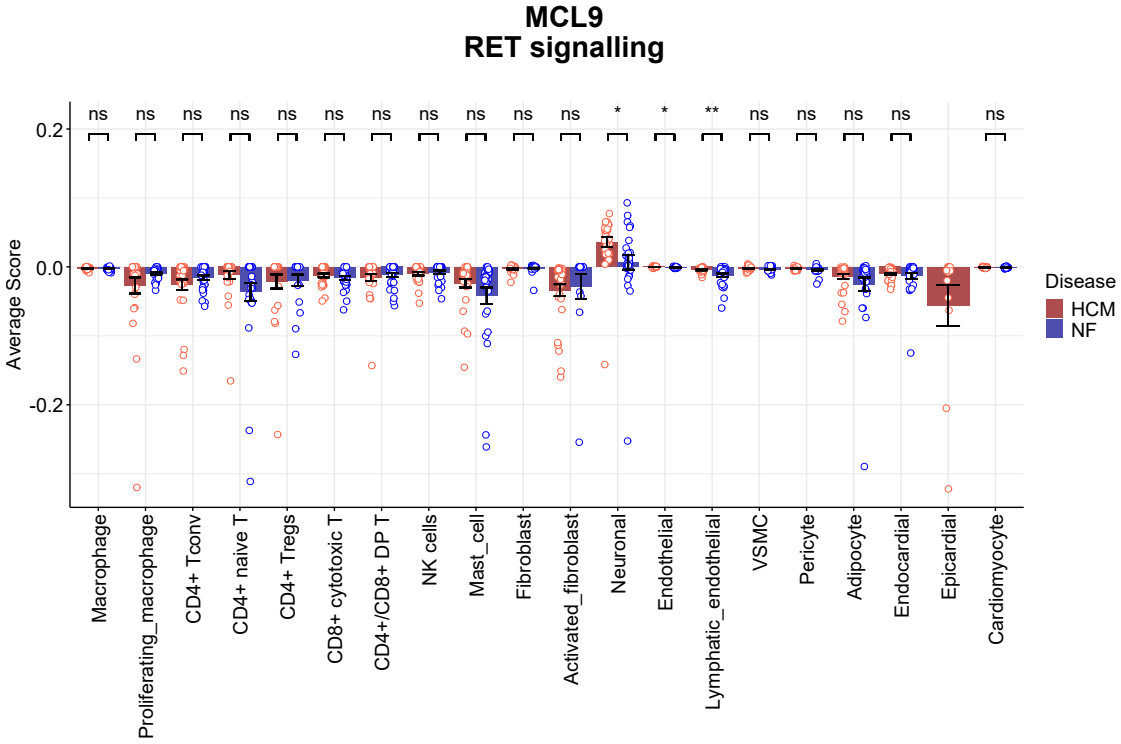

Figure D.10. Gene set scoring for MCL sub-cluster 9 of Cluster 1 (early up-regulation followed by a late surge) in late-stage human cell types. This sub-cluster is a constituent of Cluster 1. The bar chart displays the gene set score for this specific sub-cluster across various cell types from late-stage human HCM snRNA-seq data. Scores were calculated for each sample using the `score_genes` function in `scanpy` v1.10.1 [267]. Bars represent the mean score, with error bars indicating the standard error of the mean. Statistical significance between disease and control samples was determined using a t-test, with p-values adjusted for multiple comparisons using the Benjamini-Hochberg method. Asterisks denote significance levels: * $p < 0.05$, ** $p < 0.01$, *** $p < 0.001$, **** $p < 0.0001$.

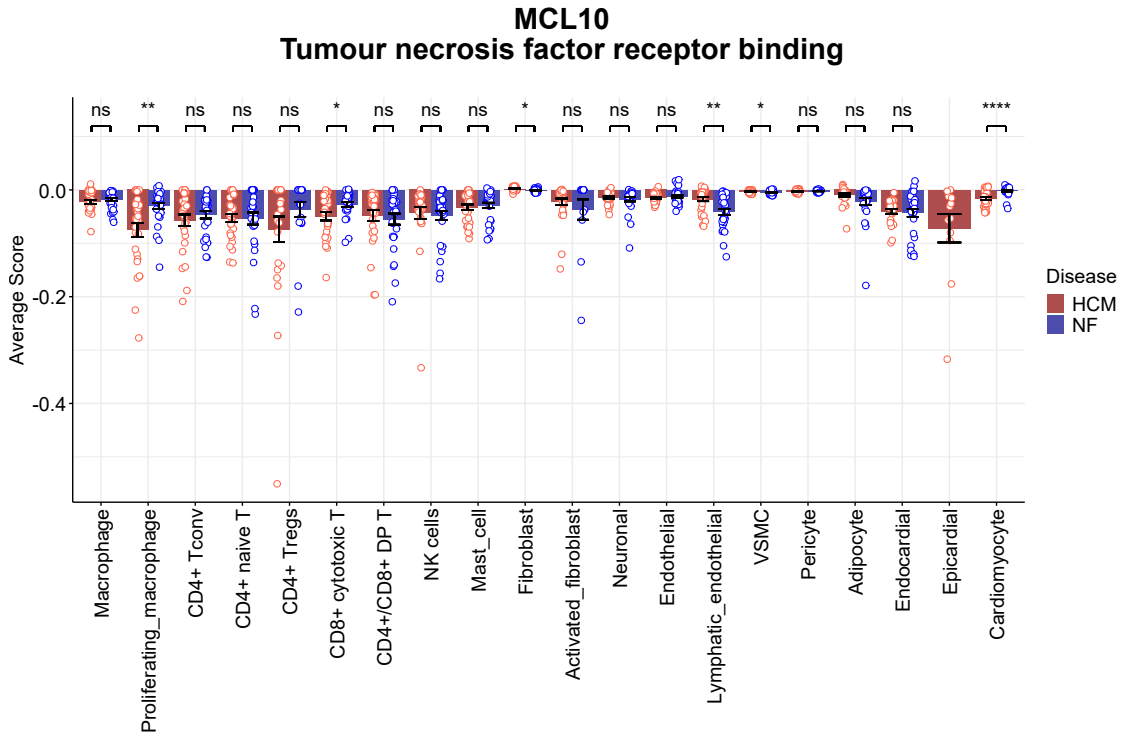

Figure D.11. Gene set scoring for MCL sub-cluster 10 of Cluster 1 (early up-regulation followed by a late surge) in late-stage human cell types. This sub-cluster is a constituent of Cluster 1. The bar chart displays the gene set score for this specific sub-cluster across various cell types from late-stage human HCM snRNA-seq data. Scores were calculated for each sample using the `score_genes` function in `scanpy` v1.10.1 [267]. Bars represent the mean score, with error bars indicating the standard error of the mean. Statistical significance between disease and control samples was determined using a t-test, with p-values adjusted for multiple comparisons using the Benjamini-Hochberg method. Asterisks denote significance levels: * $p < 0.05$, ** $p < 0.01$, *** $p < 0.001$, **** $p < 0.0001$.

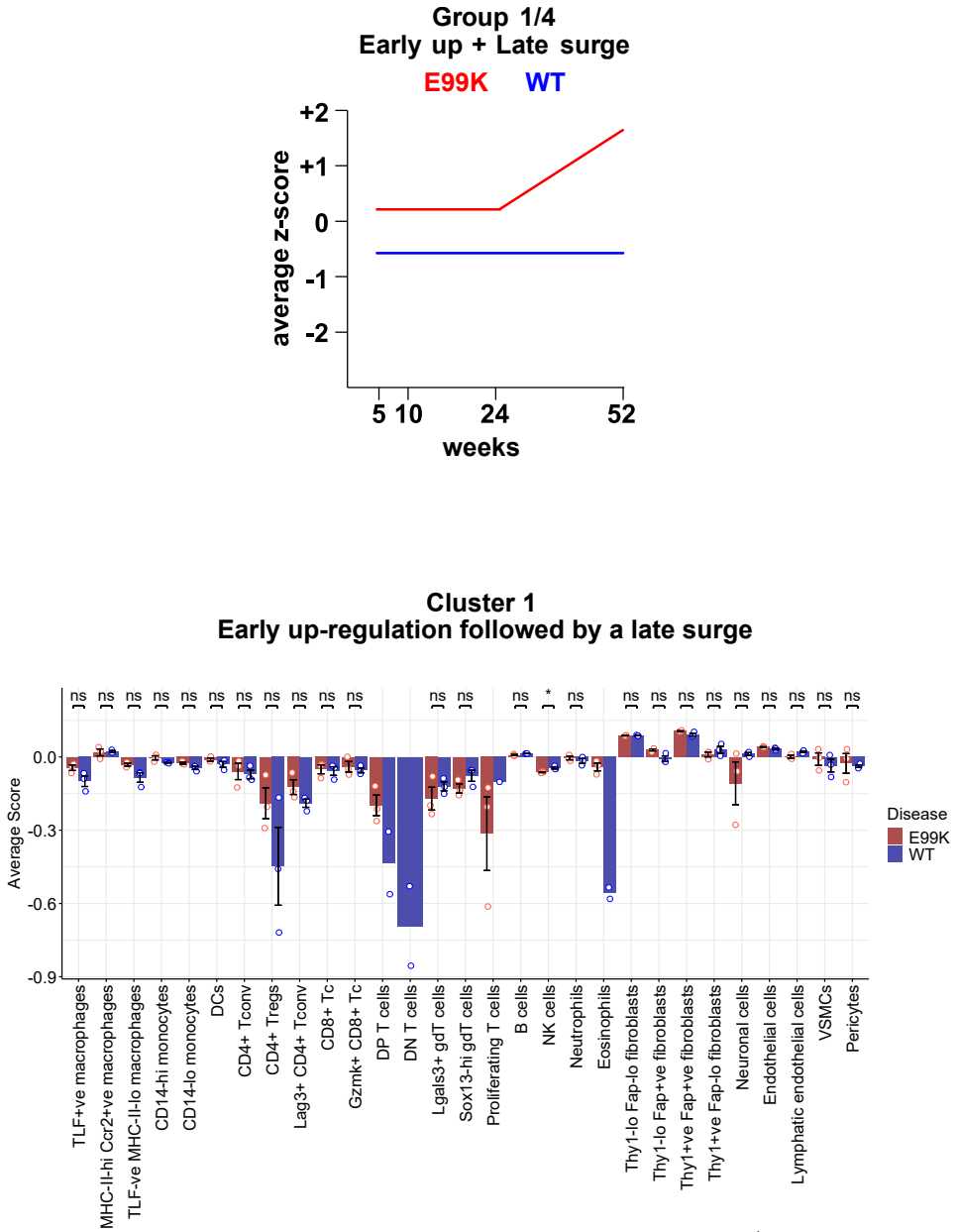

Figure D.12. Gene set scoring and statistics of cluster 1 (early up-regulation followed by a late surge) in late-stage mouse cell types. The upper panel schematically illustrates the temporal expression trend for Cluster 1, derived from bulk RNA-seq data of Actc1^{E99K} (red line) and wild-type (blue line) hearts over time. The lower panel displays the gene set score for all genes within Cluster 1 across various cell types identified in late-stage Actc1^{E99K} mouse scRNA-seq data. Scores were calculated for each sample using the `score_genes` function in `scanpy` v1.10.1 [267]. Bars represent the mean score, with error bars indicating the standard error of the mean. Statistical significance between disease and control samples was determined using a t-test, with p-values adjusted for multiple comparisons using the Benjamini-Hochberg method. Asterisks denote significance levels: * $p < 0.05$, ** $p < 0.01$, *** $p < 0.001$, **** $p < 0.0001$.

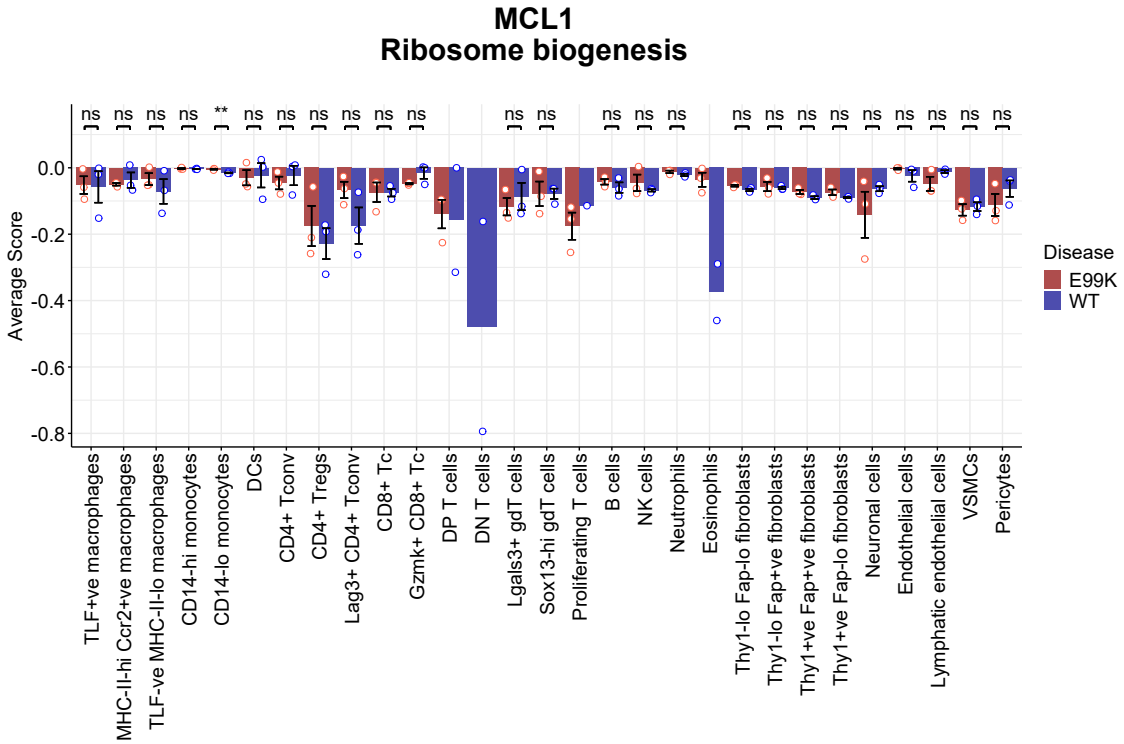

Figure D.13. Gene set scoring for MCL sub-cluster 1 of Cluster 1 (early up-regulation followed by a late surge) in late-stage mouse cell types. This sub-cluster is a constituent of Cluster 1. The bar chart displays the gene set score for this specific sub-cluster across various cell types from late-stage Actc1^{E99K} mouse scRNA-seq data. Scores were calculated for each sample using the `score_genes` function in `scanpy` v1.10.1 [267]. Bars represent the mean score, with error bars indicating the standard error of the mean. Statistical significance between disease and control samples was determined using a t-test, with p-values adjusted for multiple comparisons using the Benjamini-Hochberg method. Asterisks denote significance levels: * $p < 0.05$, ** $p < 0.01$, *** $p < 0.001$, **** $p < 0.0001$.

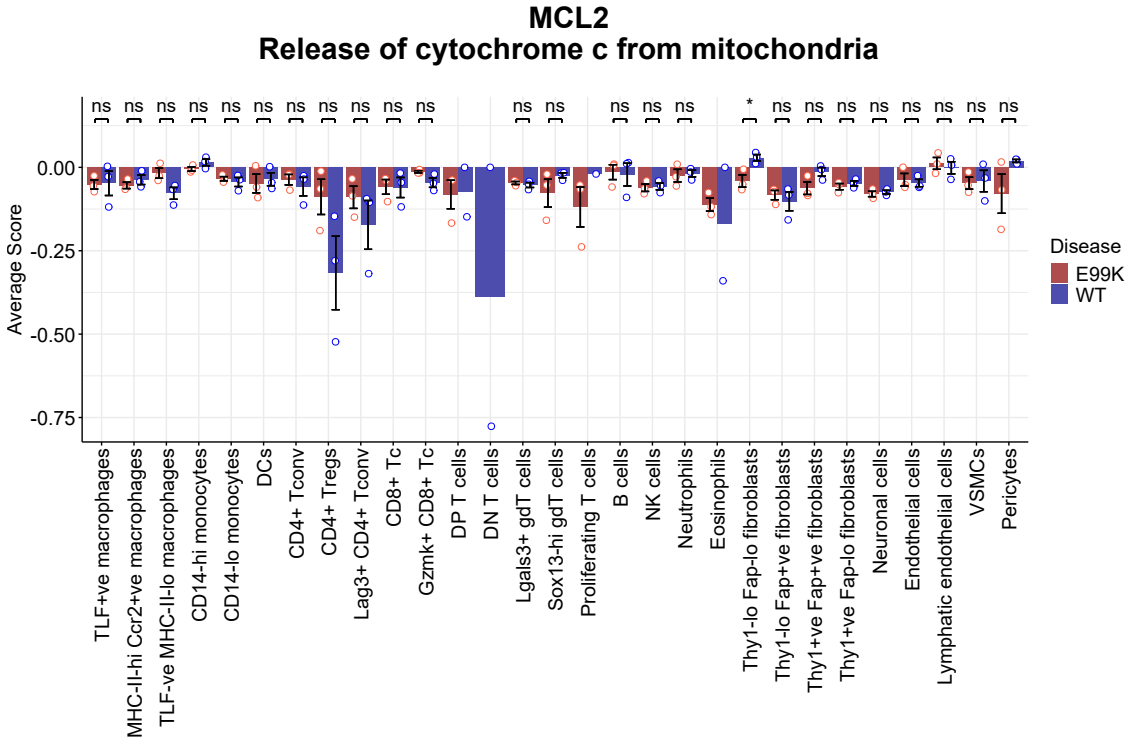

Figure D.14. Gene set scoring for MCL sub-cluster 2 of Cluster 1 (early up-regulation followed by a late surge) in late-stage mouse cell types. This sub-cluster is a constituent of Cluster 1. The bar chart displays the gene set score for this specific sub-cluster across various cell types from late-stage Actc1^{E99K} mouse scRNA-seq data. Scores were calculated for each sample using the `score_genes` function in `scanpy` v1.10.1 [267]. Bars represent the mean score, with error bars indicating the standard error of the mean. Statistical significance between disease and control samples was determined using a t-test, with p-values adjusted for multiple comparisons using the Benjamini-Hochberg method. Asterisks denote significance levels: * $p < 0.05$, ** $p < 0.01$, *** $p < 0.001$, **** $p < 0.0001$.

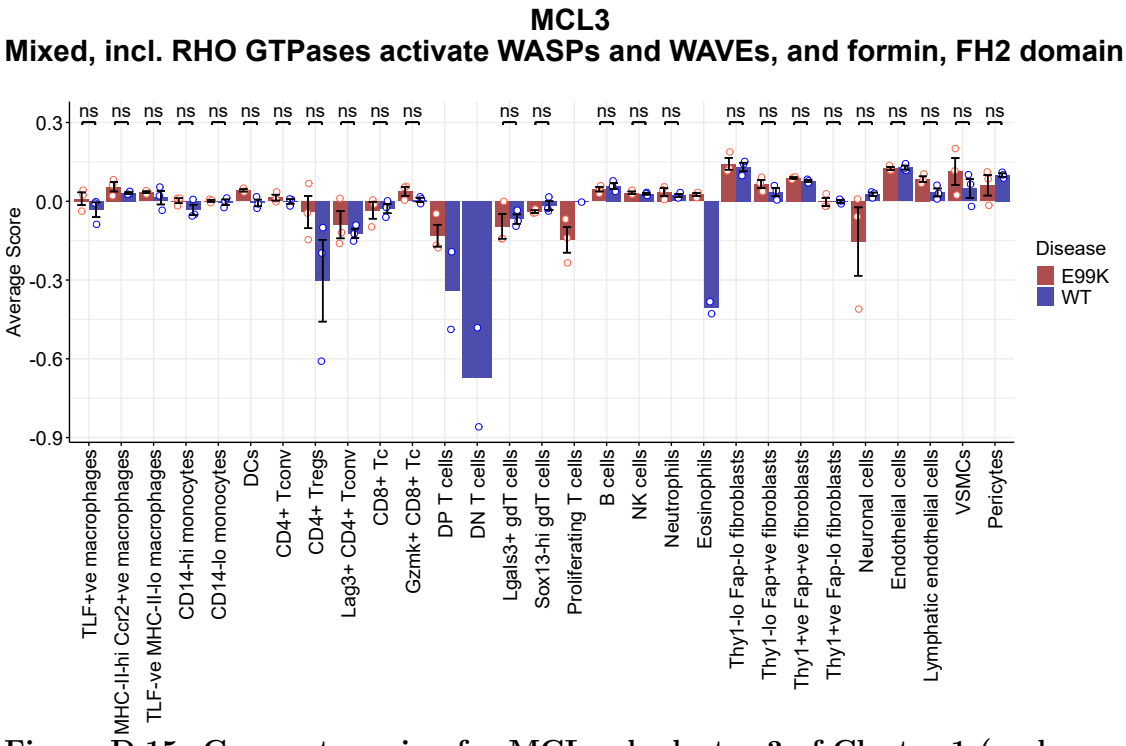

Figure D.15. Gene set scoring for MCL sub-cluster 3 of Cluster 1 (early up-regulation followed by a late surge) in late-stage mouse cell types. This sub-cluster is a constituent of Cluster 1. The bar chart displays the gene set score for this specific sub-cluster across various cell types from late-stage Actc1^{E99K} mouse scRNA-seq data. Scores were calculated for each sample using the `score_genes` function in `scanpy` v1.10.1 [267]. Bars represent the mean score, with error bars indicating the standard error of the mean. Statistical significance between disease and control samples was determined using a t-test, with p-values adjusted for multiple comparisons using the Benjamini-Hochberg method. Asterisks denote significance levels: * $p < 0.05$, ** $p < 0.01$, *** $p < 0.001$, **** $p < 0.0001$.

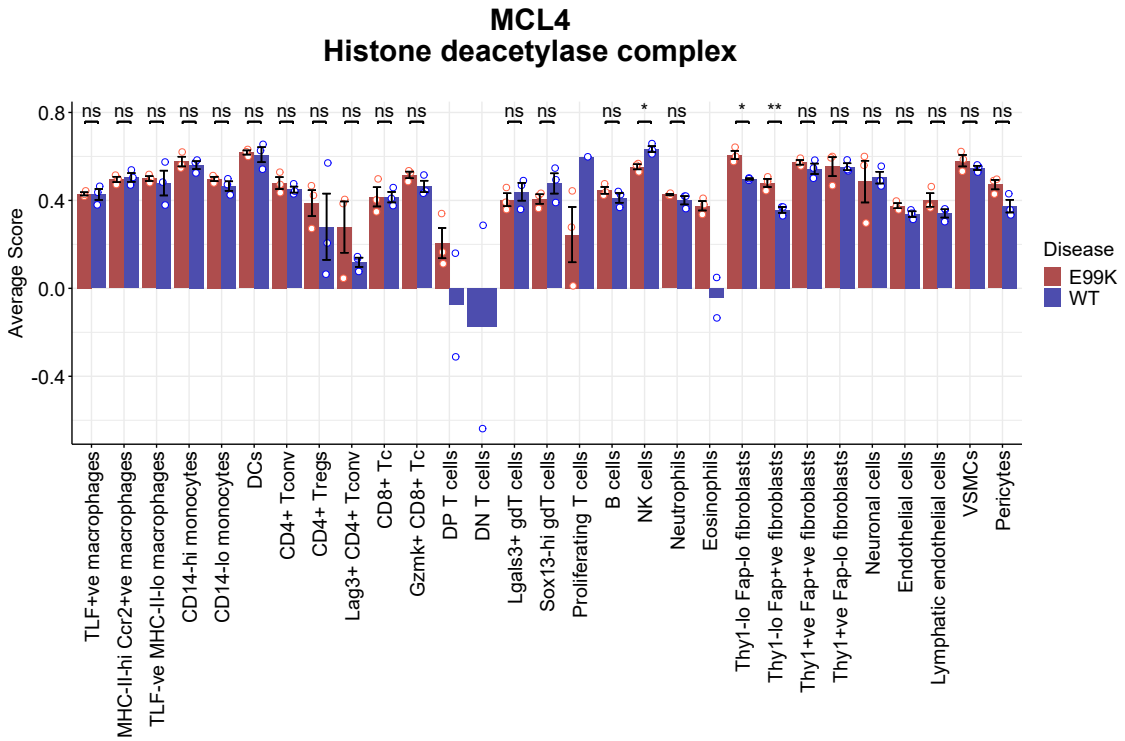

Figure D.16. Gene set scoring for MCL sub-cluster 4 of Cluster 1 (early up-regulation followed by a late surge) in late-stage mouse cell types. This sub-cluster is a constituent of Cluster 1. The bar chart displays the gene set score for this specific sub-cluster across various cell types from late-stage Actc1^{E99K} mouse scRNA-seq data. Scores were calculated for each sample using the `score_genes` function in `scanpy` v1.10.1 [267]. Bars represent the mean score, with error bars indicating the standard error of the mean. Statistical significance between disease and control samples was determined using a t-test, with p-values adjusted for multiple comparisons using the Benjamini-Hochberg method. Asterisks denote significance levels: * $p < 0.05$, ** $p < 0.01$, *** $p < 0.001$, **** $p < 0.0001$.

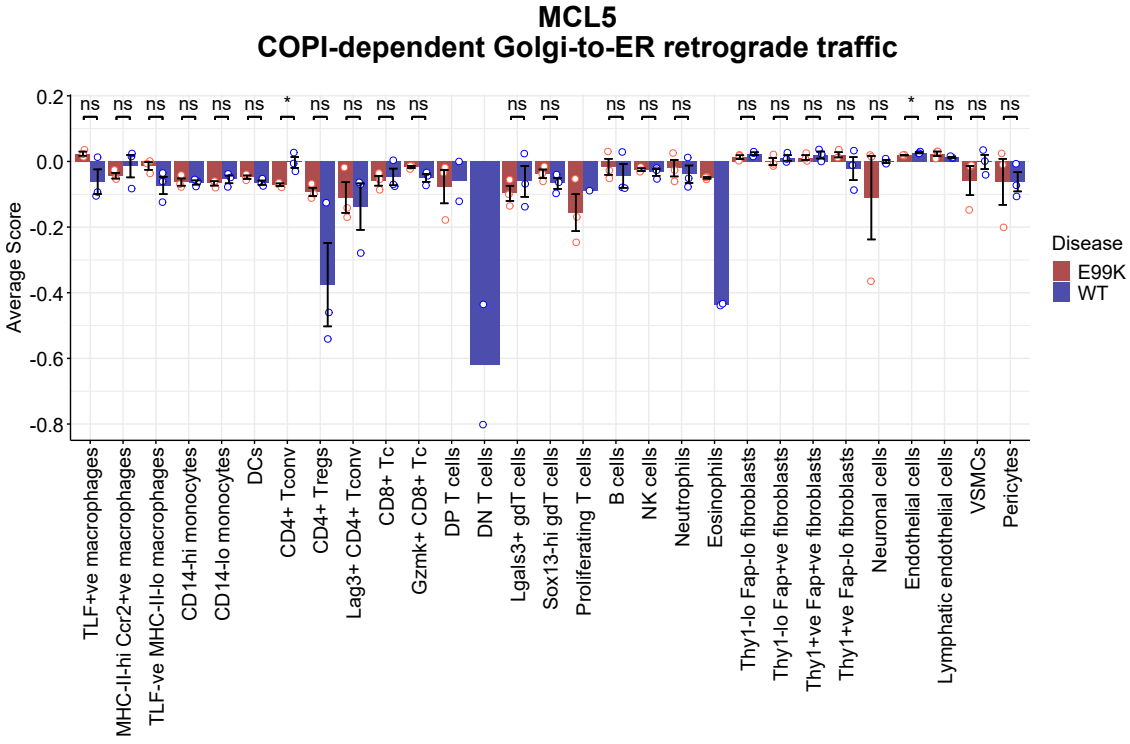

Figure D.17. Gene set scoring for MCL sub-cluster 5 of Cluster 1 (early up-regulation followed by a late surge) in late-stage mouse cell types. This sub-cluster is a constituent of Cluster 1. The bar chart displays the gene set score for this specific sub-cluster across various cell types from late-stage Actc1^{E99K} mouse scRNA-seq data. Scores were calculated for each sample using the `score_genes` function in `scanpy` v1.10.1 [267]. Bars represent the mean score, with error bars indicating the standard error of the mean. Statistical significance between disease and control samples was determined using a t-test, with p-values adjusted for multiple comparisons using the Benjamini-Hochberg method. Asterisks denote significance levels: * $p < 0.05$, ** $p < 0.01$, *** $p < 0.001$, **** $p < 0.0001$.

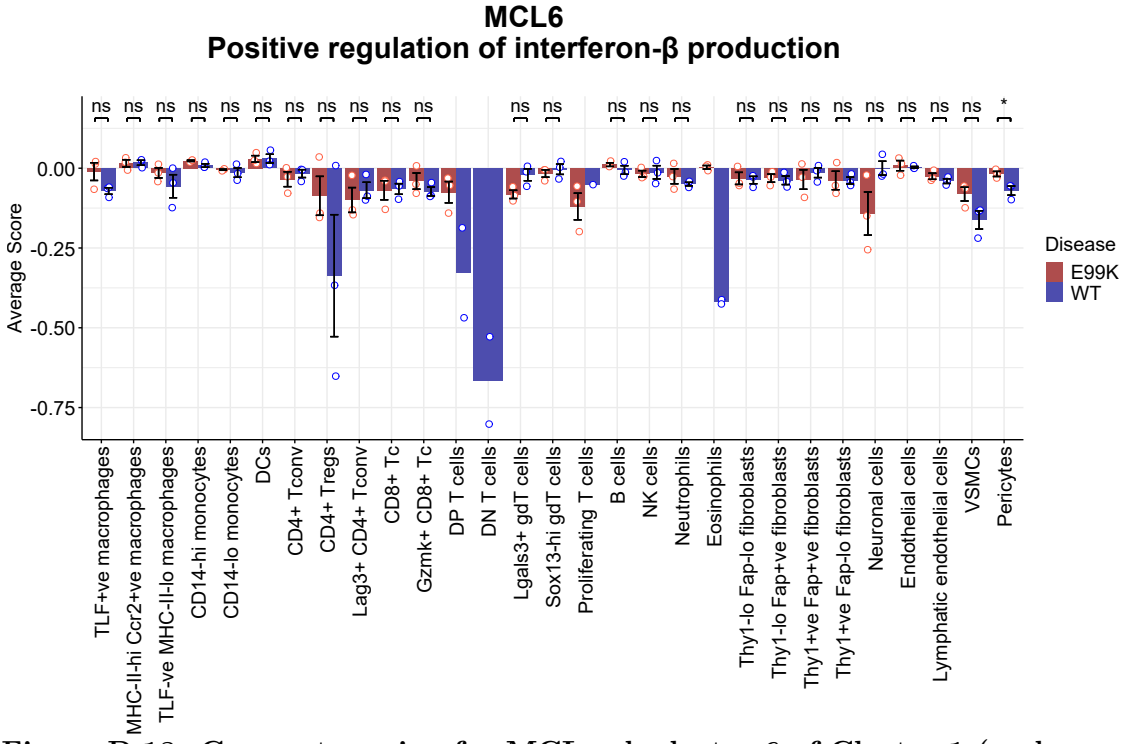

Figure D.18. Gene set scoring for MCL sub-cluster 6 of Cluster 1 (early up-regulation followed by a late surge) in late-stage mouse cell types. This sub-cluster is a constituent of Cluster 1. The bar chart displays the gene set score for this specific sub-cluster across various cell types from late-stage $Actc1^{E99K}$ mouse scRNA-seq data. Scores were calculated for each sample using the `score_genes` function in `scanpy` v1.10.1 [267]. Bars represent the mean score, with error bars indicating the standard error of the mean. Statistical significance between disease and control samples was determined using a t-test, with p-values adjusted for multiple comparisons using the Benjamini-Hochberg method. Asterisks denote significance levels: * $p < 0.05$, ** $p < 0.01$, *** $p < 0.001$, **** $p < 0.0001$.

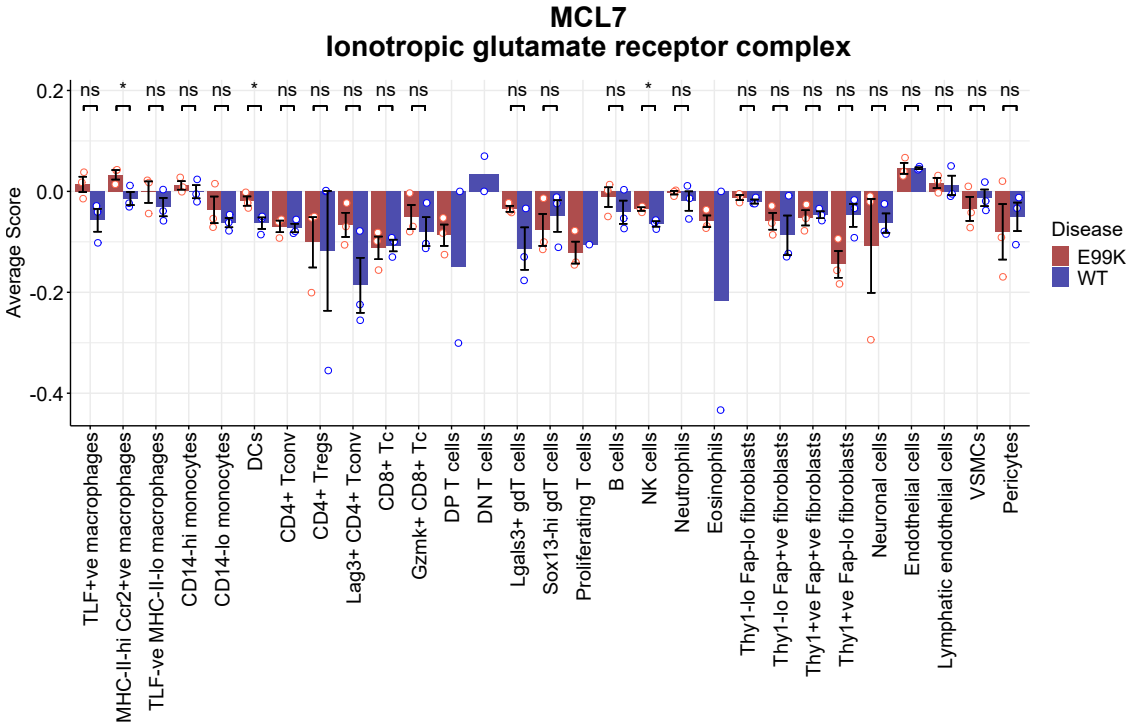

Figure D.19. Gene set scoring for MCL sub-cluster 7 of Cluster 1 (early up-regulation followed by a late surge) in late-stage mouse cell types. This sub-cluster is a constituent of Cluster 1. The bar chart displays the gene set score for this specific sub-cluster across various cell types from late-stage Actc1^{E99K} mouse scRNA-seq data. Scores were calculated for each sample using the `score_genes` function in `scanpy` v1.10.1 [267]. Bars represent the mean score, with error bars indicating the standard error of the mean. Statistical significance between disease and control samples was determined using a t-test, with p-values adjusted for multiple comparisons using the Benjamini-Hochberg method. Asterisks denote significance levels: * $p < 0.05$, ** $p < 0.01$, *** $p < 0.001$, **** $p < 0.0001$.

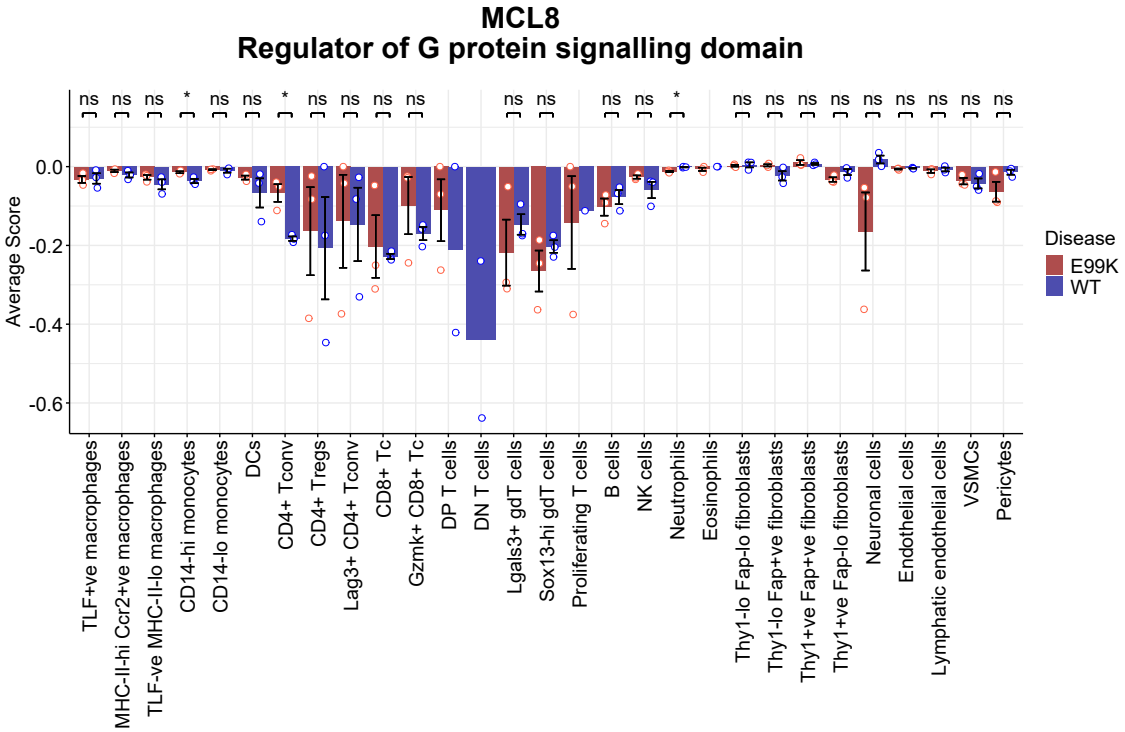

Figure D.20. Gene set scoring for MCL sub-cluster 8 of Cluster 1 (early up-regulation followed by a late surge) in late-stage mouse cell types. This sub-cluster is a constituent of Cluster 1. The bar chart displays the gene set score for this specific sub-cluster across various cell types from late-stage Actc1^{E99K} mouse scRNA-seq data. Scores were calculated for each sample using the `score_genes` function in `scanpy` v1.10.1 [267]. Bars represent the mean score, with error bars indicating the standard error of the mean. Statistical significance between disease and control samples was determined using a t-test, with p-values adjusted for multiple comparisons using the Benjamini-Hochberg method. Asterisks denote significance levels: * $p < 0.05$, ** $p < 0.01$, *** $p < 0.001$, **** $p < 0.0001$.

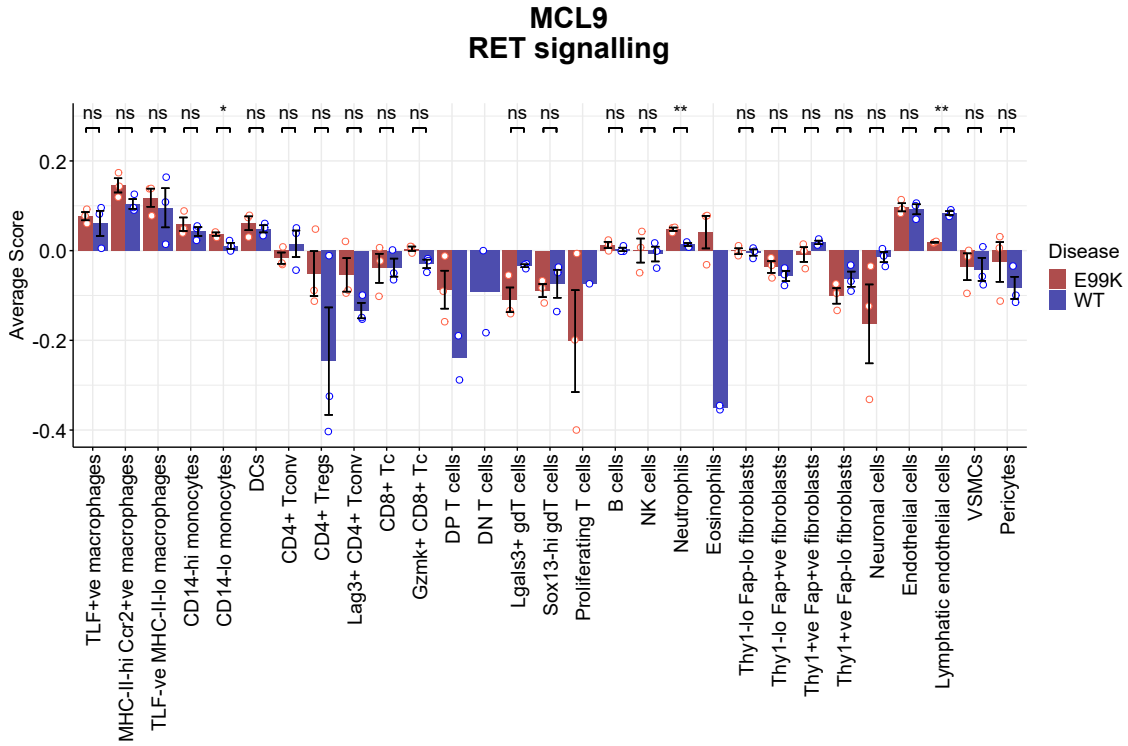

Figure D.21. Gene set scoring for MCL sub-cluster 9 of Cluster 1 (early up-regulation followed by a late surge) in late-stage mouse cell types. This sub-cluster is a constituent of Cluster 1. The bar chart displays the gene set score for this specific sub-cluster across various cell types from late-stage Actc1^{E99K} mouse scRNA-seq data. Scores were calculated for each sample using the `score_genes` function in `scanpy` v1.10.1 [267]. Bars represent the mean score, with error bars indicating the standard error of the mean. Statistical significance between disease and control samples was determined using a t-test, with p-values adjusted for multiple comparisons using the Benjamini-Hochberg method. Asterisks denote significance levels: * $p < 0.05$, ** $p < 0.01$, *** $p < 0.001$, **** $p < 0.0001$.

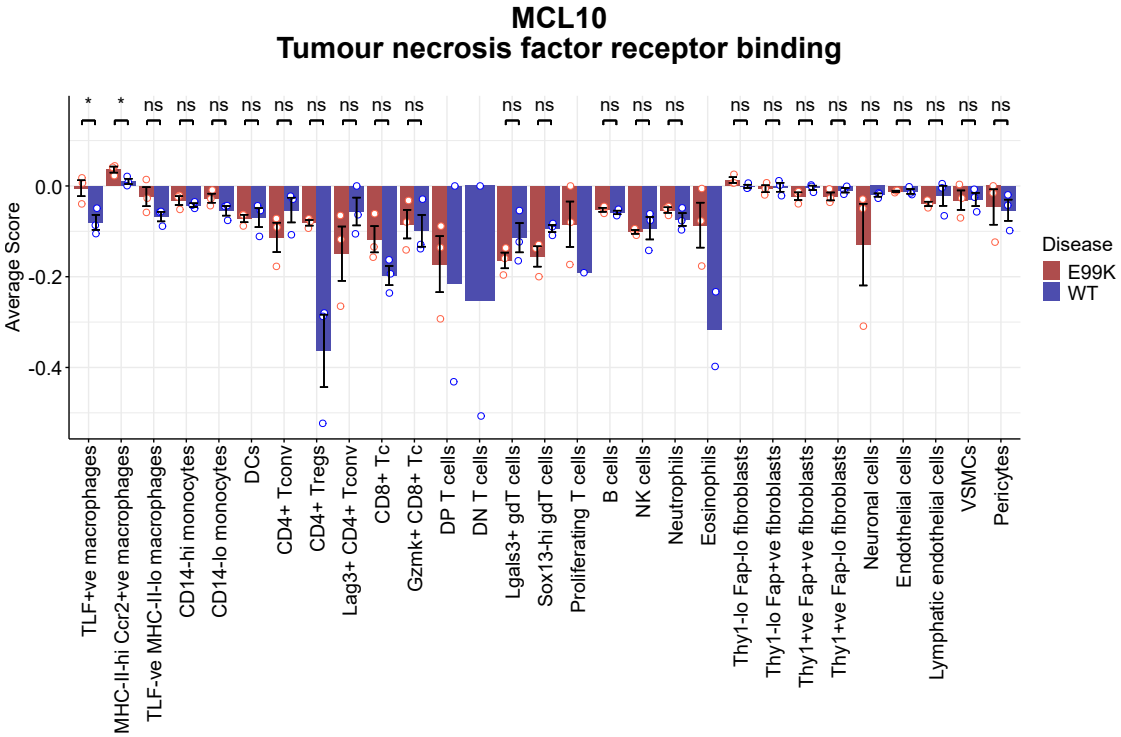

Figure D.22. Gene set scoring for MCL sub-cluster 10 of Cluster 1 (early up-regulation followed by a late surge) in late-stage mouse cell types. This sub-cluster is a constituent of Cluster 1. The bar chart displays the gene set score for this specific sub-cluster across various cell types from late-stage Actc1^{E99K} mouse scRNA-seq data. Scores were calculated for each sample using the `score_genes` function in `scanpy` v1.10.1 [267]. Bars represent the mean score, with error bars indicating the standard error of the mean. Statistical significance between disease and control samples was determined using a t-test, with p-values adjusted for multiple comparisons using the Benjamini-Hochberg method. Asterisks denote significance levels: * $p < 0.05$, ** $p < 0.01$, *** $p < 0.001$, **** $p < 0.0001$.

Cluster 4, also exhibiting an early up-regulation followed by a late surge, was primarily associated with immune response and inflammation (Figures D.23 and D.34). Sub-cluster analysis highlighted cytokine-cytokine receptor interaction (MCL sub-cluster 1; Figure D.24), adaptive immune response (MCL sub-cluster 2; Figure D.25), antifungal and immunoglobulin related processes (MCL sub-cluster 3; Figure D.26), complement and coagulation cascades (MCL sub-cluster 4; Figure D.27), FcϵRI-mediated signalling and B cell receptor complex formation (MCL sub-cluster 5; Figure D.28), interferon-β response and antiviral mechanisms (MCL sub-cluster 6; Figure D.29), plasma lipoprotein particles (MCL sub-cluster 7; Figure D.30), WNT signalling (MCL sub-cluster 8; Figure D.31),

phosphatidylcholine metabolism (MCL sub-cluster 9; Figure D.32), and a largely uncharacterised sub-cluster containing GTPase related genes (MCL sub-cluster 10; Figure D.33). In late-stage human HCM, the overall cluster 4 signature was significantly upregulated in activated fibroblasts, NK cells, lymphatic endothelial cells, VSMCs, and cardiomyocytes, while downregulated in proliferating macrophages (Figure D.23). Analysis of individual sub-clusters revealed further cell-type specific patterns. The cytokine-cytokine receptor interaction sub-cluster (MCL sub-cluster 1; Figure D.24) showed a similar pattern to the overall cluster, with upregulation in activated fibroblasts, NK cells, lymphatic endothelial cells, and VSMCs. The adaptive immune response sub-cluster (MCL sub-cluster 2; Figure D.25) was upregulated in Tregs and downregulated in activated fibroblasts, suggesting a complex interplay between immune cell activation and fibroblast responses in late-stage HCM. In the mouse scRNA-seq data, the overall cluster 4 signature was upregulated in two fibroblast populations ($Thy1^{lo}Fap^{lo}$ and $Thy1^{lo}Fap^{+}$ fibroblasts) and downregulated in B cells (Figure D.34). Sub-cluster analysis revealed upregulation of the cytokine-cytokine receptor interaction sub-cluster (MCL sub-cluster 1; Figure D.35) in $TLF^{-}MHC\text{-}II^{lo}$ macrophages and $Thy1^{lo}Fap^{+}$ fibroblasts. The adaptive immune response sub-cluster (MCL sub-cluster 2; Figure D.36) was downregulated in several immune cell populations, including $CD14^{lo}$ monocytes, $\gamma\delta$T cells, NK cells, and neutrophils.

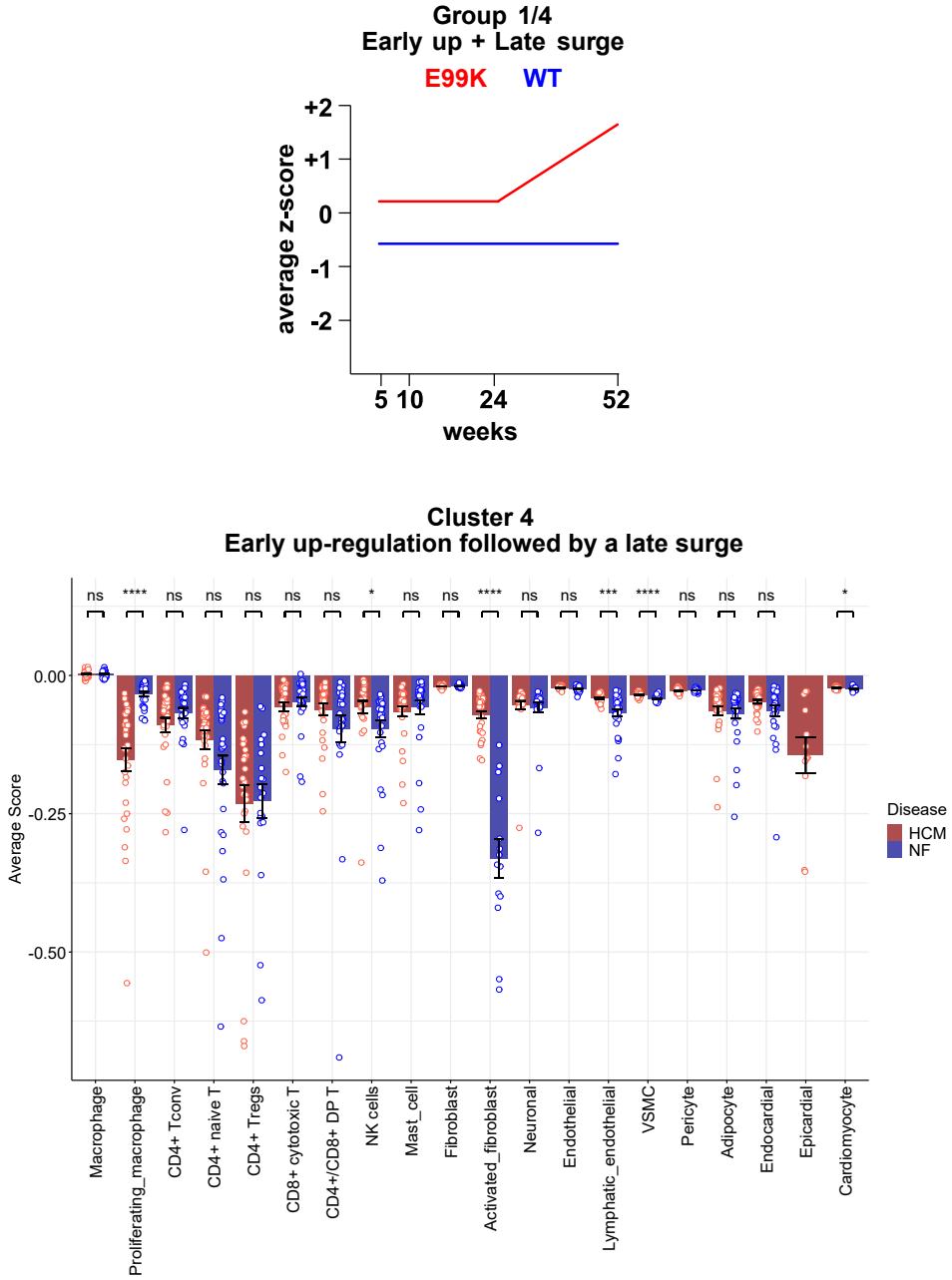

Figure D.23. Gene set scoring and statistics of Cluster 4 (early up-regulation followed by a late surge) in late-stage human cell types. The upper panel schematically illustrates the temporal expression trend for Cluster 4, derived from bulk RNA-seq data of Actc1^{E99K} (red line) and wild-type (blue line) hearts over time. The lower panel displays the gene set score for all genes within Cluster 4 across various cell types identified in late-stage human HCM snRNA-seq data. Scores were calculated for each sample using the `score_genes` function in `scanpy` v1.10.1 [267]. Bars represent the mean score, with error bars indicating the standard error of the mean. Statistical significance between disease and control samples was determined using a t-test, with p-values adjusted for multiple comparisons using the Benjamini-Hochberg method. Asterisks denote significance levels: * $p < 0.05$, ** $p < 0.01$, *** $p < 0.001$, **** $p < 0.0001$.

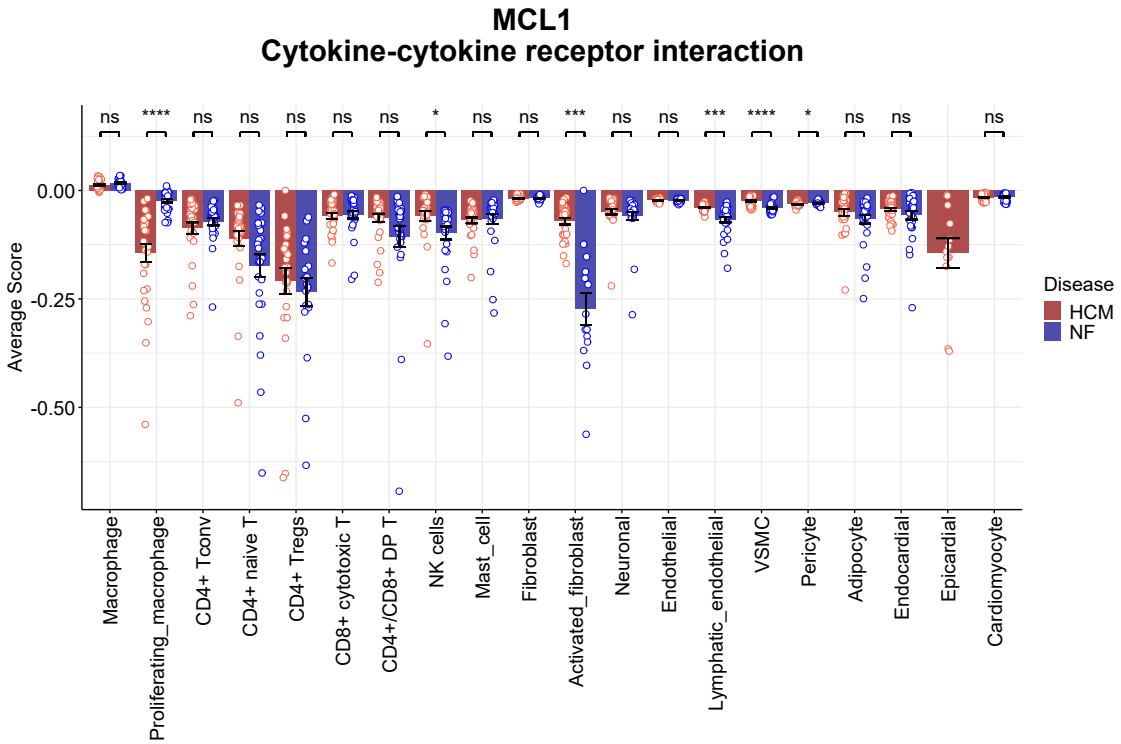

Figure D.24. Gene set scoring for MCL sub-cluster 1 of Cluster 4 (early up-regulation followed by a late surge) in late-stage human cell types. This sub-cluster is a constituent of Cluster 4. The bar chart displays the gene set score for this specific sub-cluster across various cell types from late-stage human HCM snRNA-seq data. Scores were calculated for each sample using the `score_genes` function in `scanpy` v1.10.1 [267]. Bars represent the mean score, with error bars indicating the standard error of the mean. Statistical significance between disease and control samples was determined using a t-test, with p-values adjusted for multiple comparisons using the Benjamini-Hochberg method. Asterisks denote significance levels: * $p < 0.05$, ** $p < 0.01$, *** $p < 0.001$, **** $p < 0.0001$.

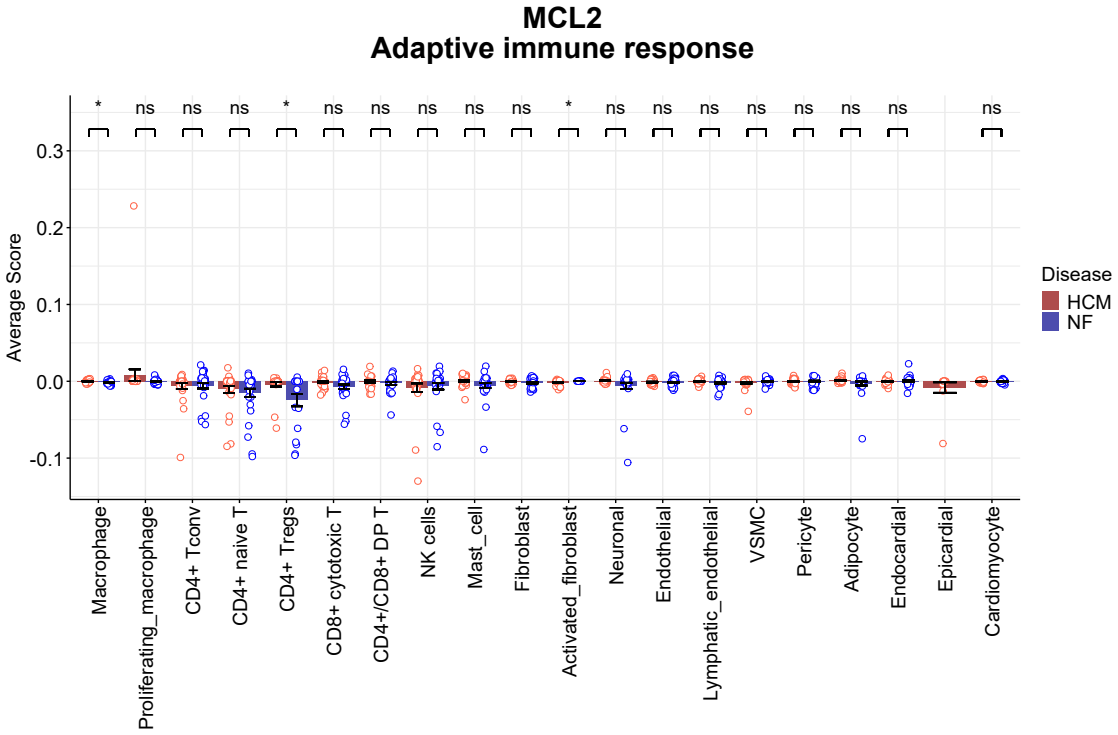

Figure D.25. Gene set scoring for MCL sub-cluster 2 of Cluster 4 (early up-regulation followed by a late surge) in late-stage human cell types. This sub-cluster is a constituent of Cluster 4. The bar chart displays the gene set score for this specific sub-cluster across various cell types from late-stage human HCM snRNA-seq data. Scores were calculated for each sample using the `score_genes` function in `scanpy` v1.10.1 [267]. Bars represent the mean score, with error bars indicating the standard error of the mean. Statistical significance between disease and control samples was determined using a t-test, with p-values adjusted for multiple comparisons using the Benjamini-Hochberg method. Asterisks denote significance levels: * $p < 0.05$, ** $p < 0.01$, *** $p < 0.001$, **** $p < 0.0001$.

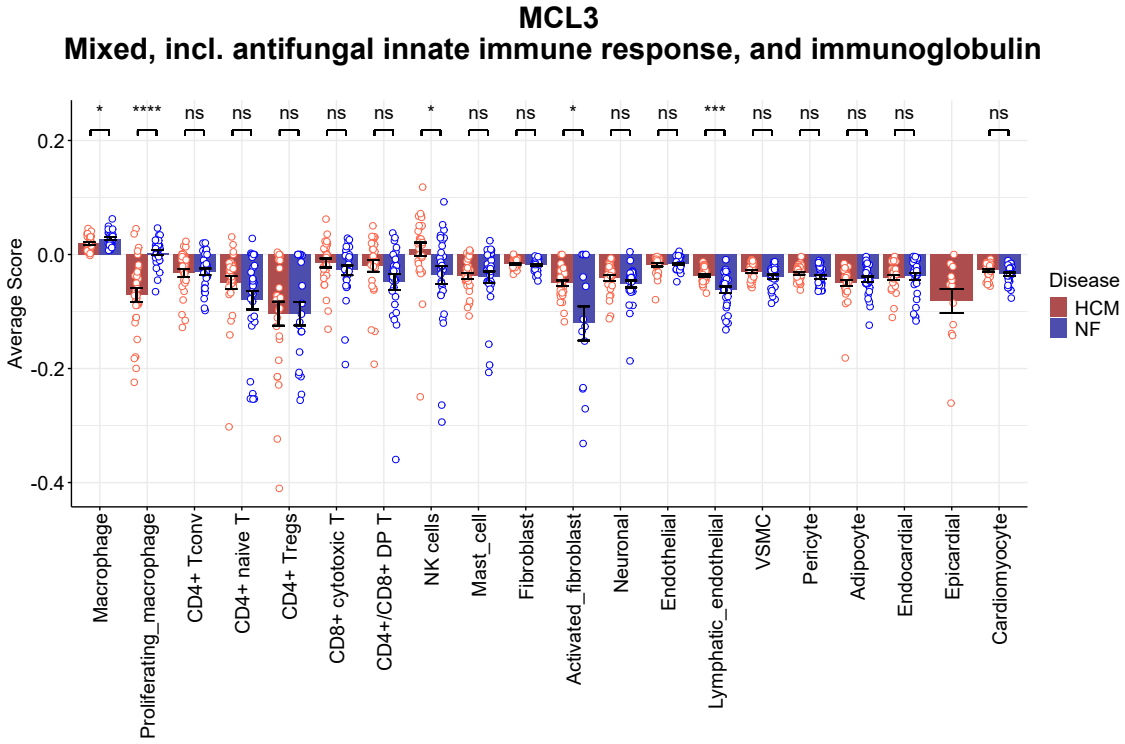

Figure D.26. Gene set scoring for MCL sub-cluster 3 of Cluster 4 (early up-regulation followed by a late surge) in late-stage human cell types. This sub-cluster is a constituent of Cluster 4. The bar chart displays the gene set score for this specific sub-cluster across various cell types from late-stage human HCM snRNA-seq data. Scores were calculated for each sample using the `score_genes` function in `scanpy` v1.10.1 [267]. Bars represent the mean score, with error bars indicating the standard error of the mean. Statistical significance between disease and control samples was determined using a t-test, with p-values adjusted for multiple comparisons using the Benjamini-Hochberg method. Asterisks denote significance levels: * $p < 0.05$, ** $p < 0.01$, *** $p < 0.001$, **** $p < 0.0001$.

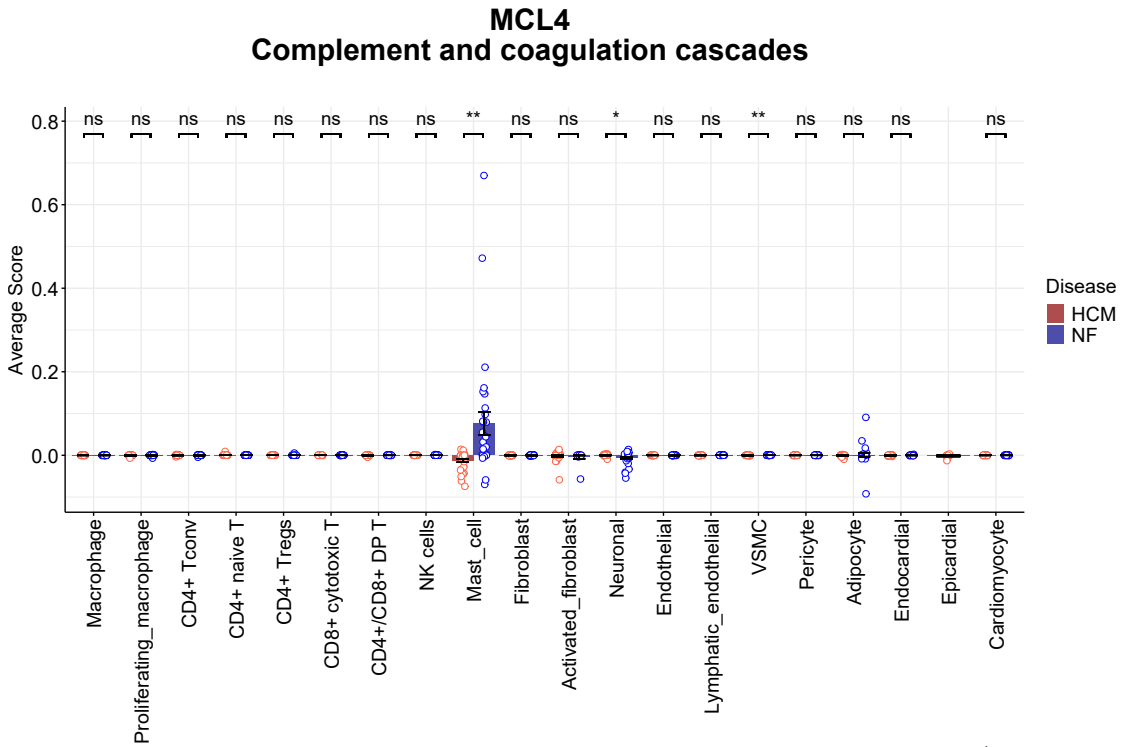

Figure D.27. Gene set scoring for MCL sub-cluster 4 of Cluster 4 (early up-regulation followed by a late surge) in late-stage human cell types. This sub-cluster is a constituent of Cluster 4. The bar chart displays the gene set score for this specific sub-cluster across various cell types from late-stage human HCM snRNA-seq data. Scores were calculated for each sample using the `score_genes` function in `scanpy` v1.10.1 [267]. Bars represent the mean score, with error bars indicating the standard error of the mean. Statistical significance between disease and control samples was determined using a t-test, with p-values adjusted for multiple comparisons using the Benjamini-Hochberg method. Asterisks denote significance levels: * $p < 0.05$, ** $p < 0.01$, *** $p < 0.001$, **** $p < 0.0001$.

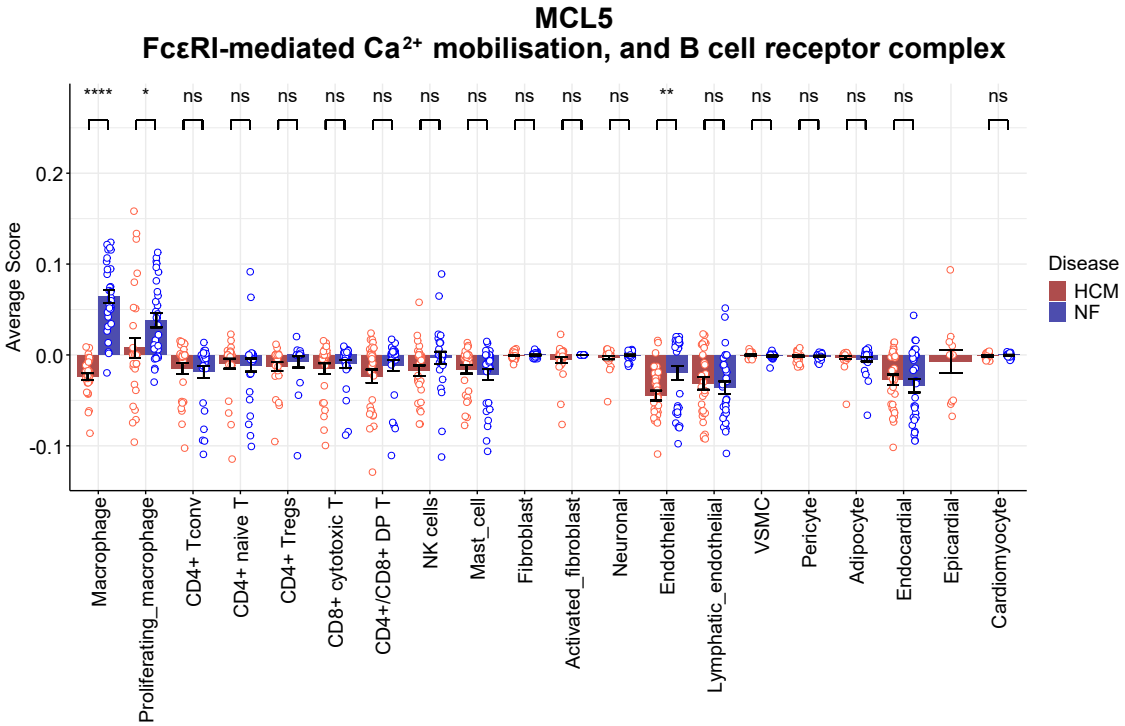

Figure D.28. Gene set scoring for MCL sub-cluster 5 of Cluster 4 (early up-regulation followed by a late surge) in late-stage human cell types. This sub-cluster is a constituent of Cluster 4. The bar chart displays the gene set score for this specific sub-cluster across various cell types from late-stage human HCM snRNA-seq data. Scores were calculated for each sample using the `score_genes` function in `scanpy` v1.10.1 [267]. Bars represent the mean score, with error bars indicating the standard error of the mean. Statistical significance between disease and control samples was determined using a t-test, with p-values adjusted for multiple comparisons using the Benjamini-Hochberg method. Asterisks denote significance levels: * $p < 0.05$, ** $p < 0.01$, *** $p < 0.001$, **** $p < 0.0001$.

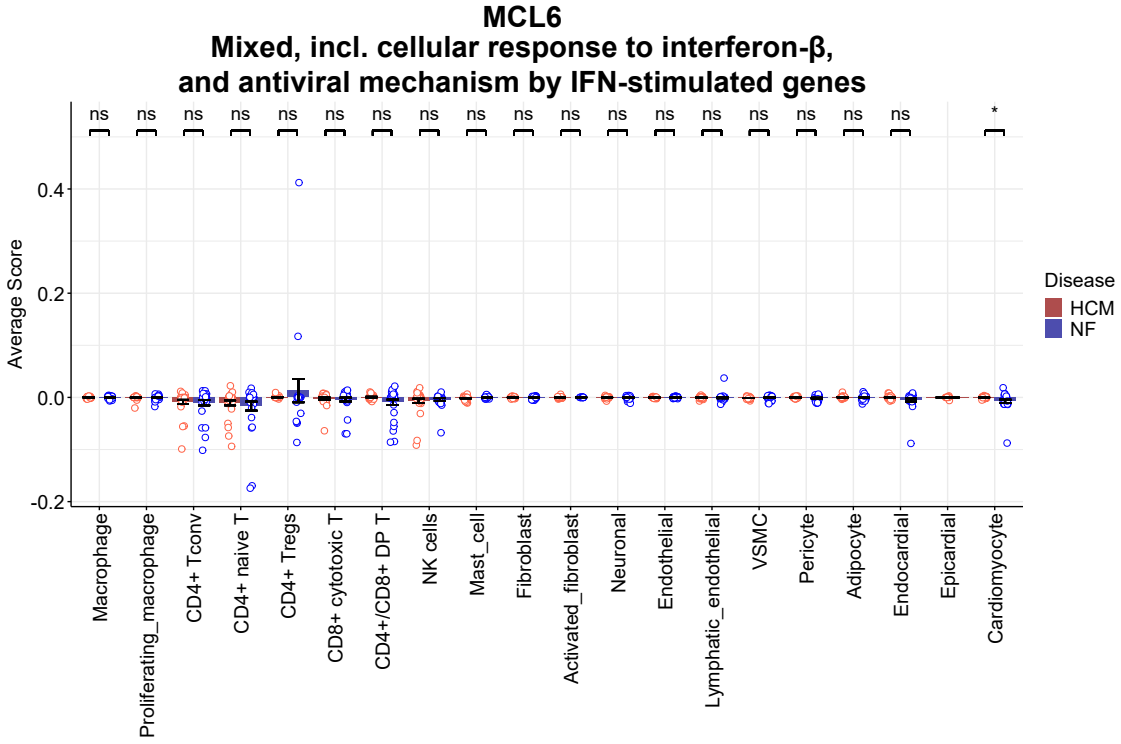

Figure D.29. Gene set scoring for MCL sub-cluster 6 of Cluster 4 (early up-regulation followed by a late surge) in late-stage human cell types. This sub-cluster is a constituent of Cluster 4. The bar chart displays the gene set score for this specific sub-cluster across various cell types from late-stage human HCM snRNA-seq data. Scores were calculated for each sample using the `score_genes` function in `scanpy` v1.10.1 [267]. Bars represent the mean score, with error bars indicating the standard error of the mean. Statistical significance between disease and control samples was determined using a t-test, with p-values adjusted for multiple comparisons using the Benjamini-Hochberg method. Asterisks denote significance levels: * $p < 0.05$, ** $p < 0.01$, *** $p < 0.001$, **** $p < 0.0001$.

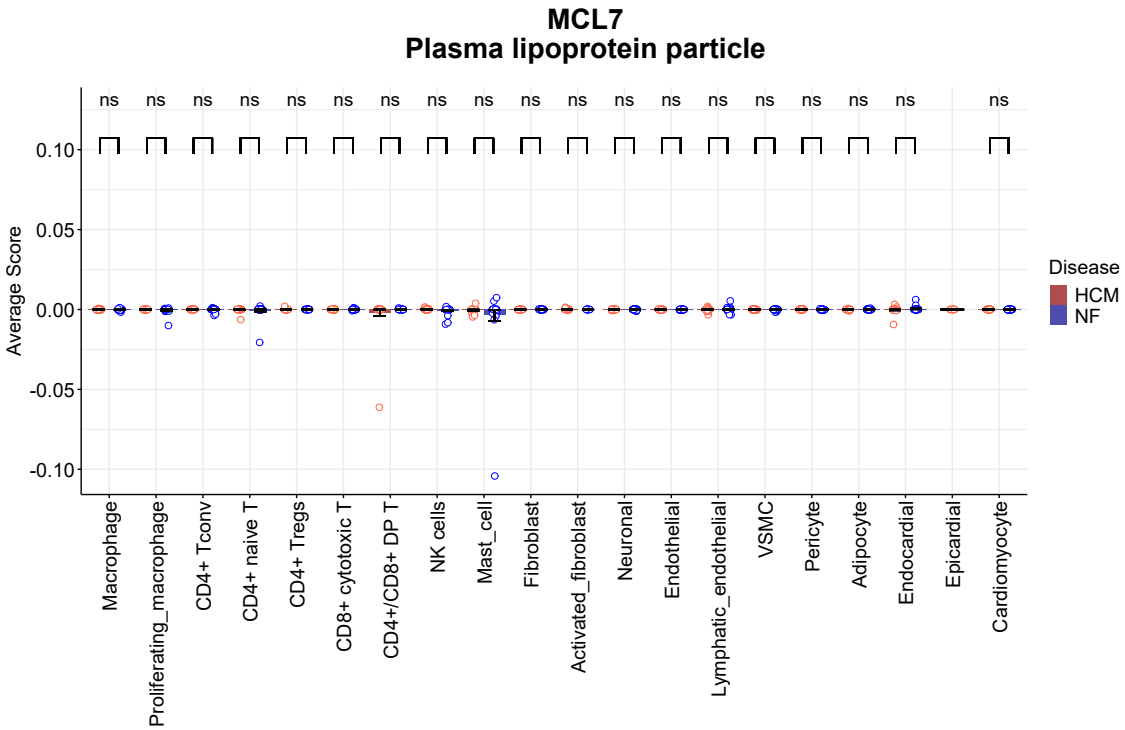

Figure D.30. Gene set scoring for MCL sub-cluster 7 of Cluster 4 (early up-regulation followed by a late surge) in late-stage human cell types. This sub-cluster is a constituent of Cluster 4. The bar chart displays the gene set score for this specific sub-cluster across various cell types from late-stage human HCM snRNA-seq data. Scores were calculated for each sample using the `score_genes` function in `scanpy` v1.10.1 [267]. Bars represent the mean score, with error bars indicating the standard error of the mean. Statistical significance between disease and control samples was determined using a t-test, with p-values adjusted for multiple comparisons using the Benjamini-Hochberg method. Asterisks denote significance levels: * $p < 0.05$, ** $p < 0.01$, *** $p < 0.001$, **** $p < 0.0001$.

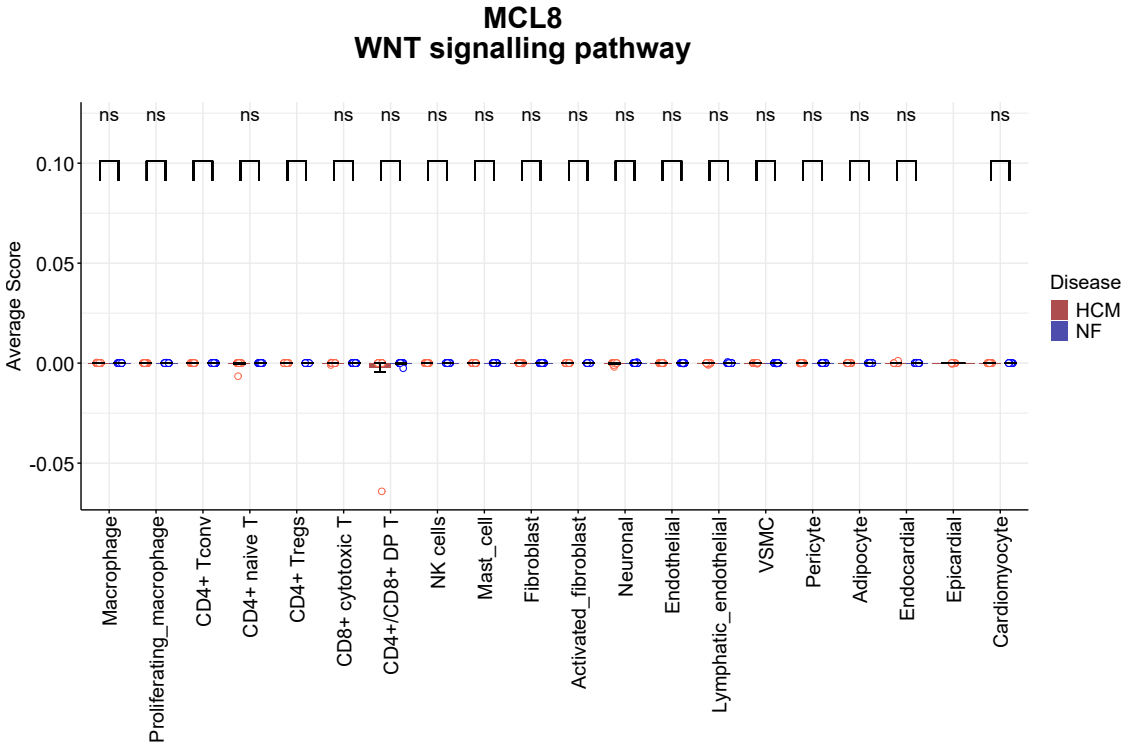

Figure D.31. Gene set scoring for MCL sub-cluster 8 of Cluster 4 (early up-regulation followed by a late surge) in late-stage human cell types. This sub-cluster is a constituent of Cluster 4. The bar chart displays the gene set score for this specific sub-cluster across various cell types from late-stage human HCM snRNA-seq data. Scores were calculated for each sample using the `score_genes` function in `scanpy` v1.10.1 [267]. Bars represent the mean score, with error bars indicating the standard error of the mean. Statistical significance between disease and control samples was determined using a t-test, with p-values adjusted for multiple comparisons using the Benjamini-Hochberg method. Asterisks denote significance levels: * $p < 0.05$, ** $p < 0.01$, *** $p < 0.001$, **** $p < 0.0001$.

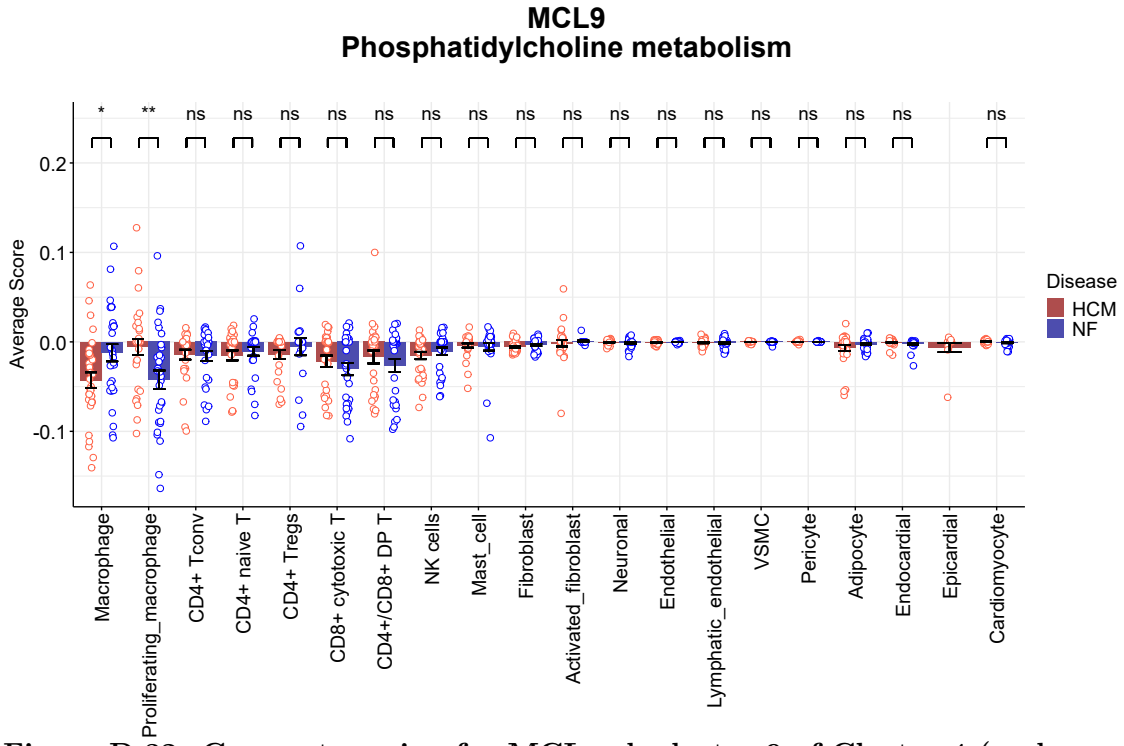

Figure D.32. Gene set scoring for MCL sub-cluster 9 of Cluster 4 (early up-regulation followed by a late surge) in late-stage human cell types. This sub-cluster is a constituent of Cluster 4. The bar chart displays the gene set score for this specific sub-cluster across various cell types from late-stage human HCM snRNA-seq data. Scores were calculated for each sample using the `score_genes` function in `scanpy` v1.10.1 [267]. Bars represent the mean score, with error bars indicating the standard error of the mean. Statistical significance between disease and control samples was determined using a t-test, with p-values adjusted for multiple comparisons using the Benjamini-Hochberg method. Asterisks denote significance levels: * $p < 0.05$, ** $p < 0.01$, *** $p < 0.001$, **** $p < 0.0001$.

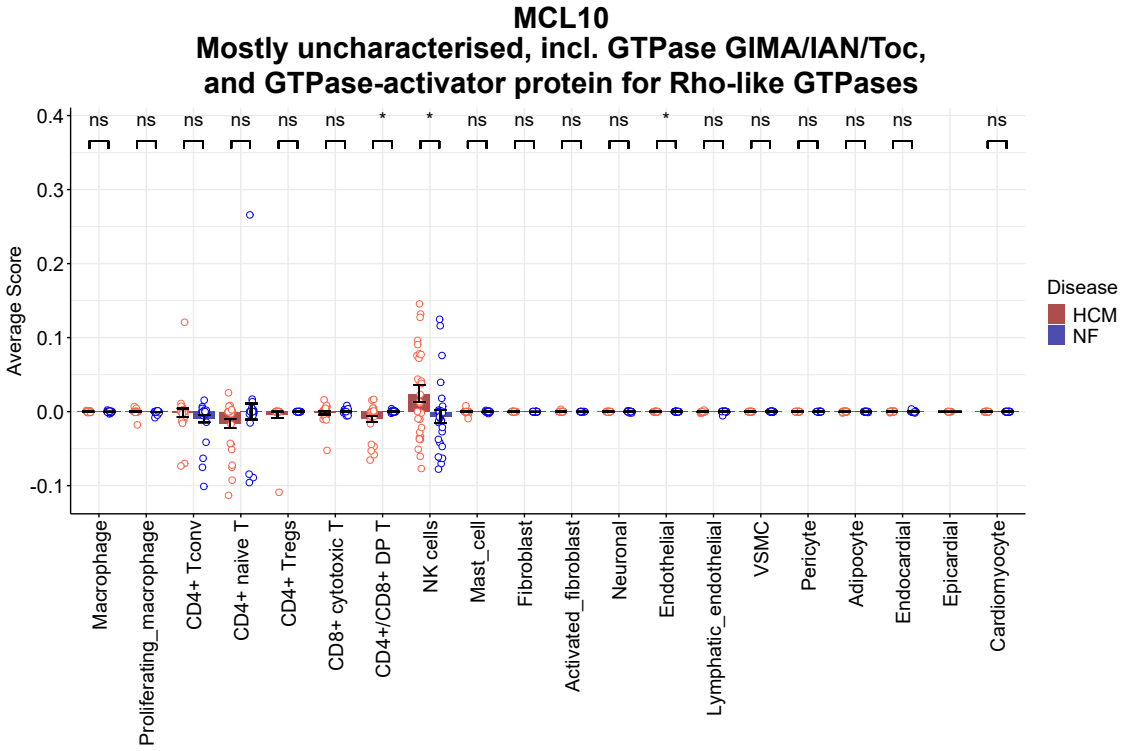

Figure D.33. Gene set scoring for MCL sub-cluster 10 of Cluster 4 (early up-regulation followed by a late surge) in late-stage human cell types. This sub-cluster is a constituent of Cluster 4. The bar chart displays the gene set score for this specific sub-cluster across various cell types from late-stage human HCM snRNA-seq data. Scores were calculated for each sample using the `score_genes` function in `scanpy` v1.10.1 [267]. Bars represent the mean score, with error bars indicating the standard error of the mean. Statistical significance between disease and control samples was determined using a t-test, with p-values adjusted for multiple comparisons using the Benjamini-Hochberg method. Asterisks denote significance levels: * $p < 0.05$, ** $p < 0.01$, *** $p < 0.001$, **** $p < 0.0001$.

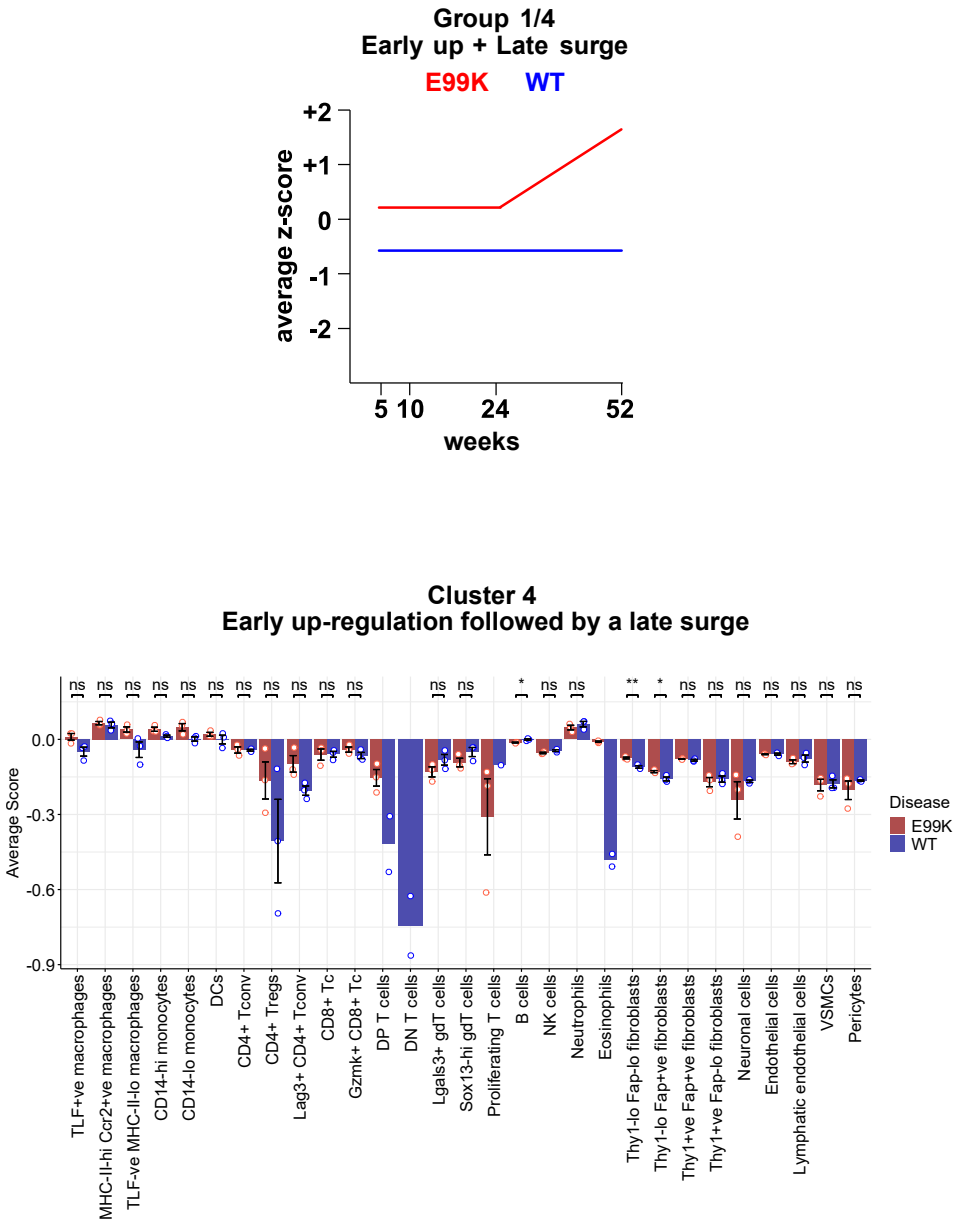

Figure D.34. Gene set scoring and statistics of cluster 4 (early up-regulation followed by a late surge) in late-stage mouse cell types. The upper panel schematically illustrates the temporal expression trend for Cluster 4, derived from bulk RNA-seq data of Actc1^{E99K} (red line) and wild-type (blue line) hearts over time. The lower panel displays the gene set score for all genes within Cluster 4 across various cell types identified in late-stage Actc1^{E99K} mouse scRNA-seq data. Scores were calculated for each sample using the `score_genes` function in `scanpy` v1.10.1 [267]. Bars represent the mean score, with error bars indicating the standard error of the mean. Statistical significance between disease and control samples was determined using a t-test, with p-values adjusted for multiple comparisons using the Benjamini-Hochberg method. Asterisks denote significance levels: * $p < 0.05$, ** $p < 0.01$, *** $p < 0.001$, **** $p < 0.0001$.

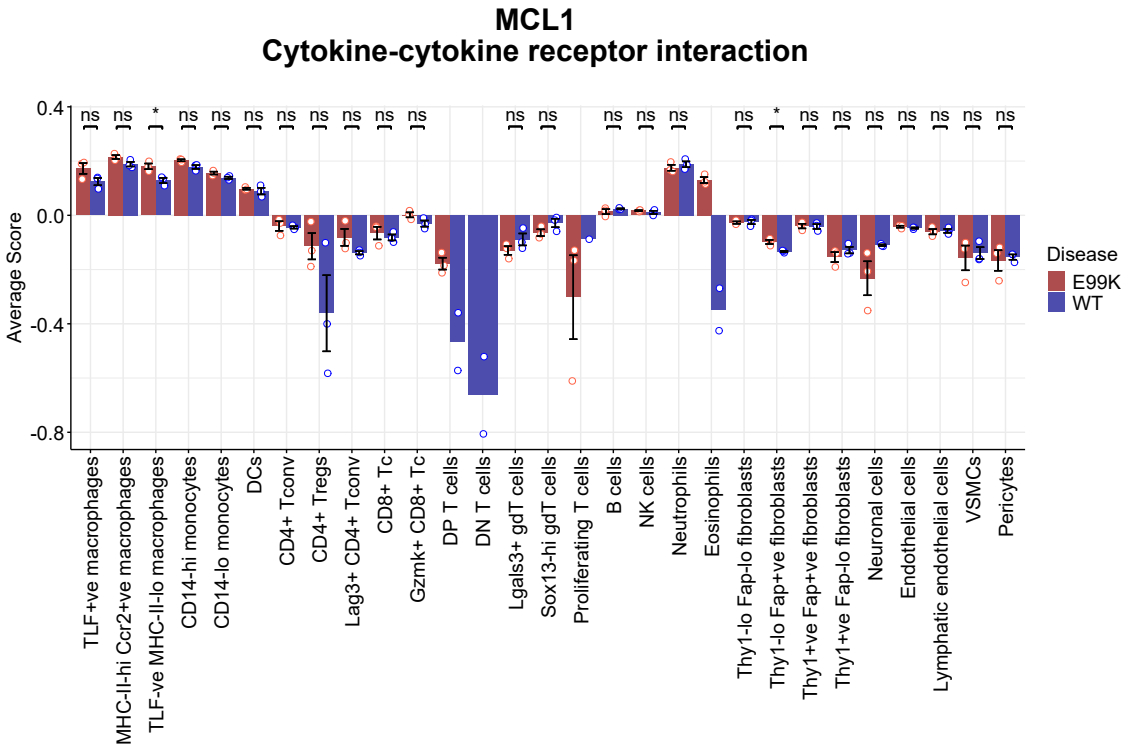

Figure D.35. Gene set scoring for MCL sub-cluster 1 of Cluster 4 (early up-regulation followed by a late surge) in late-stage mouse cell types. This sub-cluster is a constituent of Cluster 4. The bar chart displays the gene set score for this specific sub-cluster across various cell types from late-stage Actc1^{E99K} mouse scRNA-seq data. Scores were calculated for each sample using the `score_genes` function in `scanpy` v1.10.1 [267]. Bars represent the mean score, with error bars indicating the standard error of the mean. Statistical significance between disease and control samples was determined using a t-test, with p-values adjusted for multiple comparisons using the Benjamini-Hochberg method. Asterisks denote significance levels: * $p < 0.05$, ** $p < 0.01$, *** $p < 0.001$, **** $p < 0.0001$.

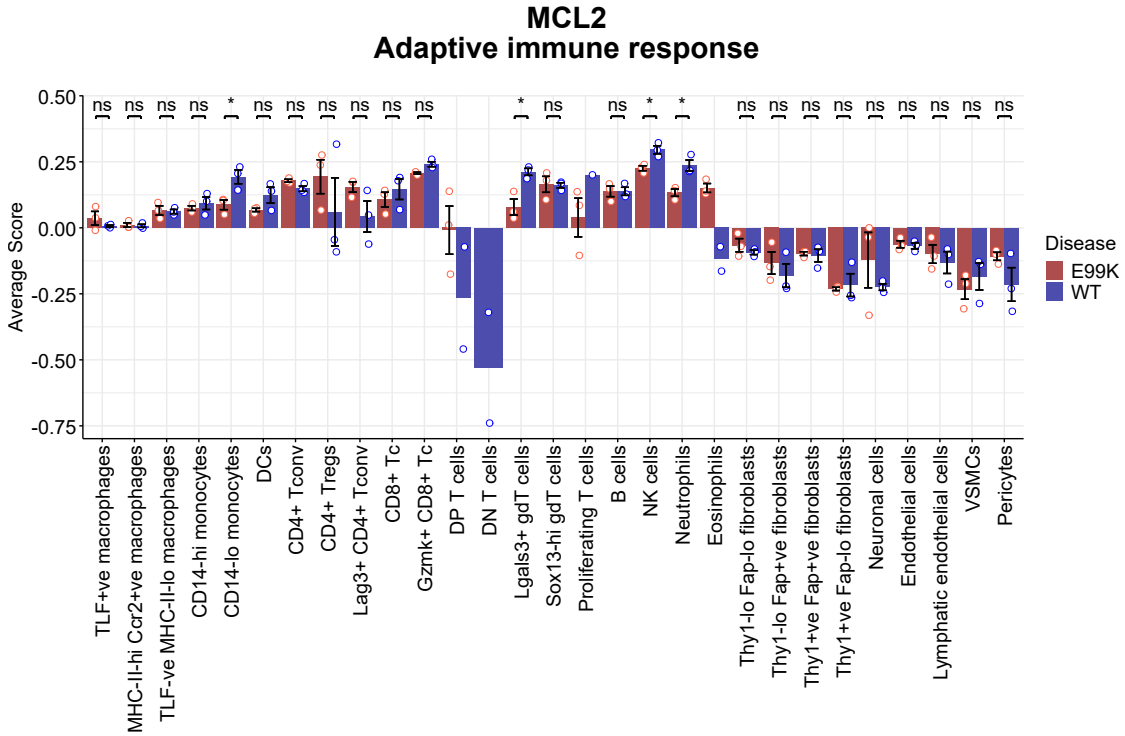

Figure D.36. Gene set scoring for MCL sub-cluster 2 of Cluster 4 (early up-regulation followed by a late surge) in late-stage mouse cell types. This sub-cluster is a constituent of Cluster 4. The bar chart displays the gene set score for this specific sub-cluster across various cell types from late-stage Actc1^{E99K} mouse scRNA-seq data. Scores were calculated for each sample using the `score_genes` function in `scanpy` v1.10.1 [267]. Bars represent the mean score, with error bars indicating the standard error of the mean. Statistical significance between disease and control samples was determined using a t-test, with p-values adjusted for multiple comparisons using the Benjamini-Hochberg method. Asterisks denote significance levels: * $p < 0.05$, ** $p < 0.01$, *** $p < 0.001$, **** $p < 0.0001$.

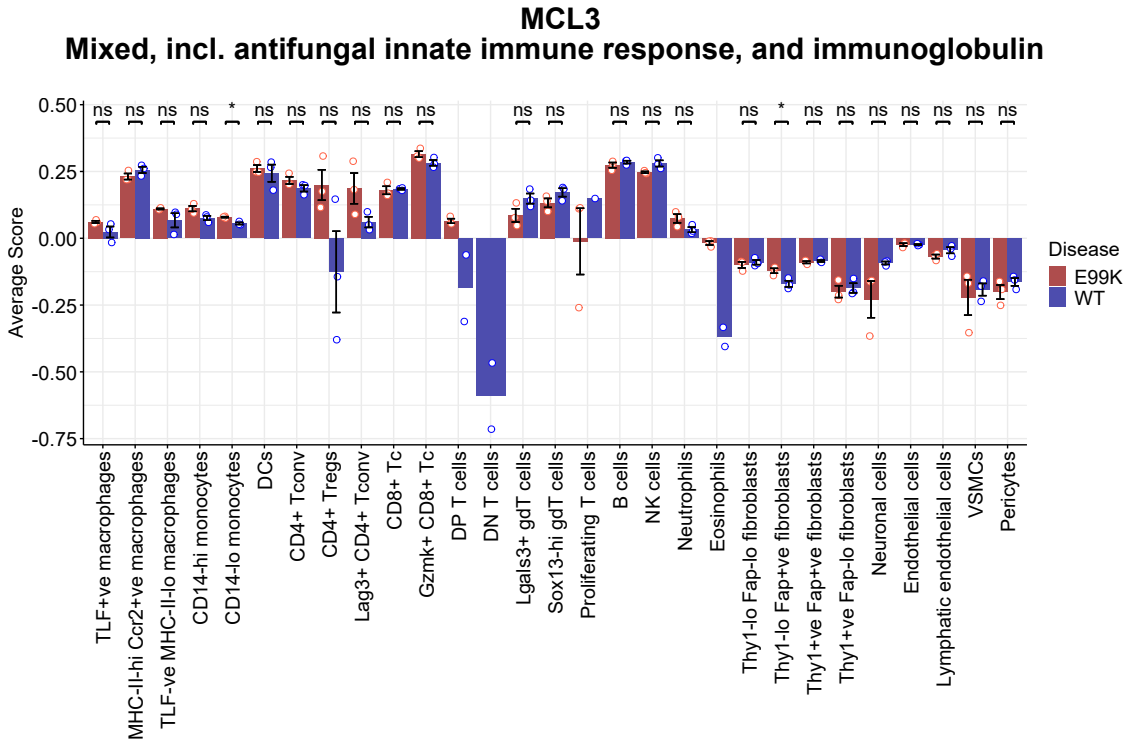

Figure D.37. Gene set scoring for MCL sub-cluster 3 of Cluster 4 (early up-regulation followed by a late surge) in late-stage mouse cell types. This sub-cluster is a constituent of Cluster 4. The bar chart displays the gene set score for this specific sub-cluster across various cell types from late-stage Actc1^{E99K} mouse scRNA-seq data. Scores were calculated for each sample using the `score_genes` function in `scanpy` v1.10.1 [267]. Bars represent the mean score, with error bars indicating the standard error of the mean. Statistical significance between disease and control samples was determined using a t-test, with p-values adjusted for multiple comparisons using the Benjamini-Hochberg method. Asterisks denote significance levels: * $p < 0.05$, ** $p < 0.01$, *** $p < 0.001$, **** $p < 0.0001$.

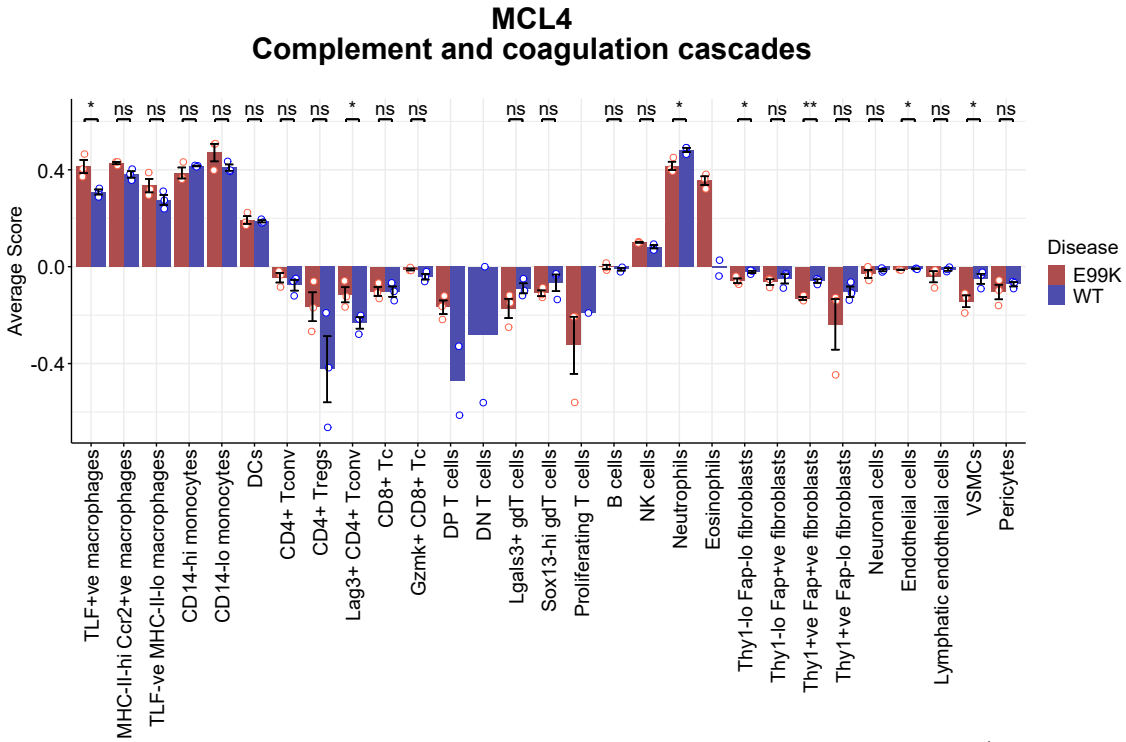

Figure D.38. Gene set scoring for MCL sub-cluster 4 of Cluster 4 (early up-regulation followed by a late surge) in late-stage mouse cell types. This sub-cluster is a constituent of Cluster 4. The bar chart displays the gene set score for this specific sub-cluster across various cell types from late-stage $Actc1^{E99K}$ mouse scRNA-seq data. Scores were calculated for each sample using the `score_genes` function in `scanpy` v1.10.1 [267]. Bars represent the mean score, with error bars indicating the standard error of the mean. Statistical significance between disease and control samples was determined using a t-test, with p-values adjusted for multiple comparisons using the Benjamini-Hochberg method. Asterisks denote significance levels: * $p < 0.05$, ** $p < 0.01$, *** $p < 0.001$, **** $p < 0.0001$.

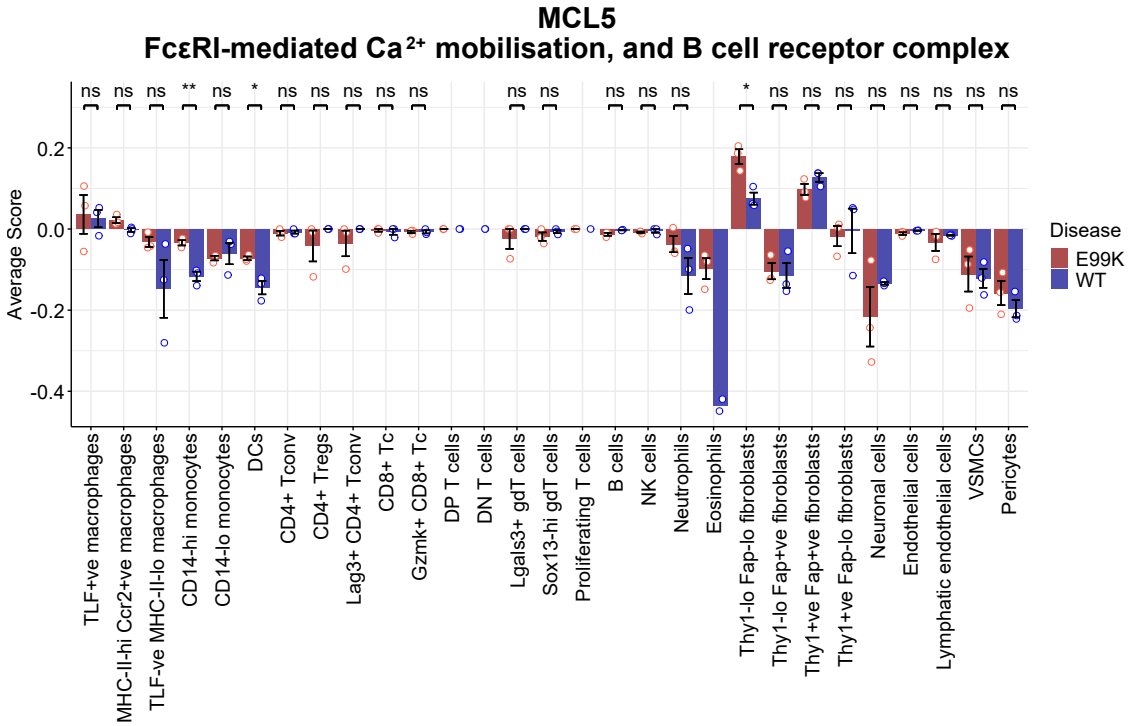

Figure D.39. Gene set scoring for MCL sub-cluster 5 of Cluster 4 (early up-regulation followed by a late surge) in late-stage mouse cell types. This sub-cluster is a constituent of Cluster 4. The bar chart displays the gene set score for this specific sub-cluster across various cell types from late-stage Actc1^{E99K} mouse scRNA-seq data. Scores were calculated for each sample using the `score_genes` function in `scanpy` v1.10.1 [267]. Bars represent the mean score, with error bars indicating the standard error of the mean. Statistical significance between disease and control samples was determined using a t-test, with p-values adjusted for multiple comparisons using the Benjamini-Hochberg method. Asterisks denote significance levels: * $p < 0.05$, ** $p < 0.01$, *** $p < 0.001$, **** $p < 0.0001$.

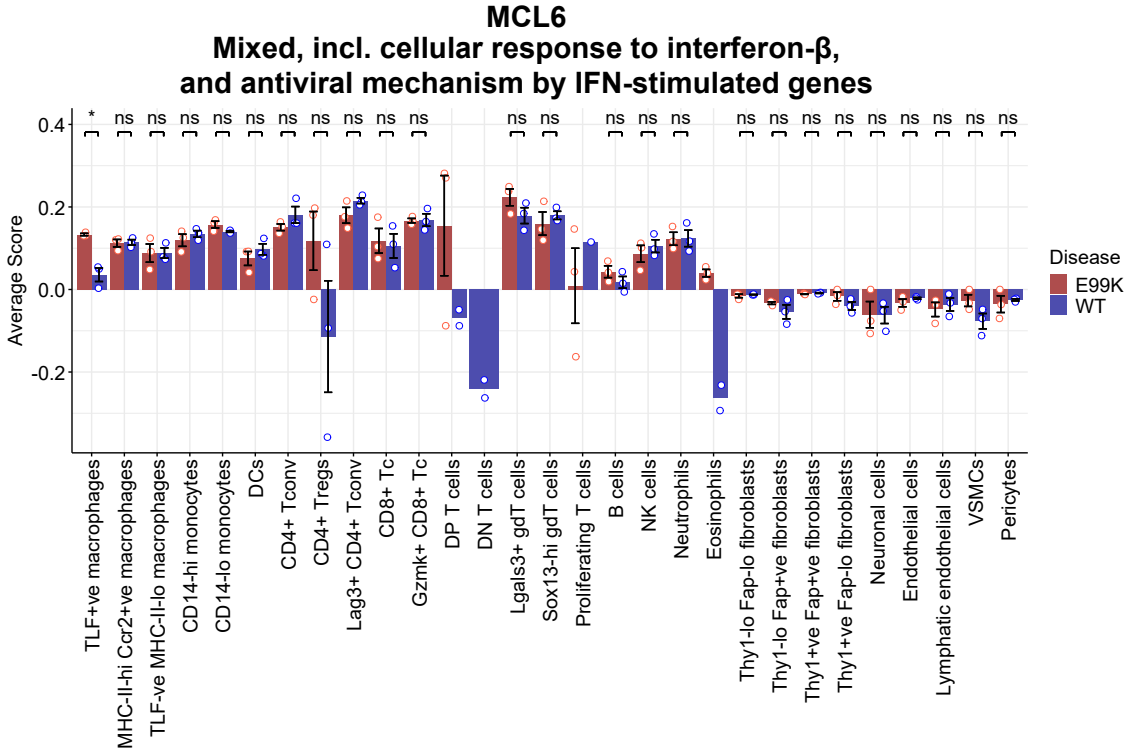

Figure D.40. Gene set scoring for MCL sub-cluster 6 of Cluster 4 (early up-regulation followed by a late surge) in late-stage mouse cell types. This sub-cluster is a constituent of Cluster 4. The bar chart displays the gene set score for this specific sub-cluster across various cell types from late-stage $\text{Actc1}^{\text{E99K}}$ mouse scRNA-seq data. Scores were calculated for each sample using the `score_genes` function in `scanpy` v1.10.1 [267]. Bars represent the mean score, with error bars indicating the standard error of the mean. Statistical significance between disease and control samples was determined using a t-test, with p-values adjusted for multiple comparisons using the Benjamini-Hochberg method. Asterisks denote significance levels: * $p < 0.05$, ** $p < 0.01$, *** $p < 0.001$, **** $p < 0.0001$.

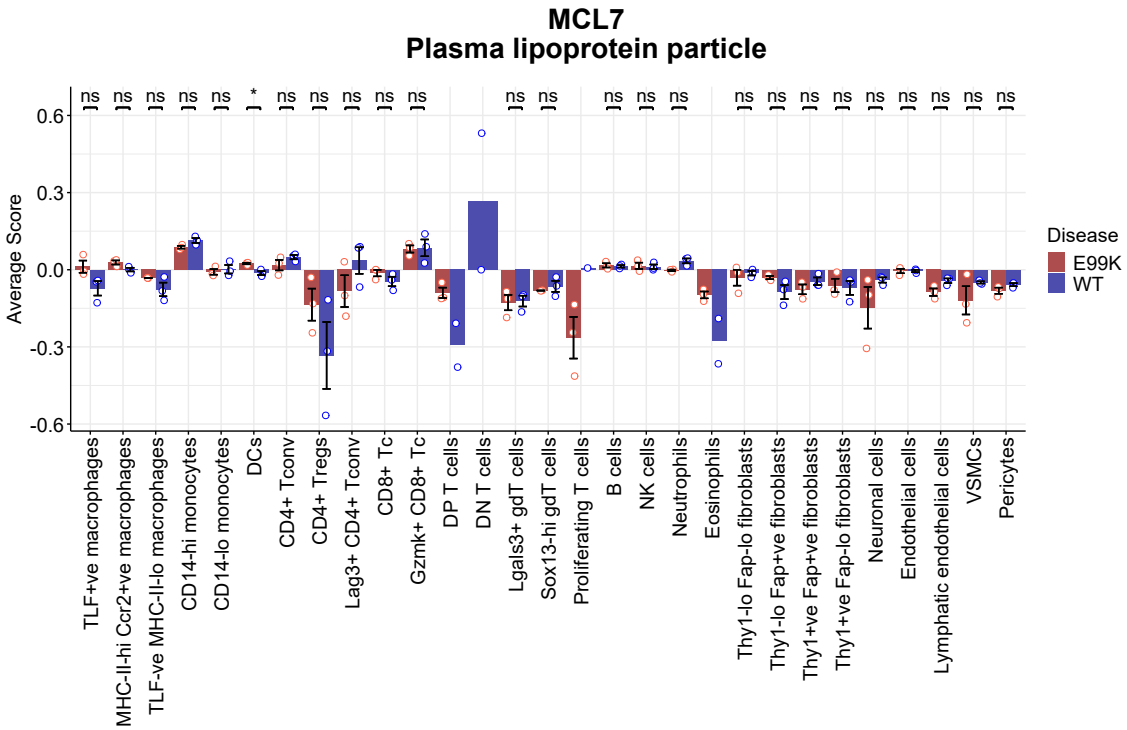

Figure D.41. Gene set scoring for MCL sub-cluster 7 of Cluster 4 (early up-regulation followed by a late surge) in late-stage mouse cell types. This sub-cluster is a constituent of Cluster 4. The bar chart displays the gene set score for this specific sub-cluster across various cell types from late-stage Actc1^{E99K} mouse scRNA-seq data. Scores were calculated for each sample using the `score_genes` function in `scanpy` v1.10.1 [267]. Bars represent the mean score, with error bars indicating the standard error of the mean. Statistical significance between disease and control samples was determined using a t-test, with p-values adjusted for multiple comparisons using the Benjamini-Hochberg method. Asterisks denote significance levels: * $p < 0.05$, ** $p < 0.01$, *** $p < 0.001$, **** $p < 0.0001$.

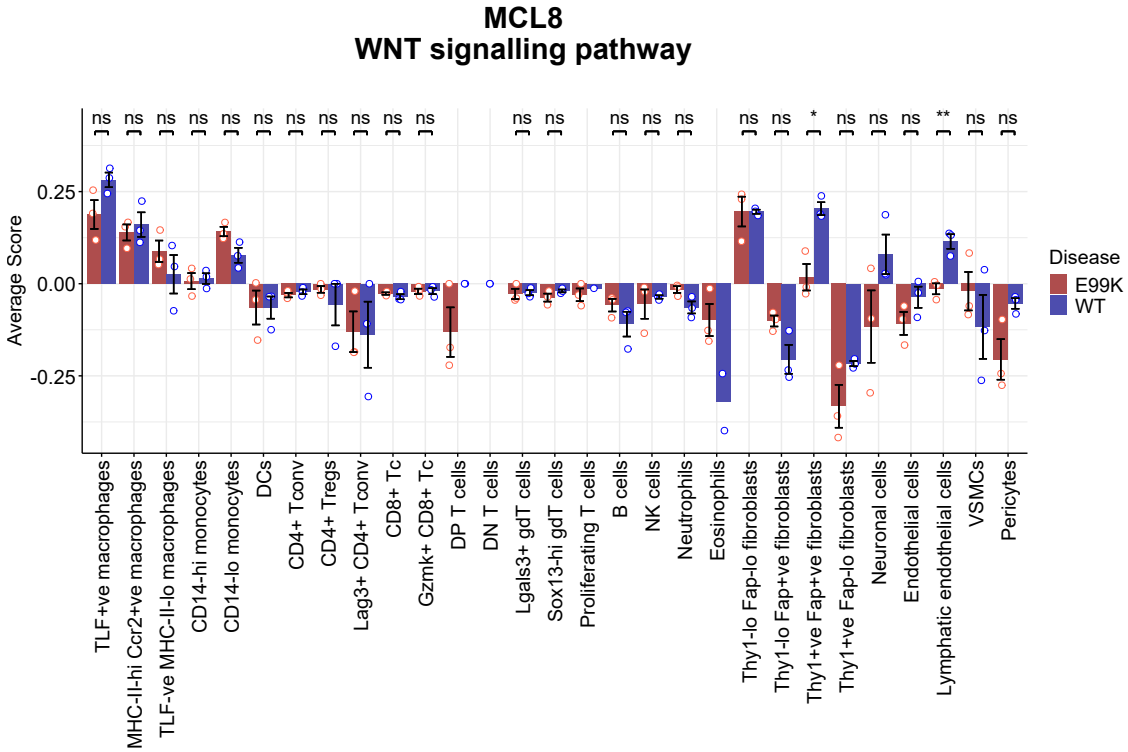

Figure D.42. Gene set scoring for MCL sub-cluster 8 of Cluster 4 (early up-regulation followed by a late surge) in late-stage mouse cell types. This sub-cluster is a constituent of Cluster 4. The bar chart displays the gene set score for this specific sub-cluster across various cell types from late-stage Actc1^{E99K} mouse scRNA-seq data. Scores were calculated for each sample using the `score_genes` function in `scanpy` v1.10.1 [267]. Bars represent the mean score, with error bars indicating the standard error of the mean. Statistical significance between disease and control samples was determined using a t-test, with p-values adjusted for multiple comparisons using the Benjamini-Hochberg method. Asterisks denote significance levels: * $p < 0.05$, ** $p < 0.01$, *** $p < 0.001$, **** $p < 0.0001$.

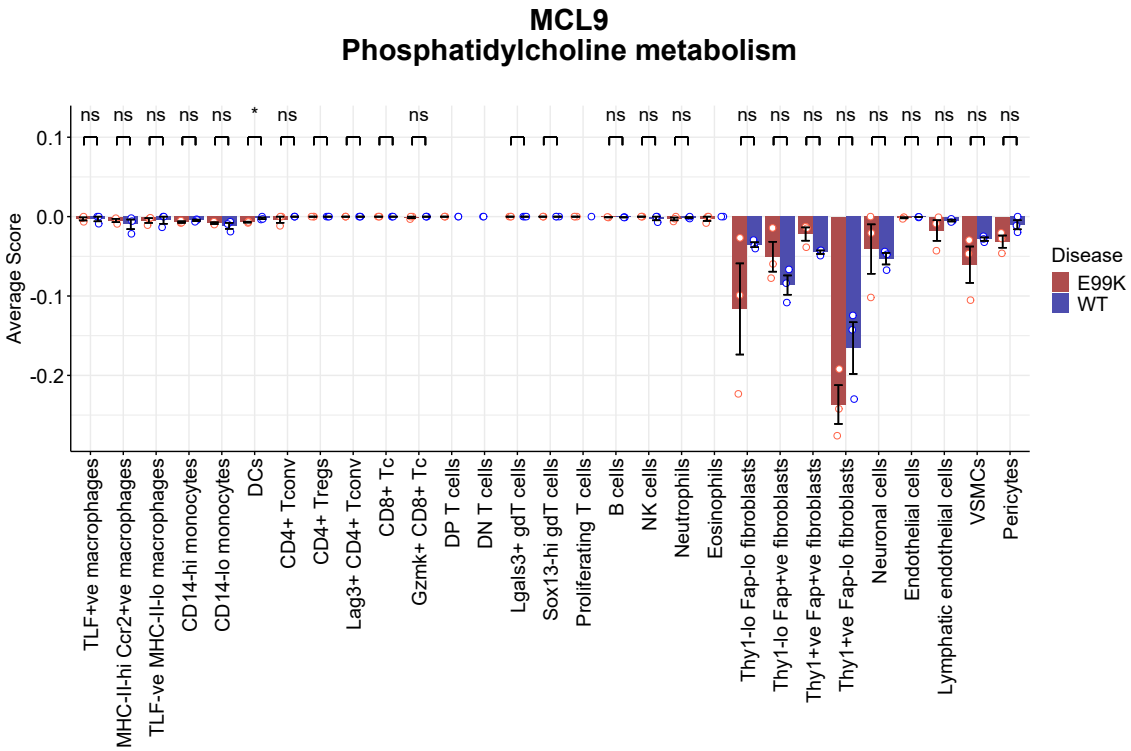

Figure D.43. Gene set scoring for MCL sub-cluster 9 of Cluster 4 (early up-regulation followed by a late surge) in late-stage mouse cell types. This sub-cluster is a constituent of Cluster 4. The bar chart displays the gene set score for this specific sub-cluster across various cell types from late-stage Actc1^{E99K} mouse scRNA-seq data. Scores were calculated for each sample using the `score_genes` function in `scanpy` v1.10.1 [267]. Bars represent the mean score, with error bars indicating the standard error of the mean. Statistical significance between disease and control samples was determined using a t-test, with p-values adjusted for multiple comparisons using the Benjamini-Hochberg method. Asterisks denote significance levels: * $p < 0.05$, ** $p < 0.01$, *** $p < 0.001$, **** $p < 0.0001$.

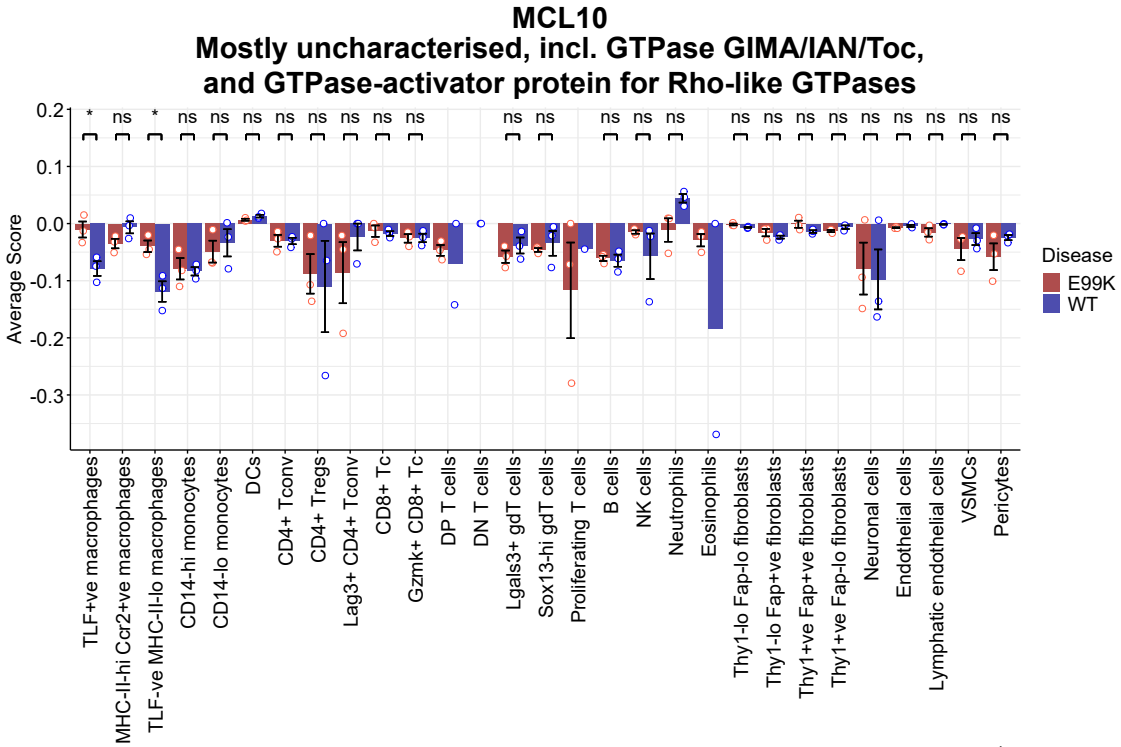

Figure D.44. Gene set scoring for MCL sub-cluster 10 of Cluster 4 (early up-regulation followed by a late surge) in late-stage mouse cell types. This sub-cluster is a constituent of Cluster 4. The bar chart displays the gene set score for this specific sub-cluster across various cell types from late-stage Actc1^{E99K} mouse scRNA-seq data. Scores were calculated for each sample using the `score_genes` function in `scanpy` v1.10.1 [267]. Bars represent the mean score, with error bars indicating the standard error of the mean. Statistical significance between disease and control samples was determined using a t-test, with p-values adjusted for multiple comparisons using the Benjamini-Hochberg method. Asterisks denote significance levels: * $p < 0.05$, ** $p < 0.01$, *** $p < 0.001$, **** $p < 0.0001$.

D.2 Cluster 9 & 10: Gradual expression increase points to ongoing cellular adaptations in the failing heart

Cluster 9, exhibiting a gradual increase in expression over time, was primarily enriched for translation-related processes. Sub-cluster analysis revealed further functional specialisation (Figures D.45 and D.56), including cytoplasmic translation (MCL sub-cluster 1; Figure D.46), preribosome and ribosome biogenesis (MCL sub-cluster 2; Figure D.47), precatalytic spliceosome and U4/U6 x U5 tri-snRNP complex formation (MCL sub-cluster 3; Figure D.48), chemokine receptor

binding (MCL sub-cluster 4; Figure D.49), glutathione metabolism (MCL sub-cluster 5; Figure D.50), aryl hydrocarbon receptor signalling (MCL sub-cluster 6; Figure D.51), mitophagy (MCL sub-cluster 7; Figure D.52), amino acid regulation of mTORC1 (MCL sub-cluster 8; Figure D.53), vesicle fusion with vacuole (MCL sub-cluster 9; Figure D.54), and S-100/ICaBP type calcium binding domain (MCL sub-cluster 10; Figure D.55). In late-stage human HCM samples, the overall cluster 9 signature was significantly downregulated in macrophages and proliferating macrophages, and upregulated in NK cells and lymphatic endothelial cells (Figure D.45). Activated fibroblasts also showed significant upregulation of the overall cluster signature. Pericytes exhibited significant downregulation. Further investigation into the sub-clusters revealed cell-type-specific patterns. For instance, the cytoplasmic translation sub-cluster (MCL sub-cluster 1; Figure D.46) was upregulated in NK cells and activated fibroblasts, mirroring the overall cluster pattern. The precatalytic spliceosome sub-cluster (MCL sub-cluster 3; Figure D.48) was downregulated in macrophages, fibroblasts, and neuronal cells, and upregulated in cardiomyocytes. Interestingly, the chemokine receptor binding sub-cluster (MCL sub-cluster 4; Figure D.49) showed upregulation in fibroblasts, pericytes, and cardiomyocytes, and downregulation in macrophages and endothelial cells. In the mouse scRNA-seq data, the overall cluster 9 signature was downregulated in $\gamma\delta$T cells and lymphatic endothelial cells (Figure D.56). Sub-cluster analysis revealed downregulation of the cytoplasmic translation sub-cluster (MCL sub-cluster 1; Figure D.57) in several immune cell populations, including $CD14^{lo}$ monocytes, DCs, $CD4^+$ Tconv cells, and $CD8^+$ Tc cells. The pre-ribosome and ribosome biogenesis sub-cluster (MCL sub-cluster 2; Figure D.58) was downregulated in $CD14^{hi}$ monocytes and neutrophils, and upregulated in $Thy1^+Fap^+$ fibroblasts.

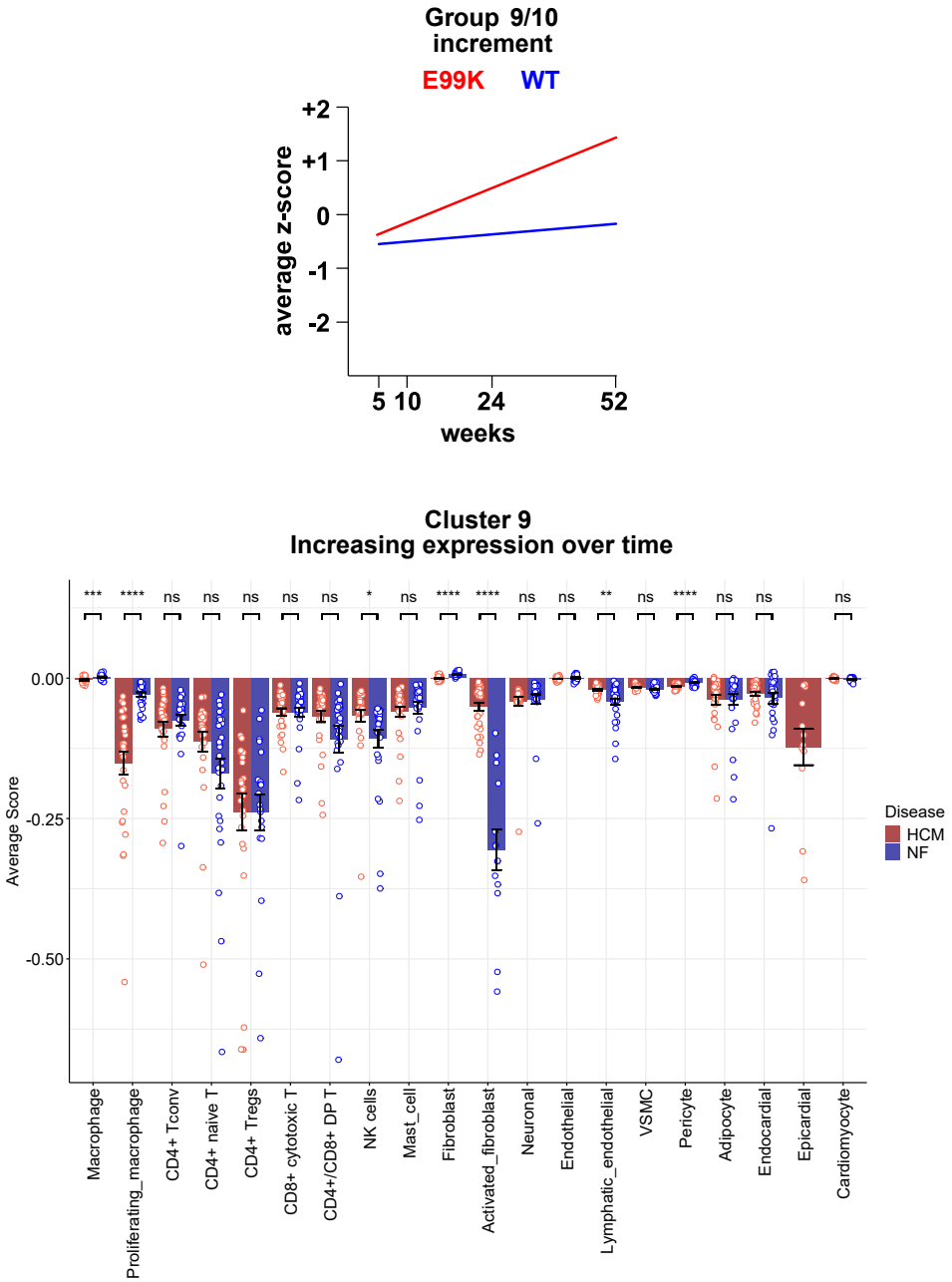

Figure D.45. Gene set scoring and statistics of Cluster 9 (increasing expression over time) in late-stage human cell types.
The upper panel schematically illustrates the temporal expression trend for Cluster 9, derived from bulk RNA-seq data of Actc1^{E99K} (red line) and wild-type (blue line) hearts over time. The lower panel displays the gene set score for all genes within Cluster 9 across various cell types identified in late-stage human HCM snRNA-seq data. Scores were calculated for each sample using the `score_genes` function in `scanpy` v1.10.1 [267]. Bars represent the mean score, with error bars indicating the standard error of the mean. Statistical significance between disease and control samples was determined using a t-test, with p-values adjusted for multiple comparisons using the Benjamini-Hochberg method. Asterisks denote significance levels: * $p < 0.05$, ** $p < 0.01$, *** $p < 0.001$, **** $p < 0.0001$.

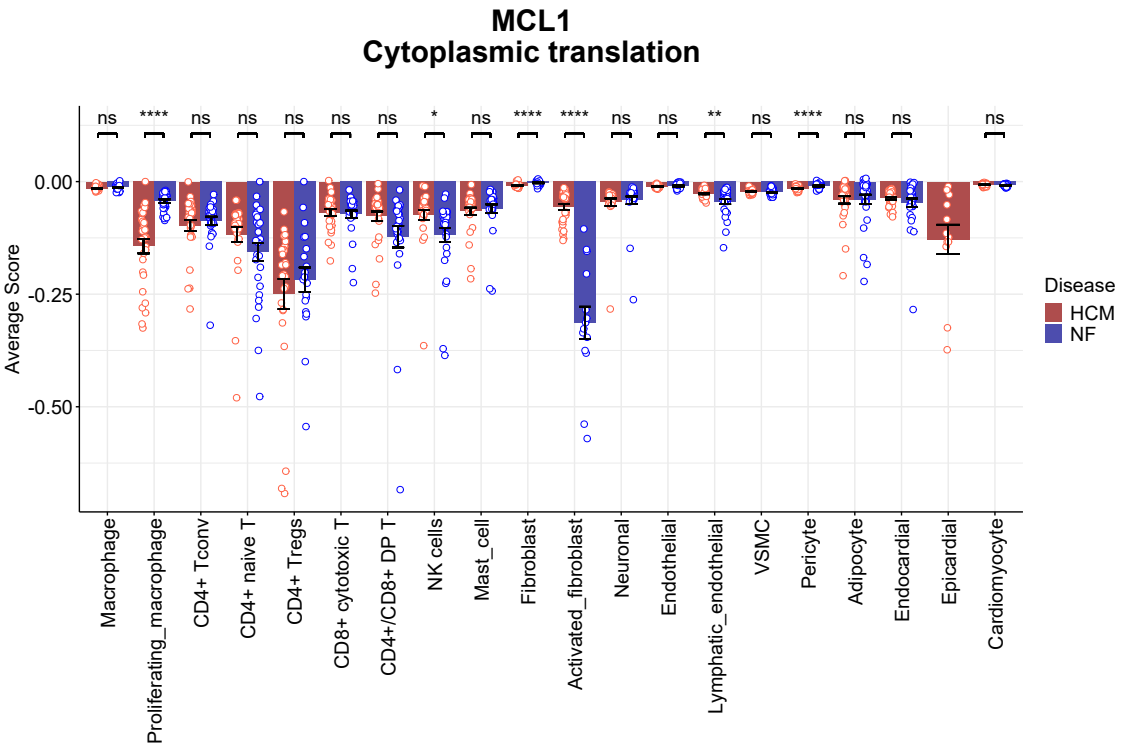

Figure D.46. Gene set scoring for MCL sub-cluster 1 of Cluster 9 (increasing expression over time) in late-stage human cell types.
This sub-cluster is a constituent of Cluster 9. The bar chart displays the gene set score for this specific sub-cluster across various cell types from late-stage human HCM snRNA-seq data. Scores were calculated for each sample using the `score_genes` function in `scanpy` v1.10.1 [267]. Bars represent the mean score, with error bars indicating the standard error of the mean. Statistical significance between disease and control samples was determined using a t-test, with p-values adjusted for multiple comparisons using the Benjamini-Hochberg method. Asterisks denote significance levels: * $p < 0.05$, ** $p < 0.01$, *** $p < 0.001$, **** $p < 0.0001$.

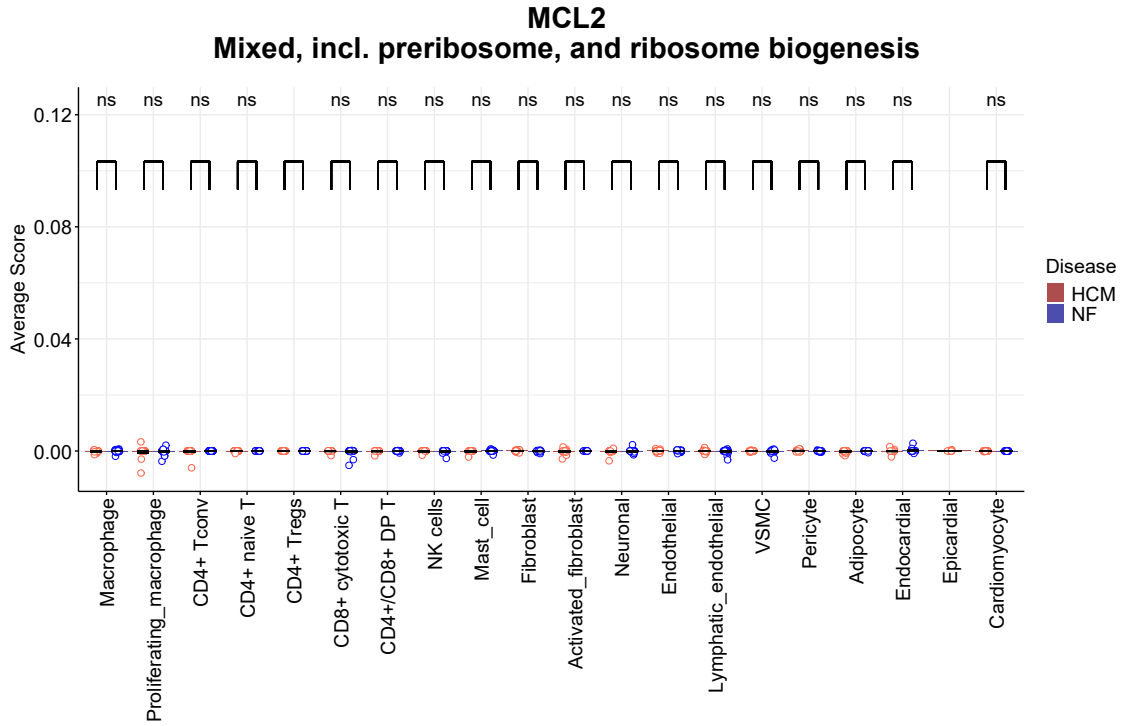

Figure D.47. Gene set scoring for MCL sub-cluster 2 of Cluster 9 (increasing expression over time) in late-stage human cell types.
This sub-cluster is a constituent of Cluster 9. The bar chart displays the gene set score for this specific sub-cluster across various cell types from late-stage human HCM snRNA-seq data. Scores were calculated for each sample using the `score_genes` function in `scanpy` v1.10.1 [267]. Bars represent the mean score, with error bars indicating the standard error of the mean. Statistical significance between disease and control samples was determined using a t-test, with p-values adjusted for multiple comparisons using the Benjamini-Hochberg method. Asterisks denote significance levels: * $p < 0.05$, ** $p < 0.01$, *** $p < 0.001$, **** $p < 0.0001$.

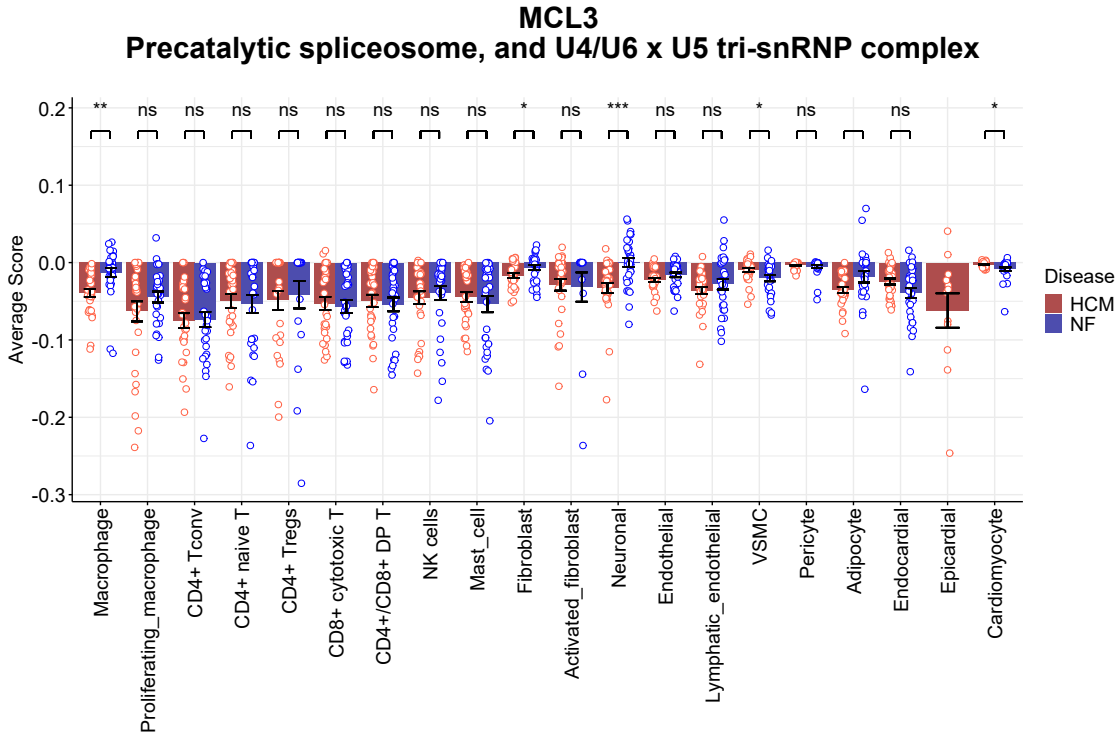

Figure D.48. Gene set scoring for MCL sub-cluster 3 of Cluster 9 (increasing expression over time) in late-stage human cell types.
This sub-cluster is a constituent of Cluster 9. The bar chart displays the gene set score for this specific sub-cluster across various cell types from late-stage human HCM snRNA-seq data. Scores were calculated for each sample using the `score_genes` function in `scanpy` v1.10.1 [267]. Bars represent the mean score, with error bars indicating the standard error of the mean. Statistical significance between disease and control samples was determined using a t-test, with p-values adjusted for multiple comparisons using the Benjamini-Hochberg method. Asterisks denote significance levels: * $p < 0.05$, ** $p < 0.01$, *** $p < 0.001$, **** $p < 0.0001$.

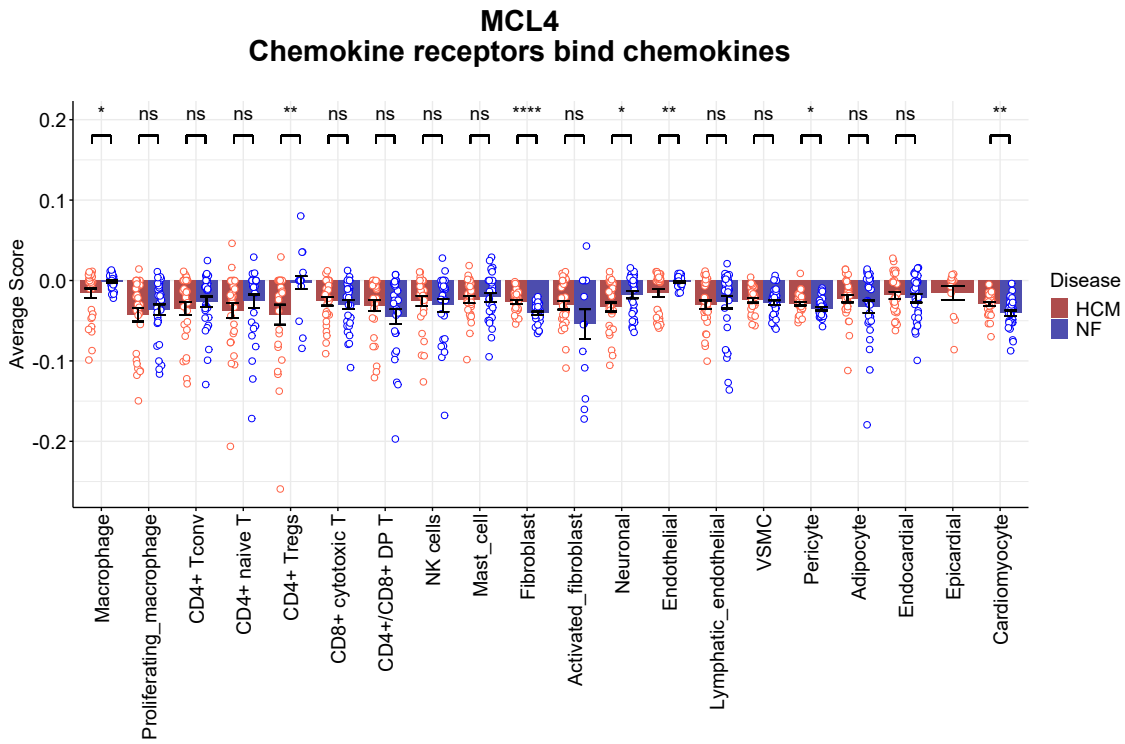

Figure D.49. Gene set scoring for MCL sub-cluster 4 of Cluster 9 (increasing expression over time) in late-stage human cell types.
This sub-cluster is a constituent of Cluster 9. The bar chart displays the gene set score for this specific sub-cluster across various cell types from late-stage human HCM snRNA-seq data. Scores were calculated for each sample using the `score_genes` function in `scanpy` v1.10.1 [267]. Bars represent the mean score, with error bars indicating the standard error of the mean. Statistical significance between disease and control samples was determined using a t-test, with p-values adjusted for multiple comparisons using the Benjamini-Hochberg method. Asterisks denote significance levels: * $p < 0.05$, ** $p < 0.01$, *** $p < 0.001$, **** $p < 0.0001$.

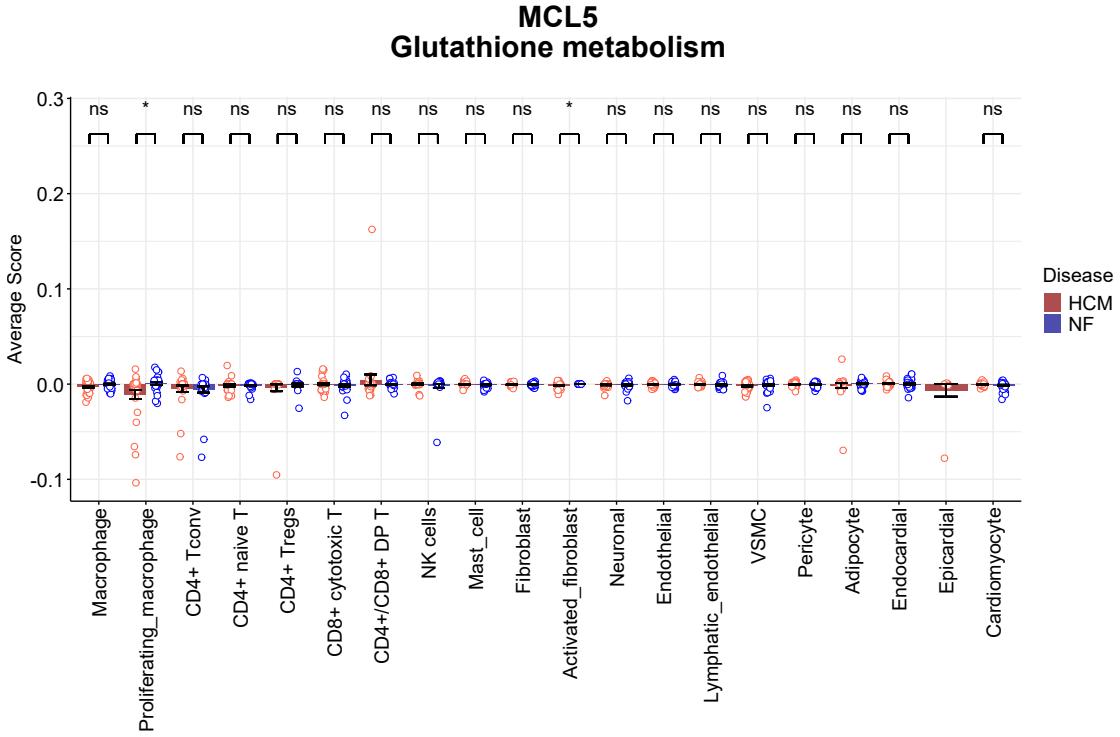

Figure D.50. Gene set scoring for MCL sub-cluster 5 of Cluster 9 (increasing expression over time) in late-stage human cell types.
This sub-cluster is a constituent of Cluster 9. The bar chart displays the gene set score for this specific sub-cluster across various cell types from late-stage human HCM snRNA-seq data. Scores were calculated for each sample using the `score_genes` function in `scanpy` v1.10.1 [267]. Bars represent the mean score, with error bars indicating the standard error of the mean. Statistical significance between disease and control samples was determined using a t-test, with p-values adjusted for multiple comparisons using the Benjamini-Hochberg method. Asterisks denote significance levels: * $p < 0.05$, ** $p < 0.01$, *** $p < 0.001$, **** $p < 0.0001$.

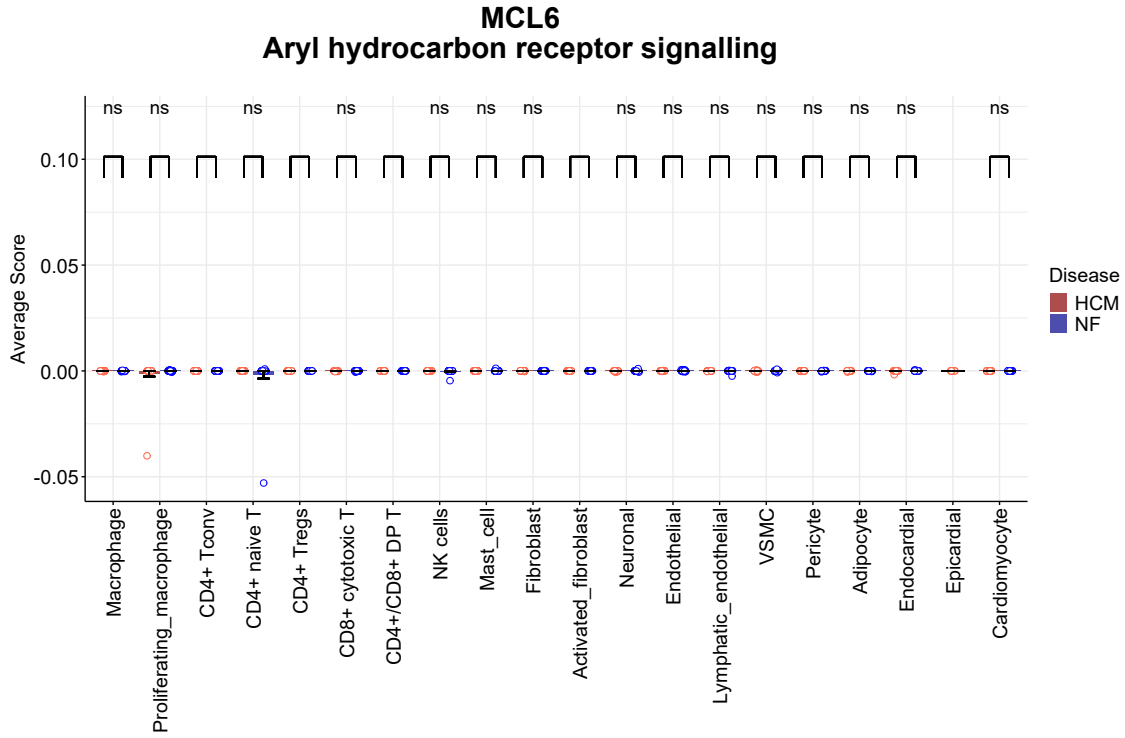

Figure D.51. Gene set scoring for MCL sub-cluster 6 of Cluster 9 (increasing expression over time) in late-stage human cell types.
This sub-cluster is a constituent of Cluster 9. The bar chart displays the gene set score for this specific sub-cluster across various cell types from late-stage human HCM snRNA-seq data. Scores were calculated for each sample using the `score_genes` function in `scanpy` v1.10.1 [267]. Bars represent the mean score, with error bars indicating the standard error of the mean. Statistical significance between disease and control samples was determined using a t-test, with p-values adjusted for multiple comparisons using the Benjamini-Hochberg method. Asterisks denote significance levels: * $p < 0.05$, ** $p < 0.01$, *** $p < 0.001$, **** $p < 0.0001$.

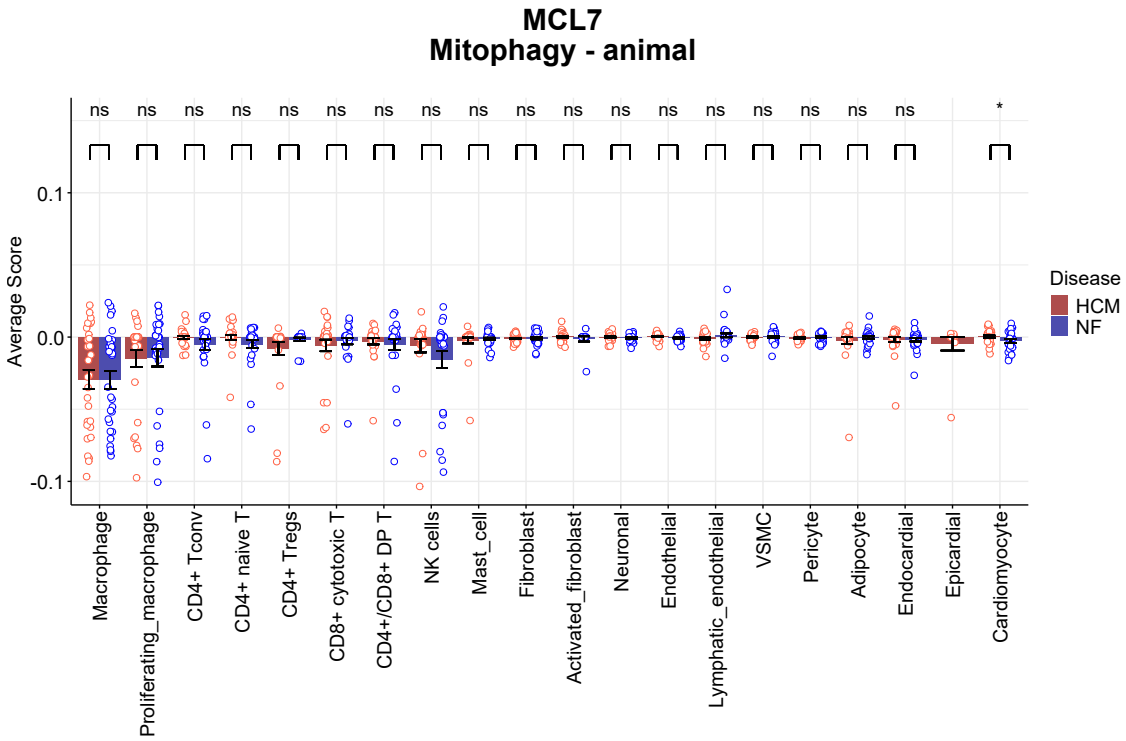

Figure D.52. Gene set scoring for MCL sub-cluster 7 of Cluster 9 (increasing expression over time) in late-stage human cell types.
This sub-cluster is a constituent of Cluster 9. The bar chart displays the gene set score for this specific sub-cluster across various cell types from late-stage human HCM snRNA-seq data. Scores were calculated for each sample using the `score_genes` function in `scanpy` v1.10.1 [267]. Bars represent the mean score, with error bars indicating the standard error of the mean. Statistical significance between disease and control samples was determined using a t-test, with p-values adjusted for multiple comparisons using the Benjamini-Hochberg method. Asterisks denote significance levels: * $p < 0.05$, ** $p < 0.01$, *** $p < 0.001$, **** $p < 0.0001$.

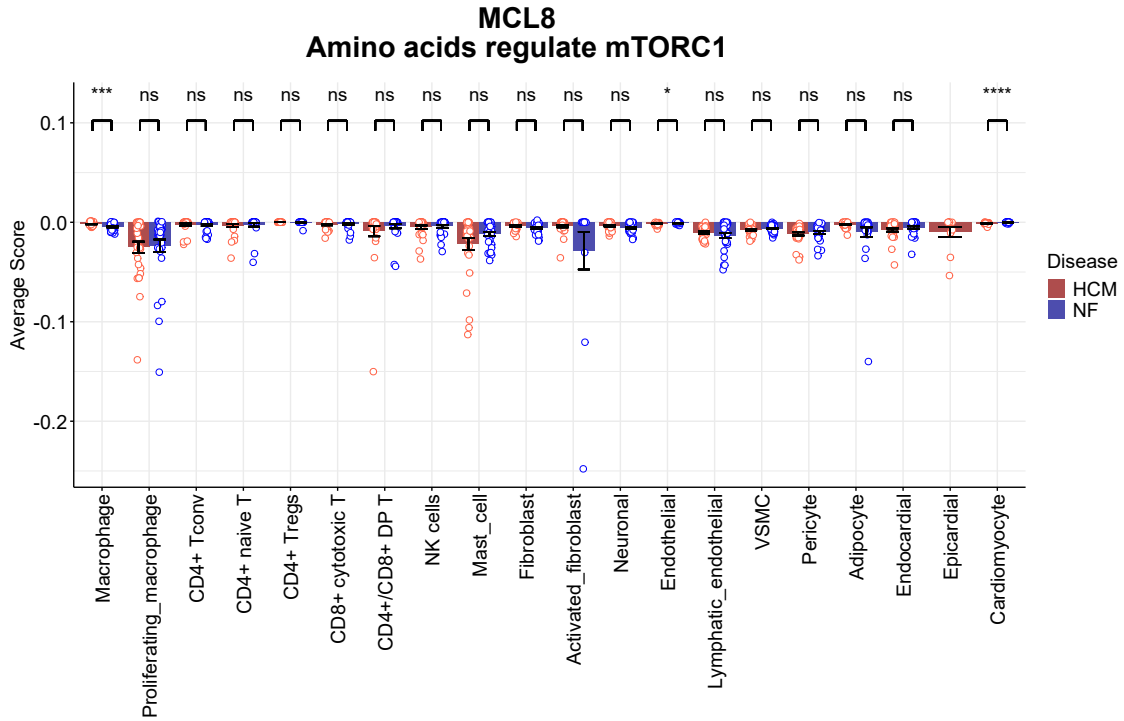

Figure D.53. Gene set scoring for MCL sub-cluster 8 of Cluster 9 (increasing expression over time) in late-stage human cell types.
This sub-cluster is a constituent of Cluster 9. The bar chart displays the gene set score for this specific sub-cluster across various cell types from late-stage human HCM snRNA-seq data. Scores were calculated for each sample using the `score_genes` function in `scanpy` v1.10.1 [267]. Bars represent the mean score, with error bars indicating the standard error of the mean. Statistical significance between disease and control samples was determined using a t-test, with p-values adjusted for multiple comparisons using the Benjamini-Hochberg method. Asterisks denote significance levels: * $p < 0.05$, ** $p < 0.01$, *** $p < 0.001$, **** $p < 0.0001$.

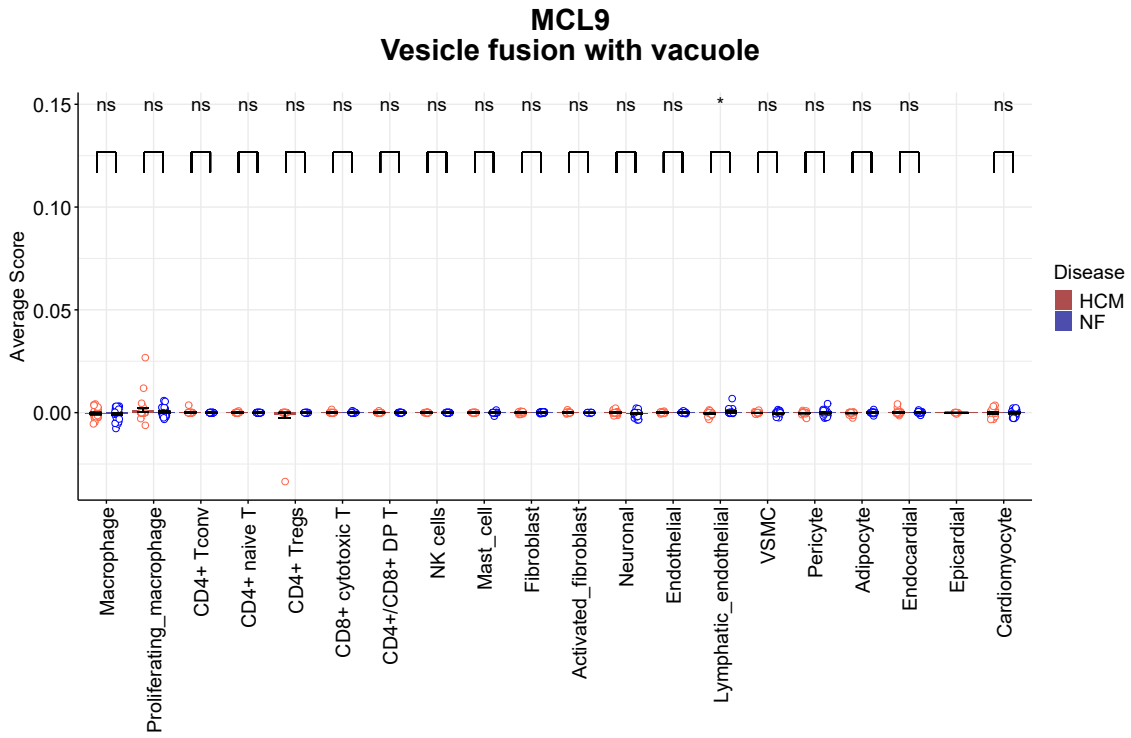

Figure D.54. Gene set scoring for MCL sub-cluster 9 of Cluster 9 (increasing expression over time) in late-stage human cell types.
This sub-cluster is a constituent of Cluster 9. The bar chart displays the gene set score for this specific sub-cluster across various cell types from late-stage human HCM snRNA-seq data. Scores were calculated for each sample using the `score_genes` function in `scanpy` v1.10.1 [267]. Bars represent the mean score, with error bars indicating the standard error of the mean. Statistical significance between disease and control samples was determined using a t-test, with p-values adjusted for multiple comparisons using the Benjamini-Hochberg method. Asterisks denote significance levels: * $p < 0.05$, ** $p < 0.01$, *** $p < 0.001$, **** $p < 0.0001$.

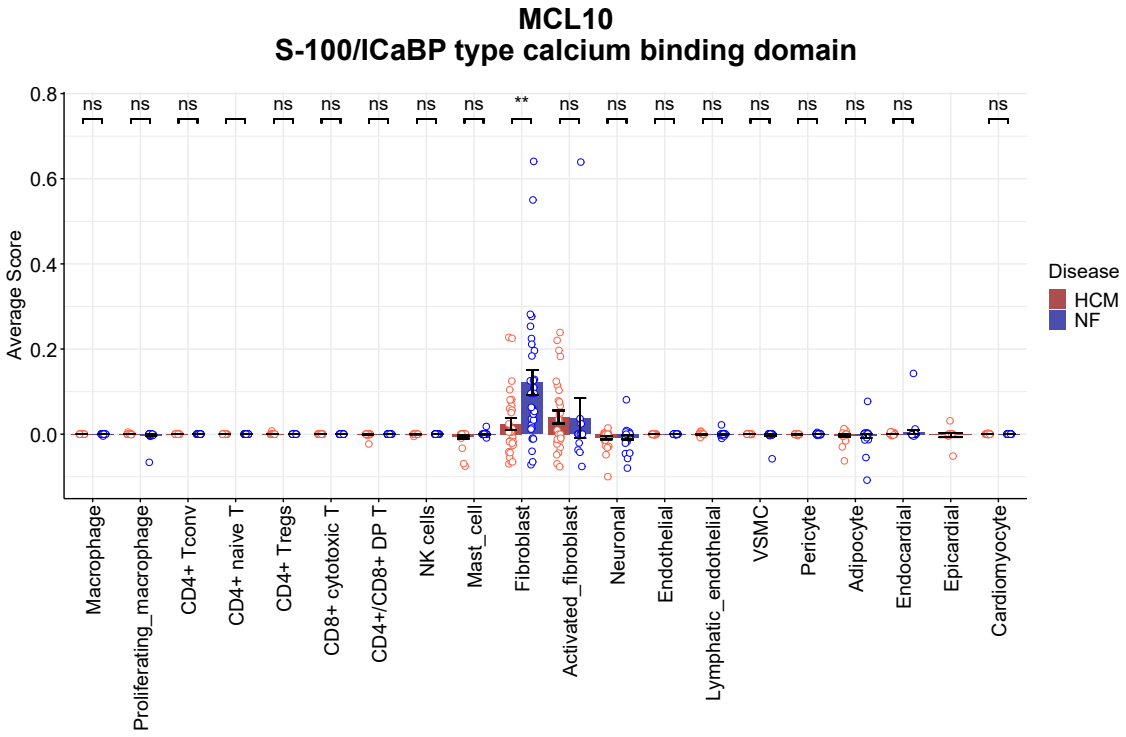

Figure D.55. Gene set scoring for MCL sub-cluster 10 of Cluster 9 (increasing expression over time) in late-stage human cell types.
This sub-cluster is a constituent of Cluster 9. The bar chart displays the gene set score for this specific sub-cluster across various cell types from late-stage human HCM snRNA-seq data. Scores were calculated for each sample using the `score_genes` function in `scanpy` v1.10.1 [267]. Bars represent the mean score, with error bars indicating the standard error of the mean. Statistical significance between disease and control samples was determined using a t-test, with p-values adjusted for multiple comparisons using the Benjamini-Hochberg method. Asterisks denote significance levels: * $p < 0.05$, ** $p < 0.01$, *** $p < 0.001$, **** $p < 0.0001$.

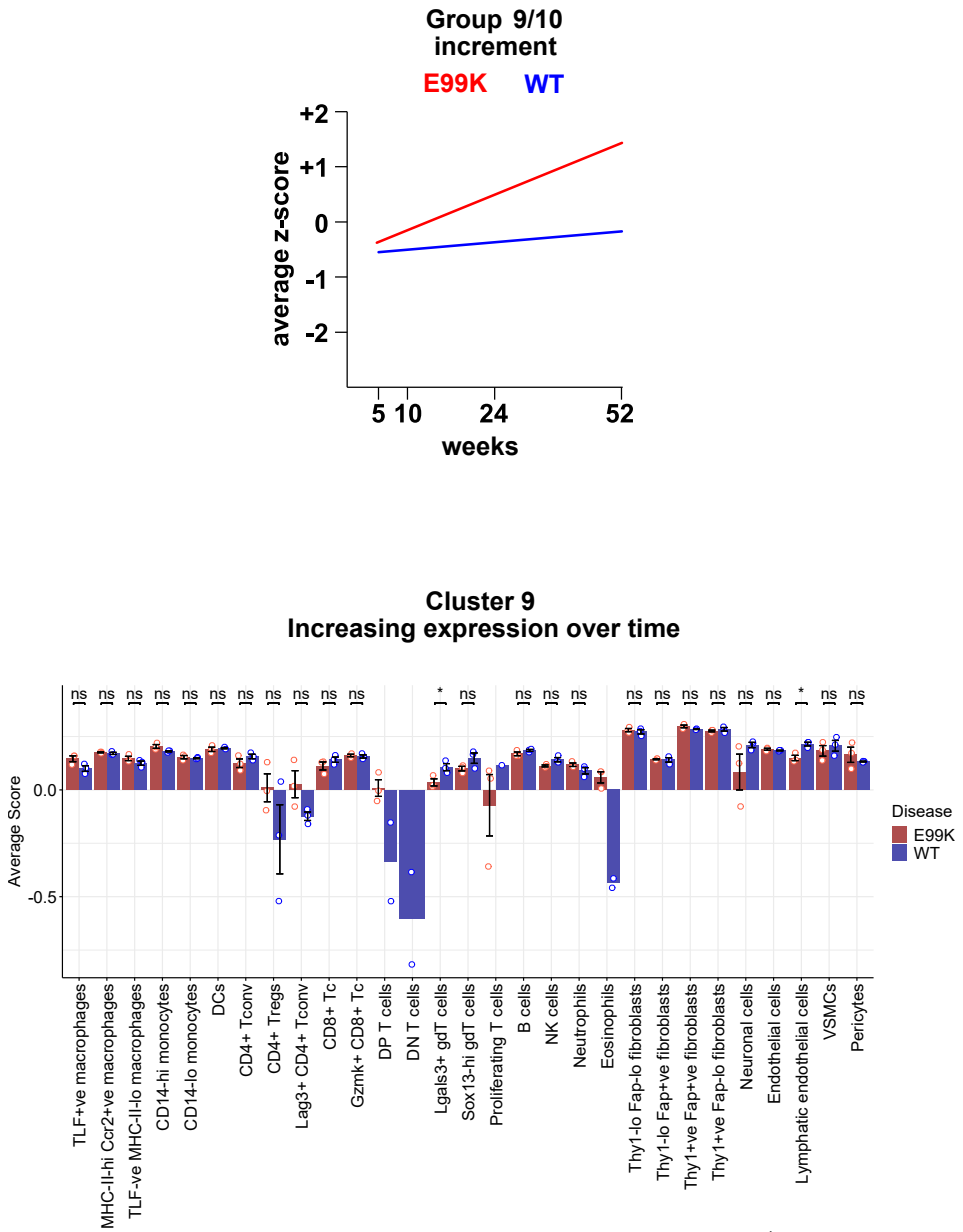

Figure D.56. Gene set scoring and statistics of Cluster 9 (increasing expression over time) in late-stage mouse cell types.
The upper panel schematically illustrates the temporal expression trend for Cluster 9, derived from bulk RNA-seq data of $Actc1^{E99K}$ (red line) and wild-type (blue line) hearts over time. The lower panel displays the gene set score for all genes within Cluster 9 across various cell types identified in late-stage $Actc1^{E99K}$ mouse scRNA-seq data. Scores were calculated for each sample using the `score_genes` function in `scanpy` v1.10.1 [267]. Bars represent the mean score, with error bars indicating the standard error of the mean. Statistical significance between disease and control samples was determined using a t-test, with p-values adjusted for multiple comparisons using the Benjamini-Hochberg method. Asterisks denote significance levels: * $p < 0.05$, ** $p < 0.01$, *** $p < 0.001$, **** $p < 0.0001$.

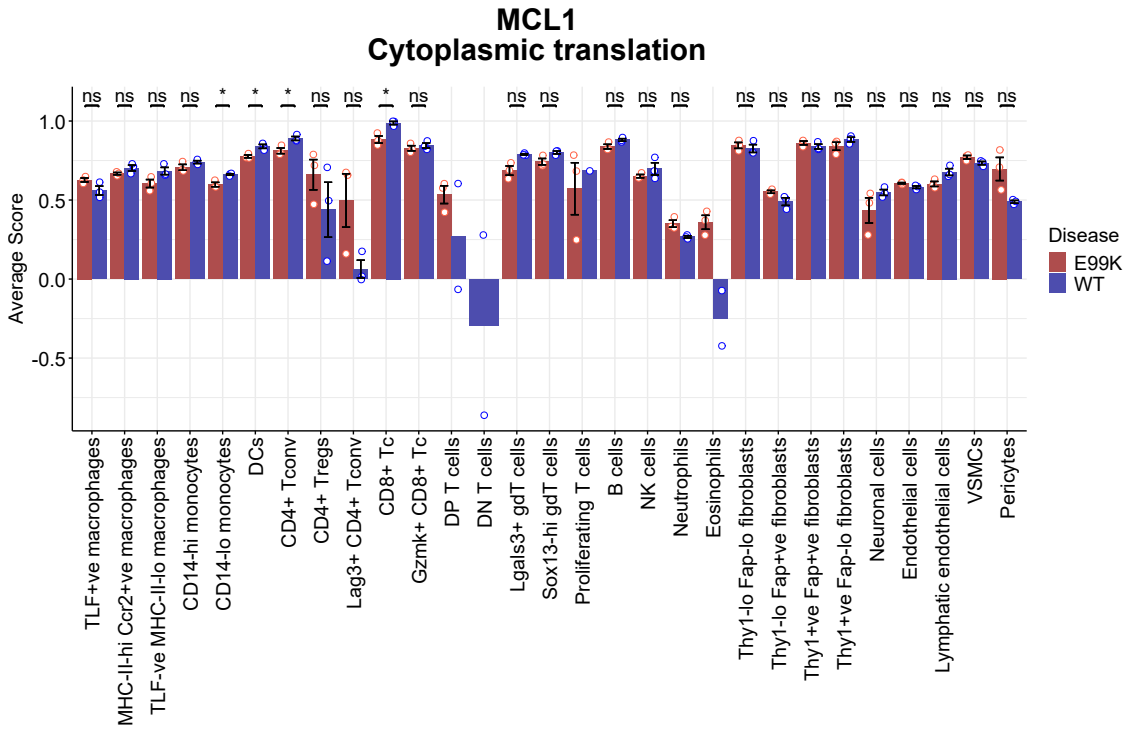

Figure D.57. Gene set scoring for MCL sub-cluster 1 of Cluster 9 (increasing expression over time) in late-stage mouse cell types.
This sub-cluster is a constituent of Cluster 9. The bar chart displays the gene set score for this specific sub-cluster across various cell types from late-stage Actc1^{E99K} mouse scRNA-seq data. Scores were calculated for each sample using the `score_genes` function in `scanpy` v1.10.1 [267]. Bars represent the mean score, with error bars indicating the standard error of the mean. Statistical significance between disease and control samples was determined using a t-test, with p-values adjusted for multiple comparisons using the Benjamini-Hochberg method. Asterisks denote significance levels: * $p < 0.05$, ** $p < 0.01$, *** $p < 0.001$, **** $p < 0.0001$.

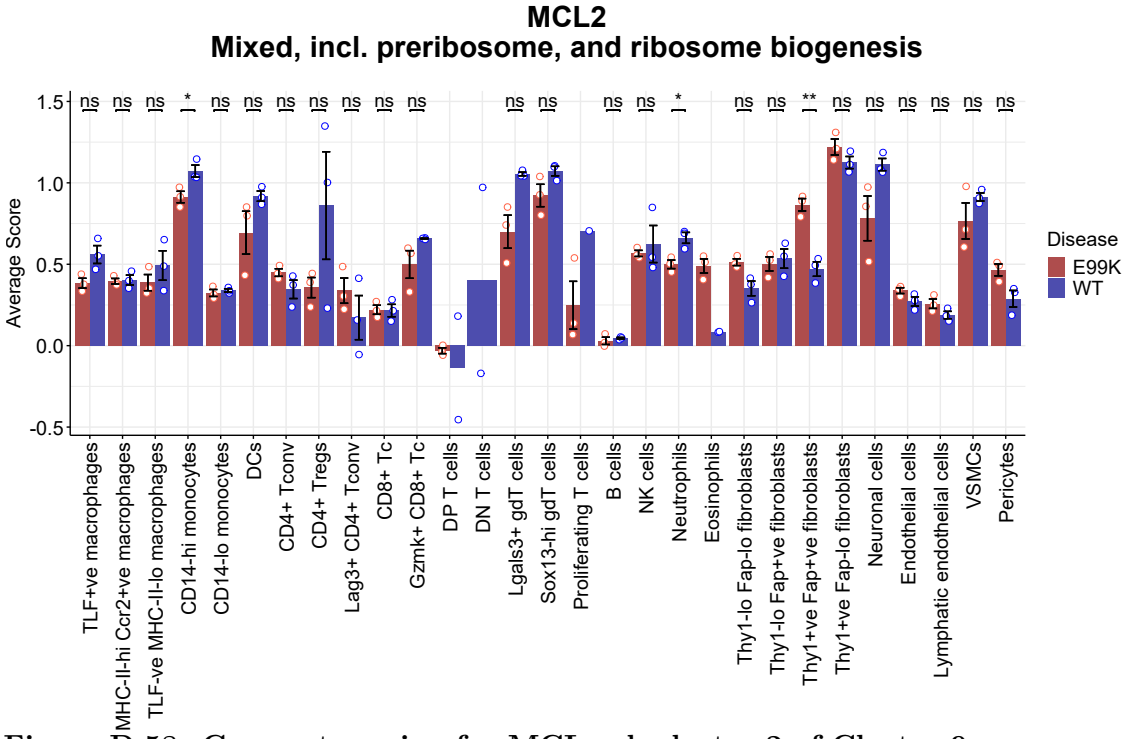

Figure D.58. Gene set scoring for MCL sub-cluster 2 of Cluster 9 (increasing expression over time) in late-stage mouse cell types.
This sub-cluster is a constituent of Cluster 9. The bar chart displays the gene set score for this specific sub-cluster across various cell types from late-stage Actc1^{E99K} mouse scRNA-seq data. Scores were calculated for each sample using the `score_genes` function in `scanpy` v1.10.1 [267]. Bars represent the mean score, with error bars indicating the standard error of the mean. Statistical significance between disease and control samples was determined using a t-test, with p-values adjusted for multiple comparisons using the Benjamini-Hochberg method. Asterisks denote significance levels: * $p < 0.05$, ** $p < 0.01$, *** $p < 0.001$, **** $p < 0.0001$.

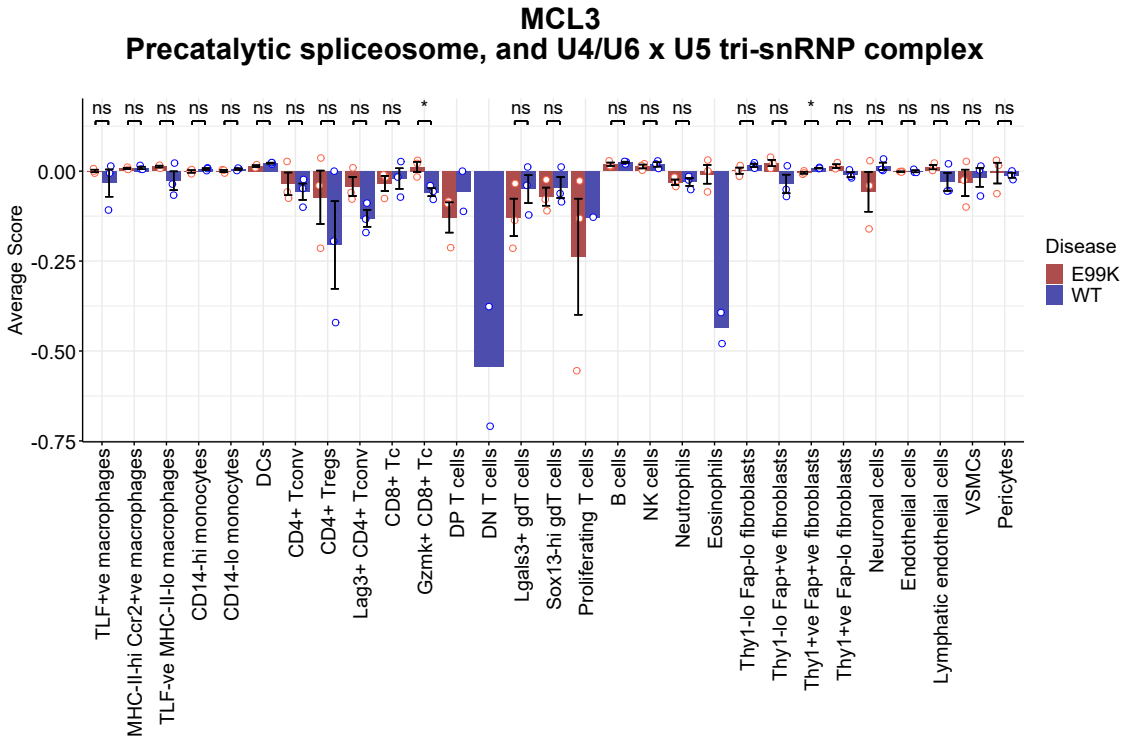

Figure D.59. Gene set scoring for MCL sub-cluster 3 of Cluster 9 (increasing expression over time) in late-stage mouse cell types.
This sub-cluster is a constituent of Cluster 9. The bar chart displays the gene set score for this specific sub-cluster across various cell types from late-stage Actc1^{E99K} mouse scRNA-seq data. Scores were calculated for each sample using the `score_genes` function in `scanpy` v1.10.1 [267]. Bars represent the mean score, with error bars indicating the standard error of the mean. Statistical significance between disease and control samples was determined using a t-test, with p-values adjusted for multiple comparisons using the Benjamini-Hochberg method. Asterisks denote significance levels: * $p < 0.05$, ** $p < 0.01$, *** $p < 0.001$, **** $p < 0.0001$.

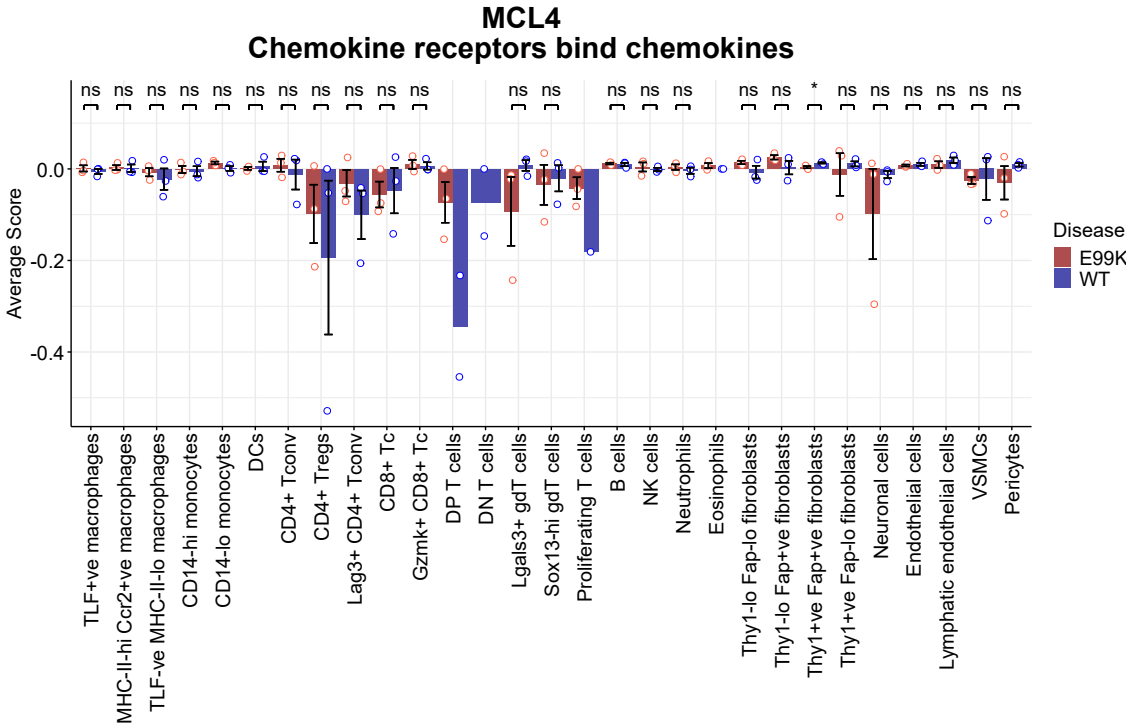

Figure D.60. Gene set scoring for MCL sub-cluster 4 of Cluster 9 (increasing expression over time) in late-stage mouse cell types.
This sub-cluster is a constituent of Cluster 9. The bar chart displays the gene set score for this specific sub-cluster across various cell types from late-stage Actc1^{E99K} mouse scRNA-seq data. Scores were calculated for each sample using the `score_genes` function in `scanpy` v1.10.1 [267]. Bars represent the mean score, with error bars indicating the standard error of the mean. Statistical significance between disease and control samples was determined using a t-test, with p-values adjusted for multiple comparisons using the Benjamini-Hochberg method. Asterisks denote significance levels: * $p < 0.05$, ** $p < 0.01$, *** $p < 0.001$, **** $p < 0.0001$.

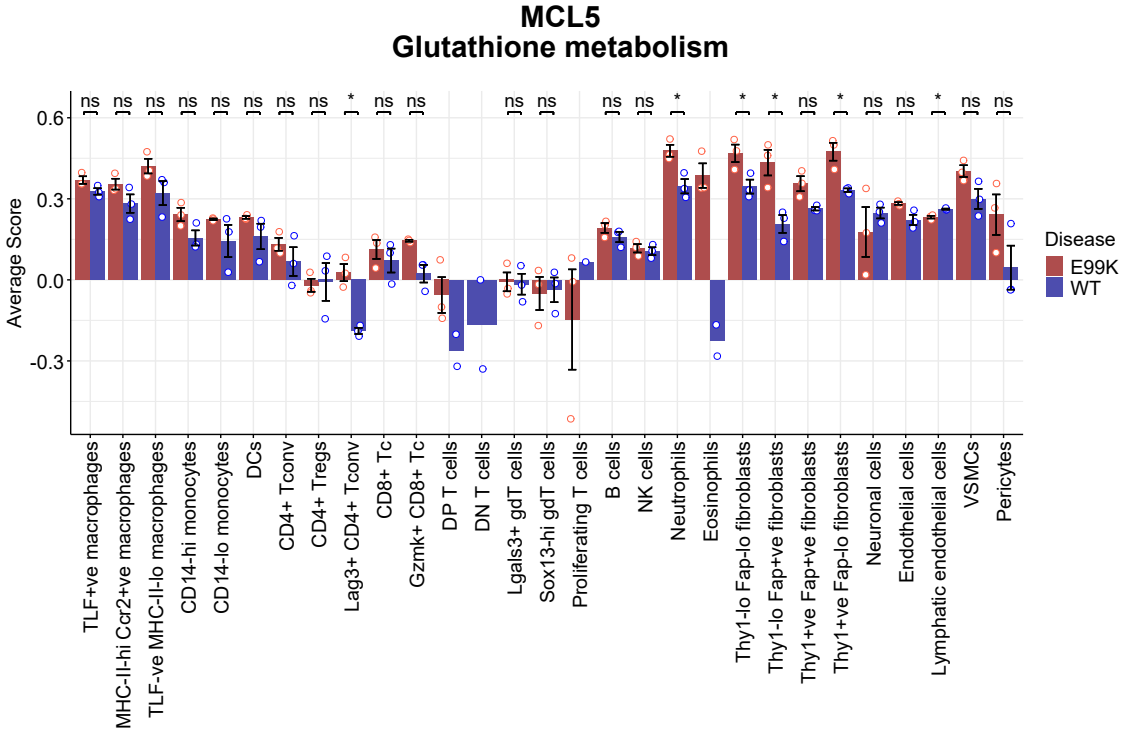

Figure D.61. Gene set scoring for MCL sub-cluster 5 of Cluster 9 (increasing expression over time) in late-stage mouse cell types.
This sub-cluster is a constituent of Cluster 9. The bar chart displays the gene set score for this specific sub-cluster across various cell types from late-stage Actc1^{E99K} mouse scRNA-seq data. Scores were calculated for each sample using the `score_genes` function in `scanpy` v1.10.1 [267]. Bars represent the mean score, with error bars indicating the standard error of the mean. Statistical significance between disease and control samples was determined using a t-test, with p-values adjusted for multiple comparisons using the Benjamini-Hochberg method. Asterisks denote significance levels: * $p < 0.05$, ** $p < 0.01$, *** $p < 0.001$, **** $p < 0.0001$.

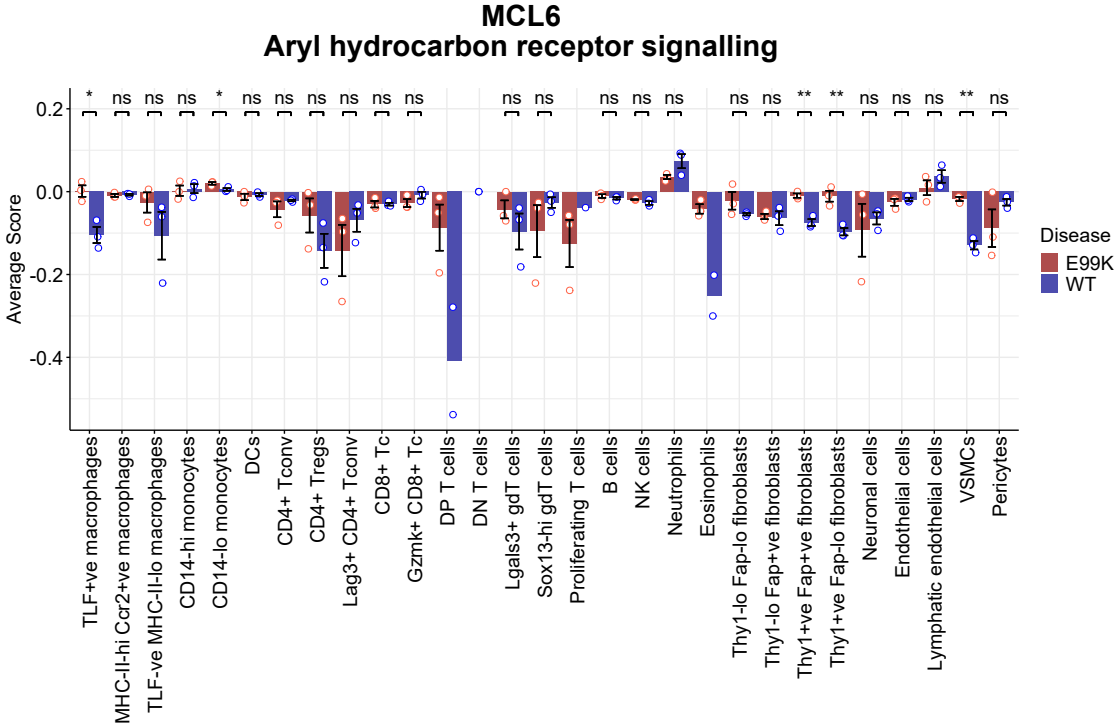

Figure D.62. Gene set scoring for MCL sub-cluster 6 of Cluster 9 (increasing expression over time) in late-stage mouse cell types.
This sub-cluster is a constituent of Cluster 9. The bar chart displays the gene set score for this specific sub-cluster across various cell types from late-stage Actc1^{E99K} mouse scRNA-seq data. Scores were calculated for each sample using the `score_genes` function in `scanpy` v1.10.1 [267]. Bars represent the mean score, with error bars indicating the standard error of the mean. Statistical significance between disease and control samples was determined using a t-test, with p-values adjusted for multiple comparisons using the Benjamini-Hochberg method. Asterisks denote significance levels: * $p < 0.05$, ** $p < 0.01$, *** $p < 0.001$, **** $p < 0.0001$.

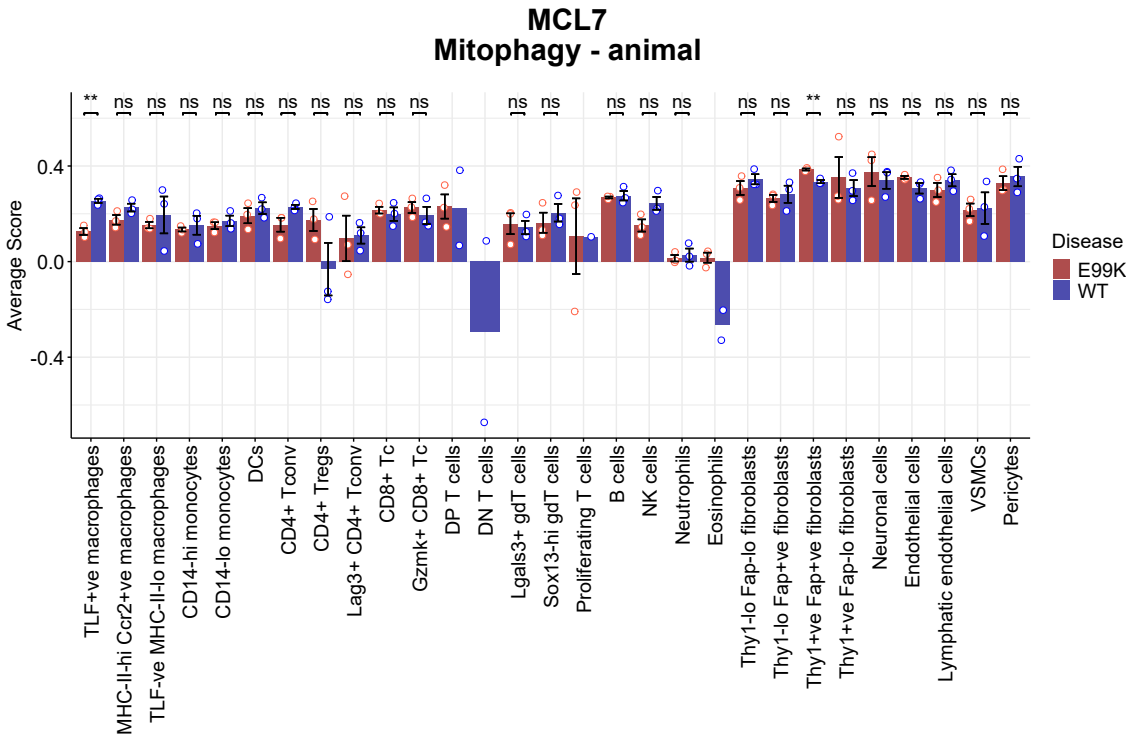

Figure D.63. Gene set scoring for MCL sub-cluster 7 of Cluster 9 (increasing expression over time) in late-stage mouse cell types.
This sub-cluster is a constituent of Cluster 9. The bar chart displays the gene set score for this specific sub-cluster across various cell types from late-stage Actc1^{E99K} mouse scRNA-seq data. Scores were calculated for each sample using the `score_genes` function in `scanpy` v1.10.1 [267]. Bars represent the mean score, with error bars indicating the standard error of the mean. Statistical significance between disease and control samples was determined using a t-test, with p-values adjusted for multiple comparisons using the Benjamini-Hochberg method. Asterisks denote significance levels: * $p < 0.05$, ** $p < 0.01$, *** $p < 0.001$, **** $p < 0.0001$.

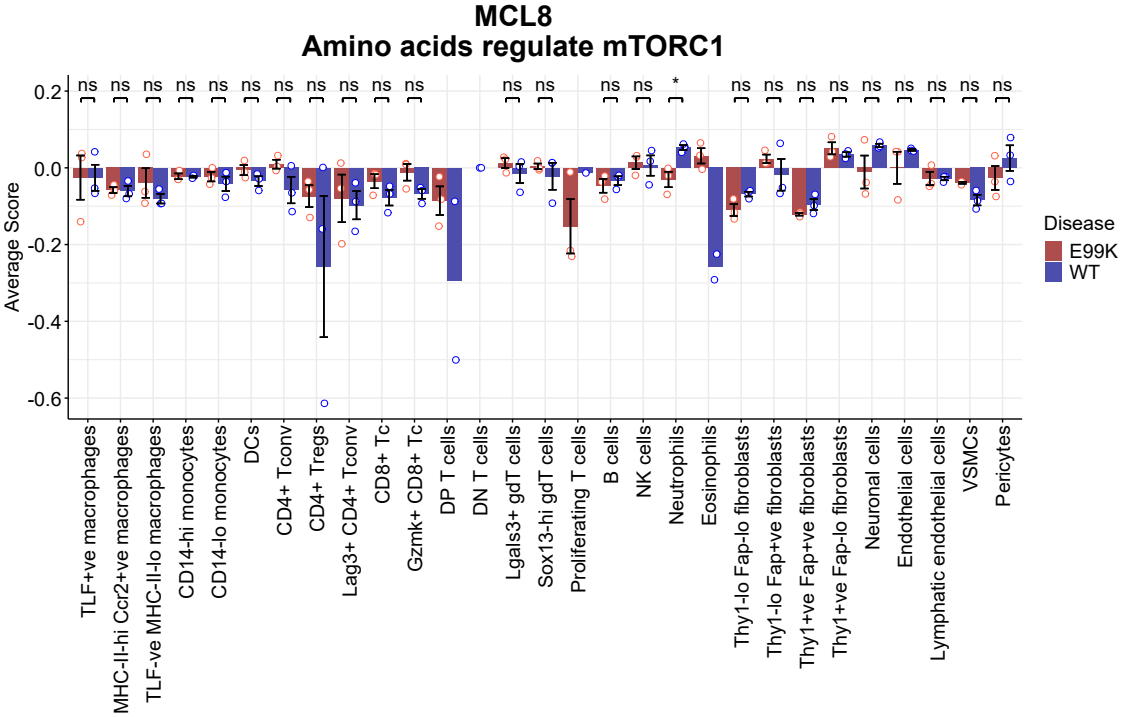

Figure D.64. Gene set scoring for MCL sub-cluster 8 of Cluster 9 (increasing expression over time) in late-stage mouse cell types.
This sub-cluster is a constituent of Cluster 9. The bar chart displays the gene set score for this specific sub-cluster across various cell types from late-stage Actc1^{E99K} mouse scRNA-seq data. Scores were calculated for each sample using the `score_genes` function in `scanpy` v1.10.1 [267]. Bars represent the mean score, with error bars indicating the standard error of the mean. Statistical significance between disease and control samples was determined using a t-test, with p-values adjusted for multiple comparisons using the Benjamini-Hochberg method. Asterisks denote significance levels: * $p < 0.05$, ** $p < 0.01$, *** $p < 0.001$, **** $p < 0.0001$.

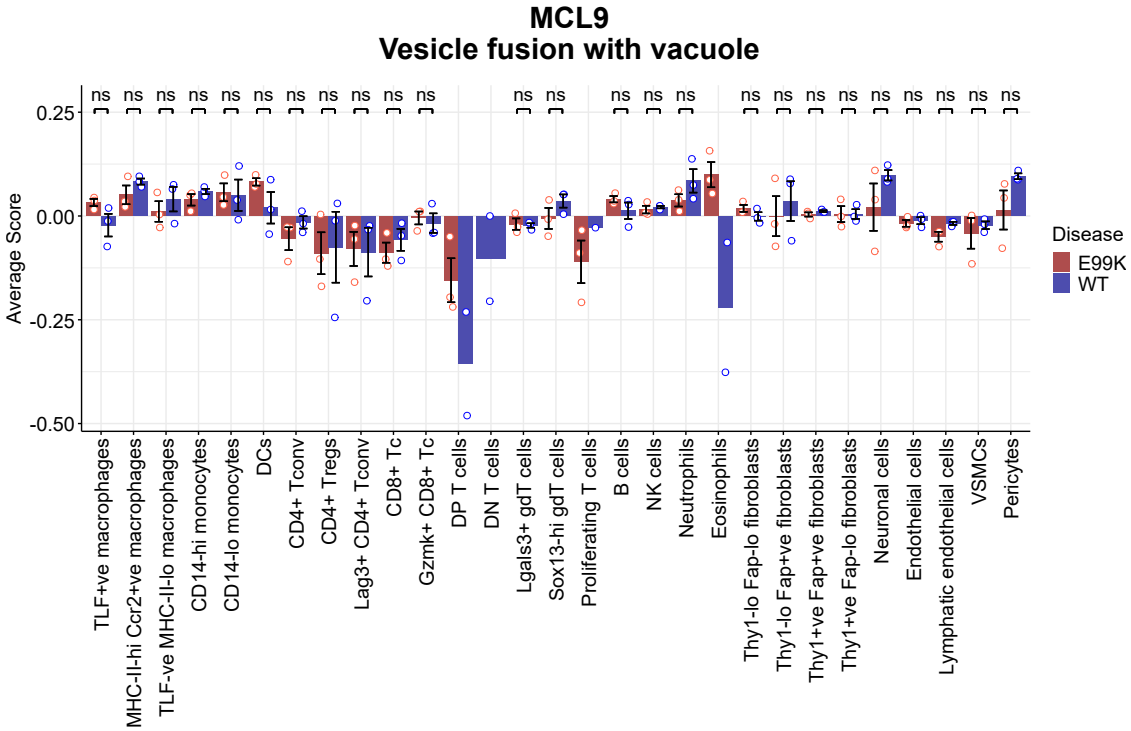

Figure D.65. Gene set scoring for MCL sub-cluster 9 of Cluster 9 (increasing expression over time) in late-stage mouse cell types.
This sub-cluster is a constituent of Cluster 9. The bar chart displays the gene set score for this specific sub-cluster across various cell types from late-stage $Actc1^{E99K}$ mouse scRNA-seq data. Scores were calculated for each sample using the `score_genes` function in `scanpy` v1.10.1 [267]. Bars represent the mean score, with error bars indicating the standard error of the mean. Statistical significance between disease and control samples was determined using a t-test, with p-values adjusted for multiple comparisons using the Benjamini-Hochberg method. Asterisks denote significance levels: * $p < 0.05$, ** $p < 0.01$, *** $p < 0.001$, **** $p < 0.0001$.

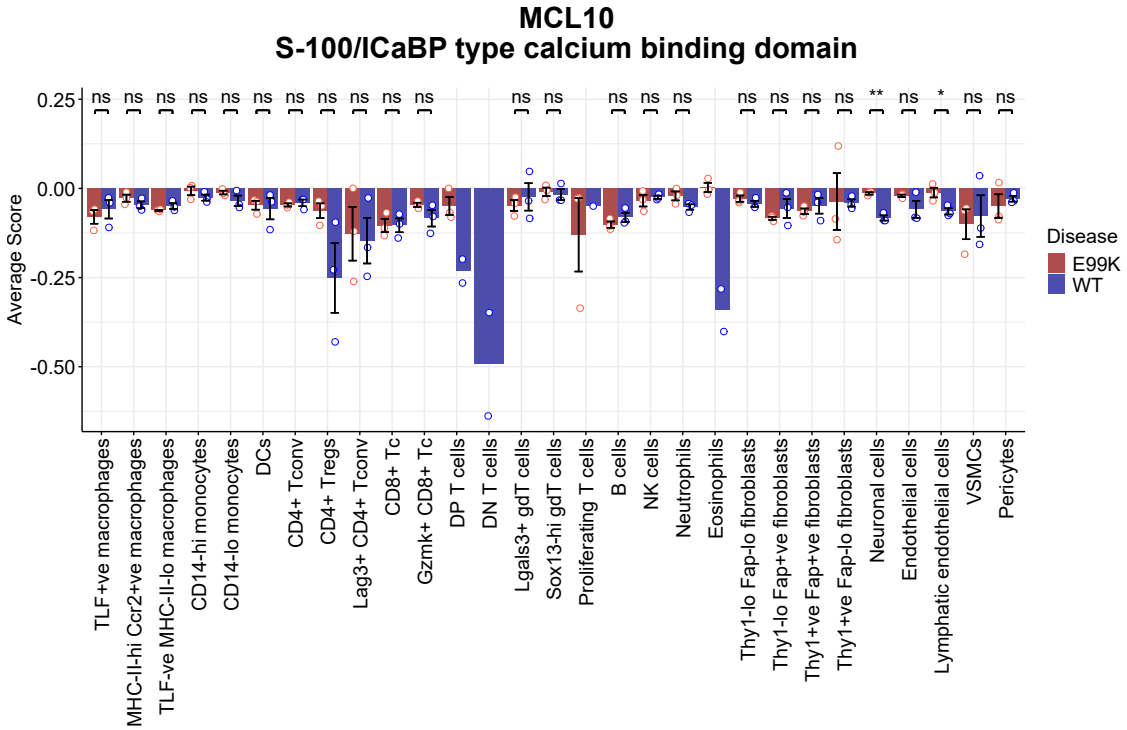

Figure D.66. Gene set scoring for MCL sub-cluster 10 of Cluster 9 (increasing expression over time) in late-stage mouse cell types.
This sub-cluster is a constituent of Cluster 9. The bar chart displays the gene set score for this specific sub-cluster across various cell types from late-stage Actc1^{E99K} mouse scRNA-seq data. Scores were calculated for each sample using the `score_genes` function in `scanpy` v1.10.1 [267]. Bars represent the mean score, with error bars indicating the standard error of the mean. Statistical significance between disease and control samples was determined using a t-test, with p-values adjusted for multiple comparisons using the Benjamini-Hochberg method. Asterisks denote significance levels: * $p < 0.05$, ** $p < 0.01$, *** $p < 0.001$, **** $p < 0.0001$.

Cluster 10, also showing increasing expression over time, encompassed a diverse range of functions (Figures D.67 and D.78). Sub-cluster analysis identified enrichment for tight junction assembly (MCL sub-cluster 1; Figure D.68), phase I functionalisation of compounds (MCL sub-cluster 2; Figure D.69), CoA-ligase activity (MCL sub-cluster 3; Figure D.70), axonemal dynein complex and inner dynein arm assembly (MCL sub-cluster 4; Figure D.71), tektin and establishment of left/right asymmetry (MCL sub-cluster 5; Figure D.72), inner dynein arm (MCL sub-cluster 6; Figure D.73), myosin II complex and mesenchyme migration (MCL sub-cluster 7; Figure D.74), adrenaline and noradrenaline inhibition of insulin secretion (MCL sub-cluster 8; Figure D.75), Wnt and frizzled/secreted frizzled-related protein signalling (MCL sub-cluster 9; Figure D.76), and a mixed

sub-cluster containing genes related to surface film and alveolar lamellar body (MCL sub-cluster 10; Figure D.77). In late-stage human HCM, the overall cluster 10 signature was significantly upregulated in NK cells, activated fibroblasts, lymphatic endothelial cells, VSMCs, and cardiomyocytes, while downregulated in proliferating macrophages (Figure D.67). Sub-cluster analysis revealed further cell-type specific patterns. The tight junction assembly sub-cluster (MCL sub-cluster 1; Figure D.68) was upregulated in endothelial cells. The CoA-ligase activity sub-cluster (MCL sub-cluster 3; Figure D.70) was upregulated in fibroblasts and VSMCs. The axonemal dynein complex sub-cluster (MCL sub-cluster 4; Figure D.71) was upregulated in VSMCs. The Wnt signalling sub-cluster (MCL sub-cluster 9; Figure D.76) was downregulated in neuronal cells and epicardial cells, and showed negligible change in lymphatic endothelial cells. In the mouse scRNA-seq data, the overall cluster 10 signature was upregulated in $CD14^{hi}$ monocytes and $Thy1^{lo}Fap^{+}$ fibroblasts, and downregulated in $Thy1^{lo}Fap^{lo}$ fibroblasts (Figure D.78). Sub-cluster analysis revealed upregulation of the CoA-ligase activity sub-cluster (MCL sub-cluster 3; Figure D.81) in $Thy1^{lo}Fap^{+}$ fibroblasts. The axonemal dynein complex sub-cluster (MCL sub-cluster 4; Figure D.82) was upregulated in $Lag3^{+}$ $CD4^{+}$ Tconv cells and downregulated in VSMCs. The Wnt signalling sub-cluster (MCL sub-cluster 9; Figure D.87) was upregulated in VSMCs and downregulated in lymphatic endothelial cells.

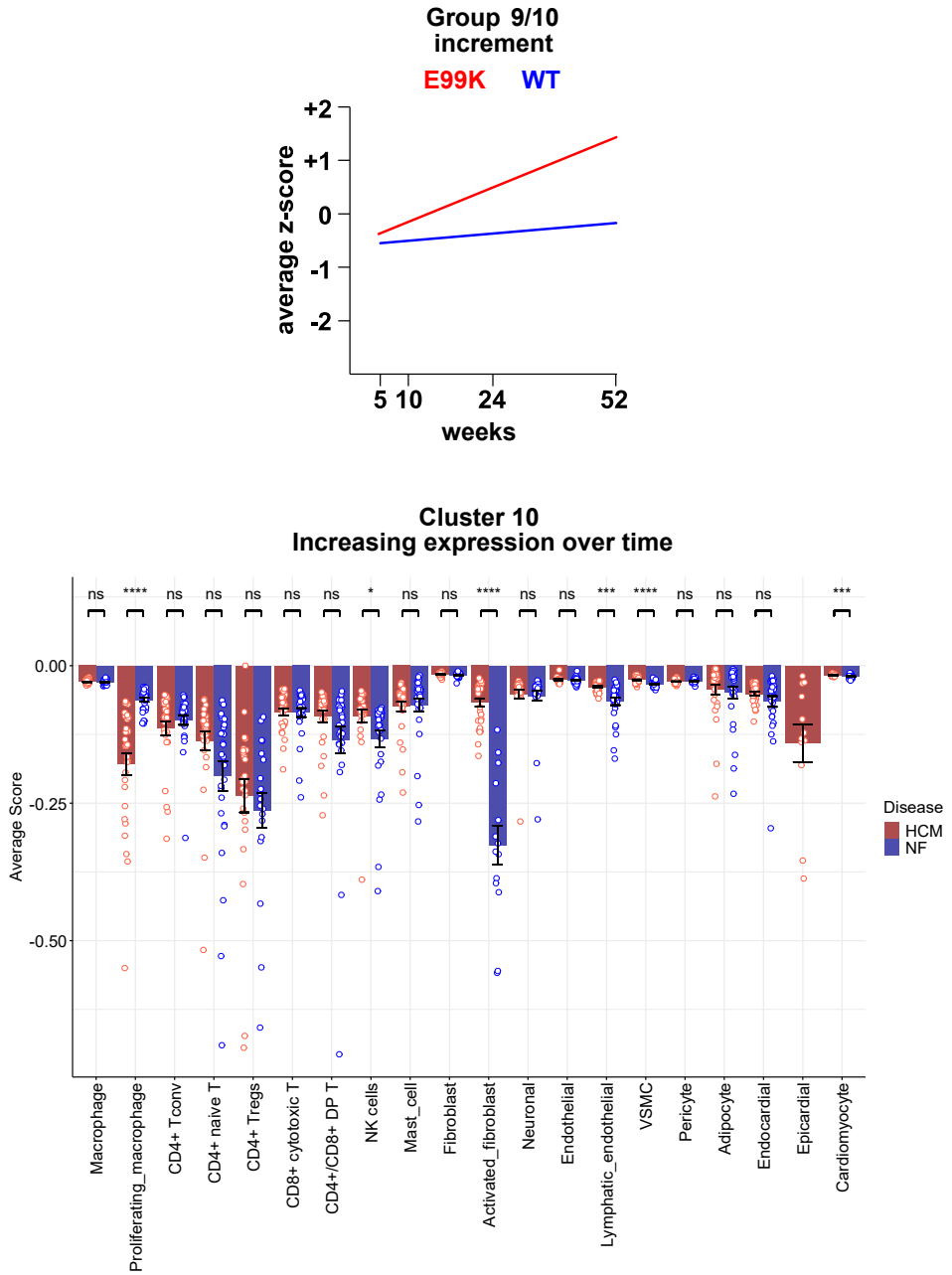

Figure D.67. Gene set scoring and statistics of Cluster 10 (increasing expression over time) in late-stage human cell types.
The upper panel schematically illustrates the temporal expression trend for Cluster 10, derived from bulk RNA-seq data of Actc1^{E99K} (red line) and wild-type (blue line) hearts over time. The lower panel displays the gene set score for all genes within Cluster 10 across various cell types identified in late-stage human HCM snRNA-seq data. Scores were calculated for each sample using the `score_genes` function in `scanpy` v1.10.1 [267]. Bars represent the mean score, with error bars indicating the standard error of the mean. Statistical significance between disease and control samples was determined using a t-test, with p-values adjusted for multiple comparisons using the Benjamini-Hochberg method. Asterisks denote significance levels: * $p < 0.05$, ** $p < 0.01$, *** $p < 0.001$, **** $p < 0.0001$.

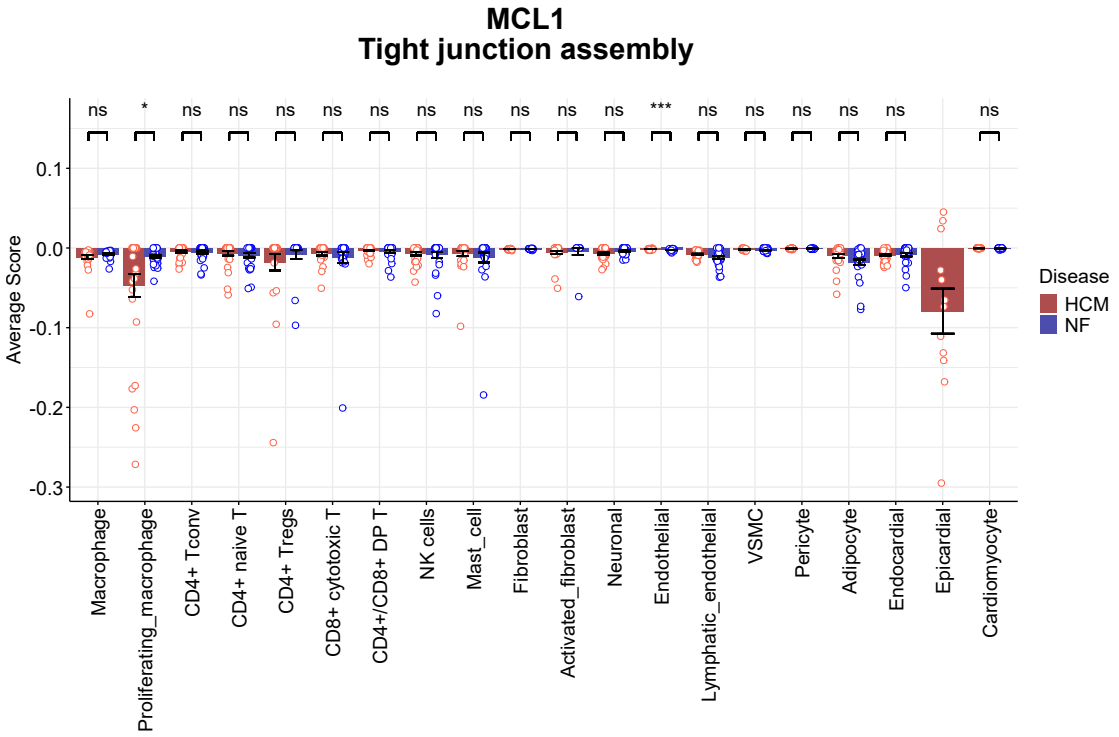

Figure D.68. Gene set scoring for MCL sub-cluster 1 of Cluster 10 (increasing expression over time) in late-stage human cell types.
This sub-cluster is a constituent of Cluster 10. The bar chart displays the gene set score for this specific sub-cluster across various cell types from late-stage human HCM snRNA-seq data. Scores were calculated for each sample using the `score_genes` function in `scanpy` v1.10.1 [267]. Bars represent the mean score, with error bars indicating the standard error of the mean. Statistical significance between disease and control samples was determined using a t-test, with p-values adjusted for multiple comparisons using the Benjamini-Hochberg method. Asterisks denote significance levels: * $p < 0.05$, ** $p < 0.01$, *** $p < 0.001$, **** $p < 0.0001$.

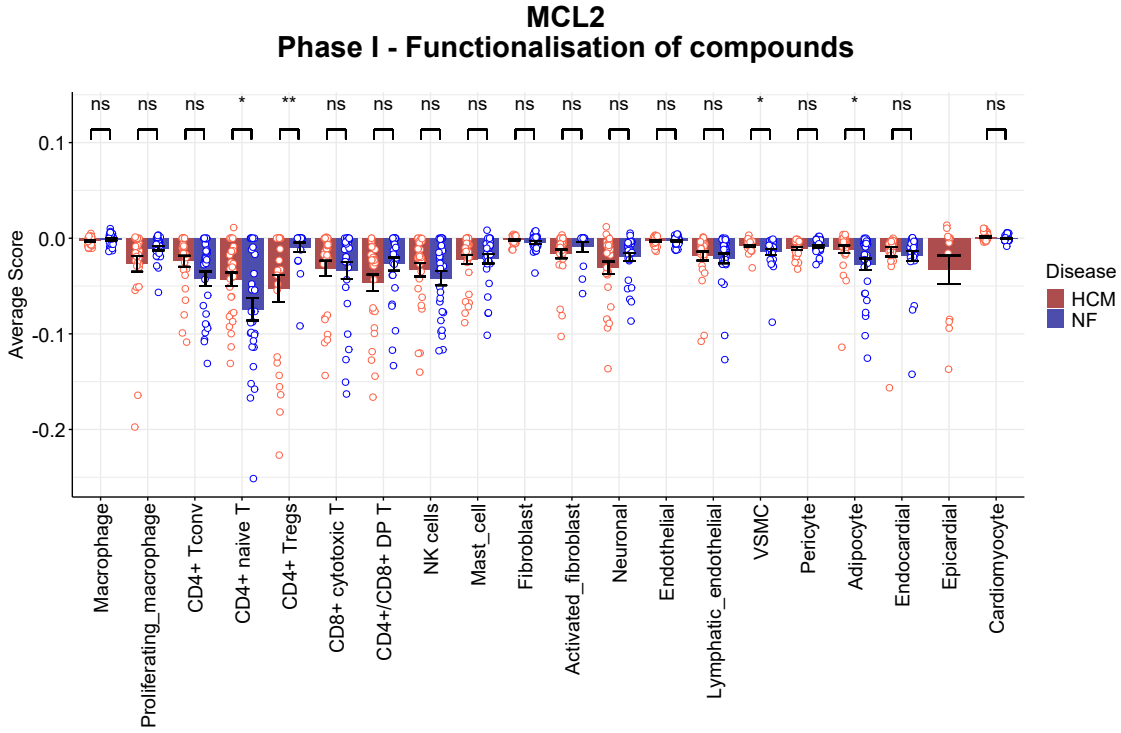

Figure D.69. Gene set scoring for MCL sub-cluster 2 of Cluster 10 (increasing expression over time) in late-stage human cell types.
This sub-cluster is a constituent of Cluster 10. The bar chart displays the gene set score for this specific sub-cluster across various cell types from late-stage human HCM snRNA-seq data. Scores were calculated for each sample using the `score_genes` function in `scanpy` v1.10.1 [267]. Bars represent the mean score, with error bars indicating the standard error of the mean. Statistical significance between disease and control samples was determined using a t-test, with p-values adjusted for multiple comparisons using the Benjamini-Hochberg method. Asterisks denote significance levels: * $p < 0.05$, ** $p < 0.01$, *** $p < 0.001$, **** $p < 0.0001$.

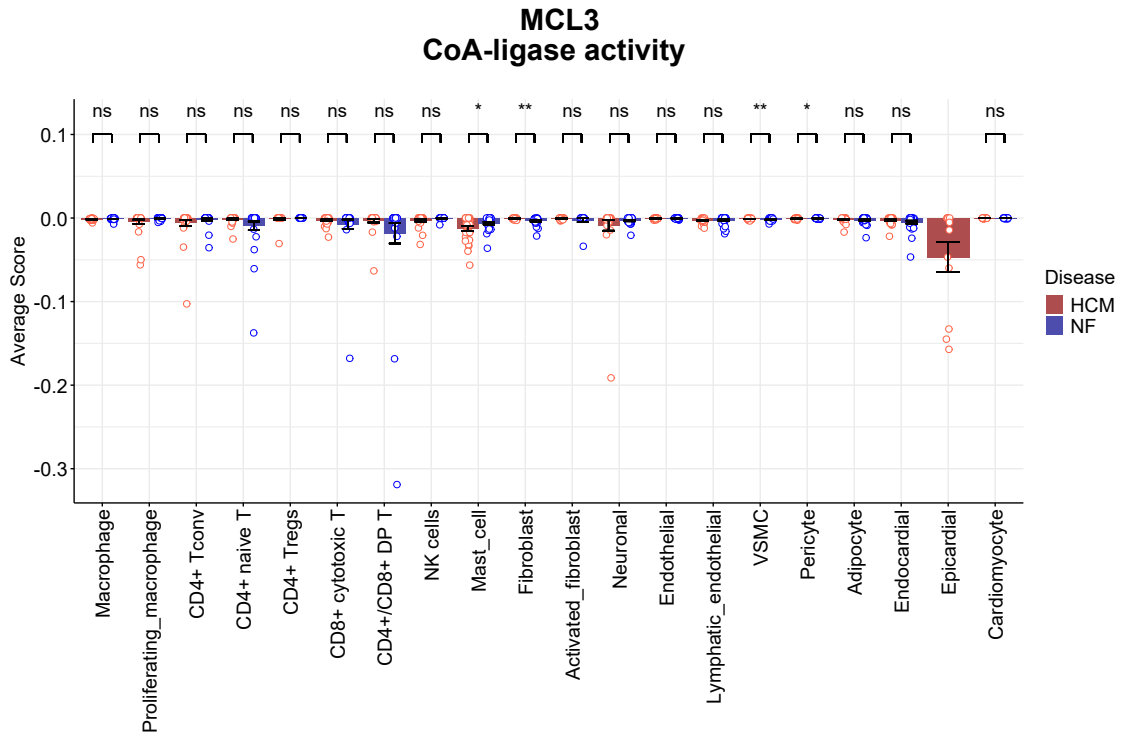

Figure D.70. Gene set scoring for MCL sub-cluster 3 of Cluster 10 (increasing expression over time) in late-stage human cell types.
This sub-cluster is a constituent of Cluster 10. The bar chart displays the gene set score for this specific sub-cluster across various cell types from late-stage human HCM snRNA-seq data. Scores were calculated for each sample using the `score_genes` function in `scanpy` v1.10.1 [267]. Bars represent the mean score, with error bars indicating the standard error of the mean. Statistical significance between disease and control samples was determined using a t-test, with p-values adjusted for multiple comparisons using the Benjamini-Hochberg method. Asterisks denote significance levels: * $p < 0.05$, ** $p < 0.01$, *** $p < 0.001$, **** $p < 0.0001$.

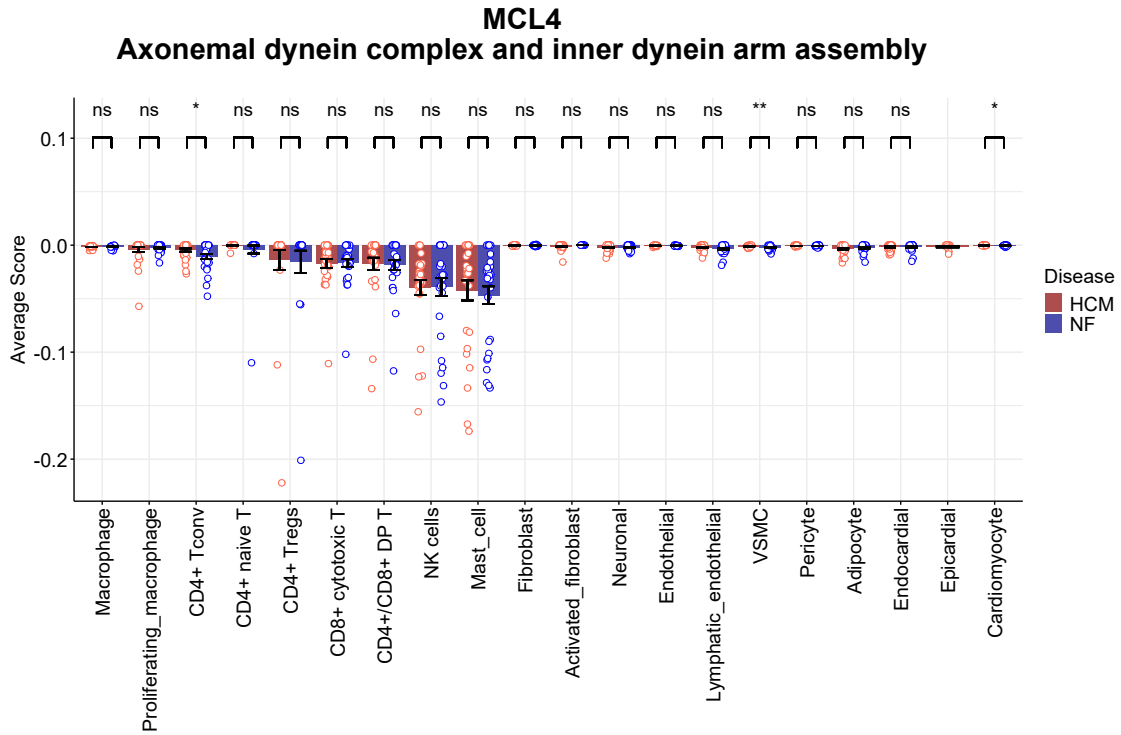

Figure D.71. Gene set scoring for MCL sub-cluster 4 of Cluster 10 (increasing expression over time) in late-stage human cell types.
This sub-cluster is a constituent of Cluster 10. The bar chart displays the gene set score for this specific sub-cluster across various cell types from late-stage human HCM snRNA-seq data. Scores were calculated for each sample using the `score_genes` function in `scanpy` v1.10.1 [267]. Bars represent the mean score, with error bars indicating the standard error of the mean. Statistical significance between disease and control samples was determined using a t-test, with p-values adjusted for multiple comparisons using the Benjamini-Hochberg method. Asterisks denote significance levels: * $p < 0.05$, ** $p < 0.01$, *** $p < 0.001$, **** $p < 0.0001$.

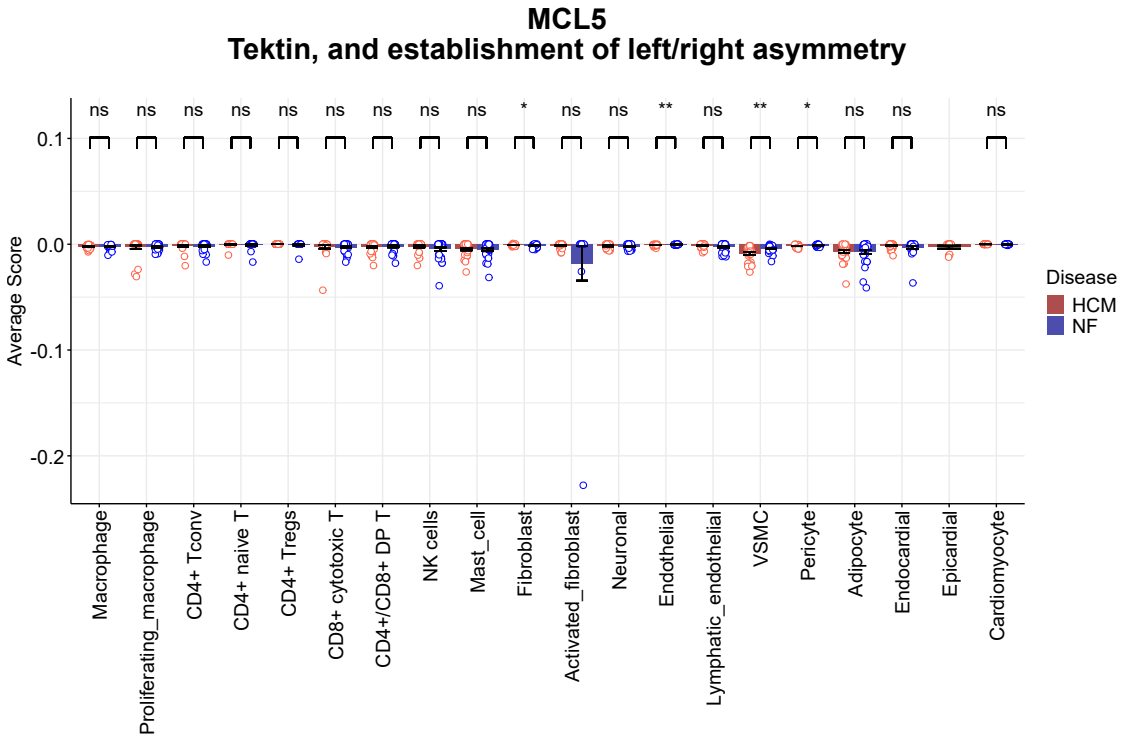

Figure D.72. Gene set scoring for MCL sub-cluster 5 of Cluster 10 (increasing expression over time) in late-stage human cell types.
This sub-cluster is a constituent of Cluster 10. The bar chart displays the gene set score for this specific sub-cluster across various cell types from late-stage human HCM snRNA-seq data. Scores were calculated for each sample using the `score_genes` function in `scanpy` v1.10.1 [267]. Bars represent the mean score, with error bars indicating the standard error of the mean. Statistical significance between disease and control samples was determined using a t-test, with p-values adjusted for multiple comparisons using the Benjamini-Hochberg method. Asterisks denote significance levels: * $p < 0.05$, ** $p < 0.01$, *** $p < 0.001$, **** $p < 0.0001$.

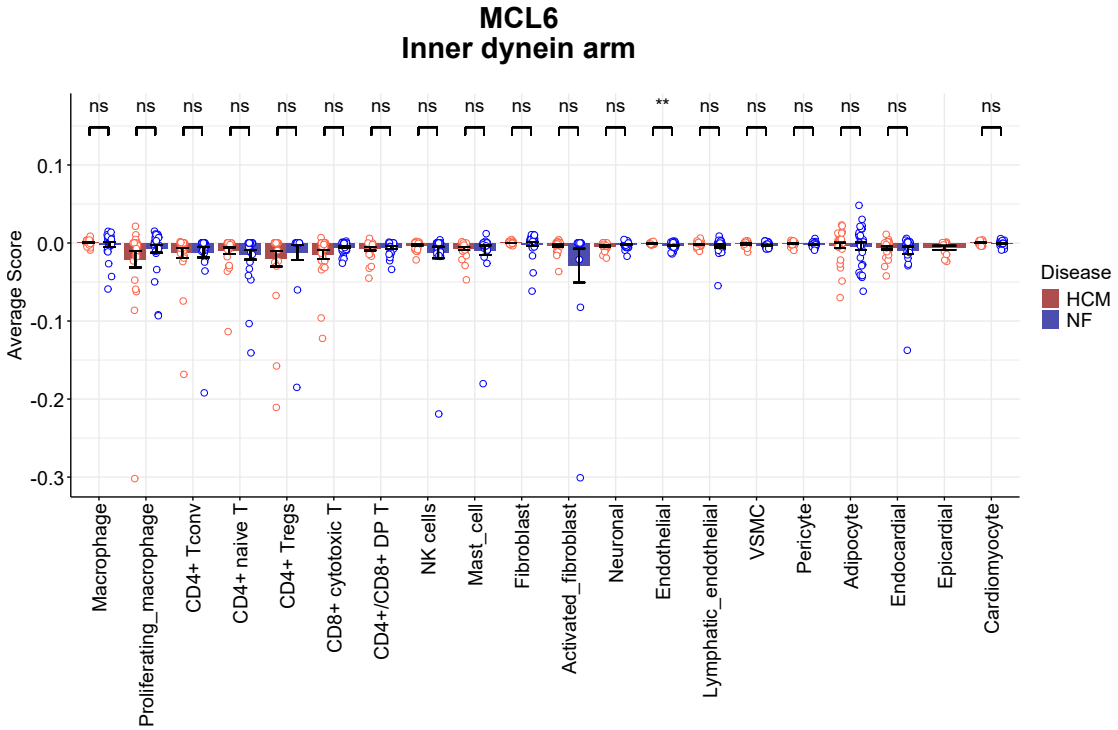

Figure D.73. Gene set scoring for MCL sub-cluster 6 of Cluster 10 (increasing expression over time) in late-stage human cell types.
This sub-cluster is a constituent of Cluster 10. The bar chart displays the gene set score for this specific sub-cluster across various cell types from late-stage human HCM snRNA-seq data. Scores were calculated for each sample using the `score_genes` function in `scanpy` v1.10.1 [267]. Bars represent the mean score, with error bars indicating the standard error of the mean. Statistical significance between disease and control samples was determined using a t-test, with p-values adjusted for multiple comparisons using the Benjamini-Hochberg method. Asterisks denote significance levels: * $p < 0.05$, ** $p < 0.01$, *** $p < 0.001$, **** $p < 0.0001$.

Figure D.74. Gene set scoring for MCL sub-cluster 7 of Cluster 10 (increasing expression over time) in late-stage human cell types.
This sub-cluster is a constituent of Cluster 10. The bar chart displays the gene set score for this specific sub-cluster across various cell types from late-stage human HCM snRNA-seq data. Scores were calculated for each sample using the `score_genes` function in `scanpy` v1.10.1 [267]. Bars represent the mean score, with error bars indicating the standard error of the mean. Statistical significance between disease and control samples was determined using a t-test, with p-values adjusted for multiple comparisons using the Benjamini-Hochberg method. Asterisks denote significance levels: * $p < 0.05$, ** $p < 0.01$, *** $p < 0.001$, **** $p < 0.0001$.

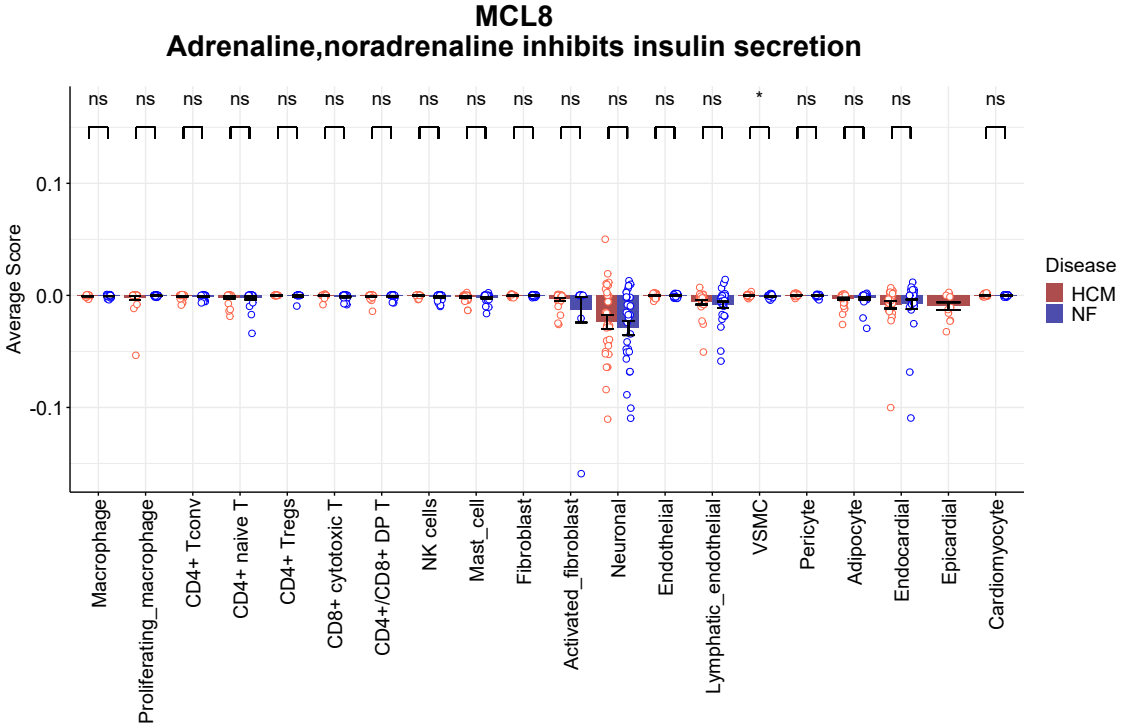

Figure D.75. Gene set scoring for MCL sub-cluster 8 of Cluster 10 (increasing expression over time) in late-stage human cell types.
This sub-cluster is a constituent of Cluster 10. The bar chart displays the gene set score for this specific sub-cluster across various cell types from late-stage human HCM snRNA-seq data. Scores were calculated for each sample using the `score_genes` function in `scanpy` v1.10.1 [267]. Bars represent the mean score, with error bars indicating the standard error of the mean. Statistical significance between disease and control samples was determined using a t-test, with p-values adjusted for multiple comparisons using the Benjamini-Hochberg method. Asterisks denote significance levels: * $p < 0.05$, ** $p < 0.01$, *** $p < 0.001$, **** $p < 0.0001$.

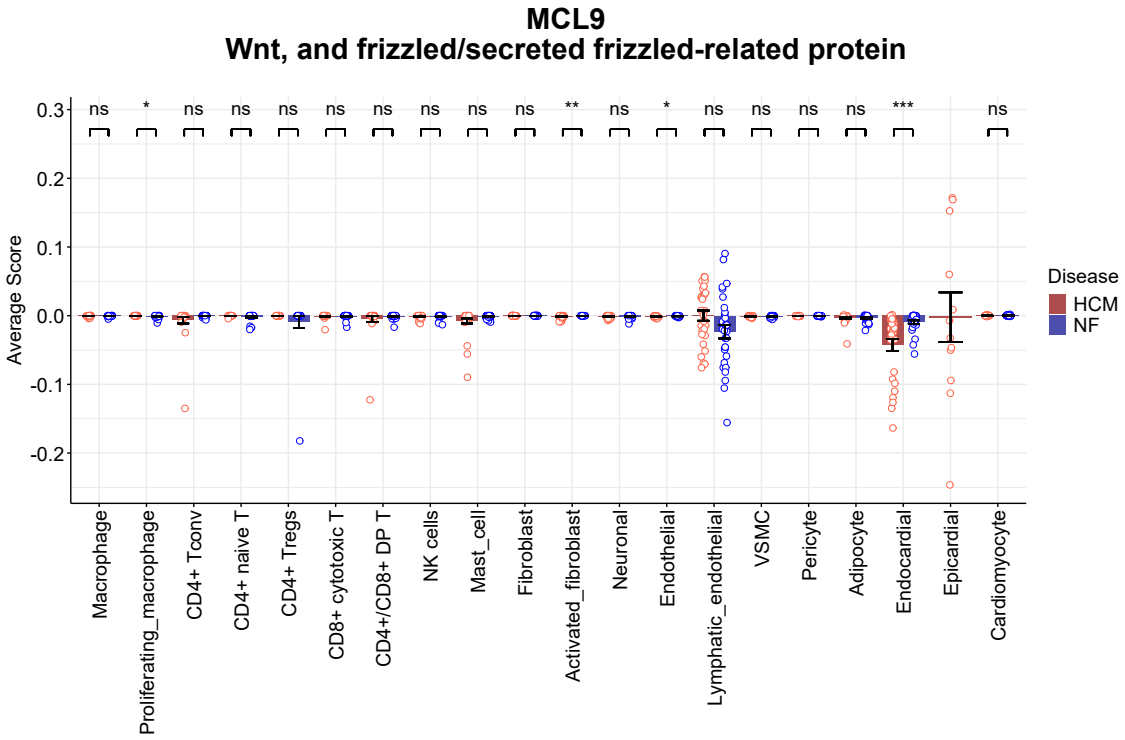

Figure D.76. Gene set scoring for MCL sub-cluster 9 of Cluster 10 (increasing expression over time) in late-stage human cell types.
This sub-cluster is a constituent of Cluster 10. The bar chart displays the gene set score for this specific sub-cluster across various cell types from late-stage human HCM snRNA-seq data. Scores were calculated for each sample using the `score_genes` function in `scanpy` v1.10.1 [267]. Bars represent the mean score, with error bars indicating the standard error of the mean. Statistical significance between disease and control samples was determined using a t-test, with p-values adjusted for multiple comparisons using the Benjamini-Hochberg method. Asterisks denote significance levels: * $p < 0.05$, ** $p < 0.01$, *** $p < 0.001$, **** $p < 0.0001$.

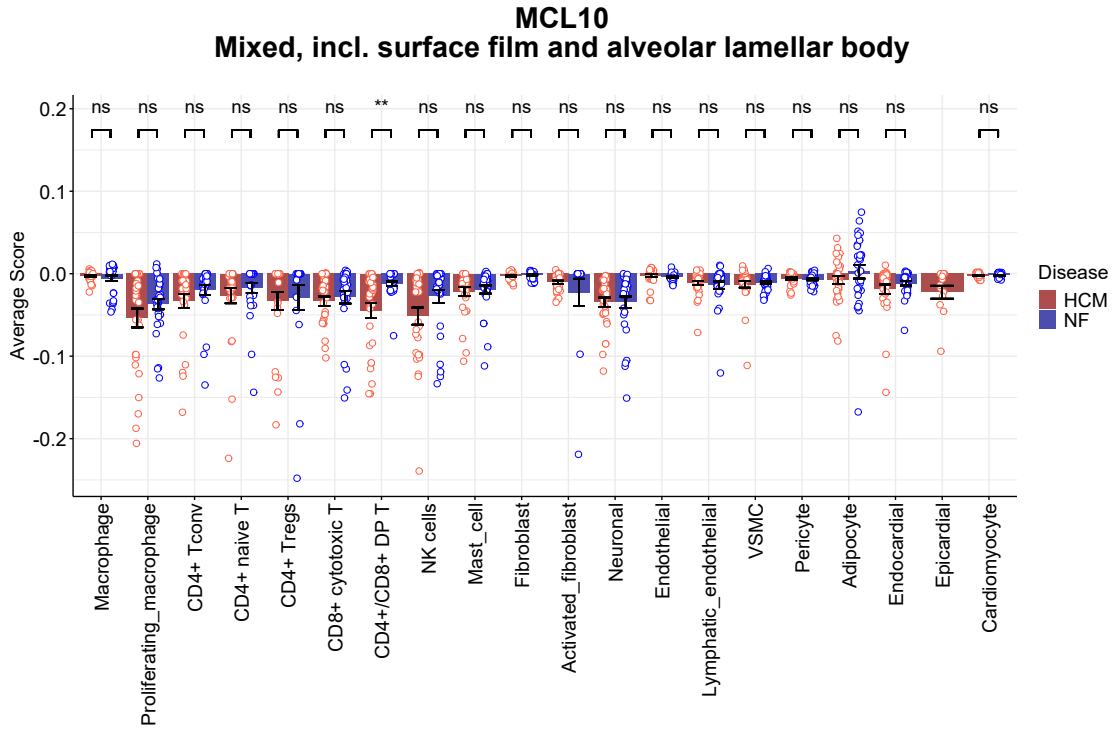

Figure D.77. Gene set scoring for MCL sub-cluster 10 of Cluster 10 (increasing expression over time) in late-stage human cell types.
This sub-cluster is a constituent of Cluster 10. The bar chart displays the gene set score for this specific sub-cluster across various cell types from late-stage human HCM snRNA-seq data. Scores were calculated for each sample using the `score_genes` function in `scanpy` v1.10.1 [267]. Bars represent the mean score, with error bars indicating the standard error of the mean. Statistical significance between disease and control samples was determined using a t-test, with p-values adjusted for multiple comparisons using the Benjamini-Hochberg method. Asterisks denote significance levels: * $p < 0.05$, ** $p < 0.01$, *** $p < 0.001$, **** $p < 0.0001$.

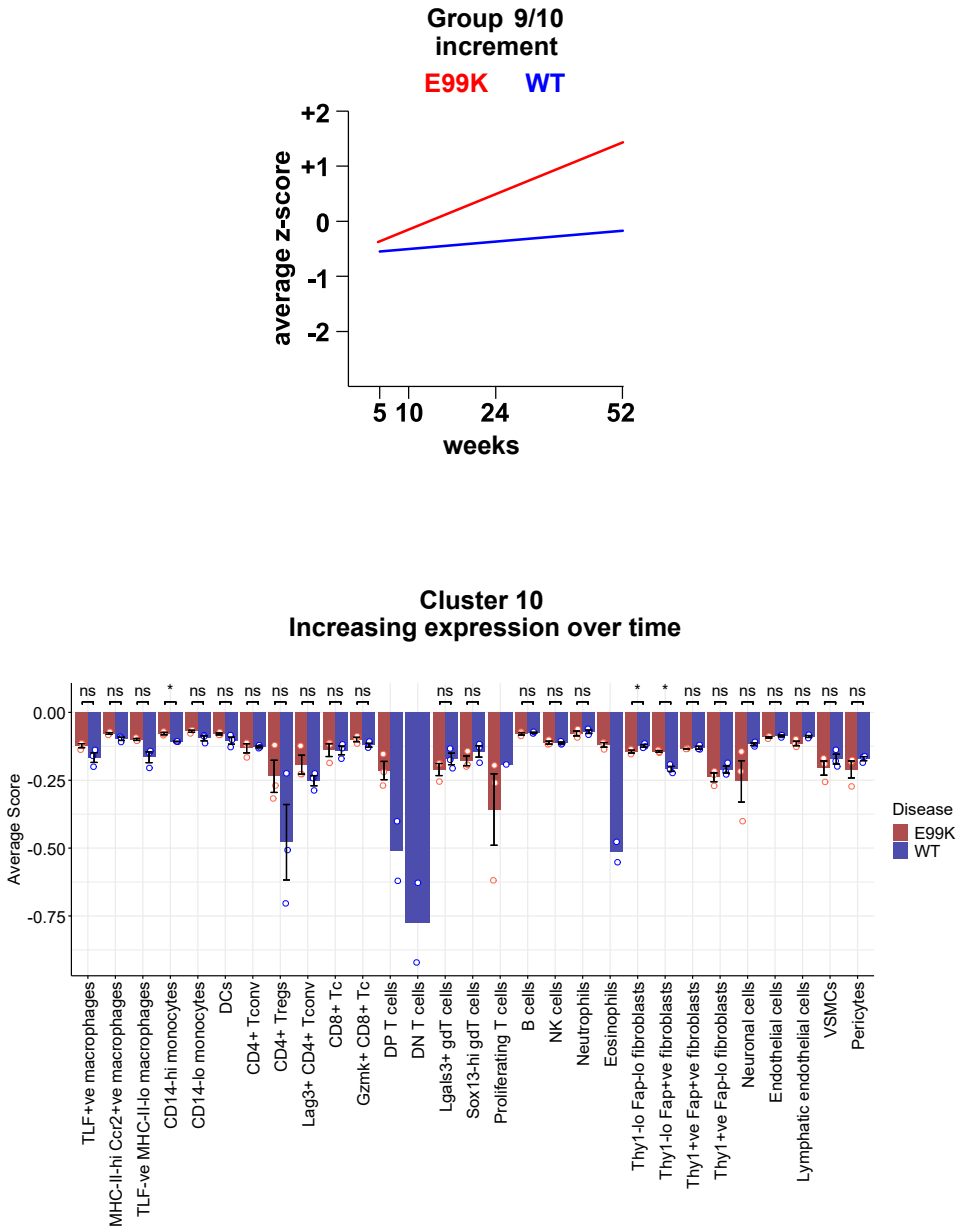

Figure D.78. Gene set scoring and statistics of Cluster 10 (increasing expression over time) in late-stage mouse cell types.
The upper panel schematically illustrates the temporal expression trend for Cluster 10, derived from bulk RNA-seq data of Actc1^{E99K} (red line) and wild-type (blue line) hearts over time. The lower panel displays the gene set score for all genes within Cluster 10 across various cell types identified in late-stage Actc1^{E99K} mouse scRNA-seq data. Scores were calculated for each sample using the `score_genes` function in `scanpy` v1.10.1 [267]. Bars represent the mean score, with error bars indicating the standard error of the mean. Statistical significance between disease and control samples was determined using a t-test, with p-values adjusted for multiple comparisons using the Benjamini-Hochberg method. Asterisks denote significance levels: * $p < 0.05$, ** $p < 0.01$, *** $p < 0.001$, **** $p < 0.0001$.

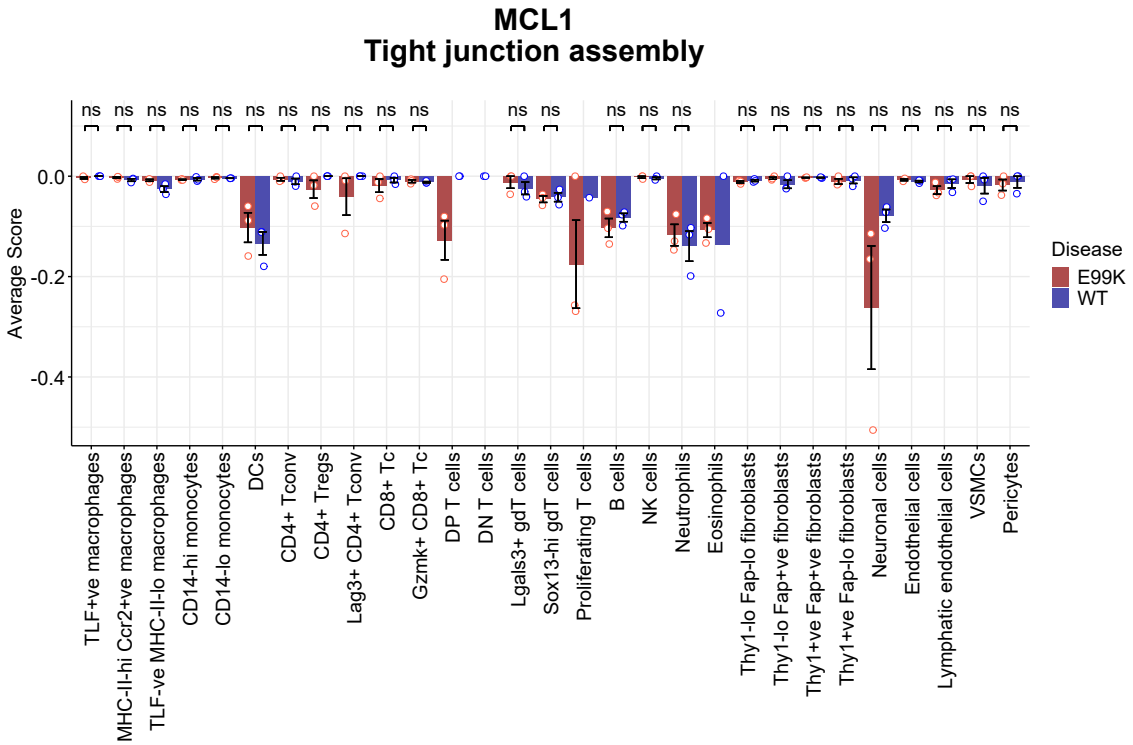

Figure D.79. Gene set scoring for MCL sub-cluster 1 of Cluster 10 (increasing expression over time) in late-stage mouse cell types.
This sub-cluster is a constituent of Cluster 10. The bar chart displays the gene set score for this specific sub-cluster across various cell types from late-stage Actc1^{E99K} mouse scRNA-seq data. Scores were calculated for each sample using the `score_genes` function in `scanpy` v1.10.1 [267]. Bars represent the mean score, with error bars indicating the standard error of the mean. Statistical significance between disease and control samples was determined using a t-test, with p-values adjusted for multiple comparisons using the Benjamini-Hochberg method. Asterisks denote significance levels: * $p < 0.05$, ** $p < 0.01$, *** $p < 0.001$, **** $p < 0.0001$.

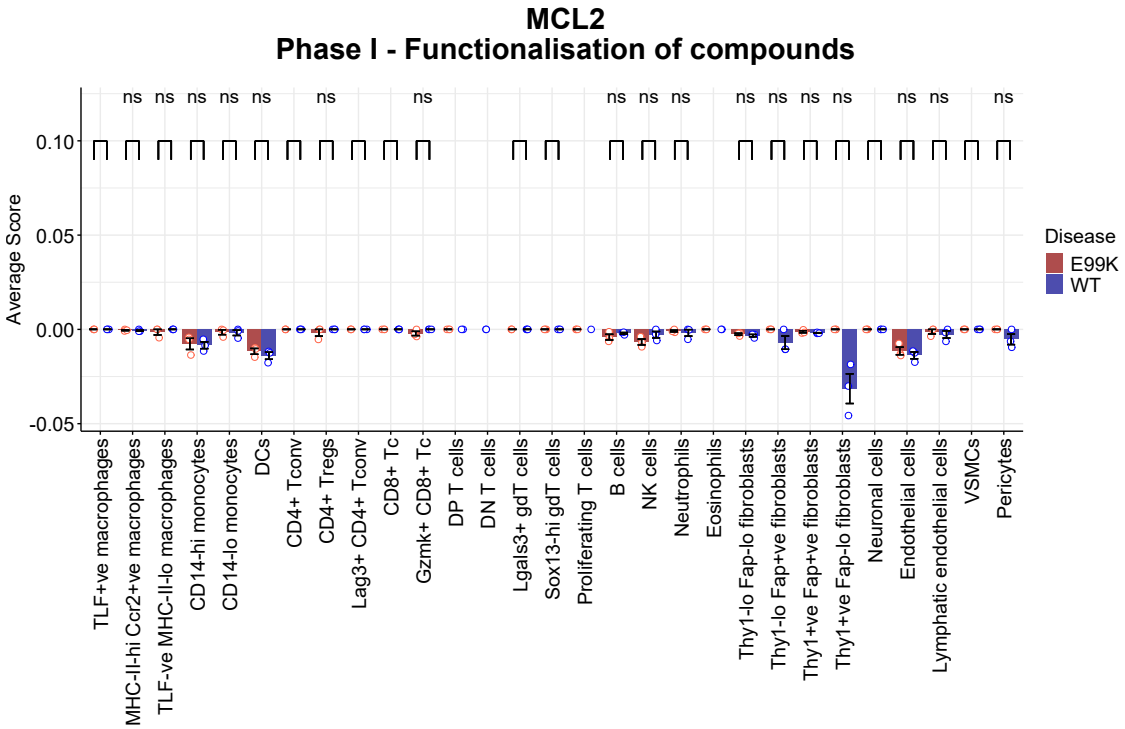

Figure D.80. Gene set scoring for MCL sub-cluster 2 of Cluster 10 (increasing expression over time) in late-stage mouse cell types.
This sub-cluster is a constituent of Cluster 10. The bar chart displays the gene set score for this specific sub-cluster across various cell types from late-stage Actc1^{E99K} mouse scRNA-seq data. Scores were calculated for each sample using the `score_genes` function in `scanpy` v1.10.1 [267]. Bars represent the mean score, with error bars indicating the standard error of the mean. Statistical significance between disease and control samples was determined using a t-test, with p-values adjusted for multiple comparisons using the Benjamini-Hochberg method. Asterisks denote significance levels: * $p < 0.05$, ** $p < 0.01$, *** $p < 0.001$, **** $p < 0.0001$.

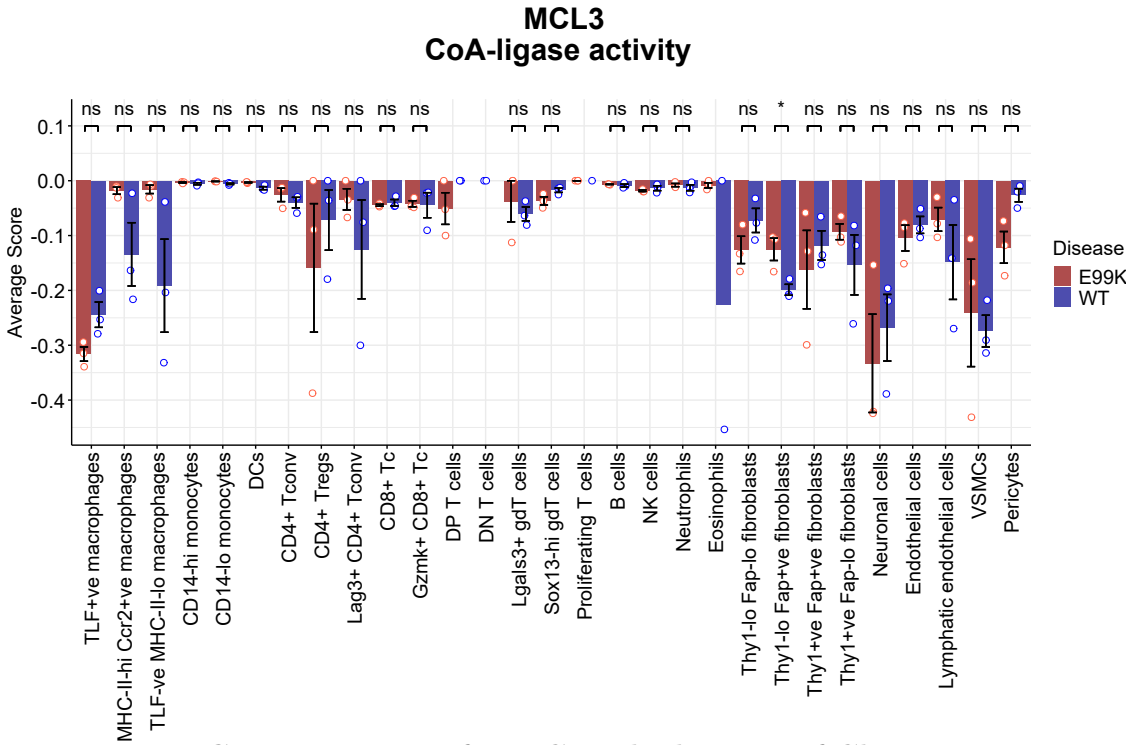

Figure D.81. Gene set scoring for MCL sub-cluster 3 of Cluster 10 (increasing expression over time) in late-stage mouse cell types.
This sub-cluster is a constituent of Cluster 10. The bar chart displays the gene set score for this specific sub-cluster across various cell types from late-stage Actc1^{E99K} mouse scRNA-seq data. Scores were calculated for each sample using the `score_genes` function in `scanpy` v1.10.1 [267]. Bars represent the mean score, with error bars indicating the standard error of the mean. Statistical significance between disease and control samples was determined using a t-test, with p-values adjusted for multiple comparisons using the Benjamini-Hochberg method. Asterisks denote significance levels: * $p < 0.05$, ** $p < 0.01$, *** $p < 0.001$, **** $p < 0.0001$.

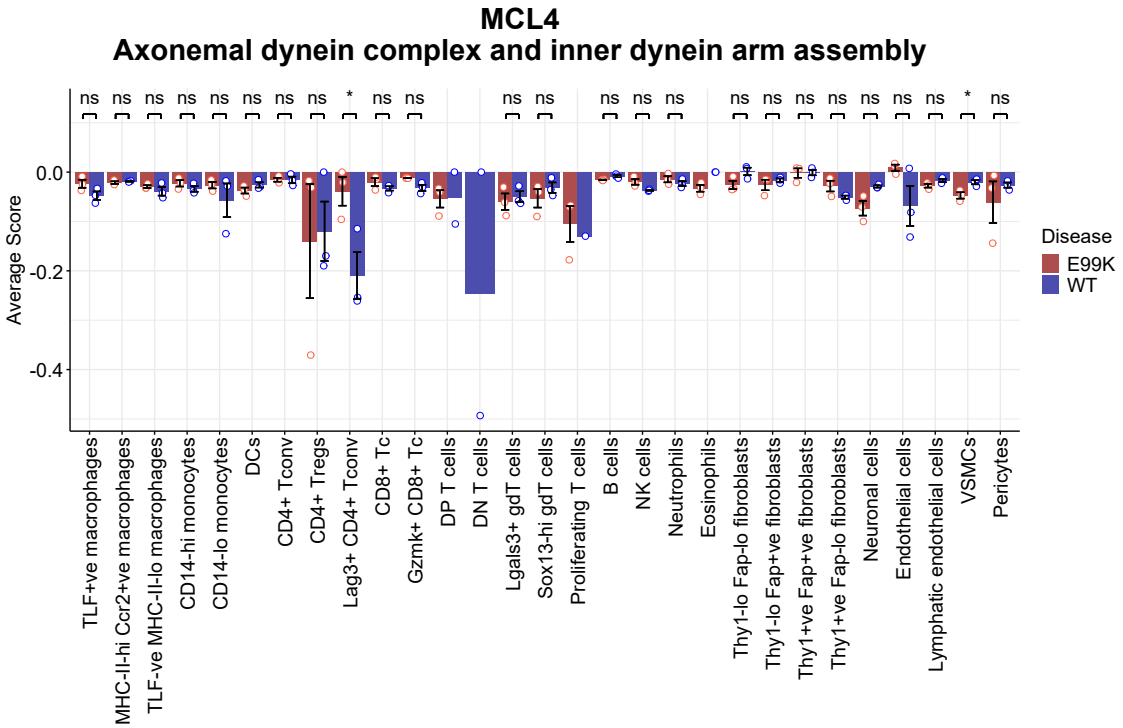

Figure D.82. Gene set scoring for MCL sub-cluster 4 of Cluster 10 (increasing expression over time) in late-stage mouse cell types.
This sub-cluster is a constituent of Cluster 10. The bar chart displays the gene set score for this specific sub-cluster across various cell types from late-stage Actc1^{E99K} mouse scRNA-seq data. Scores were calculated for each sample using the `score_genes` function in `scanpy` v1.10.1 [267]. Bars represent the mean score, with error bars indicating the standard error of the mean. Statistical significance between disease and control samples was determined using a t-test, with p-values adjusted for multiple comparisons using the Benjamini-Hochberg method. Asterisks denote significance levels: * $p < 0.05$, ** $p < 0.01$, *** $p < 0.001$, **** $p < 0.0001$.

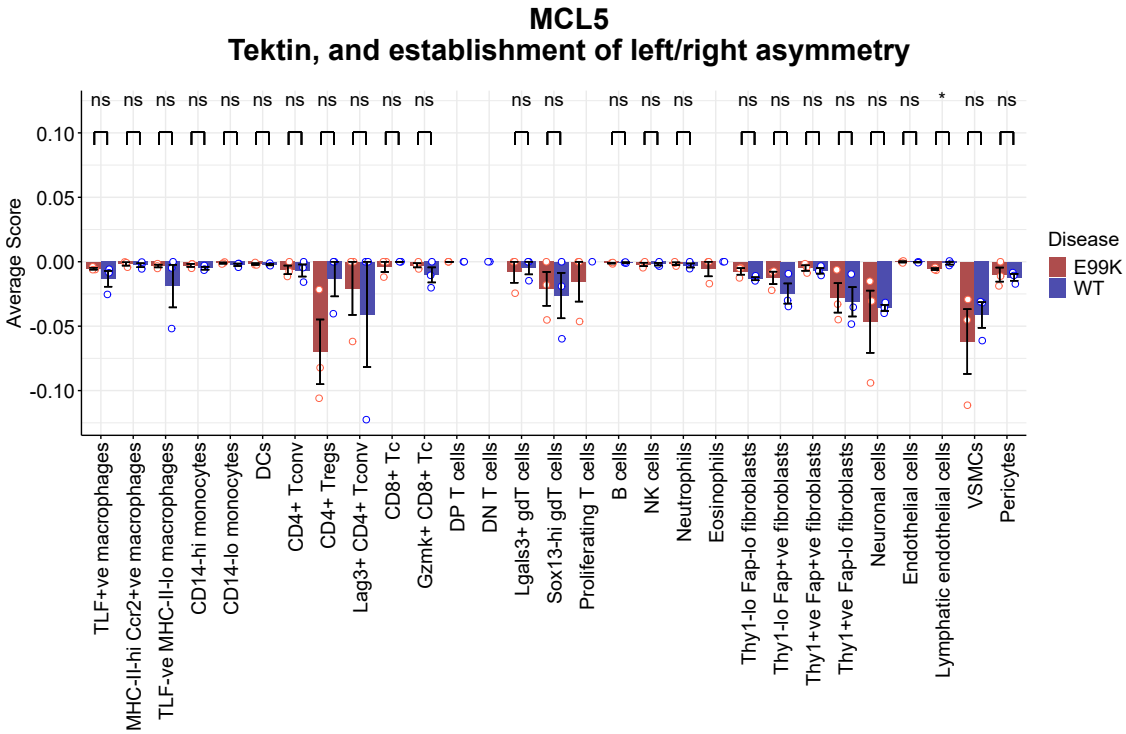

Figure D.83. Gene set scoring for MCL sub-cluster 5 of Cluster 10 (increasing expression over time) in late-stage mouse cell types.
This sub-cluster is a constituent of Cluster 10. The bar chart displays the gene set score for this specific sub-cluster across various cell types from late-stage Actc1^{E99K} mouse scRNA-seq data. Scores were calculated for each sample using the `score_genes` function in `scanpy` v1.10.1 [267]. Bars represent the mean score, with error bars indicating the standard error of the mean. Statistical significance between disease and control samples was determined using a t-test, with p-values adjusted for multiple comparisons using the Benjamini-Hochberg method. Asterisks denote significance levels: * $p < 0.05$, ** $p < 0.01$, *** $p < 0.001$, **** $p < 0.0001$.

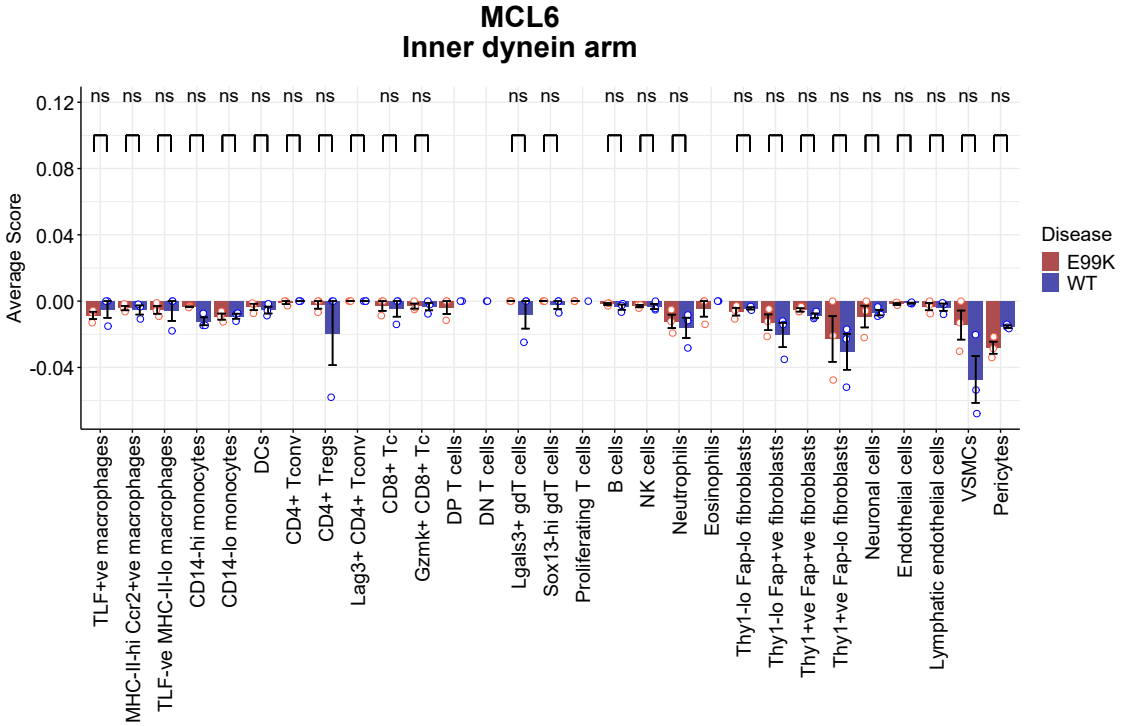

Figure D.84. Gene set scoring for MCL sub-cluster 6 of Cluster 10 (increasing expression over time) in late-stage mouse cell types.
This sub-cluster is a constituent of Cluster 10. The bar chart displays the gene set score for this specific sub-cluster across various cell types from late-stage Actc1^{E99K} mouse scRNA-seq data. Scores were calculated for each sample using the `score_genes` function in `scanpy` v1.10.1 [267]. Bars represent the mean score, with error bars indicating the standard error of the mean. Statistical significance between disease and control samples was determined using a t-test, with p-values adjusted for multiple comparisons using the Benjamini-Hochberg method. Asterisks denote significance levels: * $p < 0.05$, ** $p < 0.01$, *** $p < 0.001$, **** $p < 0.0001$.

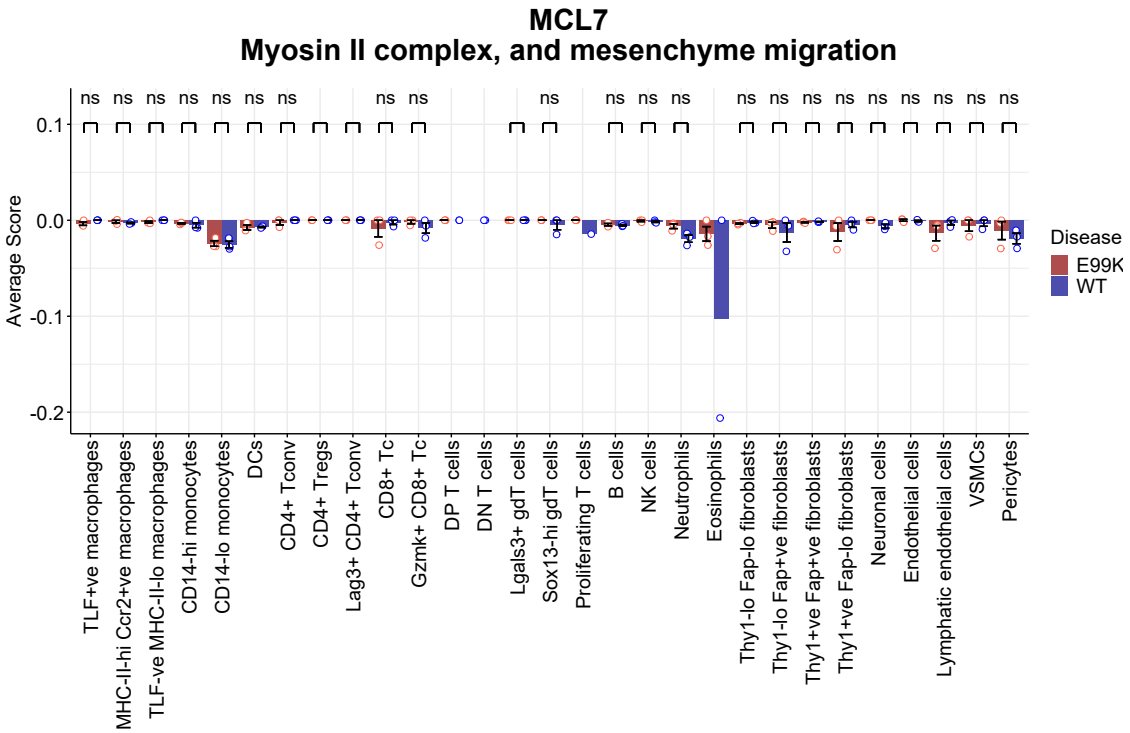

Figure D.85. Gene set scoring for MCL sub-cluster 7 of Cluster 10 (increasing expression over time) in late-stage mouse cell types.
This sub-cluster is a constituent of Cluster 10. The bar chart displays the gene set score for this specific sub-cluster across various cell types from late-stage Actc1^{E99K} mouse scRNA-seq data. Scores were calculated for each sample using the `score_genes` function in `scanpy` v1.10.1 [267]. Bars represent the mean score, with error bars indicating the standard error of the mean. Statistical significance between disease and control samples was determined using a t-test, with p-values adjusted for multiple comparisons using the Benjamini-Hochberg method. Asterisks denote significance levels: * $p < 0.05$, ** $p < 0.01$, *** $p < 0.001$, **** $p < 0.0001$.

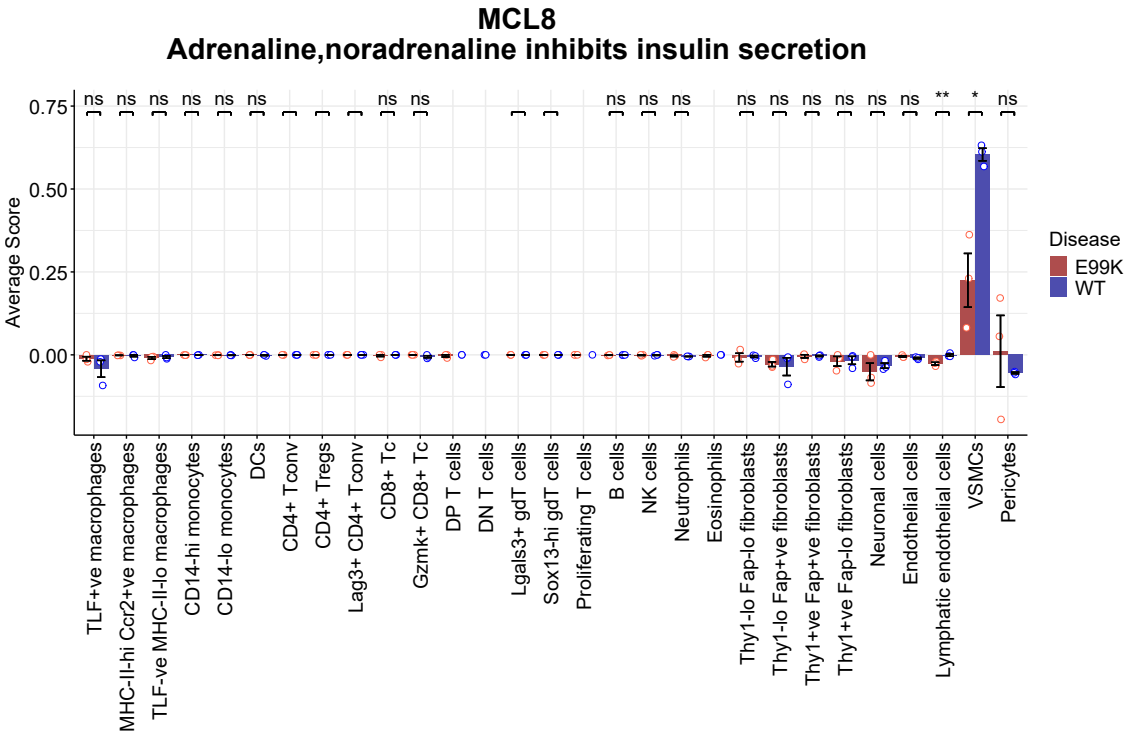

Figure D.86. Gene set scoring for MCL sub-cluster 8 of Cluster 10 (increasing expression over time) in late-stage mouse cell types.
This sub-cluster is a constituent of Cluster 10. The bar chart displays the gene set score for this specific sub-cluster across various cell types from late-stage Actc1^{E99K} mouse scRNA-seq data. Scores were calculated for each sample using the `score_genes` function in `scanpy` v1.10.1 [267]. Bars represent the mean score, with error bars indicating the standard error of the mean. Statistical significance between disease and control samples was determined using a t-test, with p-values adjusted for multiple comparisons using the Benjamini-Hochberg method. Asterisks denote significance levels: * $p < 0.05$, ** $p < 0.01$, *** $p < 0.001$, **** $p < 0.0001$.

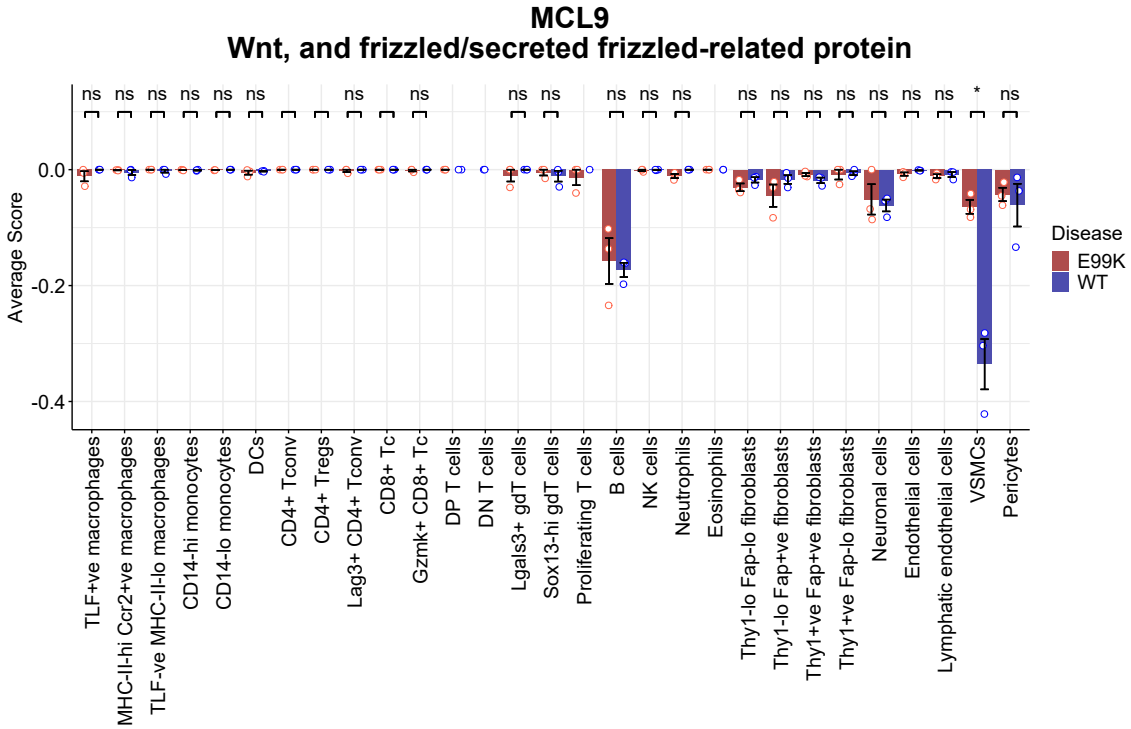

Figure D.87. Gene set scoring for MCL sub-cluster 9 of Cluster 10 (increasing expression over time) in late-stage mouse cell types.
This sub-cluster is a constituent of Cluster 10. The bar chart displays the gene set score for this specific sub-cluster across various cell types from late-stage Actc1^{E99K} mouse scRNA-seq data. Scores were calculated for each sample using the `score_genes` function in `scanpy` v1.10.1 [267]. Bars represent the mean score, with error bars indicating the standard error of the mean. Statistical significance between disease and control samples was determined using a t-test, with p-values adjusted for multiple comparisons using the Benjamini-Hochberg method. Asterisks denote significance levels: * $p < 0.05$, ** $p < 0.01$, *** $p < 0.001$, **** $p < 0.0001$.

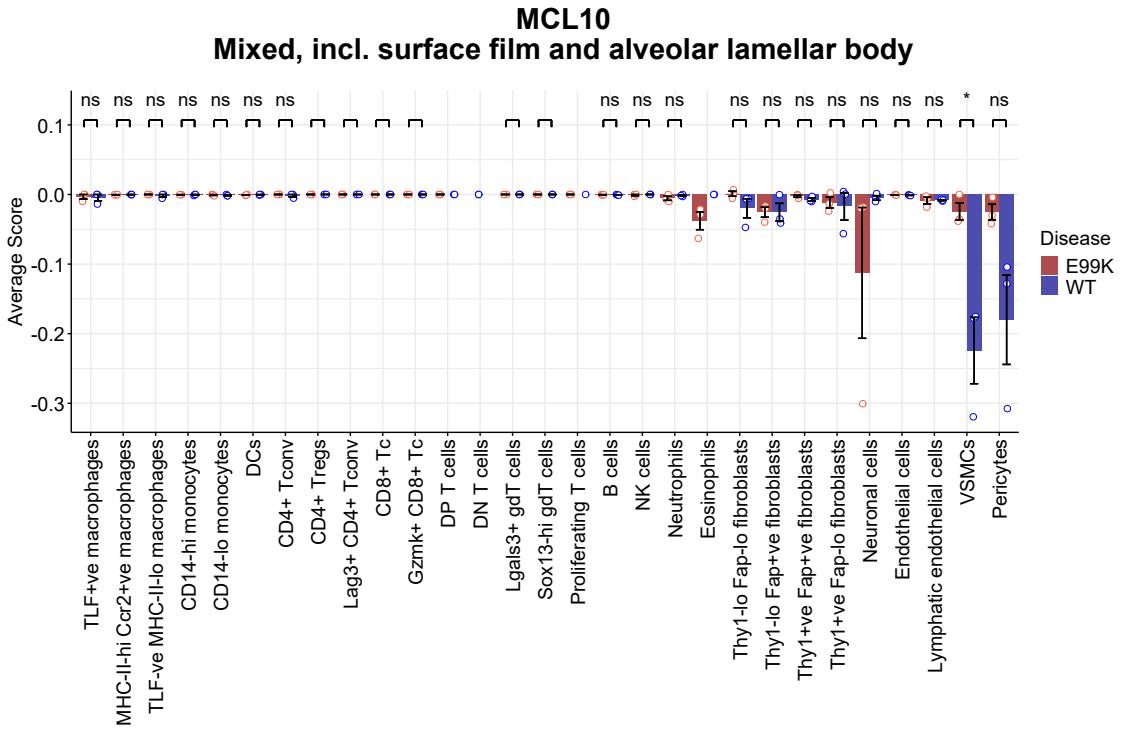

Figure D.88. Gene set scoring for MCL sub-cluster 10 of Cluster 10 (increasing expression over time) in late-stage mouse cell types.
This sub-cluster is a constituent of Cluster 10. The bar chart displays the gene set score for this specific sub-cluster across various cell types from late-stage Actc1^{E99K} mouse scRNA-seq data. Scores were calculated for each sample using the `score_genes` function in `scanpy` v1.10.1 [267]. Bars represent the mean score, with error bars indicating the standard error of the mean. Statistical significance between disease and control samples was determined using a t-test, with p-values adjusted for multiple comparisons using the Benjamini-Hochberg method. Asterisks denote significance levels: * $p < 0.05$, ** $p < 0.01$, *** $p < 0.001$, **** $p < 0.0001$.

D.3 Cluster 11 & 12: Biphasic expression patterns reveal dynamic shifts in stress response and repair mechanisms

Cluster 11, displaying a U-shaped trend with downregulation in the mid-stage and upregulation in both early and late stages, encompassed a diverse range of functions (Figures D.89 and D.100). Sub-cluster analysis revealed enrichment for processes such as the regulation of transcription from RNA polymerase II promoter in response to stress (MCL sub-cluster 1; Figure D.90), homology-directed repair (HDR) through homologous recombination (MCL sub-cluster 2; Figure D.91),

ceramide metabolism (MCL sub-cluster 3; Figure D.92), RHO GTPases activating WASPs and WAVEs (MCL sub-cluster 4; Figure D.93), polysomal ribosome (MCL sub-cluster 5; Figure D.94), a mixed sub-cluster including homeobox genes (MCL sub-cluster 6; Figure D.95), procollagen-proline dioxygenase activity (MCL sub-cluster 7; Figure D.96), response to interleukin-18 (MCL sub-cluster 8; Figure D.97), nuclear-transcribed mRNA catabolism, NMD (MCL sub-cluster 9; Figure D.98), and the tubulin/FtsZ family, C-terminal domain (MCL sub-cluster 10; Figure D.99). In late-stage human HCM samples, the overall cluster 11 signature was significantly upregulated in activated fibroblasts, NK cells, lymphatic endothelial cells, VSMCs, and cardiomyocytes, while downregulated in macrophages and proliferating macrophages (Figure D.89). Further examination of individual sub-clusters revealed more specific cell-type contributions. For instance, the regulation of transcription sub-cluster (MCL sub-cluster 1; Figure D.90) was upregulated in NK cells and activated fibroblasts, and downregulated in proliferating macrophages. The HDR sub-cluster (MCL sub-cluster 2; Figure D.91) was downregulated in proliferating macrophages. The ceramide metabolism sub-cluster (MCL sub-cluster 3; Figure D.92) was upregulated in activated fibroblasts and endothelial cells. The RHO GTPases sub-cluster (MCL sub-cluster 4; Figure D.93) showed upregulation in macrophages and cardiomyocytes. The polysomal ribosome sub-cluster (MCL sub-cluster 5; Figure D.94) was upregulated in mast cells and $CD4^{+}CD8^{+}$ DP T cells, and downregulated in proliferating macrophages. In the mouse scRNA-seq data, the overall cluster 11 signature was downregulated in B cells and $Thy1^{lo}Fap^{lo}$ fibroblasts (Figure D.100). Sub-cluster analysis revealed downregulation of the regulation of transcription sub-cluster (MCL sub-cluster 1; Figure D.101) in $CD14^{hi}$ and $CD14^{lo}$ monocytes, neutrophils, and $Thy1^{+}Fap^{lo}$ fibroblasts, while the $Sox13^{hi}$ $\gamma\delta$T cells showed upregulation.

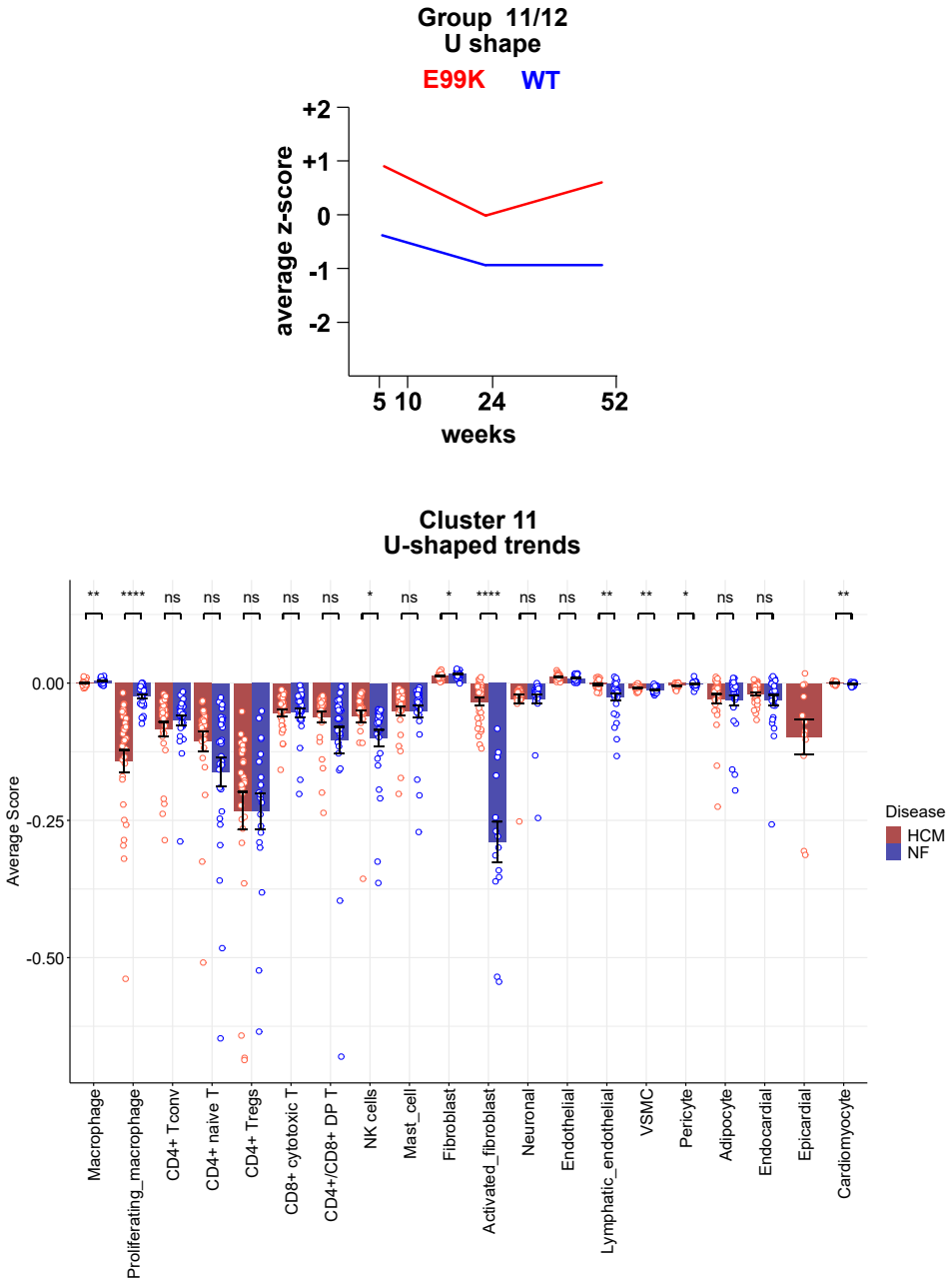

Figure D.89. Gene set scoring and statistics of Cluster 11 (U-shaped trends) in late-stage human cell types.

The upper panel schematically illustrates the temporal expression trend for Cluster 11, derived from bulk RNA-seq data of Actc1^{E99K} (red line) and wild-type (blue line) hearts over time. The lower panel displays the gene set score for all genes within Cluster 11 across various cell types identified in late-stage human HCM snRNA-seq data. Scores were calculated for each sample using the `score_genes` function in `scanpy` v1.10.1 [267]. Bars represent the mean score, with error bars indicating the standard error of the mean. Statistical significance between disease and control samples was determined using a t-test, with p-values adjusted for multiple comparisons using the Benjamini-Hochberg method. Asterisks denote significance levels: * $p < 0.05$, ** $p < 0.01$, *** $p < 0.001$, **** $p < 0.0001$.

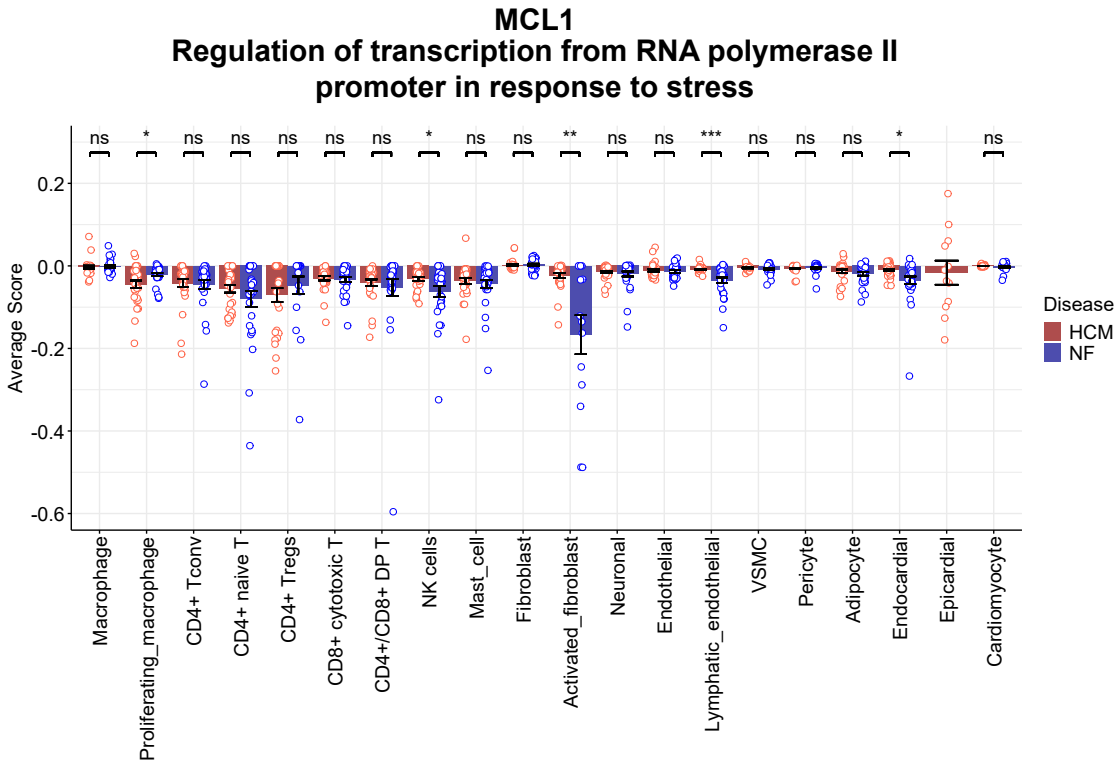

Figure D.90. Gene set scoring for MCL sub-cluster 1 of Cluster 11 (U-shaped trends) in late-stage human cell types.
This sub-cluster is a constituent of Cluster 11. The bar chart displays the gene set score for this specific sub-cluster across various cell types from late-stage human HCM snRNA-seq data. Scores were calculated for each sample using the `score_genes` function in `scanpy` v1.10.1 [267]. Bars represent the mean score, with error bars indicating the standard error of the mean. Statistical significance between disease and control samples was determined using a t-test, with p-values adjusted for multiple comparisons using the Benjamini-Hochberg method. Asterisks denote significance levels: * $p < 0.05$, ** $p < 0.01$, *** $p < 0.001$, **** $p < 0.0001$.

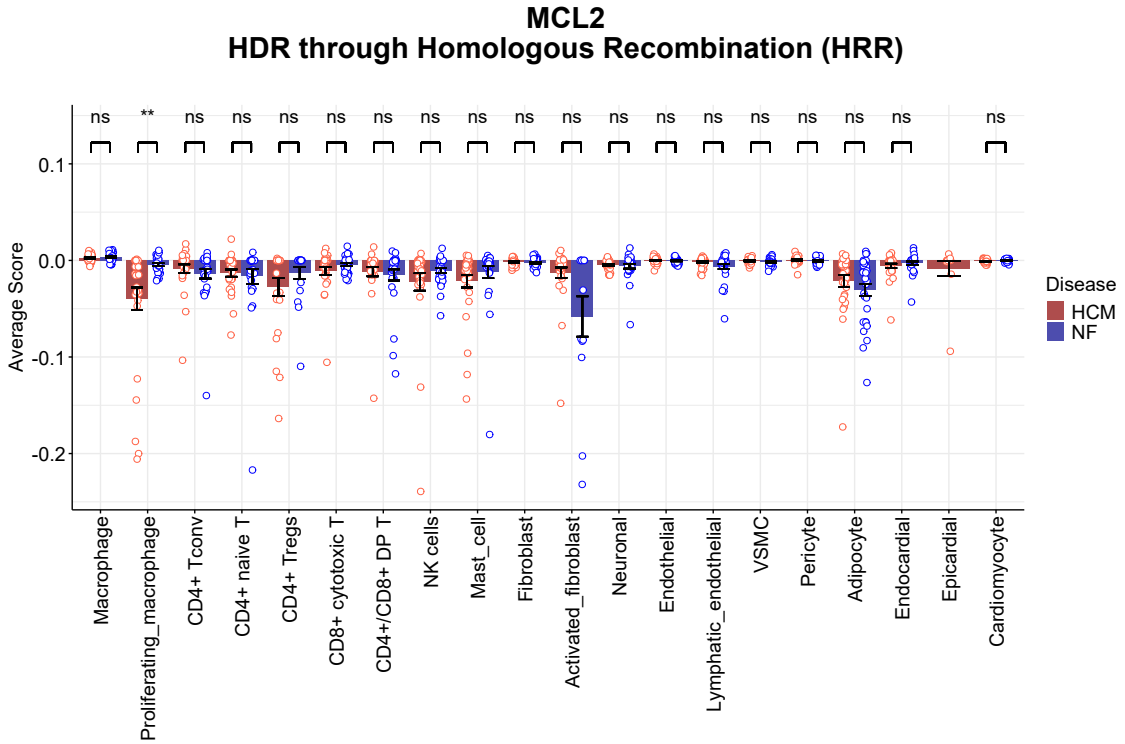

Figure D.91. Gene set scoring for MCL sub-cluster 2 of Cluster 11 (U-shaped trends) in late-stage human cell types.
This sub-cluster is a constituent of Cluster 11. The bar chart displays the gene set score for this specific sub-cluster across various cell types from late-stage human HCM snRNA-seq data. Scores were calculated for each sample using the `score_genes` function in `scanpy` v1.10.1 [267]. Bars represent the mean score, with error bars indicating the standard error of the mean. Statistical significance between disease and control samples was determined using a t-test, with p-values adjusted for multiple comparisons using the Benjamini-Hochberg method. Asterisks denote significance levels: * $p < 0.05$, ** $p < 0.01$, *** $p < 0.001$, **** $p < 0.0001$.

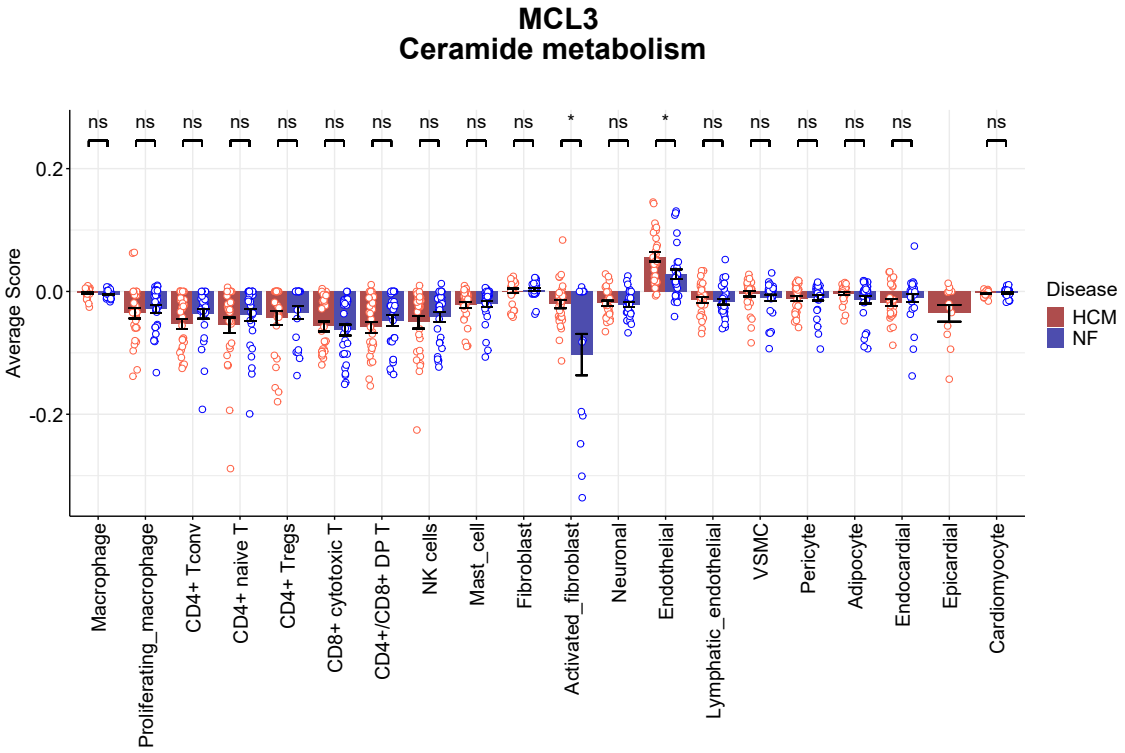

Figure D.92. Gene set scoring for MCL sub-cluster 3 of Cluster 11 (U-shaped trends) in late-stage human cell types.
This sub-cluster is a constituent of Cluster 11. The bar chart displays the gene set score for this specific sub-cluster across various cell types from late-stage human HCM snRNA-seq data. Scores were calculated for each sample using the `score_genes` function in `scanpy` v1.10.1 [267]. Bars represent the mean score, with error bars indicating the standard error of the mean. Statistical significance between disease and control samples was determined using a t-test, with p-values adjusted for multiple comparisons using the Benjamini-Hochberg method. Asterisks denote significance levels: * $p < 0.05$, ** $p < 0.01$, *** $p < 0.001$, **** $p < 0.0001$.

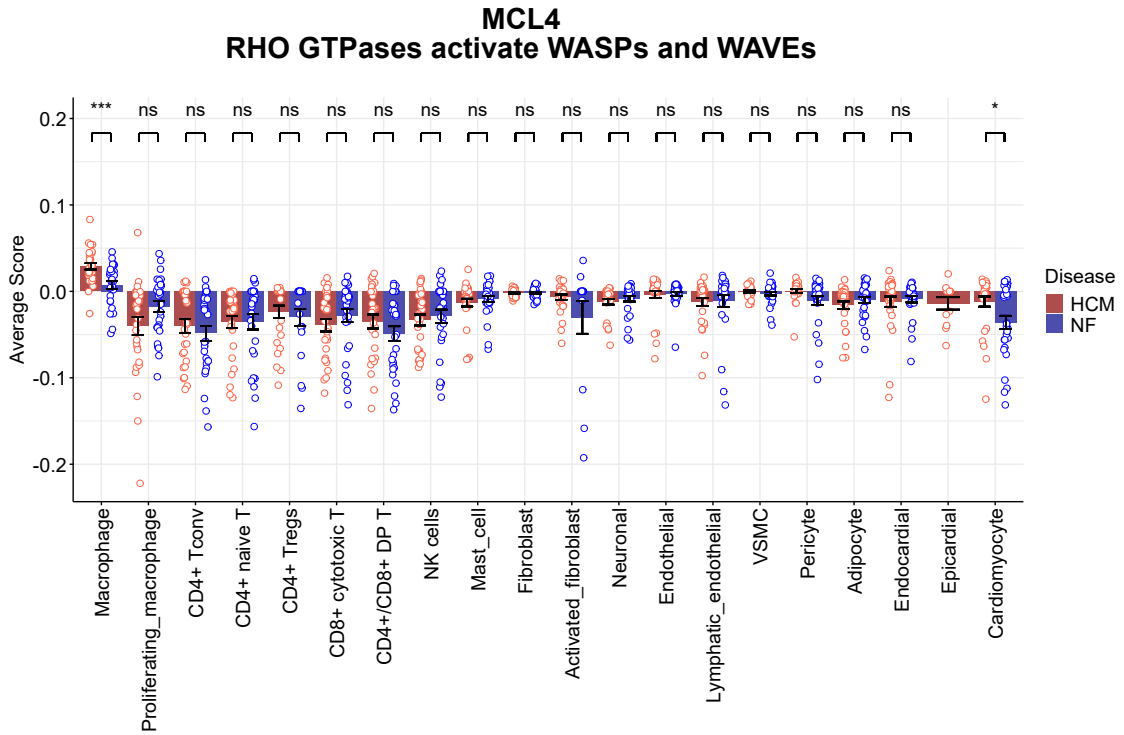

Figure D.93. Gene set scoring for MCL sub-cluster 4 of Cluster 11 (U-shaped trends) in late-stage human cell types.
This sub-cluster is a constituent of Cluster 11. The bar chart displays the gene set score for this specific sub-cluster across various cell types from late-stage human HCM snRNA-seq data. Scores were calculated for each sample using the `score_genes` function in `scanpy` v1.10.1 [267]. Bars represent the mean score, with error bars indicating the standard error of the mean. Statistical significance between disease and control samples was determined using a t-test, with p-values adjusted for multiple comparisons using the Benjamini-Hochberg method. Asterisks denote significance levels: * $p < 0.05$, ** $p < 0.01$, *** $p < 0.001$, **** $p < 0.0001$.

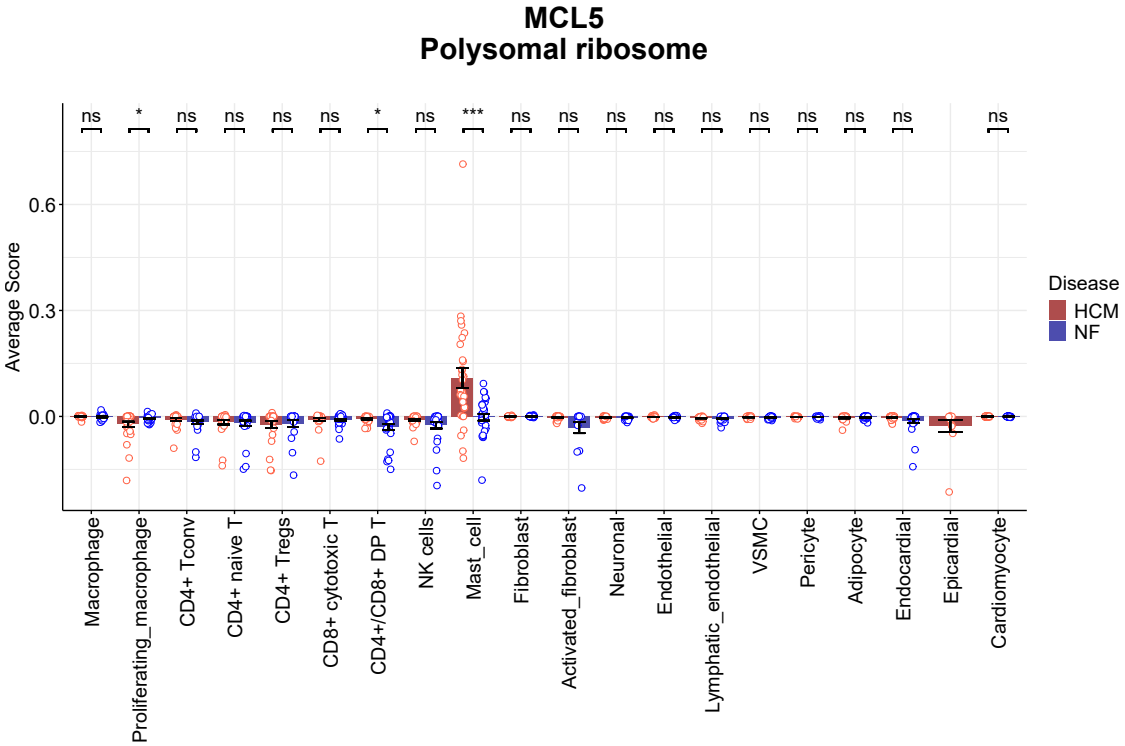

Figure D.94. Gene set scoring for MCL sub-cluster 5 of Cluster 11 (U-shaped trends) in late-stage human cell types.
This sub-cluster is a constituent of Cluster 11. The bar chart displays the gene set score for this specific sub-cluster across various cell types from late-stage human HCM snRNA-seq data. Scores were calculated for each sample using the `score_genes` function in `scanpy` v1.10.1 [267]. Bars represent the mean score, with error bars indicating the standard error of the mean. Statistical significance between disease and control samples was determined using a t-test, with p-values adjusted for multiple comparisons using the Benjamini-Hochberg method. Asterisks denote significance levels: * $p < 0.05$, ** $p < 0.01$, *** $p < 0.001$, **** $p < 0.0001$.

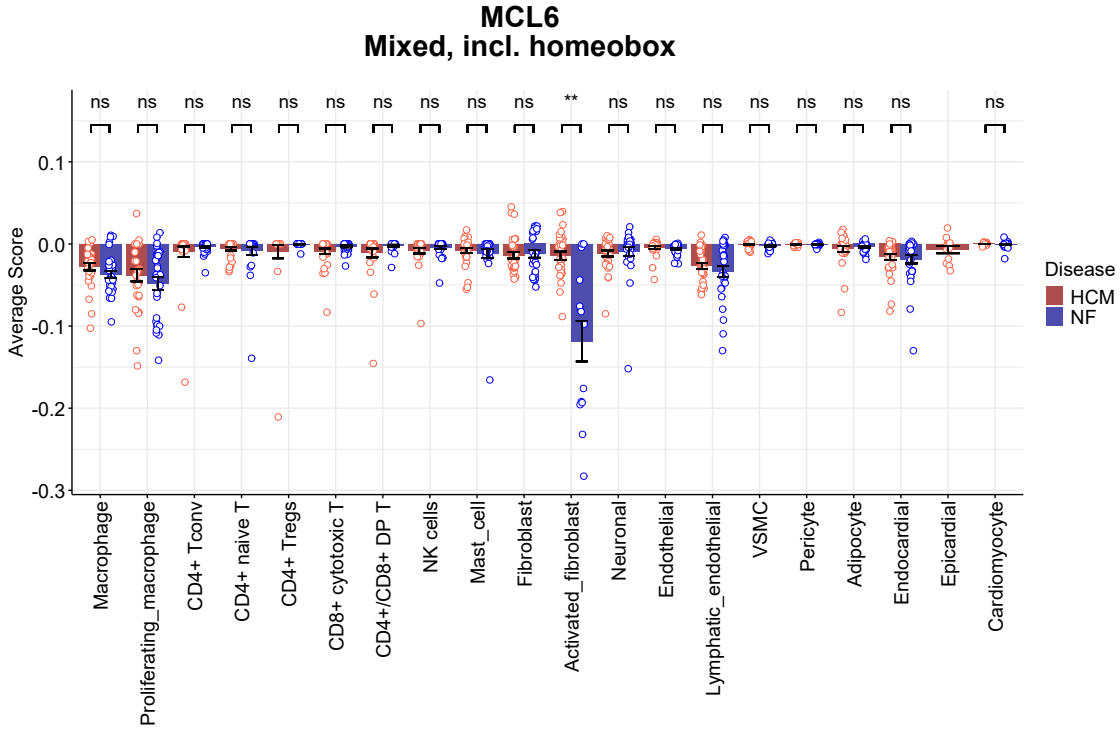

Figure D.95. Gene set scoring for MCL sub-cluster 6 of Cluster 11 (U-shaped trends) in late-stage human cell types.
This sub-cluster is a constituent of Cluster 11. The bar chart displays the gene set score for this specific sub-cluster across various cell types from late-stage human HCM snRNA-seq data. Scores were calculated for each sample using the `score_genes` function in `scanpy` v1.10.1 [267]. Bars represent the mean score, with error bars indicating the standard error of the mean. Statistical significance between disease and control samples was determined using a t-test, with p-values adjusted for multiple comparisons using the Benjamini-Hochberg method. Asterisks denote significance levels: * $p < 0.05$, ** $p < 0.01$, *** $p < 0.001$, **** $p < 0.0001$.

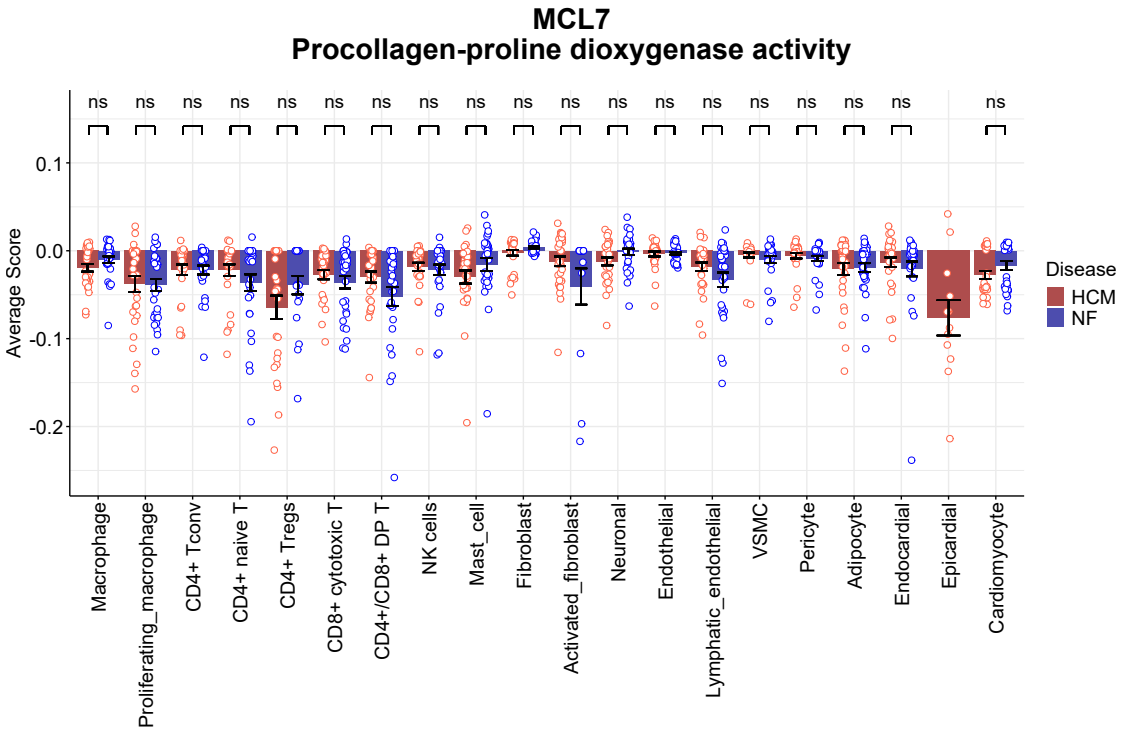

Figure D.96. Gene set scoring for MCL sub-cluster 7 of Cluster 11 (U-shaped trends) in late-stage human cell types.
This sub-cluster is a constituent of Cluster 11. The bar chart displays the gene set score for this specific sub-cluster across various cell types from late-stage human HCM snRNA-seq data. Scores were calculated for each sample using the `score_genes` function in `scanpy` v1.10.1 [267]. Bars represent the mean score, with error bars indicating the standard error of the mean. Statistical significance between disease and control samples was determined using a t-test, with p-values adjusted for multiple comparisons using the Benjamini-Hochberg method. Asterisks denote significance levels: * $p < 0.05$, ** $p < 0.01$, *** $p < 0.001$, **** $p < 0.0001$.

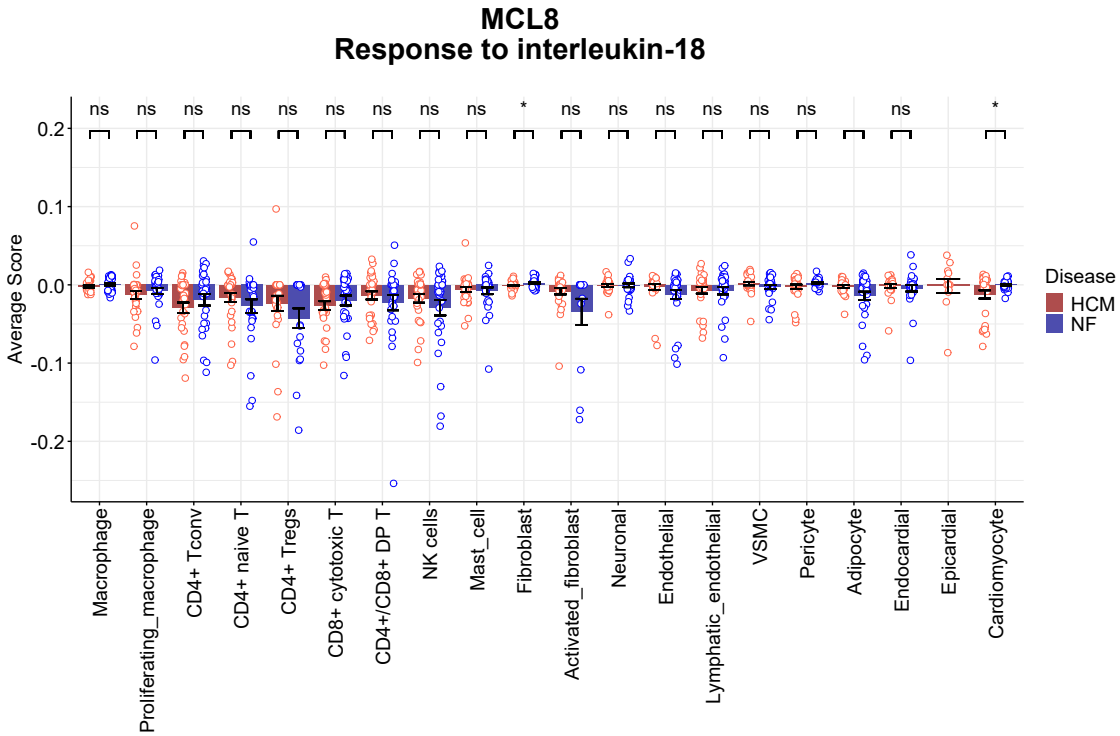

Figure D.97. Gene set scoring for MCL sub-cluster 8 of Cluster 11 (U-shaped trends) in late-stage human cell types.
This sub-cluster is a constituent of Cluster 11. The bar chart displays the gene set score for this specific sub-cluster across various cell types from late-stage human HCM snRNA-seq data. Scores were calculated for each sample using the `score_genes` function in `scanpy` v1.10.1 [267]. Bars represent the mean score, with error bars indicating the standard error of the mean. Statistical significance between disease and control samples was determined using a t-test, with p-values adjusted for multiple comparisons using the Benjamini-Hochberg method. Asterisks denote significance levels: * $p < 0.05$, ** $p < 0.01$, *** $p < 0.001$, **** $p < 0.0001$.

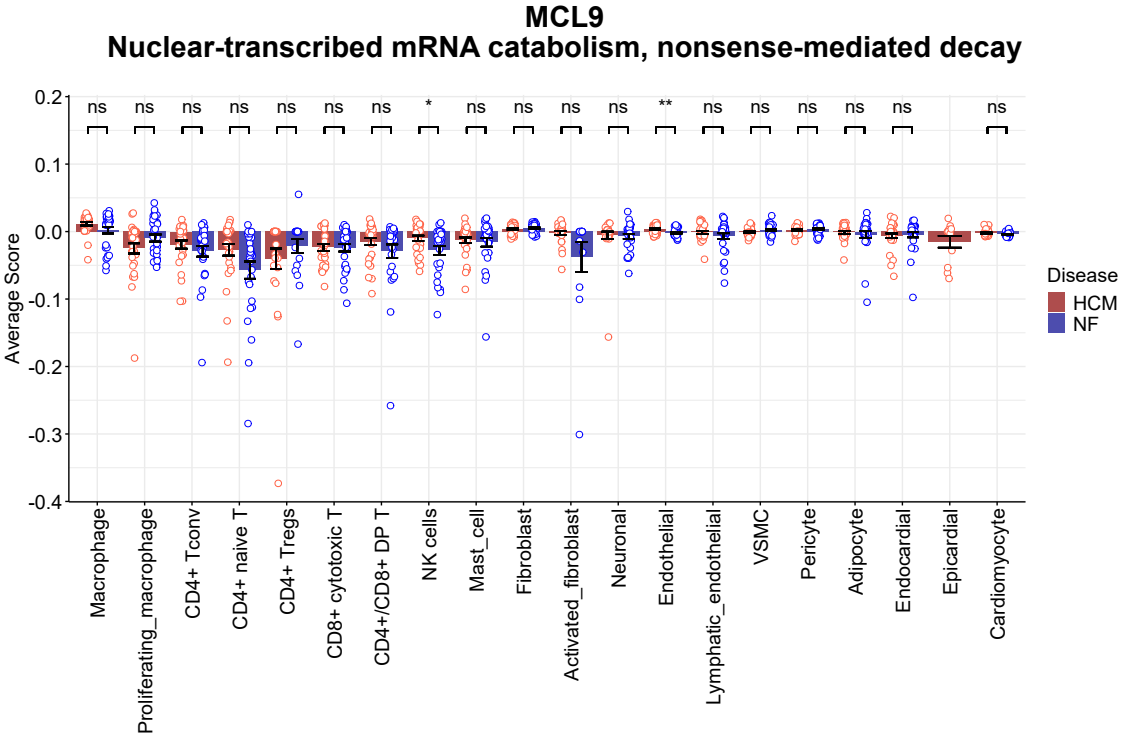

Figure D.98. Gene set scoring for MCL sub-cluster 9 of Cluster 11 (U-shaped trends) in late-stage human cell types.
This sub-cluster is a constituent of Cluster 11. The bar chart displays the gene set score for this specific sub-cluster across various cell types from late-stage human HCM snRNA-seq data. Scores were calculated for each sample using the `score_genes` function in `scanpy` v1.10.1 [267]. Bars represent the mean score, with error bars indicating the standard error of the mean. Statistical significance between disease and control samples was determined using a t-test, with p-values adjusted for multiple comparisons using the Benjamini-Hochberg method. Asterisks denote significance levels: * $p < 0.05$, ** $p < 0.01$, *** $p < 0.001$, **** $p < 0.0001$.

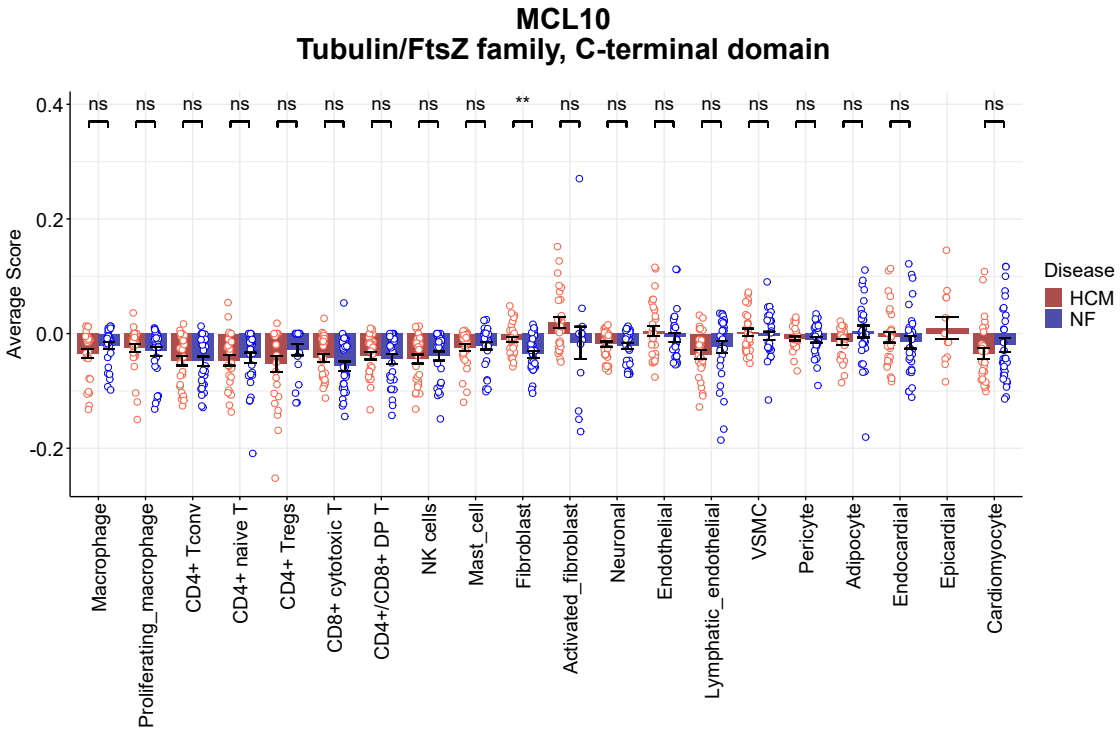

Figure D.99. Gene set scoring for MCL sub-cluster 10 of Cluster 11 (U-shaped trends) in late-stage human cell types.
This sub-cluster is a constituent of Cluster 11. The bar chart displays the gene set score for this specific sub-cluster across various cell types from late-stage human HCM snRNA-seq data. Scores were calculated for each sample using the `score_genes` function in `scanpy` v1.10.1 [267]. Bars represent the mean score, with error bars indicating the standard error of the mean. Statistical significance between disease and control samples was determined using a t-test, with p-values adjusted for multiple comparisons using the Benjamini-Hochberg method. Asterisks denote significance levels: * $p < 0.05$, ** $p < 0.01$, *** $p < 0.001$, **** $p < 0.0001$.

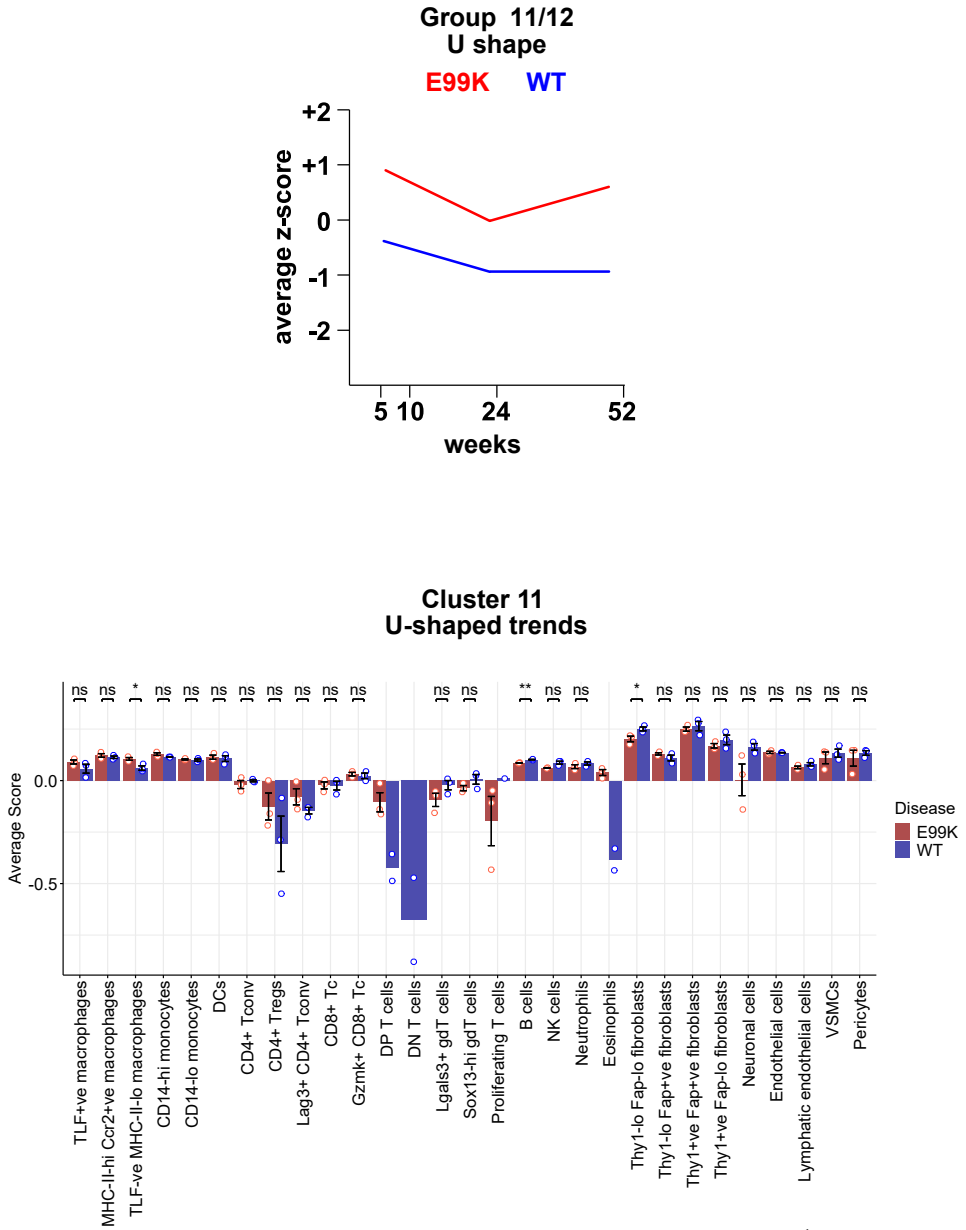

Figure D.100. Gene set scoring and statistics of Cluster 11 (U-shaped trends) in late-stage mouse cell types.
The upper panel schematically illustrates the temporal expression trend for Cluster 11, derived from bulk RNA-seq data of Actc1^{E99K} (red line) and wild-type (blue line) hearts over time. The lower panel displays the gene set score for all genes within Cluster 11 across various cell types identified in late-stage Actc1^{E99K} mouse scRNA-seq data. Scores were calculated for each sample using the `score_genes` function in `scanpy` v1.10.1 [267]. Bars represent the mean score, with error bars indicating the standard error of the mean. Statistical significance between disease and control samples was determined using a t-test, with p-values adjusted for multiple comparisons using the Benjamini-Hochberg method. Asterisks denote significance levels: * $p < 0.05$, ** $p < 0.01$, *** $p < 0.001$, **** $p < 0.0001$.

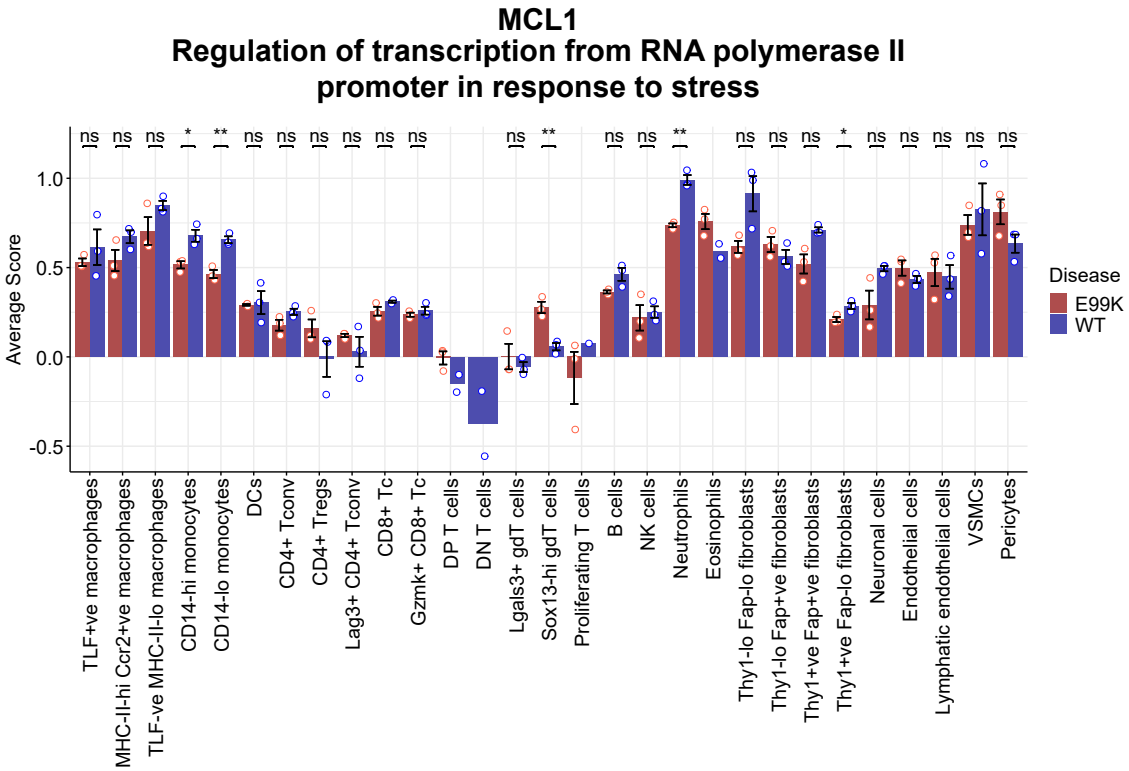

Figure D.101. Gene set scoring for MCL sub-cluster 1 of Cluster 11 (U-shaped trends) in late-stage mouse cell types.
This sub-cluster is a constituent of Cluster 11. The bar chart displays the gene set score for this specific sub-cluster across various cell types from late-stage Actc1^{E99K} mouse scRNA-seq data. Scores were calculated for each sample using the `score_genes` function in `scanpy` v1.10.1 [267]. Bars represent the mean score, with error bars indicating the standard error of the mean. Statistical significance between disease and control samples was determined using a t-test, with p-values adjusted for multiple comparisons using the Benjamini-Hochberg method. Asterisks denote significance levels: * $p < 0.05$, ** $p < 0.01$, *** $p < 0.001$, **** $p < 0.0001$.

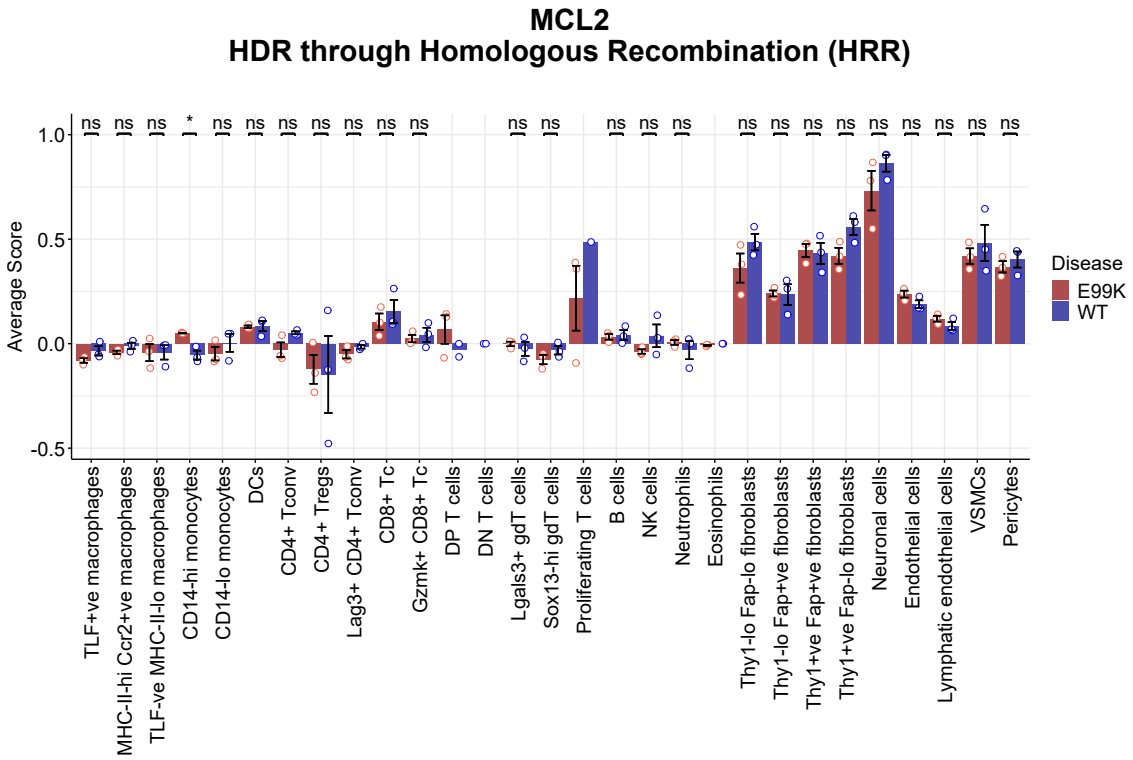

Figure D.102. Gene set scoring for MCL sub-cluster 2 of Cluster 11 (U-shaped trends) in late-stage mouse cell types.
This sub-cluster is a constituent of Cluster 11. The bar chart displays the gene set score for this specific sub-cluster across various cell types from late-stage Actc1^{E99K} mouse scRNA-seq data. Scores were calculated for each sample using the `score_genes` function in `scanpy` v1.10.1 [267]. Bars represent the mean score, with error bars indicating the standard error of the mean. Statistical significance between disease and control samples was determined using a t-test, with p-values adjusted for multiple comparisons using the Benjamini-Hochberg method. Asterisks denote significance levels: * $p < 0.05$, ** $p < 0.01$, *** $p < 0.001$, **** $p < 0.0001$.

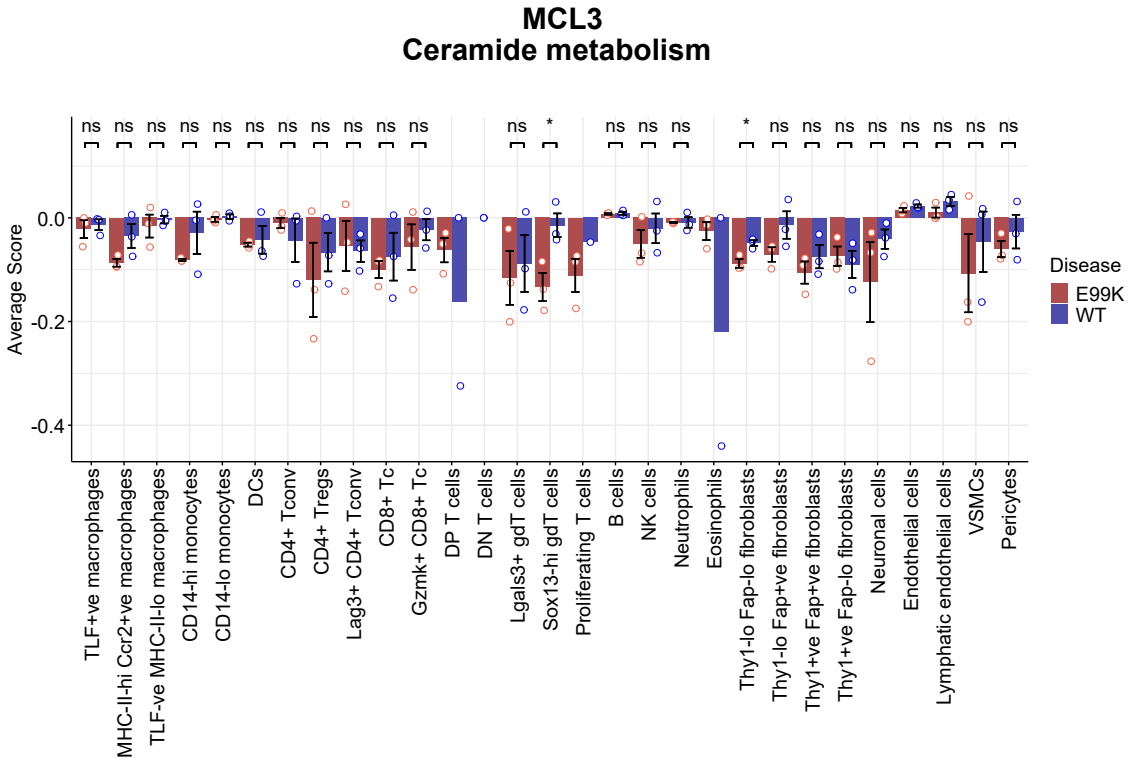

Figure D.103. Gene set scoring for MCL sub-cluster 3 of Cluster 11 (U-shaped trends) in late-stage mouse cell types.
This sub-cluster is a constituent of Cluster 11. The bar chart displays the gene set score for this specific sub-cluster across various cell types from late-stage Actc1^{E99K} mouse scRNA-seq data. Scores were calculated for each sample using the `score_genes` function in `scanpy` v1.10.1 [267]. Bars represent the mean score, with error bars indicating the standard error of the mean. Statistical significance between disease and control samples was determined using a t-test, with p-values adjusted for multiple comparisons using the Benjamini-Hochberg method. Asterisks denote significance levels: * $p < 0.05$, ** $p < 0.01$, *** $p < 0.001$, **** $p < 0.0001$.

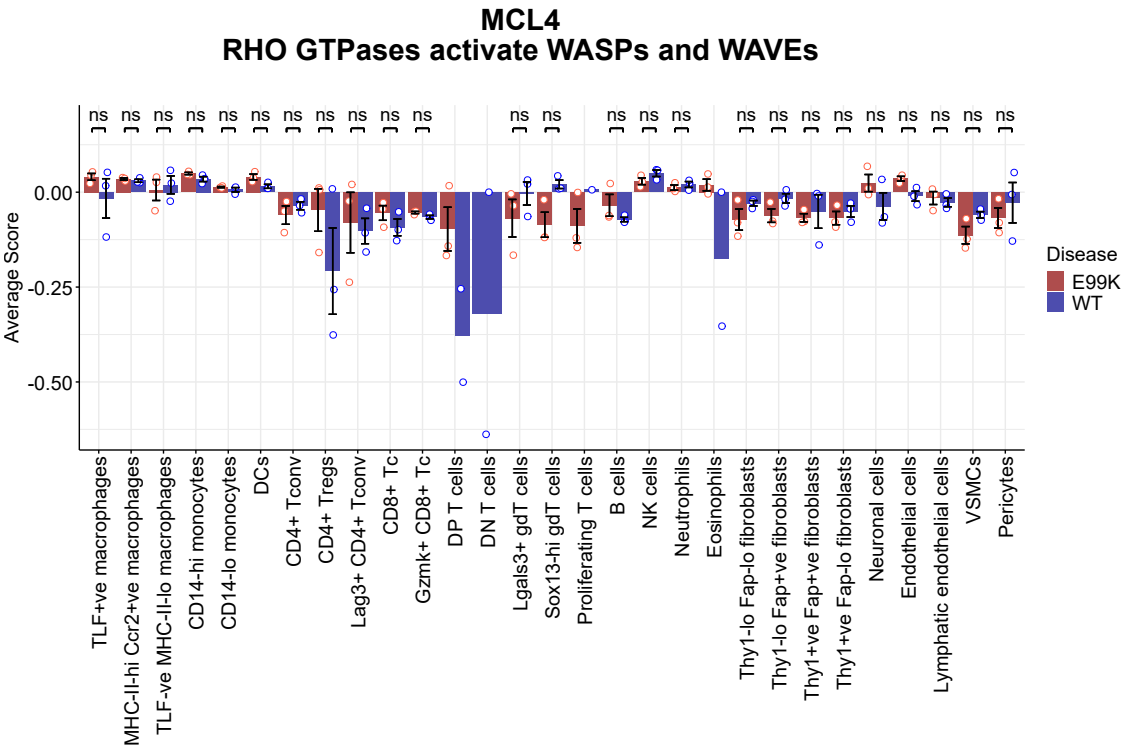

Figure D.104. Gene set scoring for MCL sub-cluster 4 of Cluster 11 (U-shaped trends) in late-stage mouse cell types.
This sub-cluster is a constituent of Cluster 11. The bar chart displays the gene set score for this specific sub-cluster across various cell types from late-stage $Actc1^{E99K}$ mouse scRNA-seq data. Scores were calculated for each sample using the `score_genes` function in `scanpy` v1.10.1 [267]. Bars represent the mean score, with error bars indicating the standard error of the mean. Statistical significance between disease and control samples was determined using a t-test, with p-values adjusted for multiple comparisons using the Benjamini-Hochberg method. Asterisks denote significance levels: * $p < 0.05$, ** $p < 0.01$, *** $p < 0.001$, **** $p < 0.0001$.

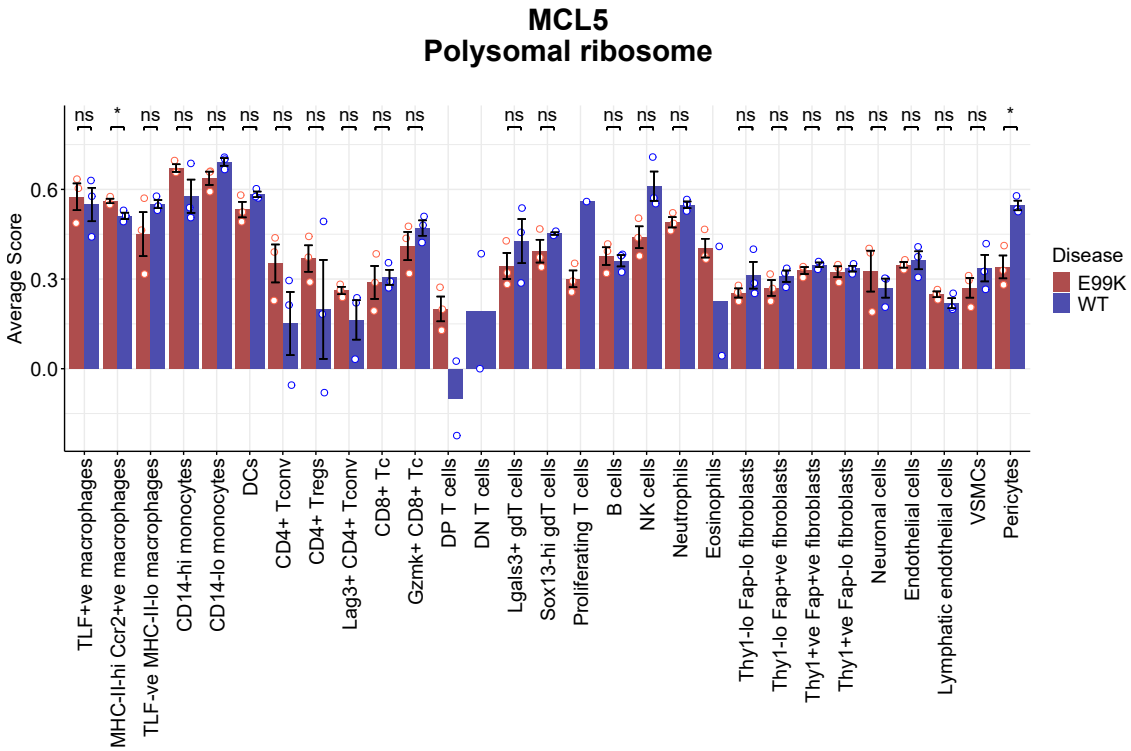

Figure D.105. Gene set scoring for MCL sub-cluster 5 of Cluster 11 (U-shaped trends) in late-stage mouse cell types.
This sub-cluster is a constituent of Cluster 11. The bar chart displays the gene set score for this specific sub-cluster across various cell types from late-stage Actc1^{E99K} mouse scRNA-seq data. Scores were calculated for each sample using the `score_genes` function in `scanpy` v1.10.1 [267]. Bars represent the mean score, with error bars indicating the standard error of the mean. Statistical significance between disease and control samples was determined using a t-test, with p-values adjusted for multiple comparisons using the Benjamini-Hochberg method. Asterisks denote significance levels: * $p < 0.05$, ** $p < 0.01$, *** $p < 0.001$, **** $p < 0.0001$.

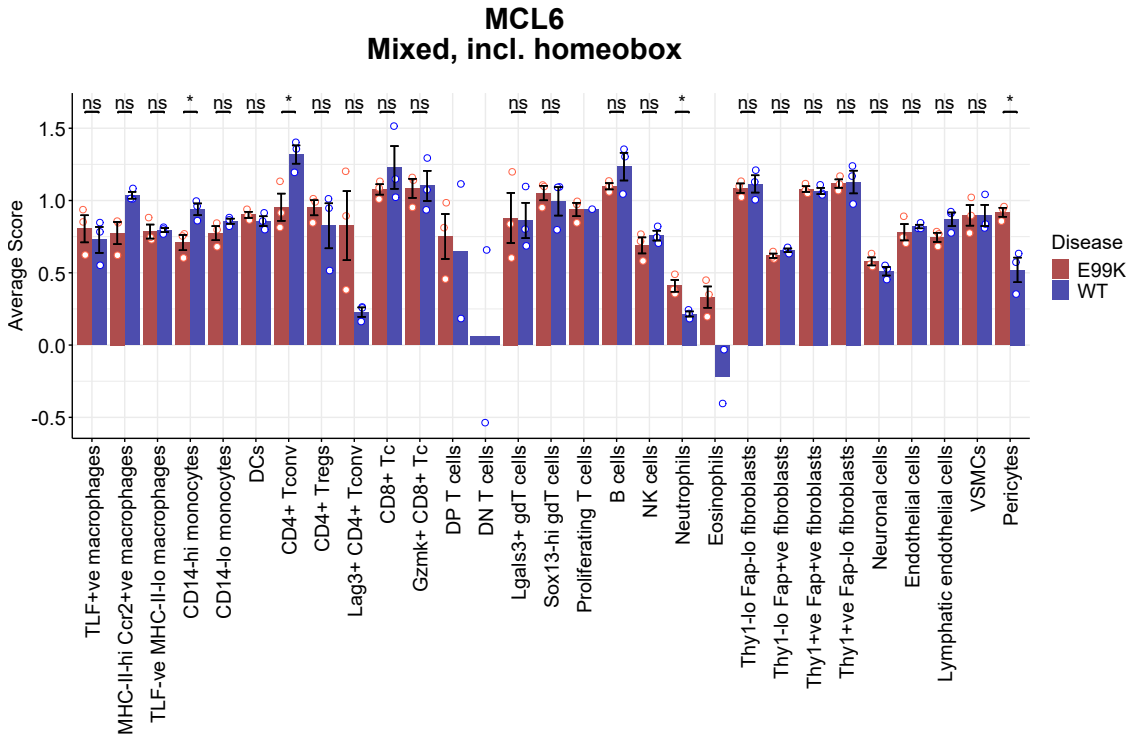

Figure D.106. Gene set scoring for MCL sub-cluster 6 of Cluster 11 (U-shaped trends) in late-stage mouse cell types.
This sub-cluster is a constituent of Cluster 11. The bar chart displays the gene set score for this specific sub-cluster across various cell types from late-stage Actc1^{E99K} mouse scRNA-seq data. Scores were calculated for each sample using the `score_genes` function in `scanpy` v1.10.1 [267]. Bars represent the mean score, with error bars indicating the standard error of the mean. Statistical significance between disease and control samples was determined using a t-test, with p-values adjusted for multiple comparisons using the Benjamini-Hochberg method. Asterisks denote significance levels: * $p < 0.05$, ** $p < 0.01$, *** $p < 0.001$, **** $p < 0.0001$.

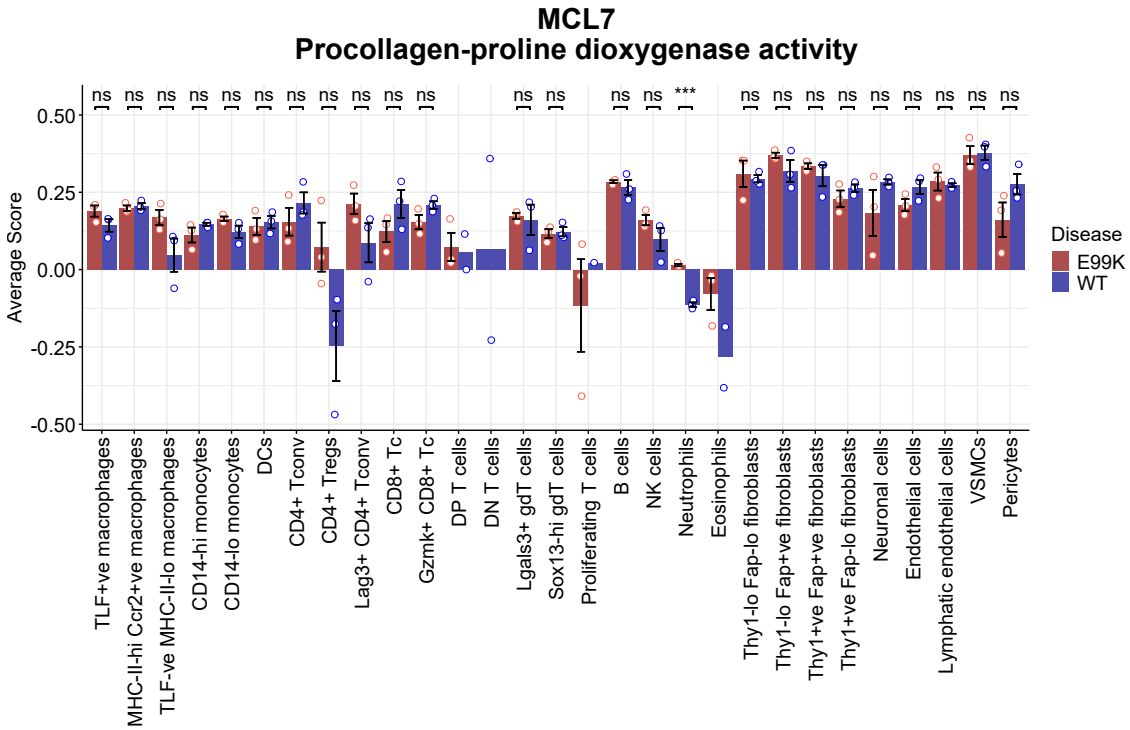

Figure D.107. Gene set scoring for MCL sub-cluster 7 of Cluster 11 (U-shaped trends) in late-stage mouse cell types.
This sub-cluster is a constituent of Cluster 11. The bar chart displays the gene set score for this specific sub-cluster across various cell types from late-stage $Actc1^{E99K}$ mouse scRNA-seq data. Scores were calculated for each sample using the `score_genes` function in `scanpy` v1.10.1 [267]. Bars represent the mean score, with error bars indicating the standard error of the mean. Statistical significance between disease and control samples was determined using a t-test, with p-values adjusted for multiple comparisons using the Benjamini-Hochberg method. Asterisks denote significance levels: * $p < 0.05$, ** $p < 0.01$, *** $p < 0.001$, **** $p < 0.0001$.

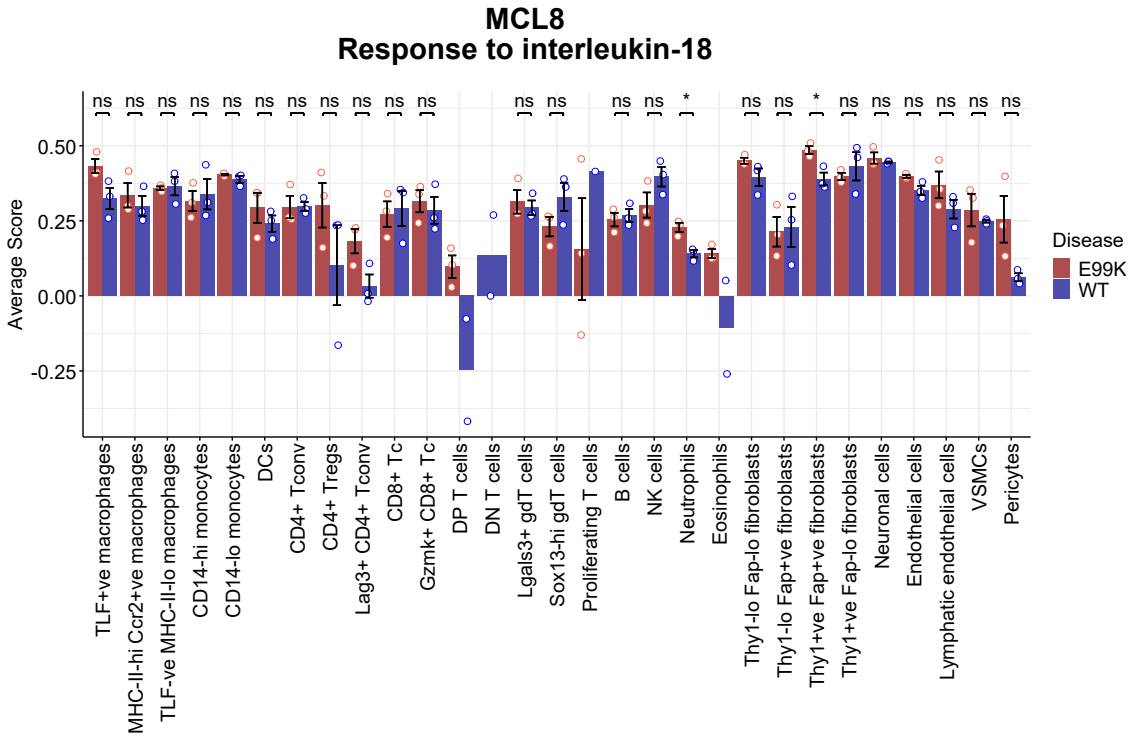

Figure D.108. Gene set scoring for MCL sub-cluster 8 of Cluster 11 (U-shaped trends) in late-stage mouse cell types.
This sub-cluster is a constituent of Cluster 11. The bar chart displays the gene set score for this specific sub-cluster across various cell types from late-stage $Actc1^{E99K}$ mouse scRNA-seq data. Scores were calculated for each sample using the `score_genes` function in `scanpy` v1.10.1 [267]. Bars represent the mean score, with error bars indicating the standard error of the mean. Statistical significance between disease and control samples was determined using a t-test, with p-values adjusted for multiple comparisons using the Benjamini-Hochberg method. Asterisks denote significance levels: * $p < 0.05$, ** $p < 0.01$, *** $p < 0.001$, **** $p < 0.0001$.

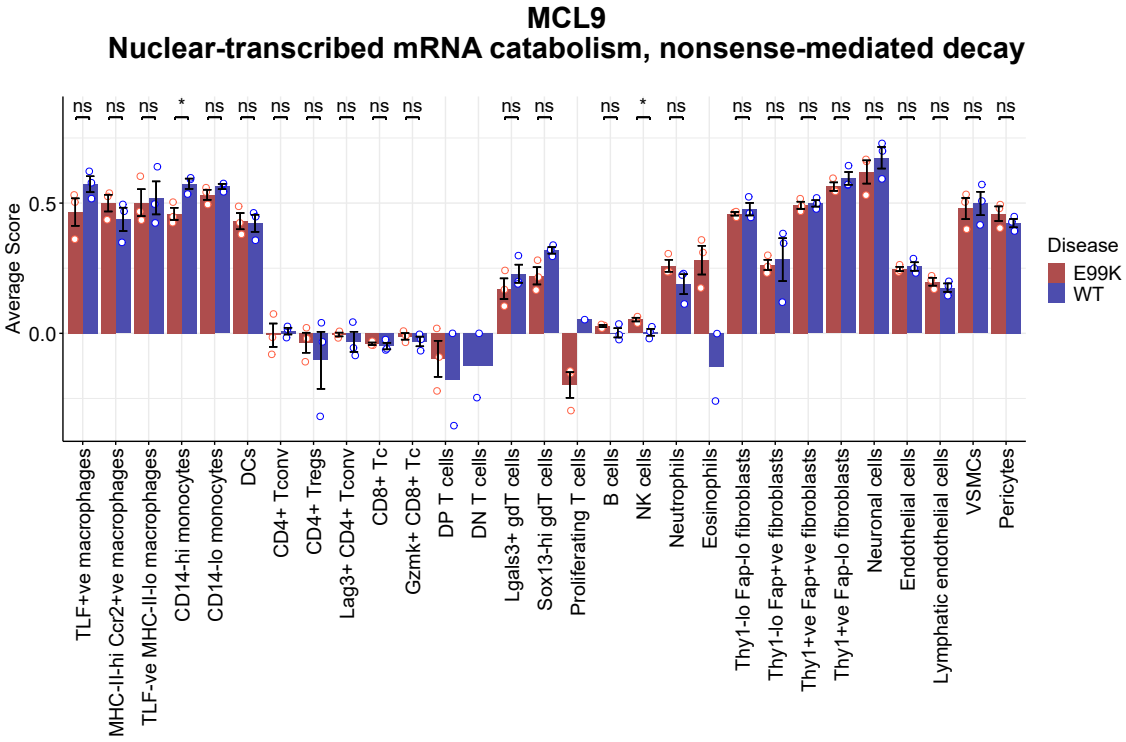

Figure D.109. Gene set scoring for MCL sub-cluster 9 of Cluster 11 (U-shaped trends) in late-stage mouse cell types.
This sub-cluster is a constituent of Cluster 11. The bar chart displays the gene set score for this specific sub-cluster across various cell types from late-stage Actc1^{E99K} mouse scRNA-seq data. Scores were calculated for each sample using the `score_genes` function in `scanpy` v1.10.1 [267]. Bars represent the mean score, with error bars indicating the standard error of the mean. Statistical significance between disease and control samples was determined using a t-test, with p-values adjusted for multiple comparisons using the Benjamini-Hochberg method. Asterisks denote significance levels: * $p < 0.05$, ** $p < 0.01$, *** $p < 0.001$, **** $p < 0.0001$.

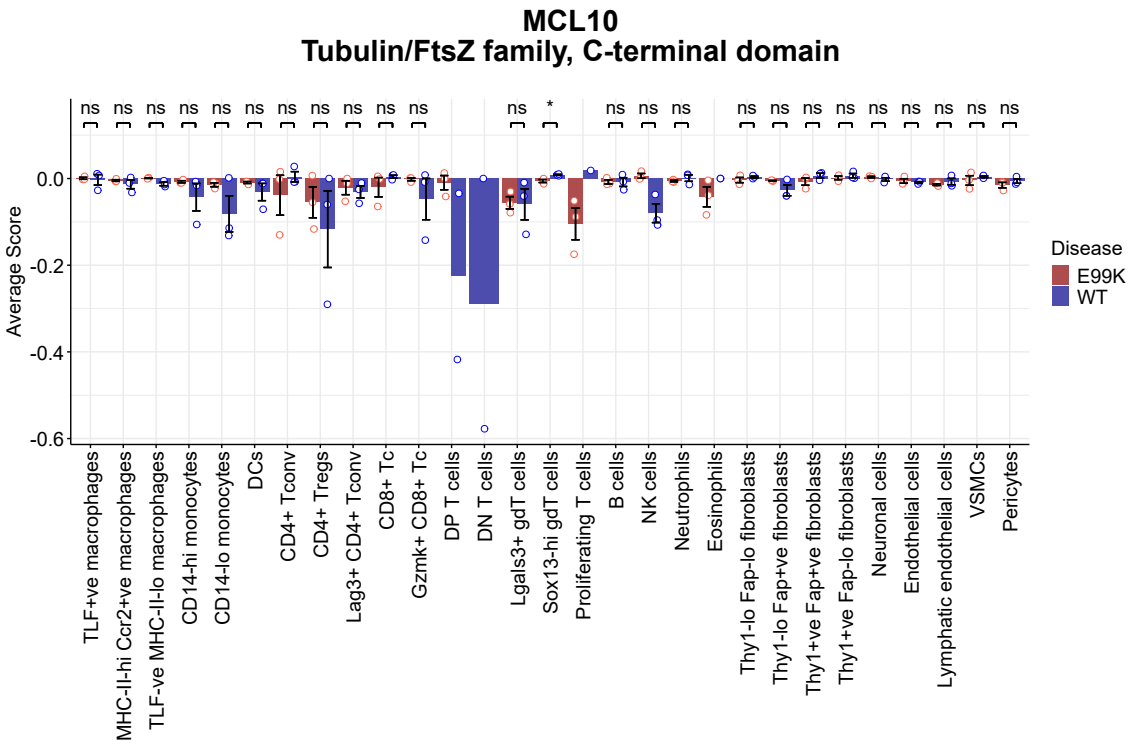

Figure D.110. Gene set scoring for MCL sub-cluster 10 of Cluster 11 (U-shaped trends) in late-stage mouse cell types.
This sub-cluster is a constituent of Cluster 11. The bar chart displays the gene set score for this specific sub-cluster across various cell types from late-stage Actc1^{E99K} mouse scRNA-seq data. Scores were calculated for each sample using the `score_genes` function in `scanpy` v1.10.1 [267]. Bars represent the mean score, with error bars indicating the standard error of the mean. Statistical significance between disease and control samples was determined using a t-test, with p-values adjusted for multiple comparisons using the Benjamini-Hochberg method. Asterisks denote significance levels: * $p < 0.05$, ** $p < 0.01$, *** $p < 0.001$, **** $p < 0.0001$.

Cluster 12, also exhibiting a U-shaped trend, was primarily associated with cell cycle regulation (Figures D.111 and D.115). The dominant sub-cluster (MCL sub-cluster 1; Figure D.112) was enriched for genes involved in the mitotic spindle checkpoint and mitotic sister chromatid segregation. Two smaller sub-clusters were identified, one uncharacterised (MCL sub-cluster 2; Figure D.113) and the other related to the tenascin complex (MCL sub-cluster 3; Figure D.114). Given the small number of genes in sub-clusters 2 and 3, the primary focus will be on the larger, functionally defined sub-cluster 1. In late-stage human HCM, the overall cluster 12 signature was upregulated in activated fibroblasts, NK cells, endothelial cells, lymphatic endothelial cells, VSMCs, and cardiomyocytes, while

downregulated in proliferating macrophages (Figure D.111). The mitotic spindle checkpoint sub-cluster (MCL sub-cluster 1; Figure D.112) showed a similar pattern, with upregulation in fibroblasts, activated fibroblasts, endothelial cells, lymphatic endothelial cells, and VSMCs. In the mouse scRNA-seq data, the overall cluster 12 signature was upregulated in TLF^{-}MHC-II^{lo} macrophages, CD14^{hi} monocytes, and VSMCs (Figure D.115). The mitotic spindle checkpoint sub-cluster (MCL sub-cluster 1; Figure D.116) was upregulated in MHC-II^{hi}Ccr2^{+} macrophages, TLF^{-}MHC-II^{lo} macrophages, CD14^{hi} and CD14^{lo} monocytes, and VSMCs, while downregulated in Thy1^{lo}Fap^{lo} fibroblasts.

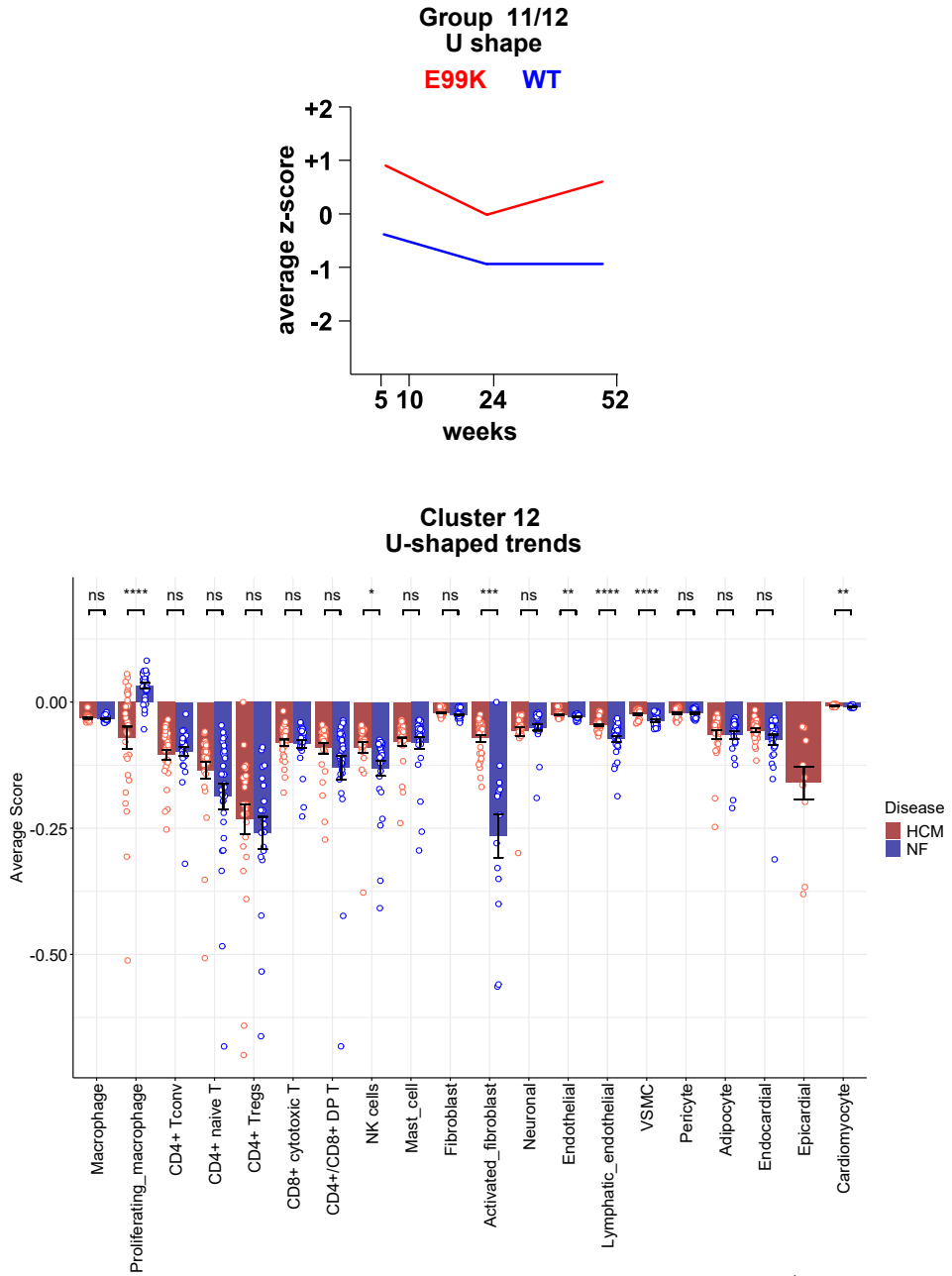

Figure D.111. Gene set scoring and statistics of Cluster 12 (U-shaped trends) in late-stage human cell types.
The upper panel schematically illustrates the temporal expression trend for Cluster 12, derived from bulk RNA-seq data of Actc1^{E99K} (red line) and wild-type (blue line) hearts over time. The lower panel displays the gene set score for all genes within Cluster 12 across various cell types identified in late-stage human HCM snRNA-seq data. Scores were calculated for each sample using the `score_genes` function in `scanpy` v1.10.1 [267]. Bars represent the mean score, with error bars indicating the standard error of the mean. Statistical significance between disease and control samples was determined using a t-test, with p-values adjusted for multiple comparisons using the Benjamini-Hochberg method. Asterisks denote significance levels: * $p < 0.05$, ** $p < 0.01$, *** $p < 0.001$, **** $p < 0.0001$.

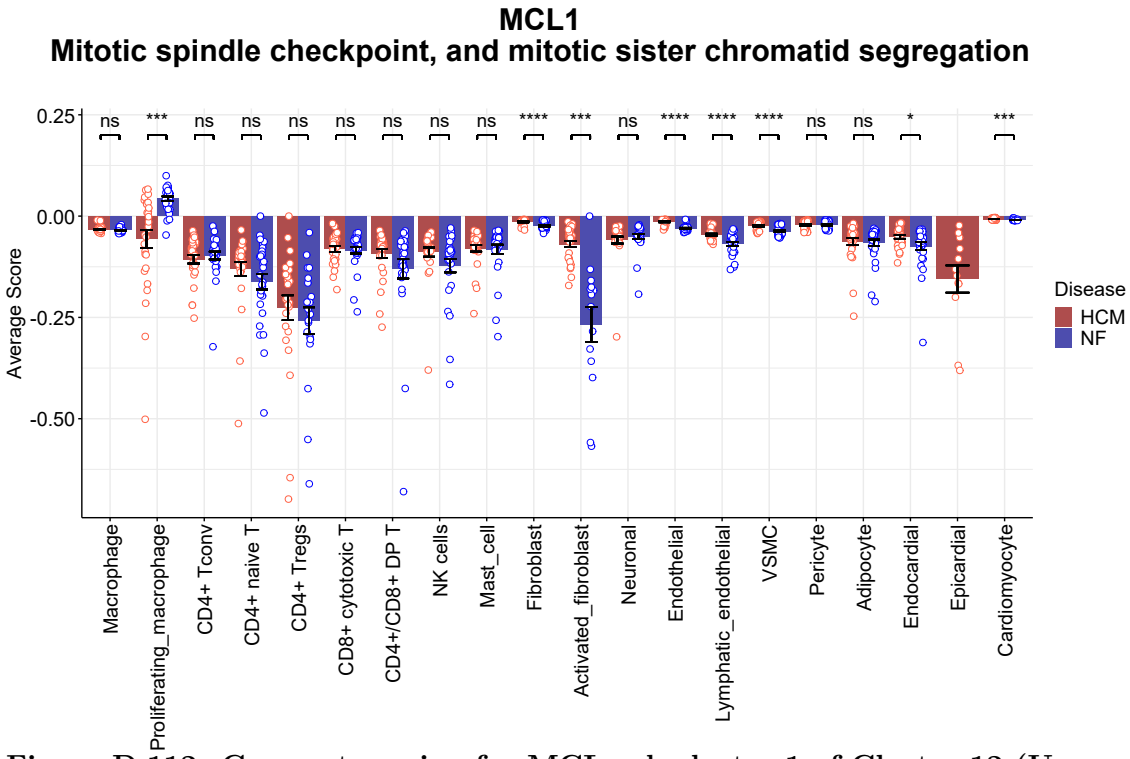

Figure D.112. Gene set scoring for MCL sub-cluster 1 of Cluster 12 (U-shaped trends) in late-stage human cell types.
This sub-cluster is a constituent of Cluster 12. The bar chart displays the gene set score for this specific sub-cluster across various cell types from late-stage human HCM snRNA-seq data. Scores were calculated for each sample using the `score_genes` function in `scanpy` v1.10.1 [267]. Bars represent the mean score, with error bars indicating the standard error of the mean. Statistical significance between disease and control samples was determined using a t-test, with p-values adjusted for multiple comparisons using the Benjamini-Hochberg method. Asterisks denote significance levels: * $p < 0.05$, ** $p < 0.01$, *** $p < 0.001$, **** $p < 0.0001$.

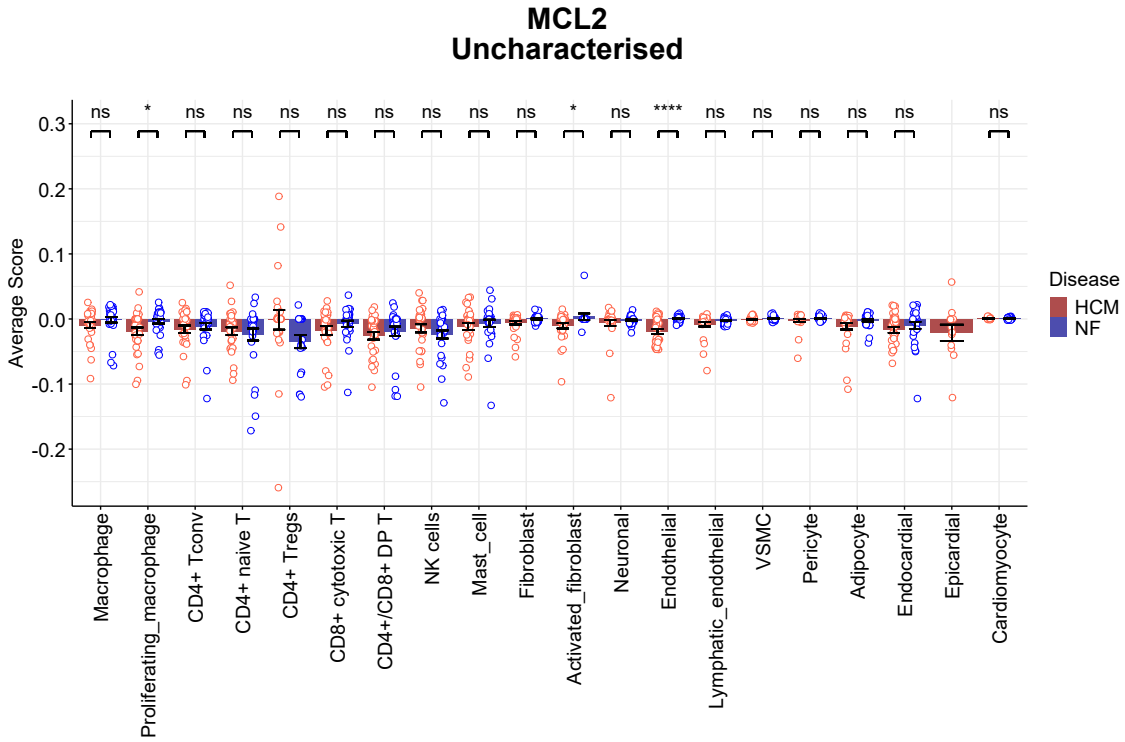

Figure D.113. Gene set scoring for MCL sub-cluster 2 of Cluster 12 (U-shaped trends) in late-stage human cell types.
This sub-cluster is a constituent of Cluster 12. The bar chart displays the gene set score for this specific sub-cluster across various cell types from late-stage human HCM snRNA-seq data. Scores were calculated for each sample using the `score_genes` function in `scanpy` v1.10.1 [267]. Bars represent the mean score, with error bars indicating the standard error of the mean. Statistical significance between disease and control samples was determined using a t-test, with p-values adjusted for multiple comparisons using the Benjamini-Hochberg method. Asterisks denote significance levels: * $p < 0.05$, ** $p < 0.01$, *** $p < 0.001$, **** $p < 0.0001$.

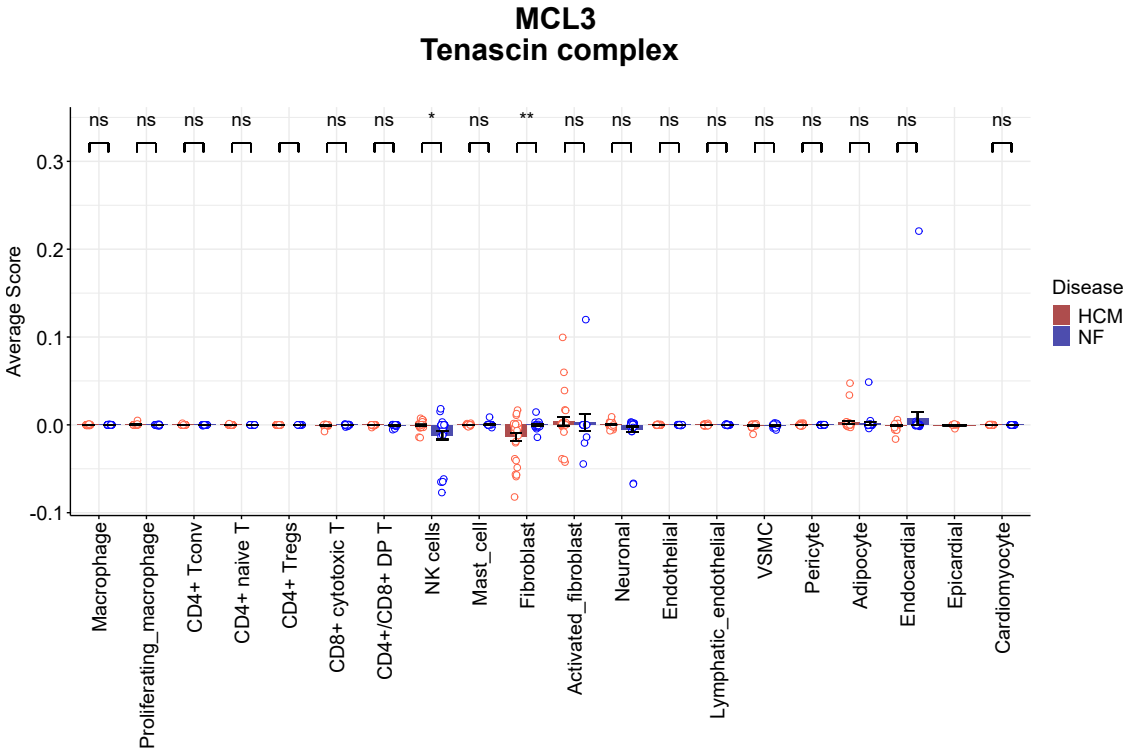

Figure D.114. Gene set scoring for MCL sub-cluster 3 of Cluster 12 (U-shaped trends) in late-stage human cell types.
This sub-cluster is a constituent of Cluster 12. The bar chart displays the gene set score for this specific sub-cluster across various cell types from late-stage human HCM snRNA-seq data. Scores were calculated for each sample using the `score_genes` function in `scanpy` v1.10.1 [267]. Bars represent the mean score, with error bars indicating the standard error of the mean. Statistical significance between disease and control samples was determined using a t-test, with p-values adjusted for multiple comparisons using the Benjamini-Hochberg method. Asterisks denote significance levels: * $p < 0.05$, ** $p < 0.01$, *** $p < 0.001$, **** $p < 0.0001$.

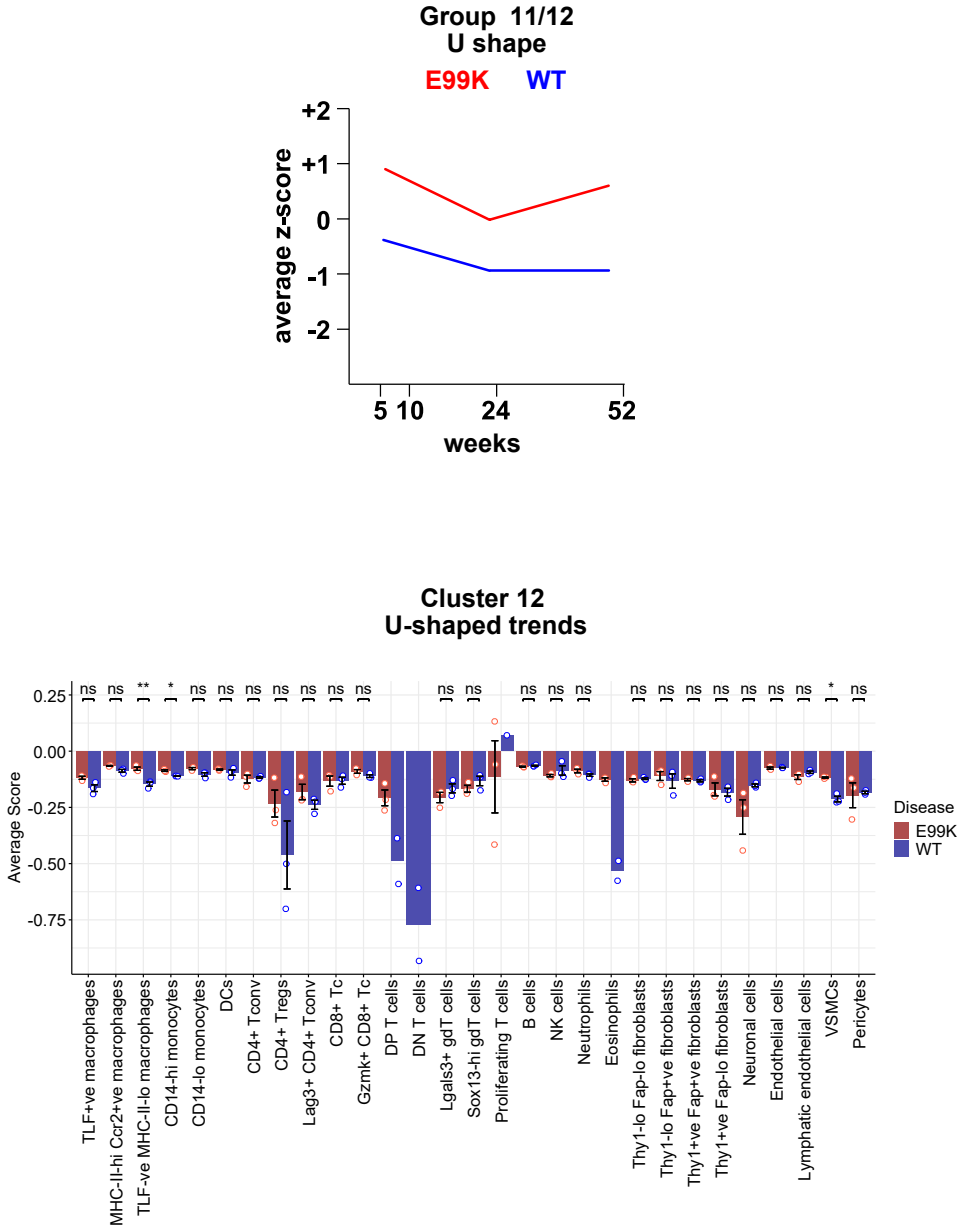

Figure D.115. Gene set scoring and statistics of Cluster 12 (U-shaped trends) in late-stage mouse cell types.
The upper panel schematically illustrates the temporal expression trend for Cluster 12, derived from bulk RNA-seq data of Actc1^{E99K} (red line) and wild-type (blue line) hearts over time. The lower panel displays the gene set score for all genes within Cluster 12 across various cell types identified in late-stage Actc1^{E99K} mouse scRNA-seq data. Scores were calculated for each sample using the `score_genes` function in `scanpy` v1.10.1 [267]. Bars represent the mean score, with error bars indicating the standard error of the mean. Statistical significance between disease and control samples was determined using a t-test, with p-values adjusted for multiple comparisons using the Benjamini-Hochberg method. Asterisks denote significance levels: * $p < 0.05$, ** $p < 0.01$, *** $p < 0.001$, **** $p < 0.0001$.

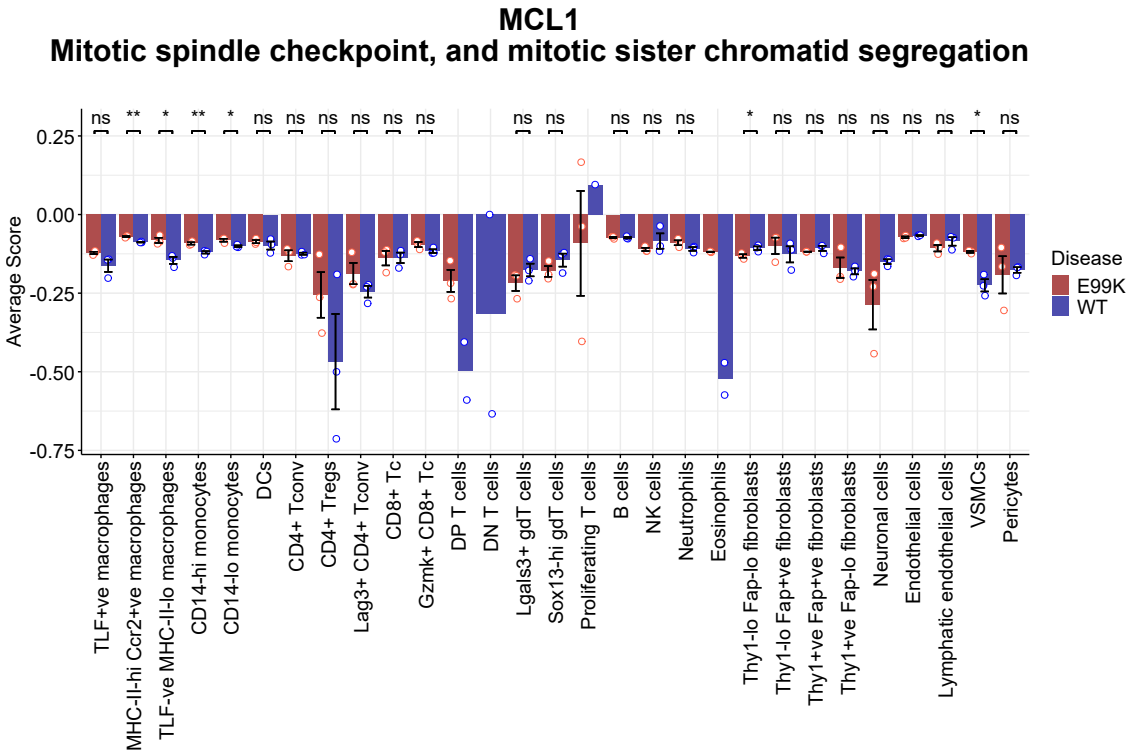

Figure D.116. Gene set scoring for MCL sub-cluster 1 of Cluster 12 (U-shaped trends) in late-stage mouse cell types.
This sub-cluster is a constituent of Cluster 12. The bar chart displays the gene set score for this specific sub-cluster across various cell types from late-stage Actc1^{E99K} mouse scRNA-seq data. Scores were calculated for each sample using the `score_genes` function in `scanpy` v1.10.1 [267]. Bars represent the mean score, with error bars indicating the standard error of the mean. Statistical significance between disease and control samples was determined using a t-test, with p-values adjusted for multiple comparisons using the Benjamini-Hochberg method. Asterisks denote significance levels: * $p < 0.05$, ** $p < 0.01$, *** $p < 0.001$, **** $p < 0.0001$.

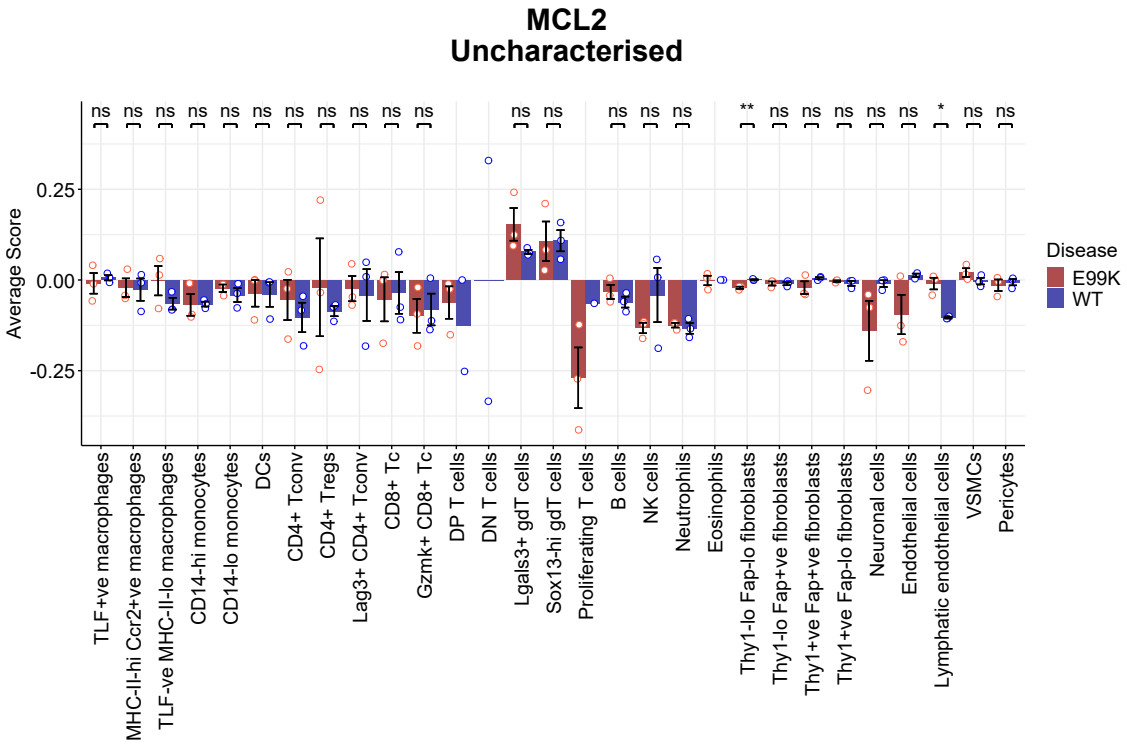

Figure D.117. Gene set scoring for MCL sub-cluster 2 of Cluster 12 (U-shaped trends) in late-stage mouse cell types.
This sub-cluster is a constituent of Cluster 12. The bar chart displays the gene set score for this specific sub-cluster across various cell types from late-stage Actc1^{E99K} mouse scRNA-seq data. Scores were calculated for each sample using the `score_genes` function in `scanpy` v1.10.1 [267]. Bars represent the mean score, with error bars indicating the standard error of the mean. Statistical significance between disease and control samples was determined using a t-test, with p-values adjusted for multiple comparisons using the Benjamini-Hochberg method. Asterisks denote significance levels: * $p < 0.05$, ** $p < 0.01$, *** $p < 0.001$, **** $p < 0.0001$.

D.4 Cluster 5 & 6: Progressive down-regulation in key clusters signals metabolic and functional decline during HCM

Cluster 5, exhibiting an initial down-regulation followed by a further decline in the late stage, was enriched for metabolic processes and cellular functions (Figures D.119 and D.130). Sub-cluster analysis revealed enrichment for ribonucleoside monophosphate metabolism (MCL sub-cluster 1; Figure D.120), cardiac muscle cell contraction (MCL sub-cluster 2; Figure D.121), a mixed sub-cluster including nucleoid and regulation of mitochondrial translation (MCL sub-cluster 3; Figure D.122), BTB and C-terminal Kelch (MCL sub-cluster 4;

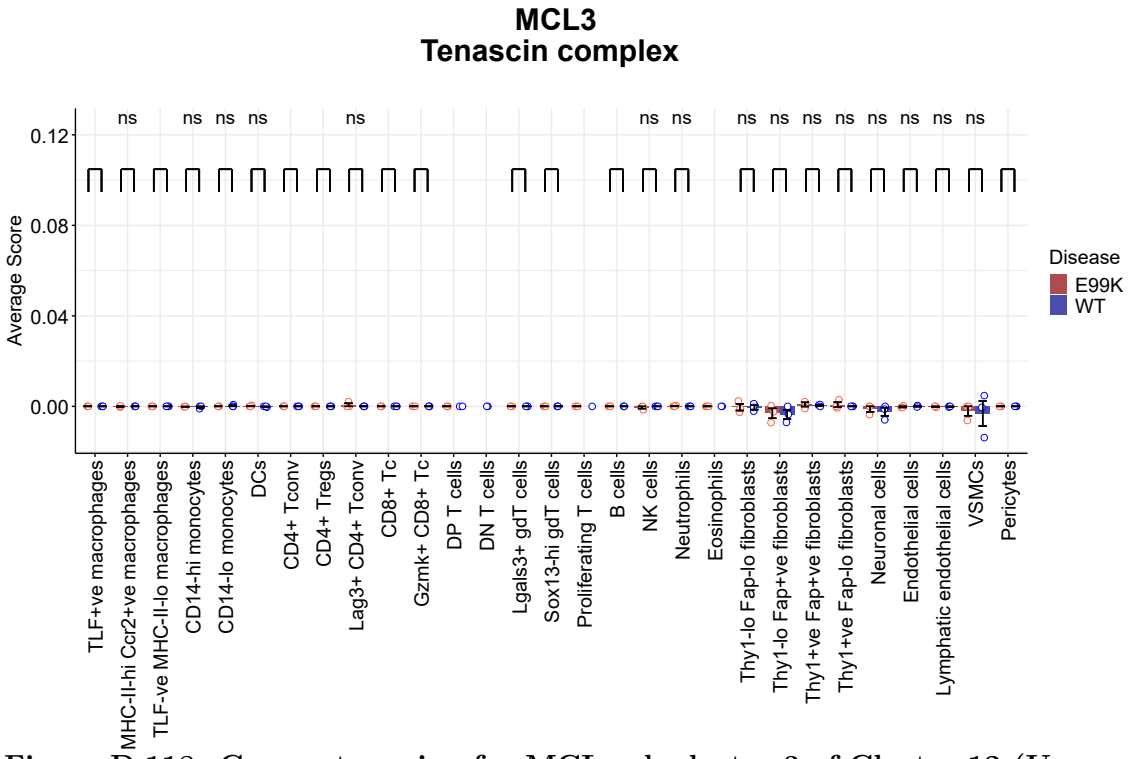

Figure D.118. Gene set scoring for MCL sub-cluster 3 of Cluster 12 (U-shaped trends) in late-stage mouse cell types.
This sub-cluster is a constituent of Cluster 12. The bar chart displays the gene set score for this specific sub-cluster across various cell types from late-stage Actc1^{E99K} mouse scRNA-seq data. Scores were calculated for each sample using the `score_genes` function in `scanpy` v1.10.1 [267]. Bars represent the mean score, with error bars indicating the standard error of the mean. Statistical significance between disease and control samples was determined using a t-test, with p-values adjusted for multiple comparisons using the Benjamini-Hochberg method. Asterisks denote significance levels: * $p < 0.05$, ** $p < 0.01$, *** $p < 0.001$, **** $p < 0.0001$.

Figure D.123), vesicle tethering involved in exocytosis (MCL sub-cluster 5; Figure D.124), cysteine-type deubiquitinase activity (MCL sub-cluster 6; Figure D.125), mRNA surveillance pathway (MCL sub-cluster 7; Figure D.126), mitochondrial translation (MCL sub-cluster 8; Figure D.127), complex I biogenesis (MCL sub-cluster 9; Figure D.128), and propanoate metabolism (MCL sub-cluster 10; Figure D.129). In late-stage human HCM samples, the overall cluster 5 signature was significantly upregulated in activated fibroblasts, lymphatic endothelial cells, and VSMCs, while downregulated in macrophages and proliferating macrophages (Figure D.119). Further examination of individual sub-clusters revealed distinct cell-type specific patterns. For instance, the ribonucleoside monophosphate metabolism

sub-cluster (MCL sub-cluster 1; Figure D.120) showed upregulation in activated fibroblasts, lymphatic endothelial cells, and VSMCs, and downregulation in macrophages, proliferating macrophages, and endothelial cells. The cardiac muscle cell contraction sub-cluster (MCL sub-cluster 2; Figure D.121) was upregulated in fibroblasts and downregulated in NK cells. The mixed sub-cluster containing nucleoid and regulation of mitochondrial translation processes (MCL sub-cluster 3; Figure D.122) was upregulated in activated fibroblasts and downregulated in macrophages, proliferating macrophages, fibroblasts, pericytes, adipocytes, and cardiomyocytes. In the mouse scRNA-seq data, the overall cluster 5 signature was downregulated in B cells and $Thy1^{lo}Fap^{lo}$ fibroblasts (Figure D.130). Sub-cluster analysis revealed downregulation of the ribonucleoside monophosphate metabolism sub-cluster (MCL sub-cluster 1; Figure D.131) in neuronal cells, downregulation of the cardiac muscle cell contraction sub-cluster (MCL sub-cluster 2; Figure D.132) in $\gamma\delta$T cells, a negligible downregulation of the mixed sub-cluster containing nucleoid and regulation of mitochondrial translation processes (MCL sub-cluster 3; Figure D.133) in MHC-$II^{hi}Ccr2^{+}$ macrophages, $CD14^{hi}$ monocytes, and pericytes, and downregulation of the BTB and C-terminal Kelch sub-cluster (MCL sub-cluster 4; Figure D.134) in lymphatic endothelial cells.

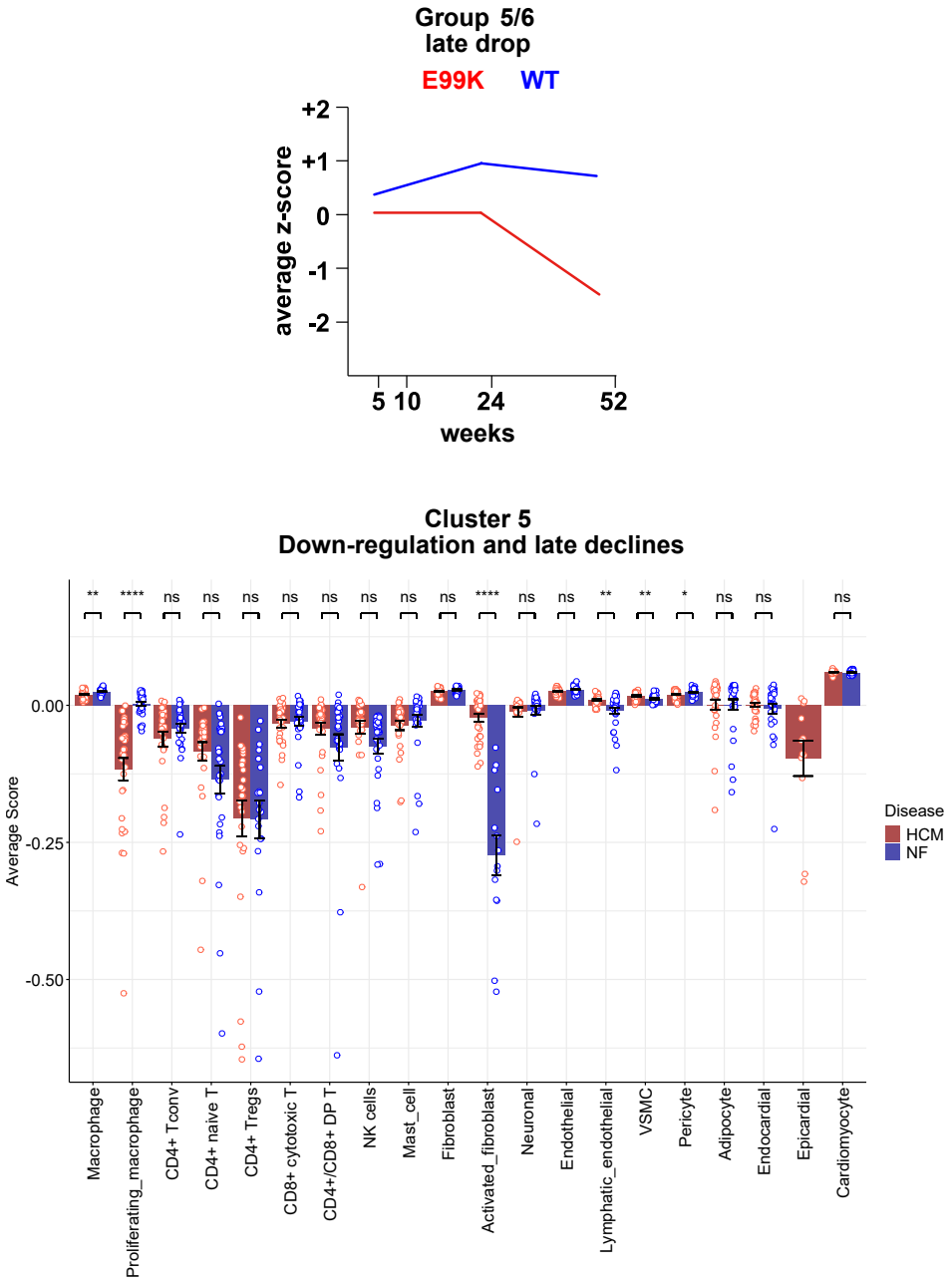

Figure D.119. Gene set scoring and statistics of Cluster 5 (down-regulation and late declines) in late-stage human cell types.
The upper panel schematically illustrates the temporal expression trend for Cluster 5, derived from bulk RNA-seq data of Actc1^{E99K} (red line) and wild-type (blue line) hearts over time. The lower panel displays the gene set score for all genes within Cluster 5 across various cell types identified in late-stage human HCM snRNA-seq data. Scores were calculated for each sample using the `score_genes` function in `scanpy` v1.10.1 [267]. Bars represent the mean score, with error bars indicating the standard error of the mean. Statistical significance between disease and control samples was determined using a t-test, with p-values adjusted for multiple comparisons using the Benjamini-Hochberg method. Asterisks denote significance levels: * $p < 0.05$, ** $p < 0.01$, *** $p < 0.001$, **** $p < 0.0001$.

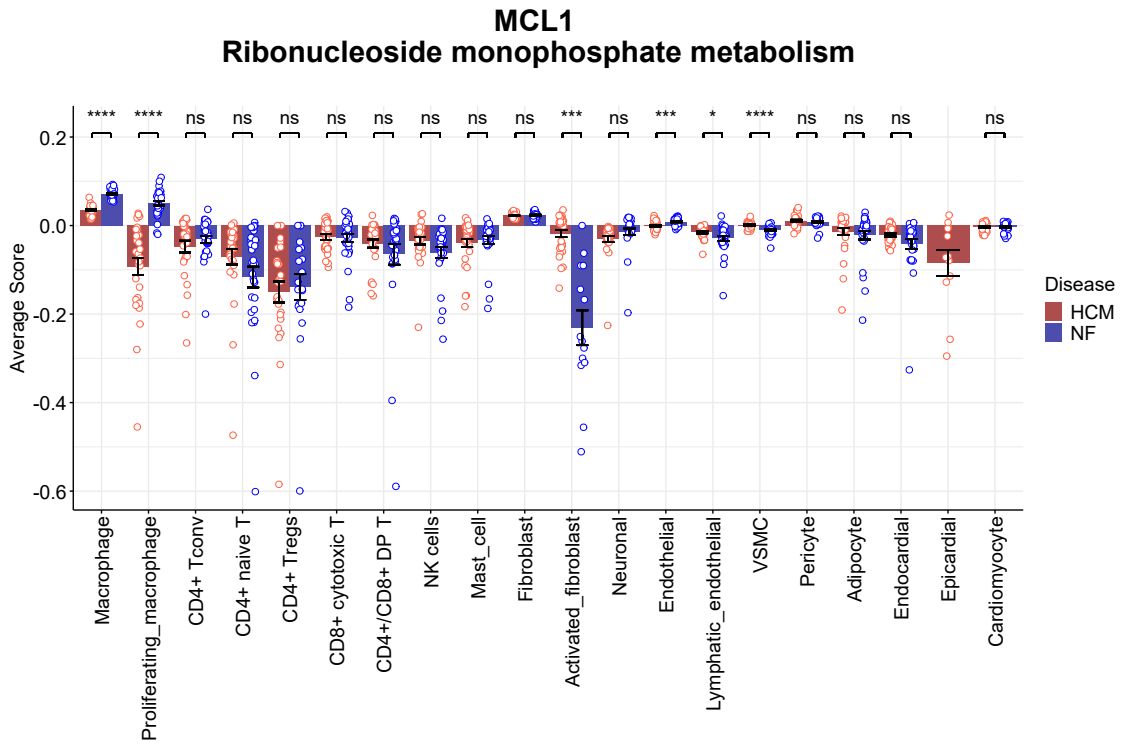

Figure D.120. Gene set scoring for MCL sub-cluster 1 of Cluster 5 (down-regulation and late declines) in late-stage human cell types.
This sub-cluster is a constituent of Cluster 5. The bar chart displays the gene set score for this specific sub-cluster across various cell types from late-stage human HCM snRNA-seq data. Scores were calculated for each sample using the `score_genes` function in `scanpy` v1.10.1 [267]. Bars represent the mean score, with error bars indicating the standard error of the mean. Statistical significance between disease and control samples was determined using a t-test, with p-values adjusted for multiple comparisons using the Benjamini-Hochberg method. Asterisks denote significance levels: * $p < 0.05$, ** $p < 0.01$, *** $p < 0.001$, **** $p < 0.0001$.

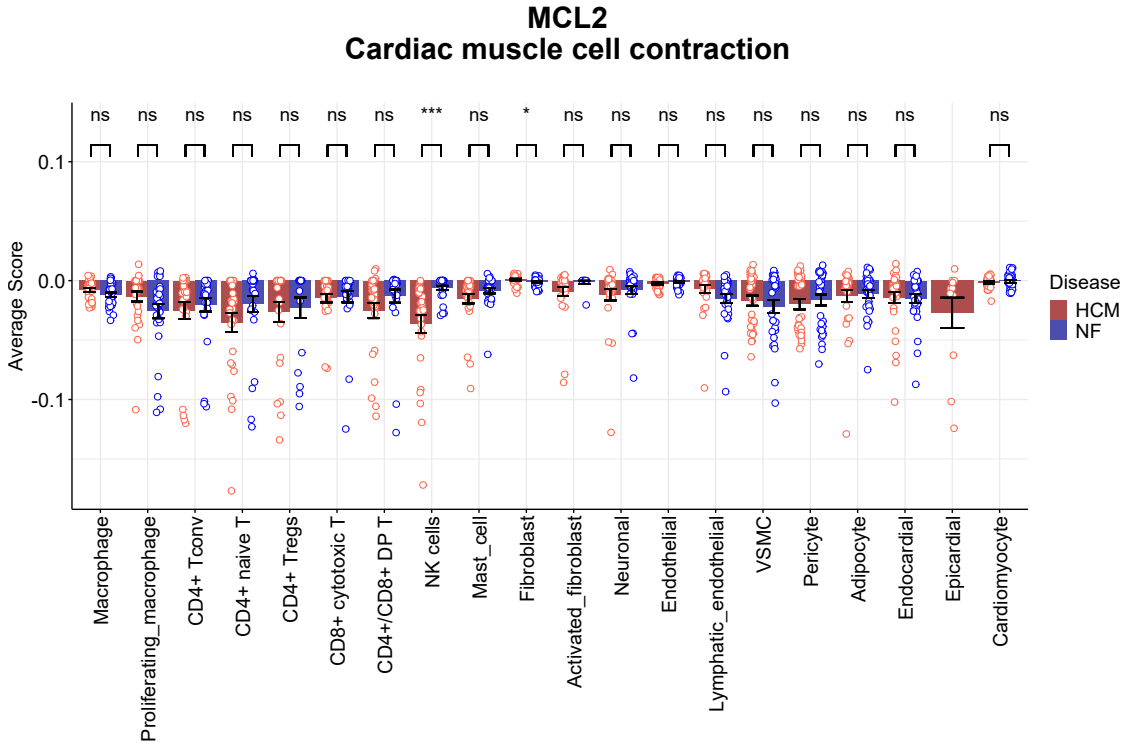

Figure D.121. Gene set scoring for MCL sub-cluster 2 of Cluster 5 (down-regulation and late declines) in late-stage human cell types.
This sub-cluster is a constituent of Cluster 5. The bar chart displays the gene set score for this specific sub-cluster across various cell types from late-stage human HCM snRNA-seq data. Scores were calculated for each sample using the `score_genes` function in `scanpy` v1.10.1 [267]. Bars represent the mean score, with error bars indicating the standard error of the mean. Statistical significance between disease and control samples was determined using a t-test, with p-values adjusted for multiple comparisons using the Benjamini-Hochberg method. Asterisks denote significance levels: * $p < 0.05$, ** $p < 0.01$, *** $p < 0.001$, **** $p < 0.0001$.

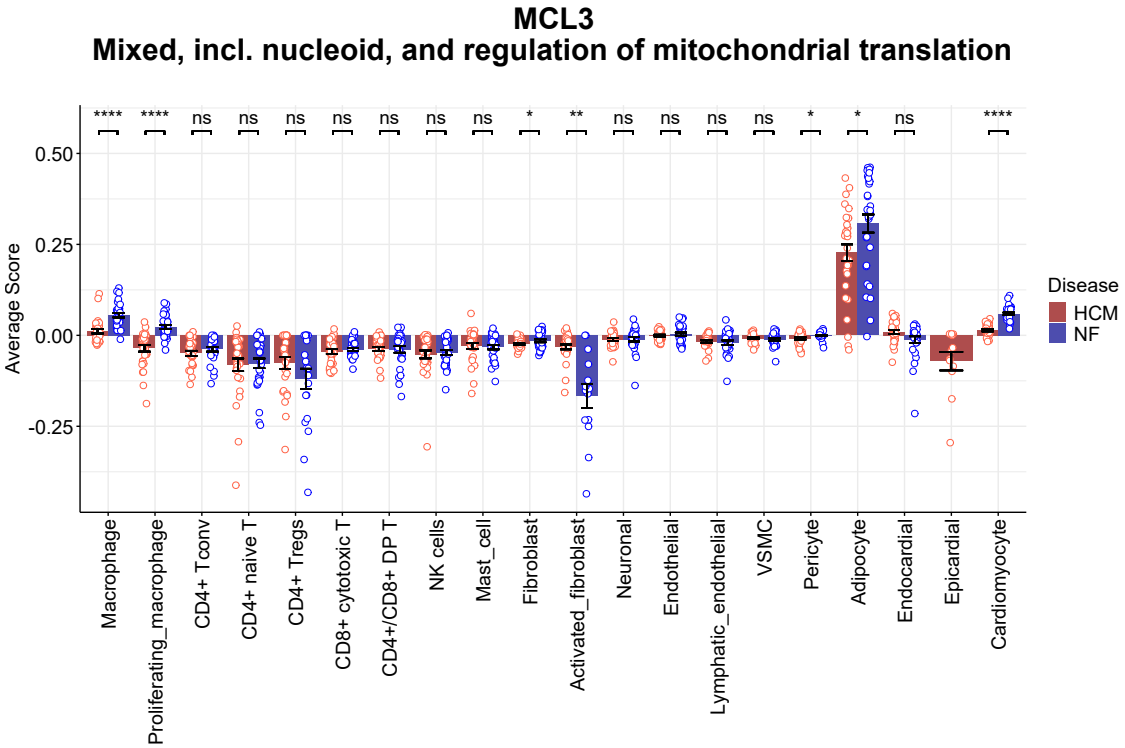

Figure D.122. Gene set scoring for MCL sub-cluster 3 of Cluster 5 (down-regulation and late declines) in late-stage human cell types.
This sub-cluster is a constituent of Cluster 5. The bar chart displays the gene set score for this specific sub-cluster across various cell types from late-stage human HCM snRNA-seq data. Scores were calculated for each sample using the `score_genes` function in `scanpy` v1.10.1 [267]. Bars represent the mean score, with error bars indicating the standard error of the mean. Statistical significance between disease and control samples was determined using a t-test, with p-values adjusted for multiple comparisons using the Benjamini-Hochberg method. Asterisks denote significance levels: * $p < 0.05$, ** $p < 0.01$, *** $p < 0.001$, **** $p < 0.0001$.

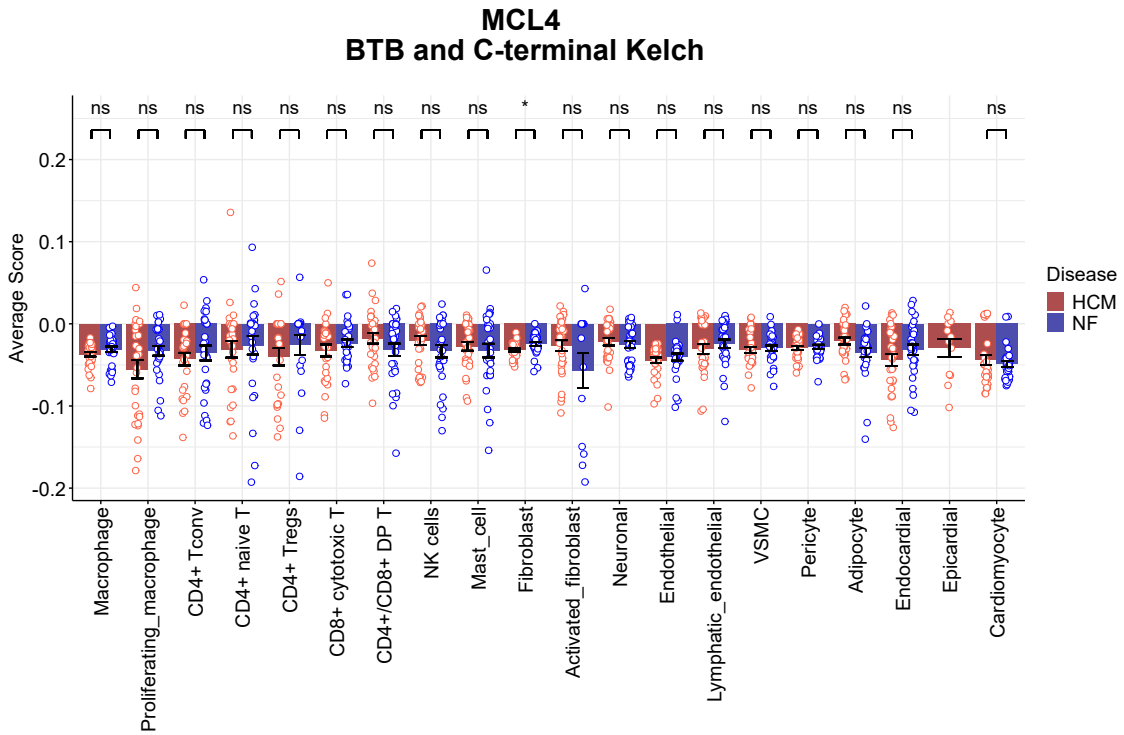

Figure D.123. Gene set scoring for MCL sub-cluster 4 of Cluster 5 (down-regulation and late declines) in late-stage human cell types.
This sub-cluster is a constituent of Cluster 5. The bar chart displays the gene set score for this specific sub-cluster across various cell types from late-stage human HCM snRNA-seq data. Scores were calculated for each sample using the `score_genes` function in `scanpy` v1.10.1 [267]. Bars represent the mean score, with error bars indicating the standard error of the mean. Statistical significance between disease and control samples was determined using a t-test, with p-values adjusted for multiple comparisons using the Benjamini-Hochberg method. Asterisks denote significance levels: * $p < 0.05$, ** $p < 0.01$, *** $p < 0.001$, **** $p < 0.0001$.

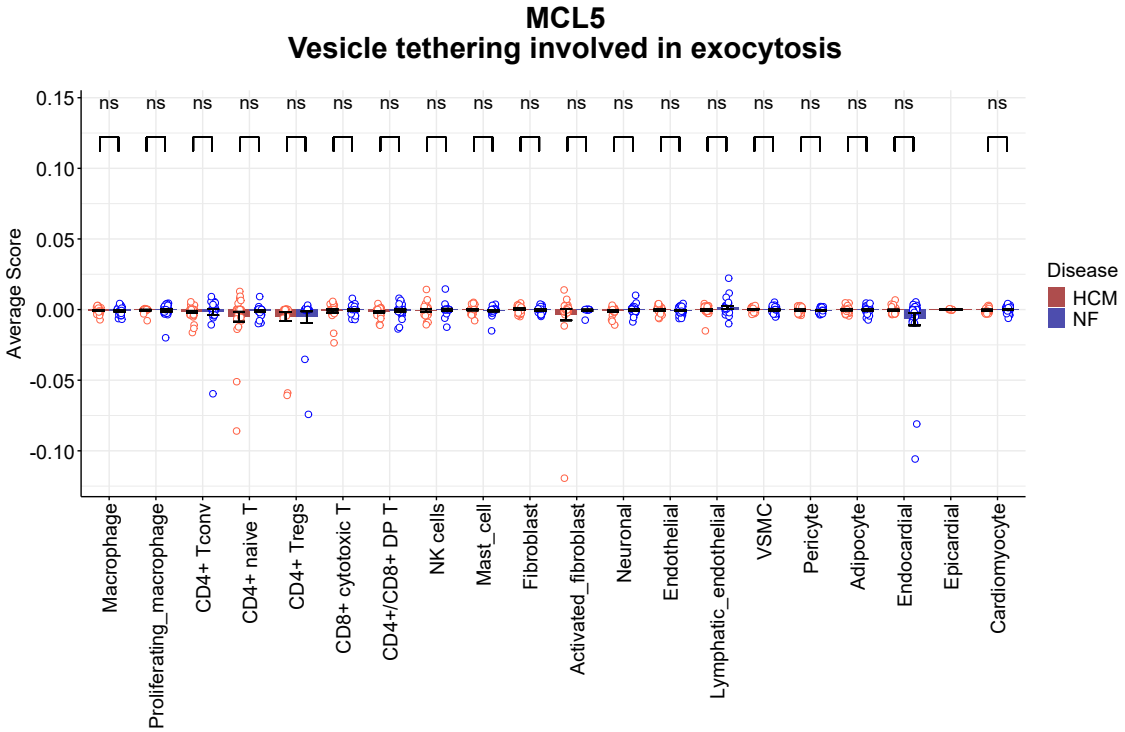

Figure D.124. Gene set scoring for MCL sub-cluster 5 of Cluster 5 (down-regulation and late declines) in late-stage human cell types.
This sub-cluster is a constituent of Cluster 5. The bar chart displays the gene set score for this specific sub-cluster across various cell types from late-stage human HCM snRNA-seq data. Scores were calculated for each sample using the `score_genes` function in `scanpy` v1.10.1 [267]. Bars represent the mean score, with error bars indicating the standard error of the mean. Statistical significance between disease and control samples was determined using a t-test, with p-values adjusted for multiple comparisons using the Benjamini-Hochberg method. Asterisks denote significance levels: * $p < 0.05$, ** $p < 0.01$, *** $p < 0.001$, **** $p < 0.0001$.

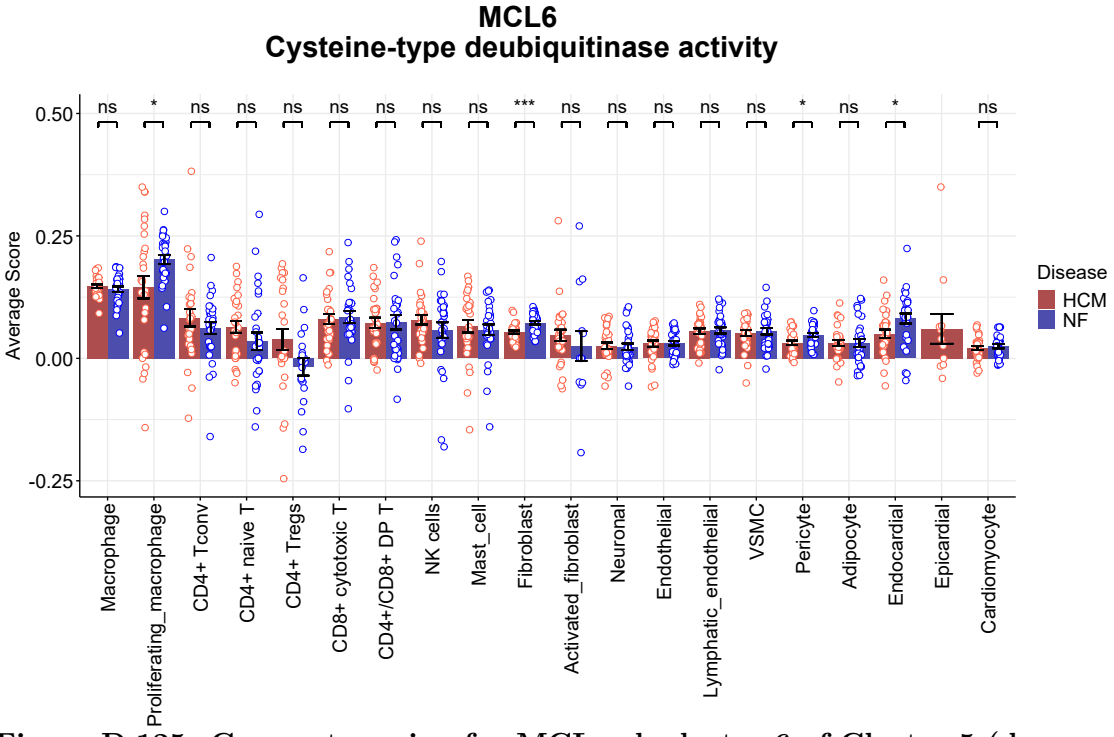

Figure D.125. Gene set scoring for MCL sub-cluster 6 of Cluster 5 (down-regulation and late declines) in late-stage human cell types.
This sub-cluster is a constituent of Cluster 5. The bar chart displays the gene set score for this specific sub-cluster across various cell types from late-stage human HCM snRNA-seq data. Scores were calculated for each sample using the `score_genes` function in `scanpy` v1.10.1 [267]. Bars represent the mean score, with error bars indicating the standard error of the mean. Statistical significance between disease and control samples was determined using a t-test, with p-values adjusted for multiple comparisons using the Benjamini-Hochberg method. Asterisks denote significance levels: * $p < 0.05$, ** $p < 0.01$, *** $p < 0.001$, **** $p < 0.0001$.

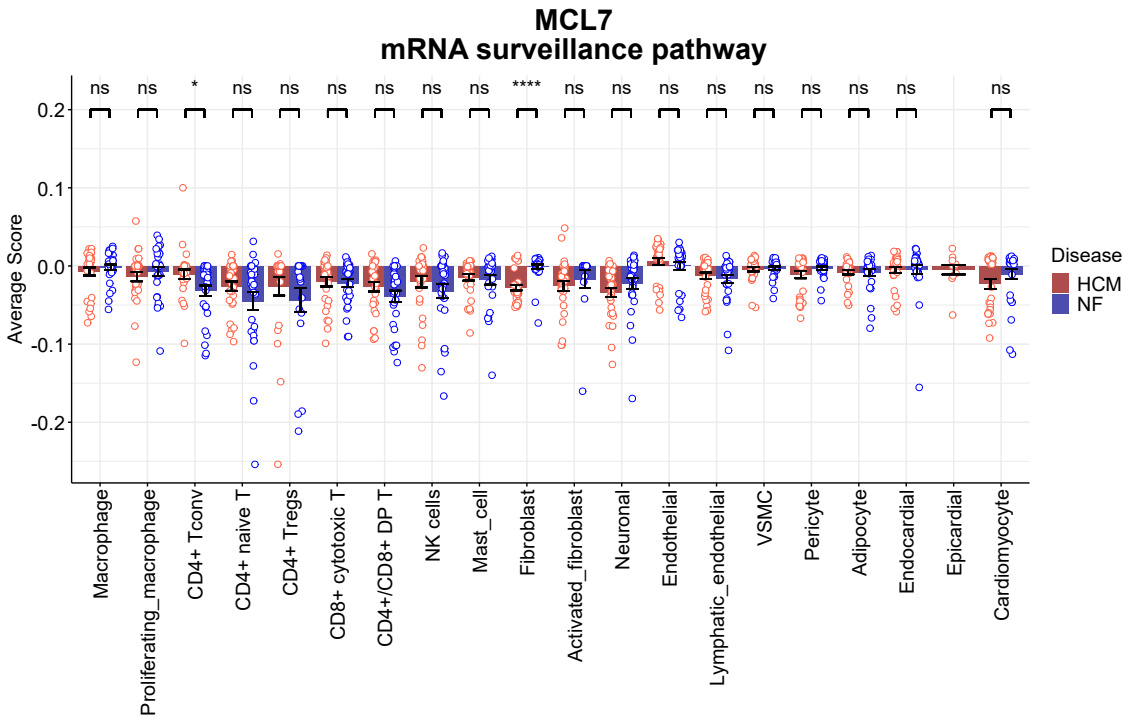

Figure D.126. Gene set scoring for MCL sub-cluster 7 of Cluster 5 (down-regulation and late declines) in late-stage human cell types.
This sub-cluster is a constituent of Cluster 5. The bar chart displays the gene set score for this specific sub-cluster across various cell types from late-stage human HCM snRNA-seq data. Scores were calculated for each sample using the `score_genes` function in `scanpy` v1.10.1 [267]. Bars represent the mean score, with error bars indicating the standard error of the mean. Statistical significance between disease and control samples was determined using a t-test, with p-values adjusted for multiple comparisons using the Benjamini-Hochberg method. Asterisks denote significance levels: * $p < 0.05$, ** $p < 0.01$, *** $p < 0.001$, **** $p < 0.0001$.

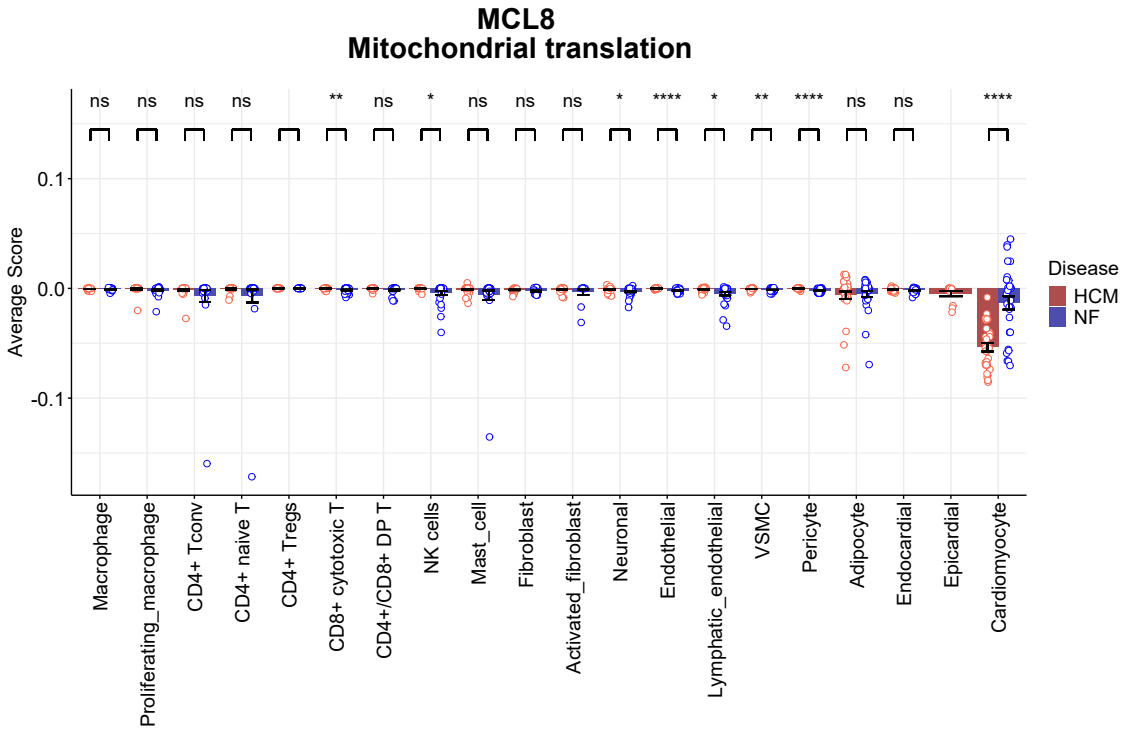

Figure D.127. Gene set scoring for MCL sub-cluster 8 of Cluster 5 (down-regulation and late declines) in late-stage human cell types.
This sub-cluster is a constituent of Cluster 5. The bar chart displays the gene set score for this specific sub-cluster across various cell types from late-stage human HCM snRNA-seq data. Scores were calculated for each sample using the `score_genes` function in `scanpy` v1.10.1 [267]. Bars represent the mean score, with error bars indicating the standard error of the mean. Statistical significance between disease and control samples was determined using a t-test, with p-values adjusted for multiple comparisons using the Benjamini-Hochberg method. Asterisks denote significance levels: * $p < 0.05$, ** $p < 0.01$, *** $p < 0.001$, **** $p < 0.0001$.

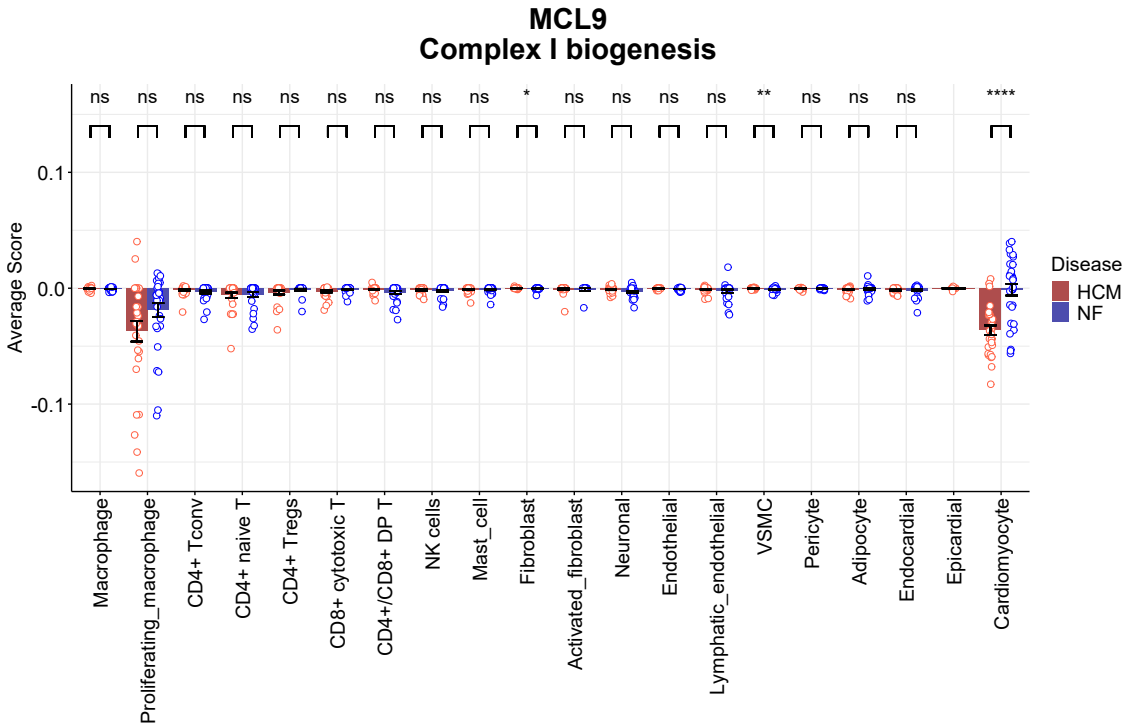

Figure D.128. Gene set scoring for MCL sub-cluster 9 of Cluster 5 (down-regulation and late declines) in late-stage human cell types.
This sub-cluster is a constituent of Cluster 5. The bar chart displays the gene set score for this specific sub-cluster across various cell types from late-stage human HCM snRNA-seq data. Scores were calculated for each sample using the `score_genes` function in `scanpy` v1.10.1 [267]. Bars represent the mean score, with error bars indicating the standard error of the mean. Statistical significance between disease and control samples was determined using a t-test, with p-values adjusted for multiple comparisons using the Benjamini-Hochberg method. Asterisks denote significance levels: * $p < 0.05$, ** $p < 0.01$, *** $p < 0.001$, **** $p < 0.0001$.

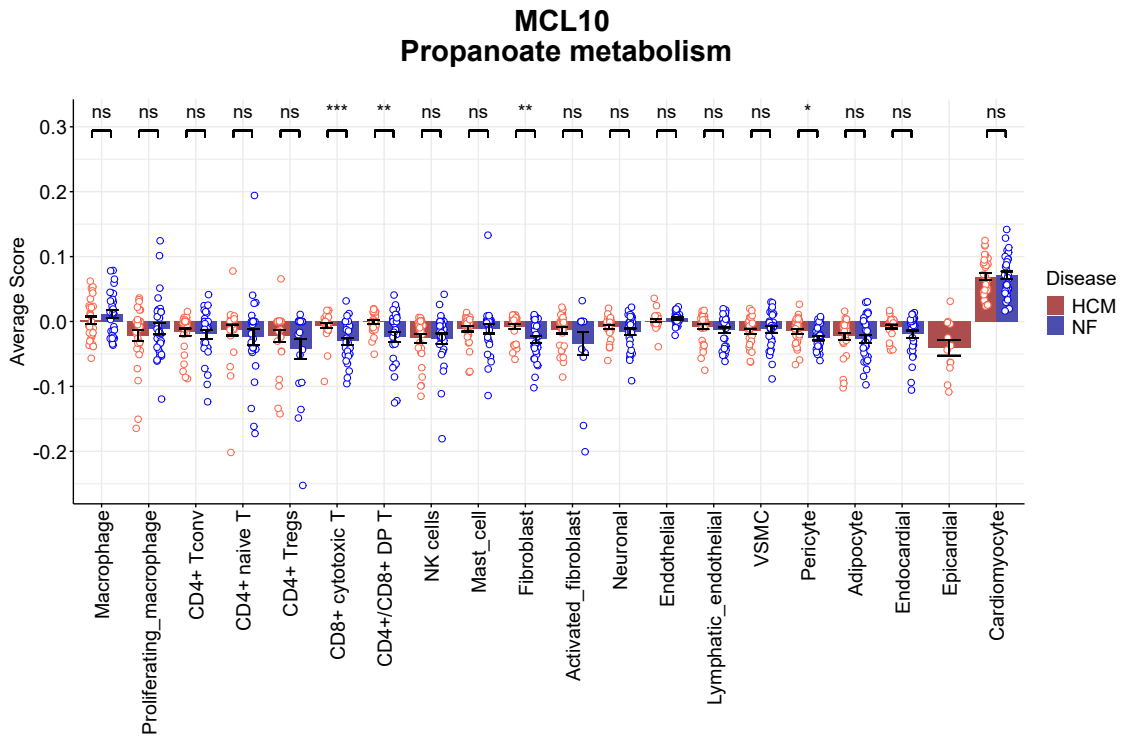

Figure D.129. Gene set scoring for MCL sub-cluster 10 of Cluster 5 (down-regulation and late declines) in late-stage human cell types.
This sub-cluster is a constituent of Cluster 5. The bar chart displays the gene set score for this specific sub-cluster across various cell types from late-stage human HCM snRNA-seq data. Scores were calculated for each sample using the `score_genes` function in `scanpy` v1.10.1 [267]. Bars represent the mean score, with error bars indicating the standard error of the mean. Statistical significance between disease and control samples was determined using a t-test, with p-values adjusted for multiple comparisons using the Benjamini-Hochberg method. Asterisks denote significance levels: * $p < 0.05$, ** $p < 0.01$, *** $p < 0.001$, **** $p < 0.0001$.

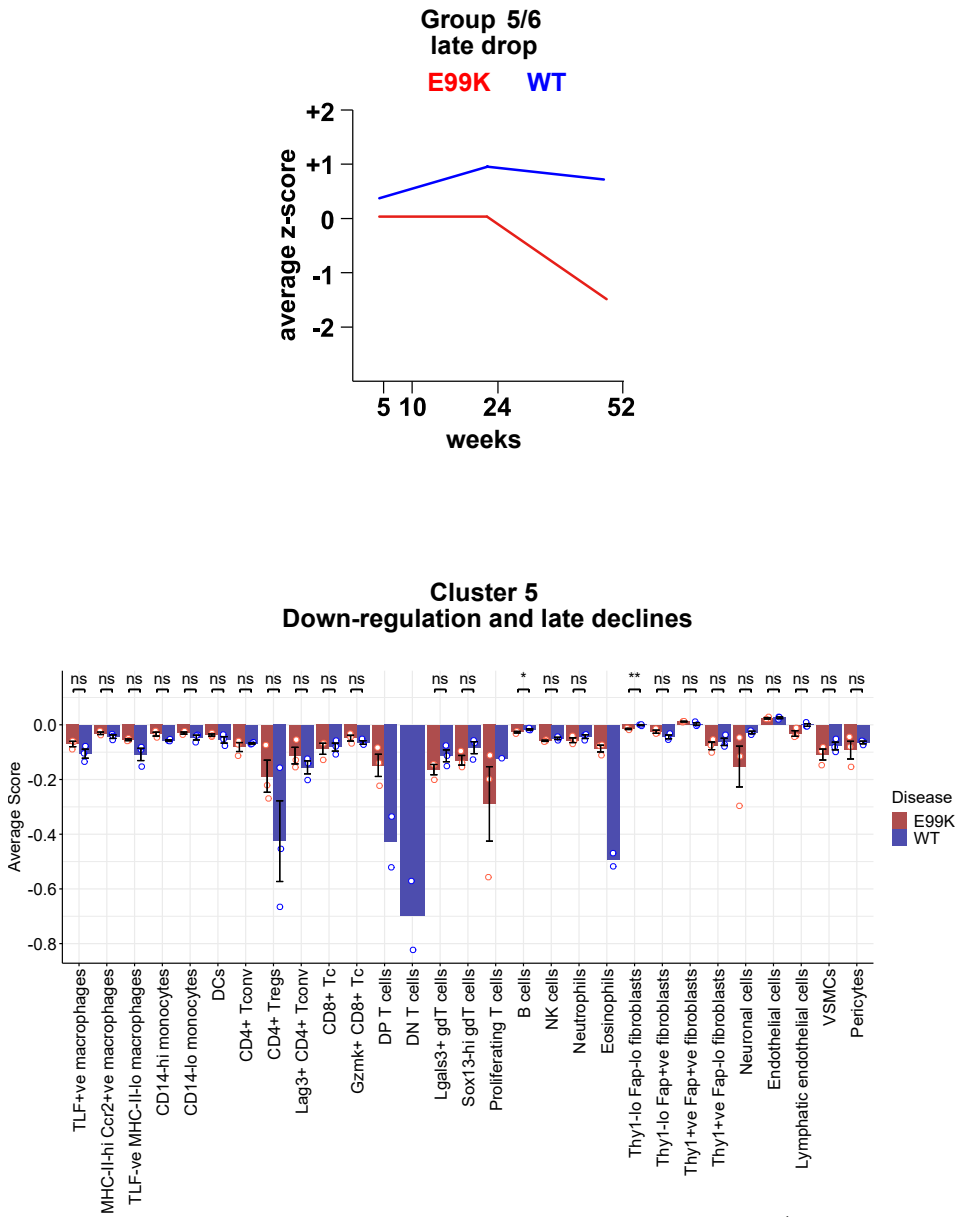

Figure D.130. Gene set scoring and statistics of Cluster 5 (down-regulation and late declines) in late-stage mouse cell types.
The upper panel schematically illustrates the temporal expression trend for Cluster 5, derived from bulk RNA-seq data of Actc1^{E99K} (red line) and wild-type (blue line) hearts over time. The lower panel displays the gene set score for all genes within Cluster 5 across various cell types identified in late-stage Actc1^{E99K} mouse scRNA-seq data. Scores were calculated for each sample using the `score_genes` function in `scanpy` v1.10.1 [267]. Bars represent the mean score, with error bars indicating the standard error of the mean. Statistical significance between disease and control samples was determined using a t-test, with p-values adjusted for multiple comparisons using the Benjamini-Hochberg method. Asterisks denote significance levels: * $p < 0.05$, ** $p < 0.01$, *** $p < 0.001$, **** $p < 0.0001$.

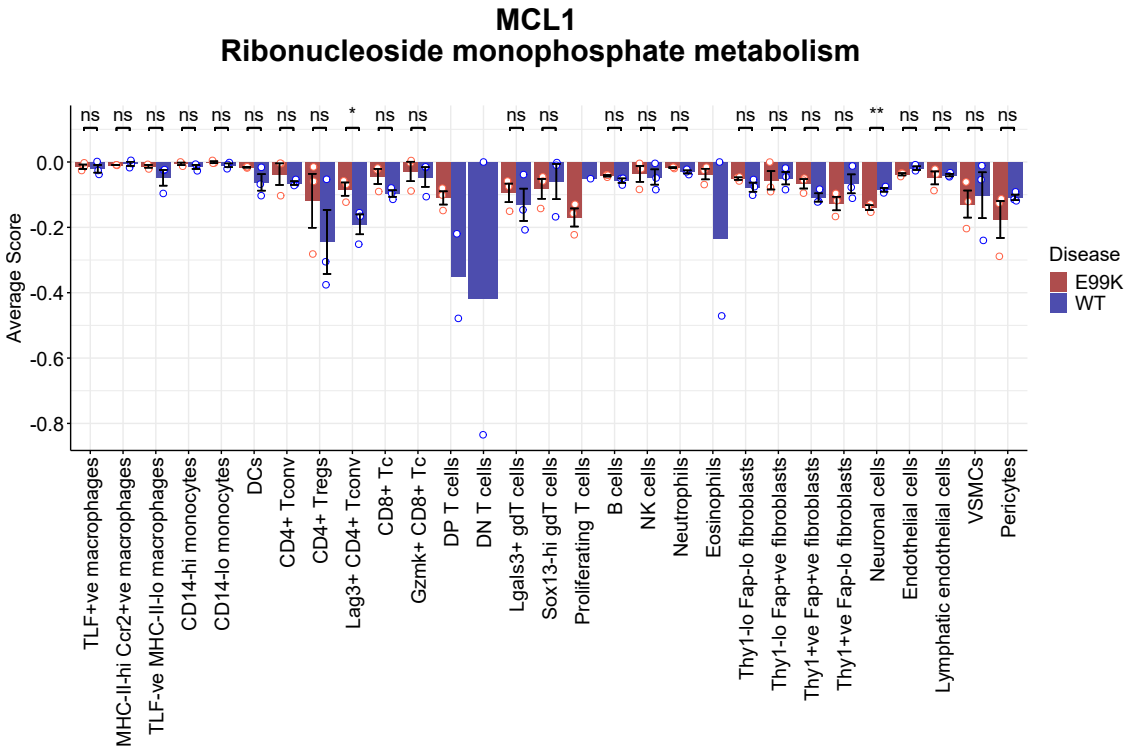

Figure D.131. Gene set scoring for MCL sub-cluster 1 of Cluster 5 (down-regulation and late declines) in late-stage mouse cell types.
This sub-cluster is a constituent of Cluster 5. The bar chart displays the gene set score for this specific sub-cluster across various cell types from late-stage Actc1^{E99K} mouse scRNA-seq data. Scores were calculated for each sample using the `score_genes` function in `scanpy` v1.10.1 [267]. Bars represent the mean score, with error bars indicating the standard error of the mean. Statistical significance between disease and control samples was determined using a t-test, with p-values adjusted for multiple comparisons using the Benjamini-Hochberg method. Asterisks denote significance levels: * $p < 0.05$, ** $p < 0.01$, *** $p < 0.001$, **** $p < 0.0001$.

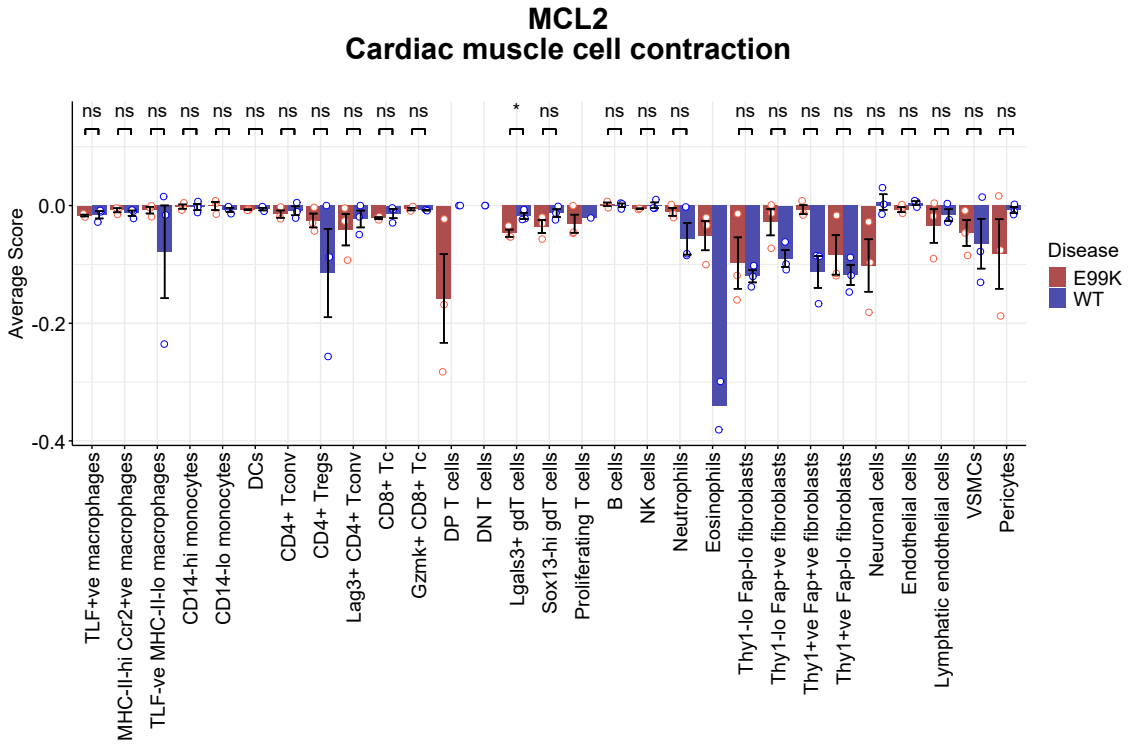

Figure D.132. Gene set scoring for MCL sub-cluster 2 of Cluster 5 (down-regulation and late declines) in late-stage mouse cell types.
This sub-cluster is a constituent of Cluster 5. The bar chart displays the gene set score for this specific sub-cluster across various cell types from late-stage Actc1^{E99K} mouse scRNA-seq data. Scores were calculated for each sample using the `score_genes` function in `scanpy` v1.10.1 [267]. Bars represent the mean score, with error bars indicating the standard error of the mean. Statistical significance between disease and control samples was determined using a t-test, with p-values adjusted for multiple comparisons using the Benjamini-Hochberg method. Asterisks denote significance levels: * $p < 0.05$, ** $p < 0.01$, *** $p < 0.001$, **** $p < 0.0001$.

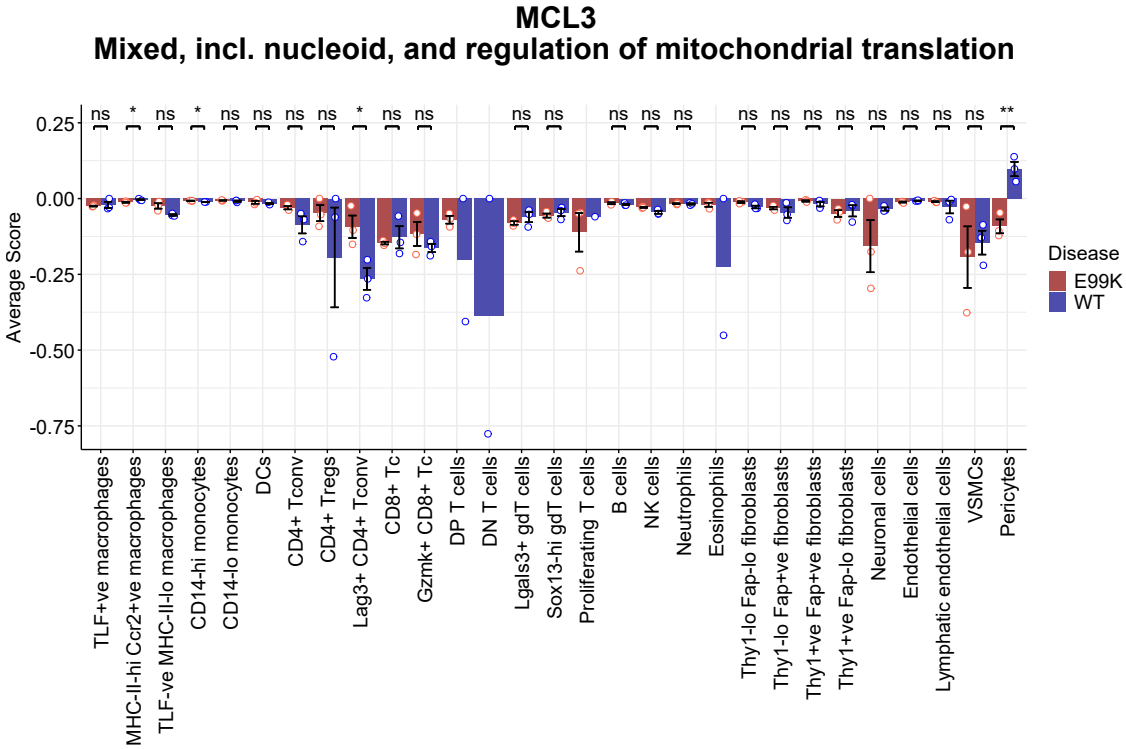

Figure D.133. Gene set scoring for MCL sub-cluster 3 of Cluster 5 (down-regulation and late declines) in late-stage mouse cell types.
This sub-cluster is a constituent of Cluster 5. The bar chart displays the gene set score for this specific sub-cluster across various cell types from late-stage $Actc1^{E99K}$ mouse scRNA-seq data. Scores were calculated for each sample using the `score_genes` function in `scanpy` v1.10.1 [267]. Bars represent the mean score, with error bars indicating the standard error of the mean. Statistical significance between disease and control samples was determined using a t-test, with p-values adjusted for multiple comparisons using the Benjamini-Hochberg method. Asterisks denote significance levels: * $p < 0.05$, ** $p < 0.01$, *** $p < 0.001$, **** $p < 0.0001$.

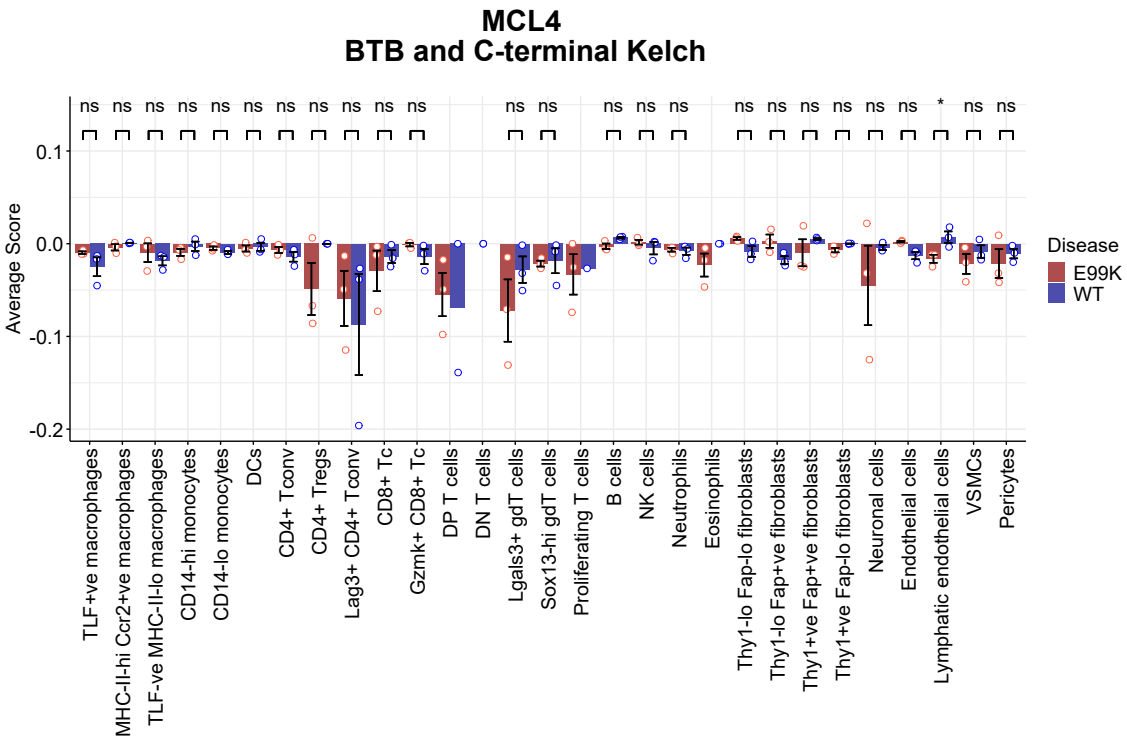

Figure D.134. Gene set scoring for MCL sub-cluster 4 of Cluster 5 (down-regulation and late declines) in late-stage mouse cell types.
This sub-cluster is a constituent of Cluster 5. The bar chart displays the gene set score for this specific sub-cluster across various cell types from late-stage Actc1^{E99K} mouse scRNA-seq data. Scores were calculated for each sample using the `score_genes` function in `scanpy` v1.10.1 [267]. Bars represent the mean score, with error bars indicating the standard error of the mean. Statistical significance between disease and control samples was determined using a t-test, with p-values adjusted for multiple comparisons using the Benjamini-Hochberg method. Asterisks denote significance levels: * $p < 0.05$, ** $p < 0.01$, *** $p < 0.001$, **** $p < 0.0001$.

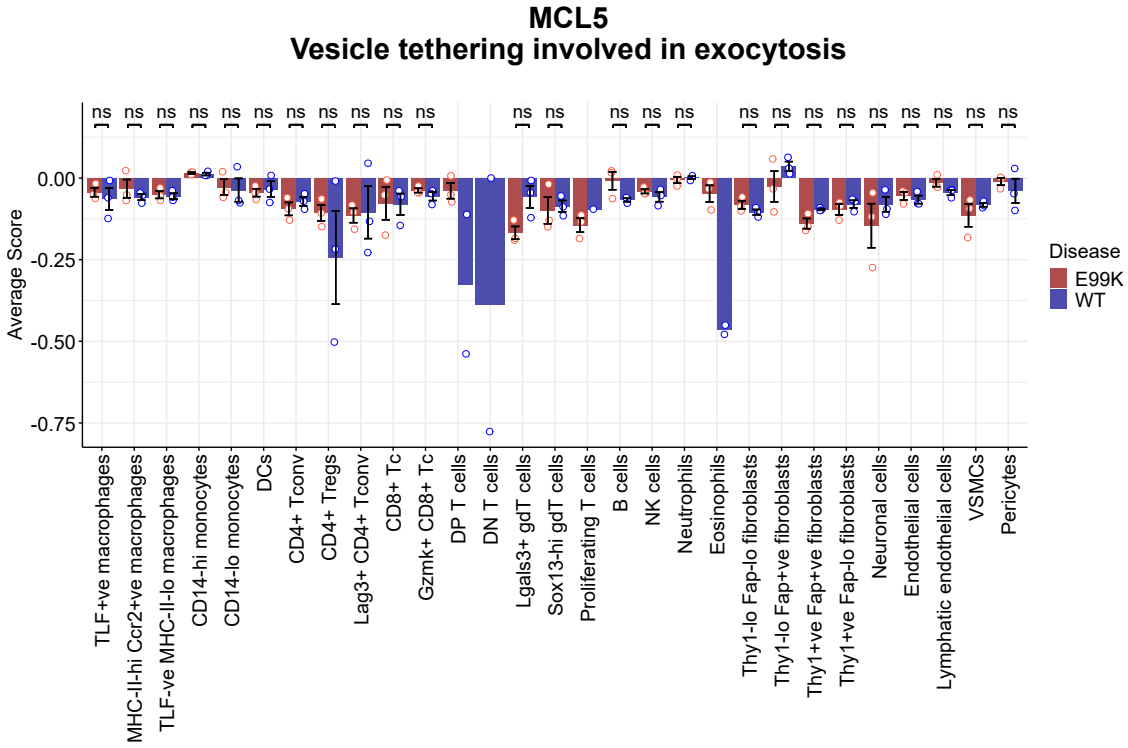

Figure D.135. Gene set scoring for MCL sub-cluster 5 of Cluster 5 (down-regulation and late declines) in late-stage mouse cell types.
This sub-cluster is a constituent of Cluster 5. The bar chart displays the gene set score for this specific sub-cluster across various cell types from late-stage Actc1^{E99K} mouse scRNA-seq data. Scores were calculated for each sample using the `score_genes` function in `scanpy` v1.10.1 [267]. Bars represent the mean score, with error bars indicating the standard error of the mean. Statistical significance between disease and control samples was determined using a t-test, with p-values adjusted for multiple comparisons using the Benjamini-Hochberg method. Asterisks denote significance levels: * $p < 0.05$, ** $p < 0.01$, *** $p < 0.001$, **** $p < 0.0001$.

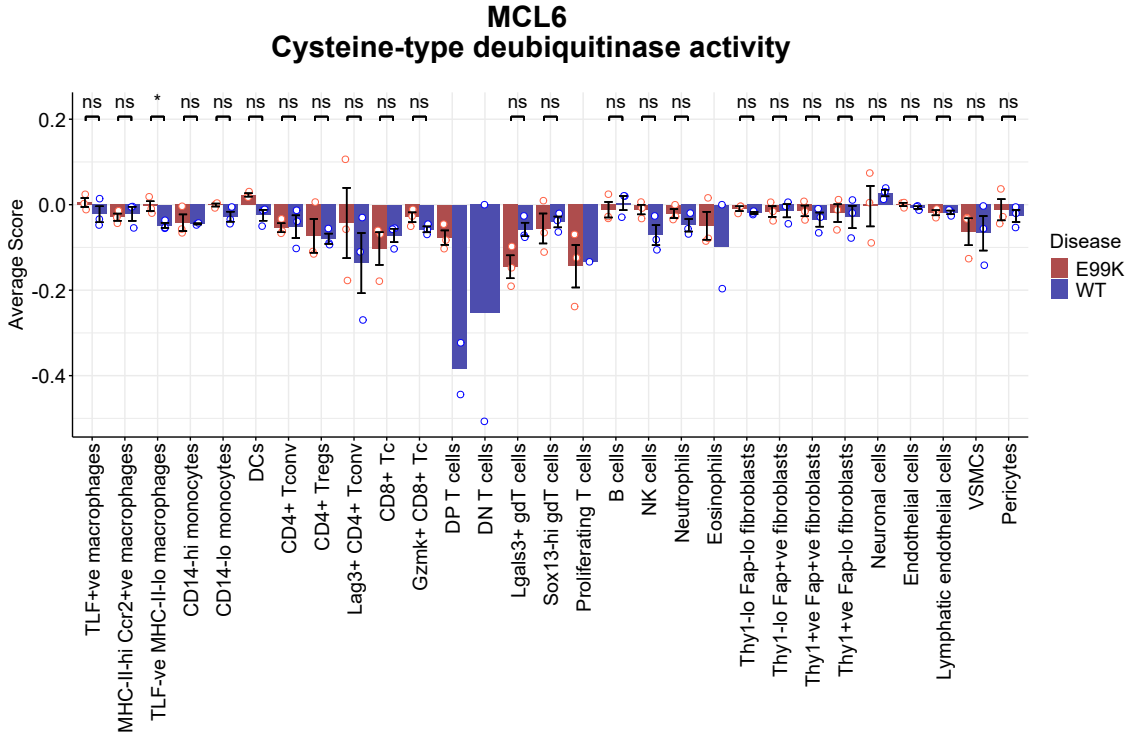

Figure D.136. Gene set scoring for MCL sub-cluster 6 of Cluster 5 (down-regulation and late declines) in late-stage mouse cell types.
This sub-cluster is a constituent of Cluster 5. The bar chart displays the gene set score for this specific sub-cluster across various cell types from late-stage Actc1^{E99K} mouse scRNA-seq data. Scores were calculated for each sample using the `score_genes` function in `scanpy` v1.10.1 [267]. Bars represent the mean score, with error bars indicating the standard error of the mean. Statistical significance between disease and control samples was determined using a t-test, with p-values adjusted for multiple comparisons using the Benjamini-Hochberg method. Asterisks denote significance levels: * $p < 0.05$, ** $p < 0.01$, *** $p < 0.001$, **** $p < 0.0001$.

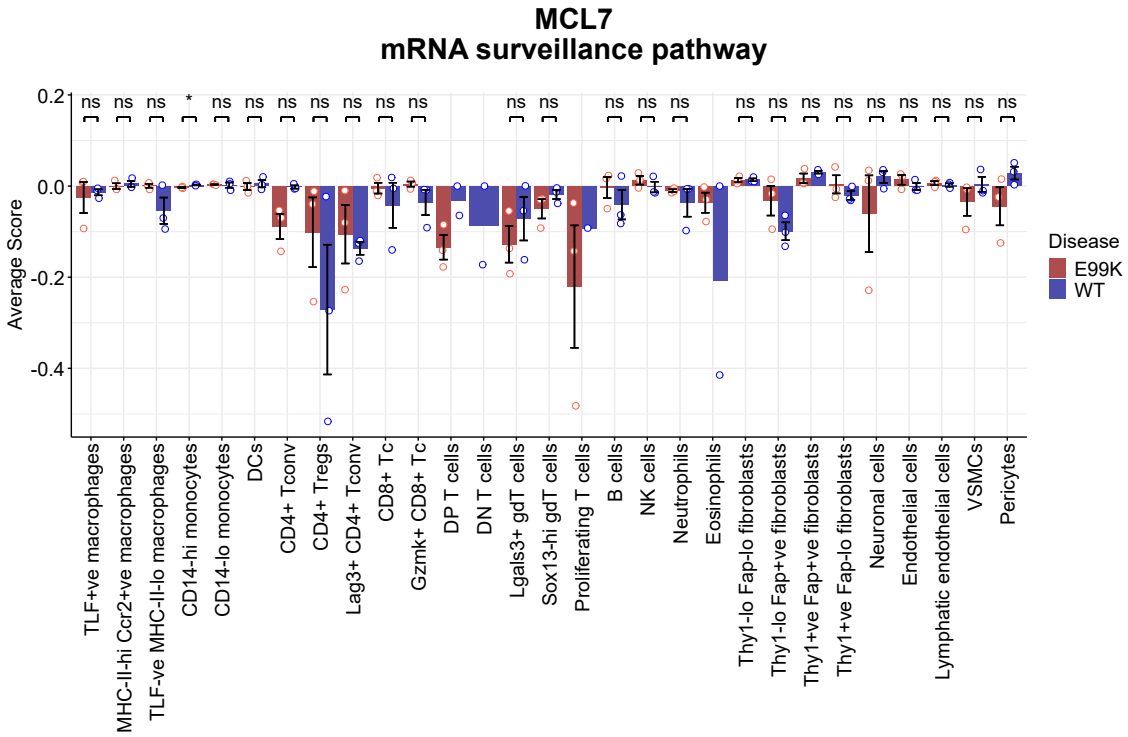

Figure D.137. Gene set scoring for MCL sub-cluster 7 of Cluster 5 (down-regulation and late declines) in late-stage mouse cell types.
This sub-cluster is a constituent of Cluster 5. The bar chart displays the gene set score for this specific sub-cluster across various cell types from late-stage $Actc1^{E99K}$ mouse scRNA-seq data. Scores were calculated for each sample using the `score_genes` function in `scanpy` v1.10.1 [267]. Bars represent the mean score, with error bars indicating the standard error of the mean. Statistical significance between disease and control samples was determined using a t-test, with p-values adjusted for multiple comparisons using the Benjamini-Hochberg method. Asterisks denote significance levels: * $p < 0.05$, ** $p < 0.01$, *** $p < 0.001$, **** $p < 0.0001$.

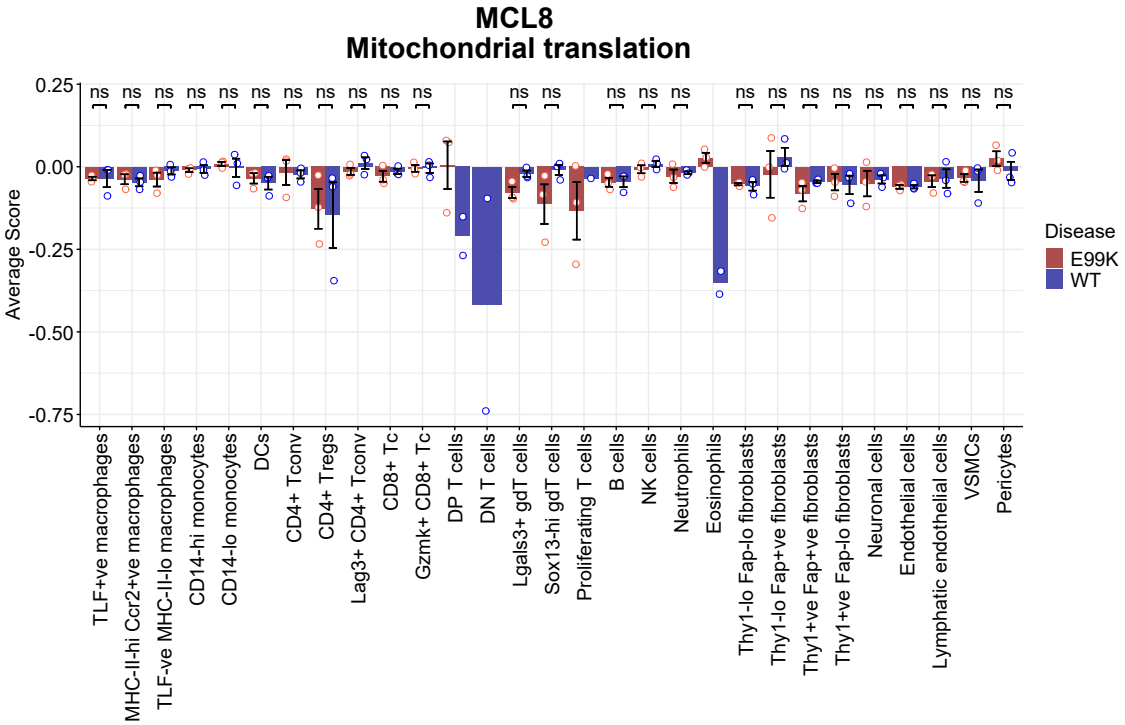

Figure D.138. Gene set scoring for MCL sub-cluster 8 of Cluster 5 (down-regulation and late declines) in late-stage mouse cell types.
This sub-cluster is a constituent of Cluster 5. The bar chart displays the gene set score for this specific sub-cluster across various cell types from late-stage Actc1^{E99K} mouse scRNA-seq data. Scores were calculated for each sample using the `score_genes` function in `scanpy` v1.10.1 [267]. Bars represent the mean score, with error bars indicating the standard error of the mean. Statistical significance between disease and control samples was determined using a t-test, with p-values adjusted for multiple comparisons using the Benjamini-Hochberg method. Asterisks denote significance levels: * $p < 0.05$, ** $p < 0.01$, *** $p < 0.001$, **** $p < 0.0001$.

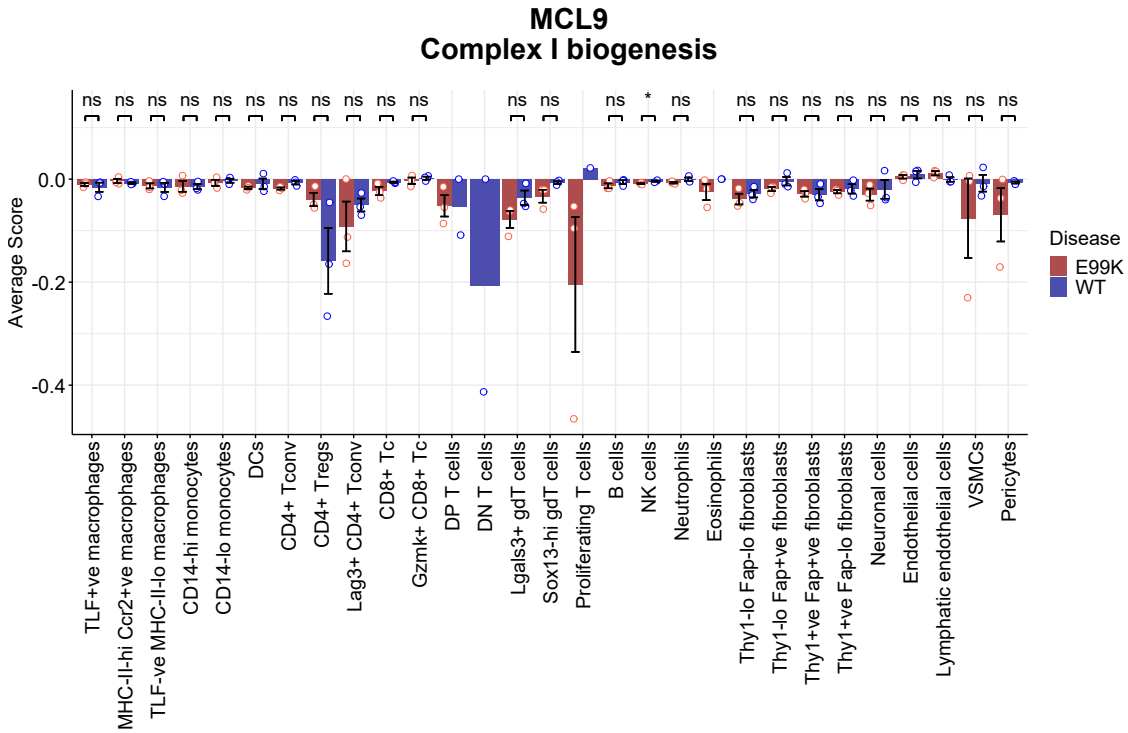

Figure D.139. Gene set scoring for MCL sub-cluster 9 of Cluster 5 (down-regulation and late declines) in late-stage mouse cell types.
This sub-cluster is a constituent of Cluster 5. The bar chart displays the gene set score for this specific sub-cluster across various cell types from late-stage $Actc1^{E99K}$ mouse scRNA-seq data. Scores were calculated for each sample using the `score_genes` function in `scanpy` v1.10.1 [267]. Bars represent the mean score, with error bars indicating the standard error of the mean. Statistical significance between disease and control samples was determined using a t-test, with p-values adjusted for multiple comparisons using the Benjamini-Hochberg method. Asterisks denote significance levels: * $p < 0.05$, ** $p < 0.01$, *** $p < 0.001$, **** $p < 0.0001$.

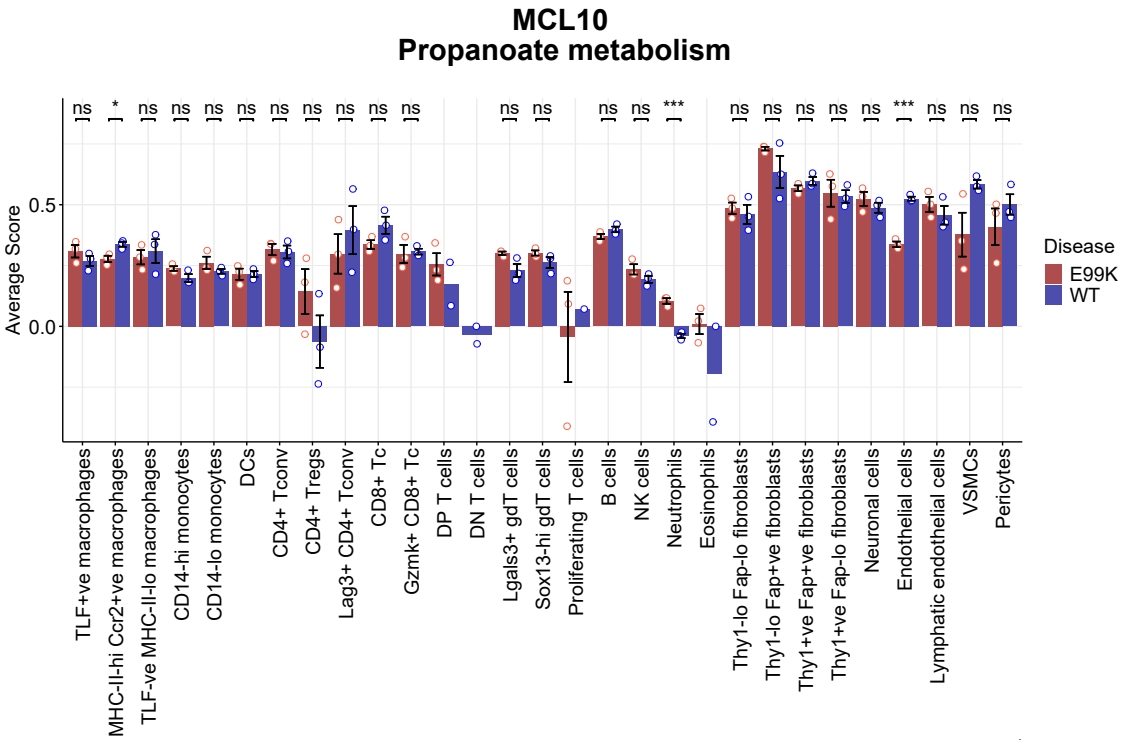

Figure D.140. Gene set scoring for MCL sub-cluster 10 of Cluster 5 (down-regulation and late declines) in late-stage mouse cell types.
This sub-cluster is a constituent of Cluster 5. The bar chart displays the gene set score for this specific sub-cluster across various cell types from late-stage Actc1^{E99K} mouse scRNA-seq data. Scores were calculated for each sample using the `score_genes` function in `scanpy` v1.10.1 [267]. Bars represent the mean score, with error bars indicating the standard error of the mean. Statistical significance between disease and control samples was determined using a t-test, with p-values adjusted for multiple comparisons using the Benjamini-Hochberg method. Asterisks denote significance levels: * $p < 0.05$, ** $p < 0.01$, *** $p < 0.001$, **** $p < 0.0001$.

Cluster 6, also showing a pattern of down-regulation followed by further decline in late-stage disease, was associated with a variety of cellular processes, including autophagy, signalling pathways, and ECM interactions (Figures D.141 and D.152). Sub-cluster analysis revealed enrichment for autophagy (MCL sub-cluster 1; Figure D.142), histone H3 acetylation (MCL sub-cluster 2; Figure D.143), nucleocytoplasmic carrier activity (MCL sub-cluster 3; Figure D.144), thyroid hormone signalling pathway (MCL sub-cluster 4; Figure D.145), U2-type spliceosomal complex and spliceosomal complex (MCL sub-cluster 5; Figure D.146), dystrophin-associated glycoprotein complex (MCL sub-cluster 6; Figure D.147), a mixed sub-cluster including ECM-receptor interaction and cell-ECM interactions

(MCL sub-cluster 7; Figure D.148), clathrin-dependent endocytosis (MCL sub-cluster 8; Figure D.149), cardiac muscle cell development (MCL sub-cluster 9; Figure D.150), and Cul3-RING ubiquitin ligase complex (MCL sub-cluster 10; Figure D.151). In late-stage human HCM, the overall cluster 6 signature was significantly upregulated in activated fibroblasts, lymphatic endothelial cells, VSMCs, and cardiomyocytes, while downregulated in proliferating macrophages (Figure D.141). Analysis of individual sub-clusters revealed further cell-type specific patterns. The autophagy sub-cluster (MCL sub-cluster 1; Figure D.142) showed upregulation in activated fibroblasts, NK cells, and cardiomyocytes, and downregulation in endothelial cells and proliferating macrophages. The histone H3 acetylation sub-cluster (MCL sub-cluster 2; Figure D.143) was upregulated in proliferating macrophages. The nucleocytoplasmic carrier activity sub-cluster (MCL sub-cluster 3; Figure D.144) was upregulated in macrophages, lymphatic endothelial cells, VSMCs, and pericytes, and downregulated in fibroblasts and proliferating macrophages. In the mouse scRNA-seq data, the overall cluster 6 signature was downregulated in B cells and $Thy1^{lo}Fap^{lo}$ fibroblasts (Figure D.152). Sub-cluster analysis revealed upregulation of the autophagy sub-cluster (MCL sub-cluster 1) in $TLF^{-}MHC\text{-}II^{lo}$ macrophages and downregulation in neuronal cells. The histone H3 acetylation sub-cluster (MCL sub-cluster 2; Figure D.154) was upregulated in $Thy1^{+}Fap^{+}$ fibroblasts. The nucleocytoplasmic carrier activity sub-cluster (MCL sub-cluster 3; Figure D.155) was upregulated in $CD14^{lo}$ monocytes and downregulated in VSMCs and pericytes.

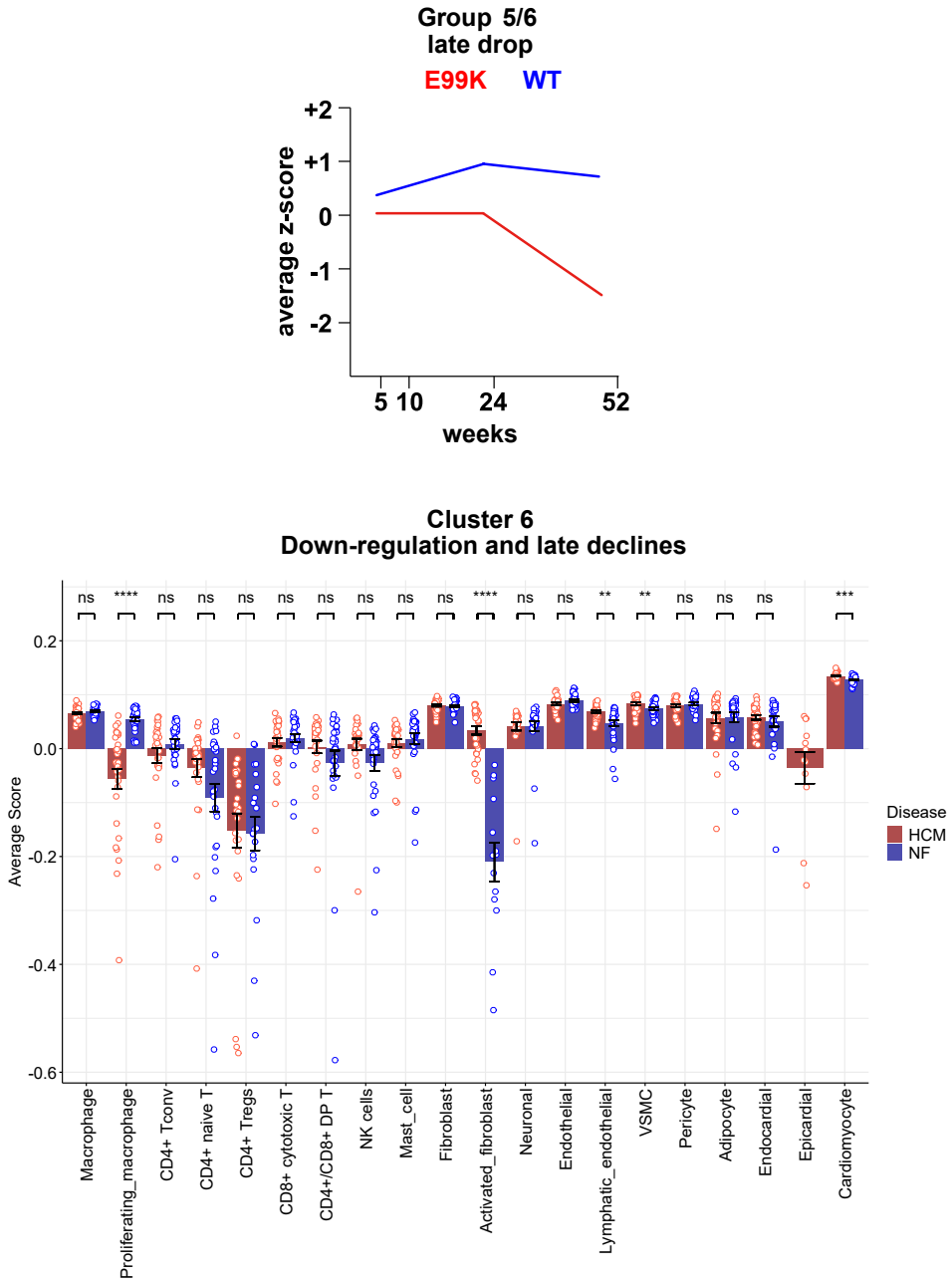

Figure D.141. Gene set scoring and statistics of Cluster 6 (down-regulation and late declines) in late-stage human cell types.
The upper panel schematically illustrates the temporal expression trend for Cluster 6, derived from bulk RNA-seq data of Actc1^{E99K} (red line) and wild-type (blue line) hearts over time. The lower panel displays the gene set score for all genes within Cluster 6 across various cell types identified in late-stage human HCM snRNA-seq data. Scores were calculated for each sample using the `score_genes` function in `scanpy` v1.10.1 [267]. Bars represent the mean score, with error bars indicating the standard error of the mean. Statistical significance between disease and control samples was determined using a t-test, with p-values adjusted for multiple comparisons using the Benjamini-Hochberg method. Asterisks denote significance levels: * $p < 0.05$, ** $p < 0.01$, *** $p < 0.001$, **** $p < 0.0001$.

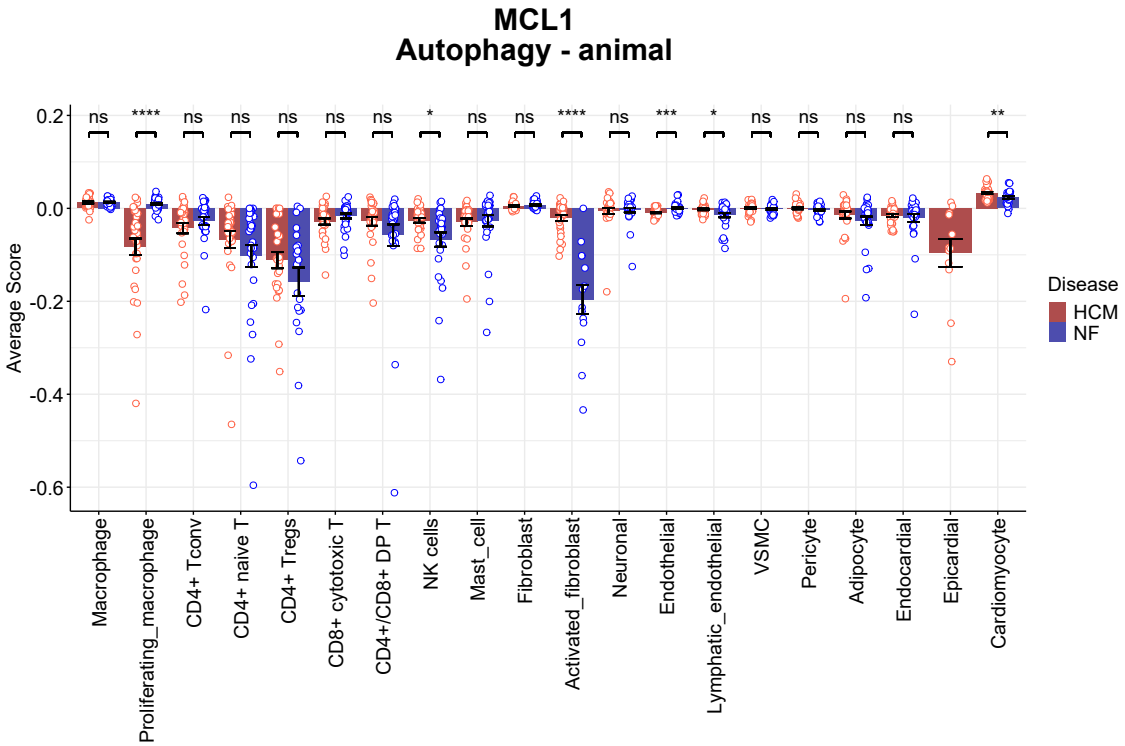

Figure D.142. Gene set scoring for MCL sub-cluster 1 of Cluster 6 (down-regulation and late declines) in late-stage human cell types.
This sub-cluster is a constituent of Cluster 6. The bar chart displays the gene set score for this specific sub-cluster across various cell types from late-stage human HCM snRNA-seq data. Scores were calculated for each sample using the `score_genes` function in `scanpy` v1.10.1 [267]. Bars represent the mean score, with error bars indicating the standard error of the mean. Statistical significance between disease and control samples was determined using a t-test, with p-values adjusted for multiple comparisons using the Benjamini-Hochberg method. Asterisks denote significance levels: * $p < 0.05$, ** $p < 0.01$, *** $p < 0.001$, **** $p < 0.0001$.

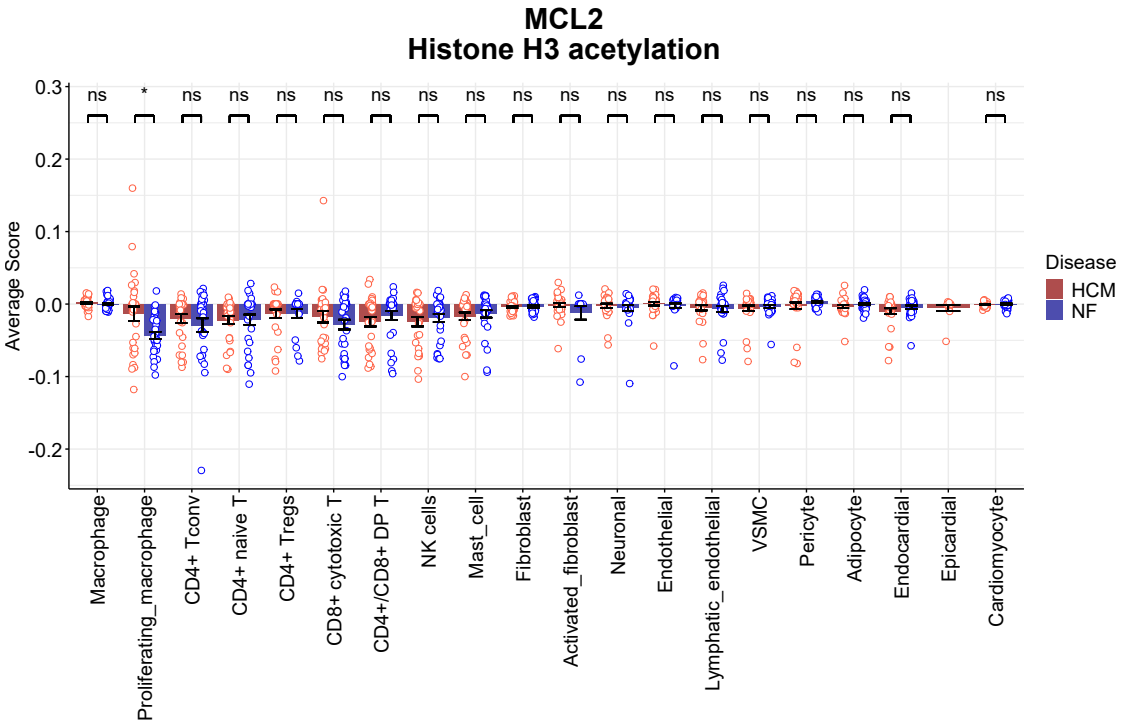

Figure D.143. Gene set scoring for MCL sub-cluster 2 of Cluster 6 (down-regulation and late declines) in late-stage human cell types.
This sub-cluster is a constituent of Cluster 6. The bar chart displays the gene set score for this specific sub-cluster across various cell types from late-stage human HCM snRNA-seq data. Scores were calculated for each sample using the `score_genes` function in `scanpy` v1.10.1 [267]. Bars represent the mean score, with error bars indicating the standard error of the mean. Statistical significance between disease and control samples was determined using a t-test, with p-values adjusted for multiple comparisons using the Benjamini-Hochberg method. Asterisks denote significance levels: * $p < 0.05$, ** $p < 0.01$, *** $p < 0.001$, **** $p < 0.0001$.

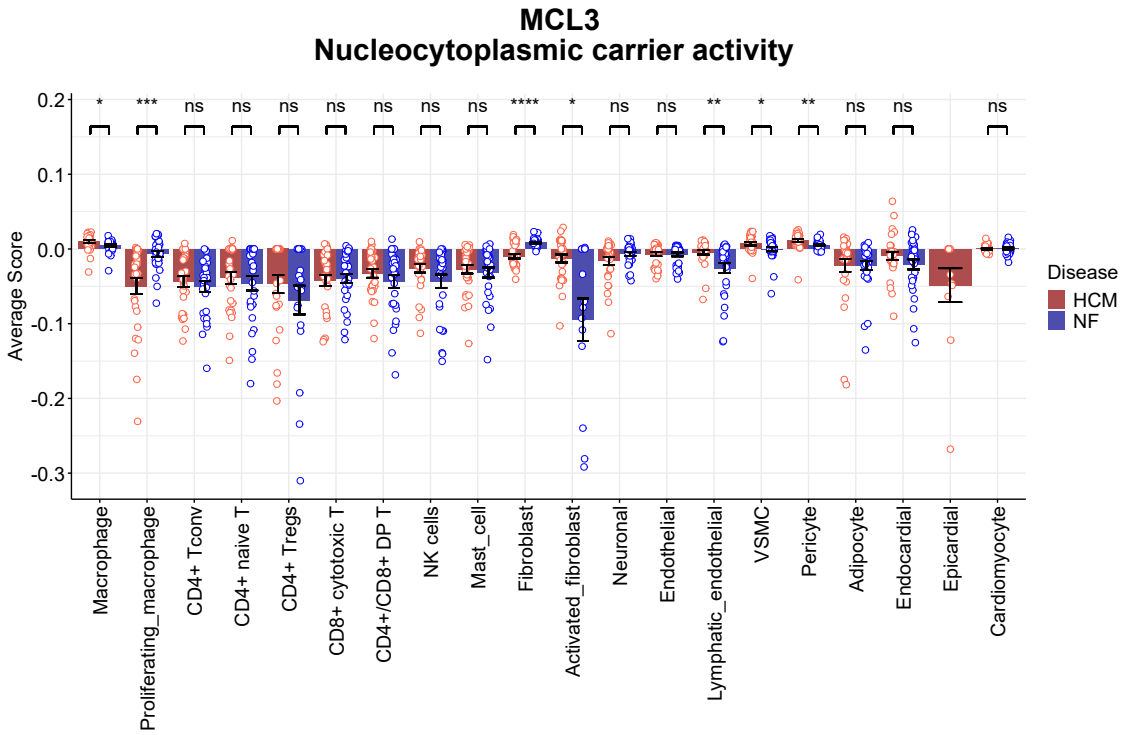

Figure D.144. Gene set scoring for MCL sub-cluster 3 of Cluster 6 (down-regulation and late declines) in late-stage human cell types.
This sub-cluster is a constituent of Cluster 6. The bar chart displays the gene set score for this specific sub-cluster across various cell types from late-stage human HCM snRNA-seq data. Scores were calculated for each sample using the `score_genes` function in `scanpy` v1.10.1 [267]. Bars represent the mean score, with error bars indicating the standard error of the mean. Statistical significance between disease and control samples was determined using a t-test, with p-values adjusted for multiple comparisons using the Benjamini-Hochberg method. Asterisks denote significance levels: * $p < 0.05$, ** $p < 0.01$, *** $p < 0.001$, **** $p < 0.0001$.

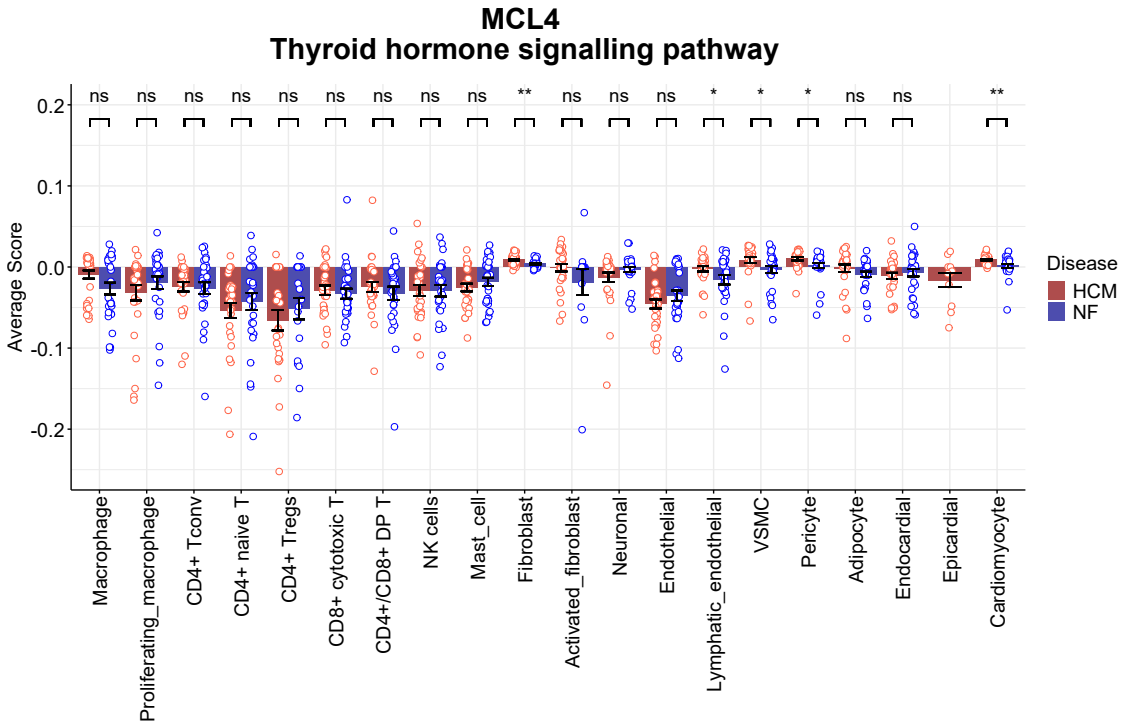

Figure D.145. Gene set scoring for MCL sub-cluster 4 of Cluster 6 (down-regulation and late declines) in late-stage human cell types.
This sub-cluster is a constituent of Cluster 6. The bar chart displays the gene set score for this specific sub-cluster across various cell types from late-stage human HCM snRNA-seq data. Scores were calculated for each sample using the `score_genes` function in `scanpy` v1.10.1 [267]. Bars represent the mean score, with error bars indicating the standard error of the mean. Statistical significance between disease and control samples was determined using a t-test, with p-values adjusted for multiple comparisons using the Benjamini-Hochberg method. Asterisks denote significance levels: * $p < 0.05$, ** $p < 0.01$, *** $p < 0.001$, **** $p < 0.0001$.

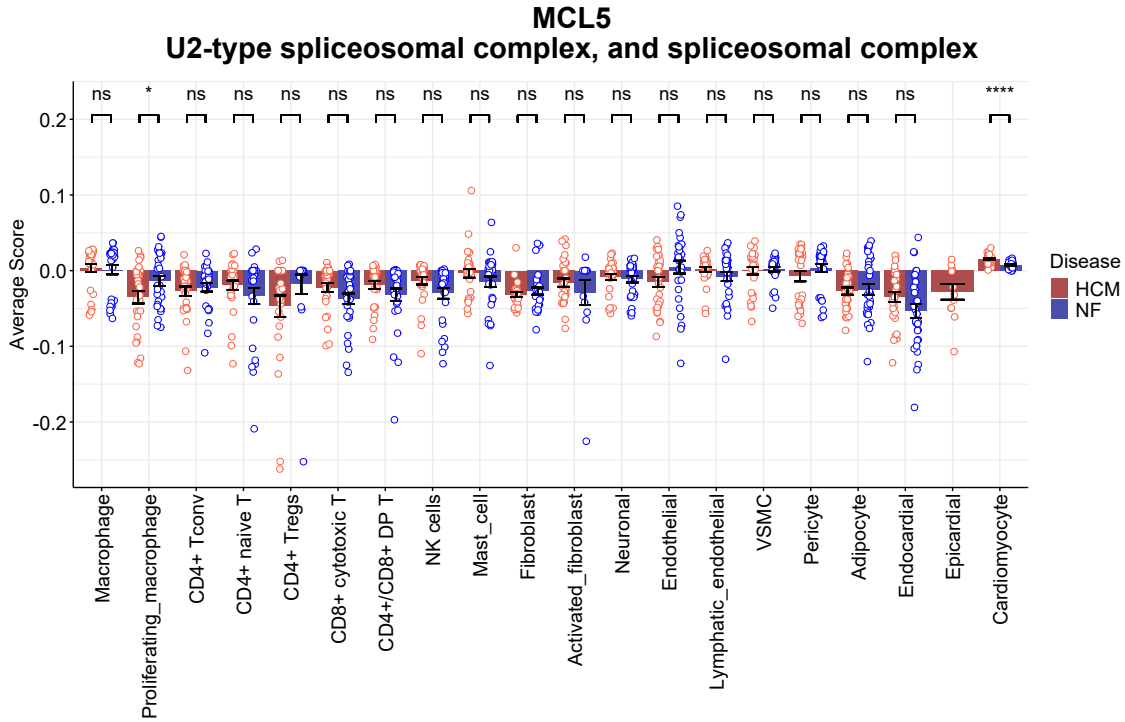

Figure D.146. Gene set scoring for MCL sub-cluster 5 of Cluster 6 (down-regulation and late declines) in late-stage human cell types.
This sub-cluster is a constituent of Cluster 6. The bar chart displays the gene set score for this specific sub-cluster across various cell types from late-stage human HCM snRNA-seq data. Scores were calculated for each sample using the `score_genes` function in `scanpy` v1.10.1 [267]. Bars represent the mean score, with error bars indicating the standard error of the mean. Statistical significance between disease and control samples was determined using a t-test, with p-values adjusted for multiple comparisons using the Benjamini-Hochberg method. Asterisks denote significance levels: * $p < 0.05$, ** $p < 0.01$, *** $p < 0.001$, **** $p < 0.0001$.

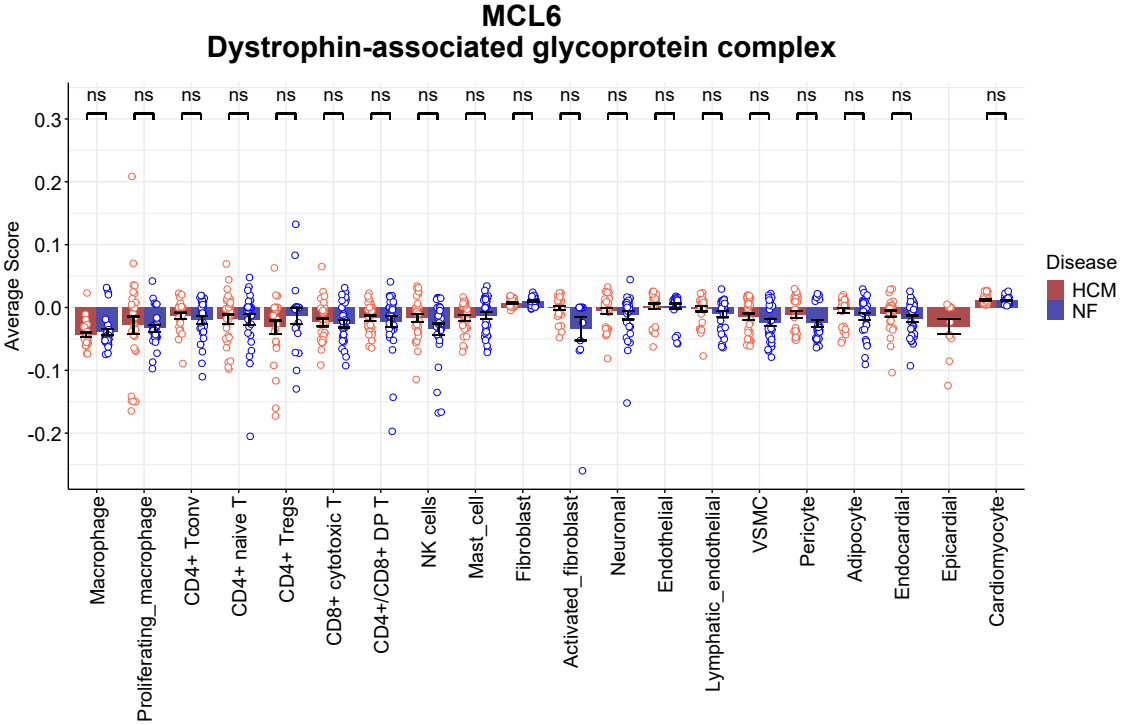

Figure D.147. Gene set scoring for MCL sub-cluster 6 of Cluster 6 (down-regulation and late declines) in late-stage human cell types.
This sub-cluster is a constituent of Cluster 6. The bar chart displays the gene set score for this specific sub-cluster across various cell types from late-stage human HCM snRNA-seq data. Scores were calculated for each sample using the `score_genes` function in `scanpy` v1.10.1 [267]. Bars represent the mean score, with error bars indicating the standard error of the mean. Statistical significance between disease and control samples was determined using a t-test, with p-values adjusted for multiple comparisons using the Benjamini-Hochberg method. Asterisks denote significance levels: * $p < 0.05$, ** $p < 0.01$, *** $p < 0.001$, **** $p < 0.0001$.

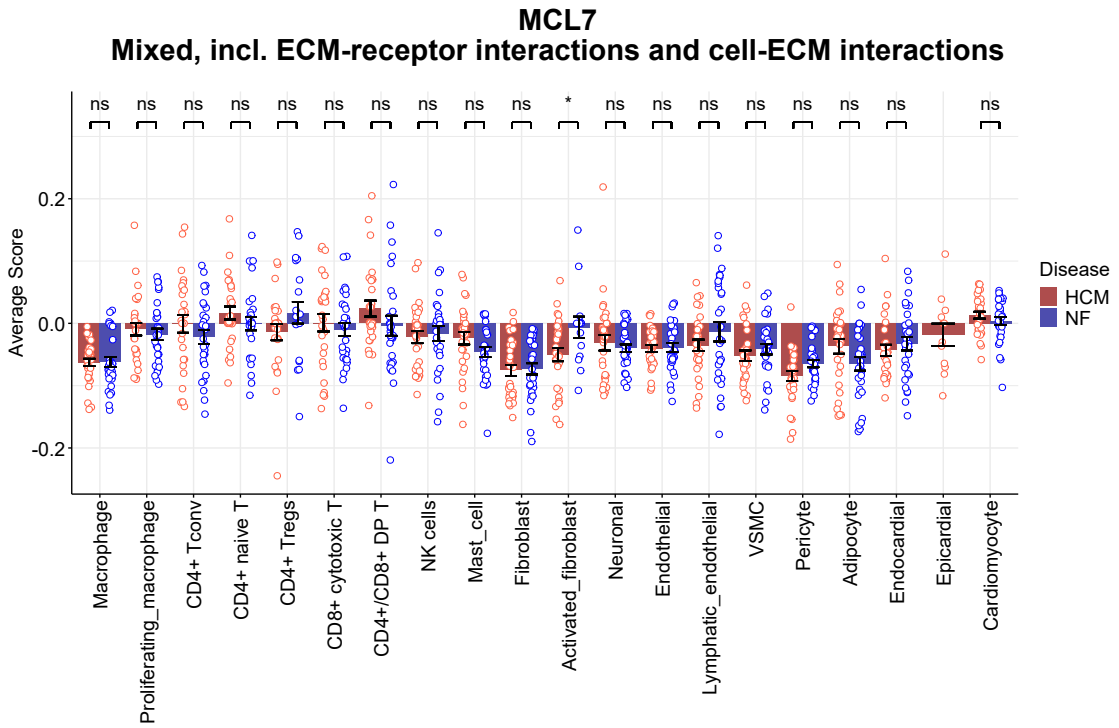

Figure D.148. Gene set scoring for MCL sub-cluster 7 of Cluster 6 (down-regulation and late declines) in late-stage human cell types.
This sub-cluster is a constituent of Cluster 6. The bar chart displays the gene set score for this specific sub-cluster across various cell types from late-stage human HCM snRNA-seq data. Scores were calculated for each sample using the `score_genes` function in `scanpy` v1.10.1 [267]. Bars represent the mean score, with error bars indicating the standard error of the mean. Statistical significance between disease and control samples was determined using a t-test, with p-values adjusted for multiple comparisons using the Benjamini-Hochberg method. Asterisks denote significance levels: * $p < 0.05$, ** $p < 0.01$, *** $p < 0.001$, **** $p < 0.0001$.

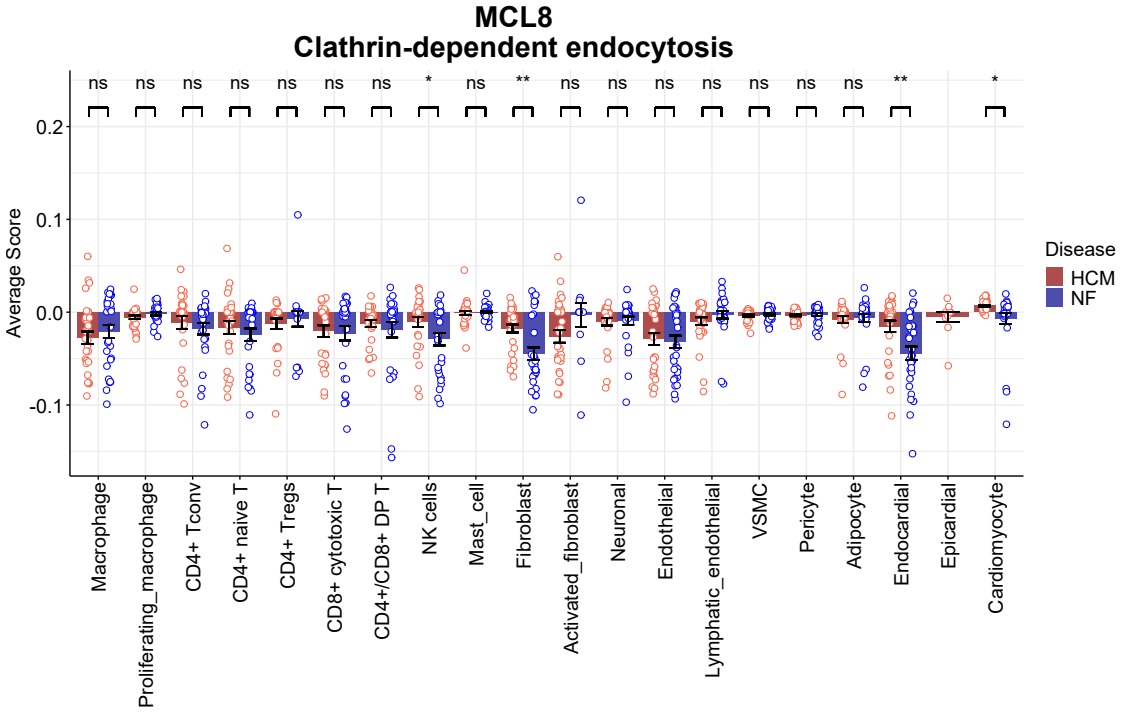

Figure D.149. Gene set scoring for MCL sub-cluster 8 of Cluster 6 (down-regulation and late declines) in late-stage human cell types.
This sub-cluster is a constituent of Cluster 6. The bar chart displays the gene set score for this specific sub-cluster across various cell types from late-stage human HCM snRNA-seq data. Scores were calculated for each sample using the `score_genes` function in `scanpy` v1.10.1 [267]. Bars represent the mean score, with error bars indicating the standard error of the mean. Statistical significance between disease and control samples was determined using a t-test, with p-values adjusted for multiple comparisons using the Benjamini-Hochberg method. Asterisks denote significance levels: * $p < 0.05$, ** $p < 0.01$, *** $p < 0.001$, **** $p < 0.0001$.

Figure D.150. Gene set scoring for MCL sub-cluster 9 of Cluster 6 (down-regulation and late declines) in late-stage human cell types.
This sub-cluster is a constituent of Cluster 6. The bar chart displays the gene set score for this specific sub-cluster across various cell types from late-stage human HCM snRNA-seq data. Scores were calculated for each sample using the `score_genes` function in `scanpy` v1.10.1 [267]. Bars represent the mean score, with error bars indicating the standard error of the mean. Statistical significance between disease and control samples was determined using a t-test, with p-values adjusted for multiple comparisons using the Benjamini-Hochberg method. Asterisks denote significance levels: * $p < 0.05$, ** $p < 0.01$, *** $p < 0.001$, **** $p < 0.0001$.

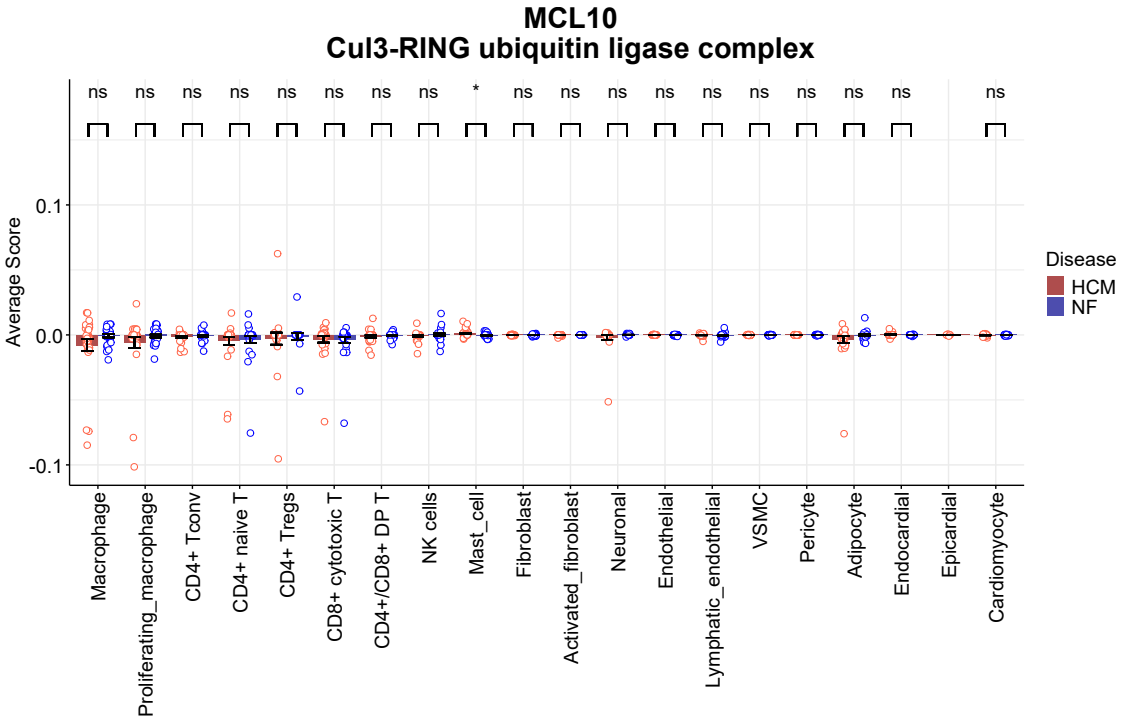

Figure D.151. Gene set scoring for MCL sub-cluster 10 of Cluster 6 (down-regulation and late declines) in late-stage human cell types.
This sub-cluster is a constituent of Cluster 6. The bar chart displays the gene set score for this specific sub-cluster across various cell types from late-stage human HCM snRNA-seq data. Scores were calculated for each sample using the `score_genes` function in `scanpy` v1.10.1 [267]. Bars represent the mean score, with error bars indicating the standard error of the mean. Statistical significance between disease and control samples was determined using a t-test, with p-values adjusted for multiple comparisons using the Benjamini-Hochberg method. Asterisks denote significance levels: * $p < 0.05$, ** $p < 0.01$, *** $p < 0.001$, **** $p < 0.0001$.

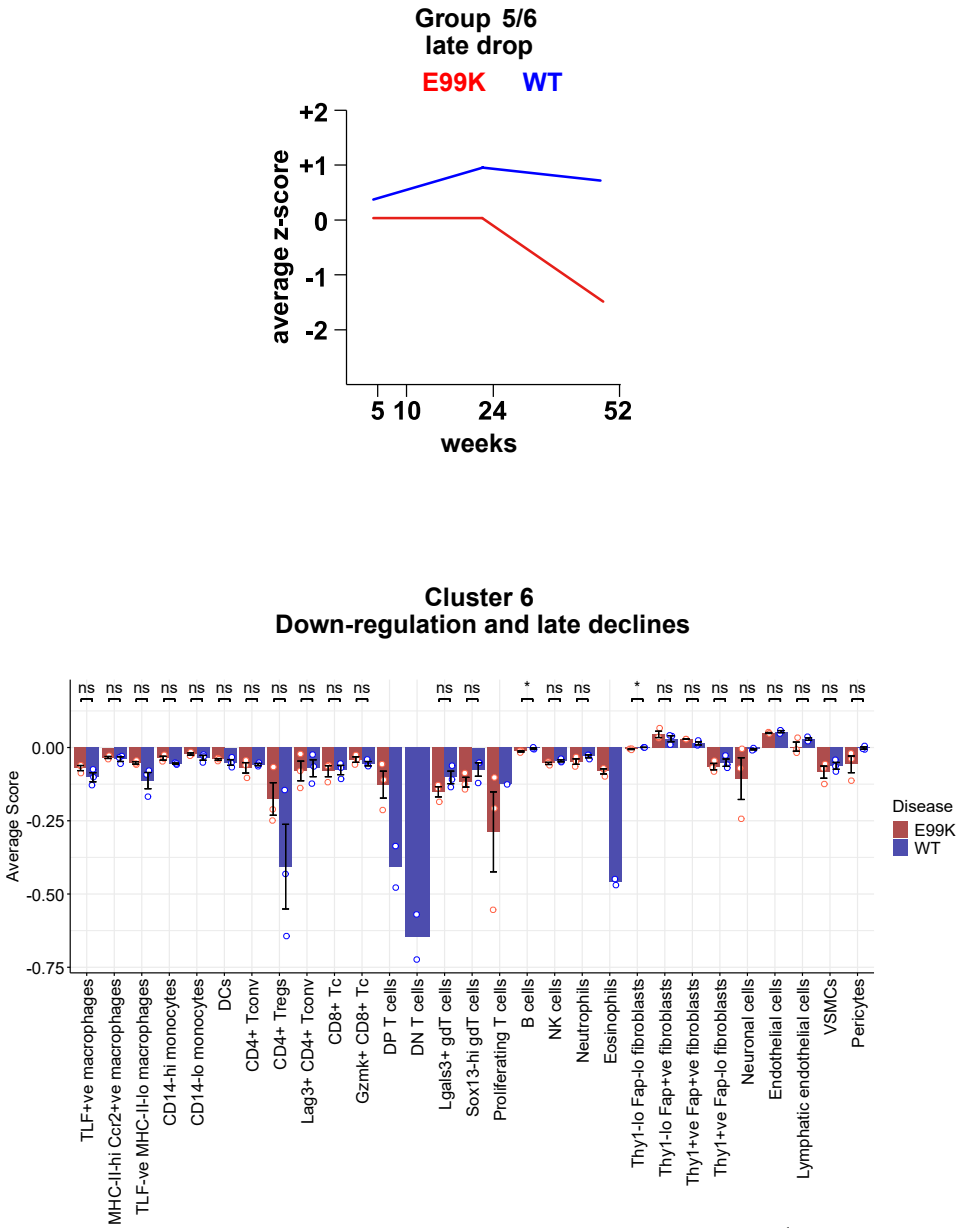

Figure D.152. Gene set scoring and statistics of Cluster 6 (down-regulation and late declines) in late-stage mouse cell types.
The upper panel schematically illustrates the temporal expression trend for Cluster 6, derived from bulk RNA-seq data of Actc1^{E99K} (red line) and wild-type (blue line) hearts over time. The lower panel displays the gene set score for all genes within Cluster 6 across various cell types identified in late-stage Actc1^{E99K} mouse scRNA-seq data. Scores were calculated for each sample using the `score_genes` function in `scanpy` v1.10.1 [267]. Bars represent the mean score, with error bars indicating the standard error of the mean. Statistical significance between disease and control samples was determined using a t-test, with p-values adjusted for multiple comparisons using the Benjamini-Hochberg method. Asterisks denote significance levels: * $p < 0.05$, ** $p < 0.01$, *** $p < 0.001$, **** $p < 0.0001$.

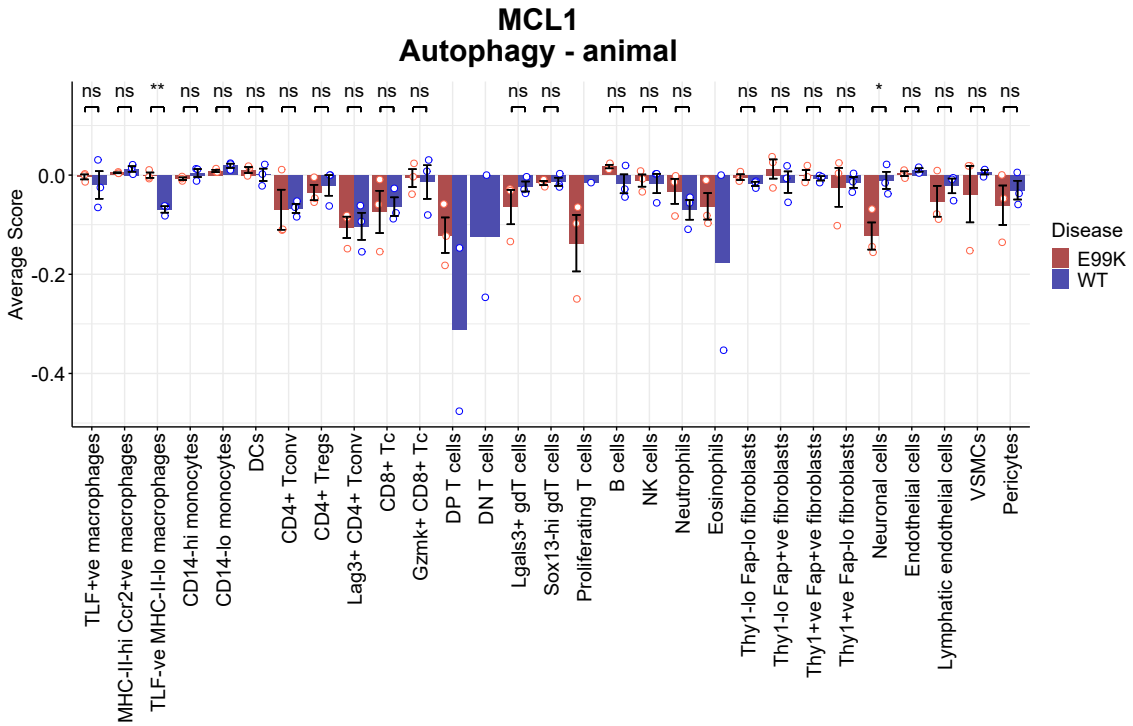

Figure D.153. Gene set scoring for MCL sub-cluster 1 of Cluster 6 (down-regulation and late declines) in late-stage mouse cell types.
This sub-cluster is a constituent of Cluster 6. The bar chart displays the gene set score for this specific sub-cluster across various cell types from late-stage Actc1^{E99K} mouse scRNA-seq data. Scores were calculated for each sample using the `score_genes` function in `scanpy` v1.10.1 [267]. Bars represent the mean score, with error bars indicating the standard error of the mean. Statistical significance between disease and control samples was determined using a t-test, with p-values adjusted for multiple comparisons using the Benjamini-Hochberg method. Asterisks denote significance levels: * $p < 0.05$, ** $p < 0.01$, *** $p < 0.001$, **** $p < 0.0001$.

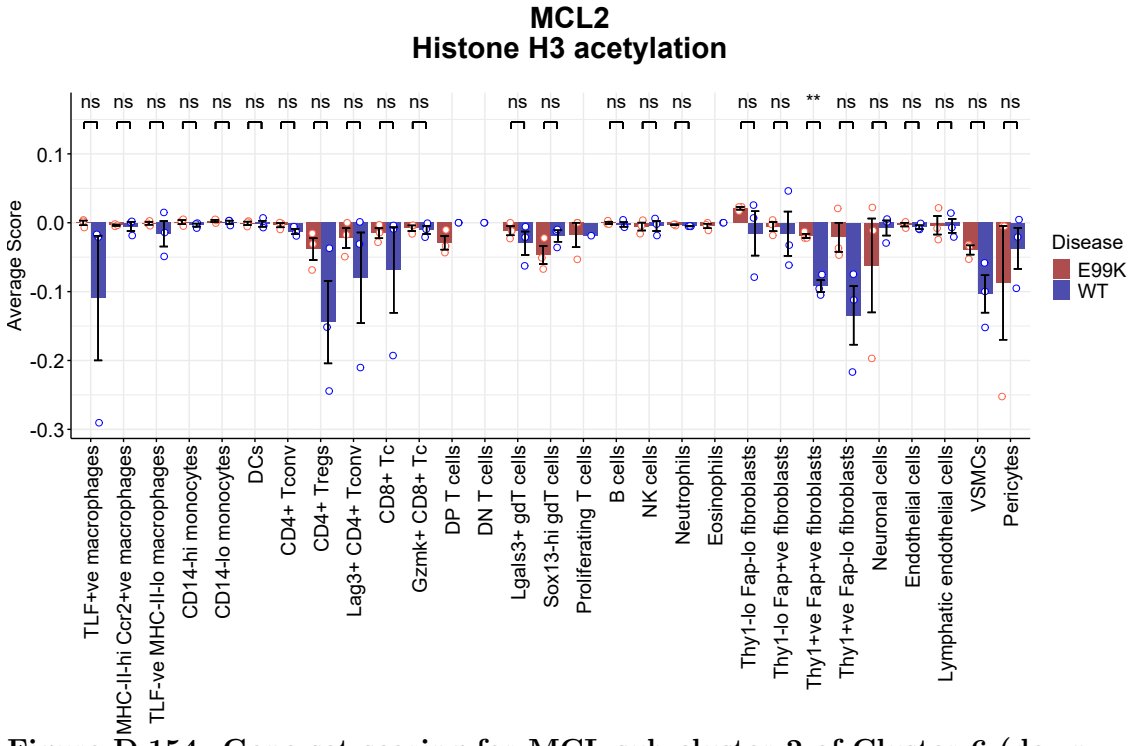

Figure D.154. Gene set scoring for MCL sub-cluster 2 of Cluster 6 (down-regulation and late declines) in late-stage mouse cell types.
This sub-cluster is a constituent of Cluster 6. The bar chart displays the gene set score for this specific sub-cluster across various cell types from late-stage $Actc1^{E99K}$ mouse scRNA-seq data. Scores were calculated for each sample using the `score_genes` function in `scanpy` v1.10.1 [267]. Bars represent the mean score, with error bars indicating the standard error of the mean. Statistical significance between disease and control samples was determined using a t-test, with p-values adjusted for multiple comparisons using the Benjamini-Hochberg method. Asterisks denote significance levels: * $p < 0.05$, ** $p < 0.01$, *** $p < 0.001$, **** $p < 0.0001$.

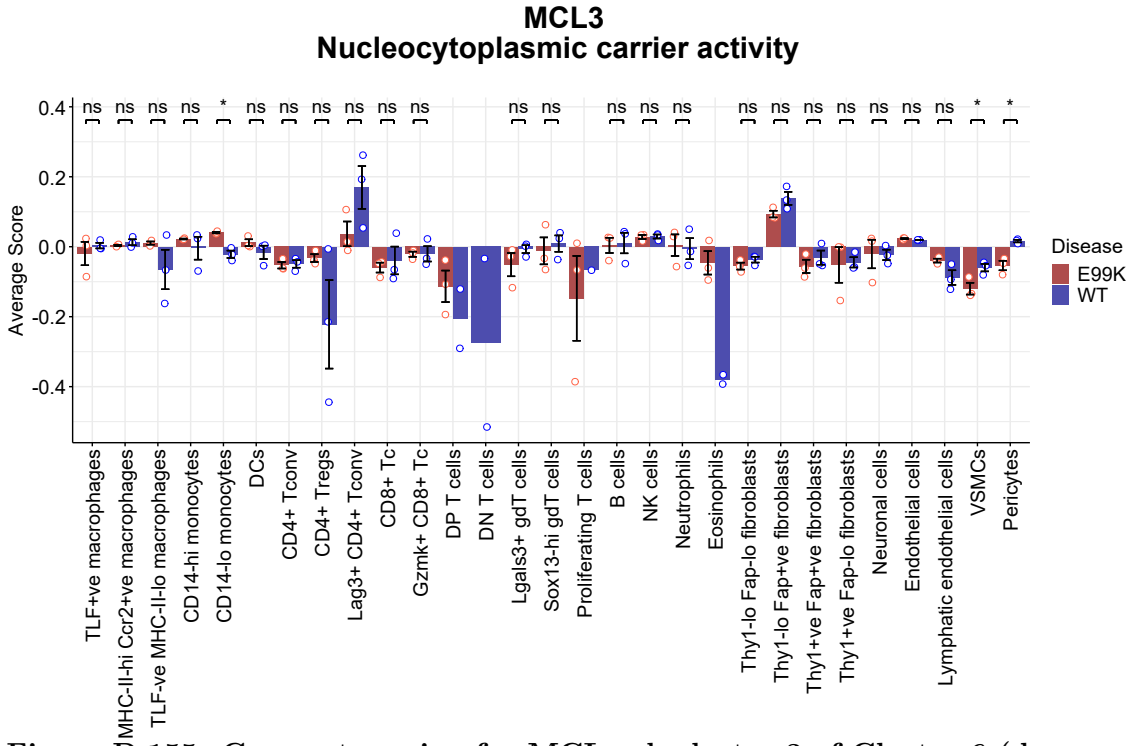

Figure D.155. Gene set scoring for MCL sub-cluster 3 of Cluster 6 (down-regulation and late declines) in late-stage mouse cell types.
This sub-cluster is a constituent of Cluster 6. The bar chart displays the gene set score for this specific sub-cluster across various cell types from late-stage Actc1^{E99K} mouse scRNA-seq data. Scores were calculated for each sample using the `score_genes` function in `scanpy` v1.10.1 [267]. Bars represent the mean score, with error bars indicating the standard error of the mean. Statistical significance between disease and control samples was determined using a t-test, with p-values adjusted for multiple comparisons using the Benjamini-Hochberg method. Asterisks denote significance levels: * $p < 0.05$, ** $p < 0.01$, *** $p < 0.001$, **** $p < 0.0001$.

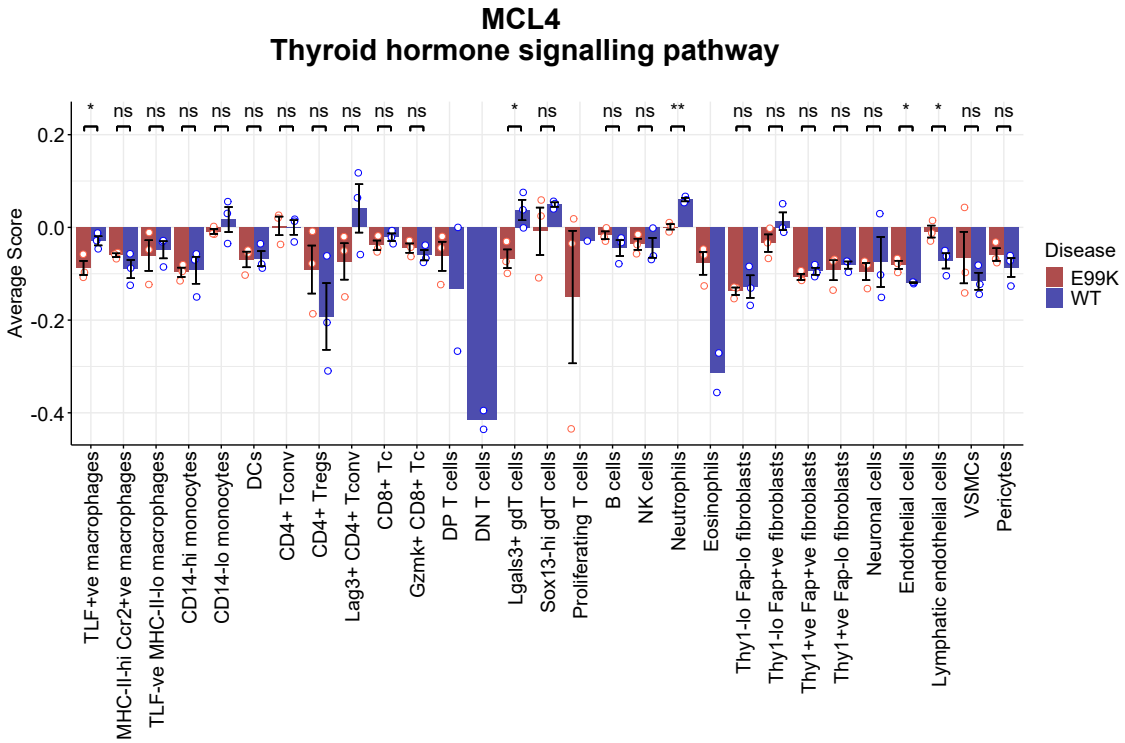

Figure D.156. Gene set scoring for MCL sub-cluster 4 of Cluster 6 (down-regulation and late declines) in late-stage mouse cell types.
This sub-cluster is a constituent of Cluster 6. The bar chart displays the gene set score for this specific sub-cluster across various cell types from late-stage Actc1^{E99K} mouse scRNA-seq data. Scores were calculated for each sample using the `score_genes` function in `scanpy` v1.10.1 [267]. Bars represent the mean score, with error bars indicating the standard error of the mean. Statistical significance between disease and control samples was determined using a t-test, with p-values adjusted for multiple comparisons using the Benjamini-Hochberg method. Asterisks denote significance levels: * $p < 0.05$, ** $p < 0.01$, *** $p < 0.001$, **** $p < 0.0001$.

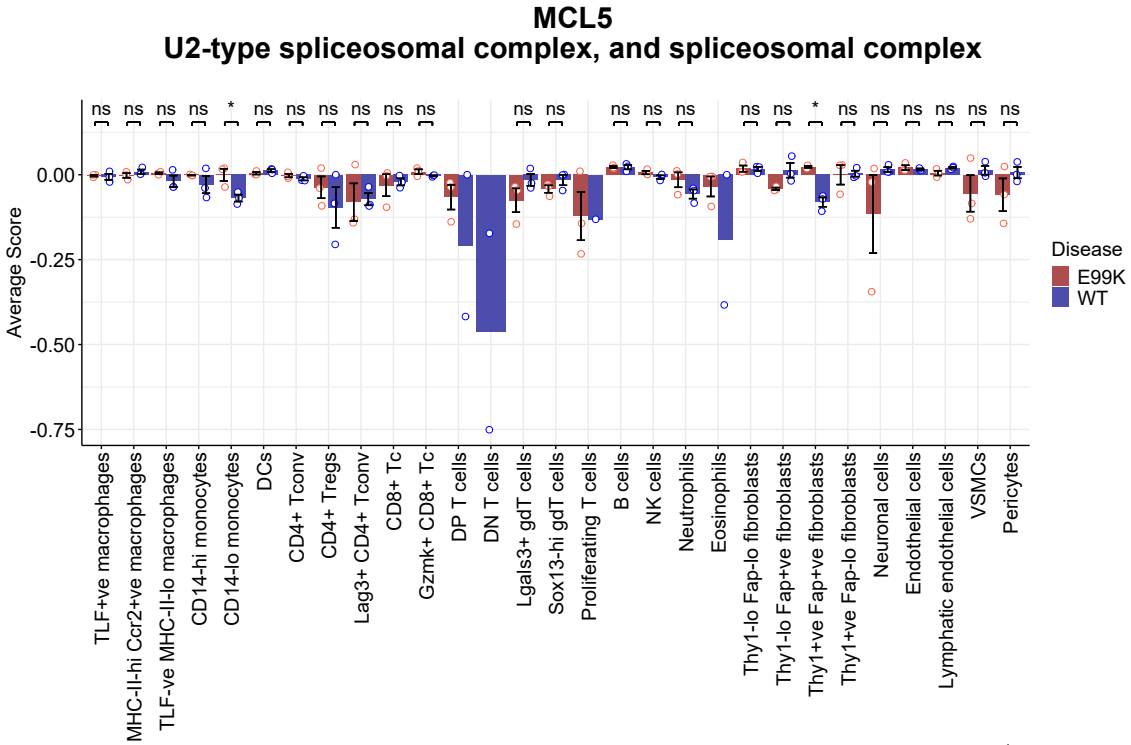

Figure D.157. Gene set scoring for MCL sub-cluster 5 of Cluster 6 (down-regulation and late declines) in late-stage mouse cell types.
This sub-cluster is a constituent of Cluster 6. The bar chart displays the gene set score for this specific sub-cluster across various cell types from late-stage Actc1^{E99K} mouse scRNA-seq data. Scores were calculated for each sample using the `score_genes` function in `scanpy` v1.10.1 [267]. Bars represent the mean score, with error bars indicating the standard error of the mean. Statistical significance between disease and control samples was determined using a t-test, with p-values adjusted for multiple comparisons using the Benjamini-Hochberg method. Asterisks denote significance levels: * $p < 0.05$, ** $p < 0.01$, *** $p < 0.001$, **** $p < 0.0001$.

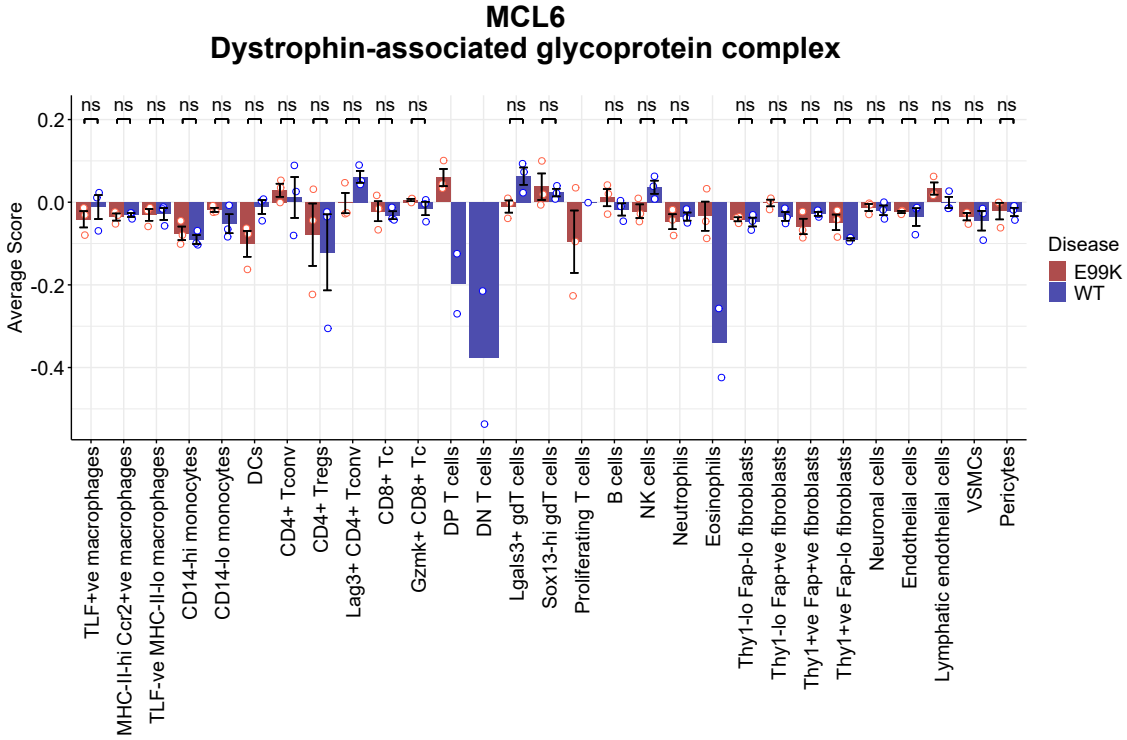

Figure D.158. Gene set scoring for MCL sub-cluster 6 of Cluster 6 (down-regulation and late declines) in late-stage mouse cell types.
This sub-cluster is a constituent of Cluster 6. The bar chart displays the gene set score for this specific sub-cluster across various cell types from late-stage $Actc1^{E99K}$ mouse scRNA-seq data. Scores were calculated for each sample using the `score_genes` function in `scanpy` v1.10.1 [267]. Bars represent the mean score, with error bars indicating the standard error of the mean. Statistical significance between disease and control samples was determined using a t-test, with p-values adjusted for multiple comparisons using the Benjamini-Hochberg method. Asterisks denote significance levels: * $p < 0.05$, ** $p < 0.01$, *** $p < 0.001$, **** $p < 0.0001$.

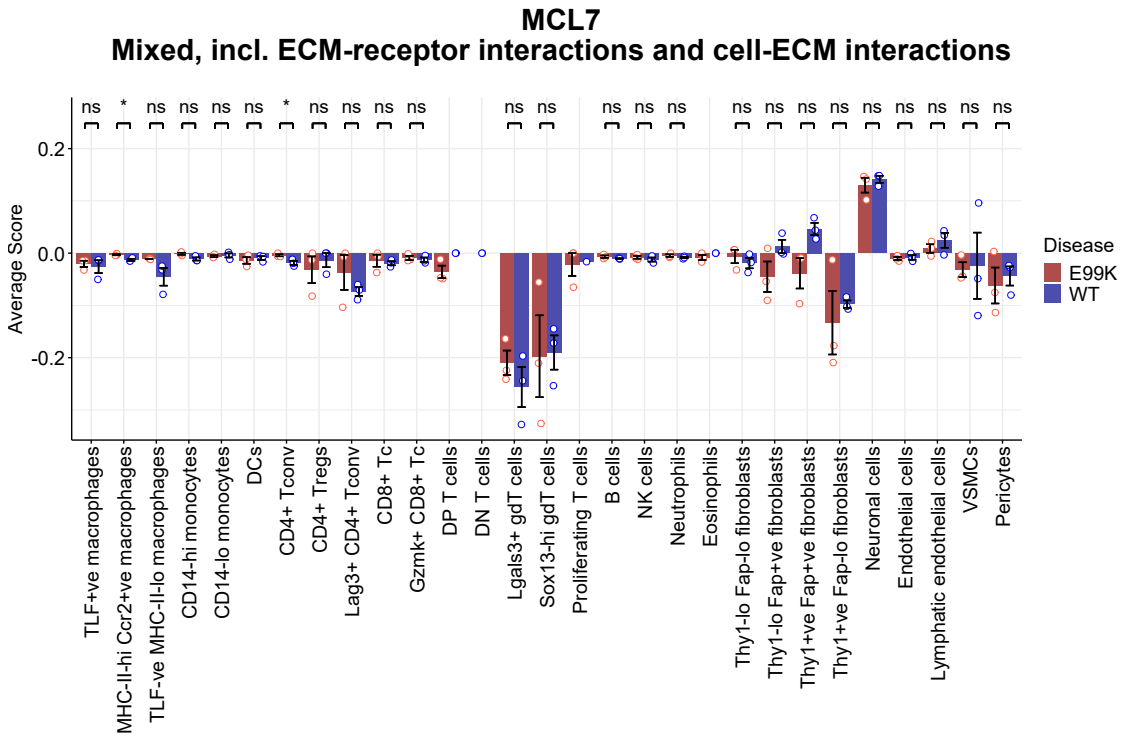

Figure D.159. Gene set scoring for MCL sub-cluster 7 of Cluster 6 (down-regulation and late declines) in late-stage mouse cell types.
This sub-cluster is a constituent of Cluster 6. The bar chart displays the gene set score for this specific sub-cluster across various cell types from late-stage Actc1^{E99K} mouse scRNA-seq data. Scores were calculated for each sample using the `score_genes` function in `scanpy` v1.10.1 [267]. Bars represent the mean score, with error bars indicating the standard error of the mean. Statistical significance between disease and control samples was determined using a t-test, with p-values adjusted for multiple comparisons using the Benjamini-Hochberg method. Asterisks denote significance levels: * $p < 0.05$, ** $p < 0.01$, *** $p < 0.001$, **** $p < 0.0001$.

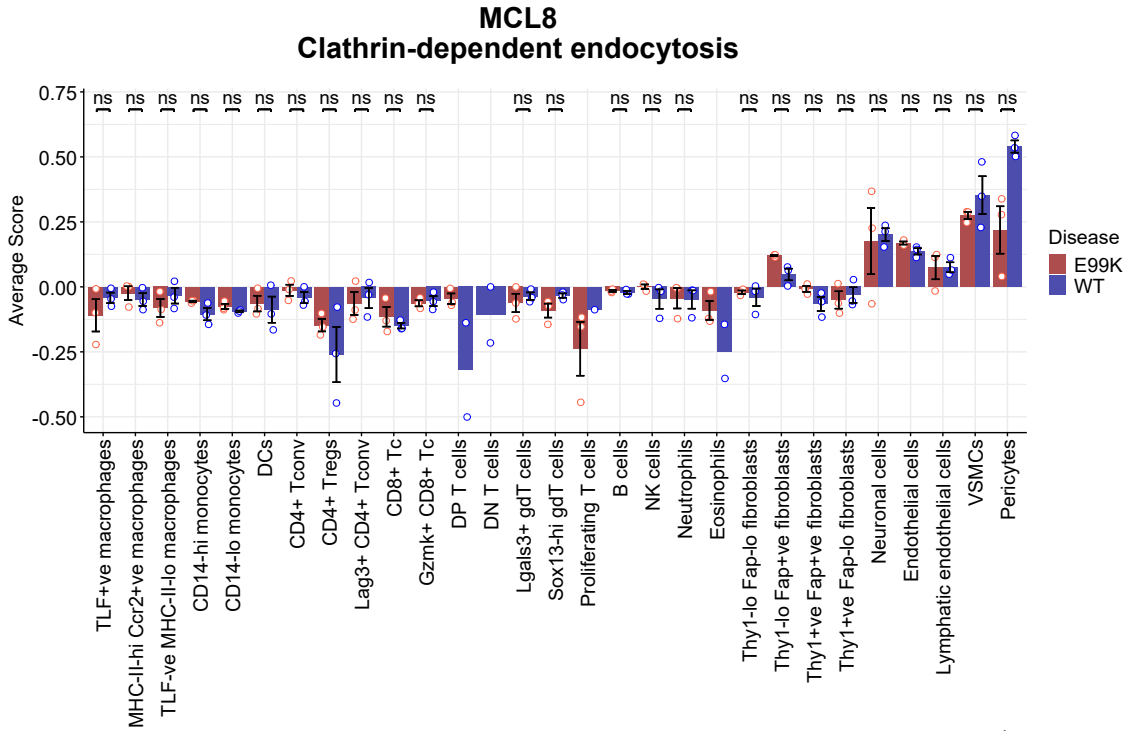

Figure D.160. Gene set scoring for MCL sub-cluster 8 of Cluster 6 (down-regulation and late declines) in late-stage mouse cell types.
This sub-cluster is a constituent of Cluster 6. The bar chart displays the gene set score for this specific sub-cluster across various cell types from late-stage $Actc1^{E99K}$ mouse scRNA-seq data. Scores were calculated for each sample using the `score_genes` function in `scanpy` v1.10.1 [267]. Bars represent the mean score, with error bars indicating the standard error of the mean. Statistical significance between disease and control samples was determined using a t-test, with p-values adjusted for multiple comparisons using the Benjamini-Hochberg method. Asterisks denote significance levels: * $p < 0.05$, ** $p < 0.01$, *** $p < 0.001$, **** $p < 0.0001$.

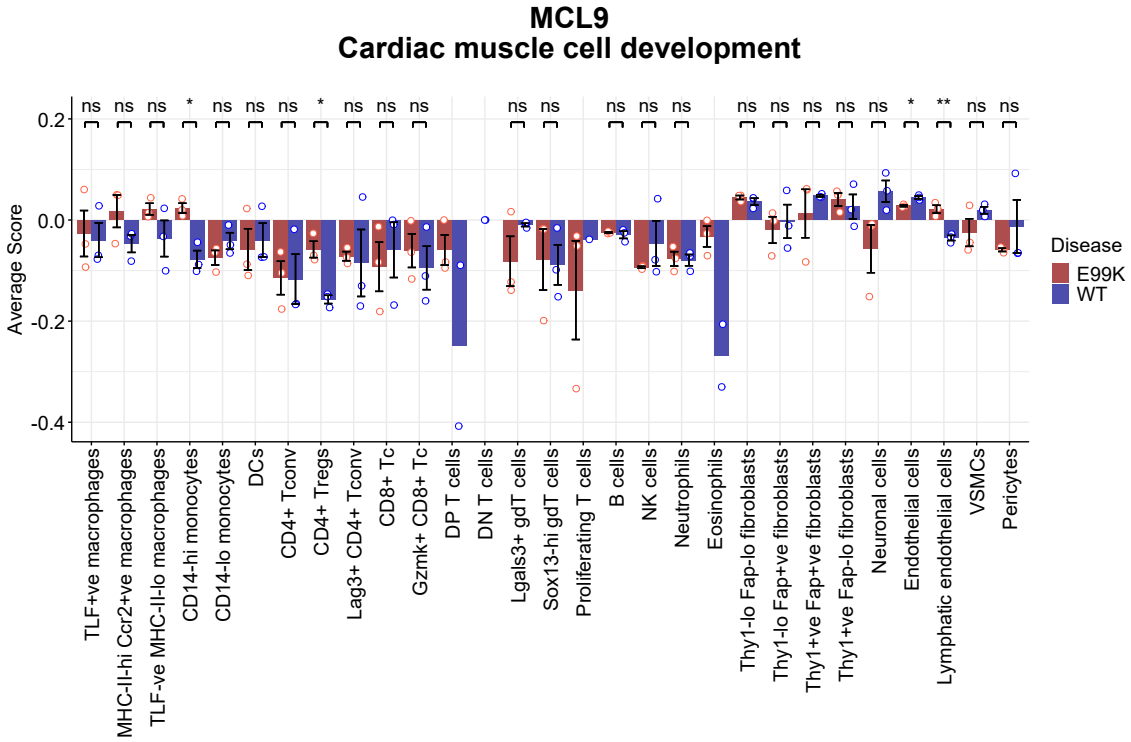

Figure D.161. Gene set scoring for MCL sub-cluster 9 of Cluster 6 (down-regulation and late declines) in late-stage mouse cell types.
This sub-cluster is a constituent of Cluster 6. The bar chart displays the gene set score for this specific sub-cluster across various cell types from late-stage Actc1^{E99K} mouse scRNA-seq data. Scores were calculated for each sample using the `score_genes` function in `scanpy` v1.10.1 [267]. Bars represent the mean score, with error bars indicating the standard error of the mean. Statistical significance between disease and control samples was determined using a t-test, with p-values adjusted for multiple comparisons using the Benjamini-Hochberg method. Asterisks denote significance levels: * $p < 0.05$, ** $p < 0.01$, *** $p < 0.001$, **** $p < 0.0001$.

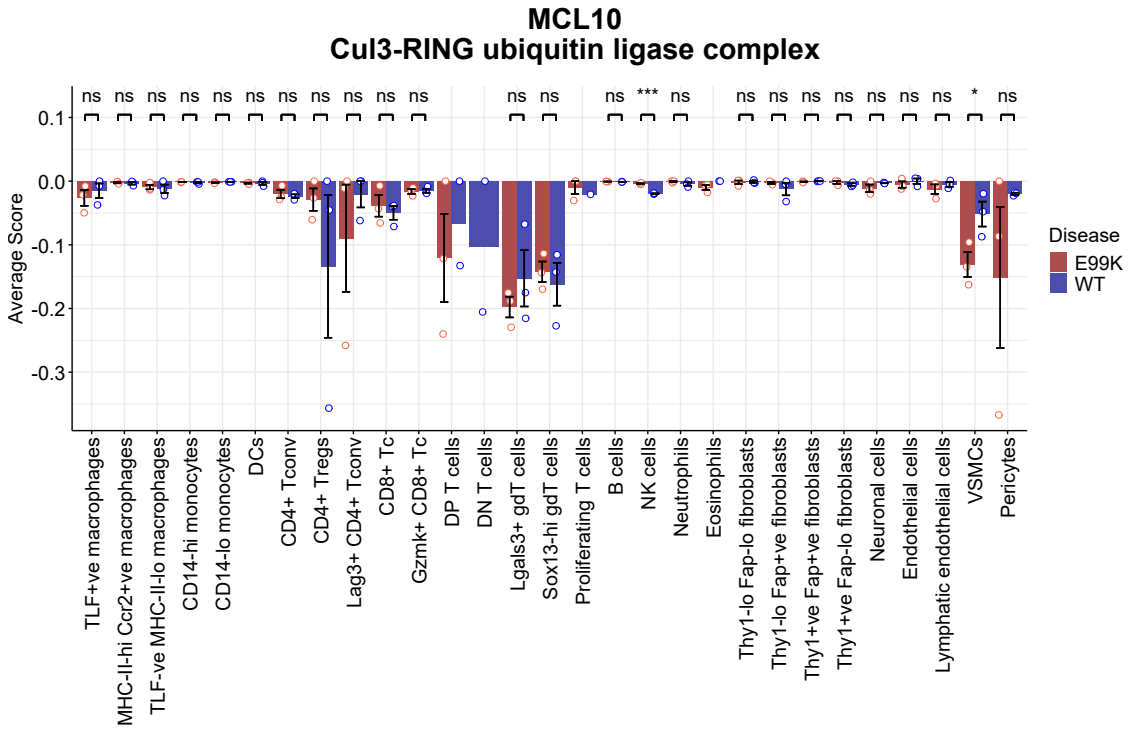

Figure D.162. Gene set scoring for MCL sub-cluster 10 of Cluster 6 (down-regulation and late declines) in late-stage mouse cell types.
This sub-cluster is a constituent of Cluster 6. The bar chart displays the gene set score for this specific sub-cluster across various cell types from late-stage $Actc1^{E99K}$ mouse scRNA-seq data. Scores were calculated for each sample using the `score_genes` function in `scanpy` v1.10.1 [267]. Bars represent the mean score, with error bars indicating the standard error of the mean. Statistical significance between disease and control samples was determined using a t-test, with p-values adjusted for multiple comparisons using the Benjamini-Hochberg method. Asterisks denote significance levels: * $p < 0.05$, ** $p < 0.01$, *** $p < 0.001$, **** $p < 0.0001$.

E

Intercellular dialogue uncovers critical remodelling cues

Endothelial cells emerge as crucial communicators in cardiac remodelling

Endothelial cells, crucial for vascular homeostasis and myocardial function, were examined to understand their specific contributions to the intercellular communication network in early-stage disease. In mid-stage human HCM, endothelial cells exhibited complex changes in signalling (Figure E.1). FGF12 signalling via FGFR1 was broadly downregulated, targeting pericytes, VSMCs, $CD4^+$ naïve T cells, cardiomyocytes, $Thy1^{lo}Fap^{lo}$ fibroblasts, and endothelial cells. This suggests potential disruption of FGF12-mediated processes, such as angiogenesis and vascular remodelling, in HCM [661–663]. Downregulated NCAM1 signalling via CACNA1C targeting immune and structural cells may impact cell adhesion and migration [664, 665]. Conversely, increased NLGN1-NRXN1 signalling between endothelial and neuronal cells suggests potential neuro-vascular coupling alterations [666, 667].

In contrast, early-stage mouse HCM endothelial cells showed a simpler communication pattern (Figure E.1). Upregulated Col4a1-Cd93 signalling between endothelial cells potentially reflects changes in ECM composition and interaction [597]. Downregulation of Igf2-Igf1r signalling between endothelial cells suggests

potential alterations in growth and survival pathways [515, 668, 669]. The limited altered interactions in early-stage mouse endothelial cells underscore the relatively quiescent endothelial state at this disease stage.

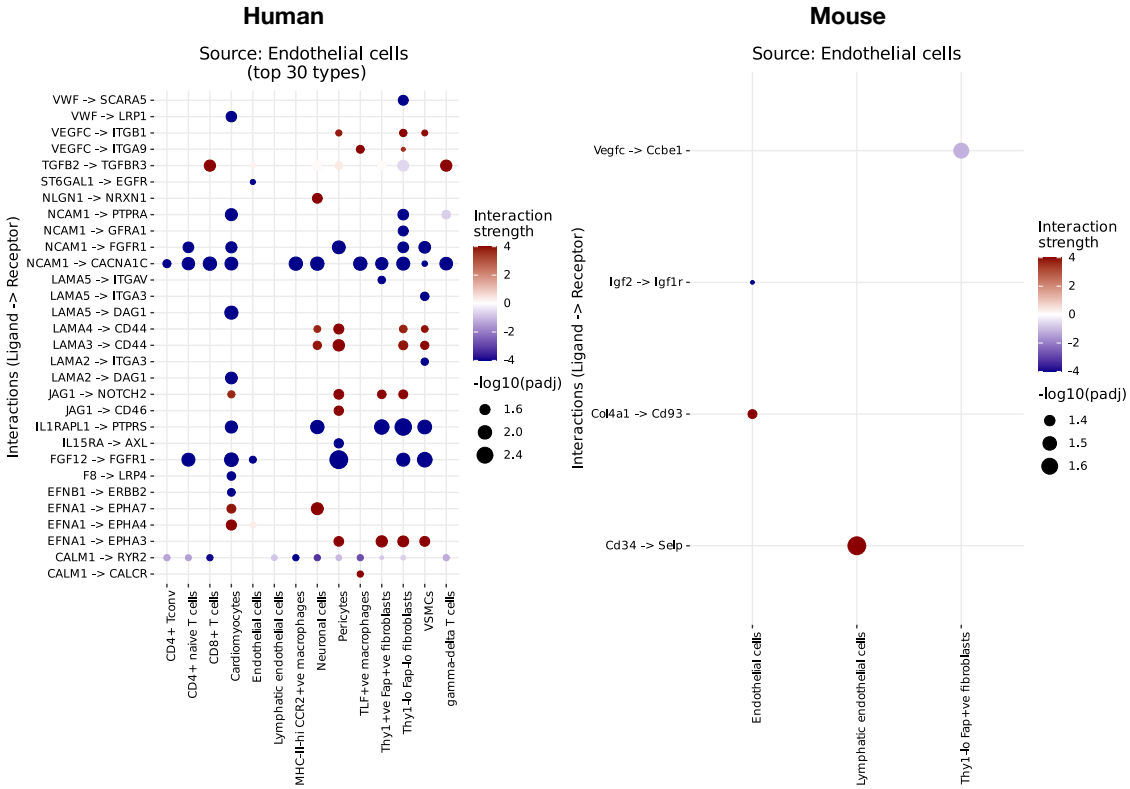

Figure E.1. Cell-cell communication involving endothelial cells in mid-stage human and early-stage mouse HCM.
Positive interaction strength indicates up-regulation of ligand-receptor genes in HCM or Actc1^{E99K} samples, while negative strength indicates down-regulation. P-values were adjusted using the Benjamini-Hochberg method. Human interactions appear on the left and mouse interactions on the right.

Fibroblasts drive remodelling dynamics through altered signalling

Cardiac fibroblast populations, specifically Thy1^{+}Fap^{+} and Thy1^{lo}Fap^{lo} fibroblast subtypes, play critical roles in ECM remodelling and contribute significantly to the HCM phenotype.

In mid-stage human HCM, Thy1^{+}Fap^{+} fibroblasts exhibited a complex signalling profile (Figure E.2). For example, reduced FGF12 signalling via FGFR1 was observed, targeting diverse cell types including pericytes, VSMCs, CD4^{+} naïve T cells, cardiomyocytes, Thy1^{lo}Fap^{lo} fibroblasts, and endothelial cells. This FGF12

downregulation may disrupt angiogenesis and vascular remodelling, potentially contributing to the adverse remodelling seen in HCM [662, 670]. Conversely, increased NLGN1-NRXN1 signalling was observed between $Thy1^{+}Fap^{+}$ fibroblasts and neuronal cells, suggesting potential neuro-vascular coupling alterations [666, 667]. Further signalling changes included upregulated PTN signalling via PTPRZ1 to neuronal cells and via NRP1 to TLF^{+} macrophages, and downregulated COL6A6 signalling via GP6 to cardiomyocytes. These diverse signalling alterations highlight the multifaceted role of $Thy1^{+}Fap^{+}$ fibroblasts in the complex intercellular communication network of mid-stage human HCM.

In contrast, early-stage mouse HCM displayed a simpler $Thy1^{+}Fap^{+}$ fibroblast communication pattern (Figure E.2). The most prominent change was downregulated Thbs1 signalling via Lrp5, targeting $Thy1^{lo}Fap^{lo}$ fibroblasts. This suggests a potential role for Thbs1 in early ECM remodelling [671–673]. Additionally, Apoe signalling via Lrp5, targeting $Thy1^{lo}Fap^{lo}$ fibroblasts, and Cd34 signalling via Selp, targeting lymphatic endothelial cells, were upregulated. The relative paucity of altered interactions in early-stage mouse $Thy1^{+}Fap^{+}$ fibroblasts underscores the less developed nature of the disease at this stage compared to the mid-stage human samples.

Shifting focus to the $Thy1^{lo}Fap^{lo}$ fibroblast subtype, mid-stage human HCM samples again displayed a complex interplay of upregulated and downregulated signalling pathways (Figure E.2). Downregulated COL6A3 signalling via GP6 and ITGA3, targeting cardiomyocytes and VSMCs respectively, suggests potential disruptions in ECM organisation and cell-matrix interactions [597]. Increased COL4A5 signalling via CD44 and CD47, targeting pericytes, cardiomyocytes, and $Thy1^{lo}Fap^{lo}$ fibroblasts themselves, points towards potential alterations in ECM composition and cell adhesion [597]. Furthermore, downregulated ADAM10 signalling via GPNMB, TSPAN14, and NOTCH1, targeting TLF^{+} macrophages, neuronal cells, and pericytes, may impact cell-cell communication and signalling pathways [560, 674].

In early-stage mouse HCM, $Thy1^{lo}Fap^{lo}$ fibroblasts exhibited a less complex communication profile compared to their human counterparts (Figure E.2). Similar to $Thy1^{+}Fap^{+}$ fibroblasts, downregulated Thbs1 signalling via Lrp5 was observed, targeting $Thy1^{lo}Fap^{lo}$ fibroblasts. Upregulated Cd34 signalling via Selp, targeting lymphatic endothelial cells, and Fn1 signalling via Plaur, targeting B cells, were also noted. These findings further emphasise the relatively quiescent state of fibroblasts in early-stage mouse HCM.

Downregulation of Igf1 signalling via Igf1r, targeting endothelial cells, may also contribute to the altered vascular microenvironment in early-stage disease [675, 676]. The less pronounced changes in cell-cell communication observed in early-stage mouse $Thy1^{lo}Fap^{lo}$ fibroblasts, compared to their human counterparts (Figure E.2), further reinforces the concept of a less complex disease state in the early stages of the mouse model.

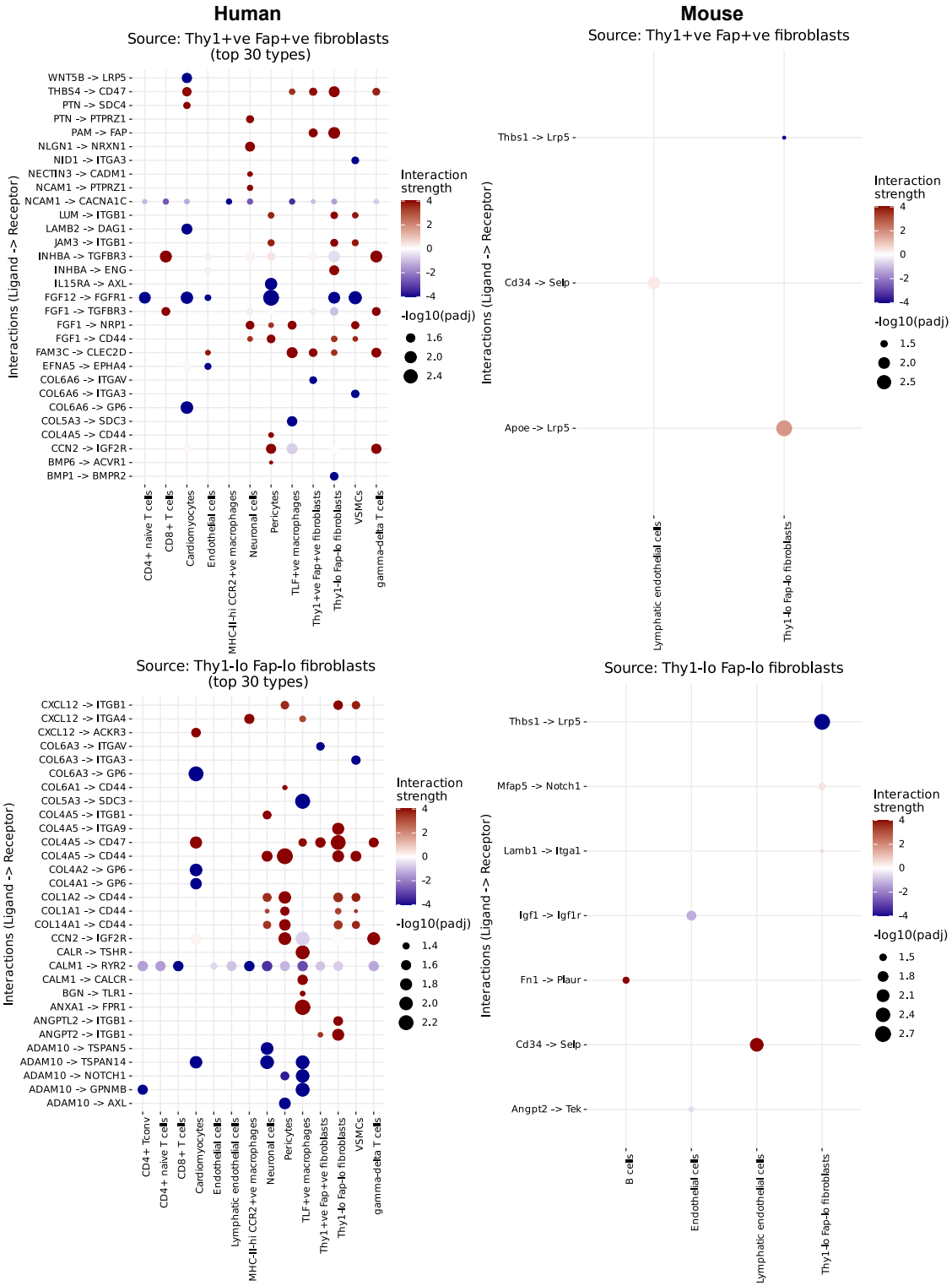

Figure E.2. Cell-cell communication involving fibroblasts in mid-stage human and early-stage mouse HCM.
Positive interaction strength indicates up-regulation of ligand-receptor genes in HCM or Actc1^{E99K} samples, while negative strength indicates down-regulation. P-values were adjusted using the Benjamini-Hochberg method. Human interactions appear on the left and mouse interactions on the right.

F

Integrating bulk trends with single-cell insights reveals early HCM changes

F.1 Cluster 7: Early activation then decline reveals specific modulations of cellular processes

Cluster 7, characterised by an initial up-regulation in early-stage Actc1^{E99K} followed by a subsequent decline in later stages, encompasses a diverse array of biological processes (Figure F.1). Sub-cluster analysis revealed enrichment for several distinct functional categories, including ECM-receptor interaction (MCL sub-cluster 1; Figure F.2), digestive system development (MCL sub-cluster 2; Figure F.3), cellular response to interferon-β and antiviral mechanisms by IFN-stimulated genes (MCL sub-cluster 3; Figure F.4), regulation of RAS by GAPs (MCL sub-cluster 4; Figure F.5), smooth muscle cell differentiation (MCL sub-cluster 5; Figure F.6), striated muscle contraction (MCL sub-cluster 6; Figure F.7), small-subunit processome and positive regulation of rRNA processing (MCL sub-cluster 7; Figure F.8), COPI-independent Golgi-to-ER retrograde traffic (MCL sub-cluster 8; Figure F.9), clathrin coat assembly (MCL sub-cluster 9; Figure F.10), and apoptosis (MCL sub-cluster 10; Figure F.11). In early-stage Actc1^{E99K} mouse hearts, the overall Cluster 7 signature did not show significant

changes in any of the analysed cell types (Figure F.1). However, examination of individual sub-clusters revealed more nuanced patterns. The ECM-receptor interaction sub-cluster was significantly down-regulated in both *Thy1*^{lo}*Fap*$^{+}$ and *Thy1*$^{+}$*Fap*$^{+}$ fibroblasts (MCL sub-cluster 1; Figure F.2). Interestingly, the digestive system development sub-cluster was significantly up-regulated in neutrophils (MCL sub-cluster 2; Figure F.3). The remaining sub-clusters, including those related to interferon response (MCL sub-cluster 3; Figure F.4), RAS regulation (MCL sub-cluster 4; Figure F.5), smooth muscle differentiation (MCL sub-cluster 5; Figure F.6), muscle contraction (MCL sub-cluster 6; Figure F.7), rRNA processing (MCL sub-cluster 7; Figure F.8), Golgi-to-ER traffic (MCL sub-cluster 8; Figure F.9), clathrin coat assembly (MCL sub-cluster 9; Figure F.10), and apoptosis (MCL sub-cluster 10; Figure F.11), did not exhibit significant changes in expression within any of the analysed cell populations in early-stage Actc1^{E99K} mice.

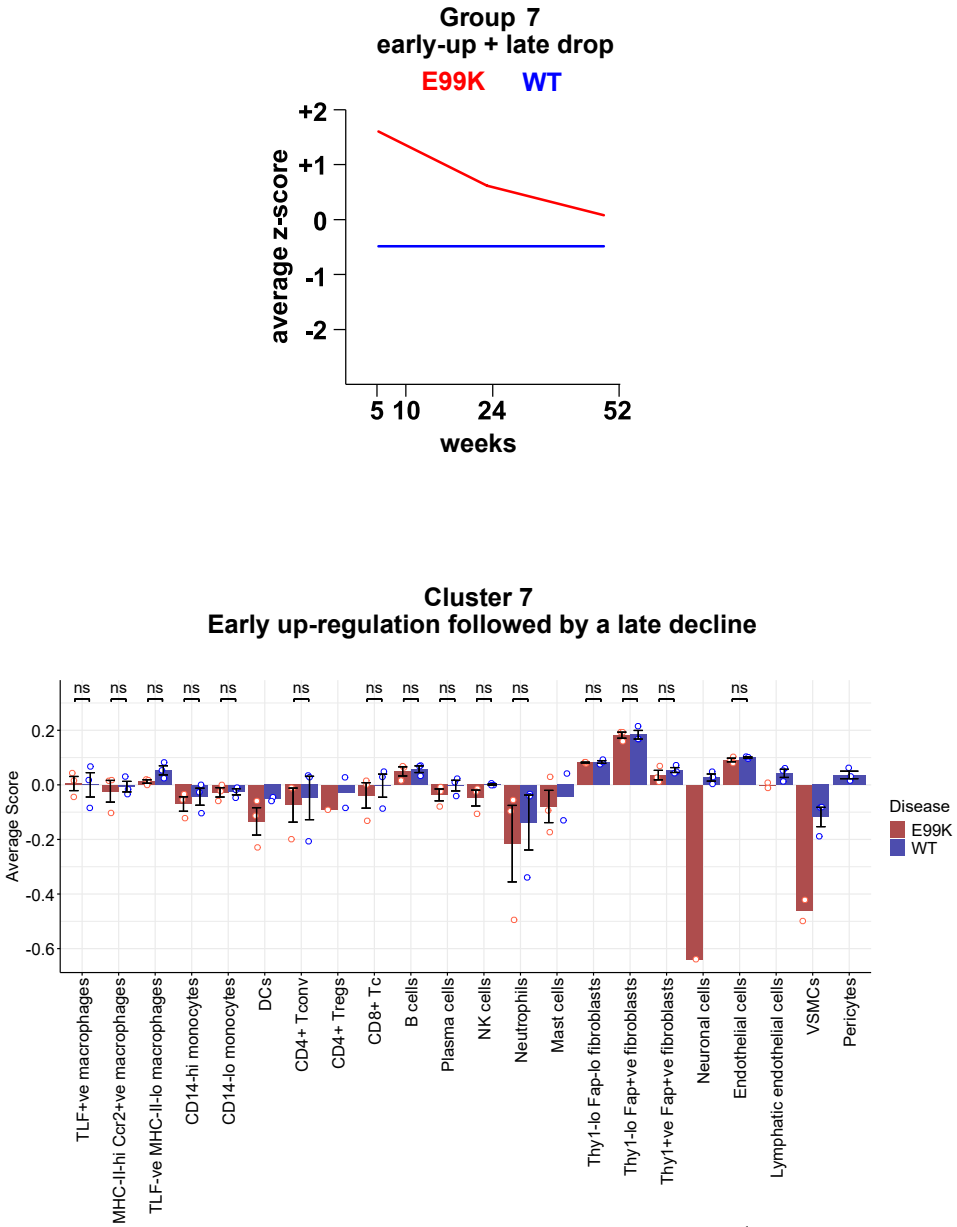

Figure F.1. Gene set scoring and statistics of Cluster 7 (early upregulation followed by late decline) in late-stage mouse cell types.
The upper panel schematically illustrates the temporal expression trend for Cluster 7, derived from bulk RNA-seq data of Actc1^{E99K} (red line) and wild-type (blue line) hearts over time. The lower panel displays the gene set score for all genes within Cluster 7 across various cell types identified in early-stage Actc1^{E99K} mouse scRNA-seq data. Scores were calculated for each sample using the `score_genes` function in `scanpy` v1.10.1 [267]. Bars represent the mean score, with error bars indicating the standard error of the mean. Statistical significance between disease and control samples was determined using a t-test, with p-values adjusted for multiple comparisons using the Benjamini-Hochberg method. Asterisks denote significance levels: * $p < 0.05$, ** $p < 0.01$, *** $p < 0.001$, **** $p < 0.0001$.

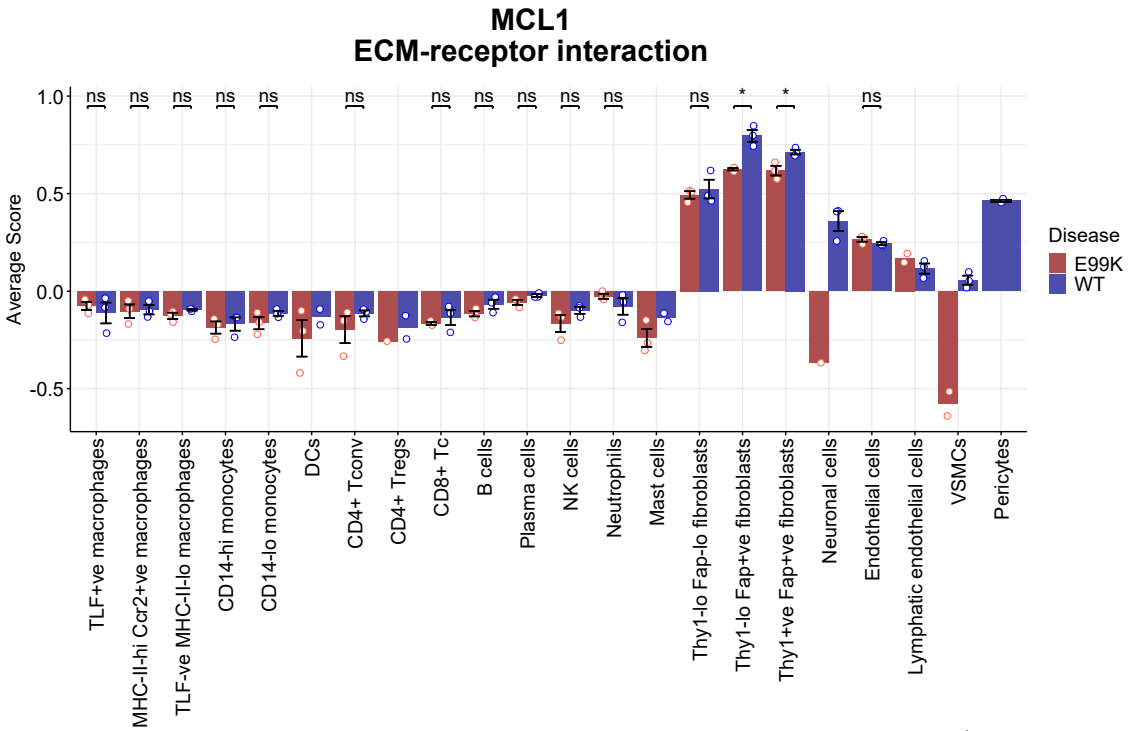

Figure F.2. Gene set scoring for MCL sub-cluster 1 of Cluster 7 (early upregulation followed by late decline) in late-stage mouse cell types. This sub-cluster is a constituent of Cluster 7. The bar chart displays the gene set score for this specific sub-cluster across various cell types from early-stage Actc1^{E99K} mouse scRNA-seq data. Scores were calculated for each sample using the `score_genes` function in `scanpy` v1.10.1 [267]. Bars represent the mean score, with error bars indicating the standard error of the mean. Statistical significance between disease and control samples was determined using a t-test, with p-values adjusted for multiple comparisons using the Benjamini-Hochberg method. Asterisks denote significance levels: * $p < 0.05$, ** $p < 0.01$, *** $p < 0.001$, **** $p < 0.0001$.

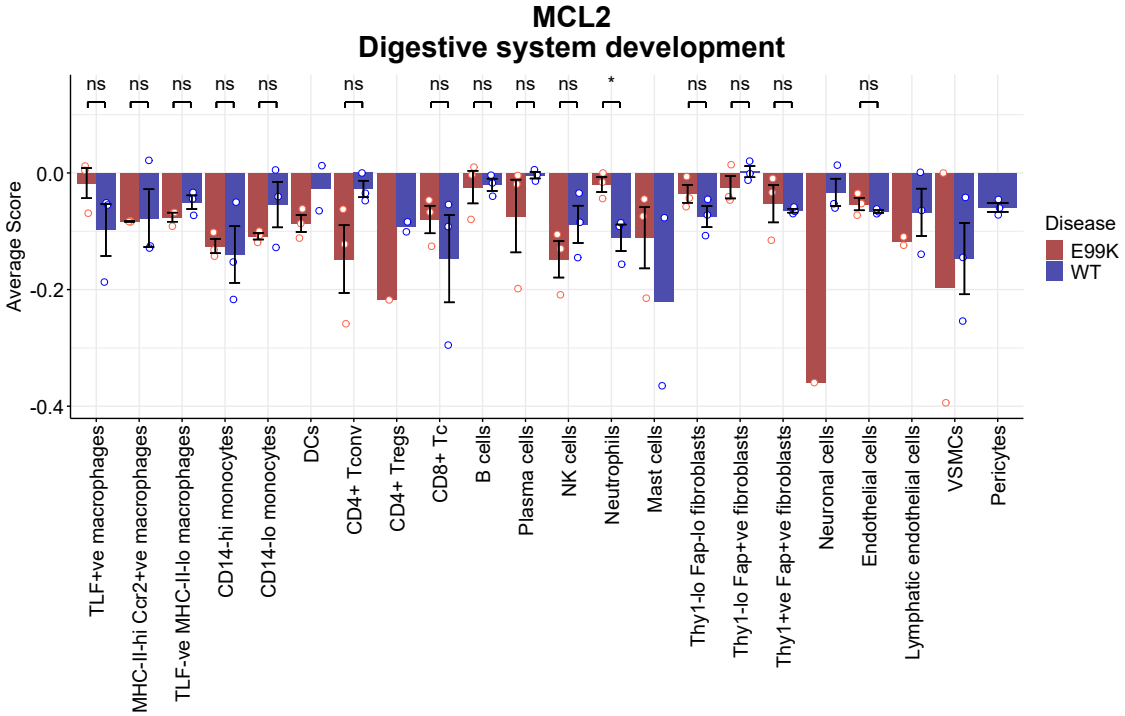

Figure F.3. Gene set scoring for MCL sub-cluster 2 of Cluster 7 (early upregulation followed by late decline) in late-stage mouse cell types. This sub-cluster is a constituent of Cluster 7. The bar chart displays the gene set score for this specific sub-cluster across various cell types from early-stage Actc1^{E99K} mouse scRNA-seq data. Scores were calculated for each sample using the `score_genes` function in `scanpy` v1.10.1 [267]. Bars represent the mean score, with error bars indicating the standard error of the mean. Statistical significance between disease and control samples was determined using a t-test, with p-values adjusted for multiple comparisons using the Benjamini-Hochberg method. Asterisks denote significance levels: * $p < 0.05$, ** $p < 0.01$, *** $p < 0.001$, **** $p < 0.0001$.

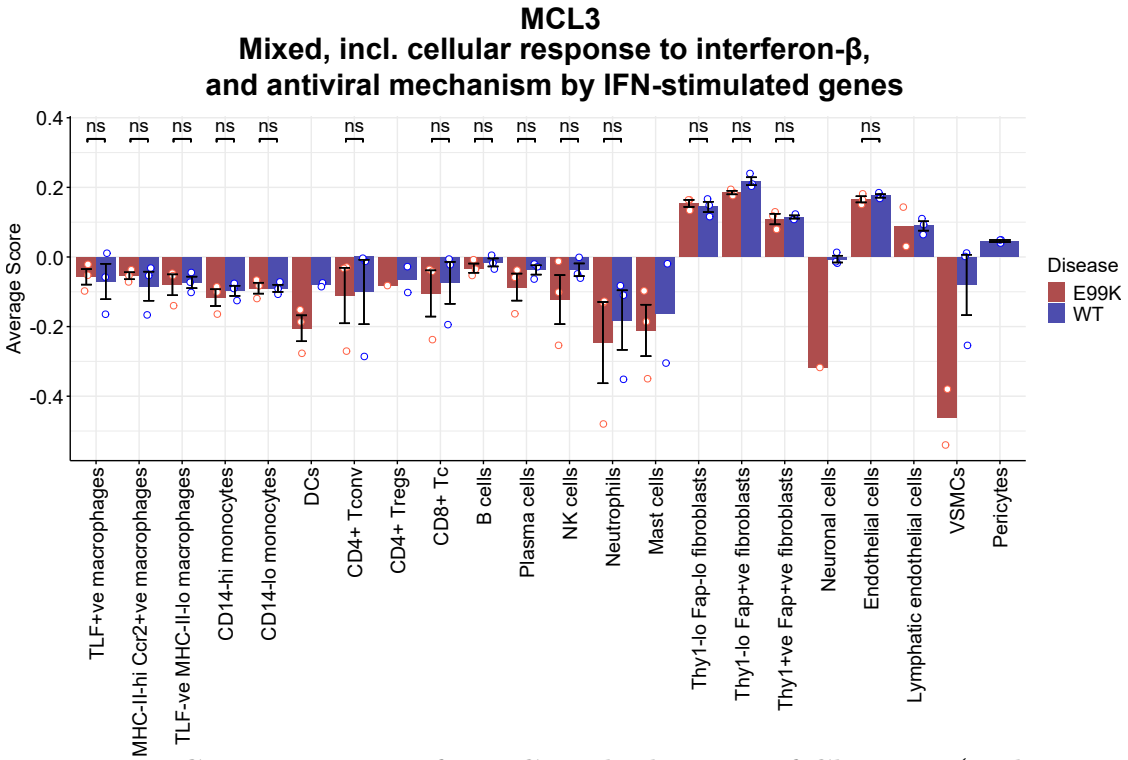

Figure F.4. Gene set scoring for MCL sub-cluster 3 of Cluster 7 (early upregulation followed by late decline) in late-stage mouse cell types. This sub-cluster is a constituent of Cluster 7. The bar chart displays the gene set score for this specific sub-cluster across various cell types from early-stage Actc1^{E99K} mouse scRNA-seq data. Scores were calculated for each sample using the `score_genes` function in `scanpy` v1.10.1 [267]. Bars represent the mean score, with error bars indicating the standard error of the mean. Statistical significance between disease and control samples was determined using a t-test, with p-values adjusted for multiple comparisons using the Benjamini-Hochberg method. Asterisks denote significance levels: * $p < 0.05$, ** $p < 0.01$, *** $p < 0.001$, **** $p < 0.0001$.

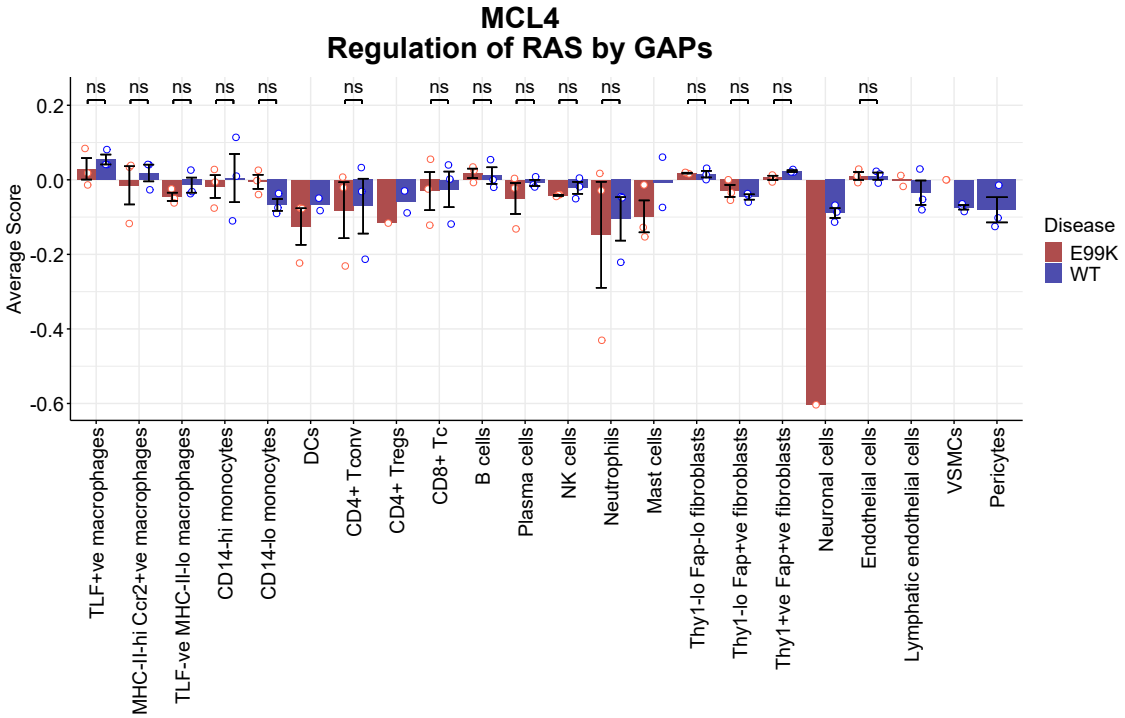

Figure F.5. Gene set scoring for MCL sub-cluster 4 of Cluster 7 (early upregulation followed by late decline) in late-stage mouse cell types. This sub-cluster is a constituent of Cluster 7. The bar chart displays the gene set score for this specific sub-cluster across various cell types from early-stage Actc1^{E99K} mouse scRNA-seq data. Scores were calculated for each sample using the `score_genes` function in `scanpy` v1.10.1 [267]. Bars represent the mean score, with error bars indicating the standard error of the mean. Statistical significance between disease and control samples was determined using a t-test, with p-values adjusted for multiple comparisons using the Benjamini-Hochberg method. Asterisks denote significance levels: * $p < 0.05$, ** $p < 0.01$, *** $p < 0.001$, **** $p < 0.0001$.

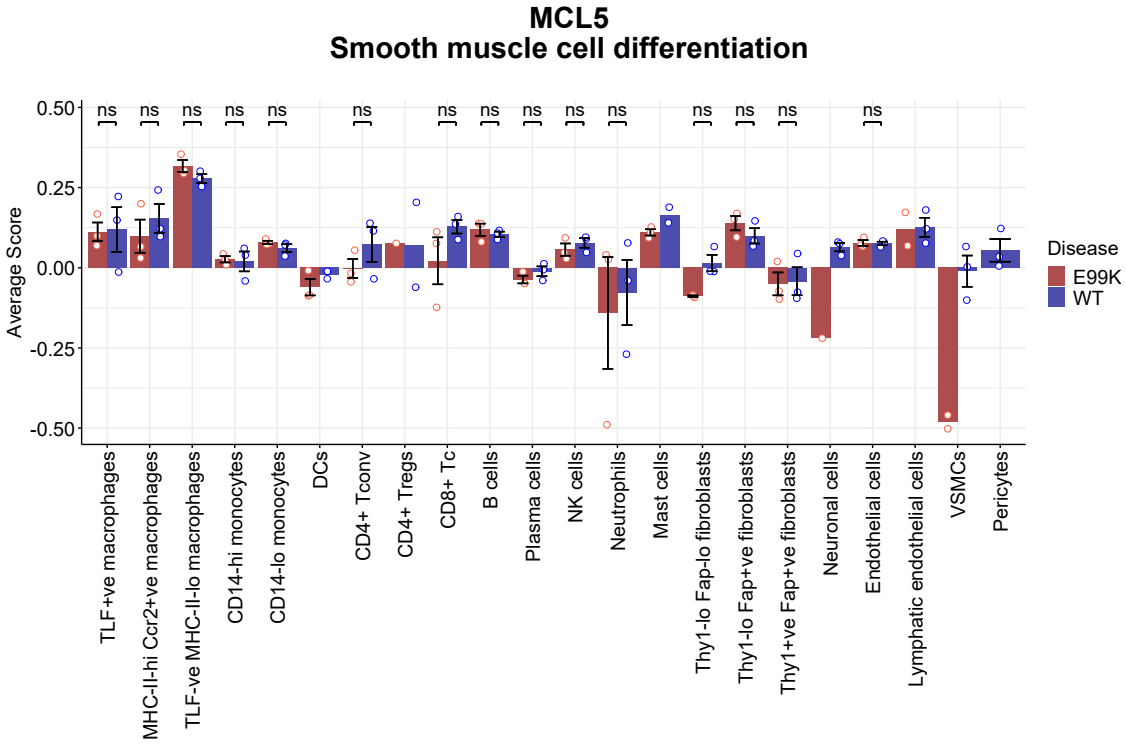

Figure F.6. Gene set scoring for MCL sub-cluster 5 of Cluster 7 (early upregulation followed by late decline) in late-stage mouse cell types.
This sub-cluster is a constituent of Cluster 7. The bar chart displays the gene set score for this specific sub-cluster across various cell types from early-stage Actc1^{E99K} mouse scRNA-seq data. Scores were calculated for each sample using the `score_genes` function in `scanpy` v1.10.1 [267]. Bars represent the mean score, with error bars indicating the standard error of the mean. Statistical significance between disease and control samples was determined using a t-test, with p-values adjusted for multiple comparisons using the Benjamini-Hochberg method. Asterisks denote significance levels: * $p < 0.05$, ** $p < 0.01$, *** $p < 0.001$, **** $p < 0.0001$.

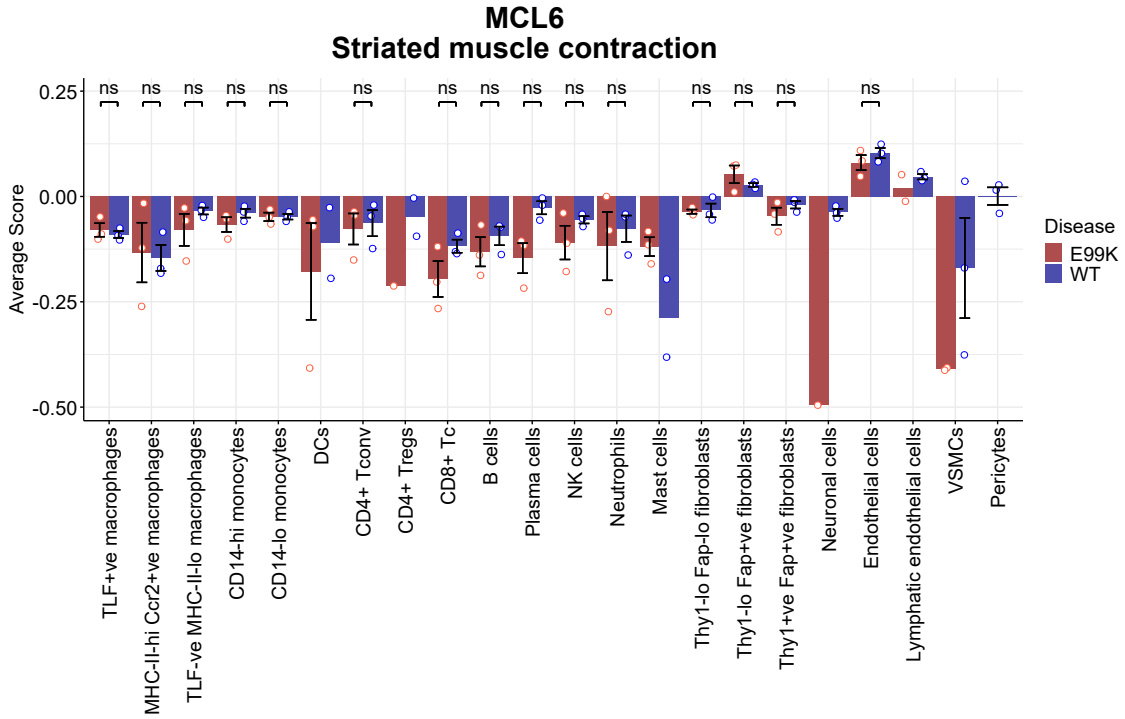

Figure F.7. Gene set scoring for MCL sub-cluster 6 of Cluster 7 (early upregulation followed by late decline) in late-stage mouse cell types. This sub-cluster is a constituent of Cluster 7. The bar chart displays the gene set score for this specific sub-cluster across various cell types from early-stage Actc1^{E99K} mouse scRNA-seq data. Scores were calculated for each sample using the `score_genes` function in `scanpy` v1.10.1 [267]. Bars represent the mean score, with error bars indicating the standard error of the mean. Statistical significance between disease and control samples was determined using a t-test, with p-values adjusted for multiple comparisons using the Benjamini-Hochberg method. Asterisks denote significance levels: * $p < 0.05$, ** $p < 0.01$, *** $p < 0.001$, **** $p < 0.0001$.

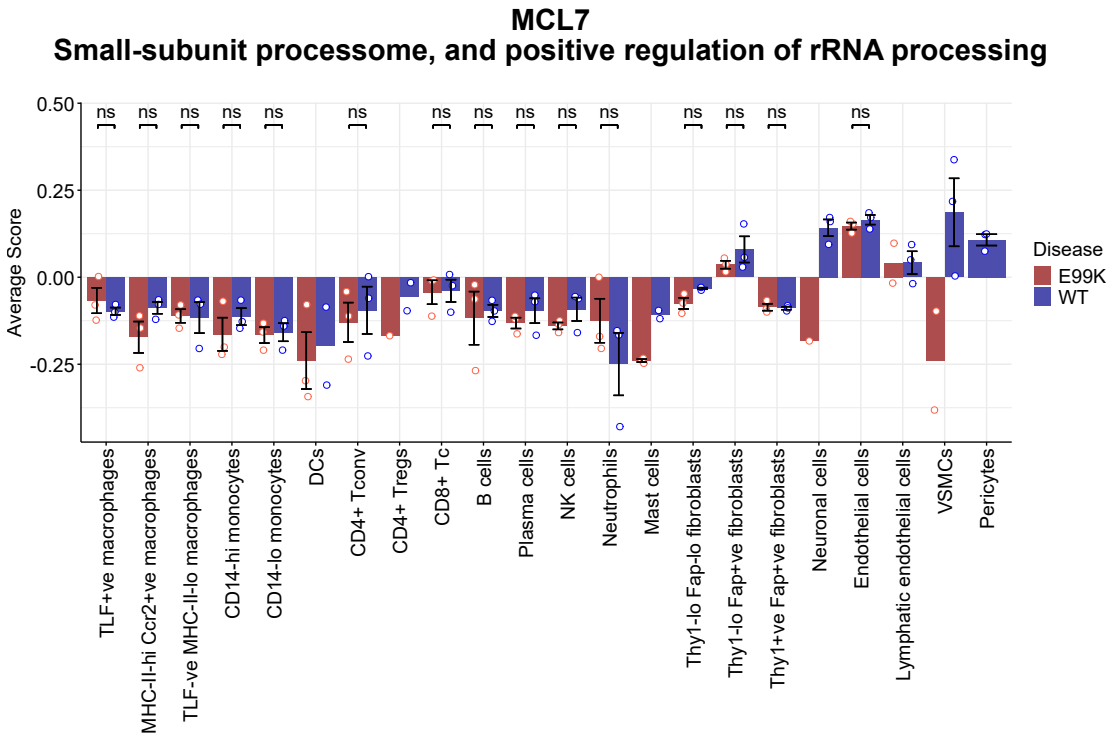

Figure F.8. Gene set scoring for MCL sub-cluster 7 of Cluster 7 (early upregulation followed by late decline) in late-stage mouse cell types. This sub-cluster is a constituent of Cluster 7. The bar chart displays the gene set score for this specific sub-cluster across various cell types from early-stage Actc1^{E99K} mouse scRNA-seq data. Scores were calculated for each sample using the `score_genes` function in `scanpy` v1.10.1 [267]. Bars represent the mean score, with error bars indicating the standard error of the mean. Statistical significance between disease and control samples was determined using a t-test, with p-values adjusted for multiple comparisons using the Benjamini-Hochberg method. Asterisks denote significance levels: * $p < 0.05$, ** $p < 0.01$, *** $p < 0.001$, **** $p < 0.0001$.

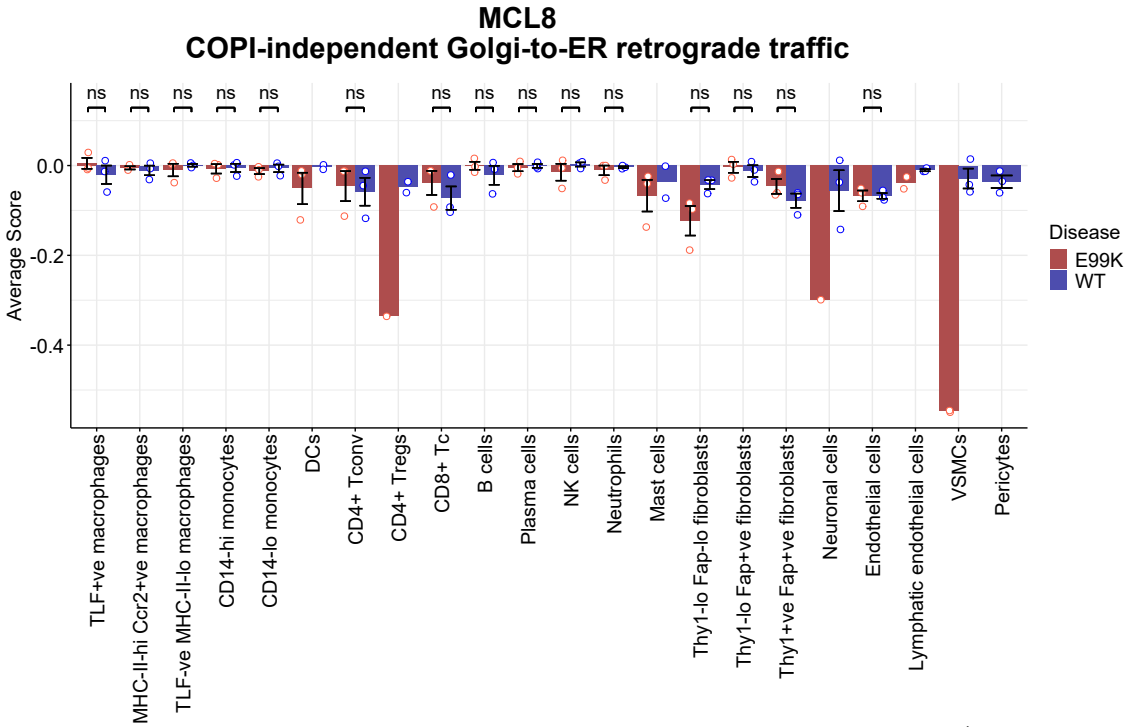

Figure F.9. Gene set scoring for MCL sub-cluster 8 of Cluster 7 (early upregulation followed by late decline) in late-stage mouse cell types. This sub-cluster is a constituent of Cluster 7. The bar chart displays the gene set score for this specific sub-cluster across various cell types from early-stage Actc1^{E99K} mouse scRNA-seq data. Scores were calculated for each sample using the `score_genes` function in `scanpy` v1.10.1 [267]. Bars represent the mean score, with error bars indicating the standard error of the mean. Statistical significance between disease and control samples was determined using a t-test, with p-values adjusted for multiple comparisons using the Benjamini-Hochberg method. Asterisks denote significance levels: * $p < 0.05$, ** $p < 0.01$, *** $p < 0.001$, **** $p < 0.0001$.

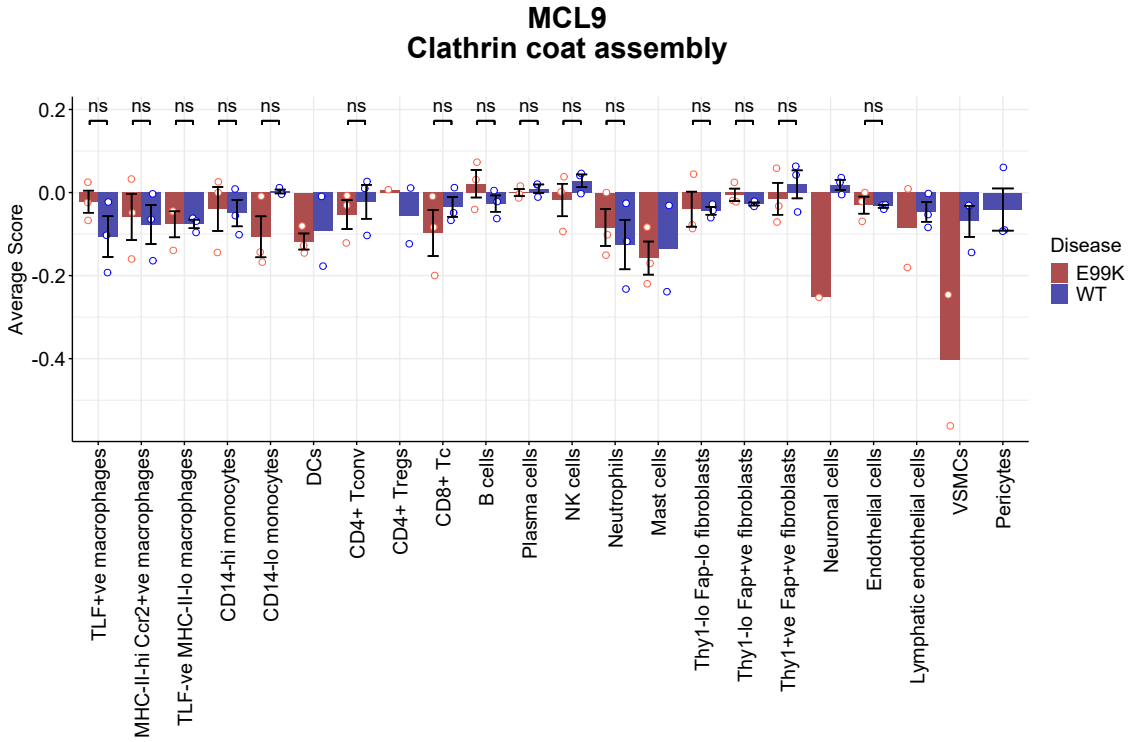

Figure F.10. Gene set scoring for MCL sub-cluster 9 of Cluster 7 (early upregulation followed by late decline) in late-stage mouse cell types. This sub-cluster is a constituent of Cluster 7. The bar chart displays the gene set score for this specific sub-cluster across various cell types from early-stage Actc1^{E99K} mouse scRNA-seq data. Scores were calculated for each sample using the `score_genes` function in `scanpy` v1.10.1 [267]. Bars represent the mean score, with error bars indicating the standard error of the mean. Statistical significance between disease and control samples was determined using a t-test, with p-values adjusted for multiple comparisons using the Benjamini-Hochberg method. Asterisks denote significance levels: * $p < 0.05$, ** $p < 0.01$, *** $p < 0.001$, **** $p < 0.0001$.

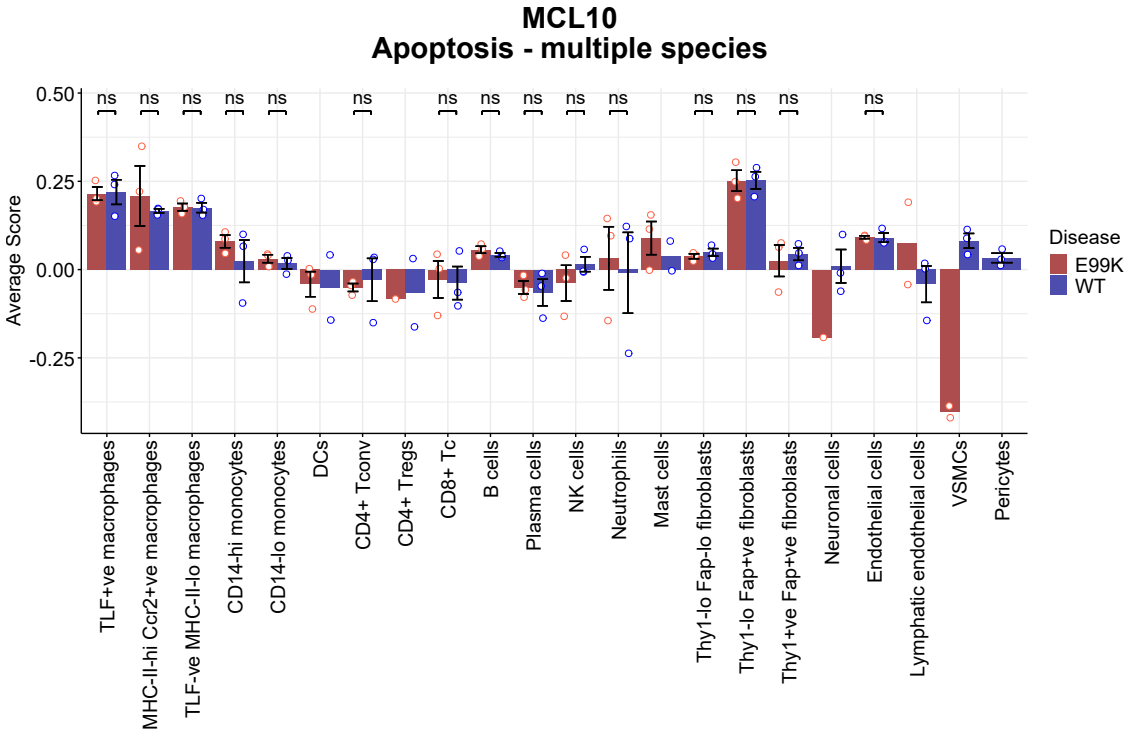

Figure F.11. Gene set scoring for MCL sub-cluster 10 of Cluster 7 (early upregulation followed by late decline) in late-stage mouse cell types. This sub-cluster is a constituent of Cluster 7. The bar chart displays the gene set score for this specific sub-cluster across various cell types from early-stage Actc1^{E99K} mouse scRNA-seq data. Scores were calculated for each sample using the `score_genes` function in `scanpy` v1.10.1 [267]. Bars represent the mean score, with error bars indicating the standard error of the mean. Statistical significance between disease and control samples was determined using a t-test, with p-values adjusted for multiple comparisons using the Benjamini-Hochberg method. Asterisks denote significance levels: * $p < 0.05$, ** $p < 0.01$, *** $p < 0.001$, **** $p < 0.0001$.

F.2 Cluster 11 & 12: Biphasic expression patterns reflect shifting cellular homeostasis

Cluster 11, exhibiting a U-shaped temporal expression pattern with down-regulation in the mid-stage and up-regulation in both early and late stages of HCM, also encompassed a diverse range of functions (Figure F.12). Sub-cluster analysis revealed enrichment for processes such as the regulation of transcription from RNA polymerase II promoter in response to stress (MCL sub-cluster 1; Figure F.13), HDR through homologous recombination (MCL sub-cluster 2; Figure F.14), ceramide metabolism (MCL sub-cluster 3; Figure F.15), RHO GTPases activat-

ing WASPs and WAVEs (MCL sub-cluster 4; Figure F.16), polysomal ribosome (MCL sub-cluster 5; Figure F.17), a mixed sub-cluster including homeobox genes (MCL sub-cluster 6; Figure F.18), procollagen-proline dioxygenase activity (MCL sub-cluster 7; Figure F.19), response to interleukin-18 (MCL sub-cluster 8; Figure F.20), nuclear-transcribed mRNA catabolism and NMD (MCL sub-cluster 9; Figure F.21), and the tubulin/FtsZ family, C-terminal domain (MCL sub-cluster 10; Figure F.22). In early-stage Actc1^{E99K} mouse hearts, the overall Cluster 11 signature was significantly down-regulated in endothelial cells and *Thy1*$^{+}$*Fap*$^{+}$ fibroblasts (Figure F.12). Further investigation of the individual sub-clusters revealed that the regulation of transcription sub-cluster was up-regulated in *Thy1*^{lo}*Fap*^{lo} fibroblasts and *Thy1*^{lo}*Fap*$^{+}$ fibroblasts, and also up-regulated in TLF^{-}MHC-II^{lo} macrophages (MCL sub-cluster 1; Figure F.13). The ceramide metabolism sub-cluster was down-regulated in CD14^{hi} monocytes (MCL sub-cluster 3; Figure F.15). The mixed homeobox sub-cluster was down-regulated in TLF^{-}MHC-II^{lo} macrophages (MCL sub-cluster 6; Figure F.18). The procollagen-proline dioxygenase activity sub-cluster was down-regulated in *Thy1*^{lo}*Fap*^{lo} fibroblasts (MCL sub-cluster 7; Figure F.19). The response to interleukin-18 sub-cluster was down-regulated in TLF^{-}MHC-II^{lo} macrophages (MCL sub-cluster 8; Figure F.20). Finally, the nuclear-transcribed mRNA catabolism and NMD sub-cluster was up-regulated in endothelial cells (MCL sub-cluster 9; Figure F.21). The remaining sub-clusters did not show significant differential expression in any cell type within the early-stage Actc1^{E99K} mouse data.

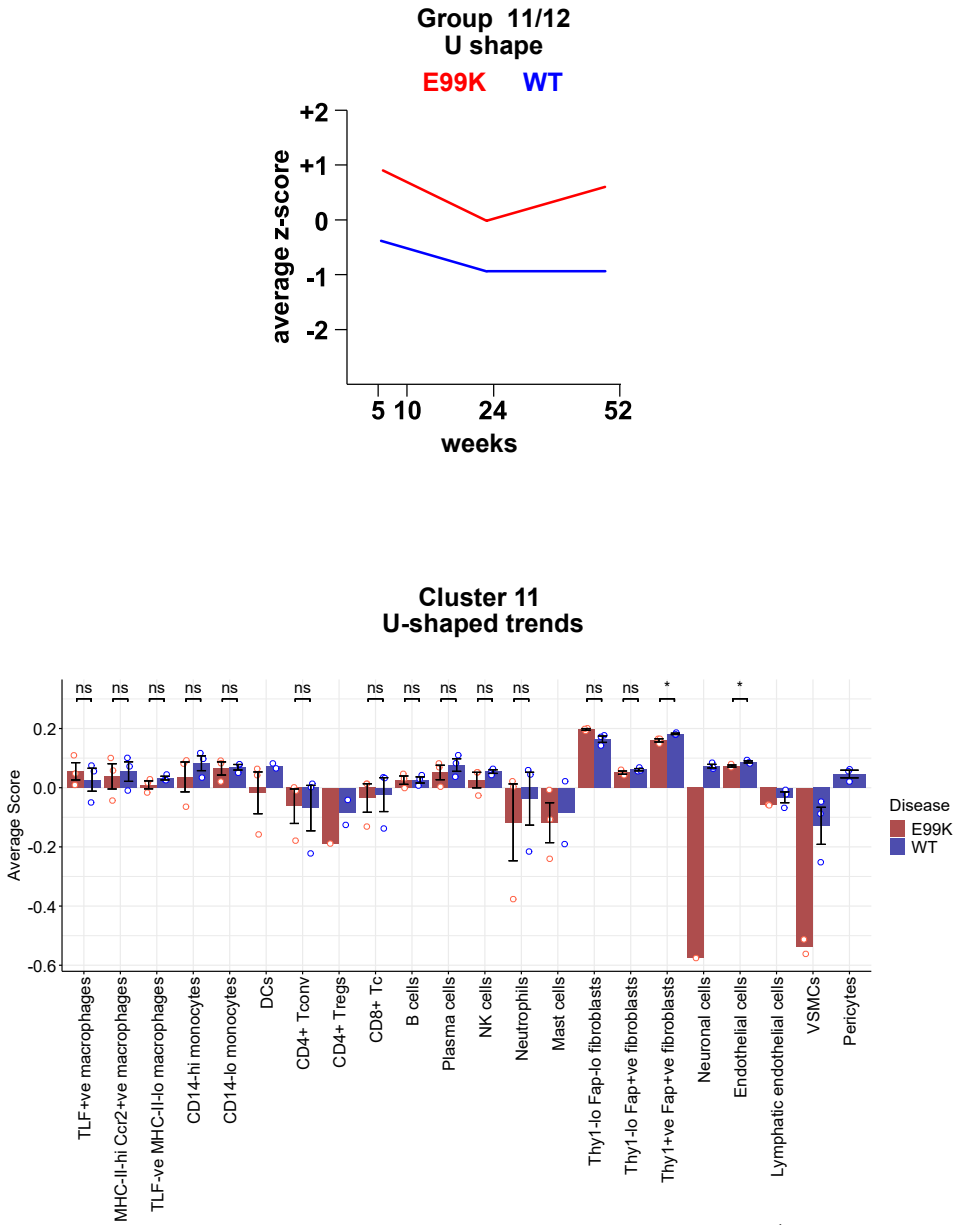

Figure F.12. Gene set scoring and statistics of Cluster 11 (U-shaped trends) in late-stage mouse cell types.
The upper panel schematically illustrates the temporal expression trend for Cluster 11, derived from bulk RNA-seq data of Actc1^{E99K} (red line) and wild-type (blue line) hearts over time. The lower panel displays the gene set score for all genes within Cluster 11 across various cell types identified in early-stage Actc1^{E99K} mouse scRNA-seq data. Scores were calculated for each sample using the `score_genes` function in `scanpy` v1.10.1 [267]. Bars represent the mean score, with error bars indicating the standard error of the mean. Statistical significance between disease and control samples was determined using a t-test, with p-values adjusted for multiple comparisons using the Benjamini-Hochberg method. Asterisks denote significance levels: * $p < 0.05$, ** $p < 0.01$, *** $p < 0.001$, **** $p < 0.0001$.

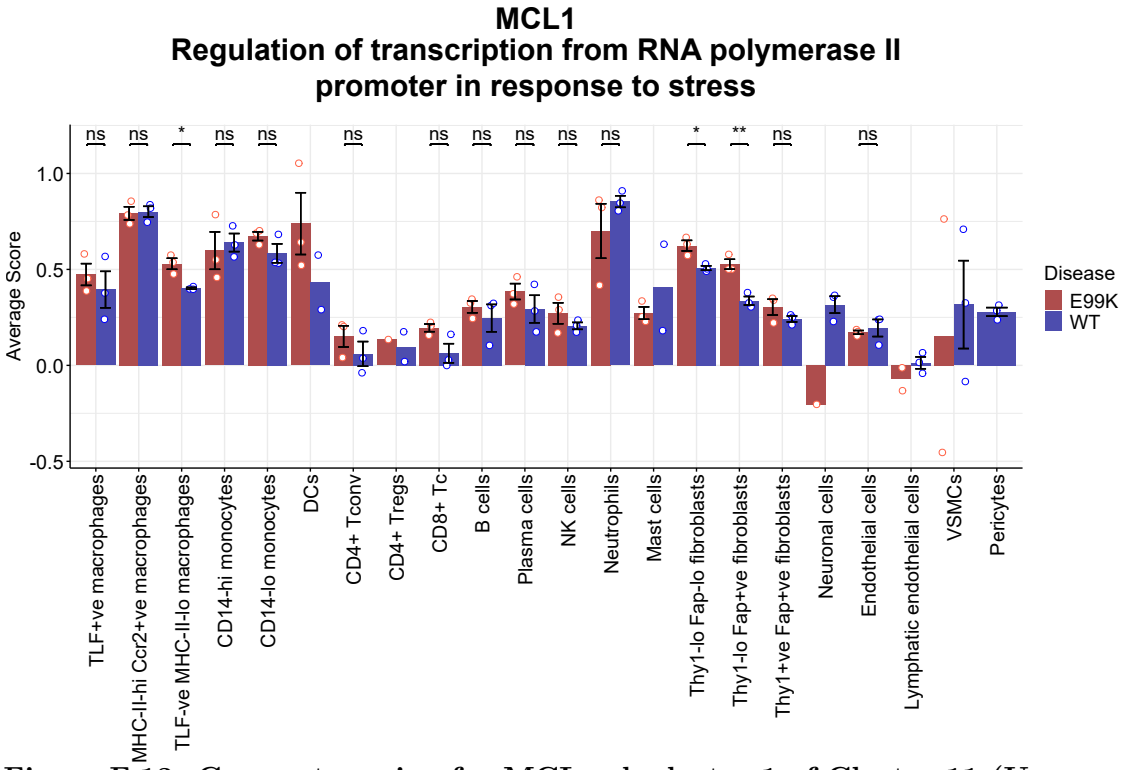

Figure F.13. Gene set scoring for MCL sub-cluster 1 of Cluster 11 (U-shaped trends) in late-stage mouse cell types.
This sub-cluster is a constituent of Cluster 11. The bar chart displays the gene set score for this specific sub-cluster across various cell types from early-stage Actc1^{E99K} mouse scRNA-seq data. Scores were calculated for each sample using the `score_genes` function in `scanpy` v1.10.1 [267]. Bars represent the mean score, with error bars indicating the standard error of the mean. Statistical significance between disease and control samples was determined using a t-test, with p-values adjusted for multiple comparisons using the Benjamini-Hochberg method. Asterisks denote significance levels: * $p < 0.05$, ** $p < 0.01$, *** $p < 0.001$, **** $p < 0.0001$.

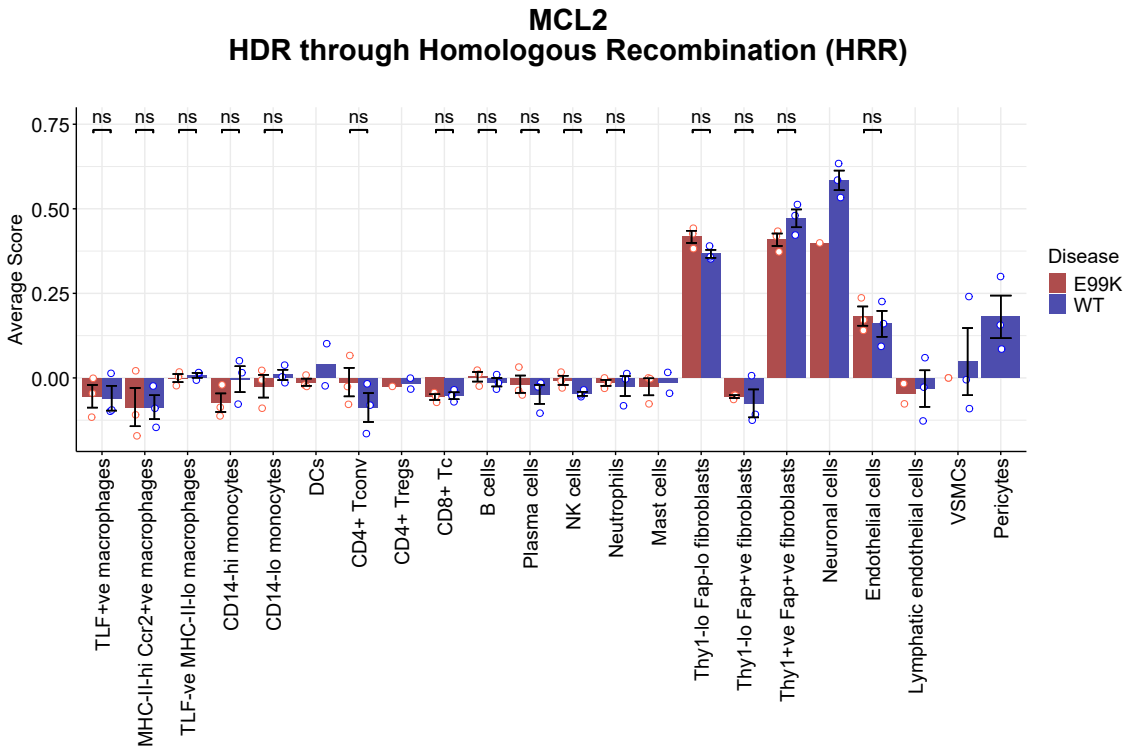

Figure F.14. Gene set scoring for MCL sub-cluster 2 of Cluster 11 (U-shaped trends) in late-stage mouse cell types.
This sub-cluster is a constituent of Cluster 11. The bar chart displays the gene set score for this specific sub-cluster across various cell types from early-stage Actc1^{E99K} mouse scRNA-seq data. Scores were calculated for each sample using the `score_genes` function in `scanpy` v1.10.1 [267]. Bars represent the mean score, with error bars indicating the standard error of the mean. Statistical significance between disease and control samples was determined using a t-test, with p-values adjusted for multiple comparisons using the Benjamini-Hochberg method. Asterisks denote significance levels: * $p < 0.05$, ** $p < 0.01$, *** $p < 0.001$, **** $p < 0.0001$.

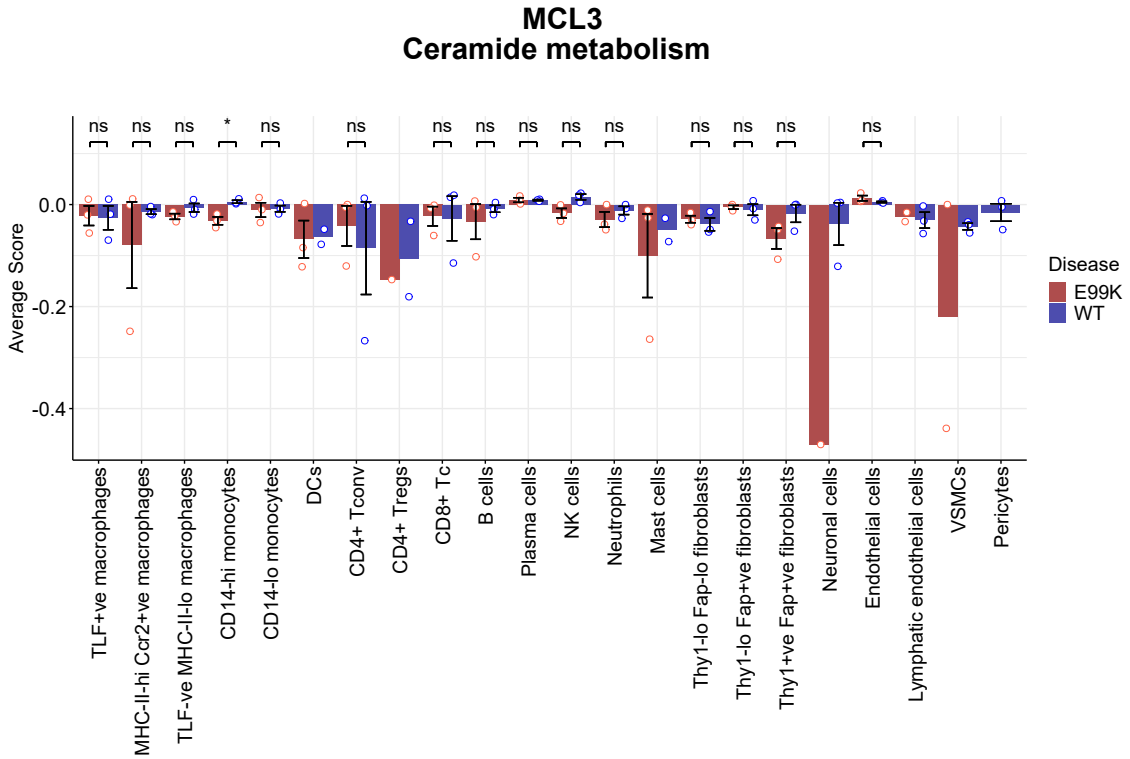

Figure F.15. Gene set scoring for MCL sub-cluster 3 of Cluster 11 (U-shaped trends) in late-stage mouse cell types.
This sub-cluster is a constituent of Cluster 11. The bar chart displays the gene set score for this specific sub-cluster across various cell types from early-stage Actc1^{E99K} mouse scRNA-seq data. Scores were calculated for each sample using the `score_genes` function in `scanpy` v1.10.1 [267]. Bars represent the mean score, with error bars indicating the standard error of the mean. Statistical significance between disease and control samples was determined using a t-test, with p-values adjusted for multiple comparisons using the Benjamini-Hochberg method. Asterisks denote significance levels: * $p < 0.05$, ** $p < 0.01$, *** $p < 0.001$, **** $p < 0.0001$.

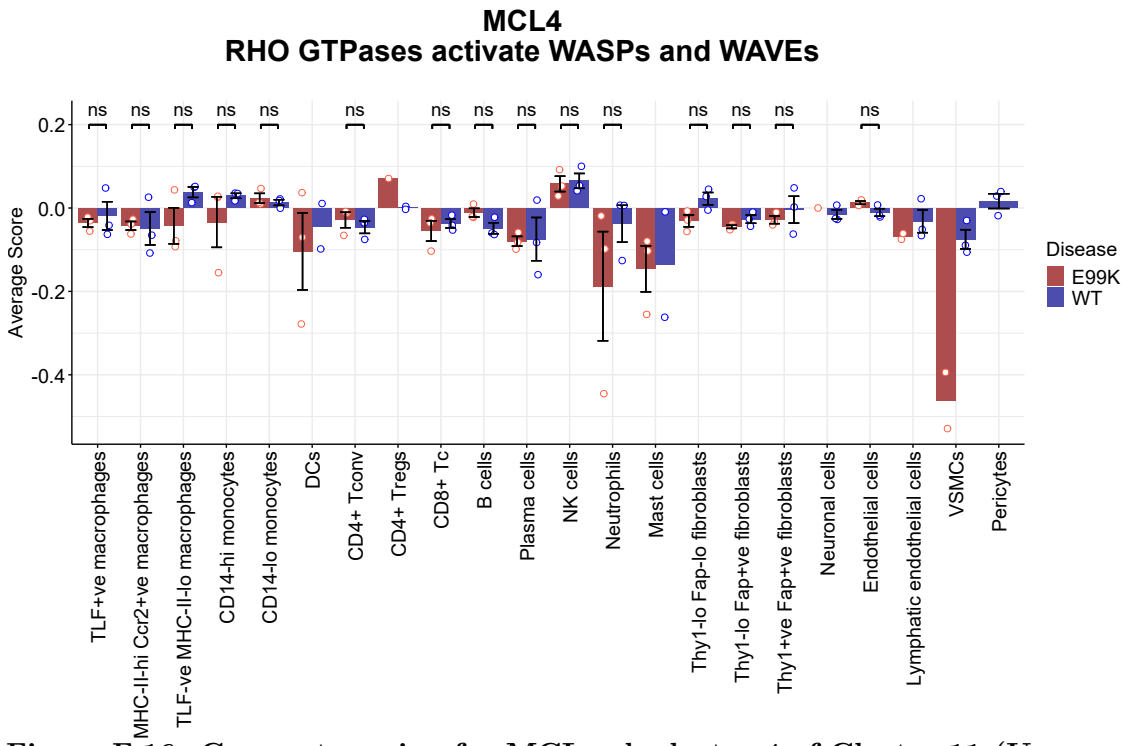

Figure F.16. Gene set scoring for MCL sub-cluster 4 of Cluster 11 (U-shaped trends) in late-stage mouse cell types.
This sub-cluster is a constituent of Cluster 11. The bar chart displays the gene set score for this specific sub-cluster across various cell types from early-stage Actc1^{E99K} mouse scRNA-seq data. Scores were calculated for each sample using the `score_genes` function in `scanpy` v1.10.1 [267]. Bars represent the mean score, with error bars indicating the standard error of the mean. Statistical significance between disease and control samples was determined using a t-test, with p-values adjusted for multiple comparisons using the Benjamini-Hochberg method. Asterisks denote significance levels: * $p < 0.05$, ** $p < 0.01$, *** $p < 0.001$, **** $p < 0.0001$.

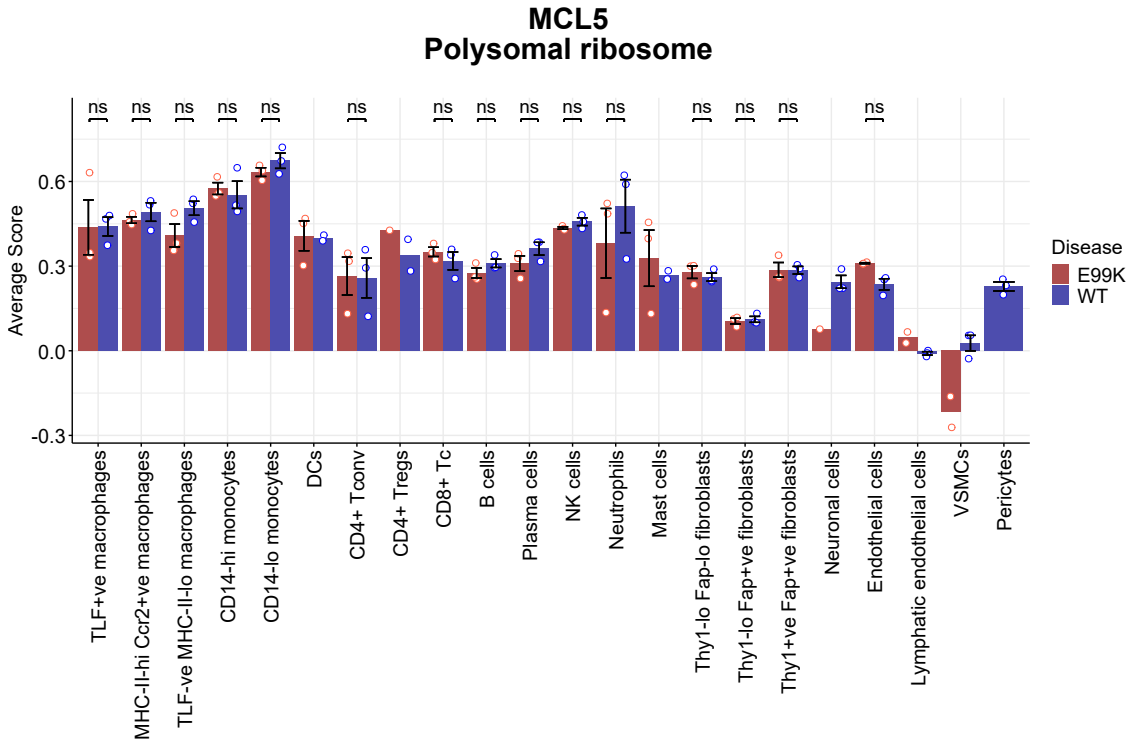

Figure F.17. Gene set scoring for MCL sub-cluster 5 of Cluster 11 (U-shaped trends) in late-stage mouse cell types.
This sub-cluster is a constituent of Cluster 11. The bar chart displays the gene set score for this specific sub-cluster across various cell types from early-stage Actc1^{E99K} mouse scRNA-seq data. Scores were calculated for each sample using the `score_genes` function in `scanpy` v1.10.1 [267]. Bars represent the mean score, with error bars indicating the standard error of the mean. Statistical significance between disease and control samples was determined using a t-test, with p-values adjusted for multiple comparisons using the Benjamini-Hochberg method. Asterisks denote significance levels: * $p < 0.05$, ** $p < 0.01$, *** $p < 0.001$, **** $p < 0.0001$.

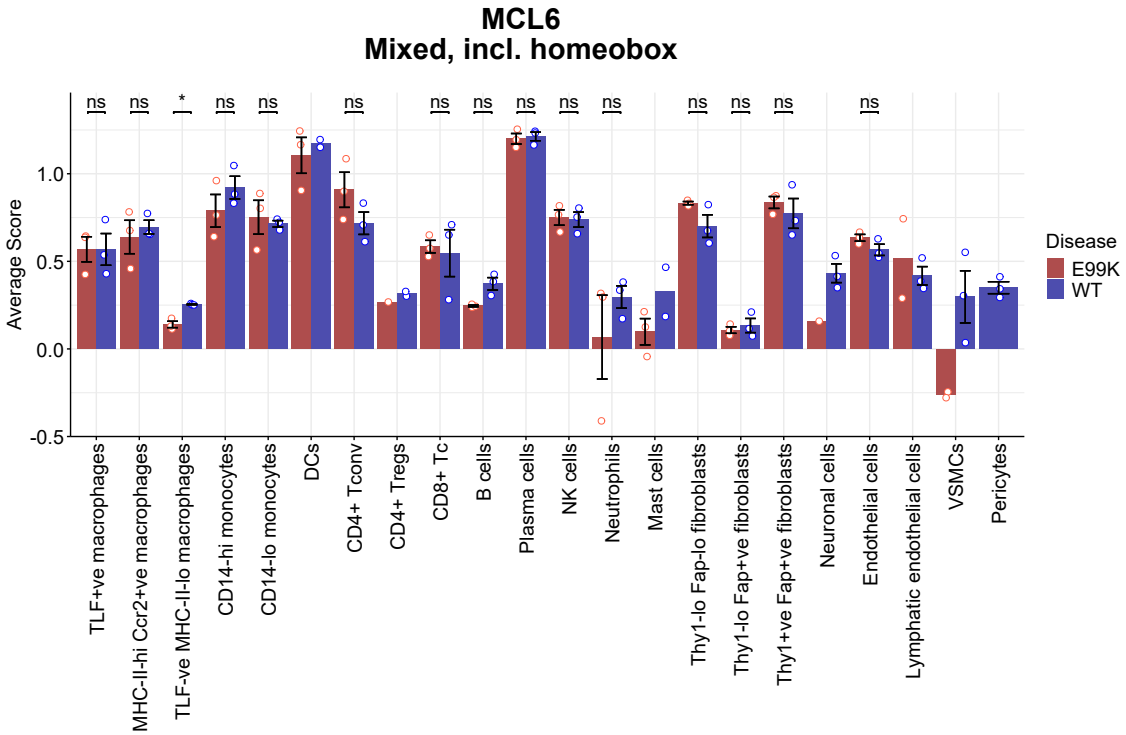

Figure F.18. Gene set scoring for MCL sub-cluster 6 of Cluster 11 (U-shaped trends) in late-stage mouse cell types.
This sub-cluster is a constituent of Cluster 11. The bar chart displays the gene set score for this specific sub-cluster across various cell types from early-stage Actc1^{E99K} mouse scRNA-seq data. Scores were calculated for each sample using the `score_genes` function in `scanpy` v1.10.1 [267]. Bars represent the mean score, with error bars indicating the standard error of the mean. Statistical significance between disease and control samples was determined using a t-test, with p-values adjusted for multiple comparisons using the Benjamini-Hochberg method. Asterisks denote significance levels: * $p < 0.05$, ** $p < 0.01$, *** $p < 0.001$, **** $p < 0.0001$.

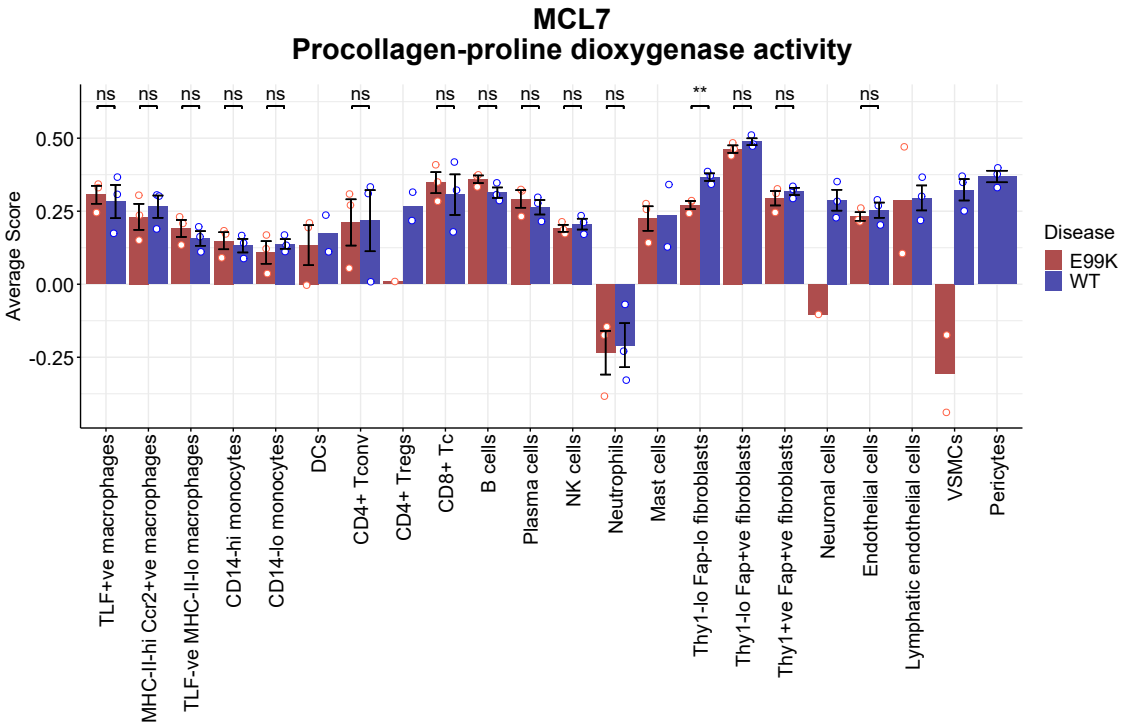

Figure F.19. Gene set scoring for MCL sub-cluster 7 of Cluster 11 (U-shaped trends) in late-stage mouse cell types.
This sub-cluster is a constituent of Cluster 11. The bar chart displays the gene set score for this specific sub-cluster across various cell types from early-stage Actc1^{E99K} mouse scRNA-seq data. Scores were calculated for each sample using the `score_genes` function in `scanpy` v1.10.1 [267]. Bars represent the mean score, with error bars indicating the standard error of the mean. Statistical significance between disease and control samples was determined using a t-test, with p-values adjusted for multiple comparisons using the Benjamini-Hochberg method. Asterisks denote significance levels: * $p < 0.05$, ** $p < 0.01$, *** $p < 0.001$, **** $p < 0.0001$.

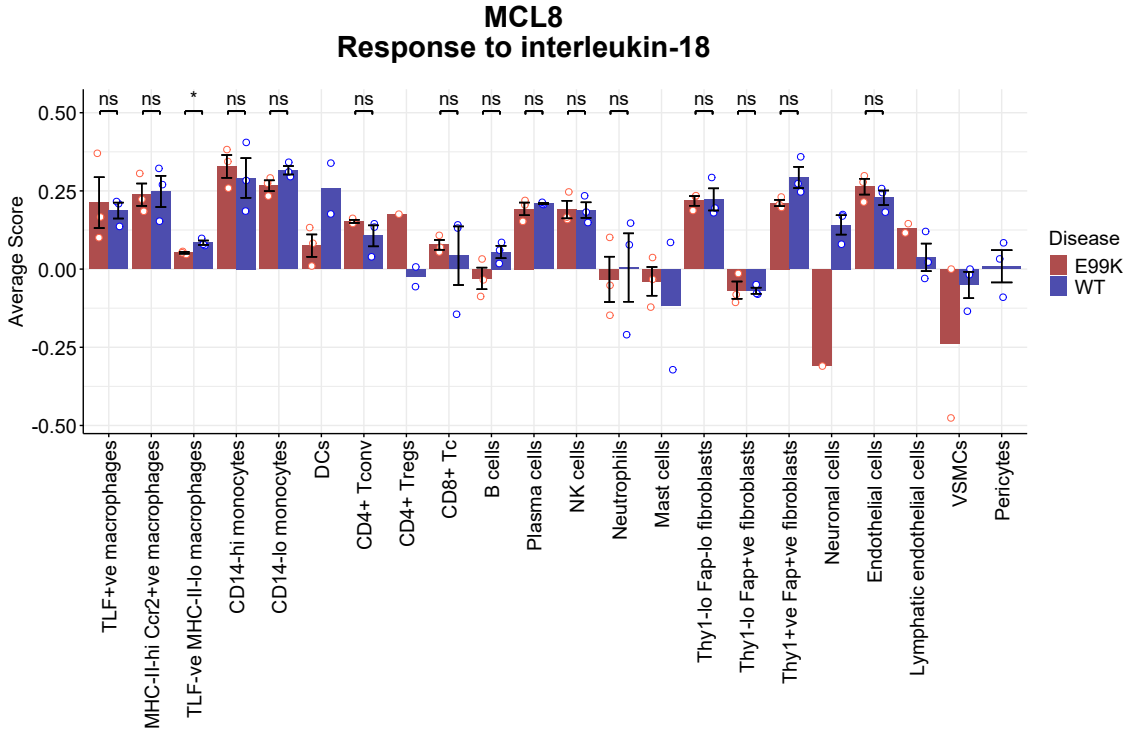

Figure F.20. Gene set scoring for MCL sub-cluster 8 of Cluster 11 (U-shaped trends) in late-stage mouse cell types.
This sub-cluster is a constituent of Cluster 11. The bar chart displays the gene set score for this specific sub-cluster across various cell types from early-stage Actc1^{E99K} mouse scRNA-seq data. Scores were calculated for each sample using the `score_genes` function in `scanpy` v1.10.1 [267]. Bars represent the mean score, with error bars indicating the standard error of the mean. Statistical significance between disease and control samples was determined using a t-test, with p-values adjusted for multiple comparisons using the Benjamini-Hochberg method. Asterisks denote significance levels: * $p < 0.05$, ** $p < 0.01$, *** $p < 0.001$, **** $p < 0.0001$.

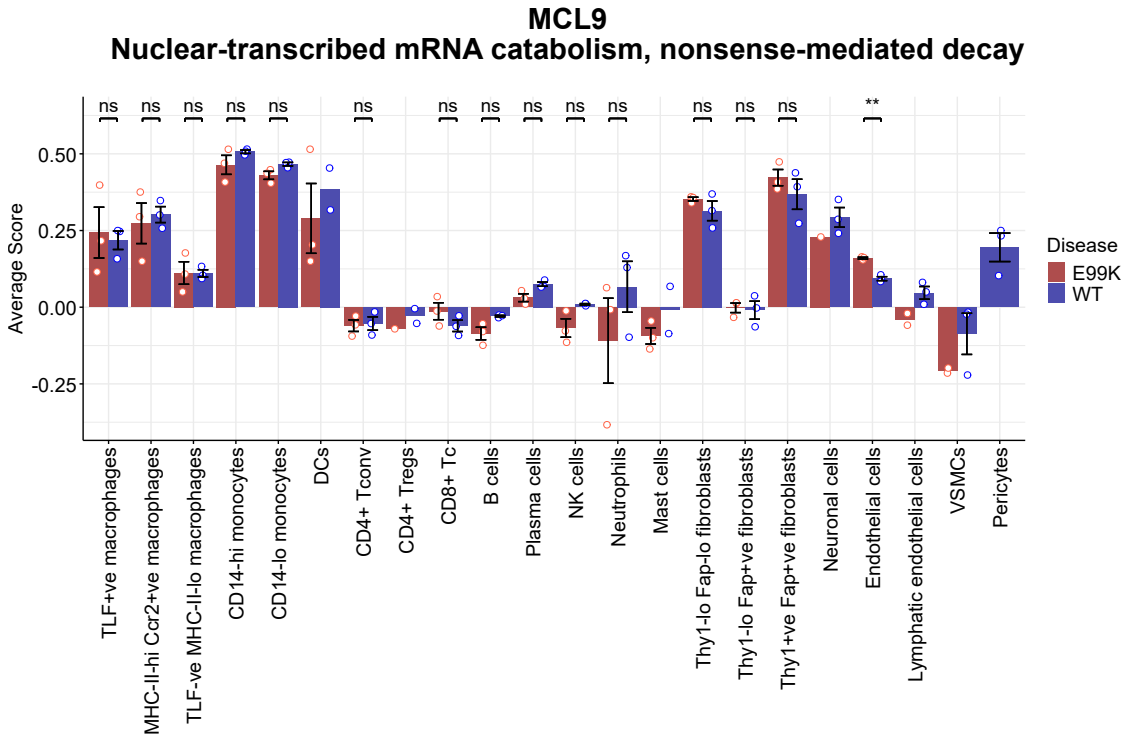

Figure F.21. Gene set scoring for MCL sub-cluster 9 of Cluster 11 (U-shaped trends) in late-stage mouse cell types.
This sub-cluster is a constituent of Cluster 11. The bar chart displays the gene set score for this specific sub-cluster across various cell types from early-stage Actc1^{E99K} mouse scRNA-seq data. Scores were calculated for each sample using the `score_genes` function in `scanpy` v1.10.1 [267]. Bars represent the mean score, with error bars indicating the standard error of the mean. Statistical significance between disease and control samples was determined using a t-test, with p-values adjusted for multiple comparisons using the Benjamini-Hochberg method. Asterisks denote significance levels: * $p < 0.05$, ** $p < 0.01$, *** $p < 0.001$, **** $p < 0.0001$.

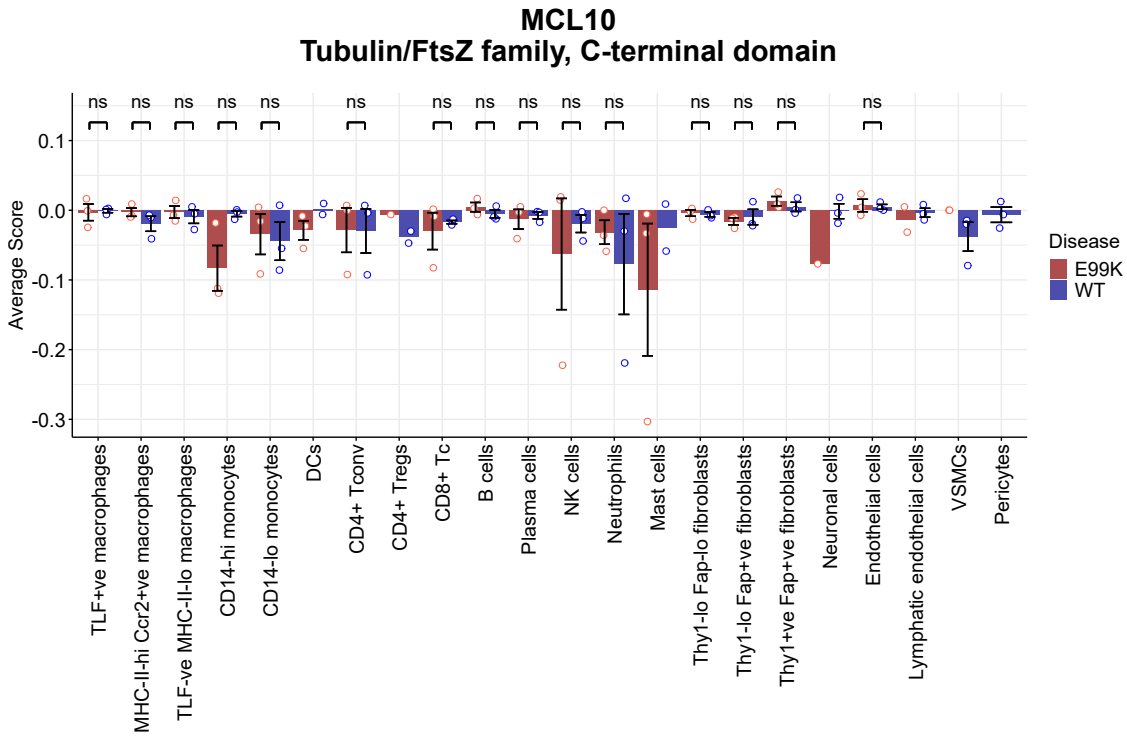

Figure F.22. Gene set scoring for MCL sub-cluster 10 of Cluster 11 (U-shaped trends) in late-stage mouse cell types.
This sub-cluster is a constituent of Cluster 11. The bar chart displays the gene set score for this specific sub-cluster across various cell types from early-stage Actc1^{E99K} mouse scRNA-seq data. Scores were calculated for each sample using the `score_genes` function in `scanpy` v1.10.1 [267]. Bars represent the mean score, with error bars indicating the standard error of the mean. Statistical significance between disease and control samples was determined using a t-test, with p-values adjusted for multiple comparisons using the Benjamini-Hochberg method. Asterisks denote significance levels: * $p < 0.05$, ** $p < 0.01$, *** $p < 0.001$, **** $p < 0.0001$.

Cluster 12, the final cluster exhibiting a U-shaped trend, was primarily associated with cell cycle regulation (Figure F.23). The dominant sub-cluster was enriched for genes involved in the mitotic spindle checkpoint and mitotic sister chromatid segregation (MCL sub-cluster 1; Figure F.24). Two smaller sub-clusters were identified, one uncharacterised (MCL sub-cluster 2; Figure F.25) and the other related to the tenascin complex (MCL sub-cluster 2; Figure F.25). Given the limited number of genes in these smaller sub-clusters, the focus here remains on the larger, functionally defined sub-cluster related to the mitotic spindle checkpoint (MCL sub-cluster 1; Figure F.24). In early-stage Actc1^{E99K} mice, neither the overall Cluster 12 signature nor its dominant sub-cluster showed sig-

nificant changes in expression across the analysed cell populations. This suggests that while cell cycle-related genes exhibit dynamic regulation throughout the course of HCM progression, these changes are not prominently reflected within the non-cardiomyocyte populations at this early stage of the disease in the Actc1^{E99K} mouse model.

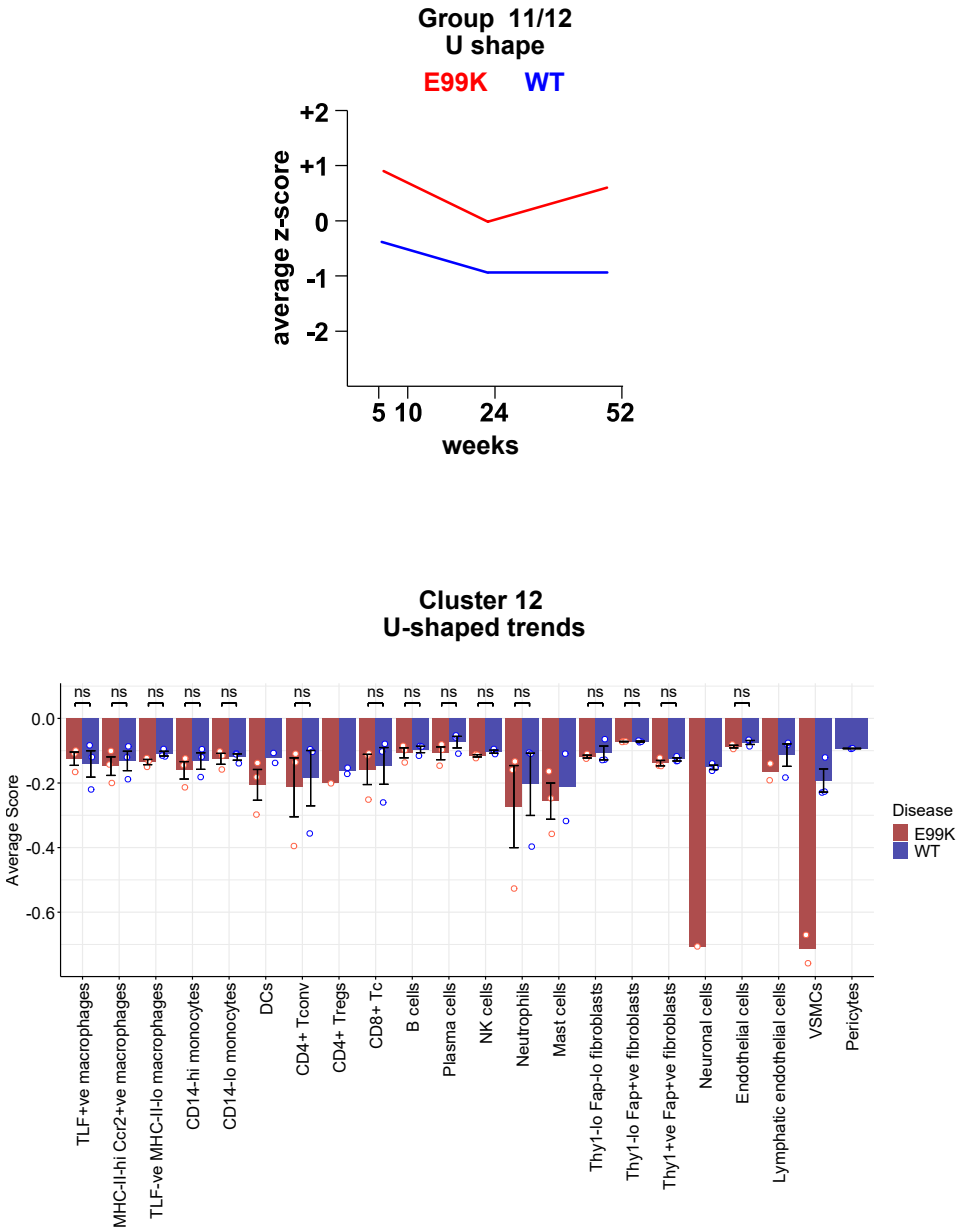

Figure F.23. Gene set scoring and statistics of Cluster 12 (U-shaped trends) in late-stage mouse cell types.

The upper panel schematically illustrates the temporal expression trend for Cluster 12, derived from bulk RNA-seq data of Actc1^{E99K} (red line) and wild-type (blue line) hearts over time. The lower panel displays the gene set score for all genes within Cluster 12 across various cell types identified in early-stage Actc1^{E99K} mouse scRNA-seq data. Scores were calculated for each sample using the `score_genes` function in `scanpy` v1.10.1 [267]. Bars represent the mean score, with error bars indicating the standard error of the mean. Statistical significance between disease and control samples was determined using a t-test, with p-values adjusted for multiple comparisons using the Benjamini-Hochberg method. Asterisks denote significance levels: * $p < 0.05$, ** $p < 0.01$, *** $p < 0.001$, **** $p < 0.0001$.

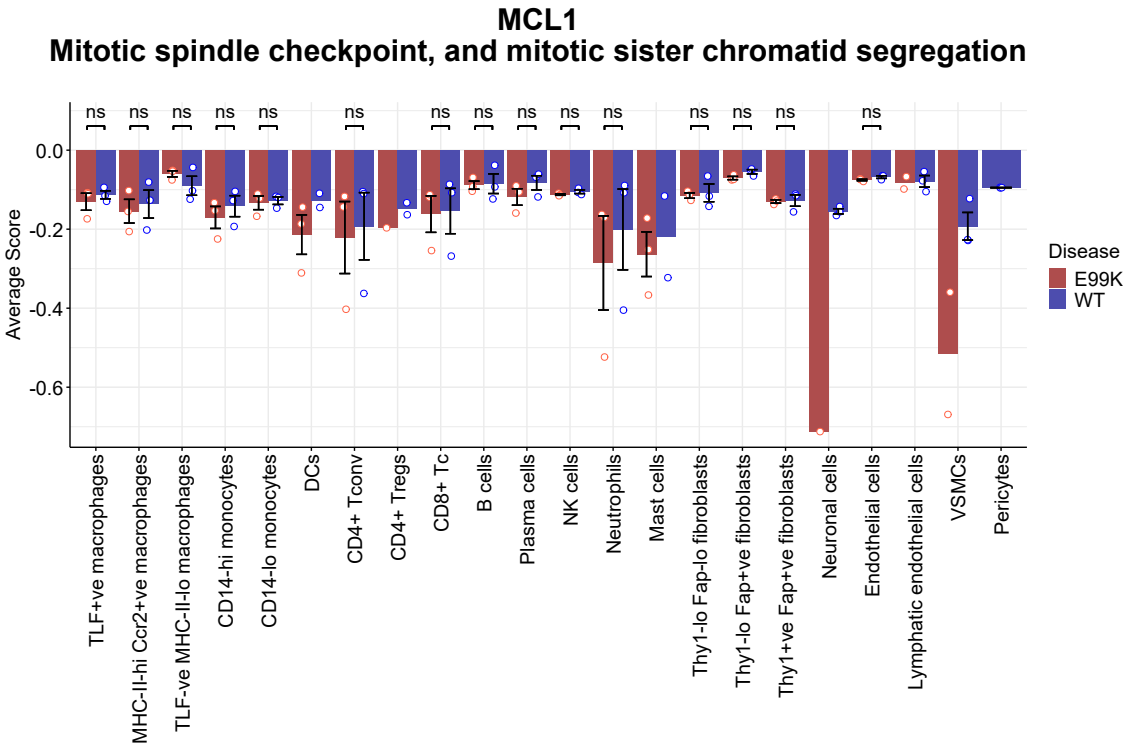

Figure F.24. Gene set scoring for MCL sub-cluster 1 of Cluster 12 (U-shaped trends) in late-stage mouse cell types.
This sub-cluster is a constituent of Cluster 12. The bar chart displays the gene set score for this specific sub-cluster across various cell types from early-stage Actc1^{E99K} mouse scRNA-seq data. Scores were calculated for each sample using the `score_genes` function in `scanpy` v1.10.1 [267]. Bars represent the mean score, with error bars indicating the standard error of the mean. Statistical significance between disease and control samples was determined using a t-test, with p-values adjusted for multiple comparisons using the Benjamini-Hochberg method. Asterisks denote significance levels: * $p < 0.05$, ** $p < 0.01$, *** $p < 0.001$, **** $p < 0.0001$.

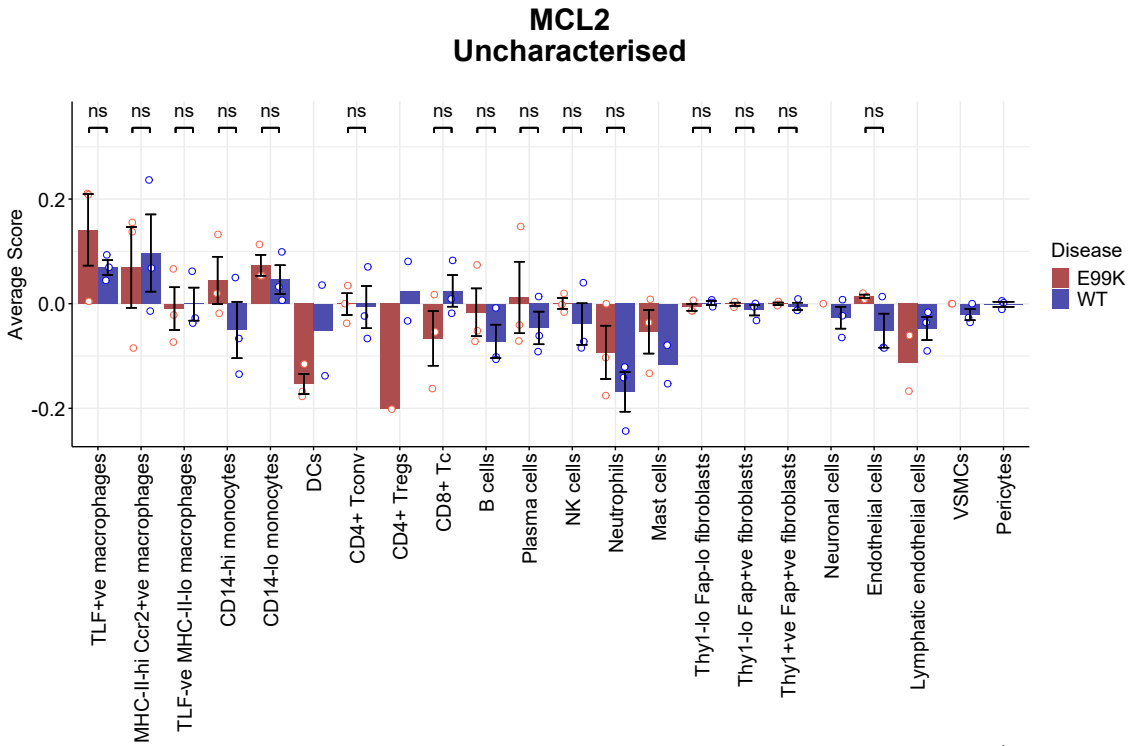

Figure F.25. Gene set scoring for MCL sub-cluster 2 of Cluster 12 (U-shaped trends) in late-stage mouse cell types.
This sub-cluster is a constituent of Cluster 12. The bar chart displays the gene set score for this specific sub-cluster across various cell types from early-stage Actc1^{E99K} mouse scRNA-seq data. Scores were calculated for each sample using the `score_genes` function in `scanpy` v1.10.1 [267]. Bars represent the mean score, with error bars indicating the standard error of the mean. Statistical significance between disease and control samples was determined using a t-test, with p-values adjusted for multiple comparisons using the Benjamini-Hochberg method. Asterisks denote significance levels: * $p < 0.05$, ** $p < 0.01$, *** $p < 0.001$, **** $p < 0.0001$.

In summary, this integrative analysis, combining temporal bulk RNA-seq data with early-stage single-cell data from the Actc1^{E99K} mouse model, has highlighted several cell type-specific transcriptional changes that occur prior to the onset of overt fibrosis. While the absence of cardiomyocytes in the single-cell dataset limits the interpretation of these findings, the observed changes in fibroblast, macrophage, monocyte, and endothelial cell populations suggest that these cell types may play a crucial role in the early stages of HCM pathogenesis.

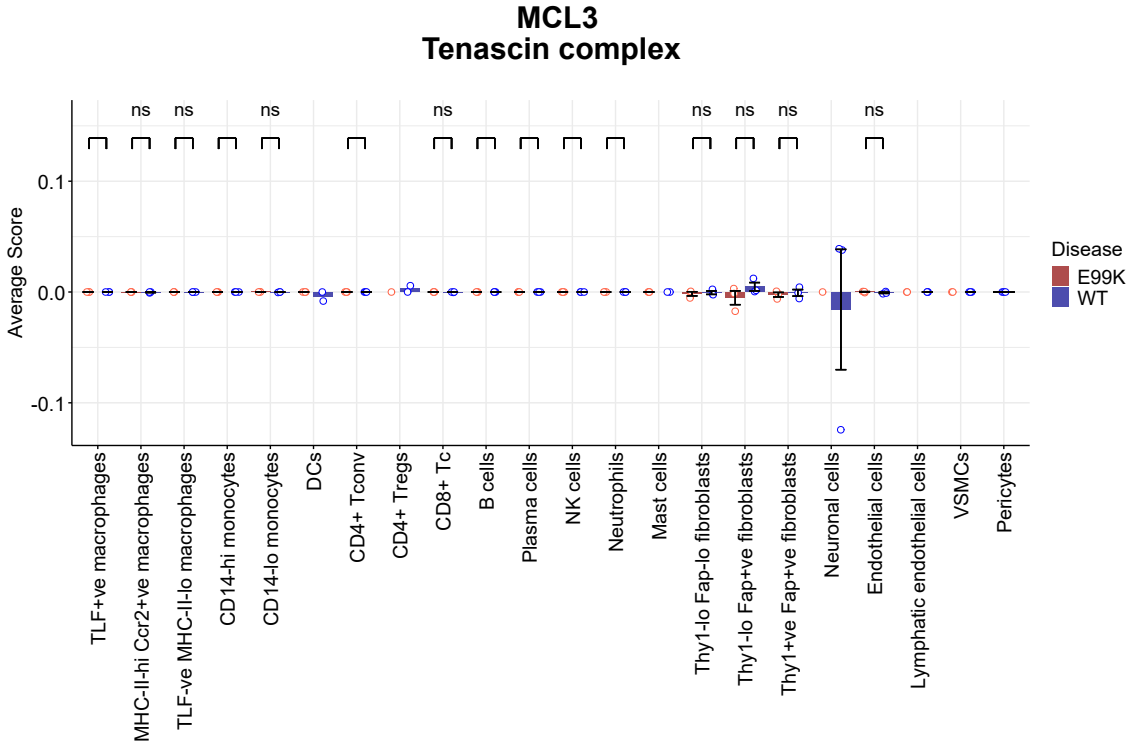

Figure F.26. Gene set scoring for MCL sub-cluster 3 of Cluster 12 (U-shaped trends) in late-stage mouse cell types.
This sub-cluster is a constituent of Cluster 12. The bar chart displays the gene set score for this specific sub-cluster across various cell types from early-stage Actc1^{E99K} mouse scRNA-seq data. Scores were calculated for each sample using the `score_genes` function in `scanpy` v1.10.1 [267]. Bars represent the mean score, with error bars indicating the standard error of the mean. Statistical significance between disease and control samples was determined using a t-test, with p-values adjusted for multiple comparisons using the Benjamini-Hochberg method. Asterisks denote significance levels: * $p < 0.05$, ** $p < 0.01$, *** $p < 0.001$, **** $p < 0.0001$.

References

[1] A. Vulpian. “Contribution à L’étude Des Rétrécissements De L’orifice Ventriculo-Aortique”. In: *Arch Physiol* 3 (1868), pp. 220–222.

[2] H. Liouville. “Retrecissement Cardiaque Sous Mortique”. In: *Gaz Med Paris* 24 (1869), pp. 161–163.

[3] M. Hallopeau. “Retrecissement Ventriculoaortique”. In: *Gaz Med Paris* 24 (1869), pp. 683–684.

[4] Russell Brock. “Functional Obstruction of the Left Ventricle; Acquired Aortic Subvalvar Stenosis”. In: 106 (1957), pp. 221–238.

[5] Donald Teare. “Asymmetrical Hypertrophy of the Heart in Young Adults”. In: *British Heart Journal* 20 (1958), p. 1.

[6] Bernard A. Bercu et al. “Pseudoaortic Stenosis Produced by Ventricular Hypertrophy”. In: *The American Journal of Medicine* 25 (1958), pp. 814–818.

[7] Edwin C. Brockenbrough, Eugene Braunwald, and Andrew G. Morrow. “A Hemodynamic Technic for the Detection of Hypertrophic Subaortic Stenosis”. In: *Circulation* 23 (1961), pp. 189–194.

[8] Eugene Braunwald and Maurice M. Aygen. “Idiopathic Myocardial Hypertrophy without Congestive Heart Failure or Obstruction to Blood Flow: Clinical, Hemodynamic and Angiocardiographic Studies in Fourteen Patients”. In: *The American Journal of Medicine* 35 (1963), pp. 7–19.

[9] A. S. Abbasi et al. “Echocardiographic Diagnosis of Idiopathic Hypertrophic Cardiomyopathy without Outflow Obstruction”. In: *Circulation* 46 (1972), pp. 897–904.

[10] Hugh Watkins, Houman Ashrafian, and Charles Redwood. “Inherited Cardiomyopathies”. In: *The New England Journal of Medicine* 364 (2011), pp. 1643–1656.

[11] B. J. Maron et al. “Prevalence of Hypertrophic Cardiomyopathy in a General Population of Young Adults. Echocardiographic Analysis of 4111 Subjects in the CARDIA Study. Coronary Artery Risk Development in (Young) Adults”. In: *Circulation* 92 (1995), pp. 785–789.

[12] B. J. Maron et al. “Clinical Profile of Hypertrophic Cardiomyopathy Identified De Novo in Rural Communities”. In: *Journal of the American College of Cardiology* 33 (1999), pp. 1590–1595.

[13] Y. Hada et al. “Prevalence of Hypertrophic Cardiomyopathy in a Population of Adult Japanese Workers As Detected by Echocardiographic Screening”. In: *The American Journal of Cardiology* 59 (1987), pp. 183–184.

[14] Yubao Zou et al. “Prevalence of Idiopathic Hypertrophic Cardiomyopathy in China: A Population-Based Echocardiographic Analysis of 8080 Adults”. In: *The American Journal of Medicine* 116 (2004), pp. 14–18.

[15] Paul J. M. Wijnker et al. “Hypertrophic Cardiomyopathy: A Vicious Cycle Triggered by Sarcomere Mutations and Secondary Disease Hits”. In: *Antioxidants & Redox Signaling* 31 (Aug. 2019), pp. 318–358.

[16] Nicholas A. Marston et al. “Clinical characteristics and outcomes in childhood-onset hypertrophic cardiomyopathy”. In: *European Heart Journal* 42 (Mar. 2021), pp. 1988–1996.

[17] Constantin-Cristian Topriceanu et al. “Abstract 13421: Meta-Analysis of Penetrance in Genetic Hypertrophic Cardiomyopathy”. In: *Circulation* 148 (Nov. 2023).

[18] Ali J. Marian and Eugene Braunwald. “Hypertrophic Cardiomyopathy: Genetics, Pathogenesis, Clinical Manifestations, Diagnosis, and Therapy”. In: *Circulation Research* 121 (2017), pp. 749–770.

[19] Polakit Teekakirikul et al. “Hypertrophic Cardiomyopathy: An Overview of Genetics and Management”. In: *Biomolecules* 9 (2019), p. 878.

[20] Bernard J. Gersh et al. “2011 ACCF/AHA Guideline for the Diagnosis and Treatment of Hypertrophic Cardiomyopathy: A Report of the American College of Cardiology Foundation/American Heart Association Task Force on Practice Guidelines. Developed in Collaboration with the American Association for Thoracic Surgery, American Society of Echocardiography, American Society of Nuclear Cardiology, Heart Failure Society of America, Heart Rhythm Society, Society for Cardiovascular Angiography and Interventions, and Society of Thoracic Surgeons”. In: *Journal of the American College of Cardiology* 58 (2011), e212–260.

[21] Barry J. Maron et al. “Sudden Deaths in Young Competitive Athletes: Analysis of 1866 Deaths in the United States, 1980-2006”. In: *Circulation* 119 (2009), pp. 1085–1092.

[22] B. J. Maron et al. “Sudden Death in Young Competitive Athletes. Clinical, Demographic, and Pathological Profiles”. In: *Jama* 276 (1996), pp. 199–204.

[23] Barry J. Maron et al. “Clinical Spectrum and Management of Heart Failure In Hypertrophic Cardiomyopathy”. In: *Jacc. Heart Failure* 6 (2018), pp. 353–363.

[24] Iacopo Olivotto et al. “Relevance of Coronary Microvascular Flow Impairment to Long-Term Remodeling and Systolic Dysfunction in Hypertrophic Cardiomyopathy”. In: *Journal of the American College of Cardiology* 47 (Mar. 2006), pp. 1043–1048.

[25] Franco Cecchi et al. “Microvascular Dysfunction, Myocardial Ischemia, and Progression to Heart Failure in Patients with Hypertrophic Cardiomyopathy”. In: *Journal of Cardiovascular Translational Research* 2 (Nov. 2009), pp. 452–461.

[26] Francesco Pelliccia et al. “Microvascular Dysfunction in Hypertrophic Cardiomyopathy”. In: *Journal of Clinical Medicine* 11 (Nov. 2022), p. 6560.

[27] Franco Cecchi et al. “Coronary Microvascular Dysfunction and Prognosis in Hypertrophic Cardiomyopathy”. In: *New England Journal of Medicine* 349 (2003), pp. 1027–1035.

[28] Martin S. Maron et al. “The Case for Myocardial Ischemia in Hypertrophic Cardiomyopathy”. In: *Journal of the American College of Cardiology* 54 (Aug. 2009), pp. 866–875.

[29] Monica Patten, Simon Pecha, and Ali Aydin. “Atrial Fibrillation in Hypertrophic Cardiomyopathy: Diagnosis and Considerations for Management”. In: *Journal of Atrial Fibrillation* 10 (2018), p. 1556.

[30] Jean Jacques Noubiap et al. “Meta-Analysis of Atrial Fibrillation in Patients With Various Cardiomyopathies”. In: *The American Journal of Cardiology* 124 (2019), pp. 262–269.

[31] William H. Maisel and Lynne Warner Stevenson. “Atrial Fibrillation in Heart Failure: Epidemiology, Pathophysiology, and Rationale for Therapy”. In: *The American Journal of Cardiology* 91 (2003), pp. 2D–8D.

[32] Polakit Teekakirikul et al. “Hypertrophic Cardiomyopathy: Translating Cellular Cross Talk into Therapeutics”. In: *The Journal of Cell Biology* 199 (2012), pp. 417–421.

[33] Michael Arad et al. “Gene Mutations in Apical Hypertrophic Cardiomyopathy”. In: *Circulation* 112 (2005), pp. 2805–2811.

[34] Sara L. Van Driest et al. “Yield of Genetic Testing in Hypertrophic Cardiomyopathy”. In: *Mayo Clinic Proceedings* 80 (2005), pp. 739–744.

[35] Hiroyuki Morita et al. “Shared Genetic Causes of Cardiac Hypertrophy in Children and Adults”. In: *The New England Journal of Medicine* 358 (2008), pp. 1899–1908.

[36] J. A. Jarcho et al. “Mapping a Gene for Familial Hypertrophic Cardiomyopathy to Chromosome 14q1”. In: *The New England Journal of Medicine* 321 (1989), pp. 1372–1378.

[37] A. A. Geisterfer-Lowrance et al. “A Molecular Basis for Familial Hypertrophic Cardiomyopathy: A Beta Cardiac Myosin Heavy Chain Gene Missense Mutation”. In: *Cell* 62 (1990), pp. 999–1006.

[38] H. Watkins et al. “Mutations in the Genes for Cardiac Troponin T and Alpha-Tropomyosin in Hypertrophic Cardiomyopathy”. In: *The New England Journal of Medicine* 332 (1995), pp. 1058–1064.

[39] A. Branzi et al. “Genetic Heterogeneity of Hypertrophic Cardiomyopathy”. In: *International Journal of Cardiology* 7 (1985), pp. 129–138.

[40] Hana Hartmannova et al. “Isolated X-Linked Hypertrophic Cardiomyopathy Caused by a Novel Mutation of the Four-and-A-Half LIM Domain 1 Gene”. In: *Circulation. Cardiovascular Genetics* 6 (2013), pp. 543–551.

[41] Gilles Millat et al. “Prevalence and Spectrum of Mutations in a Cohort of 192 Unrelated Patients with Hypertrophic Cardiomyopathy”. In: *European Journal of Medical Genetics* 53 (2010), pp. 261–267.

[42] Juan Pablo Kaski et al. “Prevalence of Sarcomere Protein Gene Mutations in Preadolescent Children with Hypertrophic Cardiomyopathy”. In: *Circulation. Cardiovascular Genetics* 2 (2009), pp. 436–441.

[43] J. Erdmann et al. “Mutation Spectrum in a Large Cohort of Unrelated Consecutive Patients with Hypertrophic Cardiomyopathy”. In: *Clinical Genetics* 64 (2003), pp. 339–349.

[44] Pascale Richard et al. “Hypertrophic Cardiomyopathy: Distribution of Disease Genes, Spectrum of Mutations, and Implications for a Molecular Diagnosis Strategy”. In: *Circulation* 107 (2003), pp. 2227–2232.

[45] L. Thierfelder et al. “Alpha-Tropomyosin and Cardiac Troponin T Mutations Cause Familial Hypertrophic Cardiomyopathy: A Disease of the Sarcomere”. In: *Cell* 77 (1994), pp. 701–712.

[46] A. Kimura et al. “Mutations in the Cardiac Troponin I Gene Associated with Hypertrophic Cardiomyopathy”. In: *Nature Genetics* 16 (1997), pp. 379–382.

[47] J. Mogensen et al. “Alpha-Cardiac Actin Is a Novel Disease Gene in Familial Hypertrophic Cardiomyopathy”. In: *The Journal of Clinical Investigation* 103 (1999), R39–43.

[48] K. Poetter et al. “Mutations in Either the Essential or Regulatory Light Chains of Myosin Are Associated with a Rare Myopathy in Human Heart and Skeletal Muscle”. In: *Nature Genetics* 13 (1996), pp. 63–69.

[49] Christian Geier et al. “Beyond the Sarcomere: CSRP3 Mutations Cause Hypertrophic Cardiomyopathy”. In: *Human Molecular Genetics* 17 (2008), pp. 2753–2765.

[50] Iacopo Olivotto et al. “Myofilament Protein Gene Mutation Screening and Outcome of Patients with Hypertrophic Cardiomyopathy”. In: *Mayo Clinic Proceedings* 83 (2008), pp. 630–638.

[51] Iacopo Olivotto et al. “Microvascular Function Is Selectively Impaired in Patients with Hypertrophic Cardiomyopathy and Sarcomere Myofilament Gene Mutations”. In: *Journal of the American College of Cardiology* 58 (2011), pp. 839–848.

[52] Roddy Walsh et al. “Reassessment of Mendelian Gene Pathogenicity Using 7,855 Cardiomyopathy Cases and 60,706 Reference Samples”. In: *Genetics in Medicine: Official Journal of the American College of Medical Genetics* 19 (2017), pp. 192–203.

[53] Ahmed A. Alfares et al. “Results of Clinical Genetic Testing of 2,912 Probands with Hypertrophic Cardiomyopathy: Expanded Panels Offer Limited Additional Sensitivity”. In: *Genetics in Medicine: Official Journal of the American College of Medical Genetics* 17 (2015), pp. 880–888.

[54] Jenifer G. Crilley et al. “Hypertrophic Cardiomyopathy Due to Sarcomeric Gene Mutations Is Characterized by Impaired Energy Metabolism Irrespective of the Degree of Hypertrophy”. In: *Journal of the American College of Cardiology* 41 (2003), pp. 1776–1782.

[55] Styliani Vakrou and M. Roselle Abraham. “Hypertrophic Cardiomyopathy: A Heart in Need of an Energy Bar?” In: *Frontiers in Physiology* 5 (2014), p. 309.

[56] Jolanda van der Velden et al. "Metabolic Changes in Hypertrophic Cardiomyopathies: Scientific Update from the Working Group of Myocardial Function of the European Society of Cardiology". In: *Cardiovascular Research* 114 (2018), pp. 1273–1280.

[57] M. Satoh et al. "Structural Analysis of the Titin Gene in Hypertrophic Cardiomyopathy: Identification of a Novel Disease Gene". In: *Biochemical and Biophysical Research Communications* 262 (1999), pp. 411–417.

[58] Takeharu Hayashi et al. "Tcap Gene Mutations in Hypertrophic Cardiomyopathy and Dilated Cardiomyopathy". In: *Journal of the American College of Cardiology* 44 (2004), pp. 2192–2201.

[59] Ali J. Marian. "Hypertrophic Cardiomyopathy: From Genetics to Treatment". In: *European Journal of Clinical Investigation* 40 (2010), pp. 360–369.

[60] Akinori Kimura. "Molecular Genetics and Pathogenesis of Cardiomyopathy". In: *Journal of Human Genetics* 61 (2016), pp. 41–50.

[61] Carolyn Y. Ho et al. "Genetic Advances in Sarcomeric Cardiomyopathies: State of the Art". In: *Cardiovascular Research* 105 (2015), pp. 397–408.

[62] Adriana Osio et al. "Myozenin 2 Is a Novel Gene for Human Hypertrophic Cardiomyopathy". In: *Circulation Research* 100 (2007), pp. 766–768.

[63] Suet Nee Chen et al. "Human Molecular Genetic and Functional Studies Identify TRIM63, Encoding Muscle RING Finger Protein 1, As a Novel Gene for Human Hypertrophic Cardiomyopathy". In: *Circulation Research* 111 (2012), pp. 907–919.

[64] Felix W. Friedrich et al. "Evidence for FHL1 As a Novel Disease Gene for Isolated Hypertrophic Cardiomyopathy". In: *Human Molecular Genetics* 21 (2012), pp. 3237–3254.

[65] Andrew P. Landstrom et al. "Molecular and Functional Characterization of Novel Hypertrophic Cardiomyopathy Susceptibility Mutations in TNNC1-Encoded Troponin C". In: *Journal of Molecular and Cellular Cardiology* 45 (2008), pp. 281–288.

[66] Elisa Carniel et al. "Alpha-Myosin Heavy Chain: A Sarcomeric Gene Associated with Dilated and Hypertrophic Phenotypes of Cardiomyopathy". In: *Circulation* 112 (2005), pp. 54–59.

[67] Andrew P. Landstrom et al. "PLN-Encoded Phospholamban Mutation in a Large Cohort of Hypertrophic Cardiomyopathy Cases: Summary of the Literature and Implications for Genetic Testing". In: *American Heart Journal* 161 (2011), pp. 165–171.

[68] Takeharu Hayashi et al. "Identification and Functional Analysis of a Caveolin-3 Mutation Associated with Familial Hypertrophic Cardiomyopathy". In: *Biochemical and Biophysical Research Communications* 313 (2004), pp. 178–184.

[69] Rowida Almomani et al. "Biallelic Truncating Mutations in ALPK3 Cause Severe Pediatric Cardiomyopathy". In: *Journal of the American College of Cardiology* 67 (2016), pp. 515–525.

[70] Andrew P. Landstrom et al. “Mutations in JPH2-Encoded Junctophilin-2 Associated with Hypertrophic Cardiomyopathy in Humans”. In: *Journal of Molecular and Cellular Cardiology* 42 (2007), pp. 1026–1035.

[71] Ali J. Marian. “Causality in Genetics: The Gradient of Genetic Effects and Back to Koch’s Postulates of Causality”. In: *Circulation Research* 114 (2014), e18–21.

[72] Ali J. Marian. “The Case of ”Missing Causal Genes” and the Practice of Medicine: A Sherlock Holmes Approach of Deductive Reasoning”. In: *Circulation Research* 119 (2016), pp. 21–24.

[73] D. G. MacArthur et al. “Guidelines for Investigating Causality of Sequence Variants in Human Disease”. In: *Nature* 508 (2014), pp. 469–476.

[74] 1000 Genomes Project Consortium et al. “A Global Reference for Human Genetic Variation”. In: *Nature* 526 (2015), pp. 68–74.

[75] 1000 Genomes Project Consortium et al. “A Map of Human Genome Variation from Population-Scale Sequencing”. In: *Nature* 467 (2010), pp. 1061–1073.

[76] Adam J. Saltzman et al. “Short Communication: The Cardiac Myosin Binding Protein C Arg502Trp Mutation: A Common Cause of Hypertrophic Cardiomyopathy”. In: *Circulation Research* 106 (2010), pp. 1549–1552.

[77] Stephen P. Page et al. “Cardiac Myosin Binding Protein-C Mutations in Families with Hypertrophic Cardiomyopathy: Disease Expression in Relation to Age, Gender, and Long Term Outcome”. In: *Circulation. Cardiovascular Genetics* 5 (2012), pp. 156–166.

[78] Akihiko Hodatsu et al. “Compound Heterozygosity Deteriorates Phenotypes of Hypertrophic Cardiomyopathy with Founder MYBPC3 Mutation: Evidence from Patients and Zebrafish Models”. In: *American Journal of Physiology. Heart and Circulatory Physiology* 307 (2014), H1594–1604.

[79] E. Dausse et al. “Familial Hypertrophic Cardiomyopathy. Microsatellite Haplotyping and Identification of a Hot Spot for Mutations in the Beta-Myosin Heavy Chain Gene”. In: *The Journal of Clinical Investigation* 92 (1993), pp. 2807–2813.

[80] J. F. Forissier et al. “Codon 102 of the Cardiac Troponin T Gene Is a Putative Hot Spot for Mutations in Familial Hypertrophic Cardiomyopathy”. In: *Circulation* 94 (1996), pp. 3069–3073.

[81] D. A. Coviello et al. “Clinical Features of Hypertrophic Cardiomyopathy Caused by Mutation of a ”hot Spot” in the Alpha-Tropomyosin Gene”. In: *Journal of the American College of Cardiology* 29 (1997), pp. 635–640.

[82] A. J. Marian et al. “Detection of a New Mutation in the Beta-Myosin Heavy Chain Gene in an Individual with Hypertrophic Cardiomyopathy”. In: *The Journal of Clinical Investigation* 90 (1992), pp. 2156–2165.

[83] H. Watkins et al. “Expression and Functional Assessment of a Truncated Cardiac Troponin T That Causes Hypertrophic Cardiomyopathy. Evidence for a Dominant Negative Action”. In: *The Journal of Clinical Investigation* 98 (1996), pp. 2456–2461.

[84] Edward Blair et al. “Mutations of the Light Meromyosin Domain of the Beta-Myosin Heavy Chain Rod in Hypertrophic Cardiomyopathy”. In: *Circulation Research* 90 (2002), pp. 263–269.

[85] Julian R. Homburger et al. “Multidimensional Structure-Function Relationships in Human β-Cardiac Myosin from Population-Scale Genetic Variation”. In: *Proceedings of the National Academy of Sciences of the United States of America* 113 (2016), pp. 6701–6706.

[86] Roddy Walsh et al. “Defining the genetic architecture of hypertrophic cardiomyopathy: re-evaluating the role of non-sarcomeric genes”. In: *European Heart Journal* (2017), ehw603.

[87] E. Blair. “Mutations in the gamma2 subunit of AMP-activated protein kinase cause familial hypertrophic cardiomyopathy: evidence for the central role of energy compromise in disease pathogenesis”. In: *Human Molecular Genetics* 10 (2001), pp. 1215–1220.

[88] Jiri Bonaventura et al. “Genetic Testing in Patients with Hypertrophic Cardiomyopathy”. In: *International Journal of Molecular Sciences* 22 (2021), p. 10401.

[89] Sirish Vullaganti et al. “Fibrosis in Hypertrophic Cardiomyopathy Patients With and Without Sarcomere Gene Mutations”. In: *Heart, Lung and Circulation* 30 (2021), pp. 1496–1501.

[90] S. Zheng et al. “Polygenic risk score for hypertrophic cardiomyopathy predicts population disease risk, penetrance in sarcomeric rare variant carriers and survival in cases”. In: *European Heart Journal* 44 (2023).

[91] Daniel Reichart et al. “Pathogenic variants damage cell composition and single cell transcription in cardiomyopathies”. In: *Science* 377 (2022).

[92] Snigdha Tripathi et al. “Unequal Allelic Expression of Wild-Type and Mutated β-Myosin in Familial Hypertrophic Cardiomyopathy”. In: *Basic Research in Cardiology* 106 (2011), pp. 1041–1055.

[93] Theresia Kraft et al. “Hypertrophic Cardiomyopathy: Cell-To-Cell Imbalance in Gene Expression and Contraction Force As Trigger for Disease Phenotype Development”. In: *Circulation Research* 119 (2016), pp. 992–995.

[94] Adam S. Helms et al. “Sarcomere Mutation-Specific Expression Patterns in Human Hypertrophic Cardiomyopathy”. In: *Circulation. Cardiovascular Genetics* 7 (2014), pp. 434–443.

[95] Marcin Wolny et al. “Cardiomyopathy Mutations in the Tail of β-Cardiac Myosin Modify the Coiled-Coil Structure and Affect Integration into Thick Filaments in Muscle Sarcomeres in Adult Cardiomyocytes”. In: *The Journal of Biological Chemistry* 288 (2013), pp. 31952–31962.

[96] E. Rosalie Witjas-Paalberends et al. “Mutations in MYH7 Reduce the Force Generating Capacity of Sarcomeres in Human Familial Hypertrophic Cardiomyopathy”. In: *Cardiovascular Research* 99 (2013), pp. 432–441.

[97] Hideshi Niimura et al. “Sarcomere Protein Gene Mutations in Hypertrophic Cardiomyopathy of the Elderly”. In: *Circulation* 105 (2002), pp. 446–451.

[98] Sabine J. van Dijk et al. “Cardiac Myosin-Binding Protein C Mutations and Hypertrophic Cardiomyopathy: Haploinsufficiency, Deranged Phosphorylation, and Cardiomyocyte Dysfunction”. In: *Circulation* 119 (2009), pp. 1473–1483.

[99] Maximilian W. Popp and Lynne E. Maquat. “Leveraging Rules of Nonsense-Mediated mRNA Decay for Genome Engineering and Personalized Medicine”. In: *Cell* 165 (2016), pp. 1319–1322.

[100] Aleksandra Siwaszek, Marta Ukleja, and Andrzej Dziembowski. “Proteins Involved in the Degradation of Cytoplasmic mRNA in the Major Eukaryotic Model Systems”. In: *Rna Biology* 11 (2014), pp. 1122–1136.

[101] L. Carrier et al. “Organization and Sequence of Human Cardiac Myosin Binding Protein C Gene (MYBPC3) and Identification of Mutations Predicted to Produce Truncated Proteins in Familial Hypertrophic Cardiomyopathy”. In: *Circulation Research* 80 (1997), pp. 427–434.

[102] Saskia Schlossarek, Giulia Mearini, and Lucie Carrier. “Cardiac Myosin-Binding Protein C in Hypertrophic Cardiomyopathy: Mechanisms and Therapeutic Opportunities”. In: *Journal of Molecular and Cellular Cardiology* 50 (2011), pp. 613–620.

[103] Antonio Sarikas et al. “Impairment of the Ubiquitin-Proteasome System by Truncated Cardiac Myosin Binding Protein C Mutants”. In: *Cardiovascular Research* 66 (2005), pp. 33–44.

[104] David Barefield et al. “Haploinsufficiency of MYBPC3 Exacerbates the Development of Hypertrophic Cardiomyopathy in Heterozygous Mice”. In: *Journal of Molecular and Cellular Cardiology* 79 (2015), pp. 234–243.

[105] Andrew R. Harper et al. “Common genetic variants and modifiable risk factors underpin hypertrophic cardiomyopathy susceptibility and expressivity”. In: *Nature Genetics* 53 (Feb. 2021), pp. 135–142. (Visited on 04/13/2025).

[106] Aya Kataoka, Carolyn Hemmer, and P. Bryant Chase. “Computational simulation of hypertrophic cardiomyopathy mutations in troponin I: influence of increased myofilament calcium sensitivity on isometric force, ATPase and [Ca2+]i”. In: *Journal of Biomechanics* 40 (2007), pp. 2044–2052.

[107] Vasco Sequeira et al. “Perturbed Length-Dependent Activation in Human Hypertrophic Cardiomyopathy with Missense Sarcomeric Gene Mutations”. In: *Circulation Research* 112 (2013), pp. 1491–1505.

[108] Adam S. Helms et al. “Genotype-Dependent and -Independent Calcium Signaling Dysregulation in Human Hypertrophic Cardiomyopathy”. In: *Circulation* 134 (2016), pp. 1738–1748.

[109] Guangli Guo et al. “Enhanced myofilament calcium sensitivity aggravates abnormal calcium handling and diastolic dysfunction in patient-specific induced pluripotent stem cell-derived cardiomyocytes with MYH7 mutation”. In: *Cell Calcium* 117 (2024), p. 102822.

[110] Paul Robinson et al. “Hypertrophic cardiomyopathy mutations increase myofilament Ca2+ buffering, alter intracellular Ca2+ handling, and stimulate Ca2+-dependent signaling”. In: *The Journal of Biological Chemistry* 293 (2018), pp. 10487–10499.

[111] R. John Solaro et al. "Molecular Mechanisms of Cardiac Myofilament Activation: Modulation by pH and a Troponin T Mutant R92Q". In: *Basic Research in Cardiology* 97 Suppl 1 (2002), pp. I102–110.

[112] Nico Kresin et al. "Analysis of Contractile Function of Permeabilized Human Hypertrophic Cardiomyopathy Multicellular Heart Tissue". In: *Frontiers in Physiology* 10 (Mar. 2019).

[113] Julian C. Braz et al. "Targeted inhibition of p38 MAPK promotes hypertrophic cardiomyopathy through upregulation of calcineurin-NFAT signaling". In: *Journal of Clinical Investigation* 111 (2003), pp. 1475–1486.

[114] J. Molkentin. "Calcineurin-NFAT signaling regulates the cardiac hypertrophic response in coordination with the MAPKs". In: *Cardiovascular Research* 63 (2004), pp. 467–475.

[115] R. K. Li et al. "Overexpression of Transforming Growth Factor-Beta1 and Insulin-Like Growth Factor-I in Patients with Idiopathic Hypertrophic Cardiomyopathy". In: *Circulation* 96 (1997), pp. 874–881.

[116] Marcin Dobaczewski, Wei Chen, and Nikolaos G. Frangogiannis. "Transforming Growth Factor (TGF)-β Signaling in Cardiac Remodeling". In: *Journal of Molecular and Cellular Cardiology* 51 (2011), pp. 600–606.

[117] Michael J. Previs et al. "Defects in the Proteome and Metabolome in Human Hypertrophic Cardiomyopathy". In: *Circulation: Heart Failure* 15 (June 2022).

[118] Stephan Rosenkranz. "TGF-beta1 and angiotensin networking in cardiac remodeling". In: *Cardiovascular Research* 63 (2004), pp. 423–432.

[119] Yufeng Yao et al. "ADAMTS16 activates latent TGF- , accentuating fibrosis and dysfunction of the pressure-overloaded heart". In: *Cardiovascular Research* 116 (2019), pp. 956–969.

[120] John A. Spertus et al. "Mavacamten for treatment of symptomatic obstructive hypertrophic cardiomyopathy (EXPLORER-HCM): health status analysis of a randomised, double-blind, placebo-controlled, phase 3 trial". In: *Lancet (London, England)* 397 (June 2021), pp. 2467–2475.

[121] Bristol-Myers Squibb. *A Randomized, Double-blind, Placebo-controlled Study to Evaluate Mavacamten in Adults With Symptomatic Obstructive Hypertrophic Cardiomyopathy Who Are Eligible for Septal Reduction Therapy*. Tech. rep. submitted: 2020-04-07. June 2024. URL: `https://clinicaltrials.gov/study/NCT04349072` (visited on 03/23/2025).

[122] Zhuang Tian et al. "Effect of Mavacamten on Chinese Patients With Symptomatic Obstructive Hypertrophic Cardiomyopathy: The EXPLORER-CN Randomized Clinical Trial". In: *JAMA cardiology* 8 (Oct. 2023), pp. 957–965.

[123] Cytokinetics. *A Phase 3, Multi-Center, Randomized, Double-blind, Placebo-controlled Trial to Evaluate the Efficacy and Safety of CK-3773274 in Adults With Symptomatic Hypertrophic Cardiomyopathy and Left Ventricular Outflow Tract Obstruction*. Tech. rep. submitted: 2021-12-23. Feb. 2025. URL: `https://clinicaltrials.gov/study/NCT05186818` (visited on 03/23/2025).

[124] Giulia Mearini et al. “Mybpc3 Gene Therapy for Neonatal Cardiomyopathy Enables Long-Term Disease Prevention in Mice”. In: *Nature Communications* 5 (2014), p. 5515.

[125] Amara Greer-Short et al. *Gene Therapy Mediates Therapeutic Improvement in Cardiac Hypertrophy and Survival in a Murine Model of MYBPC3-Associated Cardiomyopathy*. Tech. rep. Type: article. bioRxiv, 2024. Chap. New Results, p. 2024.02.19.581102.

[126] Tenaya Therapeutics. *First-in-Human, Open-Label, Safety, Tolerability, Dose-Finding, Pharmacodynamic and Cardiac Transgene Expression Study of TN-201, a Recombinant Adeno-associated Virus Serotype 9 (AAV9) Containing Myosin Binding Protein C Transgene, in Adults With MYBPC3 Mutation-associated Hypertrophic Cardiomyopathy (HCM)*. Tech. rep. submitted: 2023-04-18. Nov. 2024. URL: `https://clinicaltrials.gov/study/NCT05836259` (visited on 03/23/2025).

[127] Jianming Jiang et al. “Allele-Specific Silencing of Mutant Myh6 Transcripts in Mice Suppresses Hypertrophic Cardiomyopathy”. In: *Science (new York, N.y.)* 342 (2013), pp. 111–114.

[128] Hong Ma et al. “Correction of a Pathogenic Gene Mutation in Human Embryos”. In: *Nature* 548 (2017), pp. 413–419.

[129] Annemieke Aartsma-Rus et al. “Development of Exon Skipping Therapies for Duchenne Muscular Dystrophy: A Critical Review and a Perspective on the Outstanding Issues”. In: *Nucleic Acid Therapeutics* 27 (2017), pp. 251–259.

[130] Giulia Mearini et al. “Repair of Mybpc3 mRNA by 5’-Trans-Splicing in a Mouse Model of Hypertrophic Cardiomyopathy”. In: *Molecular Therapy. Nucleic Acids* 2 (2013), e102.

[131] Maksymilian Prondzynski et al. “Evaluation of MYBPC3 Trans-Splicing and Gene Replacement As Therapeutic Options in Human iPSC-Derived Cardiomyocytes”. In: *Molecular Therapy. Nucleic Acids* 7 (2017), pp. 475–486.

[132] Johanna Kuusisto et al. “Low-Grade Inflammation and the Phenotypic Expression of Myocardial Fibrosis in Hypertrophic Cardiomyopathy”. In: *Heart (British Cardiac Society)* 98 (2012), pp. 1007–1013.

[133] Maja Schlittler et al. “Myocardial Fibrosis in Hypertrophic Cardiomyopathy: A Perspective from Fibroblasts”. In: *International Journal of Molecular Sciences* 24 (2023), p. 14845.

[134] Ke Sheng et al. “PTN secreted by cardiac fibroblasts promotes myocardial fibrosis and inflammation of pressure overload-induced hypertrophic cardiomyopathy through the PTN-SDC4 pathway”. In: *Life Sciences* 363 (Feb. 2025), p. 123356.

[135] Mark Chaffin et al. “Single-Nucleus Profiling of Human Dilated and Hypertrophic Cardiomyopathy”. In: *Nature* 608 (2022), pp. 174–180.

[136] Xuanyu Liu et al. “Lineage-Specific Regulatory Changes in Hypertrophic Cardiomyopathy Unraveled by Single-Nucleus RNA-Seq and Spatial Transcriptomics”. In: *Cell Discovery* 9 (2023), p. 6.

[137] Lu Fang et al. “Systemic inflammation is associated with myocardial fibrosis, diastolic dysfunction, and cardiac hypertrophy in patients with hypertrophic cardiomyopathy”. In: *American Journal of Translational Research* 9 (2017), pp. 5063–5073.

[138] Xinli Guo et al. “Systemic inflammation is associated with myocardial fibrosis in patients with obstructive hypertrophic cardiomyopathy”. In: *ESC Heart Failure* 12 (Oct. 2024), pp. 582–591.

[139] David K. Zach et al. “Low-grade systemic inflammation and left ventricular dysfunction in hypertensive compared to non-hypertensive hypertrophic cardiomyopathy”. In: *International Journal of Cardiology* 399 (Mar. 2024), p. 131661.

[140] Polakit Teekakirikul et al. “Cardiac Fibrosis in Mice with Hypertrophic Cardiomyopathy Is Mediated by Non-Myocyte Proliferation and Requires Tgf-β”. In: *The Journal of Clinical Investigation* 120 (2010), pp. 3520–3529.

[141] A. Matsumori et al. “Increased circulating cytokines in patients with myocarditis and cardiomyopathy”. In: *British Heart Journal* 72 (Dec. 1994), pp. 561–566.

[142] Márta Högye et al. “Comparison of circulating levels of interleukin-6 and tumor necrosis factor-alpha in hypertrophic cardiomyopathy and in idiopathic dilated cardiomyopathy”. In: *The American Journal of Cardiology* 94 (July 2004), pp. 249–251.

[143] Kan Zen et al. “Analysis of circulating apoptosis mediators and proinflammatory cytokines in patients with idiopathic hypertrophic cardiomyopathy: comparison between nonobstructive and dilated-phase hypertrophic cardiomyopathy”. In: *International Heart Journal* 46 (Mar. 2005), pp. 231–244.

[144] Siamon Gordon and Annette Plüddemann. “Tissue macrophages: heterogeneity and functions”. In: *BMC Biology* 15 (June 2017).

[145] Xudong Liao et al. “Distinct Roles of Resident and Nonresident Macrophages in Nonischemic Cardiomyopathy”. In: *Proceedings of the National Academy of Sciences* 115 (2018).

[146] Maarten Hulsmans et al. “Macrophages Facilitate Electrical Conduction in the Heart”. In: *Cell* 169 (2017), 510–522.e20.

[147] Kory J. Lavine et al. “The Macrophage in Cardiac Homeostasis and Disease”. In: *Journal of the American College of Cardiology* 72 (Oct. 2018), pp. 2213–2230.

[148] William P. Lafuse, Daniel J. Wozniak, and Murugesan V. S. Rajaram. “Role of Cardiac Macrophages on Cardiac Inflammation, Fibrosis and Tissue Repair”. In: *Cells* 10 (2020), p. 51.

[149] Rysa Zaman and Slava Epelman. “Resident cardiac macrophages: Heterogeneity and function in health and disease”. In: *Immunity* 55 (Sept. 2022), pp. 1549–1563.

[150] Stephane Heymans et al. “Macrophage microRNA-155 promotes cardiac hypertrophy and failure”. In: *Circulation* 128 (Sept. 2013), pp. 1420–1432.

[151] Hui Yu et al. “Exosomes Derived From Hypertrophic Cardiomyocytes Induce Inflammation in Macrophages via miR-155 Mediated MAPK Pathway”. In: *Frontiers in Immunology* 11 (2020), p. 606045.

[152] Deepak Ramanujam et al. “MicroRNA-21-Dependent Macrophage-to-Fibroblast Signaling Determines the Cardiac Response to Pressure Overload”. In: *Circulation* 143 (Apr. 2021), pp. 1513–1525.

[153] Xavier S. Revelo et al. “Cardiac Resident Macrophages Prevent Fibrosis and Stimulate Angiogenesis”. In: *Circulation Research* 129 (Dec. 2021), pp. 1086–1101.

[154] Shi-Hao Ni et al. “Single-cell transcriptomic analyses of cardiac immune cells reveal that Rel-driven CD72-positive macrophages induce cardiomyocyte injury”. In: *Cardiovascular Research* 118 (Mar. 2022), pp. 1303–1320.

[155] Ke Sheng et al. “Integrated single-cell RNA-seq analysis revealed PTN secreted by fibroblasts acting on itself and macrophages via SDC4 ligand in myocardial hypertrophy”. In: (June 2024).

[156] Huijuan Lv et al. “Impaired Thymic Tolerance to α-Myosin Directs Autoimmunity to the Heart in Mice and Humans”. In: *The Journal of Clinical Investigation* 121 (2011), pp. 1561–1573.

[157] Tania Nevers et al. “Left Ventricular T-Cell Recruitment Contributes to the Pathogenesis of Heart Failure”. In: *Circulation. Heart Failure* 8 (2015), pp. 776–787.

[158] Dario A. A. Vignali, Lauren W. Collison, and Creg J. Workman. “How Regulatory T Cells Work”. In: *Nature Reviews. Immunology* 8 (2008), pp. 523–532.

[159] Xiao Meng et al. “Regulatory T cells in cardiovascular diseases”. In: *Nature Reviews. Cardiology* 13 (Mar. 2016), pp. 167–179.

[160] Shyam S. Bansal et al. “Dysfunctional and Proinflammatory Regulatory T-Lymphocytes Are Essential for Adverse Cardiac Remodeling in Ischemic Cardiomyopathy”. In: *Circulation* 139 (Jan. 2019), pp. 206–221.

[161] Yuanliang Xia et al. “Role of Treg cell subsets in cardiovascular disease pathogenesis and potential therapeutic targets”. In: *Frontiers in Immunology* 15 (2024), p. 1331609.

[162] Kai Zhang et al. “Regulatory T cells protect against diabetic cardiomyopathy in db/db mice”. In: *Journal of Diabetes Investigation* 15 (Sept. 2024), pp. 1191–1201.

[163] Yonggang Ma. “Role of Neutrophils in Cardiac Injury and Repair Following Myocardial Infarction”. In: *Cells* 10 (July 2021), p. 1676.

[164] Dongjian Han et al. “Enhancing Cardioprotection Through Neutrophil-Mediated Delivery of 18 -Glycyrrhetinic Acid in Myocardial Ischemia/Reperfusion Injury”. In: *Advanced Science (Weinheim, Baden-Wurttemberg, Germany)* 11 (Nov. 2024), e2406124.

[165] Han Na Suh et al. “Dissect the immunity using cytokine profiling and NF-κB target gene analysis in systemic inflammatory minipig model”. In: *PLOS ONE* 16 (June 2021). Ed. by Michal A. Olszewski, e0252947.

[166] Bikash Mishra and Lionel Ivashkiv. "Regulation of Inflammatory NF-κB Target Gene Activation by Jak-STAT Signaling". In: *The Journal of Immunology* 210 (May 2023), pp. 162.01–162.01.

[167] George W. Booz, Jonathan N. E. Day, and Kenneth M. Baker. "Interplay Between the Cardiac Renin Angiotensin System and JAK-STAT Signaling: Role in Cardiac Hypertrophy, Ischemia/Reperfusion Dysfunction, and Heart Failure". In: *Journal of Molecular and Cellular Cardiology* 34 (Nov. 2002), pp. 1443–1453.

[168] Seán P. Barry et al. "Role of the JAK–STAT pathway in myocardial injury". In: *Trends in Molecular Medicine* 13 (Feb. 2007), pp. 82–89.

[169] Shai S. Shen-Orr et al. "Defective Signaling in the JAK-STAT Pathway Tracks with Chronic Inflammation and Cardiovascular Risk in Aging Humans". In: *Cell Systems* 3 (Oct. 2016), 374–384.e4.

[170] Qiuyu Pang et al. "Regulation of the JAK/STAT signaling pathway: The promising targets for cardiovascular disease". In: *Biochemical Pharmacology* 213 (July 2023), p. 115587.

[171] Cecile Ancey et al. "Human cardiomyocyte hypertrophy induced in vitro by gp130 stimulation". In: *Cardiovascular Research* 59 (July 2003), pp. 78–85.

[172] Edith K. Podewski et al. "Alterations in Janus kinase (JAK)-signal transducers and activators of transcription (STAT) signaling in patients with end-stage dilated cardiomyopathy". In: *Circulation* 107 (Feb. 2003), pp. 798–802.

[173] P. Fischer and D. Hilfiker-Kleiner. "Survival pathways in hypertrophy and heart failure: the gp130-STAT3 axis". In: *Basic Research in Cardiology* 102 (July 2007), pp. 279–297.

[174] Ahmed Fahmi et al. "p42/p44-MAPK and PI3K are sufficient for IL-6 family cytokines/gp130 to signal to hypertrophy and survival in cardiomyocytes in the absence of JAK/STAT activation". In: *Cellular Signalling* 25 (Apr. 2013), pp. 898–909.

[175] Surinder M. Soond, David S. Latchman, and Anastasis Stephanou. "STAT signalling in the heart and cardioprotection". In: *Expert Reviews in Molecular Medicine* 8 (July 2006), pp. 1–16.

[176] Raj Kishore and Suresh K. Verma. "Roles of STATs signaling in cardiovascular diseases". In: *JAK-STAT* 1 (Apr. 2012), pp. 118–124.

[177] K. E. O'Sullivan et al. "Understanding STAT3 signaling in cardiac ischemia". In: *Basic Research in Cardiology* 111 (Mar. 2016).

[178] Ryan A. Frieler and R. Mortensen. "Immune Cell and Other Noncardiomyocyte Regulation of Cardiac Hypertrophy and Remodeling." In: *Circulation* 131 11 (2015), pp. 1019–30.

[179] Simona Nemska et al. "Kinetic mRNA Profiling in a Rat Model of Left-Ventricular Hypertrophy Reveals Early Expression of Chemokines and Their Receptors". In: *PloS One* 11 (2016), e0161273.

[180] Lei Wang et al. "CXCL1-CXCR2 axis mediates angiotensin II-induced cardiac hypertrophy and remodelling through regulation of monocyte infiltration". In: *European Heart Journal* 39 (May 2018), pp. 1818–1831.

[181] Juan Liu, Qin Shen, and Yang Wu. “Simvastatin prevents cardiac hypertrophy in vitro and in vivo via JAK/STAT pathway”. In: *Life Sciences* 82 (May 2008), pp. 991–996.

[182] Alberto Aimo et al. “Pirfenidone As a Novel Cardiac Protective Treatment”. In: *Heart Failure Reviews* 27 (2021), pp. 525–532.

[183] Zhenhuan Chen et al. “Pirfenidone attenuates cardiac hypertrophy against isoproterenol by inhibiting activation of the janus tyrosine kinase-2/signal transducer and activator of transcription 3 (JAK-2/STAT3) signaling pathway”. In: *Bioengineered* 13 (May 2022), pp. 12772–12782.

[184] Gavin A. Lewis et al. “Impact of Myocardial Fibrosis on Cardiovascular Structure, Function and Functional Status in Heart Failure with Preserved Ejection Fraction”. In: *Journal of Cardiovascular Translational Research* 15 (2022), pp. 1436–1443.

[185] Jiong Wang et al. “β-elemene alleviates hyperglycemia-induced cardiac inflammation and remodeling by inhibiting the JAK/STAT3-NF-κB pathway”. In: *Phytomedicine: International Journal of Phytotherapy and Phytopharmacology* 119 (Oct. 2023), p. 154987.

[186] Frans A. van Nieuwenhoven and Neil A. Turner. “The role of cardiac fibroblasts in the transition from inflammation to fibrosis following myocardial infarction”. In: *Vascular Pharmacology* 58 (Mar. 2013), pp. 182–188.

[187] Monika Litviňuková et al. “Cells of the Adult Human Heart”. In: *Nature* 588 (2020), pp. 466–472.

[188] Yanan Cheng et al. “Central role of cardiac fibroblasts in myocardial fibrosis of diabetic cardiomyopathy”. In: *Frontiers in Endocrinology* 14 (2023), p. 1162754.

[189] Badder Kattih et al. “Single-nuclear transcriptome profiling identifies persistent fibroblast activation in hypertrophic and failing human hearts of patients with longstanding disease”. In: *Cardiovascular Research* 119 (Nov. 2023), pp. 2550–2562.

[190] Francesco Niro et al. “Fibrotic extracellular matrix impacts cardiomyocyte phenotype and function in an iPSC-derived isogenic model of cardiac fibrosis”. In: *Translational Research: The Journal of Laboratory and Clinical Medicine* 273 (Nov. 2024), pp. 58–77.

[191] Nikolaos G. Frangogiannis. “Cardiac Fibrosis”. In: *Cardiovascular Research* 117 (2021), pp. 1450–1488.

[192] Ratchanee Duangrat et al. “Sustained AT1R stimulation induces upregulation of growth factors in human cardiac fibroblasts via G q/TGF-β/ERK signaling that influences myocyte hypertrophy”. In: *European Journal of Pharmacology* 937 (Dec. 2022), p. 175384.

[193] C. M. Dubois et al. “Evidence that furin is an authentic transforming growth factor-beta1-converting enzyme”. In: *The American Journal of Pathology* 158 (Jan. 2001), pp. 305–316.

[194] Joanne E. Murphy-Ullrich and Mark J. Suto. "Thrombospondin-1 regulation of latent TGF-β activation: A therapeutic target for fibrotic disease". In: *Matrix Biology: Journal of the International Society for Matrix Biology* 68-69 (Aug. 2018), pp. 28–43.

[195] Cyril Anastasi et al. "BMP-1 disrupts cell adhesion and enhances TGF-β activation through cleavage of the matricellular protein thrombospondin-1". In: *Science Signaling* 13 (July 2020), eaba3880.

[196] Huan Wang et al. "Hydrogels preserve native phenotypes of valvular fibroblasts through an elasticity-regulated PI3K/AKT pathway". In: *Proceedings of the National Academy of Sciences of the United States of America* 110 (Nov. 2013), pp. 19336–19341.

[197] Svenja Hartmann et al. "Abstract 90: Modulation of Cardiac Fibroblast to Myofibroblast Transition by Rho-associated Kinases ROCK1 and ROCK2". In: *Circulation Research* 119 (July 2016), A90–A90. (Visited on 03/23/2025).

[198] Ross Bretherton et al. "Regulators of cardiac fibroblast cell state". In: *Matrix Biology: Journal of the International Society for Matrix Biology* 91-92 (Sept. 2020), pp. 117–135.

[199] Dana Rose Julian et al. "IL-4 Stimulated Macrophages Induce a Pro-Inflammatory Secretome in Fibroblasts". In: *The FASEB Journal* 34 (2020), pp. 1–1. (Visited on 03/23/2025).

[200] Maarten van der Kroef et al. "CXCL4 triggers monocytes and macrophages to produce PDGF-BB, culminating in fibroblast activation: Implications for systemic sclerosis". In: *Journal of Autoimmunity* 111 (July 2020), p. 102444.

[201] Mingzhe Zheng, Anthony Ambesi, and Paula J. McKeown-Longo. "Role of TLR4 Receptor Complex in the Regulation of the Innate Immune Response by Fibronectin". In: *Cells* 9 (Jan. 2020), p. 216.

[202] Zerina Lokmic et al. "Hypoxia and hypoxia signaling in tissue repair and fibrosis". In: *International Review of Cell and Molecular Biology* 296 (2012), pp. 139–185.

[203] Ian A. Darby and Tim D. Hewitson. "Hypoxia in tissue repair and fibrosis". In: *Cell and Tissue Research* 365 (Sept. 2016), pp. 553–562.

[204] Rana Mhaidly and Fatima Mechta-Grigoriou. "Fibroblast heterogeneity in tumor micro-environment: Role in immunosuppression and new therapies". In: *Seminars in Immunology* 48 (Apr. 2020), p. 101417.

[205] Vladan Milosevic and Arne Östman. "Interactions between cancer-associated fibroblasts and T-cells: functional crosstalk with targeting and biomarker potential". In: *Upsala Journal of Medical Sciences* 129 (2024).

[206] Alexandrine Bertaud et al. "Signaling Pathways and Potential Therapeutic Strategies in Cardiac Fibrosis". In: *International Journal of Molecular Sciences* 24 (2023), p. 1756.

[207] Joel G. Rurik et al. "CAR T cells produced in vivo to treat cardiac injury". In: *Science (New York, N.Y.)* 375 (Jan. 2022), pp. 91–96. URL: `https://www.ncbi.nlm.nih.gov/pmc/articles/PMC9983611/` (visited on 05/10/2025).

[208] Fabiana Passaro et al. “Targeting fibrosis in the failing heart with nanoparticles”. In: *Advanced Drug Delivery Reviews* 174 (2021), pp. 461–481.

[209] Jie Liu et al. “Endothelial Forkhead Box Transcription Factor P1 Regulates Pathological Cardiac Remodeling Through Transforming Growth Factor-β1-Endothelin-1 Signal Pathway”. In: *Circulation* 140 (Aug. 2019), pp. 665–680.

[210] Lindsey Dugaucquier et al. “The role of endothelial autocrine NRG1/ERBB4 signaling in cardiac remodeling”. In: *American Journal of Physiology. Heart and Circulatory Physiology* 319 (Aug. 2020), H443–H455.

[211] Meryl Musicante et al. “Regulation of endothelial nitric oxide synthase in cardiac remodeling”. In: *International Journal of Cardiology* 364 (Oct. 2022), pp. 96–101.

[212] Xing Yang et al. “The role of endothelial cell in cardiac hypertrophy: Focusing on angiogenesis and intercellular crosstalk”. In: *Biomedicine & Pharmacotherapy = Biomedecine & Pharmacotherapie* 163 (July 2023), p. 114799.

[213] Xiaoqing Zhang, Craig A. Simmons, and J. Paul Santerre. “Paracrine signalling from monocytes enables desirable extracellular matrix accumulation and temporally appropriate phenotype of vascular smooth muscle cell-like cells derived from adipose stromal cells”. In: *Acta Biomaterialia* 103 (Feb. 2020), pp. 129–141.

[214] Nerea Méndez-Barbero, Carmen Gutiérrez-Muñoz, and Luis Miguel Blanco-Colio. “Cellular Crosstalk between Endothelial and Smooth Muscle Cells in Vascular Wall Remodeling”. In: *International Journal of Molecular Sciences* 22 (July 2021), p. 7284.

[215] Brian M. Dulmovits and Ira M. Herman. “Microvascular remodeling and wound healing: a role for pericytes”. In: *The International Journal of Biochemistry & Cell Biology* 44 (Nov. 2012), pp. 1800–1812.

[216] Isaac Shaw et al. “Pericytes in the renal vasculature: roles in health and disease”. In: *Nature Reviews. Nephrology* 14 (Aug. 2018), pp. 521–534.

[217] Han Su et al. “Emerging Role of Pericytes and Their Secretome in the Heart”. In: *Cells* 10 (2021), p. 548.

[218] G. Luxan et al. “The Role of Pericytes in Cardiac Ageing and Disease”. In: *European Heart Journal* 43 (2022).

[219] Pearl Quijada et al. “Cardiac pericytes mediate the remodeling response to myocardial infarction”. In: *The Journal of Clinical Investigation* 133 (May 2023), e162188.

[220] Antonietta Fazio et al. “Signaling Role of Pericytes in Vascular Health and Tissue Homeostasis”. In: *International Journal of Molecular Sciences* 25 (June 2024), p. 6592.

[221] F. A. Recchia and V. Lionetti. “Animal Models of Dilated Cardiomyopathy for Translational Research”. In: *Veterinary Research Communications* 31 Suppl 1 (2007), pp. 35–41.

[222] Nima Milani-Nejad and Paul M. L. Janssen. "Small and Large Animal Models in Cardiac Contraction Research: Advantages and Disadvantages". In: *Pharmacology & Therapeutics* 141 (2014), pp. 235–249.

[223] A. A. Geisterfer-Lowrance et al. "A Mouse Model of Familial Hypertrophic Cardiomyopathy". In: *Science (new York, N.y.)* 272 (1996), pp. 731–734.

[224] Rocco Hueneke et al. "Early Remodeling of Repolarizing K+ Currents in the αMHC403/+ Mouse Model of Familial Hypertrophic Cardiomyopathy". In: *Journal of Molecular and Cellular Cardiology* 103 (2017), pp. 93–101.

[225] Suman Nag et al. "Contractility parameters of human -cardiac myosin with the hypertrophic cardiomyopathy mutation R403Q show loss of motor function". In: *Science Advances* 1 (Oct. 2015), e1500511.

[226] Saswata S. Sarkar et al. "The hypertrophic cardiomyopathy mutations R403Q and R663H increase the number of myosin heads available to interact with actin". In: *Science Advances* 6 (Apr. 2020), eaax0069.

[227] G. E. Lyons et al. "Developmental Regulation of Myosin Gene Expression in Mouse Cardiac Muscle". In: *The Journal of Cell Biology* 111 (1990), pp. 2427–2436.

[228] Bradley M. Palmer et al. "Reduced Cross-Bridge Dependent Stiffness of Skinned Myocardium from Mice Lacking Cardiac Myosin Binding Protein-C". In: *Molecular and Cellular Biochemistry* 263 (2004), pp. 73–80.

[229] J. James et al. "Transgenic Modeling of a Cardiac Troponin I Mutation Linked to Familial Hypertrophic Cardiomyopathy". In: *Circulation Research* 87 (2000), pp. 805–811.

[230] Cecilia Ferrantini et al. "Pathogenesis of Hypertrophic Cardiomyopathy Is Mutation Rather Than Disease Specific: A Comparison of the Cardiac Troponin T E163R and R92Q Mouse Models". In: *Journal of the American Heart Association* 6 (2017), e005407.

[231] R. Prabhakar et al. "A Familial Hypertrophic Cardiomyopathy Alpha-Tropomyosin Mutation Causes Severe Cardiac Hypertrophy and Death in Mice". In: *Journal of Molecular and Cellular Cardiology* 33 (2001), pp. 1815–1828.

[232] M. Muthuchamy et al. "Mouse Model of a Familial Hypertrophic Cardiomyopathy Mutation in Alpha-Tropomyosin Manifests Cardiac Dysfunction". In: *Circulation Research* 85 (1999), pp. 47–56.

[233] Weihua Song et al. "Molecular Mechanism of the E99K Mutation in Cardiac Actin (ACTC Gene) That Causes Apical Hypertrophy in Man and Mouse". In: *The Journal of Biological Chemistry* 286 (2011), pp. 27582–27593.

[234] A. Subramaniam et al. "Tissue-Specific Regulation of the Alpha-Myosin Heavy Chain Gene Promoter in Transgenic Mice". In: *The Journal of Biological Chemistry* 266 (1991), pp. 24613–24620.

[235] Zhonglan Chen et al. "Relation between Lymphocyte to Monocyte Ratio and Survival in Patients with Hypertrophic Cardiomyopathy: A Retrospective Cohort Study". In: *Peerj* 10 (2022), e13212.

[236] Madeleine K. D. Scott et al. “Increased Monocyte Count As a Cellular Biomarker for Poor Outcomes in Fibrotic Diseases: A Retrospective, Multicentre Cohort Study”. In: *The Lancet Respiratory Medicine* 7 (2019), pp. 497–508.

[237] Nikolaos G. Frangogiannis. “Cardiac fibrosis”. In: *Cardiovascular Research* 117 (Nov. 2020), pp. 1450–1488.

[238] Leyi Zhu et al. “Detection of myocardial fibrosis: Where we stand”. In: *Frontiers in Cardiovascular Medicine* 9 (Sept. 2022).

[239] Javier Díez, Arantxa González, and Jason C. Kovacic. “Myocardial Interstitial Fibrosis in Nonischemic Heart Disease, Part 3/4”. In: *Journal of the American College of Cardiology* 75 (May 2020), pp. 2204–2218.

[240] Katharina Schimmel et al. “Cardiac Fibrosis in the Pressure Overloaded Left and Right Ventricle as a Therapeutic Target”. In: *Frontiers in Cardiovascular Medicine* 9 (May 2022).

[241] Karan Bhatti, Manav Bandlamudi, and Juan Lopez-Mattei. “Endomyocardial Fibrosis”. In: *StatPearls*. Treasure Island (FL): StatPearls Publishing, 2025. URL: `http://www.ncbi.nlm.nih.gov/books/NBK513293/` (visited on 07/23/2025).

[242] Susan Lowey et al. “Functional Effects of the Hypertrophic Cardiomyopathy R403Q Mutation Are Different in an Alpha- or Beta-Myosin Heavy Chain Backbone”. In: *The Journal of Biological Chemistry* 283 (2008), pp. 20579–20589.

[243] Susan Lowey et al. “Transgenic Mouse α- and β-Cardiac Myosins Containing the R403Q Mutation Show Isoform-Dependent Transient Kinetic Differences”. In: *The Journal of Biological Chemistry* 288 (2013), pp. 14780–14787.

[244] Sebastiano Sciarretta, Massimo Volpe, and Junichi Sadoshima. “Mammalian Target of Rapamycin Signaling in Cardiac Physiology and Disease”. In: *Circulation Research* 114.3 (Jan. 2014), pp. 549–564.

[245] Hadi Khalil et al. “Fibroblast-specific TGF-β-Smad2/3 signaling underlies cardiac fibrosis”. In: *Journal of Clinical Investigation* 127 (Sept. 2017), pp. 3770–3783.

[246] Warisara Parichatikanond et al. “Therapeutic Targets for the Treatment of Cardiac Fibrosis and Cancer: Focusing on TGF-β Signaling”. In: *Frontiers in Cardiovascular Medicine* 7 (Mar. 2020).

[247] Richard Schulz. “Intracellular Targets of Matrix Metalloproteinase-2 in Cardiac Disease: Rationale and Therapeutic Approaches”. In: *Annual Review of Pharmacology and Toxicology* 47 (Feb. 2007), pp. 211–242.

[248] Abhijit Takawale et al. “Tissue Inhibitor of Matrix Metalloproteinase-1 Promotes Myocardial Fibrosis by Mediating CD63-Integrin β1 Interaction”. In: *Hypertension* 69 (June 2017), pp. 1092–1103.

[249] Merle M. Krebber et al. “Matrix Metalloproteinases and Tissue Inhibitors of Metalloproteinases in Extracellular Matrix Remodeling during Left Ventricular Diastolic Dysfunction and Heart Failure with Preserved Ejection Fraction: A Systematic Review and Meta-Analysis”. In: *International Journal of Molecular Sciences* 21 (Sept. 2020), p. 6742.

[250] J. Montag et al. “Successful Knock-In of Hypertrophic Cardiomyopathy-Mutation R723G into the MYH7 Gene Mimics HCM Pathology in Pigs”. In: *Scientific Reports* 8 (2018), p. 4786.

[251] Shifu Chen. “Ultrafast One-Pass FASTQ Data Preprocessing, Quality Control, and Deduplication Using Fastp”. In: *Imeta* 2 (2023), e107.

[252] Shifu Chen et al. “Fastp: An Ultra-Fast All-In-One FASTQ Preprocessor”. In: *Bioinformatics* 34 (2018), pp. i884–i890.

[253] Adam Frankish et al. “GENCODE 2021”. In: *Nucleic Acids Research* 49 (2021), pp. D916–D923.

[254] Alexander Dobin et al. “STAR: Ultrafast Universal RNA-Seq Aligner”. In: *Bioinformatics (oxford, England)* 29 (2013), pp. 15–21.

[255] Eurie L. Hong et al. “Principles of Metadata Organization at the ENCODE Data Coordination Center”. In: *Database: The Journal of Biological Databases and Curation* 2016 (2016), baw001.

[256] Yang Liao, Gordon K. Smyth, and Wei Shi. “featureCounts: An Efficient General Purpose Program for Assigning Sequence Reads to Genomic Features”. In: *Bioinformatics (oxford, England)* 30 (2014), pp. 923–930.

[257] Mark D. Robinson, Davis J. McCarthy, and Gordon K. Smyth. “edgeR: A Bioconductor Package for Differential Expression Analysis of Digital Gene Expression Data”. In: *Bioinformatics (oxford, England)* 26 (2010), pp. 139–140.

[258] Mark D. Robinson and Alicia Oshlack. “A Scaling Normalization Method for Differential Expression Analysis of RNA-Seq Data”. In: *Genome Biology* 11 (2010), R25.

[259] Gennady Korotkevich et al. “Fast Gene Set Enrichment Analysis”. In: *Biorxiv* (2016).

[260] Aravind Subramanian et al. “Gene Set Enrichment Analysis: A Knowledge-Based Approach for Interpreting Genome-Wide Expression Profiles”. In: *Proceedings of the National Academy of Sciences of the United States of America* 102 (2005), pp. 15545–15550.

[261] Arthur Liberzon et al. “Molecular Signatures Database (MSigDB) 3.0”. In: *Bioinformatics (oxford, England)* 27 (2011), pp. 1739–1740.

[262] Huaiyu Mi et al. “Large-Scale Gene Function Analysis with the PANTHER Classification System”. In: *Nature Protocols* 8 (2013), pp. 1551–1566.

[263] Uku Raudvere et al. “G:Profiler: A Web Server for Functional Enrichment Analysis and Conversions of Gene Lists (2019 Update)”. In: *Nucleic Acids Research* 47 (2019), W191–W198.

[264] Grace X. Y. Zheng et al. “Massively Parallel Digital Transcriptional Profiling of Single Cells”. In: *Nature Communications* 8 (2017), p. 14049.

[265] Matthew D. Young and Sam Behjati. “SoupX Removes Ambient RNA Contamination from Droplet-Based Single-Cell RNA Sequencing Data”. In: *Gigascience* 9 (2020), giaa151.

[266] Christopher S. McGinnis, Lyndsay M. Murrow, and Zev J. Gartner. "DoubletFinder: Doublet Detection in Single-Cell RNA Sequencing Data Using Artificial Nearest Neighbors". In: *Cell Systems* 8 (2019), 329–337.e4.

[267] F. Alexander Wolf, Philipp Angerer, and Fabian J. Theis. "SCANPY: Large-Scale Single-Cell Gene Expression Data Analysis". In: *Genome Biology* 19 (2018), p. 15.

[268] Ilya Korsunsky et al. "Fast, Sensitive and Accurate Integration of Single-Cell Data with Harmony". In: *Nature Methods* 16 (2019), pp. 1289–1296.

[269] V. A. Traag, L. Waltman, and N. J. van Eck. "From Louvain to Leiden: Guaranteeing Well-Connected Communities". In: *Scientific Reports* 9 (2019), p. 5233.

[270] Pau Badia-i-Mompel et al. "Decoupler: Ensemble of Computational Methods to Infer Biological Activities from Omics Data". In: *Bioinformatics Advances* 2 (2022). Ed. by Marieke Lydia Kuijjer.

[271] Charity W. Law et al. "Voom: Precision Weights Unlock Linear Model Analysis Tools for RNA-Seq Read Counts". In: *Genome Biology* 15 (2014), R29.

[272] Michael Schubert et al. "Perturbation-Response Genes Reveal Signaling Footprints in Cancer Gene Expression". In: *Nature Communications* 9 (2018), p. 20.

[273] Christian H. Holland, Bence Szalai, and Julio Saez-Rodriguez. "Transfer of Regulatory Knowledge from Human to Mouse for Functional Genomics Analysis". In: *Biochimica Et Biophysica Acta (bba) - Gene Regulatory Mechanisms*. Transcriptional Profiles and Regulatory Gene Networks 1863 (2020), p. 194431.

[274] Christian H. Holland et al. "Robustness and Applicability of Transcription Factor and Pathway Analysis Tools on Single-Cell RNA-Seq Data". In: *Genome Biology* 21 (2020), p. 36.

[275] Daniel Dimitrov et al. "LIANA+ provides an all-in-one framework for cell-cell communication inference". In: *Nature Cell Biology* 26 (2024), pp. 1613–1622.

[276] Gioele La Manno et al. "RNA Velocity of Single Cells". In: *Nature* 560 (2018), pp. 494–498.

[277] Volker Bergen et al. "Generalizing RNA Velocity to Transient Cell States through Dynamical Modeling". In: *Nature Biotechnology* 38 (2020), pp. 1408–1414.

[278] Styliani Vakrou et al. "Differences in Molecular Phenotype in Mouse and Human Hypertrophic Cardiomyopathy". In: *Scientific Reports* 11 (2021), p. 13163.

[279] Xuanyu Liu et al. "Long Non-Coding and Coding RNA Profiling Using Strand-Specific RNA-Seq in Human Hypertrophic Cardiomyopathy". In: *Scientific Data* 6 (2019), p. 90.

[280] Terry Therneau, Hart Stephen. *RNASeqPower*. 2017.

[281] Ana Conesa et al. "maSigPro: a method to identify significantly differential expression profiles in time-course microarray experiments". In: *Bioinformatics* 22 (2006), pp. 1096–1102.

[282] María José Nueda, Sonia Tarazona, and Ana Conesa. "Next maSigPro: updating maSigPro bioconductor package for RNA-seq time series". In: *Bioinformatics* 30 (2014), pp. 2598–2602.

[283] Jil Sander, Joachim L. Schultze, and Nir Yosef. "ImpulseDE: detection of differentially expressed genes in time series data using impulse models". In: *Bioinformatics* 33 (2016). Ed. by Ziv Bar-Joseph, pp. 757–759.

[284] David S. Fischer, Fabian J. Theis, and Nir Yosef. "Impulse model-based differential expression analysis of time course sequencing data". In: *Nucleic Acids Research* (2018).

[285] A. Thorburn et al. "HRas-Dependent Pathways Can Activate Morphological and Genetic Markers of Cardiac Muscle Cell Hypertrophy." In: *The Journal of Biological Chemistry* 268 3 (1993), pp. 2244–9.

[286] Teresa Ramírez et al. "The MEKK-JNK Pathway Is Stimulated by α1-Adrenergic Receptor and Ras Activation and Is Associated with in Vitroand in Vivo Cardiac Hypertrophy*". In: *The Journal of Biological Chemistry* 272 (1997), pp. 14057–14061.

[287] P. Sugden and A. Clerk. "Activation of the Small GTP-Binding Protein Ras in the Heart by Hypertrophic Agonists." In: *Trends in Cardiovascular Medicine* 10 1 (2000), pp. 1–8.

[288] D. Oceandy et al. "Tumor Suppressor Ras-Association Domain Family 1 Isoform A Is a Novel Regulator of Cardiac Hypertrophy". In: *Circulation* 120 (2009), pp. 607–616.

[289] M. Adamcová, Ippei Kawano, and F. Simko. "The Impact of microRNAs in Renin–Angiotensin-System-Induced Cardiac Remodelling". In: *International Journal of Molecular Sciences* 22 (2021).

[290] M. Ramos-Kuri et al. "Molecules Linked to Ras Signaling As Therapeutic Targets in Cardiac Pathologies". In: *Biological Research* 54 (2021).

[291] P. Smeets et al. "Inflammatory Pathways Are Activated during Cardiomyocyte Hypertrophy and Attenuated by Peroxisome Proliferator-Activated Receptors PPARα and PPARδ*". In: *Journal of Biological Chemistry* 283 (2008), pp. 29109–29118.

[292] Xin Liu, G. Shi, and Junli Guo. "Innate Immune Cells in Pressure Overload-Induced Cardiac Hypertrophy and Remodeling". In: *Frontiers in Cell and Developmental Biology* 9 (2021).

[293] F. Brockhaus and B. Brüne. "P53 Accumulation in Apoptotic Macrophages Is an Energy Demanding Process That Precedes Cytochrome C Release in Response to Nitric Oxide". In: *Oncogene* 18 (1999), pp. 6403–6410.

[294] J. Narula et al. "Apoptosis in Heart Failure: Release of Cytochrome C from Mitochondria and Activation of Caspase-3 in Human Cardiomyopathy." In: *Proceedings of the National Academy of Sciences of the United States of America* 96 14 (1999), pp. 8144–9.

[295] L. Cai et al. "Hyperglycemia-Induced Apoptosis in Mouse Myocardium: Mitochondrial Cytochrome C-Mediated Caspase-3 Activation Pathway." In: *Diabetes* 51 6 (2002), pp. 1938–48.

[296] M. Trinei et al. “A P53-p66Shc Signalling Pathway Controls Intracellular Redox Status, Levels of Oxidation-Damaged DNA and Oxidative Stress-Induced Apoptosis”. In: *Oncogene* 21 (2002), pp. 3872–3878.

[297] C. Baines and J. Molkentin. “STRESS Signaling Pathways That Modulate Cardiac Myocyte Apoptosis.” In: *Journal of Molecular and Cellular Cardiology* 38 1 (2005), pp. 47–62.

[298] Roua Hassoun et al. “Stress Activated Signalling Impaired Protein Quality Control Pathways in Human Hypertrophic Cardiomyopathy.” In: *International Journal of Cardiology* 344 (2021), pp. 160–169.

[299] K. Kuwahara et al. “The Effects of the Selective ROCK Inhibitor, Y27632, on ET-1-Induced Hypertrophic Response in Neonatal Rat Cardiac Myocytes – Possible Involvement of Rho/ROCK Pathway in Cardiac Muscle Cell Hypertrophy”. In: *Febs Letters* 452 (1999).

[300] T. Yanazume et al. “Rho/ROCK Pathway Contributes to the Activation of Extracellular Signal-Regulated Kinase/GATA-4 during Myocardial Cell Hypertrophy*”. In: *The Journal of Biological Chemistry* 277 (2002), pp. 8618–8625.

[301] J. Brown, Dominic P. Del Re, and Mark A. Sussman. “The Rac and Rho Hall of Fame: A Decade of Hypertrophic Signaling Hits”. In: *Circulation Research* 98 (2006), pp. 730–742.

[302] Svenja Hartmann, A. Ridley, and S. Lutz. “The Function of Rho-Associated Kinases ROCK1 and ROCK2 in the Pathogenesis of Cardiovascular Disease”. In: *Frontiers in Pharmacology* 6 (2015).

[303] A. Kluge et al. “Rho-Family GTPase 1 (Rnd1) Is a Biomechanical Stress-Sensitive Activator of Cardiomyocyte Hypertrophy.” In: *Journal of Molecular and Cellular Cardiology* 129 (2019), pp. 130–143.

[304] Veerle A. M. van de Schans, J. Smits, and W. Blankesteijn. “The Wnt/frizzled Pathway in Cardiovascular Development and Disease: Friend or Foe?” In: *European Journal of Pharmacology* 585 2-3 (2008), pp. 338–45.

[305] M. Bergmann. “WNT Signaling in Adult Cardiac Hypertrophy and Remodeling: Lessons Learned from Cardiac Development.” In: *Circulation Research* 107 10 (2010), pp. 1198–208.

[306] Pratima Malekar et al. “Wnt Signaling Is Critical for Maladaptive Cardiac Hypertrophy and Accelerates Myocardial Remodeling”. In: *Hypertension* 55 (2010), pp. 939–945.

[307] W. Liang and E. Marbán. “Wnt Signaling Selectively Inhibits Sodium Channels in Cardiac Myocytes”. In: *Biophysical Journal* 108 (2015), pp. 1–2.

[308] V. Stylianidis, Kevin C. M. Hermans, and W. Blankesteijn. “Wnt Signaling in Cardiac Remodeling and Heart Failure.” In: *Handbook of Experimental Pharmacology* 243 (2017), pp. 371–393.

[309] Li Lin et al. “Pygo1 Regulates Pathological Cardiac Hypertrophy Via a β-Catenin-Dependent Mechanism.” In: *American Journal of Physiology. Heart and Circulatory Physiology* (2021).

[310] V. Balatskyi et al. "WNT/β-Catenin Pathway Is a Key Regulator of Cardiac Function and Energetic Metabolism". In: *Acta Physiologica* 237 (2023).

[311] J. Schisler et al. "P663Cardiac Energy Dependence on Glucose Increases Metabolites Related to Glutathione and Activates Metabolic Genes Controlled by mTOR". In: *Cardiovascular Research* 103 (2014).

[312] J. Schisler et al. "Cardiac Energy Dependence on Glucose Increases Metabolites Related to Glutathione and Activates Metabolic Genes Controlled by Mechanistic Target of Rapamycin". In: *Journal of the American Heart Association: Cardiovascular and Cerebrovascular Disease* 4 (2015).

[313] Guoyong Li et al. "FUNDC1: A Promising Mitophagy Regulator at the Mitochondria-Associated Membrane for Cardiovascular Diseases". In: *Frontiers in Cell and Developmental Biology* 9 (2021).

[314] Jenna L. Jewell et al. "Differential Regulation of mTORC1 by Leucine and Glutamine". In: *Science (new York, N.y.)* 347 (2015), pp. 194–198.

[315] S. Sciarretta et al. "New Insights Into the Role of mTOR Signaling in the Cardiovascular System." In: *Circulation Research* 122 3 (2018), pp. 489–505.

[316] Delong Meng et al. "Glutamine and Asparagine Activate mTORC1 Independently of Rag GTPases". In: *The Journal of Biological Chemistry* 295 (2020), pp. 2890–2899.

[317] F. Shi and Sheila Collins. "Regulation of mTOR Signaling: Emerging Role of Cyclic Nucleotide-Dependent Protein Kinases and Implications for Cardiometabolic Disease". In: *International Journal of Molecular Sciences* 24 (2023).

[318] N. Suwaki, Kerstin Klare, and M. Tarsounas. "RAD51 Paralogs: Roles in DNA Damage Signalling, Recombinational Repair and Tumorigenesis." In: *Seminars in Cell & Developmental Biology* 22 8 (2011), pp. 898–905.

[319] A. El-Hattab and F. Scaglia. "Mitochondrial Cardiomyopathies". In: *Frontiers in Cardiovascular Medicine* 3 (2016).

[320] Sara Ranjbarvaziri et al. "Abstract 235: Hypertrophic Cardiomyopathy, a Disease of Altered Cardiac Energetics". In: *Circulation Research* (2020).

[321] Sara Ranjbarvaziri et al. "Altered Cardiac Energetics and Mitochondrial Dysfunction in Hypertrophic Cardiomyopathy". In: *Circulation* 144 (2021), pp. 1714–1731.

[322] E. Nollet et al. "Mitochondrial Dysfunction in Human Hypertrophic Cardiomyopathy Is Linked to Cardiomyocyte Architecture Disruption and Corrected by Improving NADH-Driven Mitochondrial Respiration". In: *European Heart Journal* 44 (2023), pp. 1170–1185.

[323] Zheng Li et al. "miR-199a Impairs Autophagy and Induces Cardiac Hypertrophy through mTOR Activation". In: *Cell Death and Differentiation* 24 (2015), pp. 1205–1213.

[324] Sheng Xie et al. "Chronic Intermittent Hypoxia Induces Cardiac Hypertrophy by Impairing Autophagy through the Adenosine 5'-Monophosphate-Activated Protein Kinase Pathway." In: *Archives of Biochemistry and Biophysics* 606 (2016), pp. 41–52.

[325] Sonia R. Singh et al. “Activation of Autophagy Ameliorates Cardiomyopathy in Mybpc3-Targeted Knockin Mice”. In: *Circulation: Heart Failure* 10 (2017).

[326] M. Hermiston, Zheng Xu, and A. Weiss. “CD45: A Critical Regulator of Signaling Thresholds in Immune Cells.” In: *Annual Review of Immunology* 21 (2003), pp. 107–37.

[327] Andreas Rheinländer, B. Schraven, and U. Bommhardt. “CD45 in Human Physiology and Clinical Medicine.” In: *Immunology Letters* 196 (2018), pp. 22–32.

[328] Bernard Malissen and A. Schmitt-Verhulst. “Transmembrane Signalling through the T-Cell-Receptor-CD3 Complex.” In: *Current Opinion in Immunology* 5 3 (1993), pp. 324–33.

[329] K. Wucherpfennig et al. “Structural Biology of the T-Cell Receptor: Insights into Receptor Assembly, Ligand Recognition, and Initiation of Signaling.” In: *Cold Spring Harbor Perspectives in Biology* 2 4 (2010).

[330] J. Connolly et al. “Recognition by CD8 on Cytotoxic T Lymphocytes Is Ablated by Several Substitutions in the Class I Alpha 3 Domain: CD8 and the T-Cell Receptor Recognize the Same Class I Molecule.” In: *Proceedings of the National Academy of Sciences of the United States of America* 87 6 (1990), pp. 2137–41.

[331] C. Doyle and J. Strominger. “Interaction between CD4 and Class II MHC Molecules Mediates Cell Adhesion”. In: *Nature* 330 (1987), pp. 256–259.

[332] S. Allan et al. “The Role of 2 FOXP3 Isoforms in the Generation of Human CD4+ Tregs.” In: *The Journal of Clinical Investigation* 115 11 (2005), pp. 3276–84.

[333] G. Deng et al. “Foxp3 Post-Translational Modifications and Treg Suppressive Activity”. In: *Frontiers in Immunology* 10 (2019).

[334] J. Fontenot et al. “A Function for Interleukin 2 in Foxp3-Expressing Regulatory T Cells”. In: *Nature Immunology* 6 (2005), pp. 1142–1151.

[335] K. Toomer et al. “Essential and Non-Overlapping IL-2Rα-Dependent Processes for Thymic Development and Peripheral Homeostasis of Regulatory T Cells”. In: *Nature Communications* 10 (2019).

[336] Annemieke C. Bouwman et al. “Intracellular and Extracellular Roles of Granzyme K”. In: *Frontiers in Immunology* 12 (2021).

[337] Elisa Ruffo et al. “Lymphocyte-Activation Gene 3 (LAG3): The Next Immune Checkpoint Receptor.” In: *Seminars in Immunology* 42 (2019).

[338] G. Atweh and C. Iancu-Rubin. “p27Kip1 and STMN1: Partners Again?” In: *Cell Cycle* 13 (2014), pp. 3163–3163.

[339] Paulina Gil-Kulik et al. “Potential Involvement of BIRC5 in Maintaining Pluripotency and Cell Differentiation of Human Stem Cells”. In: *Oxidative Medicine and Cellular Longevity* 2019 (2019).

[340] S. Uxa et al. “Ki-67 Gene Expression”. In: *Cell Death and Differentiation* 28 (2021), pp. 3357–3370.

[341] N. Henderson et al. “Galectin-3 Regulates Myofibroblast Activation and Hepatic Fibrosis.” In: *Proceedings of the National Academy of Sciences of the United States of America* 103 13 (2006), pp. 5060–5.

[342] Liu-Cheng Li, Jun Li, and Jian Gao. “Functions of Galectin-3 and Its Role in Fibrotic Diseases”. In: *The Journal of Pharmacology and Experimental Therapeutics* 351 (2014), pp. 336–343.

[343] Carolina Jaquenod De Giusti et al. “Macrophages and Galectin 3 Play Critical Roles in CVB3-Induced Murine Acute Myocarditis and Chronic Fibrosis.” In: *Journal of Molecular and Cellular Cardiology* 85 (2015), pp. 58–70.

[344] V. Blanda et al. “Galectin-3 in Cardiovascular Diseases”. In: *International Journal of Molecular Sciences* 21 (2020).

[345] Antje Schauer et al. “Loss of Sox9 in Cardiomyocytes Delays the Onset of Cardiac Hypertrophy and Fibrosis.” In: *International Journal of Cardiology* 282 (2019), pp. 68–75.

[346] Dennis D. HicksteinSglI, A. Back, and S. Collins. “Regulation of Expression of the CD11b and CD18 Subunits of the Neutrophil Adherence Receptor during Human Myeloid Differentiation.” In: *The Journal of Biological Chemistry* 264 36 (1989), pp. 21812–7.

[347] M. Lübbert et al. “The Human Lysozyme Gene Undergoes Stepwise Demethylation during Phagocyte Maturation”. In: *Leukemia* 11 (1997), pp. 990–997.

[348] T. Döbel et al. “FcγRIII (CD16) Equips Immature 6-Sulfo LacNAc-Expressing Dendritic Cells (slanDCs) with a Unique Capacity to Handle IgG-Complexed Antigens.” In: *Blood* 121 18 (2013), pp. 3609–18.

[349] E. Stanley and V. Chitu. “CSF-1 Receptor Signaling in Myeloid Cells.” In: *Cold Spring Harbor Perspectives in Biology* 6 6 (2014).

[350] D. Chistiakov et al. “CD68/macrosialin: Not Just a Histochemical Marker”. In: *Laboratory Investigation* 97 (2017), pp. 4–13.

[351] Lindsey A. Waddell et al. “ADGRE1 (EMR1, F4/80) Is a Rapidly-Evolving Gene Expressed in Mammalian Monocyte-Macrophages”. In: *Frontiers in Immunology* 9 (2018).

[352] Guobao Chen et al. “Molecular Mechanisms for Synchronized Transcription of Three Complement C1q Subunit Genes in Dendritic Cells and Macrophages*”. In: *The Journal of Biological Chemistry* 286 (2011), pp. 34941–34950.

[353] Yufeng Zhou et al. “Mannose Receptor Modulates Macrophage Polarization and Allergic Inflammation through miR-511-3p”. In: *The Journal of Allergy and Clinical Immunology* 141 (2018).

[354] Sarah A. Dick et al. “Three Tissue Resident Macrophage Subsets Coexist across Organs with Conserved Origins and Life Cycles”. In: *Science Immunology* 7 (2022), eabf7777.

[355] D. Depoil et al. “CD19 Is Essential for B Cell Activation by Promoting B Cell Receptor–Antigen Microcluster Formation in Response to Membrane-Bound Ligand”. In: *Nature Immunology* 9 (2008), pp. 63–72.

[356] G. Pavlasová and M. Mraz. "The Regulation and Function of CD20: An "enigma" of B-Cell Biology and Targeted Therapy". In: *Haematologica* 105 (2020), pp. 1494–1506.

[357] Anton Tkachenko, Kristyna Kupcova, and O. Havranek. "B-Cell Receptor Signaling and Beyond: The Role of Igα (CD79a)/Igβ (CD79b) in Normal and Malignant B Cells". In: *International Journal of Molecular Sciences* (2023).

[358] Virginia Andreani et al. "Cochaperone Mzb1 Is a Key Effector of Blimp1 in Plasma Cell Differentiation and β1-Integrin Function". In: *Proceedings of the National Academy of Sciences of the United States of America* 115 (2018), pp. 9630–9639.

[359] H. DeLisser et al. "Involvement of Endothelial PECAM-1/CD31 in Angiogenesis." In: *The American Journal of Pathology* 151 3 (1997), pp. 671–7.

[360] M. Shibuya. "Structure and Dual Function of Vascular Endothelial Growth Factor Receptor-1 (Flt-1)." In: *The International Journal of Biochemistry & Cell Biology* 33 4 (2001), pp. 409–20.

[361] L. Sauteur et al. "Cdh5/VE-Cadherin Promotes Endothelial Cell Interface Elongation Via Cortical Actin Polymerization during Angiogenic Sprouting." In: *Cell Reports* 9 2 (2014), pp. 504–13.

[362] Cindy Park-Windhol et al. "Endomucin Inhibits VEGF-Induced Endothelial Cell Migration, Growth, and Morphogenesis by Modulating VEGFR2 Signaling". In: *Scientific Reports* 7 (2017).

[363] D. Jackson. "Hyaluronan in the Lymphatics: The Key Role of the Hyaluronan Receptor LYVE-1 in Leucocyte Trafficking." In: *Matrix Biology : Journal of the International Society for Matrix Biology* 78-79 (2018), pp. 219–235.

[364] Jay W. Shin et al. "Prox1 Promotes Lineage-Specific Expression of Fibroblast Growth Factor (FGF) Receptor-3 in Lymphatic Endothelium: A Role for FGF Signaling in Lymphangiogenesis." In: *Molecular Biology of the Cell* 17 2 (2005), pp. 576–84.

[365] Nicole C. Johnson et al. "Lymphatic Endothelial Cell Identity Is Reversible and Its Maintenance Requires Prox1 Activity." In: *Genes & Development* 22 23 (2008), pp. 3282–91.

[366] Sunju Lee et al. "Prox1 Physically and Functionally Interacts with COUP-TFII to Specify Lymphatic Endothelial Cell Fate." In: *Blood* 113 8 (2009), pp. 1856–9.

[367] D. Meyer and H. R. Baumgartner. "Role of Von Willebrand Factor in Platelet Adhesion to the Subendothelium". In: *British Journal of Haematology* 54 (1983), pp. 1–9.

[368] D. Kerjaschki. "Lymphatic Neoangiogenesis in Human Neoplasia and Transplantation As Experiments of Nature". In: *Kidney International* 68 (2005), pp. 1967–1968.

[369] A. Randi, Koval E. Smith, and G. Castaman. "Von Willebrand Factor Regulation of Blood Vessel Formation." In: *Blood* 132 2 (2018), pp. 132–140.

[370] Y. Hashimoto et al. “Claudin-5: A Pharmacological Target to Modify the Permeability of the Blood-Brain Barrier.” In: *Biological & Pharmaceutical Bulletin* 44 10 (2021), pp. 1380–1390.

[371] Qing Ge et al. “LCZ696, an Angiotensin Receptor-Neprilysin Inhibitor, Improves Cardiac Hypertrophy and Fibrosis and Cardiac Lymphatic Remodeling in Transverse Aortic Constriction Model Mice”. In: *Biomed Research International* 2020 (2020).

[372] Jie Bai et al. “Angiotensin II Induces Cardiac Edema and Hypertrophic Remodeling through Lymphatic-Dependent Mechanisms”. In: *Oxidative Medicine and Cellular Longevity* 2022 (2022).

[373] Sylvain D. Vallet and S. Ricard-Blum. “Lysyl Oxidases: From Enzyme Activity to Extracellular Matrix Cross-Links.” In: *Essays in Biochemistry* (2019).

[374] Hanne Devos et al. “Reviewing the Regulators of COL1A1”. In: *International Journal of Molecular Sciences* 24 (2023), p. 10004.

[375] Adam P. Croft et al. “Distinct Fibroblast Subsets Drive Inflammation and Damage in Arthritis”. In: *Nature* 570 (2019), p. 246.

[376] M. Hellström et al. “Role of PDGF-B and PDGFR-Beta in Recruitment of Vascular Smooth Muscle Cells and Pericytes during Embryonic Blood Vessel Formation in the Mouse.” In: *Development* 126 14 (1999), pp. 3047–55.

[377] E. J. Chantemèle et al. “Notch3 Is a Major Regulator of Vascular Tone in Cerebral and Tail Resistance Arteries”. In: *Arteriosclerosis, Thrombosis, and Vascular Biology* 28 (2008), pp. 2216–2224.

[378] Zhiqiang Qu et al. “Functions of ANO1/TMEM16A, Ca2+-Activated Cl- Channels in Regulation of Blood Pressure and Vascular Remodeling”. In: *Journal of Cardiology and Therapy* 3 (2016), pp. 543–548.

[379] E. Demirel et al. “RGS5 Attenuates Baseline Activity of ERK1/2 and Promotes Growth Arrest of Vascular Smooth Muscle Cells”. In: *Cells* 10 (2021).

[380] H. Je et al. “Caveolin-1 Regulates Contractility in Differentiated Vascular Smooth Muscle.” In: *American Journal of Physiology. Heart and Circulatory Physiology* 286 1 (2004), pp. 91–8.

[381] D. Rockey, Nate Weymouth, and Zengdun Shi. “Smooth Muscle α Actin (Acta2) and Myofibroblast Function during Hepatic Wound Healing”. In: *Plos One* 8 (2013).

[382] J. Abrams et al. “Graded Effects of Unregulated Smooth Muscle Myosin on Intestinal Architecture, Intestinal Motility and Vascular Function in Zebrafish”. In: *Disease Models & Mechanisms* 9 (2016), pp. 529–540.

[383] Danny Halim et al. “Loss of LMOD1 Impairs Smooth Muscle Cytocontractility and Causes Megacystis Microcolon Intestinal Hypoperistalsis Syndrome in Humans and Mice”. In: *Proceedings of the National Academy of Sciences* 114 (2017), pp. 2739–2747.

[384] T. Hsieh and J. Jin. “Evolution and Function of Calponin and Transgelin”. In: *Frontiers in Cell and Developmental Biology* 11 (2023).

[385] Feng-Ju Huang et al. “Pericyte Deficiencies Lead to Aberrant Tumor Vascularizaton in the Brain of the NG2 Null Mouse.” In: *Developmental Biology* 344 2 (2010), pp. 1035–46.

[386] Toni Schumacher and R. Benndorf. “ABC Transport Proteins in Cardiovascular Disease—A Brief Summary”. In: *Molecules : A Journal of Synthetic Chemistry and Natural Product Chemistry* 22 (2017).

[387] Hajar Al Feteisi et al. “Identification and Quantification of Blood–Brain Barrier Transporters in Isolated Rat Brain Microvessels”. In: *Journal of Neurochemistry* 146 (2018).

[388] Jaesang Kim et al. “SOX10 Maintains Multipotency and Inhibits Neuronal Differentiation of Neural Crest Stem Cells”. In: *Neuron* 38 (2003), pp. 17–31.

[389] Prameet Kaur et al. “Expression Profiling of RNA Transcripts during Neuronal Maturation and Ischemic Injury”. In: *Plos One* 9 (2014).

[390] D. Lutz et al. “Myelin Basic Protein Cleaves Cell Adhesion Molecule L1 and Promotes Neuritogenesis and Cell Survival*”. In: *The Journal of Biological Chemistry* 289 (2014), pp. 13503–13518.

[391] Madoka Tonosaki et al. “L1cam Is Crucial for Cell Locomotion and Terminal Translocation of the Soma in Radial Migration during Murine Corticogenesis”. In: *Plos One* 9 (2014).

[392] Joana S. Cristóvão et al. “The Neuronal S100B Protein Is a Calcium-Tuned Suppressor of Amyloid-β Aggregation”. In: *Science Advances* 4 (2018).

[393] M. D’Adamo et al. “Kv1.1 Channelopathies: Pathophysiological Mechanisms and Therapeutic Approaches”. In: *International Journal of Molecular Sciences* 21 (2020), p. 2935.

[394] Liam J. Peck et al. “Studying Independent Kcna6 Knock-Out Mice Reveals Toxicity of Exogenous LacZ to Central Nociceptor Terminals and Differential Effects of Kv1.6 on Acute and Neuropathic Pain Sensation”. In: *The Journal of Neuroscience* 41 (2021), pp. 9141–9162.

[395] Kaikai Wang et al. “Single-Cell Transcriptomic Analysis of Somatosensory Neurons Uncovers Temporal Development of Neuropathic Pain”. In: *Cell Research* 31 (2021), pp. 904–918.

[396] Teresa Mínguez-Viñas et al. “Two Epilepsy-Associated Variants in KCNA2 (KV1.2) at Position H310 Oppositely Affect Channel Functional Expression”. In: *The Journal of Physiology* 601 (2023).

[397] Sairia Dass et al. “Patients with Hypertrophic Cardiomyopathy (hcm) and Hcm Gene Carriers Have Attenuated Myocardial Oxygenation Response to Vasodilator Stress - a Potential Mechanism for Sudden Cardiac Death”. In: *Journal of Cardiovascular Magnetic Resonance* 14 (2012).

[398] R. Lloyd et al. “Preclinical Alterations in Cardiac Energetics Amongst Sarcomere Mutation Carriers in Hypertrophic Cardiomyopathy”. In: *Journal of Cardiovascular Magnetic Resonance* 17 (2015), O83.

[399] Ahmet Güçlü et al. “Disease Stage–Dependent Changes in Cardiac Contractile Performance and Oxygen Utilization Underlie Reduced Myocardial Efficiency in Human Inherited Hypertrophic Cardiomyopathy”. In: *Circulation: Cardiovascular Imaging* 10 (2017).

[400] Rahana Y. Parbhudayal et al. “Increased Myocardial Oxygen Consumption Precedes Contractile Dysfunction in Hypertrophic Cardiomyopathy Caused by Pathogenic Tnnt2 Gene Variants”. In: *Journal of the American Heart Association* 9 (2020).

[401] Sumanth D. Prabhu and Nikolaos G. Frangogiannis. “The Biological Basis for Cardiac Repair After Myocardial Infarction: From Inflammation to Fibrosis”. In: *Circulation Research* 119 (2016), pp. 91–112.

[402] Durba Banerjee et al. “Metabolic Impairment in Response to Early Induction of C/ebpβ Leads to Compromised Cardiac Function during Pathological Hypertrophy”. In: *Journal of Molecular and Cellular Cardiology* 139 (2020), pp. 148–163.

[403] Rong Tian. “Metabolic Modulation of Cardiac Health: The Role of Glucose and Amino Acids”. In: *The Faseb Journal* 35 (2021).

[404] Li Lin and Anne A. Knowlton. “Innate Immunity and Cardiomyocytes in Ischemic Heart Disease”. In: *Life Sciences* 100 (2014), pp. 1–8.

[405] Neil A. Turner. “Inflammatory and Fibrotic Responses of Cardiac Fibroblasts to Myocardial Damage Associated Molecular Patterns (damps)”. In: *Journal of Molecular and Cellular Cardiology* 94 (2016), pp. 189–200.

[406] May-Kristin Torp, Jarle Vaage, and Kåre-Olav Stensløkken. “Mitochondria-Derived Damage-Associated Molecular Patterns and Inflammation in the Ischemic-Reperfused Heart”. In: *Acta Physiologica* 237 (2023).

[407] Sang-Ging Ong and Derek J. Hausenloy. “Hypoxia-Inducible Factor As a Therapeutic Target for Cardioprotection”. In: *Pharmacology & Therapeutics* 136 (2012), pp. 69–81.

[408] Qun Lin and Zhong Yun. “The Hypoxia-Inducible Factor Pathway in Adipocytes: The Role of Hif-2 in Adipose Inflammation and Hypertrophic Cardiomyopathy”. In: *Frontiers in Endocrinology* 6 (2015).

[409] Hajime Abe, Hiroaki Semba, and Norihiko Takeda. “The Roles of Hypoxia Signaling in the Pathogenesis of Cardiovascular Diseases”. In: *Journal of Atherosclerosis and Thrombosis* 24 (2017), pp. 884–894.

[410] Santosh Kumar et al. “HIMF (hypoxia-Induced Mitogenic Factor)-Il (interleukin)-6 Signaling Mediates Cardiomyocyte-Fibroblast Crosstalk to Promote Cardiac Hypertrophy and Fibrosis”. In: *Hypertension* 73 (2019), pp. 1058–1070.

[411] Minxuan Liu et al. “Novel Therapeutic Targets for Hypoxia-Related Cardiovascular Diseases: The Role of Hif-1”. In: *Frontiers in Physiology* 11 (2020).

[412] Carlos Silvestre-Roig et al. “Neutrophils As Regulators of Cardiovascular Inflammation”. In: *Nature Reviews Cardiology* 17 (2020), pp. 327–340.

[413] Sergey Antipenko et al. “Neutrophils Are Indispensable for Adverse Cardiac Remodeling in Heart Failure”. In: (2023).

[414] Yoshiharu Higuchi et al. “Involvement of Reactive Oxygen Species-Mediated Nf-K B Activation in Tnf- α -Induced Cardiomyocyte Hypertrophy”. In: *Journal of Molecular and Cellular Cardiology* 34 (2002), pp. 233–240.

[415] Jiao Jiao et al. “Defective Circulating Regulatory B Cells in Patients with Dilated Cardiomyopathy”. In: *Cellular Physiology and Biochemistry* 46 (2018), pp. 23–35.

[416] Gerardo García-Rivas et al. “The Role of B Cells in Heart Failure and Implications for Future Immunomodulatory Treatment Strategies”. In: *Esc Heart Failure* 7 (2020), pp. 1387–1399.

[417] Diem H. Tran and Zhao V. Wang. “Glucose Metabolism in Cardiac Hypertrophy and Heart Failure”. In: *Journal of the American Heart Association* 8 (2019).

[418] Alexander von Gise and William T. Pu. “Endocardial and Epicardial Epithelial to Mesenchymal Transitions in Heart Development and Disease”. In: *Circulation Research* 110 (2012), pp. 1628–1645.

[419] Hasse Brønnum et al. “Mir-21 Promotes Fibrogenic Epithelial-To-Mesenchymal Transition of Epicardial Mesothelial Cells Involving Programmed Cell Death 4 and Sprouty-1”. In: *Plos One* 8 (2013). Ed. by Marie Jose Goumans, e56280.

[420] Jessica N. Blom and Qingping Feng. “Cardiac Repair by Epicardial Emt: Current Targets and a Potential Role for the Primary Cilium”. In: *Pharmacology & Therapeutics* 186 (2018), pp. 114–129.

[421] Denghong Zhang et al. “Mtorc1 Regulates Cardiac Function and Myocyte Survival through 4e-Bp1 Inhibition in Mice”. In: *Journal of Clinical Investigation* 120 (2010), pp. 2805–2816.

[422] Pankaj Shende et al. “Cardiac Raptor Ablation Impairs Adaptive Hypertrophy, Alters Metabolic Gene Expression, and Causes Heart Failure in Mice”. In: *Circulation* 123 (2011), pp. 1073–1082.

[423] Giovanni E. Davogustto et al. “Metabolic Remodeling Precedes Mtorc1-Mediated Cardiac Hypertrophy”. In: *Journal of Molecular and Cellular Cardiology* 158 (2021), pp. 115–127.

[424] Ken-ichiro Okada et al. “Prolonged Endoplasmic Reticulum Stress in Hypertrophic and Failing Heart After Aortic Constriction: Possible Contribution of Endoplasmic Reticulum Stress to Cardiac Myocyte Apoptosis”. In: *Circulation* 110 (2004), pp. 705–712.

[425] Masafumi Kitakaze and Osamu Tsukamoto. “What Is the Role of Er Stress in the Heart?: Introduction and Series Overview”. In: *Circulation Research* 107 (2010), pp. 15–18.

[426] Jeffrey G. Dickhout, Rachel E. Carlisle, and Richard C. Austin. “Interrelationship between Cardiac Hypertrophy, Heart Failure, and Chronic Kidney Disease: Endoplasmic Reticulum Stress As a Mediator of Pathogenesis”. In: *Circulation Research* 108 (2011). Ed. by Masafumi Kitakaze, pp. 629–642.

[427] Luciano Cominacini et al. “Endoplasmic Reticulum Stress and Nrf2 Signaling in Cardiovascular Diseases”. In: *Free Radical Biology and Medicine* 88 (2015), pp. 233–242.

[428] Shunyao Wang et al. “Endoplasmic Reticulum Stress in the Heart: Insights into Mechanisms and Drug Targets”. In: *British Journal of Pharmacology* 175 (2017), pp. 1293–1304.

[429] Navid Omidkhoda et al. “The Role of Micrornas on Endoplasmic Reticulum Stress in Myocardial Ischemia and Cardiac Hypertrophy”. In: *Pharmacological Research* 150 (2019), p. 104516.

[430] Martyna Strzelec et al. “Immunomodulation—a general review of the current state-of-the-art and new therapeutic strategies for targeting the immune system”. In: *Frontiers in Immunology* 14 (2023).

[431] A. Gal et al. “Sustained TGFβ exposure suppresses Smad and non-Smad signalling in mammary epithelial cells, leading to EMT and inhibition of growth arrest and apoptosis”. In: *Oncogene* 27 (2007), pp. 1218–1230.

[432] Mark J. Ranek et al. “PKG1-modified TSC2 regulates mTORC1 activity to counter adverse cardiac stress”. In: *Nature* 566 (2019), pp. 264–269.

[433] Alessandra Breschi, Thomas R. Gingeras, and Roderic Guigó. “Comparative Transcriptomics in Human and Mouse”. In: *Nature Reviews Genetics* 18 (2017), pp. 425–440.

[434] Susanna T. E. Cooper et al. “Of Mouse and Man: Cross-Species Characterization of Hypertensive Cardiac Remodeling”. In: *International Journal of Molecular Sciences* 23 (2022), p. 7709.

[435] M. Cavey and T. Lecuit. “Molecular Bases of Cell-Cell Junctions Stability and Dynamics”. In: *Cold Spring Harbor Perspectives in Biology* 1 (2009), a002998–a002998.

[436] Valeria Mezzano and Farah Sheikh. “Cell–Cell Junction Remodeling in the Heart: Possible Role in Cardiac Conduction System Function and Arrhythmias?” In: *Life Sciences* 90 (2012), pp. 313–321.

[437] Alexandra D. Rusu and Marios Georgiou. “The Multifarious Regulation of the Apical Junctional Complex”. In: *Open Biology* 10 (2020).

[438] Tamer M. A. Mohamed et al. “Regulation of Cell Cycle to Stimulate Adult Cardiomyocyte Proliferation and Cardiac Regeneration”. In: *Cell* 173 (2018), 104–116.e12.

[439] Yen-Hsu Chen, Shaw-Fang Yet, and Mark A. Perrella. “Role of Heme Oxygenase-1 in the Regulation of Blood Pressure and Cardiac Function”. In: *Experimental Biology and Medicine* 228 (2003), pp. 447–453.

[440] Konrad Teodor Sawicki, Hsiang-Chun Chang, and Hossein Ardehali. “Role of Heme in Cardiovascular Physiology and Disease”. In: *Journal of the American Heart Association* 4 (2015).

[441] Anita Ayer et al. “Heme Oxygenases in Cardiovascular Health and Disease”. In: *Physiological Reviews* 96 (2016), pp. 1449–1508.

[442] Leo E. Otterbein, Roberta Foresti, and Roberto Motterlini. “Heme Oxygenase-1 and Carbon Monoxide in the Heart: The Balancing Act between Danger Signaling and Pro-Survival”. In: *Circulation Research* 118 (2016), pp. 1940–1959.

[443] Yuyang Guo et al. “Heme in Cardiovascular Diseases: A Ubiquitous Dangerous Molecule Worthy of Vigilance”. In: *Frontiers in Cell and Developmental Biology* 9 (2022).

[444] Richard C. Becker, A. Phillip Owens, and Sakthivel Sadayappan. “Tissue-Level Inflammation and Ventricular Remodeling in Hypertrophic Cardiomyopathy”. In: *Journal of Thrombosis and Thrombolysis* 49 (2020), pp. 177–183.

[445] C. Proud. “Ras, Pi3-Kinase and Mtor Signaling in Cardiac Hypertrophy”. In: *Cardiovascular Research* 63 (2004), pp. 403–413.

[446] J. Liao et al. “Regulation of Mtor Pathway in Exercise-Induced Cardiac Hypertrophy”. In: *International Journal of Sports Medicine* 36 (2015), pp. 343–350.

[447] Marcin Bujak and Nikolaos G. Frangogiannis. “The Role of TGF-Beta Signaling in Myocardial Infarction and Cardiac Remodeling”. In: *Cardiovascular Research* 74 (2007), pp. 184–195.

[448] Huisheng Liu et al. “Innate sensing of picornavirus infection involves cGAS-STING-mediated antiviral responses triggered by mitochondrial DNA release”. In: *PLOS Pathogens* 19 (2023). Ed. by Bert L. Semler, e1011132.

[449] Yue Zheng et al. “Activation of the cGAS-STING pathway by a mitochondrial DNA-targeted emissive rhodium(iii) metallointercalator”. In: *Chemical Science* 14 (2023), pp. 6890–6903.

[450] Katharina Gerlach et al. “The JAK1/3 Inhibitor to Tofacitinib Suppresses T Cell Homing and Activation in Chronic Intestinal Inflammation”. In: *Journal of Crohn’s and Colitis* 15 (Aug. 2020), pp. 244–257.

[451] Marie Febvre-James et al. “Repression of interferon -regulated cytokines by the JAK1/2 inhibitor ruxolitinib in inflammatory human macrophages”. In: *International Immunopharmacology* 54 (Jan. 2018), pp. 354–365.

[452] Remo Poto et al. “The JAK1/JAK2 inhibitor ruxolitinib inhibits mediator release from human basophils and mast cells”. In: *Frontiers in Immunology* 15 (Aug. 2024).

[453] Gina A. Montealegre Sanchez et al. “JAK1/2 inhibition with baricitinib in the treatment of autoinflammatory interferonopathies”. In: *Journal of Clinical Investigation* 128 (June 2018), pp. 3041–3052.

[454] Amanda Mogul, Katherine Corsi, and Laura McAuliffe. “Baricitinib: The Second FDA-Approved JAK Inhibitor for the Treatment of Rheumatoid Arthritis”. In: *Annals of Pharmacotherapy* 53 (Mar. 2019), pp. 947–953.

[455] Liang Chen et al. “Ruxolitinib ameliorated coxsackievirus B3-induced acute viral myocarditis by suppressing the JAK-STAT pathway”. In: *International Immunopharmacology* 124 (Nov. 2023), p. 110797.

[456] Wenqi Li et al. “Baricitinib alleviates cardiac fibrosis and inflammation induced by chronic sympathetic activation”. In: *International Immunopharmacology* 140 (Oct. 2024), p. 112894.

[457] Daniel L. Beckles, Eduardo Mascareno, and M. A. Q. Siddiqui. “Inhibition of Jak2 phosphorylation attenuates pressure overload cardiac hypertrophy”. In: *Vascular Pharmacology* 45 (Dec. 2006), pp. 350–357.

[458] Yu Chen et al. “JAK-STAT signalling and the atrial fibrillation promoting fibrotic substrate”. In: *Cardiovascular Research* 113 (Feb. 2017), pp. 310–320.

[459] Dan Yang et al. “SENP1 Protects Against Pressure Overload-Induced Cardiac Remodeling and Dysfunction Via Inhibiting STAT3 Signaling”. In: *Journal of the American Heart Association* 11 (Nov. 2022).

[460] Gaetano Zizzo et al. “Efficient Clearance of Early Apoptotic Cells by Human Macrophages Requires M2c Polarization and Mertk Induction”. In: *The Journal of Immunology* 189 (2012), pp. 3508–3520.

[461] Gaetano Zizzo and Philip L. Cohen. “The Ppar-γ Antagonist Gw9662 Elicits Differentiation of M2c-Like Cells and Upregulation of the Mertk/gas6 Axis: A Key Role for Ppar-γ in Human Macrophage Polarization”. In: *Journal of Inflammation* 12 (2015).

[462] Bishuang Cai et al. “Mertk Signaling in Macrophages Promotes the Synthesis of Inflammation Resolution Mediators by Suppressing Camkii Activity”. In: *Science Signaling* 11 (2018).

[463] Sergey V. Novitskiy et al. “Gas6/mertk Signaling Is Negatively Regulated by Nf-Kb and Supports Lung Carcinogenesis”. In: *Oncotarget* 10 (2019), pp. 7031–7042.

[464] Huajia Zhang et al. “Annexin A2/tlr2/myd88 Pathway Induces Arginase 1 Expression in Tumor-Associated Neutrophils”. In: *Journal of Clinical Investigation* 132 (2022).

[465] J. Peng et al. “Molecular Cloning and Expression Analysis of the Gnas Gene in Pig and Porcine Fibroblast Cells”. In: *Genetics and Molecular Research* 13 (2014), pp. 5463–5473.

[466] Jiangdong An et al. “Gnas Knockdown Suppresses Osteogenic Differentiation of Mesenchymal Stem Cells Via Activation of Hippo Signaling Pathway”. In: *Journal of Cellular Physiology* 234 (2019), pp. 22299–22310.

[467] Kiave-Yune Howangyin et al. “Myeloid-Epithelial-Reproductive Receptor Tyrosine Kinase and Milk Fat Globule Epidermal Growth Factor 8 Coordinately Improve Remodeling After Myocardial Infarction Via Local Delivery of Vascular Endothelial Growth Factor”. In: *Circulation* 133 (2016), pp. 826–839.

[468] Lin Zhang et al. “Chemokine Signaling Pathway Involved in Ccl2 Expression in Patients with Rheumatoid Arthritis”. In: *Yonsei Medical Journal* 56 (2015), p. 1134.

[469] Shihab Kochumon et al. “Palmitate Activates Ccl4 Expression in Human Monocytic Cells Via Tlr4/myd88 Dependent Activation of Nf-Kb/mapk/ Pi3k Signaling Systems”. In: *Cellular Physiology and Biochemistry* 46 (2018), pp. 953–964.

[470] Ji-Won Noh et al. “Cellular and Molecular Mechanisms and Effects of Berberine on Obesity-Induced Inflammation”. In: *Biomedicines* 10 (2022), p. 1739.

[471] Lucía Núñez et al. “Agt Haplotype in Itga4 Gene Is Related to Antibody-Mediated Rejection in Heart Transplant Patients”. In: *Plos One* 14 (2019). Ed. by Stanislaw Stepkowski, e0219345.

[472] Muhammad Ashraf et al. “Chemokine/itga4 Interaction Directs Ipsc-Derived Myogenic Progenitor Migration to Injury Sites in Aging Muscle for Regeneration”. In: *Cells* 12 (2023), p. 1837.

[473] J. Heger et al. “Growth Differentiation Factor 15 Acts Anti-Apoptotic and Pro-Hypertrophic in Adult Cardiomyocytes”. In: *Journal of Cellular Physiology* 224 (2010), pp. 120–126.

[474] Harding H. Luan et al. “Gdf15 Is an Inflammation-Induced Central Mediator of Tissue Tolerance”. In: *Cell* 178 (2019), 1231–1244.e11.

[475] Marian Wesseling, Julius H. C. de Poel, and Saskia C. A. de Jager. “Growth Differentiation Factor 15 in Adverse Cardiac Remodelling: From Biomarker to Causal Player”. In: *Esc Heart Failure* 7 (2020), pp. 1488–1501.

[476] Rui Shang and Brian Rodrigues. “Lipoprotein Lipase and Its Delivery of Fatty Acids to the Heart”. In: *Biomolecules* 11 (2021), p. 1016.

[477] Manoj B. Menon et al. “Lyz2-Cre-Mediated Genetic Deletion of Septin7 Reveals a Role of Septins in Macrophage Cytokinesis and Kras-Driven Tumorigenesis”. In: *Frontiers in Cell and Developmental Biology* 9 (2022).

[478] Junchang Zhang et al. “Itgal As a Prognostic Biomarker Correlated with Immune Infiltrates in Gastric Cancer”. In: *Frontiers in Cell and Developmental Biology* 10 (2022).

[479] Rysa Zaman, Homaira Hamidzada, and Slava Epelman. “Exploring Cardiac Macrophage Heterogeneity in the Healthy and Diseased Myocardium”. In: *Current Opinion in Immunology* 68 (2021), pp. 54–63.

[480] Wei Zhao et al. “Identification of the Immune Status of Hypertrophic Cardiomyopathy by Integrated Analysis of Bulk- and Single-Cell Rna Sequencing Data”. In: *Computational and Mathematical Methods in Medicine* 2022 (2022). Ed. by Liaqat Ali, pp. 1–10.

[481] Florence Tatin et al. “Apelin Modulates Pathological Remodeling of Lymphatic Endothelium After Myocardial Infarction”. In: *Jci Insight* 2 (2017).

[482] Rajinikanth Gogiraju, Magdalena L. Bochenek, and Katrin Schäfer. “Angiogenic Endothelial Cell Signaling in Cardiac Hypertrophy and Heart Failure”. In: *Frontiers in Cardiovascular Medicine* 6 (2019).

[483] Yashu Kuang et al. “Vascular Endothelial S1pr1 Ameliorates Adverse Cardiac Remodelling Via Stimulating Reparative Macrophage Proliferation After Myocardial Infarction”. In: *Cardiovascular Research* 117 (2020), pp. 585–599.

[484] Antonio Filippini, Luca Tamagnone, and Alessio D’Alessio. “Endothelial Cell Metabolism in Vascular Functions”. In: *Cancers* 14 (2022), p. 1929.

[485] Qinyu Li et al. “Lymphatic Endothelial Sphingosine 1-Phosphate Receptor 1 Enhances Macrophage Clearance Via Lymphatic System Following Myocardial Infarction”. In: *Frontiers in Cardiovascular Medicine* 9 (2022).

[486] Clint L. Miller et al. “Cyclic Nucleotide Phosphodiesterase 1a: A Key Regulator of Cardiac Fibroblast Activation and Extracellular Matrix Remodeling in the Heart”. In: *Basic Research in Cardiology* 106 (2011), pp. 1023–1039.

[487] Walter E. Knight et al. “Pde1c Deficiency Antagonizes Pathological Cardiac Remodeling and Dysfunction”. In: *Proceedings of the National Academy of Sciences* 113 (2016).

[488] Kristen Kokkonen and David A. Kass. “Nanodomain Regulation of Cardiac Cyclic Nucleotide Signaling by Phosphodiesterases”. In: *Annual Review of Pharmacology and Toxicology* 57 (2017), pp. 455–479.

[489] Si Chen, Walter E. Knight, and Chen Yan. “Roles of Pde1 in Pathological Cardiac Remodeling and Dysfunction”. In: *Journal of Cardiovascular Development and Disease* 5 (2018), p. 22.

[490] Lesley J. Stephen et al. “A Critical Role for the Epha3 Receptor Tyrosine Kinase in Heart Development”. In: *Developmental Biology* 302 (2007), pp. 66–79.

[491] Sheng-an Su et al. “Ephrinb2 Regulates Cardiac Fibrosis through Modulating the Interaction of Stat3 and Tgf-β/smad3 Signaling”. In: *Circulation Research* 121 (2017), pp. 617–627.

[492] Sheng-an Su et al. “Essential Roles of Ephrinb2 in Mammalian Heart: From Development to Diseases”. In: *Cell Communication and Signaling* 17 (2019).

[493] Kondapalli Mrudula Spurthi et al. “Toll-Like Receptor 2 Deficiency Hyperactivates the Foxo1 Transcription Factor and Induces Aging-Associated Cardiac Dysfunction in Mice”. In: *Journal of Biological Chemistry* 293 (2018), pp. 13073–13089.

[494] Shiju Ye et al. “Toll-Like Receptor 2 Signaling Deficiency in Cardiac Cells Ameliorates Ang Ii-Induced Cardiac Inflammation and Remodeling”. In: *Translational Research* 233 (2021), pp. 62–76.

[495] Jinfu Qian et al. “Toll-Like Receptor-2 in Cardiomyocytes and Macrophages Mediates Isoproterenol-Induced Cardiac Inflammation and Remodeling”. In: *The Faseb Journal* 37 (2022).

[496] Yufeng Zhai et al. “Elevated Expression of Tlr2 in Aging Hearts Exacerbates Cardiac Inflammatory Response and Adverse Remodeling Following Ischemia and Reperfusion Injury”. In: *Frontiers in Immunology* 13 (2022).

[497] Elena Revuelta-López et al. “Relationship among Lrp1 Expression, Pyk2 Phosphorylation and Mmp-9 Activation in Left Ventricular Remodelling After Myocardial Infarction”. In: *Journal of Cellular and Molecular Medicine* 21 (2017), pp. 1915–1928.

[498] Alexandra L. Matthews et al. “Regulation of a Disintegrin and Metalloproteinase (adam) Family Sheddases Adam10 and Adam17: The Emerging Role of Tetraspanins and Rhomboids”. In: *Platelets* 28 (2016), pp. 333–341.

[499] E. Klapproth et al. “Adam10 Inhibition Improves Survival and Augments Cardiac Function After Myocardial Infarction”. In: *European Heart Journal* 41 (2020).

[500] Santiago Roura et al. “Inverse Relationship between Raft Lrp1 Localization and Non-Raft Erk1,2/mmp9 Activation in Idiopathic Dilated Cardiomyopathy: Potential Impact in Ventricular Remodeling”. In: *International Journal of Cardiology* 176 (2014), pp. 805–814.

[501] Uta-Mareike Herr et al. “Lrp1 Modulates App Intraneuronal Transport and Processing in Its Monomeric and Dimeric State”. In: *Frontiers in Molecular Neuroscience* 10 (2017).

[502] Nicola Potere et al. “Low Density Lipoprotein Receptor-Related Protein-1 in Cardiac Inflammation and Infarct Healing”. In: *Frontiers in Cardiovascular Medicine* 6 (2019).

[503] Lauri Eklund et al. “Lack of Type Xv Collagen Causes a Skeletal Myopathy and Cardiovascular Defects in Mice”. In: *Proceedings of the National Academy of Sciences* 98 (2001), pp. 1194–1199.

[504] Karolina Rasi et al. “Collagen Xv Is Necessary for Modeling of the Extracellular Matrix and Its Deficiency Predisposes to Cardiomyopathy”. In: *Circulation Research* 107 (2010), pp. 1241–1252.

[505] Jessica J. Connelly et al. “Epigenetic Regulation of Col15a1 in Smooth Muscle Cell Replicative Aging and Atherosclerosis”. In: *Human Molecular Genetics* 22 (2013), pp. 5107–5120.

[506] Brittany G. Durgin et al. “Smooth Muscle Cell-Specific Deletion of Col15a1 Unexpectedly Leads to Impaired Development of Advanced Atherosclerotic Lesions”. In: *American Journal of Physiology-Heart and Circulatory Physiology* 312 (2017), H943–H958.

[507] Anjira S. Ambade et al. “Collagen 18a1/endostatin Expression in the Progression of Right Ventricular Remodeling and Dysfunction in Pulmonary Arterial Hypertension”. In: *American Journal of Respiratory Cell and Molecular Biology* 71 (2024), pp. 343–355.

[508] Darawan Rinchai et al. “Increased Abundance of Adam9 Transcripts in the Blood Is Associated with Tissue Damage”. In: *F1000research* 4 (2016), p. 89.

[509] Cheng-Wei Chou et al. “An Overview of Adam9: Structure, Activation, and Regulation in Human Diseases”. In: *International Journal of Molecular Sciences* 21 (2020), p. 7790.

[510] Weiwei Wang et al. “Mir-30e-5p Is Sponged by Kcnq1ot1 and Represses Angiotensin Ii-Induced Hypertrophic Phenotypes in Cardiomyocytes by Targeting Adam9”. In: *Experimental Cell Research* 394 (2020), p. 112140.

[511] Ziyi Liu et al. “Apoe-Notch Axis Governs Elastogenesis during Human Cardiac Valve Remodeling”. In: (2023).

[512] Yang Wu et al. “Human Apoe2 Endows Stronger Contractility in Rat Cardiomyocytes Enhancing Heart Function”. In: *Cells* 12 (2023), p. 347.

[513] Mohamed Nemir and Thierry Pedrazzini. “Functional Role of Notch Signaling in the Developing and Postnatal Heart”. In: *Journal of Molecular and Cellular Cardiology* 45 (2008), pp. 495–504.

[514] Mohamed Nemir et al. "The Notch Pathway Controls Fibrotic and Regenerative Repair in the Adult Heart". In: *European Heart Journal* 35 (2012), pp. 2174–2185.

[515] Rodrigo Troncoso et al. "New Insights into Igf-1 Signaling in the Heart". In: *Trends in Endocrinology & Metabolism* 25 (2014), pp. 128–137.

[516] N. Shan et al. "Laminin α4 (lama4) Expression Promotes Trophoblast Cell Invasion, Migration, and Angiogenesis, and Is Lowered in Preeclamptic Placentas". In: *Placenta* 36 (2015), pp. 809–820.

[517] Mariko Sato, Huai-Jen Tsai, and H. Joseph Yost. "Semaphorin3d Regulates Invasion of Cardiac Neural Crest Cells into the Primary Heart Field". In: *Developmental Biology* 298 (2006), pp. 12–21.

[518] Donatella Valdembri et al. "Class 3 Semaphorins in Cardiovascular Development". In: *Cell Adhesion & Migration* 10 (2016), pp. 641–651.

[519] Muna Suleiman et al. "The Role of Cd44, Hyaluronan and Nhe1 in Cardiac Remodeling". In: *Life Sciences* 209 (2018), pp. 197–201.

[520] M. Deckert, J. Kubar, and A. Bernard. "Cd58 and Cd59 Molecules Exhibit Potentializing Effects in T Cell Adhesion and Activation." In: *The Journal of Immunology* 148 (1992), pp. 672–677.

[521] P. Anton van der Merwe et al. "Human Cell-Adhesion Molecule Cd2 Binds Cd58 (lfa-3) with a Very Low Affinity and an Extremely Fast Dissociation Rate but Does Not Bind Cd48 or Cd59". In: *Biochemistry* 33 (1994), pp. 10149–10160.

[522] Ling Lu et al. "Integrin α5 Subunit Is Required for the Tumor Supportive Role of Fibroblasts in Colorectal Adenocarcinoma and Serves As a Potential Stroma Prognostic Marker". In: *Molecular Oncology* 13 (2019), pp. 2697–2714.

[523] Li Li et al. "Fibrillin-1–Enriched Microenvironment Drives Endothelial Injury and Vascular Rarefaction in Chronic Kidney Disease". In: *Science Advances* 7 (2021).

[524] F. Saporiti et al. "Melanocortin-1 Receptor Positively Regulates Human Artery Endothelial Cell Migration". In: *Cellular Physiology and Biochemistry* 52 (2019), pp. 1339–1360.

[525] Chen-Yuan Lin et al. "Adam9 Promotes Lung Cancer Progression through Vascular Remodeling by Vegfa, Angpt2, and Plat". In: *Scientific Reports* 7 (2017).

[526] Dongliang Liu et al. "Comprehensive Analysis of the Expression and Prognosis for Itgbs: Identification of Itgb5 As a Biomarker of Poor Prognosis and Correlated with Immune Infiltrates in Gastric Cancer". In: *Frontiers in Cell and Developmental Biology* 9 (2022).

[527] J. Bajorath. "Molecular Organization, Structural Features, and Ligand Binding Characteristics of CD44, a Highly Variable Cell Surface Glycoprotein with Multiple Functions". In: *Proteins* 39 (2000), pp. 103–111.

[528] Shizuko Tanaka et al. “Cooperativity between Far Upstream Enhancer and Proximal Promoter Elements of the Human α2(i) Collagen (col1a2) Gene Instructs Tissue Specificity in Transgenic Mice”. In: *Journal of Biological Chemistry* 279 (2004), pp. 56024–56031.

[529] Federico Galvagni et al. “Cd93 and Dystroglycan Cooperation in Human Endothelial Cell Adhesion and Migration”. In: *Oncotarget* 7 (2016), pp. 10090–10103.

[530] Gian Marco Tosi et al. “The Binding of Cd93 to Multimerin-2 Promotes Choroidal Neovascularization”. In: *Investigative Opthalmology & Visual Science* 61 (2020), p. 30.

[531] Jing Chen et al. “Carrying Both Col1a2 and Fbn2 Gene Heterozygous Mutations Results in a Severe Skeletal Clinical Phenotype: An Affected Family”. In: *Bmc Medical Genomics* 15 (2022).

[532] Laura Conti et al. “The Noninflammatory Role of High Mobility Group Box 1/toll-Like Receptor 2 Axis in the Self-Renewal of Mammary Cancer Stem Cells”. In: *The Faseb Journal* 27 (2013), pp. 4731–4744.

[533] C. Mayer et al. “Sterile Inflammation As a Factor in Human Male Infertility: Involvement of Toll like Receptor 2, Biglycan and Peritubular Cells”. In: *Scientific Reports* 6 (2016).

[534] C. Sun et al. “Adam15 Regulates Endothelial Permeability and Neutrophil Migration Via Src/erk1/2 Signalling”. In: *Cardiovascular Research* 87 (2010), pp. 348–355.

[535] Cheng-Ji Zhou et al. “Ocular Coloboma and Dorsoventral Neuroretinal Patterning Defects in Lrp6 Mutant Eyes”. In: *Developmental Dynamics* 237 (2008), pp. 3681–3689.

[536] Jia-Wei Hong et al. “Bmp4 Regulates Emt to Be Involved in Non-Syndromic Cleft Lip with or without Palate”. In: *The Cleft Palate Craniofacial Journal* 60 (2022), pp. 1462–1473.

[537] Virginie Monceau et al. “Enhanced Sensitivity to Low Dose Irradiation of Apoe-/- Mice Mediated by Early Pro-Inflammatory Profile and Delayed Activation of the Tgfβ1 Cascade Involved in Fibrogenesis”. In: *Plos One* 8 (2013). Ed. by Xiongwen Chen, e57052.

[538] Xiong-Zhi Li et al. “Astragaloside Iv Prevents Cardiac Remodeling in the Apolipoprotein E-Deficient Mice by Regulating Cardiac Homeostasis and Oxidative Stress”. In: *Cellular Physiology and Biochemistry* 44 (2017), pp. 2422–2438.

[539] Katsuhito Fujiu and Ryozo Nagai. “Fibroblast-Mediated Pathways in Cardiac Hypertrophy”. In: *Journal of Molecular and Cellular Cardiology* 70 (2014), pp. 64–73.

[540] Zetao Ma et al. “Identification of Underlying Hub Genes Associated with Hypertrophic Cardiomyopathy by Integrated Bioinformatics Analysis”. In: *Pharmacogenomics and Personalized Medicine* Volume 14 (2021), pp. 823–837.

[541] Caroline Bonnans, Jonathan Chou, and Zena Werb. "Remodelling the Extracellular Matrix in Development and Disease". In: *Nature Reviews Molecular Cell Biology* 15 (2014), pp. 786–801.

[542] Yibin Wu and Ye Xu. "Integrated Bioinformatics Analysis of Expression and Gene Regulation Network of Col12a1 in Colorectal Cancer". In: *Cancer Medicine* 9 (2020), pp. 4743–4755.

[543] Pipsa Saharinen and Kari Alitalo. "The Yin, the Yang, and the Angiopoietin-1". In: *Journal of Clinical Investigation* 121 (2011), pp. 2157–2159.

[544] Gou Young Koh. "Orchestral Actions of Angiopoietin-1 in Vascular Regeneration". In: *Trends in Molecular Medicine* 19 (2013), pp. 31–39.

[545] Qian Yan et al. "Angptl1 Interacts with Integrin $\alpha 1\beta 1$ to Suppress Hcc Angiogenesis and Metastasis by Inhibiting Jak2/stat3 Signaling". In: *Cancer Research* 77 (2017), pp. 5831–5845.

[546] Venkata J. Adapala et al. "Acute Inflammation Plays a Limited Role in the Regulation of Adipose Tissue Col1a1 Protein Abundance". In: *The Journal of Nutritional Biochemistry* 23 (2012), pp. 567–572.

[547] Emiel P. C. van der Vorst et al. "Myeloid a Disintegrin and Metalloproteinase Domain 10 Deficiency Modulates Atherosclerotic Plaque Composition by Shifting the Balance from Inflammation toward Fibrosis". In: *The American Journal of Pathology* 185 (2015), pp. 1145–1155.

[548] Valentina Dallacasagrande and Katherine A. Hajjar. "Annexin A2 in Inflammation and Host Defense". In: *Cells* 9 (2020), p. 1499.

[549] Angshumonik Angbohang et al. "X-Box Binding Protein 1–Mediated Col4a1s Secretion Regulates Communication between Vascular Smooth Muscle and Stem/progenitor Cells". In: *Journal of Biological Chemistry* 296 (2021), p. 100541.

[550] Maisa Garcia-Arguinzonis et al. "Alternative C3 Complement System: Lipids and Atherosclerosis". In: *International Journal of Molecular Sciences* 22 (2021), p. 5122.

[551] Jennifer E. Stanich et al. "Ano1 As a Regulator of Proliferation". In: *American Journal of Physiology-Gastrointestinal and Liver Physiology* 301 (2011), G1044–G1051.

[552] Huizhe Wu et al. "Cell-Specific Regulation of Proliferation by Ano1/tmem16a in Breast Cancer with Different Er, Pr, and Her2 Status". In: *Oncotarget* 8 (2017), pp. 84996–85013.

[553] V. Joukov et al. "A Novel Vascular Endothelial Growth Factor, Vegf-C, Is a Ligand for the Flt4 (vegfr-3) and Kdr (vegfr-2) Receptor Tyrosine Kinases." In: *The Embo Journal* 15 (1996), pp. 1751–1751.

[554] T. Makinen. "Isolated Lymphatic Endothelial Cells Transduce Growth, Survival and Migratory Signals Via the Vegf-C/d Receptor Vegfr-3". In: *The Embo Journal* 20 (2001), pp. 4762–4773.

[555] Ji Yoon Lee et al. "Blockade of Flt4 Suppresses Metastasis of Melanoma Cells by Impaired Lymphatic Vessels". In: *Biochemical and Biophysical Research Communications* 478 (2016), pp. 733–738.

[556] Souichi Kurita et al. “Binding between the Junctional Proteins Afadin and Plekha7 and Implication in the Formation of Adherens Junction in Epithelial Cells”. In: *Journal of Biological Chemistry* 288 (2013), pp. 29356–29368.

[557] Thao M. Nguyen et al. “Epha5 and Epha7 Forward Signaling Enhances Human Hematopoietic Stem and Progenitor Cell Maintenance, Migration, and Adhesion Via Rac1 Activation”. In: *Experimental Hematology* 48 (2017), pp. 72–78.

[558] Giorgia Simonetti et al. “Adrenomedullin Expression Characterizes Leukemia Stem Cells and Associates with an Inflammatory Signature in Acute Myeloid Leukemia”. In: *Frontiers in Oncology* 11 (2021).

[559] A. David Marais. “Apolipoprotein E in Lipoprotein Metabolism, Health and Cardiovascular Disease”. In: *Pathology* 51 (2019), pp. 165–176.

[560] Thorsten Maretzky et al. “Adam10 Mediates E-Cadherin Shedding and Regulates Epithelial Cell-Cell Adhesion, Migration, and β-Catenin Translocation”. In: *Proceedings of the National Academy of Sciences* 102 (2005), pp. 9182–9187.

[561] Karina Reiss et al. “Adam10 Cleavage of N-Cadherin and Regulation of Cell–Cell Adhesion and β-Catenin Nuclear Signalling”. In: *The Embo Journal* 24 (2005), pp. 742–752.

[562] Paola Zigrino et al. “Role of Adam-9 Disintegrin-Cysteine-Rich Domains in Human Keratinocyte Migration”. In: *Journal of Biological Chemistry* 282 (2007), pp. 30785–30793.

[563] Timothy J. Mead et al. “Adamts9-Regulated Pericellular Matrix Dynamics Governs Focal Adhesion-Dependent Smooth Muscle Differentiation”. In: *Cell Reports* 23 (2018), pp. 485–498.

[564] Elisa Gomez Perdiguero et al. “Alteration of Developmental and Pathological Retinal Angiogenesis in Angptl4-Deficient Mice”. In: *Journal of Biological Chemistry* 286 (2011), pp. 36841–36851.

[565] Elisa Gomez Perdiguero et al. “Angptl4-αvβ3 Interaction Counteracts Hypoxia-Induced Vascular Permeability by Modulating Src Signalling Downstream of Vascular Endothelial Growth Factor Receptor 2”. In: *The Journal of Pathology* 240 (2016), pp. 461–471.

[566] Athanasia Liabotis et al. “Angiopoietin-Like 4-Induced 3d Capillary Morphogenesis Correlates to Stabilization of Endothelial Adherens Junctions and Restriction of Vegf-Induced Sprouting”. In: *Biomedicines* 10 (2022), p. 206.

[567] Sanggavi Nadarajan et al. “Annexin A1 (anxa1): A Systematic Review of Its Role in Inflammation”. In: *Sains Malaysiana* 50 (2021), pp. 207–226.

[568] Guido W. M. Swart. “Activated Leukocyte Cell Adhesion Molecule (cd166/alcam): Developmental and Mechanistic Aspects of Cell Clustering and Cell Migration”. In: *European Journal of Cell Biology* 81 (2002), pp. 313–321.

[569] Christopher R. Bye et al. “Axonal Growth of Midbrain Dopamine Neurons Is Modulated by the Cell Adhesion Molecule Alcam through Trans-Heterophilic Interactions with L1cam, Chl1, and Semaphorins”. In: *The Journal of Neuroscience* 39 (2019), pp. 6656–6667.

[570] Yibin Wu and Ye Xu. "Clinical Significance of Col11a1 and Its Effect on Immune Infiltration in Colorectal Cancer". In: *Ssrn Electronic Journal* (2020).

[571] Yuanliang Yan et al. "Col12a1 As a Prognostic Biomarker Links Immunotherapy Response in Breast Cancer". In: *Endocrine-Related Cancer* 30 (2023).

[572] Daniel Ricklin et al. "Complement Component C3 – the "swiss Army Knife" of Innate Immunity and Host Defense". In: *Immunological Reviews* 274 (2016), pp. 33–58.

[573] Dina Bashir AbuSamra. "Cd34 Is a Ligand for Vascular Selectins on Human Hematopoietic Stem/progenitor Cells". In: *Blood* 126 (2015), pp. 2399–2399.

[574] Yan Luo and Yu-quan Wei. "The Regulating Roles of Angiopoietins/TEK-2 in Angiogenesis". In: *Chinese Journal of Medical Genetics* 23 (2006), pp. 63–66.

[575] Sayuri Nishiyama et al. "Angptl2 Induces Synovial Inflammation Via Lilrb2". In: *Inflammation* 44 (2021), pp. 1108–1118.

[576] Fan Yang et al. "Angptl2 Knockdown Induces Autophagy to Relieve Alveolar Macrophage Pyroptosis by Reducing Lilrb2-Mediated Inhibition of Trem2". In: *Journal of Cellular and Molecular Medicine* 28 (2024).

[577] Yoshitaka Isumi et al. "Adrenomedullin Production in Fibroblasts: Its Possible Function As a Growth Regulator of Swiss 3t3 Cells*". In: *Endocrinology* 139 (1998), pp. 2552–2563.

[578] Zoran V. Popovic et al. "The Proteoglycan Biglycan Enhances Antigen-Specific T Cell Activation Potentially Via Myd88 and Trif Pathways and Triggers Autoimmune Perimyocarditis". In: *The Journal of Immunology* 187 (2011), pp. 6217–6226.

[579] Jesus G. Vallejo. "Role of Toll-Like Receptors in Cardiovascular Diseases". In: *Clinical Science* 121 (2011), pp. 1–10.

[580] Yasutomi Higashikuni et al. "Toll-Like Receptor-2 Mediates Adaptive Cardiac Hypertrophy in Response to Pressure Overload through Interleukin-1β Upregulation Via Nuclear Factor Kb Activation". In: *Journal of the American Heart Association* 2 (2013).

[581] Zheng Xiao et al. "Key Player in Cardiac Hypertrophy, Emphasizing the Role of Toll-Like Receptor 4". In: *Frontiers in Cardiovascular Medicine* 7 (2020).

[582] Yanan Zhang et al. "Toll-Like Receptors in Cardiac Hypertrophy". In: *Frontiers in Cardiovascular Medicine* 10 (2023).

[583] Bogale Aredo et al. "A Chimeric Cfh Transgene Leads to Increased Retinal Oxidative Stress, Inflammation, and Accumulation of Activated Subretinal Microglia in Mice". In: *Investigative Opthalmology & Visual Science* 56 (2015), p. 3427.

[584] Bertrand Calippe et al. "Complement Factor H Inhibits Cd47-Mediated Resolution of Inflammation". In: *Immunity* 46 (2017), pp. 261–272.

[585] Justin T. Avery et al. "Mice Expressing the Variant Rs1143679 Allele of Itgam (cd11b) Show Impaired Dc-Mediated T Cell Proliferation". In: *Mammalian Genome* 30 (2019), pp. 245–259.

[586] Hui Wang et al. “Comp (cartilage Oligomeric Matrix Protein), a Novel Piezo1 Regulator That Controls Blood Pressure”. In: *Hypertension* 79 (2022), pp. 549–561.

[587] Roberta Martinelli et al. “The Cc Chemokine Eotaxin (ccl11) Is a Partial Agonist of Cc Chemokine Receptor 2b”. In: *Journal of Biological Chemistry* 276 (2001), pp. 42957–42964.

[588] Nigel J. Stevenson et al. “Ccl11 Blocks Il-4 and Gm-Csf Signaling in Hematopoietic Cells and Hinders Dendritic Cell Differentiation Via Suppressor of Cytokine Signaling Expression”. In: *Journal of Leukocyte Biology* 85 (2008), pp. 289–297.

[589] Clémence Hollande et al. “Inhibition of the Dipeptidyl Peptidase Dpp4 (cd26) Reveals Il-33-Dependent Eosinophil-Mediated Control of Tumor Growth”. In: *Nature Immunology* 20 (2019), pp. 257–264.

[590] Samuel Fritsch et al. “Intravenous Delivery of Pth/pthrp Type 1 Receptor Cdna to Rats Decreases Heart Rate, Blood Pressure, Renal Tone, Renin Angiotensin System, and Stress-Induced Cardiovascular Responses”. In: *Journal of the American Society of Nephrology* 15 (2004), pp. 2588–2600.

[591] Gyun Jee Song, Nathalie Fiaschi-Taesch, and Alessandro Bisello. “Endogenous Parathyroid Hormone-Related Protein Regulates the Expression of Pth Type 1 Receptor and Proliferation of Vascular Smooth Muscle Cells”. In: *Molecular Endocrinology* 23 (2009), pp. 1681–1690.

[592] Hong-Yu Wang et al. “Adrenomedullin Improves Hypertension and Vascular Remodeling Partly through the Receptor-Mediated Ampk Pathway in Rats with Obesity-Related Hypertension”. In: *International Journal of Molecular Sciences* 24 (2023), p. 3943.

[593] P. Lacolley et al. “The Vascular Smooth Muscle Cell in Arterial Pathology: A Cell That Can Take on Multiple Roles”. In: *Cardiovascular Research* 95 (2012), pp. 194–204.

[594] Yingzhi Zhuge et al. “Role of Smooth Muscle Cells in Cardiovascular Disease”. In: *International Journal of Biological Sciences* 16 (2020), pp. 2741–2751.

[595] Justyna Totoń-Żurańska et al. “Vascular Remodelling in Cardiovascular Diseases: Hypertension, Oxidation, and Inflammation”. In: *Clinical Science* 138 (2024), pp. 817–850.

[596] Sepuru K. Mohan, Sandhya G. Rani, and Chin Yu. “The Heterohexameric Complex Structure, a Component in the Non-Classical Pathway for Fibroblast Growth Factor 1 (fgf1) Secretion”. In: *Journal of Biological Chemistry* 285 (2010), pp. 15464–15475.

[597] Nikos K. Karamanos et al. “A Guide to the Composition and Functions of the Extracellular Matrix”. In: *The Febs Journal* 288 (2021), pp. 6850–6912.

[598] Peter J. Newman and Debra K. Newman. “Signal Transduction Pathways Mediated by Pecam-1: New Roles for an Old Molecule in Platelet and Vascular Cell Biology”. In: *Arteriosclerosis, Thrombosis, and Vascular Biology* 23 (2003), pp. 953–964.

[599] Fabio Morandi et al. "Cd38, a Receptor with Multifunctional Activities: From Modulatory Functions on Regulatory Cell Subsets and Extracellular Vesicles, to a Target for Therapeutic Strategies". In: *Cells* 8 (2019), p. 1527.

[600] Nicole L. Ward and Daniel J. Dumont. "The Angiopoietins and Tie2/tek: Adding to the Complexity of Cardiovascular Development". In: *Seminars in Cell & Developmental Biology* 13 (2002), pp. 19–27.

[601] Emilia A. Korhonen et al. "Tie1 Controls Angiopoietin Function in Vascular Remodeling and Inflammation". In: *Journal of Clinical Investigation* 126 (2016), pp. 3495–3510.

[602] Roger S. Holmes, Kimberley D. Spradling Reeves, and Laura A. Cox. "Mammalian Glutamyl Aminopeptidase Genes (enpep) and Proteins: Comparative Studies of a Major Contributor to Arterial Hypertension". In: *Journal of Data Mining in Genomics & Proteomics* 08 (2017).

[603] Seung-Jun Lee et al. "Angiopoietin-2 Exacerbates Cardiac Hypoxia and Inflammation After Myocardial Infarction". In: *Journal of Clinical Investigation* 128 (2018), pp. 5018–5033.

[604] Yinchuan Xu, Jiabing Rong, and Zhaocai Zhang. "The Emerging Role of Angiotensinogen in Cardiovascular Diseases". In: *Journal of Cellular Physiology* 236 (2020), pp. 68–78.

[605] B. Radotra, D. McCormick, and A. Crockard. "Cd44 Plays a Role in Adhesive Interactions between Glioma Cells and Extracellular Matrix Components". In: *Neuropathology and Applied Neurobiology* 20 (1994), pp. 399–405.

[606] M. A. Sims et al. "Cloning and Characterisation of Itgav, the Genomic Sequence for Human Cell Adhesion Protein (vitronectin) Receptor Alpha Subunit, Cd51". In: *Cytogenetic and Genome Research* 89 (2000), pp. 268–271.

[607] Jyrki Heino. "The Collagen Family Members As Cell Adhesion Proteins". In: *Bioessays* 29 (2007), pp. 1001–1010.

[608] Xiaojing He et al. "Structural Basis for Autoinhibition of the Guanine Nucleotide Exchange Factor Farp2". In: *Structure* 21 (2013), pp. 355–364.

[609] Youxin Kong et al. "Structural Basis for Plexin Activation and Regulation". In: *Neuron* 91 (2016), pp. 548–560.

[610] Jing Wang et al. "Neutrophil Infiltration during Inflammation Is Regulated by Pilrα Via Modulation of Integrin Activation". In: *Nature Immunology* 14 (2012), pp. 34–40.

[611] Raquel Reyes et al. "Tetraspanin Cd9: A Key Regulator of Cell Adhesion in the Immune System". In: *Frontiers in Immunology* 9 (2018).

[612] Weihua Shi et al. "Pilra Is Associated with Immune Cells Infiltration in Atrial Fibrillation Based on Bioinformatics and Experiment Validation". In: *Frontiers in Cardiovascular Medicine* 10 (2023).

[613] Nicola Ferri, Neil O. Carragher, and Elaine W. Raines. "Role of Discoidin Domain Receptors 1 and 2 in Human Smooth Muscle Cell-Mediated Collagen Remodeling". In: *The American Journal of Pathology* 164 (2004), pp. 1575–1585.

[614] Lianjie Miao et al. "β1 Integrins Regulate Cellular Behaviour and Cardiomyocyte Organization during Ventricular Wall Formation". In: *Cardiovascular Research* 120 (2024), pp. 1279–1294.

[615] Eun Kyung Song et al. "Itgbl1 Modulates Integrin Activity to Promote Cartilage Formation and Protect against Arthritis". In: *Science Translational Medicine* 10 (2018).

[616] Lei Zhao et al. "Cd36 Palmitoylation Disrupts Free Fatty Acid Metabolism and Promotes Tissue Inflammation in Non-Alcoholic Steatohepatitis". In: *Journal of Hepatology* 69 (2018), pp. 705–717.

[617] Vaya Chen et al. "Cd36 Restricts Lipid-Associated Macrophages Accumulation in White Adipose Tissues during Atherogenesis". In: *Frontiers in Cardiovascular Medicine* 11 (2024).

[618] Yuanjun Huang et al. "Role of Integrin β1 and Tenascin C Mediate Tgf-Smad2/3 Signaling in Chondrogenic Differentiation of Bmscs Induced by Type I Collagen Hydrogel". In: *Regenerative Biomaterials* 11 (2024).

[619] Christoforos K. Vaxevanis et al. "Biglycan As a Mediator of Proinflammatory Response and Target for Mds and Saml Therapy". In: *Oncoimmunology* 12 (2022).

[620] Eser Adiguzel et al. "Collagens in the Progression and Complications of Atherosclerosis". In: *Vascular Medicine* 14 (2009), pp. 73–89.

[621] Ciara M. Shaver et al. "The Nlrp3 Inflammasome in Macrophages Is Stimulated by Cell-Free Hemoglobin". In: *Physiological Reports* 8 (2020).

[622] Angela Armento et al. "Cfh Loss in Human Rpe Cells Leads to Inflammation and Complement System Dysregulation Via the Nf-Kb Pathway". In: *International Journal of Molecular Sciences* 22 (2021), p. 8727.

[623] Henry Velazquez-Soto et al. "Exogenous Cfh Modulates Levels of Pro-Inflammatory Mediators to Prevent Oxidative Damage of Retinal Pigment Epithelial Cells with the At-Risk Cfh Y402h Variant". In: *Antioxidants* 12 (2023), p. 1540.

[624] Qinxue Wang and Haobin Huang. "Delineating the Role of Itgam in Macrophage Dynamics and Cardiac Modulation during Sepsis-Induced Cardiomyopathy". In: (2024).

[625] Heiko Weyd. "More Than Just Innate Affairs – on the Role of Annexins in Adaptive Immunity". In: *Biological Chemistry* 397 (2016), pp. 1017–1029.

[626] Kaisa E. Happonen et al. "Regulation of Complement by Cartilage Oligomeric Matrix Protein Allows for a Novel Molecular Diagnostic Principle in Rheumatoid Arthritis". In: *Arthritis & Rheumatism* 62 (2010), pp. 3574–3583.

[627] Hongyang Shu et al. "The Role of Cd36 in Cardiovascular Disease". In: *Cardiovascular Research* 118 (2020), pp. 115–129.

[628] Yiliang Chen et al. "Cd36, a Signaling Receptor and Fatty Acid Transporter That Regulates Immune Cell Metabolism and Fate". In: *Journal of Experimental Medicine* 219 (2022).

[629] Clare Gould et al. "B2m Gene Expression Reflects an Immunologically Active Tumor Microenvironment in Dlbcl". In: *Blood* 134 (2019), pp. 2778–2778.

[630] Hanbing Wang, Baorui Liu, and Jia Wei. "Beta2-Microglobulin(b2m) in Cancer Immunotherapies: Biological Function, Resistance and Remedy". In: *Cancer Letters* 517 (2021), pp. 96–104.

[631] Daniel V. Iwamoto and David A. Calderwood. "Regulation of Integrin-Mediated Adhesions". In: *Current Opinion in Cell Biology* 36 (2015), pp. 41–47.

[632] Mohammed-Amine El Azreq et al. "Discoidin Domain Receptor 1 Promotes Th17 Cell Migration by Activating the Rhoa/rock/mapk/erk Signaling Pathway". In: *Oncotarget* 7 (2016), pp. 44975–44990.

[633] Junquan Liu et al. "A Highly Selective Humanized Ddr1 Mab Reverses Immune Exclusion by Disrupting Collagen Fiber Alignment in Breast Cancer". In: *Journal for Immunotherapy of Cancer* 11 (2023), e006720.

[634] Juanjuan Liu et al. "Lrp5 and Lrp6 Are Required for Maintaining Self-Renewal and Differentiation of Hematopoietic Stem Cells". In: *The Faseb Journal* 33 (2019), pp. 5615–5625.

[635] Iris Peröbner et al. "Lrp6 Mediates Wnt/β-Catenin Signaling and Regulates Adipogenic Differentiation in Human Mesenchymal Stem Cells". In: *The International Journal of Biochemistry & Cell Biology* 44 (2012), pp. 1970–1982.

[636] Abdul Malik Setiawan, Taty Anna Kamarudin, and Norzana Abd Ghafar. "The Role of Bmp4 in Adipose-Derived Stem Cell Differentiation: A Minireview". In: *Frontiers in Cell and Developmental Biology* 10 (2022).

[637] Hal E. Broxmeyer et al. "Modulation of Hematopoietic Chemokine Effects in Vitro and in Vivo by Dpp-4/cd26". In: *Stem Cells and Development* 25 (2016), pp. 575–585.

[638] M. Sugimoto, T. Oohashi, and Y. Ninomiya. "The Genes Col4a5 and Col4a6, Coding for Basement Membrane Collagen Chains Alpha 5(iv) and Alpha 6(iv), Are Located Head-To-Head in Close Proximity on Human Chromosome Xq22 and Col4a6 Is Transcribed from Two Alternative Promoters." In: *Proceedings of the National Academy of Sciences* 91 (1994), pp. 11679–11683.

[639] Kristopher E. Kubow et al. "Mechanical Forces Regulate the Interactions of Fibronectin and Collagen I in Extracellular Matrix". In: *Nature Communications* 6 (2015).

[640] Seung Jae Shin and Hiromi Yanagisawa. "Recent Updates on the Molecular Network of Elastic Fiber Formation". In: *Essays in Biochemistry* 63 (2019). Ed. by Josephine Adams, pp. 365–376.

[641] Samuel Bouyain and Dara J. Watkins. "The protein tyrosine phosphatases PTPRZ and PTPRG bind to distinct members of the contactin family of neural recognition molecules". In: *Proceedings of the National Academy of Sciences* 107 (2010), pp. 2443–2448.

[642] Amila Zuko et al. "Contactins in the Neurobiology of Autism". In: *European Journal of Pharmacology* 719 (2013), pp. 63–74.

[643] Christian Boni, Carlo Laudanna, and Claudio Sorio. "A Comprehensive Review of Receptor-Type Tyrosine-Protein Phosphatase Gamma (ptprg) Role in Health and Non-Neoplastic Disease". In: *Biomolecules* 12 (2022), p. 84.

[644] Giovanni Tossetta et al. “Role of Cd93 in Health and Disease”. In: *Cells* 12 (2023), p. 1778.

[645] Rosemary A. Bamford et al. “Cntn4 Modulates Neural Elongation through Interplay with App”. In: *Open Biology* 14 (2024).

[646] Kensuke Kimura et al. “Cardiac Sympathetic Rejuvenation: A Link between Nerve Function and Cardiac Hypertrophy”. In: *Circulation Research* 100 (2007), pp. 1755–1764.

[647] Kevin J. Hamill et al. “Laminin Deposition in the Extracellular Matrix: A Complex Picture Emerges”. In: *Journal of Cell Science* 122 (2009), pp. 4409–4417.

[648] Maria A. Gubbiotti, Thomas Neill, and Renato V. Iozzo. “A Current View of Perlecan in Physiology and Pathology: A Mosaic of Functions”. In: *Matrix Biology* 57–58 (2017), pp. 285–298.

[649] Tessa R. Lavorgna et al. “Perlecan: A Review of Its Role in Neurologic and Musculoskeletal Disease”. In: *Frontiers in Physiology* 14 (2023).

[650] R. Ferrari and P. Rizzo. “The Notch Pathway: A Novel Target for Myocardial Remodelling Therapy?” In: *European Heart Journal* 35 (2014), pp. 2140–2145.

[651] Donal MacGrogan, Juliane Münch, and José Luis de la Pompa. “Notch and Interacting Signalling Pathways in Cardiac Development, Disease, and Regeneration”. In: *Nature Reviews Cardiology* 15 (2018), pp. 685–704.

[652] Paulina Langa et al. “A Perspective on Notch Signalling in Progression and Arrhythmogenesis in Familial Hypertrophic and Dilated Cardiomyopathies”. In: *Philosophical Transactions of the Royal Society B: Biological Sciences* 378 (2023).

[653] Karl T. Weber. “Cardiac Interstitium in Health and Disease: The Fibrillar Collagen Network”. In: *Journal of the American College of Cardiology* 13 (1989), pp. 1637–1652.

[654] Jie Feng et al. “Versican Promotes Cardiomyocyte Proliferation and Cardiac Repair”. In: *Circulation* 149 (2024), pp. 1004–1015.

[655] Ludovic Telley et al. “Dual Function of Nrp1 in Axon Guidance and Subcellular Target Recognition in Cerebellum”. In: *Neuron* 91 (2016), pp. 1276–1291.

[656] Enza Piccolo et al. “Lgals3bp, Lectin Galactoside-Binding Soluble 3 Binding Protein, Induces Vascular Endothelial Growth Factor in Human Breast Cancer Cells and Promotes Angiogenesis”. In: *Journal of Molecular Medicine* 91 (2012), pp. 83–94.

[657] ChangHui Pak et al. “Human Neuropsychiatric Disease Modeling Using Conditional Deletion Reveals Synaptic Transmission Defects Caused by Heterozygous Mutations in Nrxn1”. In: *Cell Stem Cell* 17 (2015), pp. 316–328.

[658] Elodie Fels et al. “Role of Lgi1 Protein in Synaptic Transmission: From Physiology to Pathology”. In: *Neurobiology of Disease* 160 (2021), p. 105537.

[659] Xiaoyang Tong et al. “Role of Sostdc1 in Skeletal Biology and Cancer”. In: *Frontiers in Physiology* 13 (2022).

[660] Lacie M. Werner and Alison K. Criss. "Diverse Functions of C4b-Binding Protein in Health and Disease". In: *The Journal of Immunology* 211 (2023), pp. 1443–1449.

[661] Nobuyuki Itoh and Hiroya Ohta. "Pathophysiological Roles of Fgf Signaling in the Heart". In: *Frontiers in Physiology* 4 (2013).

[662] Yeongju Yeo et al. "Fgf12 (fibroblast Growth Factor 12) Inhibits Vascular Smooth Muscle Cell Remodeling in Pulmonary Arterial Hypertension". In: *Hypertension* 76 (2020), pp. 1778–1786.

[663] Ge Tian et al. "Fgf12 Restrains Mitochondria-Dependent Ferroptosis in Doxorubicin-Induced Cardiomyocytes through the Activation of Fgfr1/ampk/nrf2 Signaling". In: *Drug Development Research* 85 (2024).

[664] Maegen A. Ackermann et al. "Tgf-β1 Affects Cell-Cell Adhesion in the Heart in an Ncam1-Dependent Mechanism". In: *Journal of Molecular and Cellular Cardiology* 112 (2017), pp. 49–57.

[665] Yuping Qin et al. "Knockdown of lncRNA CACNA1C-AS2 Promotes Epithelial-Mesenchymal Transition and Enhances the Proliferation, Invasion and Migration of Human Esophageal Cancer Cells". In: *Chinese Journal of Cellular and Molecular Immunology* 39 (2023), pp. 249–257.

[666] Michelle D. Gjørlund et al. "Neuroligin-1 Induces Neurite Outgrowth through Interaction with Neurexin-1β and Activation of Fibroblast Growth Factor Receptor-1". In: *The Faseb Journal* 26 (2012), pp. 4174–4186.

[667] Hamide Betul Gerik-Celebi, Hilmi Bolat, and Gul Unsel-Bolat. "Rare Heterozygous Genetic Variants of Nrxn and Nlgn Gene Families Involved in Synaptic Function and Their Association with Neurodevelopmental Disorders". In: *Developmental Neurobiology* 84 (2024), pp. 158–168.

[668] Sandra Díaz del Moral et al. "The Insulin-Like Growth Factor Signalling Pathway in Cardiac Development and Regeneration". In: *International Journal of Molecular Sciences* 23 (2021), p. 234.

[669] Jiafeng Zhu et al. "Insulin-Like Growth Factor 1 Receptor Deficiency Alleviates Angiotensin Ii–Induced Cardiac Fibrosis through the Protein Kinase B/extracellular Signal-Regulated Kinase/nuclear Factor-Kb Pathway". In: *Journal of the American Heart Association* 12 (2023).

[670] Michael J. Cross and Lena Claesson-Welsh. "Fgf and Vegf Function in Angiogenesis: Signalling Pathways, Biological Responses and Therapeutic Inhibition". In: *Trends in Pharmacological Sciences* 22 (2001), pp. 201–207.

[671] Yoshito Yamashiro et al. "Matrix Mechanotransduction Mediated by Thrombospondin-1/integrin/yap Signaling Pathway in the Remodeling of Blood Vessels". In: *Biorxiv* (2019).

[672] Yoshito Yamashiro et al. "Matrix Mechanotransduction Mediated by Thrombospondin-1/integrin/yap in the Vascular Remodeling". In: *Proceedings of the National Academy of Sciences* 117 (2020), pp. 9896–9905.

[673] Eric D. Buras et al. "Thrombospondin-1 Promotes Fibro-Adipogenic Stromal Expansion and Contractile Dysfunction of the Diaphragm in Obesity". In: *Jci Insight* (2024).

[674] David R. Gibb et al. “The Emergence of Adam10 As a Regulator of Lymphocyte Development and Autoimmunity”. In: *Molecular Immunology* 48 (2011), pp. 1319–1327.

[675] Patrice Delafontaine, Yao-Hua Song, and Yangxin Li. “Expression, Regulation, and Function of Igf-1, Igf-1r, and Igf-1 Binding Proteins in Blood Vessels”. In: *Arteriosclerosis, Thrombosis, and Vascular Biology* 24 (2004), pp. 435–444.

[676] Mirjana Macvanin et al. “New Insights on the Cardiovascular Effects of Igf-1”. In: *Frontiers in Endocrinology* 14 (2023).